PHYSICAL CHEMISTRY 2018

14th International Conference
on Fundamental and Applied Aspects of
Physical Chemistry

Proceedings
Volume II

September 24-28, 2018
Belgrade, Serbia

PHYSICAL CHEMISTRY 2018

14th International Conference
on Fundamental and Applied Aspects of
Physical Chemistry

Proceedings
Volume II

September 24-28, 2018
Belgrade, Serbia

SBN 978-86-82475-37-8
Title: Physical Chemistry 2018 (Proceedings)
Editors: Željko Čupić and Slobodan Anić
Published by: Society of Physical Chemists of Serbia, Studentski Trg 12-16, 11158, Belgrade, Serbia
Publisher: Society of Physical Chemists of Serbia
For Publisher: S. Anić, President of Society of Physical Chemists of Serbia
Printed by: ″Jovan″, <Printing and Publishing Company, 200 Copies
Number og pages: 518+4, Format B5, printing finished in September 2018

Text and Layout: ″Jovan″

200 - *Copy printing*

CONTENT

G *– Organic Physical Chemistry*

APPLICATION OF PRINCIPAL COMPONENT ANALYSIS TO SETSCHENOW CONSTANTS OF ORGANIC COMPOUNDS

G. M. Nikolić [1], A. M. Veselinović [1], M. G. Nikolić [2] and J. V. Živković [1]

[1] *Department of Chemistry, Faculty of Medicine, University of Niš, Bulevar dr Zorana Đinđića 81, 18000 Niš, Serbia. (goranhem@yahoo.com)*
[2] *Department of Chemistry, Faculty of Sciences and Mathematics, University of Niš, Višegradska 33, 18000 Niš, Serbia.*

ABSTRACT

Principal component analysis was applied to elucidate relationships between Setschenow constant, molar volume calculated by the method of Le Bas (V_{LeBas}), intrinsic solubility (S_o), and octanol-water partition coefficient (in the form of $\log K_{ow}$) for 101 organic compounds. First two principal components explained about 90 % of variance in analyzed data set with PC1 explaining about 71 % and PC2 about 19%. Very similar values of loadings on both PC1 and PC2 for K_s and $\log K_{ow}$ indicate that K_s value is mainly determined by the hydrophobic effects which are well represented by the first principal component (PC1). Specific PC1 and PC2 scores for some compounds (amino acids and steroids) indicate that some other factors beside hydrophobicity must be considered for predicting their K_s values.

INTRODUCTION

The influence of inorganic salts on the solubility and distribution of organic compounds is an interesting phenomenon with numerous possible applications, most notably for improving extraction efficiency of organic compounds [1,2]. This phenomenon is best described by the empirical Setschenow constant (K_s) which can be calculated from either solubility or distribution data by the following equations:

$$\log(S/S_o) = -K_s \times C_s, \text{ or}$$

$$\log(D_o/D) = -K_s \times C_s,$$

where S and S_o are solubilities of the organic solute in aqueous salt solution and in water respectively, C_s is the molar concentration of electrolyte, while D_o and D are distribution ratios of organic solute between organic solvent and water or aqueous salt solution respectively. The majority of experimental and theoretical work on Setschenow constant was

done for sodium chloride (NaCl) because of its ubiquitous presence in nature.

Simple theoretical treatments to predict K_s values attempted to find a direct correlation between its value and one particular physicochemical property of solute molecules like molar volume calculated by the method of Le Bas (V_{LeBas}), intrinsic solubility (S_o) or octanol-water partition coefficient (K_{ow}, usually in the form of $\log K_{ow}$) but were only moderately accurate. In more recent theoretical works on K_s value prediction various approaches were employed including combination of various physicochemical properties [3], topological modeling [4], multiple linear regression, artificial neural network (ANN), and support vector machine (SVM) [5], COSMO-RS and polyparameter linear free energy relationships (pp-LFERs) [6] or integral equation formalism polarizable continuum model (IEF-PCM) [7]. Most of these theoretical models were constructed and tested by using data set employed by Ni and Yalkovsky [3] so we applied principal component analysis (PCA) on this data set to better elucidate relationships between K_s, V_{LeBas}, S_o, and $\log K_{ow}$.

EXPERIMENTAL

We applied PCA to the data set for 101 organic compounds given in the paper by Ni and Yalkovsky [3] in a manner similar to the multivariate analysis of hydrophobic descriptors described in the literature [8].

Unscrambler 9.7 software (CAMO Software, Norway) was used for performing PCA calculations.

RESULTS AND DISCUSSION

Since each compound in analyzed data set was described by four parameters (K_s, V_{LeBas}, S_o, and $\log K_{ow}$) PCA extracted four principal components. The percentages of explained variance by these four principal components were: 71.04 % (PC1), 19.03 % (PC2), 7.83 % (PC3), and 2.10 % (PC4). This means that first two principal components explained about 90 % of total variance in the analyzed data set.

The plot of PCA scores for first two principal components is given in Fig. 1. and plot of loadings on PC1 and PC2 is given in Fig. 2.

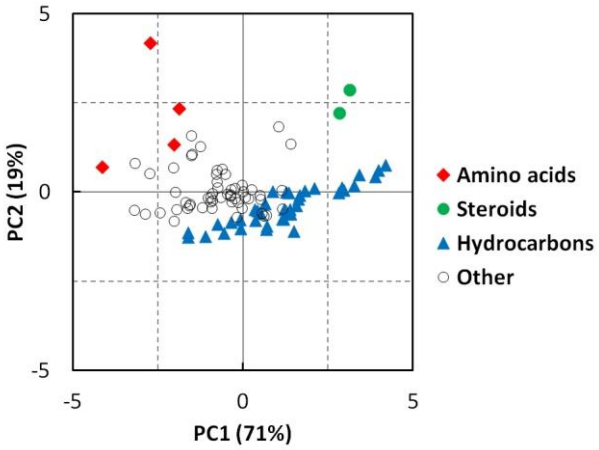

Figure 1. Plot of the scores for first two principal components extracted by PCA.

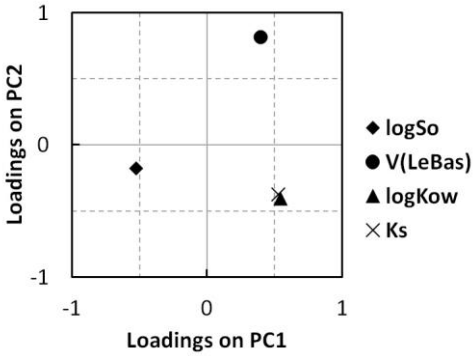

Figure 2. Plot of the loadings on first two principal components.

Very similar values of loadings on both PC1 and PC2 for K_s and $\log K_{ow}$ are in accordance with the fairly good correlation between them (r = 0.7717) [3] which indicate that K_s value is mainly determined by the hydrophobic effects which are well represented by the first principal component (PC1).

This assumption can be supported by the fact that PC2 scores of hydrocarbons (blue triangles in Fig. 1.), as typically nonpolar compounds, show very little variation. Correlations between K_s and PC scores for hydrocarbons (39 compounds) are given by the following equations:

$K_s = 0.0361 \times PC1 + 0.2191$ ($r^2 = 0.7892$)

$K_s = 0.0669 \times PC2 + 0.2101$ ($r^2 = 0.3737$)

Specific combination of PC1 and PC2 scores for amino acids (red rhombuses in Fig. 1.) and steroids (green circles in Fig. 1.) indicate that some other factors beside hydrophobicity must be considered for predicting their K_s values.

CONCLUSION

Principal component analysis of literature data for 101 organic compounds revealed that first two principal components explained about 90 % of variance in analyzed data set with PC1 explaining about 71 % and PC2 about 19%. Very similar values of loadings on both PC1 and PC2 for K_s and $\log K_{ow}$ indicate that K_s value is mainly determined by the hydrophobic effects which are well represented by the first principal component (PC1). Specific combinations of PC1 and PC2 scores for some compounds (amino acids and steroids) indicate that some other factors beside hydrophobicity must be considered for predicting their K_s values.

Acknowledgement

This work was partially supported by the Ministry for Science and Technological Development of the Republic of Serbia (Grant no. 31060).

REFERENCES

[1] A. M. Hyde, S. L. Zultanski, J. H. Waldman, Y. L. Zhong, M. Shevlin, F. Peng, Organic Process Research & Development, 2017, **21**, 1355-1370.
[2] I. M. Valente, M. M. Moreira, P. Neves, T. da Fé, L. M. Gonçalves, P. J. Almeida, J. A. Rodrigues, Phytochemical Analysis, 2017, **28**, 297-304.
[3] N. Ni, S. H. Yalkowsky, International Journal of Pharmaceutics, 2003, **254**, 167-172.
[4] Y. Li, Q. Hu, C. Zhong, Industrial & Engineering Chemistry Research, 2004, **43**, 4465-4468.
[5] J. Xu, L. Wang, L. Wang, X. Shen, W. Xu, Journal of Computational Chemistry, 2011, **32**, 3241-3252.
[6] S. Endo, A. Pfennigsdorff, K. U. Goss, Environmental Science & Technology, 2012, **46**, 1496-1503.
[7] X. Yu, R. Yu, Industrial & Engineering Chemistry Research, 2013, **52**, 11182-11188.
[8] S. Dove, ADMET & DMPK, 2014, **2**, 3-17.

DETERMINATION OF CONFIGURATION AND CONFORMATION OF DIETHYL 4-(PYRROLIDIN-1-YLMETHYLENE)PENT-2-ENEDIOATE

M. Stojanović [1], J. Aleksić [1], Z. Džambaski [1] and M. Baranac-Stojanović [2]

[1] University of Belgrade, Institute of Chemistry, Technology and Metallurgy,Center for Chemistry, Njegoševa 12, 11000 Belgrade, Serbia (milovans@chem.bg.ac.rs)
[2]University of Belgrade – Faculty of Chemistry, Studentski trg 12-16, 11000 Belgrade, Serbia

ABSTRACT
By combining experimental NMR chemical shift data and theoretical calculations we were able to determine configuration and conformational behaviour of the title polyfunctionalized conjugated diene. The major configurational isomer (*2E,4E*; ~96%) exists mainly as a mixture of *cis,trans,trans* (63%) and *cis,trans,cis* conformers (30%) with a barrier to their interconversion of 7.2 kcal/mol from the side of the former.

INTRODUCTION
The conjugated diene motif constitutes an important reactive part of many naturally occurring bioactive molecules, thus enabling access to naturally derived structures with improved or modified biological properties [1]. Conjugated dienes are also valuable building blocks used to create a variety of organic compounds [2]. In order to rationalize or predict chemical and biological action of such compounds full structure elucidation is of great importance to organic chemists. In the course of our project directed toward the development of green and simple method for the formation of substituted conjugated dienes we have synthesized trisubstituted diene **1**.

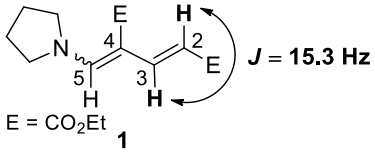

1

While *E* configuration around the C2=C3 double bond of **1** was easily recognized by the large coupling constant between the two olefinic protons, that around the C4=C5 double bond could not be determined from NMR spectral data. The main obstacle to do this was overlapping of the signals which belong to H3 and H5 protons (7.83 ppm and 7.82 ppm, respectively),

thus preventing us to obtain any useful information from NOE experiments. To solve this problem we have employed theoretical calculations with the aim to predict relative energies of the two configurational isomers. The accuracy of our conclusions was verified by an excellent agreement between experimental and calculated NMR chemical shifts, the latter based on relative portions of the most populated conformational isomers.

EXPERIMENTAL

All calculations were done by using the Gaussian 09 program package [3] at the B3LYP/6-31+G(d,p) level of theory [4,5]. The IEFPCM model [6] was employed to simulate solvent effects. The solvent chosen was the same as that used for recording the NMR spectra ($CHCl_3$; Bruker Avance III spectrometer: ^1H at 500.3 MHz, ^{13}C at 125.8 MHz). The GIAO method [7] was used for NMR calculations. Chemical shifts are referenced to tetramethylsilane (TMS) and are calculated as $\delta_i = \sigma_{TMS} - \sigma_i$. Energy minimum structures contained no imaginary frequency, while transition states for isomerization were characterized by one imaginary frequency, the vibrational mode of which corresponded to the reaction coordinate.

RESULTS AND DISCUSSION

The configurational/conformational flexibility of the studied compound allows it to adopt sixteen isomeric structures, when configuration around the C2=C3 bond is fixed. Among these, all structures having *cis* arrangement around the conjugated diene fragment and *E* configuration around the C4=C5 bond were excluded from consideration due to the expected large steric strain between pyrrolidine substituent and H2 atom. This led us to optimize twelve isomeric structures. The results of our calculations show that free energies of the eight conformational isomers having *2E,4Z* configuration are all above 2 kcal/mol (Figure 1), and this can be ascribed to the large steric strain between the *cis*-oriented pyrrolidine and ester group. To reduce the strain, the O=C–C4=C5–N fragment deviates from planarity, which, in turn, reduces resonance stabilization of the molecule.

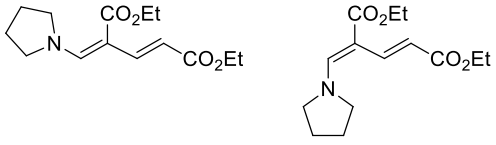

	2E,4Z configuration	*2E,4E* configuration
ΔG_{rel} (kcal/mol)	2.08-3.87	0.00-1.88
Mole fraction (%)	4.3	95.0

Figure 1. Calculated free energies and mole fractions of configurational isomers of compound **1**.

The calculated mole fraction of *2E,4Z*-configured isomers is only 4.3%, while the calculated low value for the barrier to *2E,4Z* → *2E,4E* isomerization of 17.6 kcal/mol indicates the rapid equilibrium between the two configurational isomers (the average life time of configurational isomers is about 1.3 s). The population of the major configurational isomer, *2E,4E*, is 95.7%, where 0.7% includes the high energy forms adopting *cis* conformation of the diene moiety, which were not optimized. Relative energies and percent weight of four possible conformers of *2E,4E*-configured compound are shown in Figure 2.

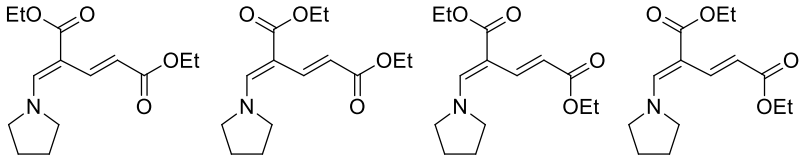

	cis,trans,trans	*cis,trans,cis*	*trans,trans,trans*	*trans,trans,cis*
ΔG_{rel} (kcal/mol)	0.00	0.44	1.59	1.88
Mole fraction (%)	63.0	30.0	4.0	3.0

Figure 2. Calculated free energies and mole fractions of conformational isomers of *2E,4E*-configured compound **1**.

The conclusion to be drawn from the given results is that the studied compound exists as an equilibrium of mainly two forms, *cis,trans,trans* and *cis,trans,cis*, of *2E,4E* configurational isomer. The barrier to their interconversion was calculated to be low: 6.8 kcal/mol, from the side of the less stable *cis,trans,cis* form and 7.2 kcal/mol from the side of the most stable *cis,trans,trans* form. Hence, they can not be distuingushed by NMR spectroscopy. To validate our conclusions, we have calculated ^{1}H NMR and ^{13}C NMR chemical shifts of selected nuclei and compared them with experimentally obtained values (Table 1). The calculated values are based on relative mole fractions of the two most populated conformations of *2E,4E* isomer, shown in Figure 2.

Table 1. Experimental and calculated ^{1}H NMR and ^{13}C NMR chemical shifts of selected nuclei of compound **1**.

	H2	H3	H5	C2	C3	C4	C5
Exp.	6.26	7.83	7.82	112.14	138.10	96.35	151.10
Calc.	6.95	7.99	8.25	108.16	139.70	98.47	147.80

As can be seen from Table 1, there is an excellent agreement between experiment and theory. The ^{13}C NMR chemical shifts deviate from each other by less than 4% and ^{1}H NMR chemical shifts by less than 11%. This is

acceptable and somewhat larger deviation observed for proton chemical shifts is expected since protons are located at the periphery of the molecule and their chemical shifts are more affected by intermolecular forces, such as solute-solvent and solute-solute interactions.

The low barrier to *2E,4Z* → *2E,4E* isomerization (17.6 kcal/mol in the given direction and 20.2 kcal/mol in the opposite direction) comes from the push-pull character of the double bond, which is due the presence of good electron-donor at one side of the bond (pyrrolidine substituent) and two electron-acceptors at the other side of the bond (CO_2Et and $CH{=}CHCO_2Et$).

CONCLUSION

In conclusion, structure elucidation of the studied trisubstituted conjugated diene, diethyl 4-(pyrrolidin-1-ylmethylene)pent-2-enedioate, was accomplished by combining experiment and theory. An excellent agreement between experimental and calculated NMR chemical shifts confirmed the relevance of conclusions obtained by calculations. Thus, the title compound can be best described as *2E,4E* configurational isomer consisting of two main forms which are in rapid equilibrium and differ in the orientation of the C4-ester group.

Acknowledgement

This work was supported by the Ministry of education, science and technological development of the Republic of Serbia (Grant no. 172020).

REFERENCES

[1] S. Carosso, M. J. Miller, Org. Biomol. Chem., 2014, 12, 7445-7468.
[2] C. Challa, J. Vellekkatt, J. Ravindran, R. S. Lankalapalli, Org. Biomol. Chem., 2014, 12, 8588-8592.
[3] M. J. Frisch et al., Gaussian 09 (Revision D.01), Gaussian Inc.: Wallingford, CT, 2013.
[4] A. D. Becke, J. Chem. Phys., 1993, 98, 5648–5652; C. Lee, W. Yang, R. G. Parr, Phys. Rev. B: Condens. Matter Mater. Phys., 1988, 37, 785–789.
[5] J. B. Foresman, A. Frisch, Exploring Chemistry with Electronic Structure Methods, Gaussian, Inc., 1996.
[6] J. Tomasi, B. Mennucci, R. Cammi, Chem. Rev., 2005, 105, 2999–3093.
[7] R. Ditchfield, Mol. Phys., 1974, 27, 789-807; K. Wolinski, J. F. Hinton, P. Pulay, J. Am. Chem. Soc., 1990, 112, 8251-8260.

TRACKING THE CHANGES OF PUSH-PULL EFFECT DURING THE FORMATION OF THIAZOLO[3,2-*c*]PYRIMIDINE FROM 2-ALKYLIDENE-4-OXOTHIAZOLIDINE

A. Rašović [1], M. Stojanović [1], J. Aleksić [1] B. Bondžić [1] and M. Baranac-Stojanović [2]

[1] University of Belgrade, Institute of Chemistry, Technology and Metallurgy,Center for Chemistry, Njegoševa 12, 11000 Belgrade, Serbia (milovans@chem.bg.ac.rs)
[2]University of Belgrade – Faculty of Chemistry, Studentski trg 12-16, 11000 Belgrade, Serbia

ABSTRACT

We have traced the subtle changes in the strength of the push-pull effect of the C2 double bond of 2-alkylidene-4-oxothiazolidine **1** occurring during the reaction leading to the condensed bicyclic product **3**, which is initiated by iodine in acetone. The push-pull effect was quantified by means of the difference in the ^{13}C NMR chemical shifts of the carbon atoms ($\Delta\delta_{CC}$), obtained experimentally and theoretically, and the quotient of the occupation numbers of π and π^* orbitals, which was calculated theoretically.

INTRODUCTION

The π-electron delocalization is an important concept in chemistry which accounts for the greater stability of conjugated vs nonconjugated systems and their special chemical reactivity [1]. In push-pull alkenes, which have one or two electron-donating groups at one end of the CC double bond and one or two electron-accepting groups at the other end, the π-electron delocalization is mainly one-directional, from donor (Don) to acceptor (Acc) groups (Figure 1). This special type of electron delocalization endows such alkenes with particular chemical reactivity, such as nucleophilic attack at the electron-deficient carbon of the CC double bond and electrophilic attack at the electron-rich carbon [2].

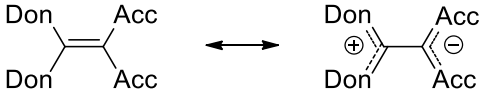

Figure 1. The π-electron delocalization in push-pull alkene.

In the course of our project directed toward the application of 2-alkylidene-4-oxothiazolidines as precursors for the synthesis of various heterocycles, we have observed an interesting iodine-induced cyclization reaction occurring between thiazolidine **1** and acetone, which resulted in the formation of thiazolo[3,2-c]pyrimidine derivative **3** (Scheme 1). We were intrigued to examine the changes of the strength of the push-pull effect along the reaction coordinate involving two sequences: i) conformational isomerization and ii) cyclization. The results will allow us to predict and compare the behaviour, particularly chemical, of the final product **3** and starting **1**.

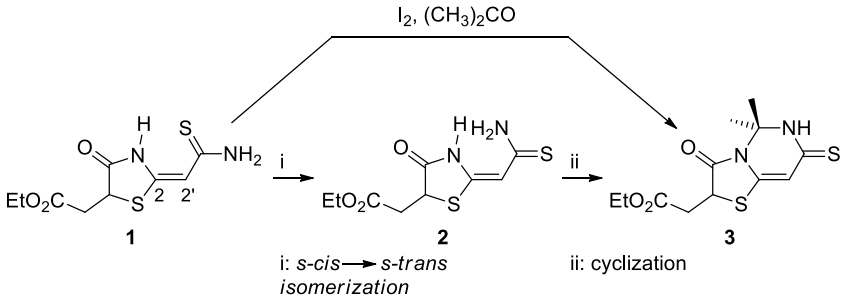

Scheme 1. Formation of bicycle **3** from thiazolidine **1**.

EXPERIMENTAL

The NMR spectra of compounds **1** and **3** were recorded on Varian Gemini spectrometer (^{1}H at 200 MHz, ^{13}C at 50.3 MHz) in DMSO-d_6. Theoretical calculations were done by using the Gaussian 09 program package [3] at the B3LYP/6-31+G(d,p) level of theory [4,5]. The structures were first optimized in vacuum, than re-optimized in the solvent (DMSO), which was used for recording the NMR spectra. All positive vibrational frequencies confirmed that the obtained structures were energy minima. Solvent effects were simulated with the aid of IEFPCM model [6]. Nuclear shielding values were calculated by using the GIAO method [7]. Chemical shifts are referenced to tetramethylsilane (TMS) and are calculated as $\delta_i = \sigma_{TMS} - \sigma_i$. Occupation values of π and π^* orbitals of the CC double bond were obtained by NBO analysis [8]. The two parameters, $\Delta\delta_{CC}$ and π^*/π, were successfully employed before to quantify the strength of the push-pull effect in various alkenes and in related 2-alkylidene-4-oxothiazolidines [9,10]. Larger values indicate larger push-pull effect.

RESULTS AND DISCUSSION

The calculated free energy difference between the starting **1** and its conformational isomer **2** is large, ΔG = 7.2 kcal/mol, meaning that **2** is

present in very small amounts in the solution, prior to cyclization reaction. Thus, the experimental chemical shifts belong solely to isomer **1**. Table 1 lists experimental and calculated ^{13}C NMR chemical shifts of **1**-**3** (only calc. for **2**), their difference, calculated occupation values of π and π^* orbitals and their quotient.

Table 1. Experimental and calculated ^{13}C NMR chemical shifts of the two carbon atoms belonging to the double bond, their difference ($\Delta\delta_{CC}$), all in ppm, occupation of π and π^* orbitals of the CC double bond (e) and their quotient (π^*/π).

compound	^{13}C NMR exp/calc		$\Delta\delta_{CC}$ exp/calc	π	π^*	π^*/π
	C2	C2'				
1	154.9/163.2	97.2/95.6	57.7/67.5	1.8126	0.3149	0.1737
2	-/150.9	-/101.4	-/49.5	1.8368	0.2946	0.1604
3	146.8/154.7	101.0/100.2	45.8/54.6	1.8160	0.3056	0.1683

Experimental and calculated ^{13}C NMR chemical shifts deviate from each other by less than 5.5% and experimental trend is well reproduced by calculations. Relative $\Delta\delta_{CC}$ (**1** vs **3**) obtained by experiment and by theory differ from each other by only 1 ppm, so that conclusions based on theory can be considered as reliable. The two parameters, $\Delta\delta_{CC}$ and π^*/π, show that upon *s-cis* $\rightarrow$ *s-trans* conformational isomerization, that is **1** $\rightarrow$ **2** (Scheme 1), the strength of the push-pull effect decreases considerably, $\Delta\delta_{CC}$(**1** − **2**) = 18 ppm and π/π^*(**1** − **2**) = 0.0133. This can mainly be ascribed to deviation from planarity of the $CSNH_2$ acceptor group in **2**, which is a consequence of the strong steric repulsion between NH_2 from the Acc and NH from the thiazolidine ring. Thus, the mean of dihedral angles around the C–C bond connecting the C=C and $C(S)NH_2$ fragments increases from 0° in **1** to 26° in **2.** The subsequent formation of bicycle **3** strengthens the π-electron delocalization over the $(Don)_2$–C=C–Acc part, $\Delta\delta_{CC}$(**3** − **2**) = 5.1 ppm and π/π^*(**3** − **2**) = 0.0079. This slight increase in the push-pull activity of the double bond results mainly from planarization of the C=C and C(S)NH groups, now having the mean of dihedral angles of 2°.

However, the push-pull effect of **3** is still significantly weaker than that in the starting **1**, $\Delta\delta_{CC}$(**1** − **3**) = 12.9 ppm and π^*/π(**1** − **3**) = 0.0054. Since in both **1** and **3** the $(Don)_2$–C=C–Acc fragments are almost planar, the resultant reduction of the push-pull activity upon going from **1** to **3** can be ascribed to the *s-cis* $\rightarrow$ *s-trans* conformational change as the major cause.

Thus, our results show that the π-electron delocalization over the push-pull substructure decreases during the **1** → **3** chemical transformation, which should affect, for example, reactivity of **3** by making carbon atoms of the double bond as less electrophilic and nucleophilic.

CONCLUSION

We have investigated subtle changes in the strength of the push-pull effect of the CC double bond of 2-alkylidene-4-oxothiazolidine **1** which occur during the chemical reaction leading to thiazolo[3,2-c]pyrimidine derivative **3**. Our results show that *s-cis* → *s-trans* conformational change within the =C−Acc fragment is the main cause for the decrease in the π-electron delocalization upon going from **1** to **3**. Additional decrease in delocalization is found in intermediate **2**, because of nonplanarity of the C=C−Acc moiety which is due to the large steric strain between NH_2 group from the Acc and NH group from thiazolidine ring. These differences in the push-pull effect between **1** and **3** may affect chemical reactivity of the CC double bond and other physical properties.

Acknowledgement

This work was supported by the Ministry of education, science and technological development of the Republic of Serbia (Grant no. 172020).

REFERENCES

[1] K. P. C. Volhardt, N. E. Schore, Organic Chemistry, W. H. Freeman and Company, New York, 1994.
[2] J. Sandström, Top. Stereochem., 1983, 14, 83-181.
[3] M. J. Frisch et al., Gaussian 09 (Revision D.01), Gaussian Inc.: Wallingford, CT, 2013.
[4] A. D. Becke, J. Chem. Phys., 1993, 98, 5648–5652; C. Lee, W. Yang, R. G. Parr, Phys. Rev. B: Condens. Matter Mater. Phys., 1988, 37, 785–789.
[5] J. B. Foresman, A. Frisch, Exploring Chemistry with Electronic Structure Methods, Gaussian, Inc., 1996.
[6] J. Tomasi, B.Mennucci, R. Cammi, Chem. Rev., 2005, 105, 2999–3093.
[7] R. Ditchfield, Mol. Phys., 1974, 27, 789-807; K. Wolinski, J. F. Hinton, P. Pulay, J. Am. Chem. Soc., 1990, 112, 8251-8260.
[8] E. D. Glendening, C. R. Landis, F. Weinhold, Wiley Interdiscip. Rev.: Comput. Mol. Sci., 2012, 2, 1−42.
[9] E. Kleinpeter, S. Klod, W.-D. Rudorf, J. Org. Chem., 2004, 4317-4329.
[10] M. Baranac-Stojanović, U. Klaumünzer, R. Marković, E. Kleinpeter, Tetrahedron 2010, 66, 8958-8967.

IS 3-AMINOACRYLIC GROUP BETTER DONOR OR ACCEPTOR OF π-ELECTRON DENSITY?

M. Stojanović [1], J. Aleksić [1] and M. Baranac-Stojanović [2]

[1] University of Belgrade, Institute of Chemistry, Technology and Metallurgy,Center for Chemistry, Njegoševa 12, 11000 Belgrade, Serbia (milovans@chem.bg.ac.rs)
[2]University of Belgrade – Faculty of Chemistry, Studentski trg 12-16, 11000 Belgrade, Serbia

ABSTRACT

Electron donating/accepting ability of 3-aminoacrylic group was examined theoretically by quantification of push-pull effect of two double bonds of (*2Z,4Z*)-dimethyl 3-amino-4-(aminomethylene)pent-2-enedioate. In this diene, 3-aminoacrylic moiety appears as electron-acceptor with respect to one double bond and as electron-donor with respect to another. The rest of substituents are the same for each bond. A slightly stronger accepting ability was inferred on the basis of two sensitive parameters, C=C bond lengths and quotient of the occupation numbers of π^* and π orbitals of the double bonds, π^*/π.

INTRODUCTION

Push-pull alkenes, having one or two electron-donating groups (Don) attached at one carbon atom of the C=C double bond and one or two electron-accepting groups (Acc) attached at another carbon atom (Figure 1), represent an interesting subclass of alkene family. They have unique physical and chemical properties due to the mostly one-directional π-electron delocalization [1-3]. Thus, push-pull polyenes emerged as important constituents of optical materials [4].

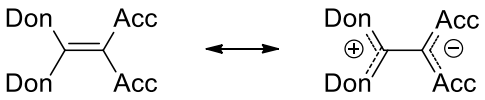

Figure 1. General formula of a push-pull alkene and its π-electron delocalization.

Knowledge about π-electron donating or accepting power of substituents is of great importance to chemists, since these properties affect physical and chemical behaviour of conjugated molecules. Herein, we investigate

electron-donating and electron-accepting ability of 3-aminoacrylic group by examining the push-pull effect of two double bonds in (*2Z,4Z*)-dimethyl 3-amino-4-(aminomethylene)pent-2-enedioate (Figure 2).

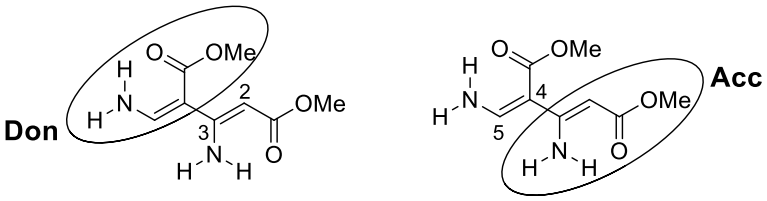

Figure 2. Structure of investigated diene.

In this diene, 3-aminoacrylic substituent behaves as π-electron donor for one CC double bond and as π-electron acceptor for another. The other two substituents, Don = NH_2 and Acc = COOMe, are the same for both double bonds and they have the same *cis*-orientation. Do these two double bonds have the same or different strength of push-pull effect? We aim to answer this question by quantifiying this property.

EXPERIMENTAL

To quantify push-pull effect of the CC double bonds we used two sensitive parameters: CC bond length and quotient of the occupation numbers of π^*-antibonding and π-bonding orbitals of the double bonds, π^*/π [5,6]. They were obtained theoretically at the B3LYP/6-31+G(d,p) level [7,8] by employing Gaussian 09 program package [9]. Structure optimizations were immediately followed by frequency analysis which confirmed that the obtained structures were energy minima and provided free energy data for the studied conformations of diene. Occupation numbers of π and π^*-orbitals were calculated by using the natural bond orbital (NBO) analysis [10]. Longer CC double bonds and larger quotient values indicate stronger push-pull effect.

RESULTS AND DISCUSSION

The studied compound is not experimentally known, so that we first evaluated energies of its three possible viable isomers, shown in Figure 3. We reasoned that hydrogen-bonding interactions would stabilize *Z* configuration around both double bonds, as well as *s-cis* conformations of the α,β-unsaturated ester moietes.

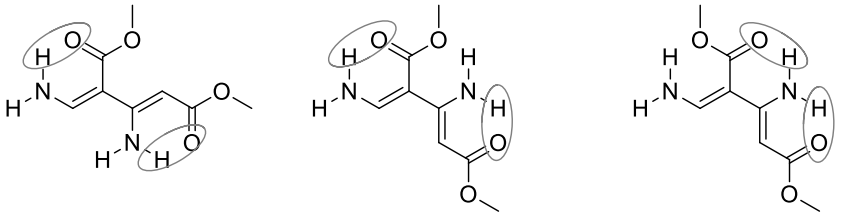

Figure 3. Three conformations of the investigated diene and their free energies in kcal/mol.

We first optimized *s-trans* and *s-cis* forms, **A** and **B**, and the latter was found to be lower in energy. Both structures suffer from steric hindrance so that the planes of the two acrylic moieties are tilted with respect to one another by 43° and 40° in **A** and **B**, respectively. This nonplanarity diminishes π-electron delocalization, but does not turn it off completely. This means that acrylic substituent may act as π-donor and π-acceptor. As rotation of the C4 ester group by 180° may result in another hydrogen-bonding stabilization, we also optimized structure **C** and found it to be by 1.99 kcal/mol higher in energy, relative to the most stable **B**, with 31° tilt of the two planar moieties.

For the study of donating/accepting ability of 3-aminoacrylic substituent we have chosen the form **A** because it is free from direct interactions of aminoacrylic substituents, that is, ester-amine interactions present in **B** and **C**, which can additionally affect the push-pull property of double bonds. We also reasoned that donor-acceptor interactions between the two *cis*-oriented amine and ester substituents would not differ in the two double bonds. Results of our calculations are presented in Table 1.

Table 1. Calculated lengths of the CC double bonds (Å), occupation numbers of π and π* orbitals (e) and their quotient (π*/π).

bond	d_{CC}	π	π*	π*/π
C2=C3	1.374	1.8152	0.2831	0.1560
C4=C5	1.381	1.7965	0.2967	0.1652

The C4=C5 double bond is slightly longer than the C2=C3 double bond, which is indicative of somewhat greater push-pull effect of the former. An analysis of occupation numbers of π-bonding and π*-antibonding orbitals corroborates this finding. Thus, the C4=C5 bond features lower density of

π-electrons in bonding orbital, but higher in antibonding orbital which results in slightly larger quotient value. Hence, we predict only slightly larger electron-accepting vs electron-donating ability of 3-aminoacrylic substituent in the studied diene.

CONCLUSION

We have compared the π-electron donating/accepting power of 3-aminoacrylic substituent by studying the strength of the push-pull effect of two double bonds in diene in which the mentioned group appears as donor for one double bond and as acceptor for another double bond, the rest of substituents are the same for both bonds. By quantifiyng the push-pull effect by means of two sensitive parameters, CC bond lengths and quotient of the occupation numbers of π and π^* orbitals, π^*/π, we have come to conclusion that electron-accepting ability slightly prevails.

Acknowledgement

This work was supported by the Ministry of education, science and technological development of the Republic of Serbia (Grant no. 172020).

REFERENCES

[1] J. Sandström, Top. Stereochem., 1983, 14, 83-181.
[2] E. Kleinpeter, J. Serb. Chem. Soc., 2006, 71, 1-17.
[3] Z. Džambaski, M. Baranac-Stojanović, ChemistrySelect, 2017, 2, 42-50.
[4] J. Luo, F. Lin, Z. Li, M. Li, T.-D. Kim, S.-H. Jang, A. K.-Y. Jen, J. Mater. Chem. C, 2017, 5, 2230-2234.
[5] E. Kleinpeter, S. Klod, W.-D. Rudorf, J. Org. Chem., 2004, 4317-4329.
[6] M. Baranac-Stojanović, U. Klaumünzer, R. Marković, E. Kleinpeter, Tetrahedron 2010, 66, 8958-8967.
[7] A. D. Becke, J. Chem. Phys., 1993, 98, 5648–5652; C. Lee, W. Yang, R. G. Parr, Phys. Rev. B: Condens. Matter Mater. Phys., 1988, 37, 785–789.
[8] J. B. Foresman, A. Frisch, Exploring Chemistry with Electronic Structure Methods, Gaussian, Inc., 1996.
[9] M. J. Frisch et al., Gaussian 09 (Revision D.01), Gaussian Inc.: Wallingford, CT, 2013.
[10] E. D. Glendening, C. R. Landis, F. Weinhold, Wiley Interdiscip. Rev.: Comput. Mol. Sci., 2012, 2, 1−42.

STACKING INTERACTIONS OF HYDROGEN-BRIDGED RINGS. ANALYSES OF CRYSTAL STRUCTURES AND QUANTUM CHEMICAL CALCULATIONS

J. P. Blagojević Filipović [1] and S. D Zarić [2]

[1] *Innovation Center of the Faculty of Chemistry, Studentski trg 12-16, 11000 Belgrade, Serbia.*
[2]*Faculty of Chemistry, University of Belgrade, Studentski trg 12-16, 11000 Belgrade, Serbia. (szaric@chem.bg.ac.rs)*

ABSTRACT
Stacking interactions were once considered as an exclusive feature of aromatic molecules. Nowadays, some non-aromatic systems are known to form this type of interactions. Study of crystal structures of resonance-assisted hydrogen-bridged rings reveals that rings are in parallel alignment, with interplane distances mostly between 3.0 and 4.0 Å, which is typical for stacking interactions. Interaction energies are calculated on dimers in the gas phase by quantum chemical methods. Interactions can be much stronger than stacking interactions in benzene dimer (-2.7 kcal/mol), since the strongest calculated interactions reach –4.8 kcal/mol.

INTRODUCTION
Stacking interactions are among the most studied non-covalent interactions, commonly found in biological systems, including higher level of organization of biomolecules and molecular recognition processes. These interactions can also be useful in material design.

Small aliphatic molecules can form stacking interactions of the strength comparable with the strength of aromatic molecules of similar size [1]. Stacking interaction in heterodimer of benzene and cyclohexane is stronger than stacking interaction in the corresponding homodimers [2, 3, 4]. Stacking interactions of planar non-aromatic species can be much stronger than stacking of aromatic molecules. For example, planar chelate rings with delocalized π-bonds can form quite strong stacking interactions mutually and with C_6-aromatic rings [5].

Hydrogen-bridged rings can act as classical rings, formed only by covalent bonding. For example, quasi-chelate rings can interact with CH-groups in a manner analogous to CH-π interactions in aromatic systems [6]. Stacking interactions of hydrogen-bridged rings with only single bonds in the ring were studied in our previous work [7, 8, 9]. Stacking interactions of

resonance-assisted hydrogen-bridged rings were observed in crystal structures [10]. In this work we systematically studied stacking interactions of resonance-assisted hydrogen-bridged rings and compared them with previously studied stacking interactions of hydrogen-bridged rings [7, 8 , 9].

METHODOLOGY

Stacking interactions of hydrogen-bridged rings have been systematically studied by analyzing crystal structures in Cambridge Structural Database (CSD) and by quantum chemical calculations on dimers in the gas phase. Model systems for the calculations are based on the CSD search, since interaction energies are calculated on dimers of molecules whose derivatives are the most frequently found in CSD.

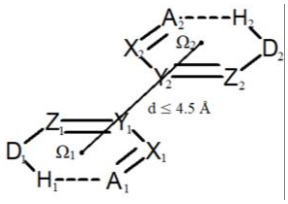

Figure 1. A system of resonance-assisted hydrogen-bridged rings studied by CSD search

All rings in the search were planar and all covalent bonds are set to be acyclic. Donor and acceptor atoms, corresponding to intramolecular hydrogen bonds, include N, O and S atoms. Search was limited to six-membered resonance-assisted hydrogen-bridged rings, due to their abundance in crystal structures. Contacts with centroid distances (d) not larger than 4.5 Å were analyzed (Figure 1).

Calculations of potential energy curves were performed by methods that showed good agreement with CCSD(T)/CBS method. Interaction energies for the geometries corresponding to the curves minima were calculated at CCSD(T)/CBS level.

RESULTS AND DISCUSSION

Large majority of contacts in crystal structures of resonance-assisted hydrogen-bridged rings are parallel contacts (91%), similar to saturated hydrogen-bridged rings (86%)[7]. In case of contacts between saturated hydrogen bridged rings and aromatic rings the percentage of parallel orientation is smaller, 45% [9].

Most of structures with parallel contacts have interplanar distances in the range between 3.0 and 4.0 Å, which is a characteristic of stacking interactions. Contacts in crystal structures of resonance-assisted hydrogen-bridged rings are mostly antiparallel, since absolute values of torsion angles $D_1\Omega_1\Omega_2D_2$ and $A_1\Omega_1\Omega_2A_2$ (Figure1) are mostly in the range from 160° to 180°.

Interaction energies of resonance-assisted hydrogen-bridged rings are calculated on homodimers of *cis*-3-hydroxyacrolein, *cis*-3-aminoacrolein and *Z*-2-hydrazinylidenacetaldehyde molecules. The most stable geometries, that are observed for *cis*-3-aminoacrolein dimer and *Z*-2-hydrazinylidenacetaldehyde dimer are parallel-displaced, like in the benzene dimer, while the most stable observed geometry of *cis*-3-hydroxyacrolein dimer is sandwich geometry. The interaction energies, together with previously calculated energies of stacking interactions of saturated hydrogen-bridged rings, mutually and with C_6-aromatic rings, are shown in Table 1.

Table 1. The strongest calculated interaction energies of hydrogen-bridged ring systems

Model-system	Interaction energy (kcal/mol)
2-methylidenecarbothioamide dimer[a]	-4.89
2-methylidenecarbothioamide/ benzene[b]	-4.38
cis-3-hydroxyacrolein dimer	-4.35
cis-3-aminoacrolein dimer	-4.76
Z-2-hydrazinylidenacetaldehyde dimer	-2.20

[a] model system for mutual interactions of saturated hydrogen-bridged rings [7]

[b] model system for interactions of saturated hydrogen-bridged rings and C_6-aromatic rings [9]

CONCLUSION

A systematic study of crystal structures of resonance-assisted hydrogen-bridged rings reveals that these systems can form stacking interactions. Quantum chemical calculations show that the mutual positions of molecules in crystals are not only a consequence of packing, since the interaction energies are significant. The interactions are stronger than stacking interactions in benzene dimer and comparable with interactions of saturated

hydrogen-bridged rings. Relatively large interaction energies make stacked hydrogen-bridged rings promising building blocks in supramolecular systems.

Acknowledgement
This work was supported by the Ministry of Education, Science and Technological development of the Republic of Serbia (Grant no. 172065).

REFERENCES

[1] S. Grimme, Angew. Chem., Int. Ed., 2008, **47**, 3430-3434.
[2] D. B. Ninković, D. Z. Vojislavljević-Vasilev, V. B. Medaković, M. B. Hall, E. N. Brothers, S. D. Zarić, Phys.Chem.Chem.Phys. 2016, **18**, 25791-25795.
[3] E. C. Lee, D. Kim, P. Jurecka, P. Tarakeshwar, P. Hobza, K. S. Kim, J. Phys. Chem. A, 2007, **111**, 3446–3457.
[4] K. S. Kim, S. Karthikeyan, N. J. Singh, J. Chem. Theory Comput. 2011, **7**, 3471–3477.
[5] D. P. Malenov, G. V. Janjić, V. B. Medaković, M. B. Hall, S. D. Zarić, Coord. Chem. Rev. 2017, **345**, 318-341.
[6] C. I. Yeo, S. N. A. Halim, S. W. Ng, S. L. Tan, J. Zukerman-Schpector, M. A. B. Ferreira, E. R. T. Tiekink, Chem. Commun. 2014, **50**, 5984-5986.
[7] J. P. Blagojević, S. D. Zarić, Chem. Commun. 2015, **51**, 12989-12991.
[8] J. P. Blagojević, G. V. Janjić, S. D. Zarić, Crystals, 2016, **6**, 34.
[9] J. P. Blagojević, D. Ž. Veljković, S. D. Zarić, CrystEngComm, 2017, **19**, 40-46.
[10] H. Karabiyik, H. Karabiyik, N. Ocaklskeleli, Acta Crystallogr., Sect. B: Struct. Sci. 2012, **68**, 71-79.

THE EFFECT OF ADDITIONAL OH GROUP ON THE ANTIRADICAL ACTIVITY IN DOPAMINE/6-OH DOPAMINE AND OCTOPAMINE/NOREPINEPHRINE PAIRS

D. Sretenović[1], G. Jovanović[1], D. Milenković[2], E. Avdović[3], J. Đorović[2], D. Dimić[1] and J. Dimitrić Marković[1]

[1]University of Belgrade, Faculty of Physical Chemistry, Studentski trg 12-16, 11000 Belgrade, Republic of Serbia. (ddimic@ffh.bg.ac.rs)
[2]Bioengineering Research and Development Center, Prvoslava Stojanovića 6, 34000 Kragujevac, Republic of Serbia.
[3]University of Kragujevac, Faculty of Science, Department of Chemistry, Radoja Domanovića 12, 34000 Kragujevac, Republic of Serbi

ABSTRACT
The antiradical activity of dopamine, 6-hydroxydopamine (6-OH dopamine), octopamine and norepinephrine was investigated towards DPPH radical. The results are explained based on the structural parameters, with special emphasis on the change of number of hydroxy groups present in molecule. The theoretical calculation of thermodynamic parameters, for the most common mechanisms, gave additional insight in the importance of catechol moiety in structure and lower significance of OH groups attached to aliphatic chain.

INTRODUCTION
The oxidative stress plays an important role in the development of many neurodegenerative disorders [1]. Therefore molecules which can cross the blood-brain barrier gain significant attention because it is believed that they present the first line of defense against reactive oxygen (ROS) and nitrogen (RNS) species. Not all of the molecules are equally potent. The aim of this contribution is to discuss the effect of additional OH group in pairs: dopamine /(6-OH dopamine) and octopamine/norepinephrine. The structures of these molecules are given in Figure 1. Out of these four molecules, only 6-OH dopamine is not present in humane body, but it is used as neurotoxin when different neurodegenerative diseases are examined *in vivo* in laboratory mice. There are several common mechanisms investigated when radical scavenging activity is considered. Three most common that are applicable for further discussion in this contribution are: hydrogen atom transfer (HAT), sequential proton loss electron transfer

(SPLET) and single electron transfer followed by proton transfer (SET-PT), with reactions and equations for parameters given elsewhere. The common thing for these three mechanism are the final products, which consist of neutral molecule of starting radical and radical specie of antioxidant. The preferability of mechanism can be discussed when the following thermodynamic parameters of the processes are calculated and compared: bond dissociation enthalpy (BDE), proton affinity (PA), electron transfer enthalpy (ETE), ionization potential (IP) and proton dissociation enthalpy (PDE)

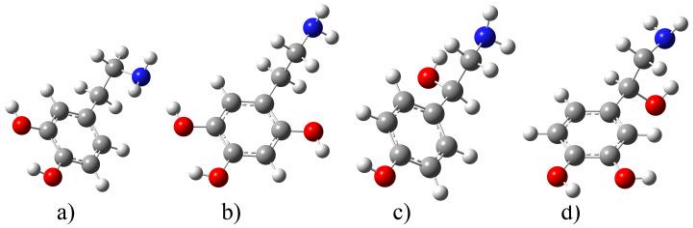

Figure 1. Optimized structures of a) dopamine, b) 6-OH dopamine, c) octopamine and d) norepinephrine.

EXPERIMENTAL/THEORETICAL METHODS

The DPPH radical scavenging activity was measured as described in reference [2]. The measurements were performed on *Thermo Scientific 220* UV-VIS spectrophotometer. The EC_{50} value was determined as the amount of selected molecule required to reduce 50% of radical, while stoichiometric coefficient (SC) was calculated as $SC = \frac{[DPPH]_0}{2EC_{50}}$, $[DPPH]_0$ was the starting concentration of DPPH. The structures of dopamine, 6-OH dopamine, octopamine and norepinephrine were optimized at B3LYP-D3/6-311G++(d,p) level of theory in Gaussian Program Package [3]. The absence of imaginary frequencies proved that the local and global minima were found. The crystallographic structures were taken as the starting conformations for the optimization and from there several other conformers were investigated in order to ensure that the most stable conformer was found. The SMD solvent model was applied so the experimental conditions could be mimicked. The thermodynamic parameters were calculated based on equation given in reference [2] after the optimization of radical cation, anion and radical species.

RESULTS AND DISCUSSION

The results of the radical scavenging activity towards DPPH radical are given in Table 1. Lower value of EC_{50} signifies the better antioxidant. Based on this value it can be concluded that dopamine, 6-OH dopamine and

norepinephrine are equally potent antioxidants. From Figure 1 and structural parameters, it should be noted that dopamine possesses two hydroxy groups, while the other two molecules have three OH groups. This proves that additional OH groups in *ortho*-position with respect to aliphatic chain in case of 6-OH dopamine and on aliphatic chain (norepinephrine) don't influence significantly the antioxidant activity. The catechol moiety allows the formation of strong hydrogen bond, which additionally stabilizes the formed radical and/or anionic species, as it will be shown in further discussion. This is experimentally proven when activity parameters are compared for octopamine and norepinephrine. The value of EC_{50} for octopamine is significantly higher than for norepinephrine, although structure differs only in one OH group. From the structural point of view there is a possibility of hydrogen bond formation between amino and hydroxy group in octopamine and norepinephrine. The value of stoichiometric coefficient is taken as the complementary factor to the EC_{50}. For "good" antioxidants it has value larger than two. When this criterion is applied, it is clear that dopamine, 6-OH dopamine and norepinephrine can be considered as good antioxidants, while octopamine showed some radical scavenging activity, but not comparable to other three.

Table 1. The experimental DPPH radical scavenging activity parameters

	EC_{50} x 10^{-6}	SC		EC_{50} x 10^{-6}	SC
Dopamine	10.50	4.76	Norepinephrine	10.60	4.71
6-OH dopamine	10.70	4.67	Octopamine	300	0.17

In order to gain better understanding of the preferred mechanism, the thermodynamic parameters for three common mechanisms in methanol are calculated [2] and presented in the following table (Table 2). The amino groups are not included in this table because it was proven in our previous contribution [2] that they show significant activity. Also, due to the large electronegativity of N atom, it wasn't possible to obtain anion from NH_2 group for octopamine and norepinephrine, due to the hydrogen transfer from OH group. The most probable mechanism can be obtained when the parameters for the first step of each path are compared. It is obvious that SPLET is the most probable for all of the investigated substances. The values of PA reflect well what was discussed before – the favorable positions for hydrogen abstraction are OH groups of catechol moiety. In 6-OH dopamine the value of PA for *ortho*-OH group is 20 kJ mol^{-1} larger than for other two. In case of octopamine the value of PA for *para*-OH group is 30 kJ mol^{-1} larger in the case when two hydroxy groups are present. The

relative low activity of OH groups attached to aliphatic chain is well reflected in values of PA that are around 200 kJ mol^{-1}. All of these findings support well the experimental observations.

Table 2. Thermodynamic parameters for the most common mechanisms (in kJ mol^{-1})

Mechanism		HAT	SET-PT		SPLET	
Parameter		BDE	IP	PDE	PA	ETE
dopamine	p-OH	316	455	23	140	338
	m-OH	321	455	27	139	344
6-OHdopamine	p-OH	305	426	41	138	329
	m-OH	298	426	34	145	315
	o-OH	316	426	52	160	329
Norepinephrine	p-OH	319	458	23	137	344
	m-OH	323	458	27	138	347
	al-OH	436	458	140	219	378
Octopamine	p-OH	345	478	28	151	355
	al-OH	389	478	73	209	342

CONCLUSION

The radical activity towards DPPH radical was measured for dopamine, 6-OH dopamine, octopamine and norepinephrine. It was shown that the position of additional OH group is a significant parameter for the antiradical activity. If catechol moiety is present and additional group is attached to aromatic ring without the possibility of hydrogen bond formation with other OH groups or if OH group is present in aliphatic chain there is no change in activity. If OH group is added to structure with only one OH group in *para*-position then the structure is stabilized with hydrogen bond formation. The most probable mechanism is SPLET, and values of PA reflect well the experimental observation and serve as quantitative parameter for analysis.

Acknowledgement

Authors acknowledge the Ministry of Education, Science and Technological Development of the Republic of Serbia for the financial support through projects No. 172040, 172015 and 174028.

REFERENCES

[1] B. Halliwell, J. M. C. Gutteridge, Free Radicals in Biology and Medicine, Clarendon Press, Oxford, 3rd edn, 1999.

[2] D. Dimić, D. Milenković, J. Dimitrić Marković, Z. Marković, Phys. Chem. Chem. Phys., 2017, 19, 12970-12980.

[3] M. J. Frisch, G. W. Trucks, H. B. Schlegel, et al. Gaussian 09, Revision C. 01, Gaussian Inc. Wallingford, CT. USA, 2010.

THE CRYSTAL STRUCTURE OF NOVEL ASYMMETRIC FLAVONE DERIVATIVES

M. Wera [1], I.E. Serdiuk [1,2] and A.D. Roshal [3]

[1] Faculty of Chemistry, University of Gdańsk,
Wita Stwosza 63, 80-308 Gdańsk, Poland (michal.wera@ug.edu.pl).
[2] Faculty of Mathematics, Physics and Informatics, University of Gdańsk,
Wita Stwosza 57, 80-308 Gdańsk, Poland.
[3] Institute of Chemistry, V. N. Karazin Kharkiv National University,
Svoboda sqr. 4, Kharkiv 61022 Ukraine.

ABSTRACT

Novel asymmetric flavones were synthesized in an attempt to create a flavone derivative able to take part in Excited State Intramolecular Double Proton Transfer (ESIDPT). The aim was to find compounds containing two proton transfer (PT) sites and investigate their luminogenic properties. The crystal structure of three of the derivatives of 3,7-dihydroxy-4-oxo-2-phenyl-4Hchromene-8-carbaldehyde was obtained and the investigation of the structural and interactions were undertaken. The results of these investigations are presented herein.

INTRODUCTION

Excited State Intramolecular Proton Transfer (ESIPT) is a process in photochemistry where electronically excited molecules relax their energy by transfer of protons between neighboring atoms. The transformation occurs frequently in the compound fragments connected *via* an intermolecular hydrogen bond and partaking in the in keto–enol and imine–amine tautomerization reactions [1-3]. The emission process is susceptible to the influence of the environment and media of the reaction due to the high sensitivity to external hydrogen bonding. Compounds exhibiting ESIPT have various applications as biological markers and probes [3].

Excited State Intramolecular Double Proton Transfer (ESIDPT) is a protontransfer light emitting process which occurs very rarely. For it to take place a compound must contain PT centers which are able to undergo the tautomerization reaction.

For the better understanding of the ESIPT and ESIDPT processes the detailed knowledge of the structure and interactions in which the compounds PT sites may be involved in is necessary. Hence, the three new

compounds were synthesized and their crystal structure was determined followed by an investigation of the interactions occurring in the solid state.

EXPERIMENTAL

The investigated flavone derivatives (Figure 1) were synthesized using methods previously described in literature [4]. Crystals suitable for X-ray analysis were obtained using the slow evaporation of the absolute methanol solvent.

X-ray data were collected at 295(2) K with ω-scan technique on the Oxford Diffraction Gemini R Ultra Ruby CCD diffractometer with graphite monochromatic MoKa radiation (λ = 0.71073 Å). Programs CrysAlis CCD [5] and CrysAlis RED [6] were used for data collection, cell refinement and data reduction with an applied multi-scan absorption correction.

Structures were solved by direct methods with SHELXS-97 [7] and refined by the full-matrix least squares method on F^2 with SHELXL2013 [8]. ORTEP-3 [9] software was used to prepare the molecular graphics, and the PLATON [10] and CrystalExplorer [11] programs to reveal and analyze the molecular interactions.

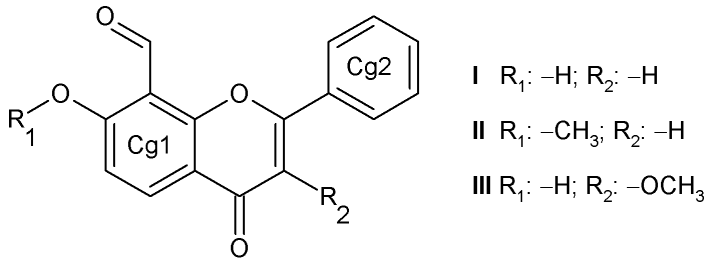

Figure 1. Structure of compounds under investigation.

RESULTS AND DISCUSSION

Crystal data and details concerning the structural refinement are given in Table 1.

The analysis of interactions occurring in the crystals of flavone derivatives reveals the presence of C–O···π (**II**,**III**), C–H···O (**I**, **III**) and C–H···π (**III**) intermolecular interactions and π–π contacts (**I**,**II**,**III**) (Tables 2–4).

Table 1. Crystal data and structure refinement parameters.

Experimental details	**I**	**II**	**III**
Empirical formula	$C_{16}H_{10}O_4$	$C_{17}H_{12}O_4$	$C17H_{12}O_5$
Formula weight	266.24	280.27	296.27
Crystal system, space group	monoclinic, P 2_1/n	monoclinic, P 2_1/n	monoclinic, C 2/c
Unit cell dimensions [Å,°]	a = 16.7029(12) b = 3.8569(2) c = 19.4969(17) β = 108.605(9)	a = 7.5768(14) b = 9.2842(8) c = 18.791(2) β = 100.003(14)	a = 14.7379(8) b = 7.2739(3) c = 26.7671(16) β = 109.952(7)
Volume [A^3]	1190.38(16)	1301.7(3)	2697.3(3)
Z, Calculated density [Mg/m^3]	4, 1.486	4, 1.430	8, 1.459
Absorption coeff. μ [mm^{-1}]	0.108	0.102	0.108
F(000)	552	584	1232
Θ range for data collection [°]	3.66–25.04	3.50–25.05	3.39–25.14
Limiting indices	-18<=h<=19, -4<=k<=4, -23<=l<=11	-8<=h<=9, -11<=k<=11, -21<=l<=22	-16<=h<=17, -8<=k<=8, -32<=l<=32
Reflections collected / unique	4716 / 2113 [R_{int} = 2.44%]	9533 / 2283 [R_{int} = 3.39%]	10131 / 2409 [R_{int} = 2.73%]
Completeness 2Θ	99.6%	99.7%	99.7%
Data / restraints / parameters	2113 / 0 / 184	2283 / 0 / 191	2409 / 0 / 203
Goodness-of-fit	1.028	1.072	1.104
Final R indices [I>2 σ (I)]	R_1 = 4.03%, wR_2 = 9.14%	R_1 = 4.99%, wR_2 = 10.63%	R_1 = 4.47%, wR_2 = 10.01%
R indices (all data)	R_1 = 6.17%, wR_2 = 10.32%	R_1 = 7.04%, wR_2 = 11.63%	R_1 = 5.57%, wR_2 = 10.55%
$\Delta\rho$max, $\Delta\rho$min (e $Å^{-3}$)	0.133, –0.176	0.151, –0.200	0.149, –0.167

Table 2. C–O···π interactions geometrical parameters [Å,°].

	Y	X	CgI	X···Cg	Y···Cg	Y–X···Cg	Symmetry codes
II	C4	O11	Cg1	3.457(1)	3.413(2)	77.7(1)	x, y + 1, z
III	C21	O22	Cg1	3.772(2)	3.799(2)	81.9(1)	–x , –y + 1, –z

Table 3. Hydrogen bonds geometrical parameters [Å,°].

	D–H···A	D–H	H···A	D···A	D–H···A	Symmetry codes
I	C6–H6···O12	0.93	2.42	3.234(3)	146	–x + 1½, y + ½, –z – ½
III	C5–H5···O22	0.93	2.58	3.429(2)	151	x – ½, y + ½, z
	C15–H15···O11	0.93	2.56	3.420(3)	155	x + ½, y – ½, z
	C17–H17···Cg2	0.93	2.83	3.572(2)	137	–x + ½, y + ½, –z + ½

Table 4. π–π contacts geometrical parameters [Å,°].

	CgI	CgJ	Cg···Cg	Dihedral angle	Interplanar distance	Offset	Symmetry codes
I	Cg1	Cg2	3.978(1)	3.8(1)	3.557(1)	2.013	–x + 2, –y + 1, –z
	Cg2	Cg1	3.978(1)	3.8(1)	3.431(1)	1.780	–x + 2, –y + 1, –z
II	Cg1	Cg1	3.857(1)	0	3.407(1)	1.808	x, y + 1, z
	Cg1	Cg1	3.857(1)	0	3.407(1)	1.808	x, y – 1, z
	Cg2	Cg2	3.857(1)	0	3.558(1)	1.490	x, y + 1, z
	Cg2	Cg2	3.857(1)	0	3.558(1)	1.490	x, y – 1, z
III	Cg1	Cg1	3.931(1)	0	3.420(1)	1.938	–x, –y + 1, –z

CONCLUSION

It was established that despite crystallizing in one crystal system the structural differences in the three flavone derivatives are the cause of diverse intermolecular interactions occurring in the crystal structure. The PT sites are show high susceptibility to formation of intermolecular interactions.

Acknowledgement

This work was partially supported by the State Funds for Scientific Research (Grant DS/530-8225-D493-18)

REFERENCES

[1] J. Zhao, S. Ji, Y. Chen, H. Guo, P. Yang, Phys. Chem. Chem. Phys., 2012, **14**, 8803–8817.
[2] J. E. Kwon, S. Y. Park, Adv. Mater., 2011, **23**, 3615–3642.
[3] S. Protti, A. Mezzetti, Photochemistry, 2012, **40**, 295–322.
[4] I.E. Serdiuk, A.D. Roshal, RSC Adv., 2015, **5**, 102191–1022203.
[5] Oxford Diffraction, CrysAlis CCD, Oxford Diffraction Ltd, Yarnton, 2008.
[6] Oxford Diffraction, CrysAlis RED, Oxford Diffraction Ltd, Yarnton, 2008.
[7] G.M. Sheldrick, Acta Cryst. **A64**, 2008, 112–122.
[8] G.M. Sheldrick, SHELXL2013, University of Göttingen, Göttingen, 2013.
[9] L.J. Farrugia, J. Appl. Cryst. 30 (1997) 565.
[10] A.L. Spek, Acta Cryst. **D65**, 2009, 148–155.
[11] S.K. Wolff, D.J. Grimwood, J.J. McKinnon, M.J. Turner, D. Jayatilaka, M.A. Spackman, CrystalExplorer (Version 3.1), University of Western Australia, 2012.

H *– Material Science*

UV SHIELDING COATINGS BASED ON GRAPHENE/CNT RADICAL SCAVENGER FILLERS

R. Tomovska,[1,2] M. Prosheva[3] and J.Blazhevska-Gilev[3]

[1] POLYMAT, University of the Basque Country, 20018 Donostia-San Sebastián, Spain (radmila.tomovska@ehu.es)
[2] Ikerbasque, Basque Foundation for Science, 48013 Bilbao, Spain
[3] Faculty of Technology and Metallurgy, University of Saints Cyril and Methodius, 1000 Skopje, R. Macedonia

ABSTRACT
This study presents synthesis of hybrid graphene/CNT filler that was used to improve photooxydation resistance of waterborne methyl methacrylate/butyl acrylate copolymer film. The hybrids has shown to be very potent radical scavengers due to facilitated charge transfer between the both fillers that improve their capability to capture and resonantly stabilize the free radicals. This was demonstrated by Electron Paramagnetic Resonance Spectroscopy and by accelerated aging performed on the composite films by irradiation with UV light at increased temperature and in air atmosphere.

INTRODUCTION
Graphene (Gr) and carbone nanotubes (CNTs) have often been used as fillers for production of reinforced polymer composites [1,2]. Additionally, due to some peculiarity of these fillers, they may introduce unusual property to the composites. For example, there are theoretical and experimental works demonstrating that Gr and CNTs have strong free-radicals scavenging potential [3-5]. As it is of great interest to find an appropriate material for UV irradiation protection of goods, these findings have turned the attention towards the CNTs and Gr polymer composites [6-8]. However, most of the presented results in these work demonstrated only a delay in the photooxidation process when the composites were exposed to accelerated aging condition of strong UV irradiation, at 50-60ºC and in presence of oxygen. In order to have improved protection and even shield the UV irradiation more efficient free-radical scavenging materials are needed.

It has been found that, due to unusual electronic properties of CNT and Gr, their combination facilitates charge transfer [9,10]. This is the effect that may improve the resonant stabilization of the captured free radicals by the hybrid materials, and subsequently the scavenging efficiency. Therefore in

this work a mixture of both carbon nano-materials is proposed as a hybrid filler to produce strong UV protection waterborne coatings.

The mixtures of Gr and multi wall CNT (MWCNT) in different ratios were prepared by air sonication and their radical scavenging ability was demonstrated by electron paramagnetic (EPR) spectroscopy. For composite synthesis in situ miniemulsion polymerization was used, because it provides physical separation of the free initiator radicals and the scavenging materials within different phases. Composites made of methyl methacrylate (MMA) and butyl acrylate (BA) copolymer and 1 wt% of the hybrid filler were prepared.The presence of Gr/MWCNT mixed filler within polymer matrix increased significantly their photostability, thus, the degradation under accelerating aging conditions (strong UV irradiation of 450 mW/m^2, temperature of 50ºC and in air atmosphere) within the irradiation time investigated (400 h) was almost completely suppressed.

EXPERIMENTAL

Preparation of the hybrids. MWCNT (Sigma Aldrich) and Gr (Graphene Supermarket) in different weight ratios (Gr:MWCNT of 10:1; 5:1; 1:1; 1:5; 1:10) were treated by sonication in air according the procedure explained elsewhere [2] and dispersed in water by sodium dodecyl sulfate (Sigma Aldrich).

In situ miniemulsion polymerization. Miniemulsion was prepared by mixing a water phase consisting of Gr/CNT hybrid dispersions, surfactant Dowfax 2A1 (2 wt% based on monomers) and an oil phase consisting of monomers: MMA, BA (both from Quimidroga), glycidyl methacrylate (GMA, Acros organic) in 49.5/49.5/1 weight ratio and costabilizer stearyl acrylate (SA, BASF, 6 wt% based on monomers). The prepared emulsion with 20% solids content was sonicated for 15 minutes and was polymerized in batch for 60 min at 70ºC, using water soluble initiator potassium persulfate (KPS) or oil soluble azobis-isobutyronitrile (AIBN) both from Sigma Aldrich. For post-polymerization to eliminate the free monomer redox couple ascorbic acid (Acros organics) and tert-Butyl hydroperoxide (sigma Aldrich) was used.

Characterization. Radical scavenging capability of the hybrid fillers containing different ratios of Gr and MWCNT were evaluated using Electron Paramagnetic Resonance (EPR) Spectroscopy and 5,5-Dimethyl-1-Pyrroline N-oxide (DMPO) as a spin trap. EPR measurements were performed at constant 25 ºC, using a Bruker ELEXSYS 500 spectrometer operating at the X-band.

The films were dried at 25ºC and 55% relative humidity. Scanning Electron Microscopy (SEM, Quanta 250 e-SEM, Philips Tecna) was employed to observe the morphology of the cross-section areas. Accelerated aging study was performed to follow the photo-oxidative resistance of the films containing 10:1 Gr/MWCNT

filer using UVA lamp (366 nm, P-Lab) with irradiation power of 550 mW/cm2 at distance of 15 cm, at temperature of 55°C for 400 hours. The progress was followed by analyzing the samples with FTIR equipped with ATR (Perkin Elmer Spectrum 100). In order to study the reproducibility of the aging process, the experiments and the analysis were triplicate.

RESULTS AND DISCUSSION

After the air sonication treatment of the mixtures of Gr/MWCNTs, they were analyzed by TEM to determine the structure of the hybrids and by Raman spectroscopy to determine the chemical changes.

Figure 1 shows TEM images of representative 1:10, 1:1 and 10:1 Gr/CNT. Obviously both materials interact between themselves, as CNTs in majority are adsorbed onto Gr surface, and their amount depends on the ratio. The Gr platelets are transparent with some visible stacks (darker areas), which may be due to the sample preparation (drop casting from dispersion).

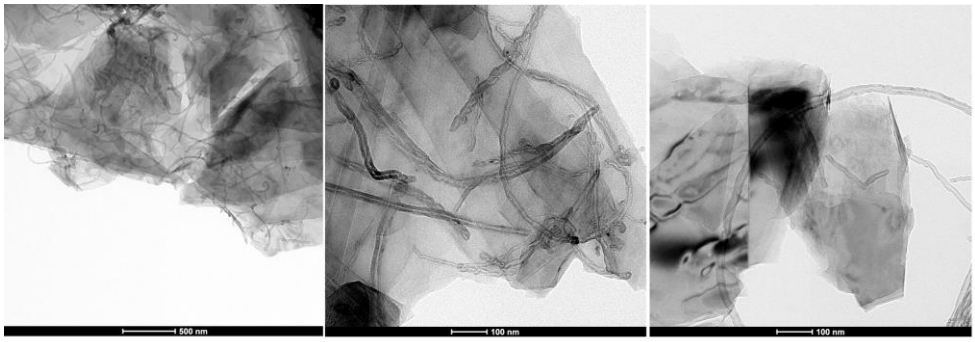

Figure 1. TEM images of the hybrids; from left to write Gr/MWCNTs ratio 1:10 (space bar 500 nm); 1:1(space bar 100 nm); and 10:1(space bar 100 nm).

Raman spectra of the hybrids are shown in Figure 2. From the spectra, the ratio between the two characteristic peaks: G (sp^2 hybridized C atoms) and the D (defects in graphenic structure, mainly represented by sp^3 hybridized carbons) was determined and presented in Table 1. The relative increment of D peak denotes increase in sp^3 hybridized carbons, or introduction of functional groups, whereas the rise in G peaks denotes recovering of the structural defects (for example atomistic vacancy defects, five or seven carbon rings) due to the high temperature to which the hybrids were exposed during the sonication.

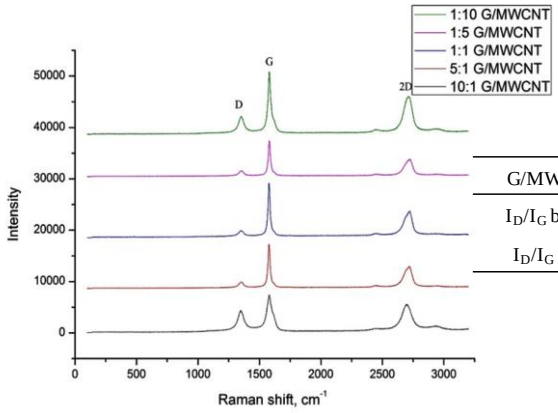

G/MWCNT	10:1	5:1	1:1	1:5	1:10
I_D/I_G before	0.13	0.12	0.14	0.11	0.18
I_D/I_G after	0.57	0.15	0.13	0.15	0.26

Figure 2. Raman spectra of the hybrids, the table shows the intensity ratio of D to G peak

The table in Figure 2 presents comparison between the intensity ratio between and after the sonication treatment. It is curious that each samples has different ratio after the treatment and that in some samples this ratio was increased (indicating higher oxidation in the structures), whereas in other samples this ratio dropped, demonstrating recovering of the graphenic structures. Likely these differences appeared due to the interaction of ultrasonic irradiation and the different aspect ratios fillers. All the samples were slightly oxidized, except 10:1 hybrid, which was oxidized importantly. Oppositely, 1:1 hybrid turns to be more hydrophobic after the treatment.

The radical scavenging activities of the hybrids measured by EPR spectroscopy using a DMPO spin trap in presence of KPS radical initiator are summarized in Table 1. In the blank sample (KPS + DMPO), the DMPO hydroxulated radical was identified. In the presence of the 1:10 hybrid, the signal of oxidized DMPA was found, meaning that DMPA was capturing and oxidizing the KPS radicals. Thus, 10:1 filler was not efficient in scavenging, in accordance with experimental results, as this was the only sample that polymerized completely using water soluble KPS.

Table 1. EPR spectroscopy results

Sample	G:CNT	Observation
Blank (KPS + DMPO)	-	Signal of DMPO-OH
Blank + G/CNT	1 : 10	Signal of DMPOX
Blank + G/CNT	1 : 5	Less intense DMPOX
Blank + G/CNT	1 : 1	No signal
Blank + G/CNT	5 : 1	No signal
Blank + G/CNT	10 : 1	No signal

Less intensive signal of oxidized DMPO was identified in presence of 1:5 hybrid. The monomer conversion in presence of 5:1 was low and it was post-polymerized with redox couple initiator. In the other hybrids no any signal of radicals was noticed, confirming effective radical scavenging and the polymerization process in the presence of these hybrids with KPS was ineffective, thus, it was necessary to perform post-polymerization with redox couple initiator. However, in the case of polymerization in presence of 10:1 hybrid no any monomer conversion was obtained using KPS, neither after few times performed post-polymerizations. To be able to polymerize it oil soluble initiators was added to the system to physical separate the 10:1 hybrid and the initiator radicals, which resulted in full monomer conversion. Taking into account the difference in the structure and surface chemistry of the G/CNTs hybrids, this is not surprising behavior. Obviously, the presence of oxygen functional groups promotes the radical stabilization effect of the hybrids.

These fillers were used to prepare aqueous polymer dispersions, from which the composite films were prepared by water evaporation at standard atmospheric conditions. The morphology of the composites were studied by SEM. Figure 3 shows only SEM images of the composites with 1 wt% of hybrids with 1:5; 1:1 and 10:1 Gr/CNTs, because the composites with 5:1 and 1:10 hybrids coagulated.

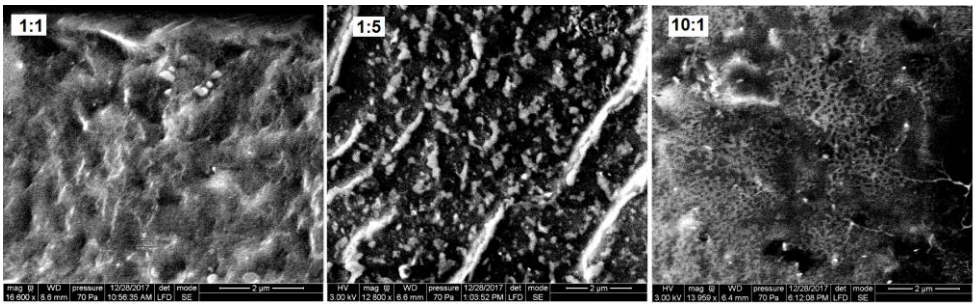

Figure 3. SEM images of the composites with 1wt% Gr/CNTs at diff. ratios

The morphology of the hybrids is different, demonstrating that the ratio of the Gr and CNTs influences the properties of the filler, and subsequently of the composites. The composite with 1:1 ratio has homogeneous distribution of the white hybrid filler within dark polymer matrix. In the 1:5 composite more aggregated structures are presented, whereas the 10:1 composites presents nice morphology of the filler surrounding each polymer particle (the dark domains), forming partially segregated network. The distribution of the filler is very good and the aggregation almost suppressed, which may be result on a larger amount of G that offer large surface are for CNT, improving the interactions between them and preventing the aggregations. This is likely the reason for the effective radical scavenging of 10:1 sample.

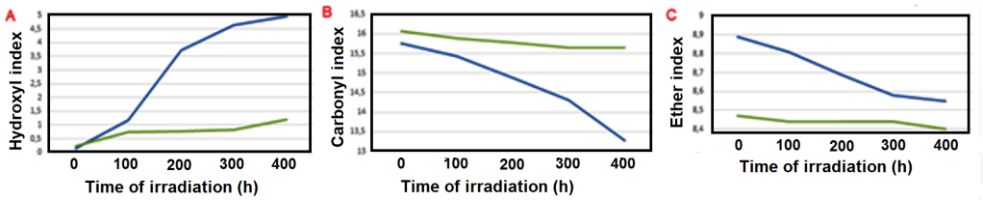

Figure 4. Comparison of hydroxyl, carbonyl and ether indices of polymer and nanocomposites during irradiation

The photoxydation studies were performed on 10:1 sample only, due to the best scavenging activity. Using FTIR, the changes in characteristic peaks of OH (3450 cm^{-1}), C=O (1727 cm^{-1}) and C-O-C functionalities (1145 cm^{-1}) were followed. Respective indexes were calculated using as reference the peak at 989 cm^{-1}. Figure 4 presents the changes of the indices with

irradiation time for neat polymer (blue line) and for nanocomposite film (green line). The indices in Figure 4 indicated that photodegradation process occurs through formation of OH groups and degradation of ester side groups of polymer chains, as C=O and C-O-C amounts dropped. The neat polymer structures changes fast, continuously and with increasing tendency, whereas the composite showed much better stability and negligible changes.

CONCLUSIONS

Hybrid fiollers were prepared by air sonication of mixtures of Gr and MWCNTs at different weight ratios. The ratio between both influences significantly the structures and the surface chemistry of the hybrids, and subsequently their radical scavenging capability. It was demonstrated that 10:1 hybrid completely scavenged the free-radicals. This was demonstrated during in situ polymerization of MMA/BA monomers in presence of this filler. This reactions proceeded only in case when oil soluble initiator was used, which men¡ans after physical separation of the initiator radicals (in droplet phase) and the hybrid filler (in aqueous phase). Due to this effective scab+venging activity of 10:1 hybrid, its presence in very small amount of 1 wt% in the polymer matrix increased significantly the photo-oxydation stability of the films, making them effective protective UV coatings for externals surfaces.

Acknowledgement

This work was supported by the NATO Science for peace project G5244.

REFERENCES

[1] A.Arzac, G.P.Leal, J.C. de la Cal, R.Tomovska, Macromol. Mater. Eng. 302 (2017) 1600315.
[2] B.T.Pérez-Martínez, L. Farías-Cepeda, V.M.Ovando-Medina, J.M.Asua, L.Rosales-Marines, R.Tomovska, Beilstein Journal of Nanotechnology, 8 (2017) 1328 – 1337.
[3] A.Martinez, A.Galano, J. Phys. Chem. C, 114 (2010) 8184-8191.
[4] R.M.Lucente-Schultz, V.C.Moore, A.D.Leonard, B.K.Price, D.V. Kosynkin, M.Lu, R.Partha, J.L.Conyers, J.M.Tour, J. Am. Chem. Soc., 131 (2009) 3934-3941.
[5] Y.Qiu, Z.Wang, A.C.E.Owens, I.Kulaots, Y.Chen, A.B.Kane, R.H.Hurt, Nanoscale, 6 (2014) 11744–11755.
[6] P.C.P.Watts, P.K. Fearon, W.K. Hsu, N.C. Billingham, H.W. Kroto, D.R.M.Walton, J. Mater. Chem., 13 (2003) 491–495.
[7] N.T.Dintcheva, R.Arrigo, F.Catalanotto, E. Morici, Polym. Degrad. Stab., 118 (2015) 24–32.

[8] M.Tang, W. Xing, J.Wu, G.Huang, K.Xiang, L. Guoa, G.Lia, J. Mater. Chem. A., 3 (2015) 5942-5948.
[9] G.L.C.Paulus, Q.H. Wang, Z.W. Ulissi, T.P. McNicholas, A.Vijaya-raghavan, C.J. Shih, Z.Jin, M.S.Strano, Small, 9 (2013) 1954-1963.
[10] Y.Liu, F.Wang, X.Wang, E.Flahaut, X.Liu, Y. Li, X.Wang, Y.Xu, Y.Shi, R.Zhang, Nature Communications, 6 (2015) 8589.

EFFECT OF ELECTRODE POTENTIAL ON MORPHOLOGY AND CHEMICAL COMPOSITION OF ELECTROSYNTHESIZED BISMUTH(III) OXIDE

M. Petrović, M. D. Radović, M. Kostić, J. Mitrović, S. Najdanović, N. Velinov and A. Bojić

University of Niš, Department of Chemistry, Faculty of Science and Mathematics, Višegradska 33, 18 000 Niš, Serbia. (mk484475@gmail.com)

ABSTRACT

Electrodeposition from acidic Bi^{3+} solution at three different constant potentials provided the materials which mutually differed in morphology and elemental composition. At electrode potential of 0.6V and 0.3V the deposited material was metallic bismuth, and at 0.1V it contained bismuth basic nitrate and possibly hydroxide. Calcination of all three deposits at 600 ^{o}C lead to a formation of Bi_2O_3 with different oxygen content, which slightly increased with the increase of electrodeposition potential at which a starting material was obtained.

INTRODUCTION

Bismuth oxide (Bi_2O_3) is an important transition metal oxide with many applications, thus various synthesis routes for this compound have been developed [1-3], including electrochemical procedure under various conditions [4,5]. The applied synthesis procedure and parameters affect some of the properties of the obtained deposits, such as grain size, morphology and oxygen content [5-7].

In this paper, the effect of the applied electrode potential on the surface morphology and oxygen content of the electrodeposited material from acidic Bi (III) solution was investigated before and after its calcination.

EXPERIMENTAL

Electrodeposition was carried out from 0.1M Bi^{3+}solution in 1M HNO_3 at constant potentials of 0.1, 0.3 and 0.6 V during 3 minutes, by chronoamperometric technique using Amel 510 DC potentiostat (Materials Mates, Italy) and VoltaScope software package. Electrodeposition was performed at 20±0.5°C in the three electrode cell with a Ti sheet as a cathode, a Pt sheet as auxillary electrode and saturated calomel electrode as a reference electrode. After the deposition, the substrate covered with deposited film was calcined at 600°C for 90 minutes in air in a furnace and

cooled in the open air. SEM was performed using the lower detector of a Hitachi SU8030 cold-cathode field emission gun scanning electron microscope and EDX was performed using a Thermo-Noran NSS system 7 with a 30mm^2 window Ultra Dry detector.

RESULTS AND DISCUSSION

Morphological differences between the deposits obtained at different potentials are observed both before and after calcination (Figure 1). Non-calcined deposit obtained at 0.1V (Figure 1A) is mostly composed of tightly packed polyhedrons of irregular, random shape and size, generally not bigger than about 5 μm, with some of them might be considered as thicker sheets.

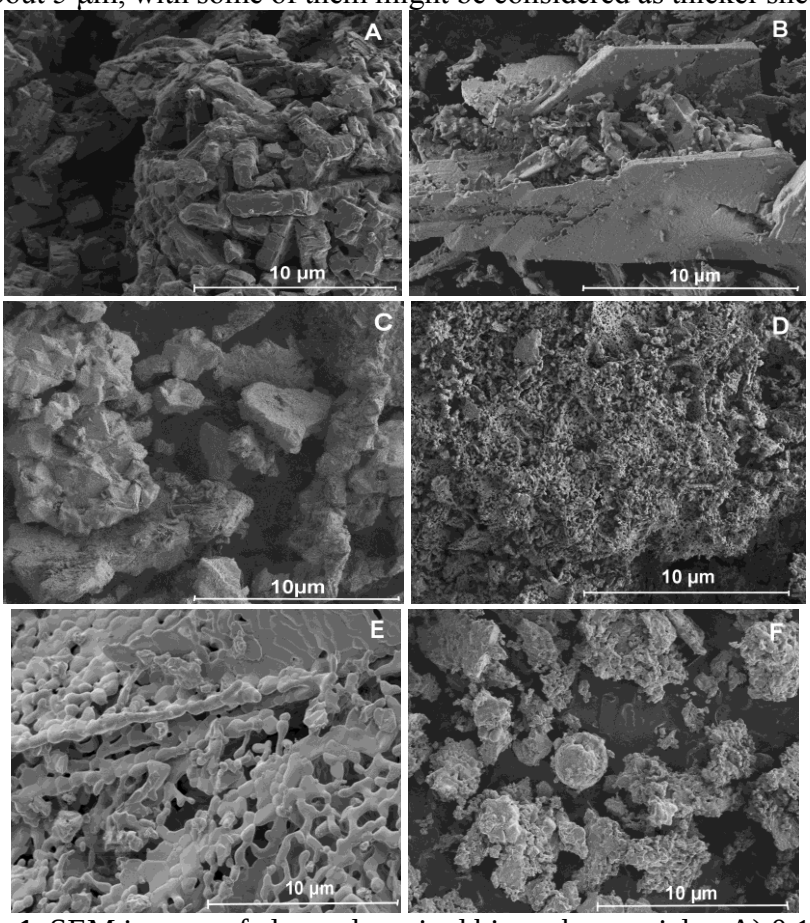

Figure 1. SEM images of electrodeposited bismuth material at A) 0.1 V, B) 0.3 V and C) 0.6 V before calcination and D) 0.1 V, F) 0.3 V and E) 0.6 V

Electrodeposition at 0.3V (Figure 1B) leads to a formation of significant fraction of plane sheet-like monoliths, some of them being bigger than 10

μm, and thick up to 1 μm, although much smaller grains of random shape are also observed. At 0.6V (Figure 1C) the obtained deposit is mostly composed of large crystal-like formations with random shape and size, with many monoliths composed of sintered polyhedrons. After calcination, the morphology of all the deposits changed significantly; their appearance differs mutually as well. In general, the sharp-edged, polyhedron and sheet-like structure turned to oval, irregular and porous structure. Deposit obtained at 0.1V after calcination (Figure 1D) is composed of mostly oval grains smaller than 1 μm, that were sintered and closely packed, yet with enough space to make porous, foam-like structure. At 0.3V, after calcination sample is similar to that at 0.1V, but the oval grains re bigger, elongated and form mostly planar sintered structures, unlike that at 0.1V. Deposit obtained at 0.6V after calcination, is composed of larger grains of very random shapes and sizes, with creased surface and it has no that "foam-like" structures found at deposits obtained at 0.1 and 0.3 V.

EDX results (Table 1) show that at 0.6V and 0.3V predominant cathodic reaction was reduction of Bi^{3+} and formation of metallic Bi; at 0.3V, however, there is little higher O content than at 0.1V, which might be a consequence of formation of small amounts of Bi-oxide and hydroxide. Deposit obtained at 0.1V significantly differs than those at higher potentials: it contains large fraction of O and N, indicating the presence of significant amount of Bi-oxide, hydroxide and basic nitrate. At this potential, H^+ ions could also be reduced at the cathode along with Bi^{3+}, forming OH^- ions, which react with the upcoming Bi^{3+} ions, and, in the presence of NO_3^-, form bismuth hydroxide and basic nitrate [7]. The process is not likely to happen at higher potentials. After calcination, all the electrodeposited materials were transformed to Bi_2O_3, as indicated by the Bi:O mass % ratio, which is close to theoretical mass ratio in Bi_2O_3 (89.69 : 10.31). Bi content in the obtained Bismuth oxide slightly decreases with the increase of electrodeposition potential for the starting material. The difference in O-content is very small between those of 0.1V and 0.3V, and little more significant for that obtained at 0.6V. Bismuth oxide obtained at 0.1V and 0.6V is apparently O-deficient, while oxide obtained at 0.6V contains more O than its theoretical value. XRD spectra showed that in all the three cases, the pure alpha Bi_2O_3 was obtained after calcination (diffractograms not shown).

CONCLUSION

Electrodeposition at three different electrode potentials from Bi^{3+} solution containing HNO_3 lead to a formation of deposits with different morphology for each of the applied potentials, both before and after calcination of the deposited materials.

Table 1. Elemental composition of deposits obtained at different potentials before and after calcination (in mass%)

Metal substrate	E (V)	%Bi + %O + %N before calcination	%Bi + %O after calcination
Ti	0.1	58.35 + 27.49 + 14.16	90.79 + 9.21
Ti	0.3	98.91+1.09	90.51 + 9.49
Ti	0.6	99.1 + 0.9	88.3 + 11.7

Deposition at higher potentials provided surfaces covered with metallic Bismuth, while at the lowest applied potential, the deposited material contained a certain amount of bismuth basic nitrates and possibly, bismuth hydroxide. Calcination of all three deposits lead to a formation of pure alpha Bi_2O_3, which also exhibited different surface appearance and different oxygen content, which slightly increased with the increase of electrodeposition potential for corresponding starting material. Bi_2O_3 obtained at 0.1 and 0.3V had little lower, and that obtained at 0.6V little higher O content than theoretical one for Bi_2O_3.

Acknowledgement
This work was partially supported by the Ministry of Education, Science and Technological Development of the Republic of Serbia (Grants no. TR 34008).

REFERENCES

[1] H. Cheng, B. Huang , J. Lu, Z. Wang, B. Xu, X. Qin, X. Zhang, Y. Dai**,** *Phys. Chem. Chem. Phys.* 2010, **12**, 15468-15475.
[2] V.Fruth**,** M. Popa**,** D. Berger**,** R. Ramer**,** M. Gartner**,** A. Ciulei**,** M. Zaharescu**,** J. Eur. Ceram. Soc. 2005, **25**, 2171-2174.
[3] A.J. Salazar-Pérez, M. A. Camacho-López, R. A. Morales-Luckie, V. Sánchez-Mendieta, F. Ureña-Núñez, J. Arenas-Alatorre, Superficies y Vacío 2005, **18**, 4-8
[4] El-G. Li**,** H.Y. Yip**,** C. Hu**,** P. K. Wong**,** Mater. Res. Bull. 2011, **46,** 153-159.
[5] K. Laurent**,** G. Y. Wang**,** S. Tusseau-Nenez**,** Y. Leprince-Wang**,** Solid State Ionics 2008, **178**, 1735-1739
[6] E.Bartonickova E., J. Cihlar, K. Castkova, , Proc. Appl. Ceram. 2007, **1**, 29–33.
[7] Bagotsky W.S., Fundamentals of electrochemistry, 2nd. ed., Wiley-Interscience, NY 2006.

KINETICS STUDIES OF REACTIVE BLUE 19 DYE ADSORPTION ON NANOSORBENT IRON(III) OXIDE PREPARED BY A MODIFIED LOW TEMPERATURE UREA METHOD

M. D. Radović, M. Kostić, M. Petrović, J. Mitrović, N. Velinov, D. Bojić and A. Bojić

University of Niš, Department of Chemistry, Faculty of Science and Mathematics, Višegradska 33, 18 000 Niš, Serbia. (mk484475@gmail.com)

ABSTRACT

In this work, low-cost non-conventional nanostructured Fe_2O_3 was produced by a modified low temperature urea method (MLTUM-Fe_2O_3). Nanoparticle MLTUM-Fe_2O_3 with bouquet like morphology is found to play as an effective sorbent media to remove textile dye Reactive Blue 19 from textile industries dye effluents. The sorption was analyzed using pseudo-first-order and pseudo-second-order kinetic models and the sorption kinetics was found to follow a pseudo-second-order kinetic model.

INTRODUCTION

One of the most important industries using synthetic dyes is the textile and garment, which produces a strongly colored wastewater, typically with a concentration in the range of 10–200 mg dm^{-3} [1]. Reactive dyes usually have a synthetic origin and complex aromatic structures, making them stable and difficult to biodegrade [2]. Reactive Blue 19 (RB 19) dye is commonly used in the textile and leather industry and may be mutagenic and toxic because of the presence of electrophilic vinyl sulfone groups [3,4]. Therefore, the strategy to eliminate the color and to reduce its effect on the industrial effluents before they are mixed up with natural water bodies is of significant importance.

Various techniques based on the physical, chemical, electrical and biological processes were developed, being used to eliminate reactive dyes from aqueous solutions [5]. Sorption is one of the most powerful and extensively used realistic methods for the removal of various forms of wastewater contaminants [6]. It has been successfully utilized in the decolorization of different classes of dyes from textile wastewater effluents [7]. High efficiency, non-toxic, simplicity and low cost, have made the sorption processes preferable among the other conventional methods, for removal of highly soluble reactive dyes from aqueous solutions.

Hence in the present investigation an attempt was made to test MLTUM-Fe_2O_3 for the Reactive Blue 19 adsorption from the aqueous solution. This study gives a comprehensive account of the adsorption kinetics, which is an essential parameter in the adsorption process because it gives an insight of the time span which is required for the complete saturation of the adsorbent surface.

EXPERIMENTAL

Ferric nitrate $Fe(NO_3)_3 \cdot 9\ H_2O$ (Sigma Aldrich, USA) and urea $(NH_2)_2CO$ (Merck, Germany) with 99% and 99.5% purities respectively, were employed as the starting materials. The dye Reactive Blue 19 (RB 19) was obtained from Sigma Aldrich (USA) and used without further purification.

Iron oxide nanoparticles were synthesized by a modified low temperature urea method. Aqueous solution of the ferric nitrate nonahydrate $Fe(NO_3)_3 \cdot 9\ H_2O$ and urea $(NH_2)_2CO$ with Fe:urea molar ratio 1:2.5 were added to a flask with reflux condenser, which were maintained at 90ºC for 3 h. After that the suspension was cooled to room temperature, filtered and washed with hot deionized water for an effective removal of ions. The final product was dried at 100ºC for 10 h.

RESULTS AND DISCUSSION

Effects of contact time

Results on Fig. 1. indicates the effect of contact time on the removal efficiency and here it is followed that the rapid sorption of RB 19 took place within 5 min (initial dye concentration was 100.0 mg dm^{-3} and sorbent dosage was 0.5 g dm^{-3}). Subsequently, sorption became slow and almost reached to equilibrium within 15 min. However, the experimental data were measured at 180 min to make sure that full equilibrium was attained.

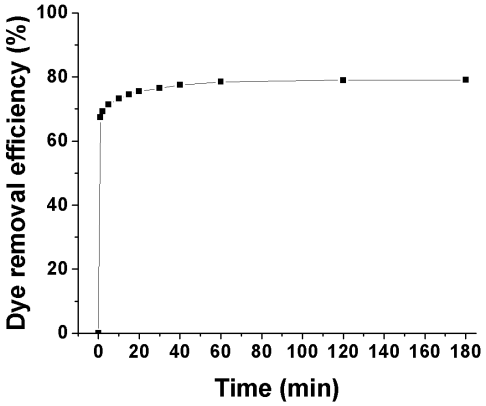

Figure 1. Effect of contact time on RB 19 removal using MLTUM-Fe_2O_3. Initial dye concentration 100 mg dm^{-3}, sorbent dose = 0.5 g dm^{-3}, native pH, temperature = 25 ± 0.5ºC.

Sorption kinetics

The rate of sorption was determined by studying the sorption kinetics at four

different initial RB 19 concentrations (10, 50, 100 and 500 mg dm^{-3}) at optimum sorbent dose. It was observed that RB 19 removal increased with the laps of time and the rate was initially rapid, after which the rate slowed down as the equilibrium approached. For evaluating the sorption reaction kinetics two models are employed, the pseudo-first and pseudo-second order models. The original equations for pseudo-first and pseudo-second order models are presented in detail in paper by Lagergren [8] and Ho and McKay [9]. The values of the kinetic models parameters calculated non-linearly are given in Table 1.

Table 1. Pseudo-first order and pseudo-second order kinetic parameters for the RB 19 dye sorption onto MLTUM-Fe_2O_3.

C_0 (mg dm^{-3})	10	50	100	500
q_e, exp (mg g^{-1})	18.977	89.341	157.224	271.002
Pseudo-first order model				
q_e, cal (mg g^{-1})	18.548	87.576	150.492	259.704
k_1 (min^{-1})	1.092	1.052	1.012	0.801
R^2	0.979	0.993	0.984	0.969
Pseudo-second order model				
q_e, cal (mg g^{-1})	19.139	88.819	153.093	273.015
k_2 (g mg^{-1} min^{-1})	0.110	0.091	0.039	0.004
R^2	0.997	0.998	0.994	0.994

CONCLUSION

The MLTUM-Fe_2O_3 nanoparticles have been synthesized using simple and fast modified low temperature urea method. MLTUM-Fe_2O_3 can be used as potential sorbent for the removal RB 19 from water with a maximum sorption capacity of 271.00 mg g^{-1} for dye at room temperature. It was shown that for initial concentration of RB 19 100.0 mg dm^{-3} equilibrium was reached in 15 min. The kinetic data shows that the present system follows pseudo-second order model.

Acknowledgement
This work was partially supported by the Ministry of Education, Science and Technological Development of the Republic of Serbia (Grants no. TR 34008).

REFERENCES

[1] C. O'Neill, F.R. Hawkes, D.L. Hawkes, N.D. Lourenco, H.M. Pinheiro, W. Delee, J. Chem. Technol. Biot., 1999, **74,** 1009–1018.
[2] S.W. Won, M.H. Han, Y.S. Yun, Water Res., 2008, **42**, 4847–4855.
[3] J.E.B. McCallum, S.A. Madison, S. Alkan, R.L. Depinto, R.U. Rohas Wahl, Environ.Sci. Technol., 2000, **34**, 5157–5164.
[4] M. Siddique, R. Farooq, Z.M. Khan, Z. Khan, S.F. Shaukat, Ultrason. Sonochem., 2011, **18**, 190–196.
[5] E. Forgacs, T. Cserhati, G. Oros, Environ. Int., 2004, **30**, 953–971.
[6] A. Dabrowski, Adv. Coll. Interface Sci., 2001, **93**, 135–224.
[7] T. Robinson, G. McMullan, R. Marchant, P. Nigam, Bioresour. Technol., 2001, **77**, 247–255.
[8] S. Lagergren, Kungliga Svenska Vetenskapsakademiens, Handl., 1898, **24**, 1–39.
[9] K.Y. Ho, G. McKay, K.L. Yeung, Langmuir, 2003, **19,** 3019–3024.

MODELING OF INTERGRANULAR MICRO-CAPACITANCE AS A FUNCTION OF NECK GROWTH DURING CERAMIC SINTERING

Z. Nikolić

University of Niš, Faculty of Electronic Engineering,
Aleksandra Medvedeva 14, 18000 Niš, Serbia. (zoran.nikolic@ni.ac.rs)

ABSTRACT
In this paper, the time-dependent intergranular micro-capacitance model based on domain methodology of regular shape and neck growth kinetics model is defined.

INTRODUCTION
Control of ceramics processing involves the raw materials used as well as the way in which they are formed and heat-treated. Sintering is widely used for consolidation of ceramics materials due to low sintering temperatures, relatively fast densification and homogenization, and high final densities which are the main advantages of this production method. Densification is based on rearrangement and shape change of solid grains.

For electronic materials design, material structure is very important. Ceramics' microstructures show that the contact region between two interacting grains can be defined as impedance with capacitance dominant [1]: approximately two contacted grains make a structure that forms a micro-capacitance, where both intergranular structure and electrical properties of ceramics depend on diffusion processes. In the paper [2] the equivalent intergranular impedance of an aggregate of grains is defined. This approach is based on the micro-capacitance of the planar capacitor formed in the contact region between two grains. The lack of this model was the over-estimated micro-capacitance due to time-dependent distance between capacitor plates, i.e. the dielectric thickness.

The purpose of the present paper is to determine new relationship between electrical, geometrical and diffusion parameters important for micro-capacitance model definition.

THEORETICAL MODEL
Sintered materials are characterized by a connected microstructure composed of solid grains. For simulation of such a structure it is convenient to use grain model of regular shape because it needs to store only the

position and size of the grain, $G^m = (x_o^m, y_o^m, R_m)$, where (x_o^m, y_o^m) is the center of the mass of *m*-th grain of radius R_m in two-dimensional space.

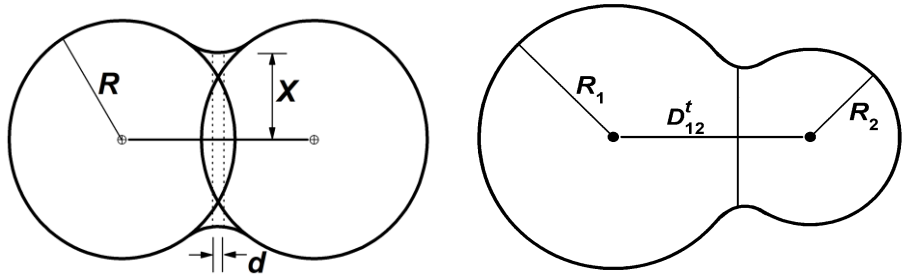

(a) (b)

Figure 1. Scheme of micro-capacitor (a) and sintering kinetics model (b).

It is convenient to assume that if loose powder particles are brought into contact, inter-atomic forces cause small circles-of-contact (necks) to form between them. The kinetics of this stage of sintering can be obtained by equating the mass transported from the materials source and change in the neck volume.

We will used an idealized microstructure of two touching grains to describe neck formation during the initial stage of sintering. The neck between the grains forms as soon as the sintering begins. The neck growth continues until it about 40-50% of the grain size [3]. Kang assumed the maximum neck size to be about 20% of the grain size [4].

We will assume that the contact region (*x* is the neck radius) can be approximately treated as micro-capacitor having dielectric thicknesses *d* (Fig. 1a), whose capacitance changes as the neck grows and the grains approaching each other, by diffusion. Since the contact surface is the circle of the area πx^2, the intergranular micro-capacitance per grain contact can be defined as $\mu C_{IG} = \varepsilon_o \varepsilon_r (\pi x^2 / d)$, where ε_o and ε_r are the dielectric constants of vacuum and the ceramic material, respectively.

The basic sintering kinetics can be obtained using an idealized two-grain sintering model (G^1 and G^2) and the equation $\Delta D/\Delta t = f(D)$, where ΔD is the decrease in center-to-center distance defined as the Euclidean distance function $D(G^1, G^2) = \sqrt{(x_o^2 - x_o^1)^2 + (y_o^2 - y_o^1)^2}$, Δt is the time step and $f(D)$ is the particular neck growth law. Assuming that at time $t + \Delta t$ the decrease of link length is $\Delta D_{ki}^{t+\Delta t} = D_{ki}^t - D_{ki}^{t+\Delta t}$ and with flat grain boundary (Fig. 1b), the intergrain distance D_{ki}^t between a pair of vertices C^k and C^i

can be updated by transformation $D_{ki}^{t+\Delta t} \mapsto D_{ki}^{t} - f(D_{ki}^{t}) \cdot \Delta t$. The simulation of neck growth will be based on the concept that sintering law $f(\bullet)$ and defined transformation can be applied within given time domain.

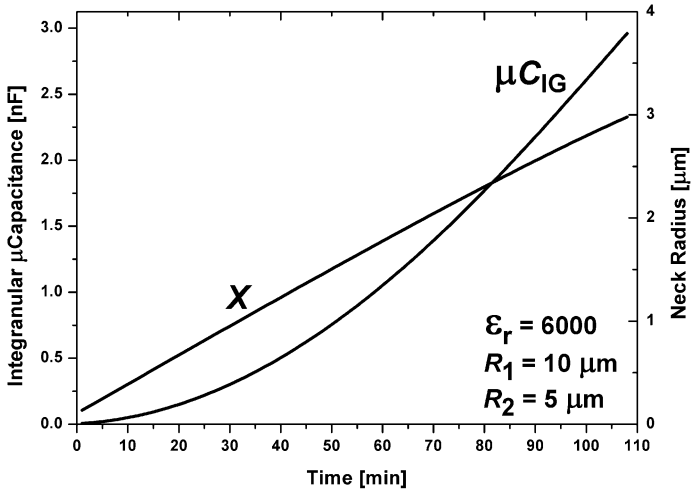

Figure 2. Time-dependent intergranular μCapacitance for two-grain model.

RESULTS AND DISCUSSION

The simulation method considered here provides an effective methodology for computation of intergranular micro-capacitance. In our approach the grain boundary as a transition region in which some atoms are not exactly aligned with either grain will be viewed as capacitors' dielectric. It needs to be pointed out here that grain boundaries in real materials, which are usually considered to be two dimensional, have a finite thickness (a few lattice parameters in very pure metals to a few hundred angstroms in ceramics, ~0.3-0.5 nm).

Having this in mind, we will apply simulation method for sintering of BaTiO3-ceramics assuming nearly constant dielectric thickness, d = 0.5 nm and constant neck growth rate between grains (relative neck size to grain size of about 0.4 after 1 h at sintering temperature, similar to calculated value from conventional sintering models [5]). Figure 2 shows a typical time-dependent intergranular micro-capacitance obtained for two-grain model with grains of sizes 10 μm and 5 μm. Due to the neck growth, densification manifested by decrease in center-to-center distance occurs, followed by relatively small grain rearrangement. This phenomenon will be more visible in the sintering of multi-grain model where the evolution of intergranular contacts (solid skeleton network) will have to be taken into account.

CONCLUSION

In this paper we have introduced a new model for predicting an evolution of intergranular micro-capacitance during ceramic sintering. The model does not need special geometric assumptions because the microstructural development can be simulated by a set of simple local rules and overall neck growth law which can be arbitrarily chosen. Even more, computer-based approach extended to multi-grain model can be used to enable establishment of interrelation between structural and electrical parameters, as well as to assist in the creation, modification, analysis and optimization of new high-performance electronic ceramics materials.

REFERENCES

[1] J. Daniels, K.H. Hardtl and Wernicke, The PTC effect of barium titanate, Philips Technical Review 38, (3) (1978/79) 73-82.
[2] Z.S. Nikolic, V.V. Mitic and I.Z. Mitrovic, TELSIKS '99, Proc. of 4th International Conference on Telecommunications in Modern Satellite, Cable and Broadcasting Services, Vol. 2, 1999, 673-676.
[3] M.N. Rahman, Sintering of Ceramics. NY: CRC Press, 2007.
[4] S.-J. L. Kang, Sintering - Densification, grain growth and microstructure. Burlington, MA: Elsevier, 2005.
[5] R.M. German, 1994 Powder Metall. Sci. (Princeton: Metal Powder Industry Federation).

EFFECT OF ANNEALING TEMPERATURE ON STRUCTURAL PROPERTIES OF TiO_2–CeO_2 POWDERS

Lj.Rožić[1], S. Petrović[1*], D. Lončarević[1], S. Stojadinović[2], V. Jović[3] and J. Lamovec[3]

[1]*University of Belgrade, IChTM–Department of Catalysis and Chemical Engineering, Njegoševa 12, Belgrade, Serbia*
[2]*University of Belgrade, Faculty of Physics, Studentski trg 12–16, 11000 Belgrade, Serbia*
[3]*University of Belgrade, IChTM–Centre of Microelectronic Technologies, Njegoševa 12, Belgrade, Serbia*

*corresponding author: srlepp@nanosys.ihtm.bg.ac.rs

ABSTRACT

In this study, TiO_2–CeO_2 powders were synthesized via a high energy ball milling process. These samples were heat treated in air at the temperature range of 500–800 °C. The effect of post-annealing temperature was studied on various structural parameters. The presented results showed that the annealing temperature accelerates the grain growth and transformation from anatase to the rutile phase. The fraction of rutile phase remarkably increases from 24 to 49.6% after annealing at 700 °C. Also, considering all the reflections of the anatase phase the lattice strain ranging from c = 9.433 to c = 9.535 is calculated, suggesting that microstrain decreases when annealing temperature increases. Overall, the temperature programmed desorption (TPD) results showed that the surface of TiO_2–CeO_2 powder annealed at 500 °C possesses redox, strong and mild Lewis acid sites in the close vicinity.

INTRODUCTION

TiO_2 is one of the most promising catalysts to initiate photocatalytic reactions, owing to its optical properties, strong oxidizing power, high stability, corrosion resistant, and environmentally benign nature as compared to other photocatalysts [1]. The structural and microstructural, morphological and photocatalytic properties of TiO_2 nanocrystals are strongly dependent on the synthesis process and calcination temperature [2]. The temperature of anatase to rutile phase transition is around 600 °C, depending on different factors such as defects, impurities and grain size. In order to control crystallinity of TiO_2 thermal treatment is usually applied but

the temperature must be carefully selected. The accommodating of CeO_2 into the TiO_2 framework not only enhances the thermal stability of the ordered mesoporous structure but also effectively extends the photoresponse of TiO_2 to the visible light region.

This work focuses on the effect of annealing temperature on the microstructural and structural properties of TiO_2–CeO_2 powders. The commercially pure TiO_2 and CeO_2 were first milled at room temperature to obtain the TiO_2–CeO_2 powder, followed by annealing at different temperatures for 2 h. By combining two analytical techniques (XRD and TPD), we determined the correlation between the change of phase composition, crystallite growth, and structural properties with annealing temperature.

EXPERIMENTAL

The results of our previous investigations have dealt with modelling and optimization process parameters of a high energy ball milling of TiO_2 and CeO_2 by a response surface methodology [3]. The experiment was conducted with three dimensionless independent parameters (TiO_2:CeO_2 weight percentage ratio, milling speed and time) which were chosen as variables and the photodegradation efficiency as dependent output response variable. The obtained model equation was used for optimization of parameters. The optimum condition to obtain the TiO_2–CeO_2 powders with highest photodegradation efficiency were as follows: TiO_2:CeO_2 weight percentage ratio 71:29, milling speed 200 rpm, and milling time 115 min. TiO_2–CeO_2 nanocrystalline powders were synthesized in the absence of solvent via the mechanochemical process using a high energy ball mill (Fritsch planetary mill Pulverisette 7 premium line). Milling was done at atmospheric conditions in a silicon nitride vial using silicon nitride balls with keeping powder to ball mass ratio at about 1:10 throughout the experiment. The prepared sample at optimal condition was subsequently annealed at the desired temperature (500, 600, 700 and 800 °C) for 2h.

The phase structure of samples was analyzed by X-ray diffraction method, using a Rigaku Ultima IV diffractometer in Bragg-Brentano geometry, with Ni-filtered CuKα radiation (40 kV, 30 mA, λ =1.54178 Å). The structural and microstructural parameters of the TiO_2–CeO_2 samples were estimated by the Williamson-Hall (WH) plot.

Temperature programmed desorption (TPD) of methanol was performed on Thermo Scientific 1100 TPDRO instrument coupled with Thermo Star GSD320 mass spectrometer. For TPD experiments, the samples were heated in argon flowing at 20 mL/min at temperature ramping rate of 5°C/min.

RESULTS AND DISCUSSION

The investigation of the crystal structure and identification of specific phases within the TiO_2–CeO_2 nanocrystalline powder were carried out by XRD. From the XRD patterns (Figure not shown), it is evident that all samples are mainly composed of anatase and rutile phases of TiO_2 and cubic CeO_2 phase. After annealing from 500 to 800 °C all diffraction peaks become more intensive, which is related to crystallization and grain growth. Also, it was found that the crystallite size of anatase phase increase from 15.2 to 22.8 nm with increase annealing temperature from 500 to 600 °C, which is believed to be mainly due to the coalescence of neighbouring crystallites resulting in an overall higher value of crystallinity. Over the same annealing temperature range, the microstrain decreased from 0.12 to 0.07%, see Fig. 1.

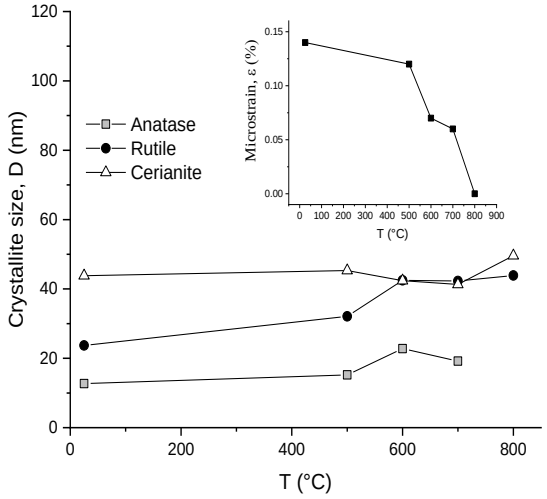

Figure 1. Variation of the grain size with the annealing temperature. Insert: variation of the microstrain with the annealing temperature

On further increase of annealing temperature to 700 °C, the crystallite size decreased to 19.2 nm, which can be attributed to degrade the crystallinity. At TiO_2–CeO_2 nanocrystalline powder annealed up to 700 °C, relaxation in strain was observed. Also, it is observed that anatase–rutile ratio decreases with annealing temperature.

As displayed in Fig. 2, desorption of molecularly adsorbed methanol takes place at the temperature lower than 110 °C while methoxy groups recombine at temperature up to 250 °C or dehydrogenate to formaldehyde. Further, increase in temperature leading to the formation of dimethyl ether at 290 °C, which is formed between two adjacent methoxy groups one adsorbed on strong and other on mild Lewis acid site. At higher temperature (340 °C) the hydro-gen transfer from surface hydroxyl to a methoxy group resulting in methane formation by C–O bond cleavage, and strongly adsorbed dehydrogenating species lead to CO formation.

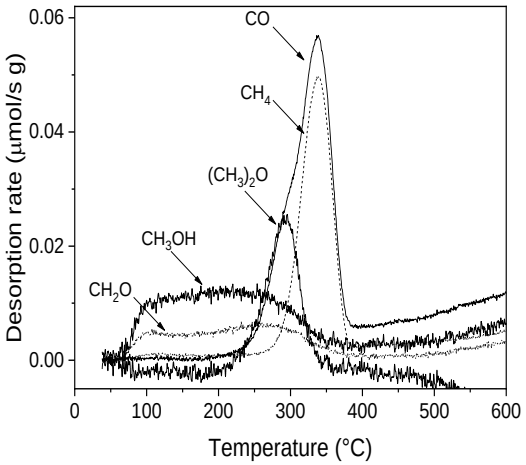

Figure 2. Methanol TPD profile of TiO_2-CeO_2 particles (annealed at 500°C)

CONCLUSIONS

The nanocrystalline TiO_2–CeO_2 powder was prepared by the high energy ball milling process. The XRD analysis revealed that TiO_2–CeO_2 powders mostly consist of anatase and rutile TiO_2 phases and cerium oxides. The rise of annealing temperature caused an increase of crystallite size and anatase–rutile ratio, while microstrain decreases continuously. Methanol TPD product distribution reveals the presence of redox and acid sites at the surface of the catalyst decreasing its number by annealing temperature.

Acknowledgments

This work was supported by the Ministry of Education, Science and Technological Development of the Republic of Serbia (Projects number 172015, 172035, 172001, TR 32 008 and III 45001).

REFERENCES

[1] A. Turolla, A. Piazzoli, J. Farner Budarz, M. Wiesner, M. Antonelli, Chem. Eng. J., 2015, **271,** 260–268.

[2] K. Ralphs, C. Hardacre, S.L. James, 2013, Chem. Soc. Rev., **42**, 7701–7718.

[3] S. Petrović, Lj. Rožić, V. Jović, S. Stojadinović, B. Grbić, N. Radić, J. Lamovec, R. Vasilić, 2018, Adv. Powder Technol., *In Press.*

ANOMALIES OF THE LOW-TEMPERATURE HEAT CAPACITY OF SOME APATITES

E.N. Bulanov, A.V. Knyazev, N.N. Smirnova, M.I. Lelet,
Z. Xu and A.G. Blokhina

Lobachevsky State University of Nizhny Novgorod, Chemical Department,
23 Gagrin av., 603950 Nizhny Novgorod, Russia.
(bulanoven@chem.unn.ru)

ABSTRACT

In present study, we describe new approach to the synthesis of two apatite-structured compounds, which allows for a reduced reaction time and temperature. Using X-ray diffraction measurements, we have refined the crystal structure of the materials, which shows that its compositions of apatites may be described as $Ca_{8.30}Bi_{1.70}(PO_4)_6O_{1.85}$ and $Ba_5(MnO_4)_3Cl$. The heat capacities of apatites were measured by precision adiabatic vacuum calorimetry over the temperature range from T = 6 to 348 K. Possible causes of the abnormal increase on the heat capacity curve in the low-temperature region are discussed.

INTRODUCTION

Apatites have general formula $A^F_2A^T_3(BO_4)_3X$ (Z=2), where A are mono- (Na, K, etc), di- (Ca, Sr, Ba, etc), tri- (Ln, Y), or tetravalent (Th, U) cations in various combinations; B are tetravalent (Si, Ge), pentavalent (P, As, V, Cr, Mn), or hexavalent (S) ions; and X are usually halogens, hydroxyl, or oxygen. Due to one of the highest isomorphic capacity among all mineral types apatite materials can be applied in different areas of industry [1].

One of the most topical field of using apatite materials is in biomaterials applications because substituted hydroxyapatite is the main mineral component of natural bones and teeth of mammals. Nowadays, hydroxyapatite-based materials are existing in different forms: from powders to ceramics [2]. To improve biological activity of apatite-based materials chemical substitutions can be utilised. Such examples can be derived by the incorporation of bismuth and antimony in apatite structure, which are well known as antimicrobial agents. There are however few reported examples in this field, and most investigations were concentrated on the antimicrobial properties and cytotoxicity of such materials. However, in order to solve real practical and technological problems, there has to be data on the physico-chemical characteristics of the materials in addition to deriving information on the

properties of matter useful from the point of view of materials science. The lack of such information makes it difficult to create new functional materials due to the difficulty of predicting the physical behaviour of this substance in the process of practical application. Apatites with Mn^{+5} and Cr^{+5} in B position are usually used as a chemical basis of inorganic pigments due to their intensive green (or blue in some solid solutions) color [3]. There are only two individual apatites with $(MnO_4)^{3-}$ tetrahedral ion: $Ba_5(MnO_4)_3F$ and $Ba_5(MnO_4)_3Cl$. A limited number of phases for the M^{+5} is associated with a number of reasons. First, the existence of manganese in the oxidation state +5 is possible only in oxocompounds in tetrahedral coordination. Secondly, the production of manganese in this oxidation state is possible only in an alkaline medium, which excludes disproportionation to more stable oxidation states (+2, +4, +6, +7). As a result, for the Mn-containing compounds of the apatite structural type a narrow crystal-chemical region of existence will be characteristic.

EXPERIMENTAL

Synthesis

Samples were synthesized via solid state reactions in accordance with following equations:

$$1.7\cdot Bi(NO_3)_3\cdot 5H_2O + 8.3\cdot Ca(NO_3)_2\cdot 4H_2O + 6\cdot (NH_4)_2HPO_4 \rightarrow$$

$$\rightarrow \mathbf{Ca_{8.30}Bi_{1.70}(PO_4)_6O_{1.85}}\ (Z=1) + \text{gases}$$

(reaction mixture was calcined at 573K, then the temperature was increased to 1223 K with 100 degrees step)

$$4.5\ BaCO_3 + 3\ MnO_2 + 0.5\ BaCl_2\cdot 2H_2O + 0.75\ O_2 \rightarrow \mathbf{Ba_5(MnO_4)_3Cl}\ (Z=2) + \text{gases}$$

(the mixture was heated in five steps: 473 K (2 hours) → 673 K (4 hours) → 773 K (4 hours) → 873 K (4 hours) → 1073 K (6 hours))

Sample Characterization

Phase purity was confirmed by powder X-ray diffraction (PXRD) using a Shimadzu XRD-6000 diffractometer equipped with a CuKα X-ray tube operated at 40 kV and 40 mA. Rietveld refinement of the PXRD data was carried out from 10 to 120° 2θ using TOPAS V3 sofware, using an initial structural model based on the hydroxyapatite crystal structure reported by Saenger *et al.* The elemental composition of the compound was determined by energy dispersive X-ray fluorescence analysis in air using a Wavelength Dispersive X-Ray Fluorescence Spectrometer LAB CENTER XRF-1800 equipped with a thermoelectrically cooled semiconductor detector. The low-temperature heat capacity, $C^{o}_{p,m}$, was determined using adiabatic calorimetry in the temperature range T = 6 to 305/350 K. The measurements were conducted using a AK-9.02/BCT-21-type calorimeter.

RESULTS AND DISCUSSION

Rietveld refinement for Bi-apatite indicated the Bi ions are located at the A^{II} (6*h*) tunnel position, which is a similar finding to other Bi containing apatites ($Bi_2La_8(GeO_4)_6O_3$) and Bi-containing apatite polysomes. The refined cation stoichiometry of $Ca_{8.30}Bi_{1.70}$ gives a slightly lower bismuth content compared to that expected from the experimental procedure, which could indicate a small amount of Bi volatization. However, the refinement procedure assumed a full occupancy of both *A* sites and the presence of cation vacancies on the A^F sites has been observed previously in apatite structure-types. This could be another possible reason for this deviation. Alternatively, the refined cation stoichiometry gives a chemical formula of $Ca_{8.30}Bi_{1.70}(PO_4)_6O_{1.85}$(Z=1), which additionally required the presence oxygen vacancies in the channel oxygen positions to enable charge balancing. Nevertheless, the calculated apatite metaprism twist angle of 21.4° is smaller than that found for un-doped hydroxyapatite (23.2°) and is consistent with an expansion of the apatite channel due to the presence of the larger Bi^{3+} ions (IR - Ca^{2+} = 0.112 nm; Bi^{3+} = 0.117 nm).

For $Ba_5(MnO_4)_3Cl$ structure φ=19.8°, while in literature data it is 22.3. Such difference can be explained by expansion of the apatite channel due to the lack of the larger Mn^{+2}-atoms, which can exist in the example due to features of the synthesis (as a consequence of the process of Mn disproportionation). Cations in 6*h* position may have different coordination number from 7 to 9. As for Ba-apatites in all available structures coordination number is 8. In our case coordination number of Ba in 6*h* position is 8 too and its polyhedron may be described as strongly distorted two-caped trigonal prism BaO_6Cl_2 with C_v symmetry. BaO_6Cl_2 polyhedrons with MnO_4 tetrahedrons form layers orthogonal to crystallographic axis *c*.

Figure 1. show an increase of the heat capacity of both apatites at temperatures below 8 K (experiment values of values of heat capacity may be found in [5-6]). Such effects have been previously observed and described for compounds with perovskite type structures: for example, $Gd_2SrCo_2O_7$, $NaGdTiO_4$ and $Na_2Gd_2Ti_3O_{10}$ [4]. This anomaly has been previously attributed to the spin ordering of the magnetic ions Gd^{3+} or Co^{3+} where the materials display magnetic disorder-order phase transitions in the low temperature region. This reason can be used to explain a heat capacity anomaly in $Ba_5(MnO_4)_3Cl$.

For the most Bi-containing compounds there were not fixed any anomalies in the low temperature range of heat capacity with the exception of the ferrite structured $BiFeO_3$ which was observed to display similar features. The increase in heat capacity below 8 K is explained by the bismuth phonon contribution or alternatively an effect from the

stereochemically active $6s^2$ lone pair electrons, which will exclusively dominates in the low-temperature lattice heat capacity. Moreover, the contributions to the heat capacity are dictated by the phonon modes in the ~0–1 THz frequency region at 5 K.

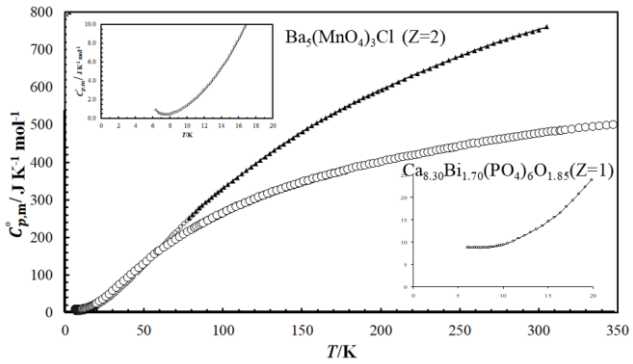

Figure 1. Temperature dependence of heat capacities of apatites under study.

CONCLUSION

Thus, in presented work it was shown for the first time that there can be phase transitions in apatites at the low temperatures, which require further structural and spectroscopic research. The presence of Mn^{5+} ion in the structure of $Ba_5(MnO_4)_3Cl$ is the most probable reason. The heat capacity of $Ca_{8.30}Bi_{1.70}(PO_4)_6O_{1.85}$ displays an anomaly in low-temperature region similar to other Bi-containing materials. Crystal structures of both apatites were refined using Rietveld method in $P6_3/m$ space group.

Acknowledgement

The work was performed with the financial support of the Russian Foundation for Basic Research (Project Number 16-33-601721 мол_а_дк).

REFERENCES

[1] J.F. Rakovan, J.D. Pasteris. Elements.11 (2015) 195-200.
[2] S.V. Dorozhkin. Ceramics International. 42 (2016) 6529-6550.
[3] E.A. Medina, J. Li, J.K. Stalick, M.A. Subramanian, Solid State Sci, 2016, 52, 97-105.
[4] A.V. Markin, A.M. Sankovich, N.N. Smirnova, I.A. Zvereva, J. Chem. & Engin. Data, 2015, 60 (11), 3069–3076.
[5] E.N. Bulanov, K.S. Korshak, M.I. Lelet, A.V. Knyazev, T. Baikie, J. Chem. Thermodyn., 2018, 124, 74-78.
[6] A.V. Knyazev, E.N. Bulanov, N.N. Smirnova, K.S. Korshak, Z. Xu, J. Chem. Thermodyn., 2018, Under Review.

SYNTHESIS AND HIGH-TEMPERATURE POLYMORPHISM OF DION-JACOBSON PHASE $KCa_2NaNb_4O_{13}$

O.V. Krasheninnikova, A.V. Knyazev, E.V. Syrov and G.A. Borisov

Lobachevsky State University of Nizhni Novgorod, Gagarin Prospekt 23/2, 603950 Nizhni Novgorod, Russia
(knyazevav@gmail.com)

ABSTRACT

Dion – Jacobson type layered perovskite phase $KCa_2NaNb_4O_{13}$ was sintered using 3 different methods. Thermal expansion behavior and phase transition of the compound were studied using high-temperature X-ray diffraction (HTXRD). Thermal stability of the phase was studied via differential thermal analysis (DTA). It was found that orthorhombic $KCa_2NaNb_4O_{13}$ transforms into tetragonal modification between 1000 and 1100 °C.

INTRODUCTION

Layered perovskites are gaining much attention recently, mostly because of their photocatalytic properties and ion-exchange abilities. Dion – Jacobson family of phases, first described by Dion et al. [1], is one of the layered perovskites families (among Aurivillius $(Bi_2O_2)[A_{n-1}B_nO_{3n+1}]$ and Ruddlesden – Popper $A_2[A_{n-1}B_nO_{3n+1}]$ [5] families). It can be described with general formula $A'[A_{n-1}B_nO_{3n+1}]$, where A' = (Li^+, Na^+, K^+, Rb^+, Cs^+, H^+, Ag^+, NH_4^{+}), A = (Ca^{2+}, Sr^{2+}, Ba^{2+}, Bi^{3+}, Ln^{3+}) and B = (Nb^{5+}, Ta^{5+}, Ti^{4+}). A Dion – Jacobson structure consists of *n* perovskite-like layers alternating with an A' cation in the interlayer space.

A $KCa_2NaNb_4O_{13}$ compound is a n=4 member of $K[Ca_2Na_{n-3}Nb_nO_{3n+1}]$ ($3 \le n \le 7$) series of Dion – Jacobson phases, first described by Jacobson et al [2]. This series was studied by different groups of authors for its dielectric [3] and ion-exchange [4] properties for photocatalytic use. In particular, Dion – Jacobson thin films with high dielectric constant (ε_r) can be used for multilayer chip capacitors, tunable devices, and random-access memory devices. On the other hand, suitable band gap energies (3-4 eV for different members of the series) allows to use Dion – Jacobson exfoliated nanosheets for water splitting under UV and visible irradiation.

Despite the fact that ferroelastic phase transition at 1000 °C was found for n=3 member of series $KCa_2Nb_3O_{10}$ [5], no further high-temperature investigations were conducted for series members with n>3. Therefore,

high-temperature investigations of the next member of the series, $KCa_2NaNb_4O_{13}$, were undertaken to fill this gap.

EXPERIMENTAL

The $KCa_2NaNb_4O_{13}$ compound was synthesized using 3 different solid-state chemistry routes:

1) Conventional solid state reaction between stoichiometric quantities of K_2CO_3, $CaCO_3$, Na_2CO_3 and Nb_2O_5 (50% mol. excess of K_2CO_3 was added due to volatilization) at 1200 °C.

2) Synthesis by «adding the layer»: reaction between n=3 $KCa_2Nb_3O_{10}$ and $NaNbO_3$ 1200 °C:

3) Synthesis by «melt solution» technique: reaction (1) at 1000 °C, but taking place in large amount of melted KCl flux [6].

SEM images of the sample were obtained using JEOL JSM-IT300LV microscope with Oxford Instruments Ultim EDS attachment*****. X-ray phase analysis and high-temperature X-ray diffraction measurements were carried out using PANalytical Empyrean diffractometer with Anton Paar HTK 1200 high-temperature camera attachment. The radiation is Cu $K\alpha_{1,2}$, 2θ range – 5-60 ° with 0.02° step, temperature range – 25-1100 °C with 100 °C step. Indexing was performed using Appleman-Evans algorithm [7]. Thermal expansion coefficients were calculated using DTC software [8]. Figures of thermal expansion were plotted using KTR-B2 algorithm [8]. DTA studies were performed using Shimadzu DTG-60H differential thermal analyzer in the temperature range of 25-1200 °C.

RESULTS AND DISCUSSION

The X-ray phase analysis of 3 obtained samples of $KCa_2NaNb_4O_{13}$ showed that only conventional solid-state reaction (1) product had no secondary phases or major impurities. The others had significant signs of $NaNbO_3$ and $KNbO_3$ impurities. Therefore, all further investigations were conducted on the first sample. SEM images show huge variety of the particles sizes (Fig.2). Energy-dispersive X-ray spectroscopy confirmed the composition to be approximately K:Ca:Na:Nb = 1:2:1:4. High-temperature X-ray analysis showed that thermal expansion of the sample is stable in the temperature range of 25-1000 °C (Fig.1 a), but after 1000 °C, XRD pattern changes (Fig.1 b) and the abrupt changes of unit cell parameters occurs, which are indications of the phase transition. Although $KCa_2NaNb_4O_{13}$ symmetry was identified as orthorhombic, its structure is not yet refined, and there is no data of its space group and atomic coordinates in literature. On the other hand, the $RbCa_2NaNb_4O_{13}$ structure was defined as tetragonal with P4/mmm space group and its XRD pattern (Fig.1 c) is matching well

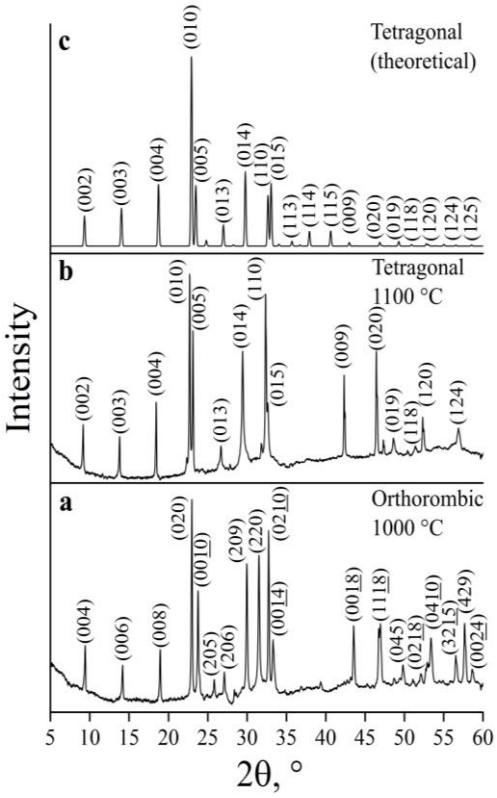

Figure1. XRD patterns of a) orthorhombic $KCa_2NaNb_4O_{13}$ at 1000 °C
b) tetragonal $KCa_2NaNb_4O_{13}$ at 1100 °C
c) theoretical XRD pattern of P4/mmm $RbCa_2NaNb_4O_{13}$

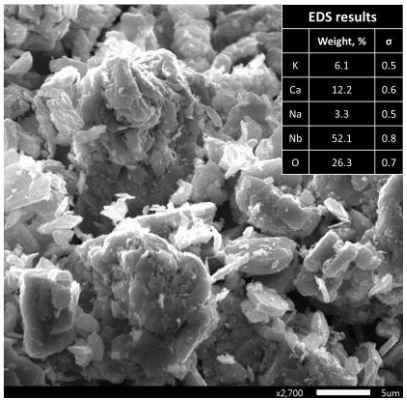

Figure 2. SEM image of $KCa_2NaNb_4O_{13}$ sample obtained by the first method (with EDS measurement results)

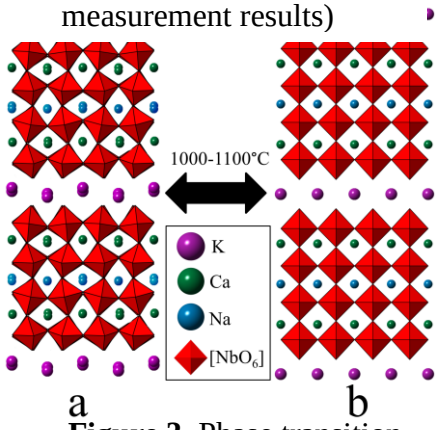

Figure 3. Phase transition between a) *proposal* orthorhombic structure and b) P4/mmm structure of $KCa_2NaNb_4O_{13}$

$KCa_2NaNb_4O_{13}$ one after phase transition. The unit cell parameters of $KCa_2NaNb_4O_{13}$, obtained through indexing (a= 7.749, b= 7.730, c= 37.38 Å), are twice as big as Rb-phase ones (a= 3.872, b= 3.872, c= 18.91 Å).

This led us to assume that the nature of discovered phase transition is transforming from orthorhombic 2x2x2 supercell type structure to tetragonal P4/mmm structure (Fig.3). The reason for K-phase structure derivation from the ideal structure is interlayer ion with a smaller radius. The smaller radius ion leads to shortening of an Nb-O bond located towards interlayer ions, and NbO_6 octahedra distortion. Moreover, the stacking of adjusted layers for

A'=K Dion – Jacobson phases is displaced by translating by 1/2 along the *a* axis, and it gives even more distortion to the structure (Fig.3 a). It is known that K ions in many oxides have the great capability of forming into a trigonal prismatic coordination [9]. On the contrary, Rb in $RbCa_2NaNb_4O_{13}$ is forming regular tetragonal coordination. Therefore, in order to transform the structure in the process of phase transition, interlayer Nb-O bond in octahedra should be shortened and adjusted layers' stacking should be translated back from its displacement. The phase transition temperature for *n*=4 phase is, as expected, slightly higher than 1000 °C for *n*=3 phase.

DTA studies of $KCa_2NaNb_4O_{13}$ showed no derivations from the baseline in the temperature range 25-1200 °C. It proves that discovered phenomenon is second-order phase transition.

CONCLUSION

Therefore, synthesis and thermal studies of *n*=4 Dion – Jacobson compound $KCa_2NaNb_4O_{13}$ were conducted. Conventional solid state reaction was chosen as an optimal synthesis strategy due to the purest reaction product. Second-order phase transition from orthorhombic 2x2x2 supercell modification to tetragonal P4/mmm modification at 1000-1100 °C was studied using high-temperature X-ray diffraction method. Descriptive mechanism for such phase transition was proposed. Thermal stability of $KCa_2NaNb_4O_{13}$ was studied up to 1200 °C using DTA.

REFERENCES

[1] M. Dion, M. Ganne, M. Tournoux, Mat. Res. Bull., 1981, 16, 1429 – 1435
[2] A.J. Jacobson, J.W. Johnson, J. T. Lewandowski, Inorg. Chem., 1985, 24 (23), 3727 – 3729
[3] B. Li, M. Osada, Y. Ebina, T. Ozawa, R. Ma, T. Sasaki, Appl. Phys. Lett., 2010, 96, 182903(1)-182903(3)
[4] Y. Ebina, K. Akatsuka, K. Fukuda, T. Sasaki, Chem. Mater., 2012, 24, 4201 – 4208
[5] S. Guertin, E. Josepha, D. Montasserasadi, J. Wiley, J. Alloys Compd., 2015, 647, 370 – 374
[6] N. Kulischow, C. Ladasiu, R. Marschall, Catal. Today, 2017, 287, 65 – 69
[7] H. Evans, D. Appleman, S. Handwerker, Amer. Crystallogr. Ass. Meeting, 1963, 3
[8] R. Belusov, S. Filatov, Phys. and chem. of glass, 2007, 33, №3, 377 – 382.
[9] M. Sato, J. Abo, T. Jin, M. Ohta, J. Alloys Compd, 1993, 192, 81 – 83

***** – The study was carried out on the equipment of the Collective Usage Center «New Materials and Resource-saving Technologies» (Lobachevsky State University of Nizhny Novgorod).

POLYURETHANE/FERRITE NANOCOMPOSITES: PREPARATION AND PHYSICAL PROPERTIES

I. D. Kodranov[1], B. P. Dojčinović[2], B. Antić[3], D. D. Manojlović[1], M. Ognjanović[3] and M. V. Pergal[2*]

[1]Faculty of Chemistry, University of Belgrade, Studentski trg 12-16, Belgrade, Serbia
[2]Institute of Chemistry, Technology and Metallurgy, University of Belgrade Njegoševa 12, Belgrade, Serbia; (marijav@chem.bg.ac.rs)
[3]The Vinca Institute of Nuclear Sciences, University of Belgrade, POB 522, Belgrade, Serbia

ABSTRACT

In the present study, polyurethane/ferrite composites (PU-NFs) were prepared using silver ferrite, copper ferrite and zinc ferrite (1 wt.%) by *in situ* two-step polymerization in solution. PU-NFs based on poly(dimethylsiloxane) as soft segment and hyperbranched polyester of the second pseudo generation/4,4′-methylenediphenyl diisocyanate as the hard segment were prepared with constant soft segment content (60 wt.%). The prepared PU-NFs and PU network (sample without nanoferrites) were characterized by FTIR, DSC and TG analyses. The glass transition of the hard segment (T_{gHS}) of PU-NFs was similar to T_{gHS} value of the unfilled PU network. The results showed that PU-NFs had better thermal stability than pure PU network.

INTRODUCTION

Polyurethanes (PUs) with poly(dimethylsiloxane) (PDMS) as a soft segment play important role in special technical and medical applications because of many unique properties of PDMS, including low glass transition temperature, low surface energy, good biocompatibility, excellent thermal stability, ultraviolet resistance and high permeability to many gases. The use of dendritic polymers (dendrimers and hyperbranched polymers) as a crosslinking agent in the synthesis of polyurethanes attracted a great deal of interest in recent years, due to their specific properties compared to analogue linear polymers [1,2]. Hyperbranched polymers have similar structure and performance as the dendrimers, and could be synthesized easily, so they have been paid more attention. Nanoparticles (nanotubes, nanospheres, nanofillers nanoflaks, nanorods and nanoplatelets) can make a

drastic change in physio-chemical properties of polyurethanes. The combination effect of nanofillers and polymer matrix has created a great interest towards researchers. Biocompatible magnetic nanoparticles, i.e. ferrites possess some unique characteristics, such as uniform size distribution, less agglomeration and stability in the biological medium. Nanocomposite materials based on PU and ferrite are important in the field of biomaterials due to their good mechanical and biocompatible properties. In this work, the influence of the different type of ferrites (content 1 wt.%) on the structure and thermal properties of prepared materials, was investigated.

EXPERIMENTAL

The polyurethane/ferrite nanocomposites were prepared by *in situ* two-step polymerization in solution (NMP/THF) using α,ω-dihydroxy-ethylene oxide-poly(dimethylsiloxane)-ethylene oxide (PDMS; ABCR; M_n = 1000 g/mol), 4,4′-methylenediphenyl diisocyanate (MDI; Sigma-Aldrich) as monomers and hyperbranched polyester of the second pseudo generation (BH-20; Boltorn®) Polymer Factory; M_n = 1780 g/mol, functionality f_{nOH} = 16) as crosslinking agent. For comparison purposes, polyurethane network without ferrite was also synthesized using the same procedure. Complete preparation procedure of the PU-NF films are described in our previous papers [1,2]. Nano ferrites (MFe_2O_4; M = Zn, Cu and $Cu_{0.5}Zn_{0.5}$) were prepared by co-precipitation with microwave-hydrothermal method. FTIR spectra were recorded on ATR Nicolet 380 spectrometer. Differential scanning calorimetry (DSC) was carried out on a DSC Q1000V9.0 Build 275 thermal analyzer. The DSC scans were recorded under a dynamic nitrogen atmosphere (50 cm^3/min), in the temperature range from -90 to 230 °C, at a heating and cooling rate of 10 and 5°C/min, respectively (two scans were run for each sample) using the so-called triple cycle of heating−cooling−heating to determine the glass transition temperature. The thermal stability of the PU-NFs and pure PU was determined by thermogravimetric (TG) analysis, using TGA Q500 V6.3 Build 189 instrument, at heating rate of 10 ºC/min under a nitrogen atmosphere.

RESULTS AND DISCUSSION

The present study made an attempt to prepare polyurethane/ferrite nanocomposites. The prepared nanocomposites and pure PU network were characterized by FTIR for structural confirmation. The characteristic stretching frequencies of the prepared PU-NFs and pure PU network appeared at 3320−3450 cm^{-1} (ν_{N-H}), 2960, 2945, and 2865 cm^{-1} (ν_{sym} and ν_{asym} of C−H), 1645−1735 cm^{-1} ($\nu_{C=O}$), 1535 and 1260 cm^{-1} (ν_{C-N} + δ_{N-H},

i.e., amide II and amide III bands), 1016 and 1080 cm^{-1} ($\nu_{Si-O-Si}$ and ν_{C-O-C}), 1597 and 1415 cm−1 ($\nu_{(C=C)arom}$), and 790 cm^{-1} (ρ_{C-H} in $SiCH_3$). The absorption bands belonging to the isocyanate (2270 cm^{-1}) and hydroxyl groups (3300 cm^{-1}) were not detected in the FTIR spectra of the prepared PU-NFs and pure PU network, indicating their complete conversion during the reaction. In FTIR spectra of PU-NFs, the peaks at 490 and 580 cm^{-1} are due to the stretching vibration of M-O band in the tetrahedral and octahedral sites, respectively. The peak at 490 cm^{-1} can be assigned to the Zn-O, Cu-O or $Cu_{0.5}Zn_{0.5}$-O band, while 534 cm^{-1} is related to the Fe-O band. Based on DSC measurements in the investigated temperature region, only the glass transition temperature of hard segments (T_{gHS}) was observed. The T_{gHS} value was in the range from 20.8 to 21.58 °C and for pure PU it was 21.20 °C (Table 1). The results showed that addition of ferrite to the PU matrix have no influence on T_{gHS} value of prepared nanocomposites. T_{gHS} value was higher for pure PU and its nanocomposites as compared to BH-20 (T_g 4.6 °C). This is attributed to the presence chemical cross-linking that restricts the molecular motion of the polymer chains and leads to the increase in T_{gHS}.

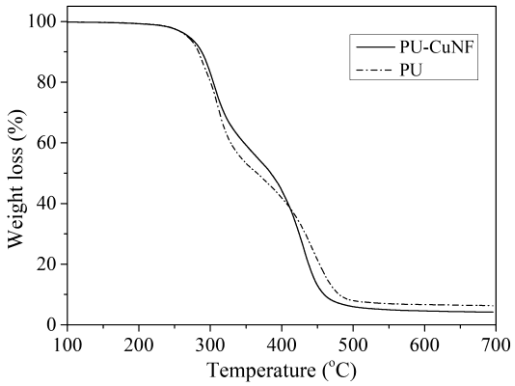

Figure 1. TG curves of PU-CuNF and pure PU

Fig. 1 presented the typical TG curves of pure PU and selected PU-CuNF film, while in Table 1 characteristic temperatures of thermal degradation and temperatures of derivative TG (DTG) peaks are listed. The $T_{10\%}$ value is considered to represent the beginning of degradation of the PU-NFs and pure PU. Thermal degradation of PU-NFs starts between 283 and 285 °C, while that for pure PU sample starts at 279 °C. Thermal stability of the prepared PU-NFs was improved with addition of the nanoferrites as compared to pure PU network. The results showed that thermal stability for all PU-NFs was similar. DTG curves (Table 1) of PU-NFs and PU sample displayed four degradation stages. The first weigh loss stage, from 300 to 309 °C for PU-NFs, is possibly attributed to the degradation of urethane bonds in the hard segment of the PU matrix. The second, third and fourth weigh losses occurred from 304 to 376 °C and from 389 to 399 °C, and from 428 to 445 °C, respectively, which is due to the degradation of the ester, the ether and the PDMS components of the PU.

Table 1. The soft segments content (SSC), glass transition temperature of the hard segment (T_{gHS}), determined by DSC, and characteristic temperatures of thermal degradation of PU-NFs and pure PU

Sample	SSC, wt.%	T_{10}, ºC	T_{50}, ºC	T_{max}, ºC	T_{gHS}, ºC
PU-CuNF	60	285	365	309/376/399/445	21.6
PU-ZnNF	60	284	368	300/304/390/440	20.8
PU- $Cu_{0.5}Zn_{0.5}NF$	60	283	368	306/325/389/428	21.8
PU	60	279	360	293/364/402/432	21.2

CONCLUSION

Novel PU/ferrite nanocomposites based on PDMS as the soft segment and MDI/BH-20 as the hard segment with different types of ferrites and small content of ferrites (1 wt.%) were prepared by *in situ* two-stage polymerization reaction. The PU-NFs formation was confirmed by FTIR. DSC results showed that glass transition of the hard segment in PU-NFs was similar to the pure PU network. TG results indicated that addition of ferrites led to increase in thermal stability of the prepared PU-NFs compared to pure PU network. In future study, the formulation of the PU-NFs needs to be evaluated for its cytotoxicity and antimicrobial properties as well as microstructure-mechanical property relationship, so that it can be further optimized to develop organic–inorganic hybrid nanocomposites showing desired biological activity.

Acknowledgement

Financial support for this study was granted by the Ministry of Science and Technological Development of the Republic of Serbia and by Magbiovin project (FP7-ERAChairs-Pilot Call-2013, Grant agreement: 621375).

REFERENCES

[1] M. V. Pergal, J. V. Džunuzović, R. Poręba, D. Micić, P. Stefanov, L. Pezo, M. Špírková, Express Polym. Lett., 2013, **7**, 806-820.

[2] M. V. Pergal, J. V. Džunuzović, R. Poręba, S. Ostojić, A. Radulović, M. Špírková, Prog. Org. Coat. 2013, **76**, 743-756.

BULK AND SURFACE STRUCTURE OF NiAl LAYERED DOUBLE HYDROXIDES AT DIFFERENT Ni/Al RATIOS

D. Nikolova [1], J. Krstić [2] and D. Crişan[3]

[1]*Institute of Catalysis, Bulgarian Academy of Sciences, Sofia 1113, Bulgaria (dimi@ic.bas.bg ;dimi_nik@abv.bg)*
[2]*University of Belgrade, IChTM-Department of Catalysis and Chemical Engineering, Belgrade, 11000, Serbia.*
[3]*Ilie Murgulescu Institute of Physical Chemistry, Romanian Academy, 202 Splaiul Independentei St., 060021 Bucharest-12, Romania.*

ABSTRACT
NiAl layered double hydroxides compounds are synthesized by co-precipitation. It was done to elucidate the effect of Ni^{2+}/Al^{3+} molar ratio from 1.5 to 4.0 on phase composition and texture properties by powder X-ray diffraction and N_2 physisorption techniques. We found that different bulk and surface structures is affected by nickel content thus makes NiAl LDH precursors potentially useful applicable in numerous catalytic processes.

INTRODUCTION
NiAl layered double hydroxides (LDHs), also known as Takovite-like (TKl) compounds, named of the mineral Takovite, $Ni_6Al_2(OH)_{16}CO_3{\cdot}4H_2O$ [1], represent lamellar materials belonging to a great group of natural or synthetic inorganic layered compounds. The Ni^{2+} and Al^{3+} ions are located in the positively charged Brucite-like hydroxide layers $[Ni^{2+}_{1-x}Al^{3+}_x(OH)_2]^{x+}$, while different kind of intercalated both charge compensating exchangeable anions and *m* number of water molecules are situated in the interlayer space $[A^{n-}_{x/n}{\cdot}mH_2O]$. The lamellar structure assumes uniform distribution of the Ni^{2+} and Al^{3+} cations, which are cross-linked through hydroxyl groups to form a bimetal hydroxide sheet, similar to that of Brucite [1-3]. By varying the proportion of Ni^{2+} and Al^{3+} cations, and/or the interlayer anions, a wide variety of LDH compositions can be obtained, which makes it possible to produce tailor-made materials able to fulfill specific requirements aiming at advantageous properties. The researcher efforts are focused on the study of the co-precipitated NiAl LDH as catalyst precursors for many industrial processes [4] based on the famous property of the both ions to remain associated with one another during the activation procedures of calcination and reduction.

As many NiAl LDHs and many of their calcination products are used as catalysts or supports, information about their physical surface and bulk properties is of significant importance. In this regard, the object of the present investigation is to elucidate the effect of nickel content on the phase composition and texture properties of the co-precipitated NiAl LDHs, changing the Ni^{2+}/Al^{3+} molar ratio.

EXPERIMENTAL

The carbonate forms of NiAl LDHs precursors with Ni^{2+}/Al^{3+} molar ratios of 1.5, 2.0, 3.0 and 4.0 were obtained by co-precipitation at 80 ºC and constant pH = 8, using nitrate salts of the corresponding metals and Na_2CO_3 as precipitating agent. All synthesized samples were dried at 80 ºC for 20 h and designated as NiAl*y*, where *y* represents the Ni^{2+}/Al^{3+} molar ratio, for example NiAl3.0. The phase composition of the as-prepared samples was established by powder X-ray diffraction (PXRD) technique and the texture properties by N_2 physisorption.

RESULTS AND DISCUSSION

The diffractograms of the NiAl LDHs reveals that the characteristic reflections of the TKl compound are clearly demonstrated by NiAl3.0 sample (Fig. 1). PXRD patterns show common features, with reflections located at the angles typical of a TKl phase containing carbonate anions in the interlayer space: sharp and symmetrical for (003), (006), (110) and (113), and broad and asymmetrical for (012), (015) and (018), respectively (JCPDF file 00-015-0087). A decrease in nickel loading in NiAl1.5 samples as well as increase in NiAl4.0 one induces lowering of the peak intensities and broadening of the TKl reflections, more pronounced in NiAl1.5 solid. No aluminum hydroxide/oxyhydroxide or $Ni(OH)_2$ phases are registered. Hence, the presence of a TKl phase in NiAl1.5 and NiAl4.0 samples is an evidence that during the co-precipitation the Ni^{2+} ions form a TKl phase engaging corresponding amounts of Al^{3+} ions in a Ni^{2+}/Al^{3+} molar ratio between 2 and

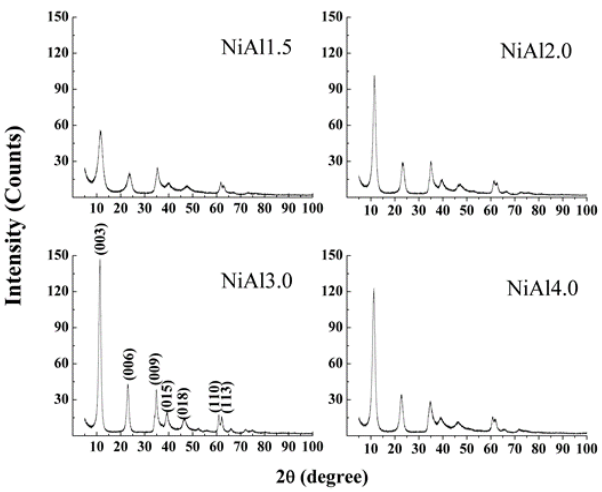

Figure 1. PXRD patterns

3, independently of Ni^{2+} ions value in the starting solution. The excess of Al^{3+} or Ni^{2+} ions precipitates as another Al- or Ni-containing XRD amorphous phases. The obtained results confirm the statement that single stoichiometric TKl phase can exist only for a narrow range of Ni^{2+}/Al^{3+} = 2–3 [2] and the references therein). Samples with a composition outside this range are poorly crystallized. The different degree of TKl samples crystallinity is in accordance with the calculated mean crystallite sizes ($L_{(006)}$, nm), precisely: 4.2 (NiAl1.5), 5.9 (NiAl2.0), 8.5 (NiAl3.0) and 6.1 (NiAl4.0).

The N_2 physisorption study provides information about obtained pore structure of as-prepared NiAl LDHs under impact of Ni^{2+}/Al^{3+} ratio. According to IUPAC classification the isotherms of all samples (Fig. 2.) are type II which is characteristic for nonporous or macroporous solids [5]. However, hysteresis loop, more or less noticeable on isotherms of all samples is an indication of presence of mesopores. This is particularly true for the NiAl3.0 sample, which shows clear indication of the change in the pore emptying mechanism at relative pressure round 0.85, on the desorption branch of isotherm. This type of hysteresis (H3 type) can be recognized in isotherms of materials containing non-rigid aggregates of plate-like particles but also in materials with pore network consistent of macropores that are not completely filled with pore condensate.

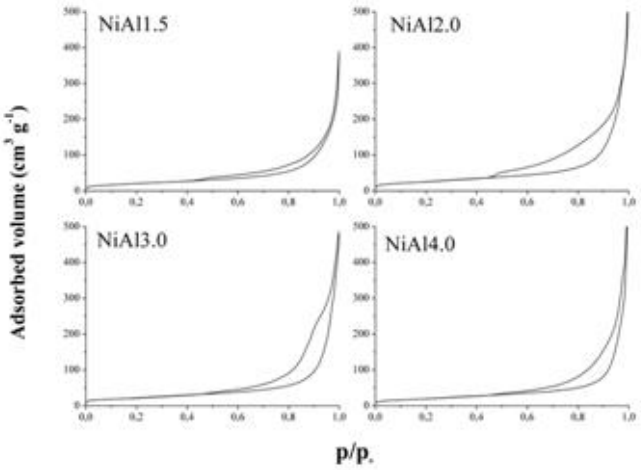

Figure 2. N_2 physisorption isotherms at 77 K

The texture parameters are collected in Table 1. The BET surface area (S_{BET}), pore volume of mesopores (V_{meso}) and average pore diameter (d_{av}) are greater at NiAl2.0 compare to NiAl1.5. Further increasing of Ni loading leads to diminution of S_{BET} and V_{meso} and rising of d_{av}. The pore volume of micropores (V_{micro}) is negligible for all NiAl LDHs.

The minimum value of mean crystallite sizes of the NiAl1.5 among all samples is associated with a non-stoichiometric amount of Ni^{2+} necessary for obtaining solely Takovite-like structure.

Table 1. Texture parameters

Sample	S_{BET} (m^2/g)	V_{meso} (cm^3/g)	V_{micro} (cm^3/g)	d_{av} (nm)
NiAl1.5	76	0.25	0.02	21.6
NiAl2.0	97	0.46	0.03	31.9
NiAl3.0	83	0.40	0.03	32.3
NiAl4.0	77	0.36	0.03	35.1

The increase in Ni^{2+} content (NiAl2.0) leads to an increase in mean crystallite size, but the considerable amount of disordered X-ray amorphous structure in synthetized material, leads to overall significant increase in S_{BET} and V_{meso}. The Ni to Al ratio (NiAl3.0 sample), for which the L_{006} of the Takovite-like structure reaches the greatest value, represents at the same time the optimal ratio for the formation of a lamellar structure. Decrease of S_{BET} value for NiAl3.0 sample is most probably driven by the disappearance of the X-ray amorphous species. Finally, for the highest content of Ni^{2+}, mean crystallite sizes of TKl phase decrease, most likely due to the disruption of such-like structure, which is caused by presence of the amorphous phase rich in Ni^{2+} content.

CONCLUSION

It was established that origin of different phase composition and texture properties is affected by the nickel content. These differences in bulk and surface structures of NiAl LDH precursors are applicable for numerous catalytic processes such as water gas shift reaction, CO_2 methanation and CO oxidation.

Acknowledgement

This work was partially supported by the Ministry for Science of the Republic of Serbia (Grants III 45001).

REFERENCES

[1] D. Bish and G. Brindley, Am. Mineral., 1977, **62**, 458-464.
[2] F. Cavani, F. Trifirò, A. Vaccari, Catal Today, 1991, **11**, 173-301.
[3] A. Vaccari, Catal Today, 1998, **41**, 53-71.
[4] A. Vaccari, Appl. Clay Sci., 1999, **14**, 161-198.
[5] M. Thommes, K. Kaneko, A.V. Niemark, J.P. Olivier, Fr. Rodriguez-Reinoso, J. Rouquerol, K.S.W. Sing, Pure Appl. Chem., 2015, **87**, 1051-1069.

THE EFFECT OF DRYING MODE ON 3D GRAPHENE/OH FUNCTIONALISED POLY(BUTYLACRYLATE -CO-METHYLMETHACRYLATE) COMPOSITES

J. Jovanović[1], B. Adnađević[1] and R. Tomovska[2]

[1]*University of Belgrade, Faculty of Physical Chemistry, Studentski Trg 12-16, Belgrade, Serbia (jelenaj@ffh.bg.ac.rs)*
[2] *University of the Basque Country, Institute for Polymer Materials (POLYMAT), Tolosa Hiribidea 76, San Sebastian, Spain*

ABSTRACT
A novel class of hydrogels based on graphene oxide and polymer latex of methyl methacrylate and butyl acrylate were synthesized. The effect of drying mode (conventional and lyophilisation) on physico-chemical and thermal properties of synthesized products were investigated. The influence of drying mode on samples bulk density, swelling degree and thermal stability was determined. The found differences in these values for different drying modes are explained with the differences in their structural properties.

INTRODUCTION
Recently, a new class of porous materials has been developed, so called graphene aerogels, offering beneficial properties: electrical conductivity and low dense 3D structure with a huge specific surface area, which contribute to further extend of the application possibilities [1]. In this work a novel composite porous materials by combination of graphene oxide and polymers were synthesized. For that aim OH functionalized polymer particles made of methyl methacrylate (MMA) and butyl acrylate (BA) in 1:1 weight ratio, were obtained in presence of 2wt% functional monomer hydroxyethyl methacrylate (HEMA). The main objective of this work was to investigate the effect of drying mode, conventional and lyophilisation, on structural and thermal properties of synthesized 3D graphene/OH functionalised poly(butylacrylate -co-methylmethacrylate) composites.

EXPERIMENTAL
2.1 Materials: Technical grade MMA, Quimidroga, BA, Quimidroga, and HEMA, Fluka were used as monomers. Potassium persulfate (Aldrich) and 4,4-azobis(4-cyanovaleric acid) (V-501, Aldrich) were used as initiators.

Graphene oxide (GO) aqueous dispersion (concentration 4 g/L GO, >95% monolayer content, Graphenea was used. **2.2 Synthesis of polymer latexes:** Details about the synthesis of MMA/BA/HEMA latex are given in previous work [2]. **2.3. Synthesis of composite hydrogels:** Three dimensional graphene based hybrid hydrogels were performed by self assembly graphene oxide aqueous dispersion under heating at 60ºC in the presence of ascorbic acid (AsA/GO ratio 1/1) and synthesized polymer latex at different ratios for 3 hours. The three different weight ratios of GO/polymer were synthesized 1/0.8 (G1); 1/1.6 (G2) and 1/2.4 (G3) In order to remove residual reactants hydrogels were dialyzed in ultrapure water controlling the conductivity until it remained constant. For that aim, a Spectral/Por dialysis membrane (Spectrumlabs) with a molecular cut-off of 12000-14000 Da was used. **2.4. Drying** of composites was performed under conventional drying in laboratory oven at 70 ºC during 72 hours and by freeze drying using lyophilisator Telstar LyoQuest-85 at -60ºC during 24 hours. Composite aerogels (A) were obtained by freeze drying of synthesized hydrogels and composite xerogels (X) were obtained by conventional drying. **2.5. Physicochemical properties** of synthesized composite materials: The bulk densities of the synthesized composites were determined gravimetrically and their swelling degrees in water (SD) were determined by the tea-bag method. The thermogravimetric analysis (TGA) were performed by Thermo gravimetric Analyser model Q500 (TA Instruments). The samples (~5 mg) were heated from 20 ºC to 800ºC in open pans with a heating rate of 10ºC/min under nitrogen atmosphere with flow rate of 100 mL/min.

RESULTS AND DISCUSSION

Figure 1 presents the appearance of the dried composites of characteristic samples of conventionally dried composites-xerogel and freeze-dried composite -aerogel.

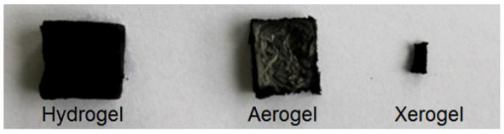

Figure 1. The images of the characteristic sample of hydrogel and dried products

Freeze-dried samples have slightly decreased their volume with respect to starting composite hydrogel indicating preservation of the formed porous structures and therefore formation of aerogel. On the contrary, the volume of conventionally dried composite was decreased drastically, which was an indication for the disintegration of porous structure and formed product are called xerogels.

The effect of drying mode on bulk densities and swelling degrees of the synthesized aerogels and xerogels is presented in Table 1.

Table 1. Bulk density and swelling degree of synthesized xerogels and freeze-dried aerogels

Sample	Bulk density ($g \cdot cm^{-3}$)	SD ($g \cdot g^{-1}$)	Sample	Bulk density ($g \cdot cm^{-3}$)	SD ($g \cdot g^{-1}$)
GO-X	0.45	2.5	GO-A	0.025	39.7
XG1	0.82	2.5	AG1	0.035	30.4
XG2	0.71	2.5	AG2	0.030	27.7
XG3	0.54	2.5	AG3	0.028	12.8

Drying mode significantly influences on the values of bulk density and swelling degree of the synthesized composite materials. Bulk density of aerogels are 25 times lower than the xerogels, whereas their SD are 16 times higher. The bulk density of aerogels is lower because of its higher porosity while porous structure is influenced by different mode of drying. The increase in bulk density and low constant value of SD is caused by the influence of capillary forces during the conventional heating.

Figure 2. shows the obtained thermogravimetric curves (TG) for the composite graphene aerogels and xerogels, respectively.

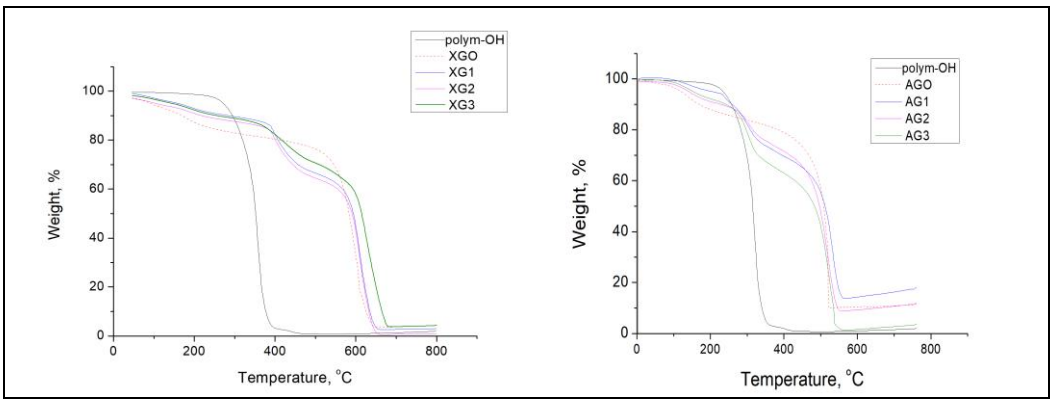

Figure 2. TG curves for the composite xerogels (left) and aerogels (right)

As the drying mode effects on composites properties: bulk densities and SD, also effects on their thermal properties**.** The dehydration process of xerogels occurs at lower temperatures than in the case of aerogels. On the contrary, the degradation processes which roughly consists in two main

stages -elimination of functional graphen oxide groups and polymer chain degradation, occurs at higher temperatures. Based on the results obtained it can be concluded that the xerogels samples are thermally more stable than the ones of aerogels which can be attributed to more compressed structure with higher coordination number.

CONCLUSION

The drying mode significantly influence on the physico-chemical and thermal properties of the obtained products – xerogels and aerogels. The density of aerogels are 25 times lower than the density of xerogels. The swelling degree of aerogels are 16 times higher than the ones of xerogels. The thermal stability is higher for the xerogels then for the composite aerogels.

Acknowledgement

This research was supported by COST action 15107, SSTM Grant No. 37974, the Ministry of Education, Science and Technological Development of the Republic of Serbia through Project No.172015G and Basque Government (GVIT373-10).

REFERENCES

[1] Z. Xu, Y.Zhang, P Li, C. Gao, ACS Nano,. 2012, **6 (**8), 7103–7113.

[2] N. Ormategui, A. Veloso, G.P. Leal, S. Rodriguez-Couto, R. Tomovska, ACS Applied Materials & Interfaces, 2015, **(7),** 14104-14112.

INITIAL REPORT ON THE MINERALS PRESENT IN A NANO-/ MISCROSTRUCTURED SEPARATE OF THE ORASU-NOU (ROMANIA) BENTONITE

G. Damian[1], F. Damian[1], Zs. Szakacs[1], G. Iepure[1], D. Aştefanei[2], D. Birgaoanu[2,3] and E. Anitas [4,5]

[1] *Technical University of Cluj Napoca, North University Center of Baia Mare, Baia Mare, Maramures, Romania. (szakacsz@yahoo.com)*
[2] *„Alexandru Ioan Cuza" University of Iaşi, Iaşi, Romania.*
[3] *Geological Institute of Romania, Bucharest, Romania*
[4] *Joint Institute for Nuclear Research, Dubna, Russian Federation.*
[5] *Horia Hulubei National Institute of Physics and Nuclear Engineering, Bucharest-Magurele, Romania.*

ABSTRACT

This work is a study, using physico-chemical methods, of the mineral content of the nano-/ microstructured separate, prepared by us, from locally available bentonite. Investigations using SEM-imaging, XRD, FT-IR spectroscopy, thermogravimetric analysis, and EDXS are complementarily identifying clay minerals. Above 66% montmorillonite and 33% finely grained cristobalite content, was determined using XRD and quantitative Rietveld phase analysis and refinement. Small amounts of halloysite are observed only in the SEM images of the raw bentonite, and not in our separate. Absence of quartz is also proven by our study. So, the way is open for the refinement of this important resource, to obtain very high quality colloidal suspensions, which can be used in its most modern applications.

INTRODUCTION

Bentonites can contain clay minerals (montmorillonite, kaolinite, illite), cristobalite, carbonates, zeolites, iron oxides and hydroxides, and relics of quartz and feldspar. They are used in their native forms, or after purification or activation, because of high water or organic compound absorption rates, and high cation exchange capacity [1,2]. Montmorillonite, their main mineral component, a hydrated di-octahedral alumino-silicate $(Na,Ca)_{0.33}(Al,Mg)_2(Si_4O_{10})(OH)_2 \cdot nH_2O$, can reversibly swell to up to 17 times in contact with water, forming gelatinous colloidal suspensions or plastic films. Its pharmaceutical applications are well known, for example under the commercial name Smecta®, as an antidiarrheic, anti-flatulent, bowel protective against viruses and bacteria, and detoxifying agent [3].

Bentonites in various refinement stages are used in over 30 industrial branches. In agriculture they enhance soils, help water and nutrient retention, and soil aeration, after drying out.

Important bentonite clay mineral resources are available around Orasu-Nou in NE Romania [4]. They are hosted in ignimbrite- and perlite-facies rhyodacites, pyroclastic volcanic rock formations transformed by hydrothermal – deuteric alteration. Geological explorations revealed 100-400m long, 50-250m wide, 3-8m thick lenticular deposits. In this whole period, no complete physico-chemical and structural description of the contained minerals was done. Just two samples were studied, without the use of modern methods, leading to a poor evaluation of their applicability in high valued, refined or activated forms.

MATRIALS AND METODS

Initially, a small sample was chipped away from the raw bentonite and observed by SEM-imaging. Then, the nano-/ microstructured material was obtained as follows. One kilogram of this white bentonite was mixed with distilled water to obtain $5dm^3$ of suspension. This was split in 5 equal parts, each part stirred for 30min, using an inox propeller-blade stirrer. Passing it through a 43μm sieve retained less than 5g of material, which was discarded. This fluid was left to rest and to settle for 24h, then the supernatant was collected. After water evaporation and left-overs dry-out at room temperature, the first couple of millimeters were scraped away from the obtained shiny surface using a celluloid film. It weighted approximately 10 grams. It was manually turned to powder using an agate mortar and pestle, until it passed through a 5μm sieve. This was the sample that we used. XRD, done on a previously calibrated Shimadzu XRD-6100, (filtered Cu-$K_{\alpha 1}$, U=40kV, I=30mA, 0.5°/min scan speed), was followed by a quantitative Rietveld phase analysis and refinement. FT-IR absorption spectrum was determined using the KBr-pellet method, on a Bruker Vertex 70V ($4cm^{-1}$ resolution, 380-$4400cm^{-1}$ domain). EDXS made on 10 different areas of 5 pelleted samples was used only as a guideline for major element content. Thermal analysis was done using a MOM TGA-DTA ($10^oC \cdot min^{-1}$ heating rate, from ambient temperature to 1000^oC). All analyses were preceded by an overnight desiccation at 110^oC [3].

RESULTS AND DISCUSSIONS

SEM micrographs of the raw bentonite (Figure 1.) prove the presence of the lamellar montmorillonite. The existence of halloysite is suggested by the rod-like mineral structures, with average lengths of 5μm, and average diameter of 175nm.

Rietveld analysis also unveils around 33% cristobalite content. This can be explained by the fact that we trapped only the finest particles in the supernatant fluid, where the cristobalite's nano-/ microscale granules, beside the clay's, tend to concentrate. The small angle scattering (SAS) region, up to about $2\theta=3.5^{o}$, deserves further investigation, using dedicated methods to describe structural agglomeration [6,7]. XRD results also demonstrate the absence of quartz. The presence of halloysite cannot be observed, because its bigger structures probably settled more rapidly during sample preparation. The FT-IT spectrum (Figure 3.) is also characteristic to montmorillonite, and, does not display the presence of other clay minerals [8].

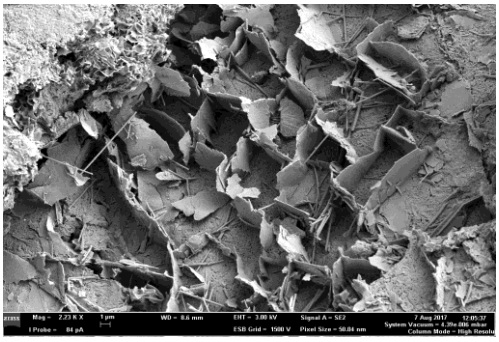

Figure 1. SEM micrograph of the freshly broken raw bentonite

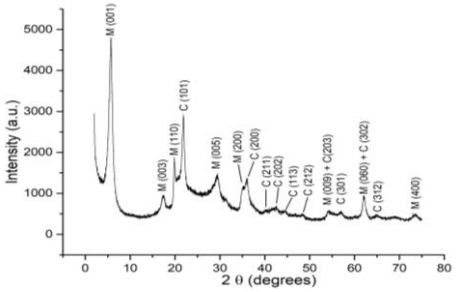

Figure 2. XRD of the sample M-montmorillonite, C-cristobalite

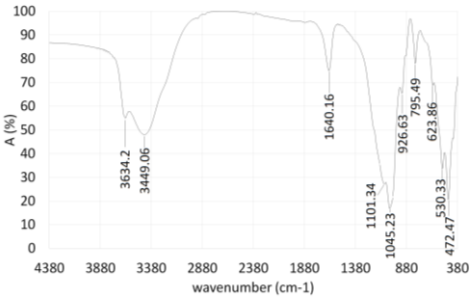

Figure 3. FT-IR spectra of the bentonite separate

Mediated EDXS results over the pelleted samples (Table 1), show high Ca and low Na percentages. Fe and low Mg contents substitute Al. K and other substitutes, can also be detected. The obtained thermogravimetric diagrams are typical for montmorillonite. Between 30-220°C they show a strong endothermic effect on the DTG curve, with a maximum value around 120-130°C. The DTA curve between the temperatures of 30-240°C has

Table 1. Major elements determined by SEM-EDXS

Element	Wt%	$\sigma_{Wt\%}$
Si	27.97	0.20
Al	9.68	0.09
Fe	1.79	0.10
Ca	1.21	0.05
Mg	0.38	0.03
K	0.19	0.04
Ti	0.11	0.05
Mn	0.04	0.06
Na	0.03	0.03

a maximum in the domain 140-150°C.

CONCLUSIONS

This is an initial study using physico-chemical methods on the mineralogical composition of the nano-/ microstructured material obtained by us from the Orasu-Nou (Romania) bentonite. SEM imaging of the raw mineral proves the presence of lamellar montmorillonite and indicates possible small quantities of halloysite. The studied sample was obtained after evaporating the distilled water used in the separation procedure, drying the left-overs at room temperature, and then scraping away the surface. XRD, FT-IR and thermogravimetric studies of the hand-milled sample give characteristic results for montmorillonite. Rietveld phase refinement also reveals around 33% cristobalite content, concentrated here due to its particle size. EDXS gives an estimate of major elemental composition. No sign of quartz, halloysite (supposedly observed in SEM images of the bulk raw material), or other clay minerals were found during these determinations. The presence of other minerals is still to be investigated in the coarser, but still microscale, separate fractions, which were not considered in this study.

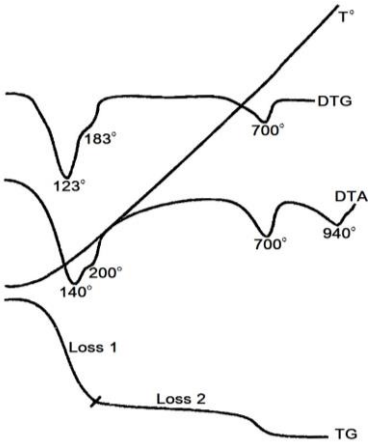

Figure 4. Thermogravimetric analysis of the bentonite separate

Acknowledgement

The authors acknowledge the financial support of JINR Dubna-TU Cluj-Napoca Joint Research Projects based on Protocol no. 4517-3-16/18.

REFERENCES

[1] M.K. Uddin, Chem. Eng. J., 2017, **308**, 438.
[2] N.M. Boeva, Yu. I. Bocharnikova, P. E. Belousov, V. V. Zhigarev, Russ. J. Phys. Chem. A, 2016, **90**, 1525.
[3] A. Meunier, Clays, Springer, Berlin, 2005.
[4] Gh. Damian, F. Damian, C. Constantina, Rom. J. Mineral Deposits, 2010, **84**, 58.
[5] A. Viani, A. Gualtieri, G. Artioli, Am. Mineral., 2002, **87**, 966.
[6] H.E. Hermes, H. Frielinghaus, W. Pyckhout-Hintzen, D. Richter, Polymer, 2006, **47**, 2147.
[7] E.M. Anitas, A. Slyamov, Zs. Szakacs, Nanoscale Res. Lett., 2017, 389
[8] B.A. Fil, C. Özmetin, M. Korkmaz, Bulg. Chem. Comm., 2014, **46**, 258.

HEAVY METAL DISTRIBUTION DEPENDENCE ON SOIL PROFILE AND PARTICLE SIZES IN SOIL TYPES

F. Damian[1], G. Damian[1], Zs. Szakacs[1], G. Iepure[1] and E. Anitas[2,3]

[1] Technical University of Cluj Napoca, North University Center of Baia Mare, Baia Mare, Maramures, Romania. (szakacsz@yahoo.com)
[2]Joint Institute for Nuclear Research, Dubna, Russian Federation
[3]Horia Hulubei National Institute of Physics and Nuclear Engineering, Bucharest-Magurele, Romania.

ABSTRACT

Heavy metal distribution in two different, but neighboring soil types (anthropic and eutricambosol) were determined by physico-chemical and granulometric studies. The heavy metal concentration is different and related to the pedogenetic soil horizons. It also depends on the particle size distribution. Sand and silt is predominant in the anthropic soil, while the clay fraction is prevalent in the eutricambosol. Pb accumulated in the coarse fraction of the anthropic top soil, while, at higher depths, Cu and Cd, in the finer fractions. In its top layer the heavy metal distribution was heterogenous. In the deeper layers the concentrations increased from gravel, through sand and silt, with a maximum reached in clay fraction. On the contrary, eutricambosol accumulated heavy metals in the top soil. The concentrations decreased with depth. In both cases, the highest heavy metal accumulations were determined in the clay fraction, because of their high number of negatively charged sites contained in the structure.

INTRODUCTION

Determining and monitoring the degree of anthropic toxic heavy metal pollution in industrial areas is of paramount importance to assess its long term negative effects. Its impact on the population's health was recently investigated [1, 2], but most determinations were made only on the top soil horizons [3-5]. In the work of F. Damian et al. [3] it was also proven that heavy metal distribution in every soil profile is influenced by its geochemical behavior.

This study describes the heavy metal distribution found in each soil profile and granulometric fraction of two neighboring soil types (anthropic and eutricambosol), polluted by the same nearby metallurgical plant.

MATRIALS AND METODS

Anthropic and eutricambosol samples were collected near a lead processing plant in Baia Mare, Romania. For eutricambosol, each pedogenetic horizon (Ao1, Ao2, Bv and C) could be sampled. But, because these horizons are mixed and cannot be distinguished for anthropic soils, two samples were taken from depths of 0-10 cm, and 20-40cm, according to Romanian legislation. Each sample was separated in granulometric classes: gravel, sand, silt and clay fractions. Heavy metals amounts were measured in hydrochloric acid solution, obtained after soil mineralization with $HClO_4$ and HNO_3, using inductively coupled plasma atomic emission spectroscopy (ICP-AES).

RESULTS AND DISCUSSIONS

Sand and silt is prevalent in the anthropic soil, while gravel and clay is present in lower ratios (Figure 1. a.) This is normal and explained by the presence of slag and construction material fragments in this soil type.

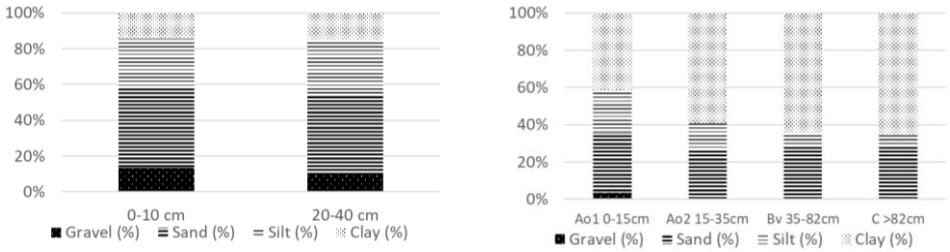

a. b.

Figure 1. Particle size distribution in soil profiles. a. anthropic; b. eutricambosol

In eutricambosol clay fraction is predominant (Figure 1.b.). Its ratio increases with depth, from horizons Ao to Bv, remaining constant in C. This is according to the pedogenetic conditions and characterizes the soil type. Sand and especially silt fractions decrease with the profile's depth in horizons Ao, and, with a high rate, in Bv and C. The very low gravel ratio, only observable in the horizon Ao1, is probably due to anthropic activities.

In the anthropic soil, Cu concentrations display an inhomogeneous distribution, as can be seen in Figure 2. It accumulates in the deeper clay fraction, because of its high mobility. These high concentrations are also found in the clay and gravel fractions of the top layer. The gravel here manly originates from slag fragments. Lead concentrations it's high in the 0-10cm layer mainly in the gravel, which contains slag. Its presence is smaller in silt and clay and it is probably due to the industrial dust eliminated in the atmosphere. At the depth of 20-40 cm the lead content is lower due to its decreased mobility within the soil profile. The high Zn concentration in the top soil's gravel fraction has the same reason as for

Pb. Its accumulation in the 20-40cm region is also like that of the leads, increasing as the fraction gets finer. Cadmium accumulates more in the finer fractions, especially in the clay, mainly at higher depths.

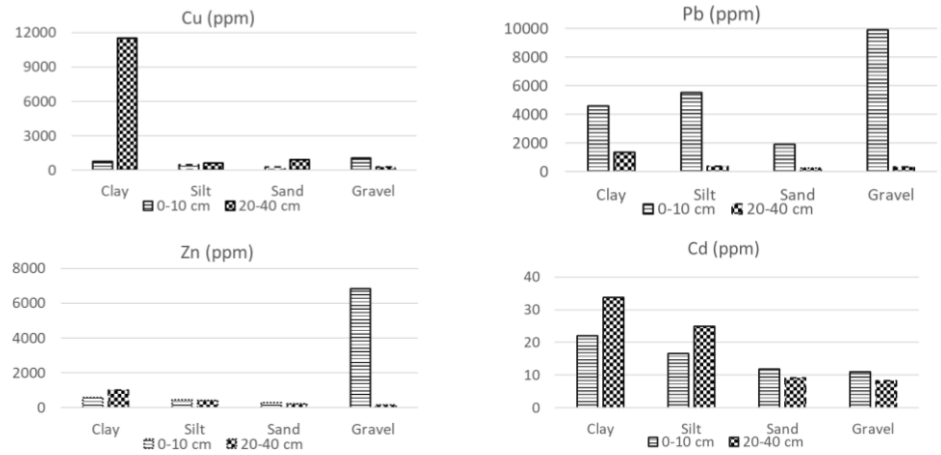

Figure 2. Heavy metal concentrations in anthropic soil

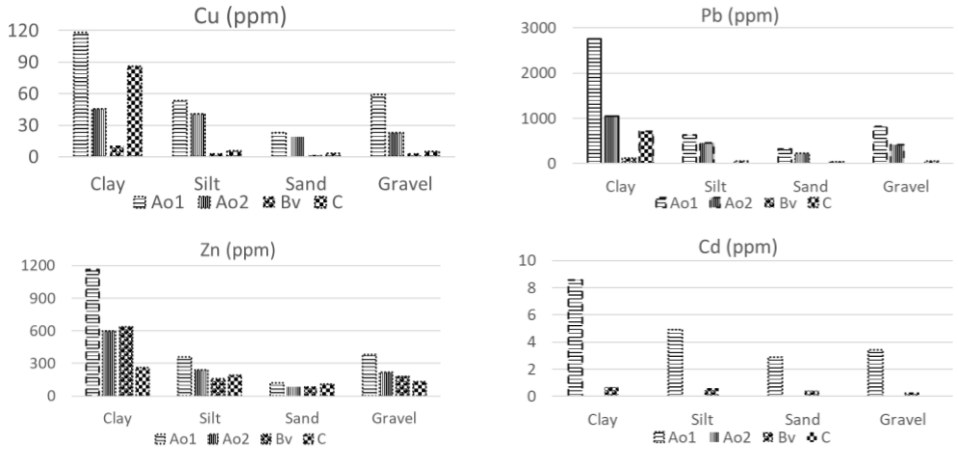

Figure 3. Heavy metal concentrations in each granulometric fraction from each pedogenetic horizons of eutricambosol

Heavy metal concentrations found in the eutricambosol are much lower, rarely exceeding alert levels. They decrease from the top soil to the Bv horizon and accumulate mainly in the clays of Ao1 (top soil). Only Pb is measured to be above intervention limit in the clay fractions of the first two horizons, and above alert limit in the other ones. The concentration increase in the C horizon can be explained by the presence of the andesitic parental rock. The gravel from Ao1 contains more heavy metals than the sand, because of

slag accumulation from industrial activity. Our research is consistent with previous studies [6, 7] proving that heavy metal concentrations increase with the decrease of the sorbent's particle size, while exceptions are explained by the presence of slag. It also agrees with M.V. D'Souza et al. [8] explaining why the high concentrations are found mainly in clays, which contain negative sites, and favor fixation of heavy metal cations.

CONCLUSION

This research demonstrates that the behavior of anthropic soils regarding heavy metal retention differs from that of the undisturbed eutricambosol, explaining the observed results using physico-chemical, geological and anthropogenic reasoning. Heavy metal distribution in the anthropic soil is inhomogeneous at different depths, while it decreases with depth down to the Bv horizon, and slightly increases in the C one for the eutricambosol because of the geological parental rock substrate. Heavy metal accumulation in the clay fractions is favorized by the negative sites found in their crystal structure that help cation retention. In both studied soils the top soil heavy metal accumulation in the gravel fraction is due to anthropic activity. Cu and Zn accumulation in the deeper profiles is due to their high mobility.

Acknowledgement

The authors acknowledge the support from JINR Dubna-TU Cluj-Napoca joint research projects based on the protocol no. 4517-3-16/18.

REFERENCES

[1] R. Lăcătuşu, C. Răuţă, N. Avram, S. Cârstea, et al., Soil Sci. J. Rom. Nat. Soc. Soil Sci., 1998, **XXXII**, 137-153.
[2] M. Nedelescu, D. Baconi, A. Neagoe, V. Iordache, et al., Sci. Total Environ., 2017, **580**, 984-995.
[3] F. Damian, G. Damian, R. Lăcătuşu, G. Macovei, et al., Carpath. J. Earth Environ. Sci., 2008, **3**, 85-98.
[4] N.V. Gulamova, Russ. J. Phys. Chem. A, 2010, **84**, 149-151.
[5] L. Paulette, T. Man, D.C. Weindorf, T. Person, Geoderma, 2014, **243-244**, 130-140.
[6] S. Mandzhieva, T. Minkina, D. Pinskiy, T. Bauer, S. Sushkova, Eurasian J. Soil Sci., 2014, **3**, 197-205.
[7] Y. Qingzhen, W. Xiaojing, J. Huimin, C. Hongtao, Yu Zhigang, Int. J. Environ. Res. Public Health, 2015, **12**, 6725-6744.
[8] M.V. D'Souza, S.M. Prasanna in: Competitive Sorption and Transport of Heavy Metals in Soils and Geological Media, H.M. Selim (Eds.), CRC Press, New York, 2017.

SOME TIME DEPENDENT ELECTRICAL AND OPTICAL PROPERTIES OF THE K-ETHYL XANTATE SOLUTION - SPHALERITE NATURAL MINERAL INTERFACE

D. Todoran[1], R. Todoran [1], Zs. Szakacs[1] and E. Anitas [2,3]

[1] Technical University of Cluj Napoca, North University Center of Baia Mare, Baia Mare, Maramures, Romania. (szakacsz@yahoo.com)
[2]Joint Institute for Nuclear Research, Dubna, Russian Federation.
[3]Horia Hulubei National Institute of Physics and Nuclear Engineering, Bucharest-Magurele, Romania.

ABSTRACT
Time dependent behavior of the spectral behavior of some optical and electrical properties of the interface formed between potassium ethyl xanthate solution and the sphalerite natural mineral is presented in this study. Measurements were done using differential optical reflectance spectroscopy over the UV-Vis/NIR domain. After extrapolations, the Kramers-Kronig formalism allowed the computation the dielectric constant, dielectric loss function, refractive index and extinction coefficient, from reflectance data. Suitable visualization led to the deduction of time dependent spectral variations. When dynamic adsorption-desorption equilibrium is reached at the interface level, the measurements tend to stabilize, marking the optimal moment to end the flotation process.

INTRODUCTION
In situ monitoring of froth flotation processes can be done using continuously repeated differential optical reflectance spectroscopy over the UV-Vis/NIR domain and almost instantaneous data processing using a PC [1-4]. Optimization of the flotation can be achieved this way and understanding of the underlaying physico-chemical processes is possible. Reflectance data processing and analysis, in the framework of the Kramers-Kronig formalism, opens the way to determine the spectral dependence of the electrical and optical functions of the rapidly evolving flotation agent - natural mineral interfaces.

MATRIALS AND METODS
The materials and methods used in our study were thoroughly described previously [1-4]. A large sample of sphalerite mineral sample was obtained from Nistru mine, in Maramures county, Romania. Cutting was done in an

arbitrary direction. Polishing was done using polishing glass and TiO_2 powder down to 0.02μm. Chemical ablation was done washing the sample 3 times for 3 m minutes in concentrated nitric acid then rinsed in distilled water [1,3,4]. The surface was further cleaned with a spray of Ar atoms in a high vacuum chamber. The xanthate was purified from industrial grade one. A concentration of 100mg/L and a pH fixed to 8 was used, as suggested by our previous studies [3,4] at a fixed temperature of 18^{o}C. Spectrometric quality check of the xanthate solution was done before each use. Spectrographic semiquantitative analysis of the sphalerite sample showed 1000ppm Sb, 300ppm Sn, 100ppm Cd, and 30ppm Bi and Co. The other elements were bellow detection limit.

Optical measurements were done on the 200-900nm (1.37-6.2eV) domain using a modified SPECORD M-40 spectrophotometer, with a prism installed to direct the incident light to the mineral's surface and the reflected light to the detector [2].

The extrapolations in the UV and NIR regions used before processing the reflectance data, and the formulae of the Kramers-Kronig formalism were thoroughly described before [2]. Finding the extrapolation coefficients and other computations were done using a home-built FreePascal language software. Reflectance measurements were made on the bare mineral surface, mineral immersed in doubly distilled water and mineral in contact with the xanthate solution.

RESULTS AND DISCUSSIONS

The measured differential reflectance values of the bare and water immersed mineral (Figure 1) were quite high, ranging between 30-80%, while a maximum of 5% of the reflectance is lost during water immersion.

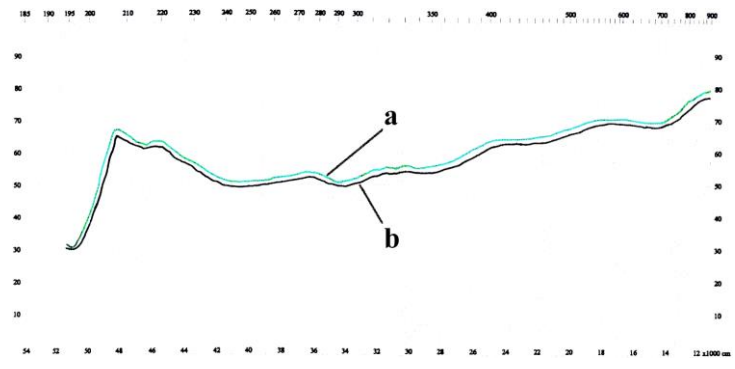

Figure 1. Differential reflectance values of the bare (curve a) and water immersed (curve b) sphalerite mineral

These measurements were used for the computation of the complex dielectric function of the sphalerite mineral and led to the determination of a

value for the electron plasma energy E_{pv}= *13.1eV* and energy band gap E_g=*1.50eV*, in good correlation with ones from the literature [1].

Continuous spectrometric monitoring of the mineral – xanthate interface resulted in registering six spectra (Figure 2.) in a period of 30min, after which they started to completely overlap. The recorded signal is much weaker now, because the light is absorbed by the xanthate solution.

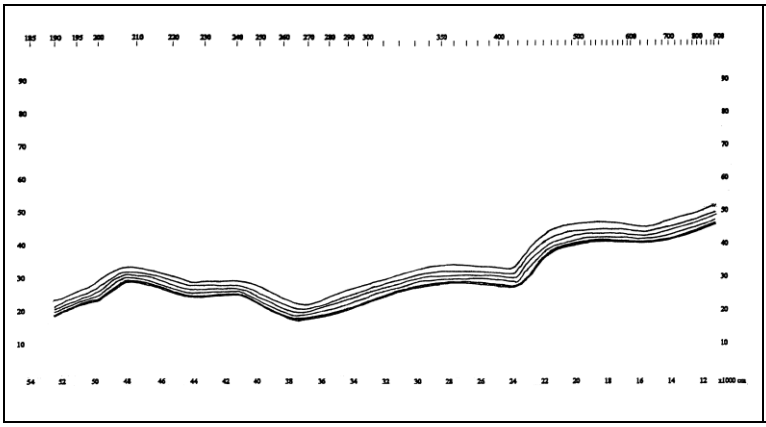

Figure 2. Differential reflectance values of sphalerite mineral- K-ethyl xanthate interface, timecoded from up to down

The dielectric constant ε_1 exhibits (Figure 3 a.) high positive values for energies up to 2,5eV, then a rapid decrease to 4 eV and a constant negative value at high energies. In time, a peak evolves around 2eV. The dielectric loss function ε_2 marks high electron energy losses in the whole UV-Vis domain with a decreasing time dependent peak around 3eV (Figure 3 b.)

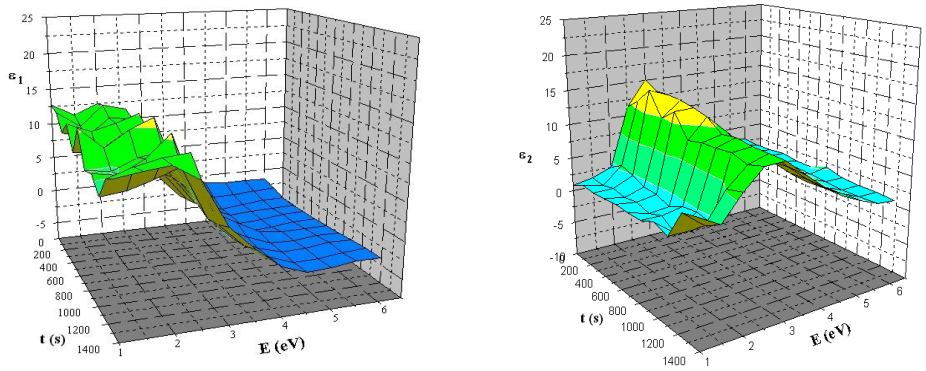

a. b.

Figure 3. Time dependent behavior of the spectral dispersion of a.) real (dielectric constant ε_1) and b.) imaginary (dielectric loss function ε_2) part of the xanthate-sphalerite interface's complex dielectric function

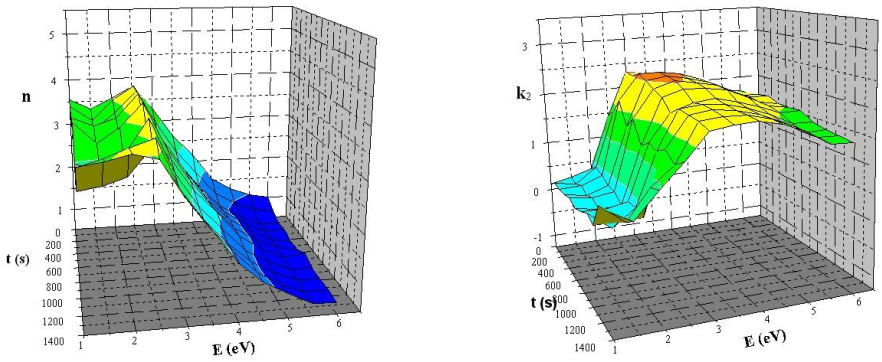

a. b.

Figure 4. Time dependent behavior of the spectral dispersion of a.) real (refraction index *n*) and b.) imaginary part (optical absorption coefficient *k*) of the xanthate-sphalerite interface's complex refraction index

The complex refraction index, with its real part (refraction index *n*) and its imaginary part (optical absorption coefficient *k*) can now be readily computed. The refraction index has high values (Figure 4 a.), characteristic to semiconductors, in the Vis-NIR region, peaking around 2eV, which then drop to n=1 in UV. The optical absorption coefficient is well correlated with ε_2, with high absorption in the whole UV-Vis region, peaking between 2-3eV, which shows a slow decrease in time.

CONCLUSION

The present work describes the time dependent behavior of the UV-Vis/NIR spectral dispersion of the dielectric constant ε_1, dielectric loss function ε_2, refraction index *n* and optical absorption coefficient *k* of the K-ethyl xanthate - sphalerite natural mineral interface using data obtained from differential reflectance spectroscopy.

Acknowledgement

The authors acknowledge the support from JINR Dubna-TU Cluj-Napoca joint research projects based on the protocol no. 4517-3-16/18.

REFERENCES

[1] R. Todoran, D. Todoran, Zs. Szakacs, Russ. J. Phys. Chem. A, 2015, **89,** 2422.
[2] D. Todoran, R. Todoran, E.M. Anitas, Zs. Szakacs, Russ. J. Phys. Chem. A, 2017, **91,** 2613.
[3] R. Todoran, D. Todoran, Zs. Szakacs, Phys. Scripta., 2013, **T157**, 014032.
[4] R. Todoran, D. Todoran, Zs. Szakacs, Spectrochim. Acta A, 2016 **152**, 591.

USING NATURAL AND Fe(III)-MODIFIED ZEOLITE ENCAPSULATED WITH ALGINATE FOR HEAVY METALS REMOVAL

M. Kragović[1*], S. Pašalić[1], I. Ristović[2], S. Krstić[1], V. Dodevski[1], J. Milojković[3] and M. Stojmenović[1]

[1] *University of Belgrade, Institute of nuclear sciences Vinča, Mike Petrovića Alasa 12-14 11000 Belgrade, Serbia*
[2] *University of Belgrade, Faculty of mining and geology, Đušina 7 11000 Belgrade, Serbia*
[3] *Institute for technology of nuclear and other mineral raw materials, Franše d'Eperea 86 11000 Belgrade, Serbia*
**email: m.kragovic@vin.bg.ac.rs*

ABSTRACT

In presented paper natural (NZ) and Fe(III)-modified (FeZ) zeolites were encapsulated with polysaccharide alginate (A) in order to obtain materials with good adsorption properties for heavy metals removal and to solve problem with water turbidity and separation of the solids from liquids. The cation exchange capacities were determined, and then samples were tested for removal lead(II), cadmium(II) and zinc(II) ions from water solutions. Results showed that it is possible to solve problem with filtration and improve adsorption properties for heavy metal ions by encapsulation. After encapsulation, cation exchange capacities remained practically unchanged (146 and 150 meq/100 g for natural and encapsulated zeolite NZA, and about 181 for Fe(III)-modified zeolite and Fe(III)-modified zeolite encapsulated with alginate) and encapsulation with alginate has positive effect on removal heavy metals ions. The removed amounts of heavy metals for encapsulated samples were also significantly higher in comparison with amounts removed by commercial carbon of known manufacturer.

INTRODUCTION

The increasing levels of toxic metals which are discharged to the environment as industrial waste represent a serious problem for human health, living resources and ecological systems. Regarding acute toxicity, Cd^{2+}, Pb^{2+} together with Hg^{2+} form ″the big three″ of heavy metals with the greatest potential hazard to human and environment [1]. There are several methods for treatment of heavy metals in contaminated effluents such as ion exchange, chemical precipitation, oxidation, adsorption, reduction or

osmosis. Adsorption and ion exchange are simple and effective processes for heavy metals removal, particularly when low-cost and eco-friendly natural materials such as zeolites are employed [2].

Although zeolites pose good properties for heavy metals removal, they are often modified in order to improve their adsorption capacity. For example, zeolites were used as substrate for iron modification, and results showed that such modified zeolites can be significantly better adsorbents for heavy metals than natural one [3]. Our previous studies [4, 5] showed that after modification of the natural zeolite-clinoptilolite (particle size <0.043 mm) with Fe(III) ions, adsorption capacity for Pb^{2+} ions increased from 66 mg/g (natural zeolite) to 133 mg/g (Fe(III) modified zeolite). From a practical standpoint, eventhough Fe(III)-modified zeolite has high adsorption capacity, its ultrafine particles may cause difficulties in filtration (separation) of solids from liquids. Results on adsorption of lead by these two adsorbents with higher particle size (-0.8+0.6mm) [4] showed decrease of adsorption capacities for Pb^{2+} ions with increasing the particle size (62 mg/g for the natural and 102 mg/g for Fe(III)modified zeolite). Thus, immobilization of the natural and Fe (III) modified zeolite powder looks like promising solution. Polymers such as polysaccharide-alginate (A) (1,4-linked β-D-mannuronic and α-L-guluronic acids) can be used as encapsulating agents due to their biodegradability, non-toxicity, gelation, water adsorption, high applicability in different industries and the most important, high adsorption capacity for heavy metals.

The aim of this study was synthesis of the natural and Fe(III)-modified zeolite encapsulated by alginate and its preliminary testing for removal of Pb^{2+}, Zn^{2+} and Cd^{2+} from water solutions.

EXPERIMENTAL

The natural zeolite-clinoptilolite from Zlatokop deposit, Serbia with a particle size <0.043 mm (NZ) was used as a starting material. The Fe(III)-modified zeolite with the same particle size (FeZ) was obtained combining the method for the goethite preparation and that for the preparation of Fe-coated zeolite [6, 7], and this procedure is given elsewhere [4].

The procedure for obtaining natural zeolite-alginate (NZA) and Fe(III)-modified zeolite-alginate (FeA) composite was based on a method used by Viraraghavan and Yuan [8]. Briefly, a 2 g of Na-alginate was dissolved in 100 cm^3 of distilled water and then agitated for 24 h to make a homogenous mixture. Then, 10 g of the natural or Fe(III)-modified zeolite were blended with 100 cm^3 of 2 % Na-alginate solution for 2 h. Spherical beads were prepared by dropping the mixed solution into 0.1 mol/dm^3 $CaCl_2$ solution. Beads were formed by drop-wise extrusion through a pipette tip. The beads

were hardened by placing them in 2 % solution of $CaCl_2$ for 24h. The remaining beads were washed in distilled water and dried at room temperature to constant weight.

The content and type of exchangeable cations and total cation exchange capacity (CEC) of the NZA and FeA were determined by treatment of 1g of each sample with 100 cm^3 of 1mol/dm^3 NH_4Cl. Results showed that after encapsulation, cation exchange capacity remains practically unchanged (146 and 150 meq/100 g for NZ and NZA, and about 181 for FeZ and FeA, respectively).

Testing of Pb^{2+}, Zn^{2+} and Cd^{2+} removal was investigated by mixing 0.5g of the NZ, FeZ, NZA or FeA with 50 cm^3 of aqueous solutions, containing initial concentration of Pb^{2+} 3200 mg/dm^3 or Cd^{2+} and Zn^{2+} 600 mg/dm^3 for 24h. Initial pH was adjusted to 4.2. After 24h, suspensions were centrifuged and the amounts of Pb^{2+}, Zn^{2+} or Cd^{2+} were determined in supernatants on atomic absorption spectrophotometer (AAS) "Analytic Jena Spekol 300".

RESULTS AND DISCUSSION

The macroscopic images of NZA or FeA are given in Fig. 1. As can be seen, the most important advantage of using alginate to immobilize natural or Fe(III)-modified zeolite is that after modification, fixed micro-sized starting materials with good formability were obtained. After encapsulation with Na-alginate the micro-sized particles of NZ or FeZ were fixed by alginate in spherical beads with size 2-3mm (Fig. 1).

Figure 1. Wet (left) and dried (right) particles of the FeA (up) and NZA(down).

The obtained samples were then tested for heavy metals cations removal. Results showed that encapsulation has positive effect on removal lead(II),

cadmium(II) and zinc(II) ions. After treatment, the removed amounts of lead were: 63, 133, 101 and 135 mg/g, cadmium: 12, 20, 20 and 28 mg/g and zinc: 7, 20, 25, 27 mg/g for PZ, FeZ, PZA and FeA. The obtained results were also compared with removal of heavy metals by commercial activated carbon (C-Ac), of known manufacturer (OMNIA AQUA), bought in Serbia. The C-Ac removed 45, 16 and 13 mg/g of Pb, Cd and Zn ions, respectively, what means that by encapsulation of zeolites it is possible to obtain material which possess better efficiency for heavy metals removal in comparison with commercial activated carbon.

CONCLUSION

Presented results indicated that modification of the natural and Fe(III)-modified zeolite with alginate could solve problems with water turbidity and filtration. After encapsulation, cation exchange capacity remained practically unchanged and encapsulation with alginate has positive effect on removal heavy metals ions. The removed amounts of heavy metals cations for encapsulated samples, and especially for Fe(III) modified zeolite were significantly higher in comparison with amounts removed by commercial carbon, what may be an indication that encapsulated samples may find practical application for heavy metals removal from contaminated waters. However, for practical application, additional experiments are needed and will be performed in the near future.

Acknowledgement

Presented results are a part of the projects TR34013 and ON172018 financed by the Ministry of Education, Science and Technological Development of the Republic of Serbia.

REFERENCES

[1] M. Hamidpoura, M. Kalbasib, M. Afyunib, H. Shariatmadarib, P.E. Holmc, H.Ch.B. Hansenc, J. Hazard. Mater., 2010, 181, 686-691;
[2] N. Bektaş, B.A. Ağim, S. Kara, J. Hazard. Mater., 2004, 112, 115-122;
[3] A. Dimirkou and M. Doula, Desalination, 2008, 224, 280-292.
[4] M. Kragović, *A. Daković, Ž. Sekulić, M. Trgo, M. Ugrina, J. Perić, G.D. Gatta, Appl.* Surf. Sci. 2012, 258, 3667-3673.
[5] M.Kragović, A. Daković, M. Marković, J. Krstić, G. Diego Gatta, N. Rotiroti, Appl. Surf. Sci. 2013, 283, 764-774.
[6] G. Mustafa, B. Singh, R.S. Kookana, Chemosphere 2004, 57, 1325–1333
[7] C. Jeon, K. Baek, J. Park, Y. Oh, S. Lee, J. Hazard. Mater. 2009, 163, 804–808
[8] T. Viraraghavan and G. Yuan, Bioresour. Technol. 2001, 78, 243-249.

CORE-SHELL STRUCTURES FOR STABILIZATION OF SIZE AND PHASE COMPOSITION OF THE OXIDE NANOPARTICLES AT ELEVATED TEMPERATURES

T. M. Karnaukhov[1,2], A. M. Volodin [1], V.O.Stoyanovskii[1] and A. A. Vedyagin[1,3]

[1]Boreskov Institute of Catalysis SB RAS, pr. Ac. Lavrentieva 5, 630090 Novosibirsk, Russian Federation. (timofey941@yandex.ru(
[2]National Research Novosibirsk State University, Pirogova str. 1, 630090 Novosibirsk, Russian Federation.
[3]National Research Tomsk Polytechnic University, Lenin Av. 30, 634050Tomsk, Russian Federation.

ABSTRACT

The particle size of different oxides (lanthanum and calcium aluminates, zirconium dioxide) was shown to be stabilized in the Oxide@C core-shell structures being subjected to a high temperature treatment. It was found that exactly the small size of the particles is responsible for stabilization of the low-temperature tetragonal phase of ZrO_2 as well as lanthanum hexaaluminate phase up to 1300-1400 °C. Since the carbon shell is not applicable for the high-temperature usage in an oxygen-containing medium, effectiveness of magnesium oxide as a shell for stabilization of Oxide@MgO systems was studied as well.

INTRODUCTION

As we have reported recently [1-3], the carbon coating supported on the surface of different oxide nanoparticles (Al_2O_3, TiO_2, calcium aluminate C12A7) can play a role of a nanoreactor shell, which allows to maintain the size of the oxide core located inside this shell even at significantly elevated temperatures, when the solid state reaction take place. A presence of the carbon coating prevents sintering (agglomeration) of the oxide nanoparticles. At the same time, the shell is permeable enough for both the gaseous [1] and liquid [4] reagents, and thus allows performing the reactions between the reagents and oxide core. The Oxide@C systems of core-shell structure are characterized with a small (initial) size of the oxide core stabilized within a wide temperature range. It gives a unique opportunity to study a role of the size effects in the phase transformations of the oxide materials at any desired temperature.

It is obvious that the carbon coating in the Oxide@C systems can provide its defending functions in a limited range of experimental conditions. First of all, the main restriction of its application at high temperatures (above 600-800 °C) is an absence of the oxidative atmosphere. It has stipulated such experiments to be carried out at elevated temperatures either in vacuum or in atmosphere of inert gas (for instance, argon). The second problem caused by the high temperatures is possibility of a carbothermal reduction of the oxide core, which leads to destruction of the Oxide@C structure. The temperature of the reduction process significantly depends on the nature of the oxide material being used. Thus, for titanium oxide this temperature lies in a range of 800-900 °C [1], while for alumina and calcium aluminate C12A7 it exceeds 1400-1450 °C [2, 3].

The present work was aimed to estimate the efficiency of the 'carbon nanoreactor' concept for the size stabilization of nanoparticles of lanthanum aluminates and zirconium oxide, which are widely used as the high-temperature supports for the catalysts. The effects of the nanoparticles' size on their phase transformations were studied precisely. Additionally, a possibility of the replacement of the carbon coating with the MgO shell stable under oxidative conditions was examined.

EXPERIMENTAL

Samples of ZrO_2 were prepared by the conventional way based on the precipitation of $ZrOCl_2$ precursor with ammonia at pH = 10.6. The precipitate was washed with a great excess of water until the pH is close to 7. The synthesized samples were dried at 110 °C for 12 h. Then, the samples were calcined in a muffle at desired temperature (500 °C and above) for 6 h.

Deposition of the carbon coating was performed by mixing ZrO_2 powder with polyvinyl alcohol (PVA) in a weight ratio of 7:3. The resulted mixture was placed into a quartz reactor, heated in an argon flow up to 500 °C with a ramping rate of 1.5 °C/min, and maintained at this temperature for 6 h.

Initial $LaAl_{11}O_{18}$ and$LaAlO_3$ samples were synthesized by a modified Pechini route from ethylene glycol-citric ester polyester precursors [5]. After decomposition of the polymeric precursors at 400 °C, the further calcination of the carbon-coated samples was carried out in argon at desired temperature (from 700 to 1300 °C). The samples without carbon coating were calcined with regard to the Pechini method.

Carbon coating for the reference samples was burnt off by its calcination in air at 500 °C (ZrO_2@C-500) or700 °C ($LaAlO_3$@C-700) for 6 h.

Deposition of the MgO shell was performed as follows. Initially, gel of magnesium hydroxide was prepared as described elsewhere [6]. Then, the oxide sample (TiO_2 or C12A7) was added into well stirred viscous gel.

After 15 min of stirring, the sample was left for 1 h before drying at a room temperature for 2 h and at 200 °C for 2 h. Finally, the sample was carefully calcined as described elsewhere [6].

High-temperature treatment of the samples was performed in a graphite crucible placed into corundum ampule inside the heating element TSR (Starbar®). The samples were heated in argon at a ramping rate of 3 °C/min up to 1400 °C and kept at the final temperature for 6 h.

RESULTSANDDISCUSSION

Figs. 1 and 2 show the impact of the calcination temperature on the specific surface area (SSA) and phase composition of the zirconia samples. The effects of the stabilization of the oxide core size (Fig. 1, ZrO_2@C-500 series) and the low-temperature cubic phase (Fig. 2, ZrO_2@C series) are well seen. However, it should be noted that the main contribution into the values of SSA of the ZrO_2@C samples is made by the carbon coating.

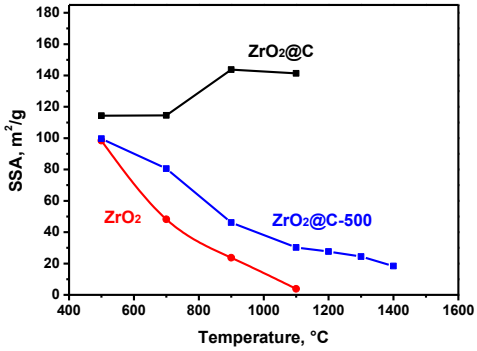

Figure 1. Specific surface area of the ZrO_2, ZrO_2@CandZrO2@C-500 samples calcined at different temperatures.

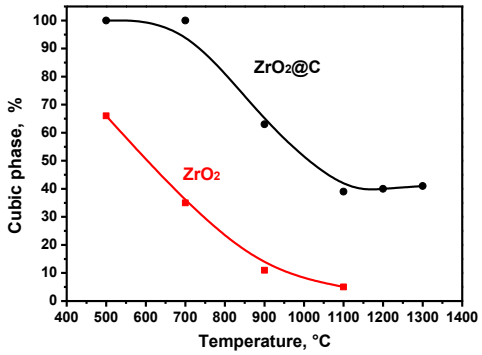

Figure 2. Content of the cubic phase in the $ZrO_2$and ZrO_2@Csamples. The rest is monoclinic phase.

In the case of the binary La_2O_3-Al_2O_3 system, depending on the initial stoichiometry, the synthesis at temperatures up to 1300 °C can be accompanied by formation of $LaAl_{11}O_{18}$with a β-alumina structure (La/Al=8.3%), and $LaAlO_3$ with a perovskite structure (La/Al=50%), which have different size areas of the thermodynamic particle stability. In the case of the sample prepared via Pechini route, formation of the $LaAlO_3$ phase starts at 700 °C (Fig. 3), and no impurity phases were found to appear during the temperature increase. As it follows from the XRD data, formation of the crystal phase does not occur at this temperature in the case of $LaAlO_3$@C-700 sample.

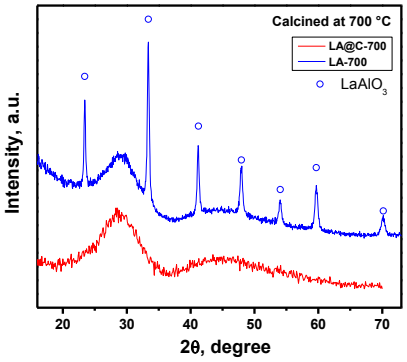

Figure 3. XRD patterns of the $LaAlO_3$ samples calcined in argon at 700 °C.

CONCLUSION

It was shown that the carbon coating allows one to stabilize the size of the oxide core in the ZrO_2@C and $LaAlO_3$@C systems. The size of the oxide particles, in its turn, affects the phase transformations in the studied systems.

Preliminary experiments have shown the possibility to synthesize the core-shell structures with the 'nanoreactor' shell represented by magnesium oxide, which is stable in the oxygen-containing atmosphere.

Acknowledgement

This study was supported by the Russian Science Foundation (Project No. 16-13-10168).

REFERENCES

[1] A. M. Volodin, A. F. Bedilo, I. V. Mishakov, V. I. Zaikovskii, A. A. Vedyagin, R. M. Kenzhin,V. O. Stoyanovskii, K. S. Golohvast, Nanotechnoln Russ, 2014, **9,** 700–706.

[2] A.M. Volodin, V.I. Zaikovskii, R.M. Kenzhin, A.F. Bedilo, I.V. Mishakov, A.A. Vedyagin, Mater. Lett., 2017, 189, 210-212.

[3] I.V.Yakovlev, A.M.Volodin, V.I.Zaikovskii, V.O.Stoyanovskii, O.B.Lapina, A.A. Vedyagin, Ceram.Int. 2018, 44,4801-4806.

[4] D.S.Heroux, A.M.Volodin, V.I.Zaikovskii, V.V.Chesnokov, A.F.Bedilo, K.J. Klabunde, J. Phys. Chem. B, 2004, 108, 3140-3144.

[5] V. Sadykov, V. Usoltsev, N. Yeremeev, N. Mezentseva, V. Pelipenko, T. Krieger, V. Belyaev, E. Sadovskaya, V. Muzykantov, Y. Fedorova, A. Ishchenko, A. Salanov, Y. Okhlupin, N. Uvarov, O. Smorygo, A. Arzhannikov, M. Korobeynikov, M. Thumm, J. Eur. Ceram. Soc., 2013, 33, 2241-2250.

[6] T.Karnaukhov, A.Vedyagin, I.Mishakov, A.Bedilo, A.Volodin, Mater. Sci. Forum, 2018, 917, 157-161.

ADSORPTION AND SURFACE PROPERTIES OF ALKALINE AND OXIDATIVE TREATED FLAX

M. Vukčević, B. Pejić, B. Lazić, M. M. Kostić and M. Laušević

University of Belgrade, Faculty of Technology and Metallurgy, Karnegijeva 4, 11000 Belgrade, Serbia (biljanap@tmf.bg.ac.rs)

ABSTRACT

Alkali and oxidative treatments were employed to obtain flax fibers with different content of hemicelluloses and lignin, to study the influence of chemical composition on sorption properties of flax fibers. The flax fibers were characterized using FTIR spectroscopy and by determination of chemical composition, carboxyl group content, electrokinetic and adsorption properties through the adsorption of lead ions. Removal of hemicelluloses led to decrease in functional groups content and consequently decrease in lead ions adsorption, while lignin removal is followed by an increase of functional groups content, namely carboxyl groups, which in turn resulted in better lead ions adsorption.

INTRODUCTION

Properties of flax fibers (Linum usitatissimum L.) originate from their heterogeneous chemical composition, location of constituents within the flax fibers and specific structure. The main components in chemical composition of flax fibers are cellulose, hemicelluloses and lignin, which determines the properties of these fibers. Cellulose is a polysaccharide with a large content of hydroxyl groups, which directly affects the hydrophilic nature of flax fiber. Hemicelluloses are strongly bound to cellulose fibrils by hydrogen bonds and occupy spaces between the fibrils in both primary and secondary walls. They are partly soluble in water and hygroscopic. Lignin is located in the secondary wall and fulfills the middle lamellae. It has very low reactivity due to the presence of strong carbon–carbon linkages and aromatic groups, which are very resistant to chemical attack [1].

Location of hemicelluloses and lignin within the structure of flax fibers, as well as their content, may adversely affect surface and adsorption properties of flax fibers [2]. Therefore, in this work flax fibers of different chemical composition were obtained by progressive removal of hemicelluloses or lignin, with intention to investigate and explain the individual roles of these components on the surface and adsorption properties of flax fibers.

EXPERIMENTAL

Flax fibers obtained from the flax plant experimentally grown in the vicinity of Banja Luka (the Republic of Srpska, Bosnia and Herzegovina) were used as a starting material in this investigation. Flax fibers (F) were chemically treated either with 18% sodium hydroxide (1:50 liquor ratio, at room temperature, for 60 min) or 2% sodium chlorite (at pH 4, 1:50 liquor ratio, at boil temperature, during 60 min) in order to obtain a raw material with different amount of hemicelluloses (Fal) and lignin (Fox), respectively.

Chemical composition of flax fibers samples was determined according to the scheme of Soutar and Bryden [1]. Carboxyl group content (Q_{COOH}) was determined using the calcium acetate method and aldehyde group content (Q_{CHO}) using copper number [2]. ATR-FTIR spectra of the samples were recorded in absorbance mode using a Nicolet™ iS™ 10 FT-IR Spectrometer (ThermoFisherScientific) with Smart iTR™ Attenuated Total Reflectance (ATR) Sampling accessories. Electrokinetic properties i.e. zeta potential (ζ) of flax fibers as a function of pH was determined by the streaming potential method using the SurPASS electrokinetic analyzer (Anton Paar GmbH, Austria). Adsorption of Pb^{2+} from aqueous solution (25 mg/dm^3, pH 5.5) was performed in batch process (24 h, 25 ^{o}C). For the determination of lead ions concentration in the solution atomic absorption spectrometer, Pye Unicam SP9 (Pye Unicam, Ltd., UK) was used.

RESULTS AND DISCUSSION

Applied chemical treatments lead to loss in weight due to the progressive removal of hemicelluloses and lignin. Content of these component and obtained weight loss are presented in Table 1.

Table 1. The chemical compositions and weight loss of all tested samples

Samples	α-cellulose	hemicelluloses	lignin	Weight loss, %
	%			
F	75.81	7.84	4.03	-
Fal	92.33	3.44	1.12	15.77
Fox	86.27	10.06	0.16	9.39

Alkaline treatment leads to decrease of hemicelluloses content for approximately 50 % in comparison with sample F. Oxidative treatment of flax fibers, resulted in significant removal of lignin since the lignin content was decreased for about 95 % (Table 1).

Removal of hemicelluloses and lignin has impact on electrokinetic properties, i.e. on surface charge (Fig. 1.). Isoelectric point (IEP, a pH value where ζ value is 0) is an indicator of the nature of functional groups. IEP of oxidative treated sample, Fox, is slightly changed compare to the origin sample due to changes in chemical composition (i.e. decrease in lignin, followed by increase in hemicelluloses content, Table 1). In the case of alkali treatment, IEP of sample Fal is shifted toward higher pH which indicates that contribution of acidic groups became lower.

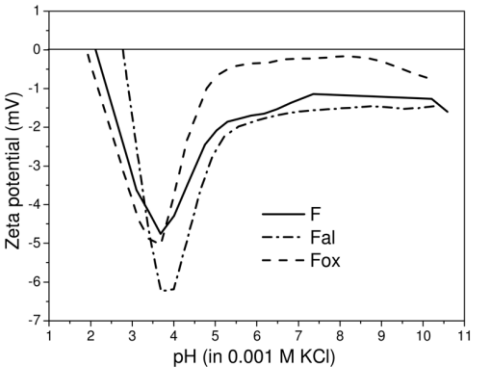

Figure 1. Zeta potential as a function of pH for all tested flax fiber samples

During the alkali treatment, a significant decrease of aldehyde group content occurs, while carboxyl group content is slightly changed (Table 2). This suggests that origin of removed carboxyl and aldehyde groups are most probably hemicelluloses. Increased content of carboxyl groups for sample Fox (Table 2) can be a consequence of oxidation of aldehyde to the carboxyl groups.

Table 2. Amount of carboxyl (Q_{COOH}) and aldehyde (Q_{CHO}) groups and adsorption capacity of flax fibers samples

Sample	Q_{CHO}	Q_{COOH}	$Q_{CHO}+Q_{COOH}$	q_e, mgPb^{2+}/g
	mmol/g			
F	0.022	0.208	0.230	7.924
Fal	0.008	0.209	0.218	4.843
Fox	0.019	0.222	0.241	8.539

The change in the amount of functional groups directly affects the capacity of flax fibers for lead ions adsorption, i.e. adsorption capacity (q_e), indicating that lead ions preferably adsorb on functional groups. This can be confirmed by FTIR spectra (Fig. 2.).

After lead ions adsorption, decrease in relative peak intensity around 1730 cm^{-1} corresponding to C=O stretching of carboxyl groups was observed for all samples, especially pronounced for sample with lower lignin content and higher amount of -COOH groups (Fox). However, ion-dipole interaction of lead ions with hydroxyl groups of cellulose should not be neglected, since decrease in relative peak intensity in the range of

3600 cm^{-1} to 3000 cm^{-1} (hydroxyl bond vibrations) indicate that hydroxyl groups of flax fibers also participate in lead ion adsorption process (Fig. 2.). This is especially pronounced for sample Fal which has similar -COOH content with sample F, but different lead ion content, indicating that -COOH groups are not the only ones responsible for adsorption of lead ions.

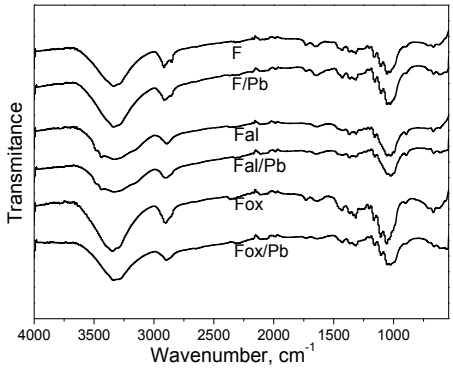

Figure 2. ATR-FTIR spectra before and after adsorption of lead ions

CONCLUSION

This work presents an attempt to explain the influences of lignin and hemicelluloses removal on surface and adsorption properties of flax fibers. The progressive removal of hemicelluloses or lignin influenced the adsorption properties through the changes in the amount of functional surface groups and electrokinetic properties of flax fibers. Removal of hemicelluloses has not brought any significant change in functional groups content and electrokinetic properties, while lignin removal resulted in an increase of functional groups content, namely carboxyl groups, which in turn influenced better lead ions adsorption.

Acknowledgement

This work was supported by Ministry of Education, Science and Technological Development Republic of Serbia through the project No 172007 and 172029.

REFERENCES

[1] M. Kostic, M. Vukcevic, B. Pejic, A. Kalijadis (2014) Textiles: History, Properties and Performance and Applications. In: Mondal IM (ed) Hemp Fibers: Old Fibers - New Applications, Nova Science Publishers, New York, pp 399-446

[2] B.D. Lazić, B.M. Pejić, A.D. Kramar, M.M. Vukčević, K.R. Mihajlovski, J.D. Rusmirović, M.M. Kostić, Cellulose, 2018, **25**, 697-709.

STRUCTURE AND MORPHOLOGY OF CALCINED LANTHANUM DOPED HYDROTALCITE

S. Pavlović[1], B. Kostić[2], D. Marinković[1], M. Gabrovska[3], D. Nikolova[3], D. Lončarević[1] and M. Stanković[1]

[1]University of Belgrade, Institute of Chemistry, Technology and Metallurgy, National Institute, Njegoševa 12, 11000 Belgrade, Serbia. (mikastan@nanosys.ihtm.bg.ac.rs)
[2]University of Belgrade, Faculty of Mining and Geology, Department of Mineralogy, Crystallography, Petrology and Geochemistry Dušina 7, 11000 Belgrade, Serbia.
[3]Institute of Catalysis, Bulgarian Academy of Sciences, Acad. G. Bonchev, str., Bldg. 11, Sofia 1113, Bulgaria.

ABSTRACT
Mg-Al hydrotalcites (Mg/Al molar ratio 3/1) doped with varying amounts of lanthanum were prepared using co-precipitation followed by calcination in order to study the effect of lanthanum on their structure and morphology. Samples were characterized by several methods: XRD, FT-IR, SEM-EDS, LDPSA and MIP. It was found that the addition of lanthanum affects the structure and morphology of the obtained metal oxides derived from La-doped Mg-Al hydrotalcites, making it effective dopant for (Mg/Al/La)O-type materials, being very promising for various catalytic reactions.

INTRODUCTION
Hydrotalcites are environmentally friendly materials which behave as solid bases and can be used in many catalytic reactions, such as transesterification of oils for biodiesel synthesis, ethanol reforming, water gas shift reactions, and CO oxidation [1, 2]. Hydrotalcites are known to be used as support for numerous catalytic species, such as rare-earth metals, alkali metals and even various anions. Their base properties are strongly related to the nature and content of doped metal as well as the temperature of calcinations.
This paper deals with the effect of La content in the mixed oxides derived from La-doped Mg-Al hydrotalcites (Mg/Al = 3/1) on the structure and morphology of prepared (Mg/Al/La)O-type materials.

EXPERIMENTAL
Preparation of HT samples
Three La-doped Mg-Al hydrotalcite samples (Mg/Al molar ratio of 3/1) were synthesized with theoretical La amount of 5, 10, and 15 wt% (calculated with

respect to $MgO-Al_2O_3$ content) by co-precipitation under stirring at 60°C and pH = 9.75±0.25, using $La(NO_3)_3 \cdot 9H_2O$, $Mg(NO_3)_2 \cdot 6H_2O$, $Al(NO_3)_3 \cdot 9H_2O$, and Na_2CO_3 as a precipitating agent. The obtained hydroxycarbonate precipitates were dried at 105°C for 20 h and subsequently calcined in an air atmosphere at 600°C for 2 h. The prepared samples were denoted as HT-LaX, where X represents the weight percentage of La. Similarly, Mg-Al hydrotalcite reference sample (Mg/Al molar ratio of 3/1) was also prepared under the same preparation conditions and denoted as HT-0.

Characterization of HT samples

X-ray diffraction data were collected using a Bruker D8 Endeavor diffracto-meter (CoKα radiation (λ = 1.78897 Å) operating at 40 mA and 40 kV). FT-IR spectra of the samples were recorded in the range of 4000-400 cm^{-1} on Thermo Scientific Nicolet 6700, diffuse reflectance infrared Fourier transform spectroscopy (DRIFTS) at room temperature under atmospheric conditions. The morphology and composition of the observed particles on the surface were determined by SEM microscopy using JEOL JCM-6610LV with energy dispersive X-ray high vacuum detector (W filament, E = 20 kV). The particle size of the samples was assessed by laser diffraction particle size analyzer (LDPSA) Malvern Mastersizer 3000C. The textural characterization of the samples was performed by mercury intrusion porosimetry (MIP) using a Carlo Erba Porosimeter 2000.

RESULTS AND DISCUSSION

The recorded X-ray diffraction lines at 41.1°, 50.4°, and 74.1° for all samples (Fig. 1) corresponded to positions of the crystalline cubic MgO phase (ICDD-PDF file 00-045-0946) indicating the formation of MgO-like phase. It is obvious that after thermal treatment at 600°C, the carbonate-containing HT structure destroyed with formation of mixed MgAl oxide, most probably a solid-solution with cubic structure [3]. The comparison with reference sample (HT-0), the lines' broadening is a consequence of the La presence. For samples with lower La contents, no peaks related to La-oxides can be observed, probably due to La low content or high dispersion of La-oxides. However, the addition of dopant in a larger amount (HT-La15) prompts formation of well-organized $La_2O_2CO_3$ (lanthanum oxy-carbonate) phase (ICDD-PDF file 00-048-1113) along with Mg-Al mixed oxide. At the applied calcination temperature the structure of $La_2O_2CO_3$ oxide is not stable, thus the pick intensity variation can be observed.

The broad and strong absorption band in the range of 3725-2570 cm^{-1}, centered at 3410 cm^{-1} (Fig. 2) appeared in the FT-IR spectra of all calcined samples and is attributed to the H-bonding stretching vibrations of the OH groups in the brucite-like layer. The bands about 1640 cm^{-1} is ascribed to the

deformation mode of H_2O molecules. It is observed two asymmetric broad bands at 1470 and 1403 cm^{-1}, at 1490 and 1409 cm^{-1} (HT-La5), at 1494 and 1411 cm^{-1} (HT-La10) and three ones at 1502, 1454 and 1368 cm^{-1} for HT-La15. This region is characterized by CO_3^{2-} and NO_3^- ions [4]. It is important to note that absorption bands for H_2O and CO_3^{2-} ions are still observed thereby indicating their present in the oxide structure ($La_2O_2CO_3$). The narrow bands, typical for interlayer NO_3^- ions at 1425 and 1385 cm^{-1} are not registered. It is likely that not all CO_3^{2-} were decomposed at the calcination temperature of 600°C or that CO_2 from the ambient air became re-adsorbed onto the basic sites of the metal oxides. The presence of water bands support the supposition that H_2O molecules could have also physically adsorbed onto the metal oxides. In fact, the HT-La15 sample shows three most intense bands at 1502, 1454 and 1368 cm^{-1} which are also potential evidence that the addition of a larger amounts of La leads to the formation of more basic sites leading to increased adsorption of CO_2.

The EDS results (Table 1) disclosed that the molar ratio of Mg/Al in each

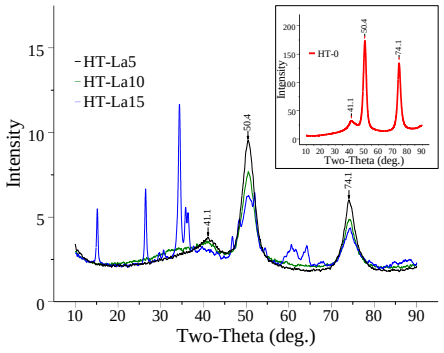

Figure 1. XRD patterns of calcined samples

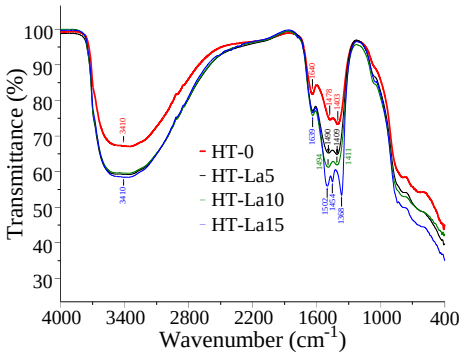

Figure 2. FT-IR spectra of calcined samples

sample is lower than the theoretical value. Bearing in mind that SEM analysis is surface one and also the limited accuracy of EDS, the obtained results correspond to the theoretical bulk ratio of Mg/Al in the samples. The La surface content increases with La loading.

The granulometry data determined by laser diffraction technique show mean particle diameters around 40 μm except for the HT-La 5 sample (Table 1). The particle diameter is roughly independent of the La content.

Table 1 Chemical composition[a], particle size[b] and porosimetry results[c]

Sample	Mg/Al molar ratio		La content		[b1]$D_{p.mean}$	[c1]ρ_{bulk}	[c2]P
	[a1]Nominal	Experimental (Mg/Al)	[a1]Nominal	[a2]wt%	μm	gcm^{-3}	vol%
HT-0	3/1	2.83/1 (26.89/9.50)	-	-	42.3	0.42	83
HT-La5	3/1	2.76/1 (24.80/9.00)	5	4.75	26.9	0.48	80
HT-La10	3/1	2.65/1 (25.62/9.67)	10	12.92	40.8	0.62	79
HT-La15	3/1	2.82/1 (24.41/8.64)	15	16.31	41.4	0.55	87

[a]EDS microanalysis; [a1]theoretical value; [a2]elemental surface analysis (EDS); [b]granulometric analysis; [b1]LDPSA; [c]MIP mercury intrusion porosimetry; [c1]bulk density; [c2]porosity.

Mercury intrusion porosimetry results showed that all calcined samples represent high-porosity materials with a porosity about 80 vol% (Table 1). SEM micrographs of calcined samples (Fig. 3) indicate the uniform hexagonal platelet structure partly destroyed due to the H_2O removal from the brucite-like layers (OH groups), interlayer H_2O molecules and CO_2 from the interlayer carbonates as well. Nevertheless, the lamellar like morphology is still kept, although with smaller platelets. The mixed Al/Mg/La oxides obtained by calcinations of La-doped Mg-Al hydrotalcites showed a different morphological structure in relation to the reference sample (Fig. 3).

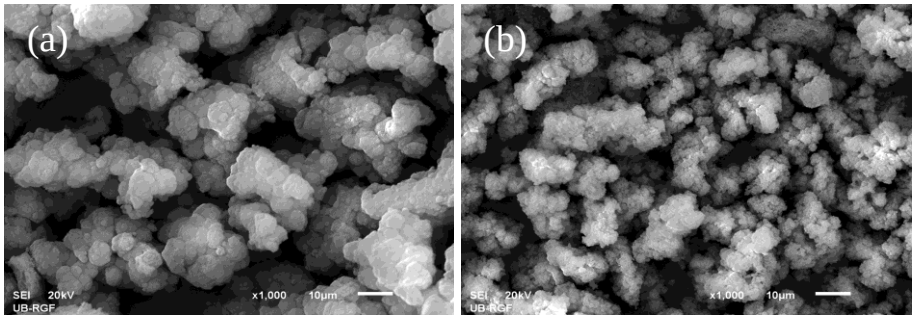

Figure 3. SEM micrographs of reference and La-doped samples

CONCLUSION

The characterization study revealed that the structure and morphology of the mixed oxides, resulting from calcination of co-precipitated La-doped Mg-Al hydrotalcites were affected by the content of La. The impact of La supplement is more significant in the oxides with higher La loading, thus permits obtaining of promising catalysts for different catalytic processes.

Acknowledgement

This work was supported by the Ministry of Education, Science and Technological Development of the Republic of Serbia (Project III 45001).

REFERENCES

[1] A. P S. Dias, J. Bernardo, P. Felizardo, M. J. N. Correia, Energy, 2012, 41, 344-353.
[2] M. Gabrovska, R. Edreva-Kardjieva, K. Tenchev, P. Tzvetkov, A. Spojakina, L. Petrov, Applied Catalysis A: General, 2011, 399, 242-251.
[3] F. Cavani, F. Trifirò, A. Vaccari, Catalysis Today, 1991, 11, 173-301.
[4] M. J. Hernandez-Moreno, M. A. Ulibarri, J. L. Rendon, C. J. Serna, Physics and Chemistry of Minerals, 1985, 12, 34-38.

SYNTHESIS AND CHARACTERIZATION OF MIXED OXIDES DERIVATE FROM Li MODIFIED Mg-Al HYDROTALCITES

D. Marinković[1], M. Gabrovska[2], D. Nikolova[2], S. Pavlović[1], B. Milovanović[3] and M. Stanković[1]*

[1]*University of Belgrade, Institute of Chemistry, Technology and Metallurgy, National Institute, Njegoševa 12, 11000 Belgrade, Serbia. (mikastan@nanosys.ihtm.bg.ac.rs)*
[2]*Institute of Catalysis, Bulgarian Academy of Sciences, Acad. G. Bonchev, str., Bldg. 11, Sofia 1113, Bulgaria.*
[3]*Alumina d.o.o., Karakaj b.b., 75400 Zvornik, Republic of Srpska, Bosnia and Herzegovina.*

ABSTRACT
Lithium modified Mg/Al hydrotalcite-like samples with different Li content were synthesized using co-precipitation followed by calcination at 500 °C. The samples were characterized by means of XRD, DRIFTS, SEM-EDS, LDPSA and MIP. Results from this study indicated that the addition of Li modifier influences the change in structural, textural and morphological characteristics, more pronounced in samples with higher lithium content.

INTRODUCTION
Hydrotalcite (HT) materials are widely used in a variety of catalytic reactions such as alkylation, isomerization, esterification, polymerization, hydro-dehydrogenation, among which the basic ones are particularly suitable for biodiesel production [1]. By changing the molar ratio of hydrotalcite cations, nature and content of metal modifier, and interlayer anions during the preparation, properties of the obtained as-synthesized hydrotalcite-like materials may be considerably influenced. After calcination, hydrotalcites decompose to mixed oxides with loss of water and CO_2 (carbonate form of HT). Calcined forms of HT are of particular interest due to their increased basicity relative to the as-synthesized HT, increased surface area and homogeneous mixing of the different elements [2].

The aim of this study is to synthesize Mg-Al hydrotalcites modified with different content of Li and to characterize the resulting mixed oxides. The effect of lithium loading on the structural, textural and morphological characteristics of the oxide (Li/Mg/Al)O-type materials as well as their use

as potential solid base catalyst in heterogeneously catalyzed transesterification reaction for biodiesel production is emphasized.

EXPERIMENTAL

Preparation of HT samples

Lithium modified Mg-Al hydrotalcite samples were synthesized in a five-necked glass reactor equipped with a steam jacket, stirrer, pH electrode, thermocouple, and reflux condenser. The carbonate forms of precursors were obtained by co-precipitation at temperature of 60 °C and pH = 9.5-10, using nitrates of the corresponding metals, $LiNO_3 \cdot 6H_2O$, $Mg(NO_3)_2 \cdot 6H_2O$, $Al(NO_3)_3 \cdot 9H_2O$, and Na_2CO_3 as a precipitating agent. The mixed Li-Mg-Al aqueous solution of nitrate salts (5, 10, and 15 wt% of Li and Mg/Al = 3/1) and the precipitant were introduced drop-wise simultaneously to the reactor. The resulting slurry was aged for 1 h in the mother liquor under stirring. Then it was filtered off and washed thoroughly with distilled water up to absence of NO_3^- ions in the filtrate. The synthesized precursors were dried at 105 °C for 20 h and subsequently thermally activated in an air atmosphere at 500 °C for 2 h. Neat Mg-Al HT sample (without the addition of Li) was also prepared for comparison purposes. The neat sample was designated as HT, while the nominal 5, 10, and 15 wt% Li-modified HT samples were labelled with 5Li-HT, 10Li-HT and 15Li-HT, respectively.

Characterization of calcined HT samples

The morphology and composition of the observed particles on the surface were determined by SEM-EDS microscopy using JEOL JCM-6610LV with energy dispersive X-ray high vacuum detector (W filament, E = 20 kV). The particle size of the samples was assessed by laser diffraction particle size analyzer (LDPSA) Malvern Mastersizer 3000C. The mercury intrusion porosimetry (MIP) measurements were performed using a Carlo Erba Porosimeter 2000. X-ray diffraction data were collected using a Bruker D8 Endeavor diffractometer (CoKα radiation, λ = 1.78897 Å). FT-IR spectra of the samples were recorded in the range of 4000-400 cm^{-1} (DRIFTS, Thermo Scientific Nicolet 6700) at room temperature under atmospheric conditions.

RESULTS AND DISCUSSION

The results of EDS elemental surface analysis, particle size, and mercury intrusion porosimetry measurements are summarized in Table 1. The EDS results revealed that the surface molar ratio of Mg/Al in each calcined sample is the identical, close to the theoretical. Since it is well known that EDS method determines the elemental composition of the mapped part of the SEM micrograph, it can be considered that experimental results satisfactorily correspond to the theoretical bulk ratio of Mg/Al in the samples. The granulometry data showed that the mean diameter of the

Table 1. Mg/Al molar ratio[a], particle size[b] and porosimetry[c] results

Sample designation	Mg/Al molar ratio		[b1]$d_{p.mean}$	[c1]S_s	[c2]P
	[a1]Nominal	[a2]Experimental	μm	m^2g^{-1}	vol%
HT	3/1	2.6/1	49	203	83
5Li-HT	3/1	2.5/1	n.d.*	199	86
10Li-HT	3/1	2.4/1	168	187	n.d.*
15Li-HT	3/1	2.5/1	226	179	85

[a]EDS microanalysis; [a1]theoretical value; [a2]elemental surface analysis (EDS); [b]granulometric analysis; [b1]mean particle diameter (LDPSA); [c]MIP; [c1]specific surface area; [c2]porosity; [*]not determined.

particles depends on the content of Li. It can be noted that the increase of Li content leads to an increase of the mean particle diameter.

The results of mercury porosimetry showed that there is no significant difference between neat and modified samples. The porosity is varied between 83 and 86%, while the specific surface area is changed from 203 to 179 m^2g^{-1} and decreasing slightly with increasing the content of lithium.

The morphology of the selected Mg/Al and Mg/Al/Li mixed oxides (neat HT and 10Li-HT) is shown in Fig. 1. The neat HT presents flat structure with "platelet" morphology, representative of layered materials, whereas the

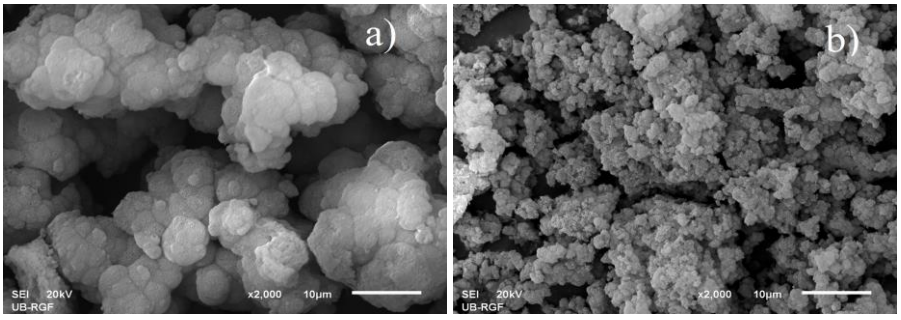

Figure 1. SEM micrographs of neat and Li-modified Mg-Al hydrotalcites: (a) neat HT and (b) 10Li-HT.

sample 10Li-HT is morphologically modified in which the large aggregates composed by round particles are observed (Fig. 1b).

Fig. 2 shows XRD diffractograms of the calcined samples. The XRD of neat HT exhibits diffractions of an Mg(Al)O mixed oxide with MgO cubic crystal structure (ICDD 00-045-0946). For the MgAlLi oxides, new diffractions were not observed (Fig. 2). The expected Li_2O was not detected, which can be due to the low scattering factor for the light atom of Li or due to high dispersion of Li_2O over the oxide matrix. Another explanation for the absence of diffractions related to the Li compounds may be found in the vicinity of the ionic radii of Li^{1+} (0.76 Å) and Mg^{2+} (0.72 Å), which allows a simple isomorphic replacement of Mg^{2+} by Li^{1+} in the MgO structure [3].

Fig. 3 illustrates the FT-IR spectra of calcined samples. All samples show a broad and intense band between 4000 and 3000 cm^{-1} due to OH stretching

vibration of layer hydroxyl groups and interlayer water molecules. The bands at 1635 cm^{-1} are originated by the bending mode of interlayer water molecules. The broad and intense bands in the region 1490-1390 cm^{-1} are due to the antisymmetric stretching mode of interlayer carbonate ions. The intensity of this band is different for modified samples and increases with increasing lithium content (Fig. 3). In fact, the 15Li-HT sample shows the most intense band centered at 1384 cm^{-1}, which is also potential evidence that the addition of larger amounts of Li leads to formation of more basic sites, leading to increased adsorption of CO_2.

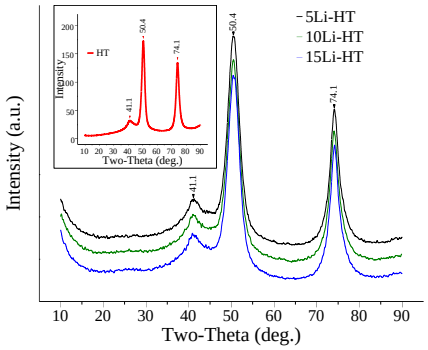

Figure 2. XRD patterns of calcined samples

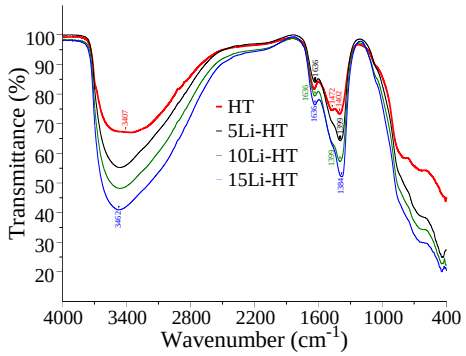

Figure 3. FT-IR spectra of calcined samples

CONCLUSION

Lithium modified Mg/Al hydrotalcite-like samples with different Li content were synthesized using co-precipitation followed by calcination at 500 °C. It was disclosed that the structure, texture and morphology of the mixed oxides, formed by calcination of co-precipitated Li modified Mg-Al hydrotalcites were altered by the content of Li. This finding is more significant in the MgAlLi oxides with higher Li content, thus allows obtaining of favorable catalysts for use in various organic conversions, especially in the reaction of oils transesterification for biodiesel production.

Acknowledgement

This work was supported by the Ministry of Education, Science and Technological Development of the Republic of Serbia (Project III 45001).

REFERENCES

[1] Y. Ma, Q. Wang, L. Zheng, Z. Gao, Q. Wang, Y. Ma, Energy, 2016, 107, 523-531.

[2] J. L. Shumaker, C. Crofcheck, S. A. Tackett, E. Santillan-Jimenez, M. Crocker, Catalysis Letters, 2007, 115, 56-61.

[3] T. Berger, J. Schuh, M. Sterrer, O. Diwald, E. Knözinger, Journal of Catalysis, 2007, 247, 61-67.

SPALATIVE ABLATION OF NANO-LAYER THIN FILMS BY SINGLE ULTRA-SHORT LASER PULSE

B. Gaković[1], P.A. Danilov[2], S. I. Kudryashov[2], S.M. Petrović[1], D. Milovanović[1], D. Peruško and A.A. Ionin[2]

[1]Institute of Nuclear Sciences "Vinča", University of Belgrade, POB.522, Belgrade, Serbia
[2] Lebedev Physical Institute of the Russian Academy of Sciences, 119991 Moscow, Russia

ABSTRACT

The effects of ultra-short laser pulses on reactive titanium-aluminium (Ti/Al) and nickel-titanium (Ni/Ti) nano-layer thin films (NLTF) were investigated. The samples, composed of five bilayers (Ti/Al and Ni/Ti, respectively), were prepared by ion sputtering on Si substrate. Single pulse irradiations were done in air with focused and linearly polarized Gaussian laser beam - 515 nm wavelength, 200 fs pulse duration and variable pulse energies. One step selective ablation of upper layer from NLTFs at low laser pulse energies and complete ablation of the thin films from Si substrate, at higher pulse energies, were registered. Effects of laser induced composition and morphological changes were monitored by different microscopies (SEM&EDS) and profilometry. Spalative ablation could be the main mechanism that caused selective ablation of the upper layers from the nano-layer thin films.

INTRODUCTION

Nano scale multi-layer thin films, new kind of nano-materials, are attractive due to their properties that cannot be obtained in the case of materials of the same bulk constituents [1]. The specific types of the NLTF are those composed of reactive metals. More than fifty reactive NLTF (RNLTF) have been known up to now and their physical-chemical properties were largely investigated [2]. Upon external energetic source, multi-layers can release stored chemical energy. This sudden exothermic reaction may become self-sustained and can propagate along the thin film alternating huge area. Surface processing of materials by laser beams is commonly used method in nanotechnology. Laser-induced processes are considered as thermally activated if laser pulse duration is longer than tens of ps [3]. Thermal effects are almost negligible if RNLTF is processing by shorter than 10 ps pulses [4]. Therefore, laser processing of RNLTF should be considered with special care due to the fact that constituents can exothermically react. Laser

processing of RNLTF with high precision and negligible alternation of the thin film substrate can be done by ultra-short fs laser pulses [5]. Selective ablation of the upper layer of the thin film, with little or no damage of the layer or the substrate beneath, is significant for applications. In this work, we have found specific values of energy /fluence at which a single 200 fs laser pulse were able to remove the first layer from the rest of the layers, without significant modification of the RNLTF beneath. In this study, we concluded that spallation is the main mechanism that caused selective ablation of upper layers in both types of RNLTFs [4].

EXPERIMENT

The samples, nano-layer thin films, were prepared by a Balzers Sputtron II vacuum system. The used substrate was n-type silicon wafer. Deposition was done in a single vacuum run, without heating the substrate. The thickness of the multilayer structures were: (i) ~200 nm - five bilayers of Ti/Al, covered by Ti as a top layer thickness of 27 nm, denoted as Ti(5x(Al/Ti))/Si; (ii) ~100 nm - five bilayers of Ni/Ti, covered by Ni as a top layer thickness of 10 nm, denoted as 5x(Ni/Ti)/Si. Laser irradiation was performed using a nano/micro fabrication setup [5], by means of single pulses of a Yb-fiber femtosecond laser with a second-harmonic wavelength of 515 nm, a FWHM of a pulse of 200 fs, a maximum pulse energy of 1.3 μJ (TEM 00 mode) and a repetition rate of 0–2 MHz. The laser pulses passed a beam splitter and were focused on the surface of the samples through a microscope. The laser beam radius at 1/e of the maximum intensity of the Gaussian beam profile was $w_0 = 3.8 \pm 0.1$ μm, and a maximum of peak laser fluence $F \approx 2.6$ J/cm^2. The sample was attached on a 3D motorized platform with a minimum step of 150 nm. Irradiation was done in air at a normal incidence. Surface morphology and composition of the irradiated surface was monitored by a JEOL 7001F scanning electron microscope (SEM), equipped with energy-dispersive x-ray (EDX) spectroscopy. The sample surfaces were examined in 2D and 3D modes by optical profilometry.

RESULTS AND DISCUSSION

In the experiment, we irradiated the RNLTF systems by single pulses with pulse energies E_p from 0.02 up to 1.3 μJ. In Fig.1(a-i), effects of single pulses on the Ti(5x(Al/Ti))/Si system are presented. The first spot, registered by SEM, was produced by a pulse of 0.04 μJ. Increasing of the pulse energy brings about different effects, ranged from partial delamination of the surface (Fig.1a), followed by clearly visible one step selective

ablation (Figs.1.b,c), two or multi step ablation (Figs.1d-h) up to complete ablation from the Si **subst**rate (Fig.1.i).

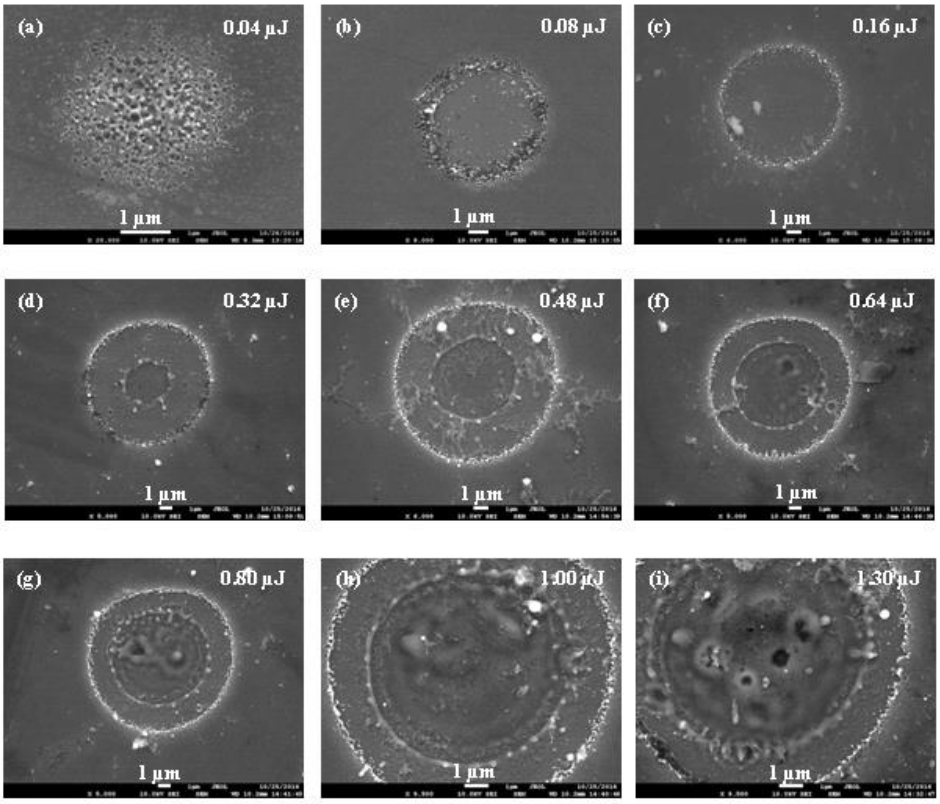

Figure 1. SEM micrographs of the Ti(5x(Al/Ti))/Si system after 200 fs single-pulse. Corresponding pulse energies are written in the upper right corners.

The similar effects, including one step ablation, multi-step ablation and complete ablation of the RNLTF, were seen after irradiation of 5x(Ni/Ti)/Si system, too. In Fig.2(a-c), the effects of only three characteristic pulse energies are presented.

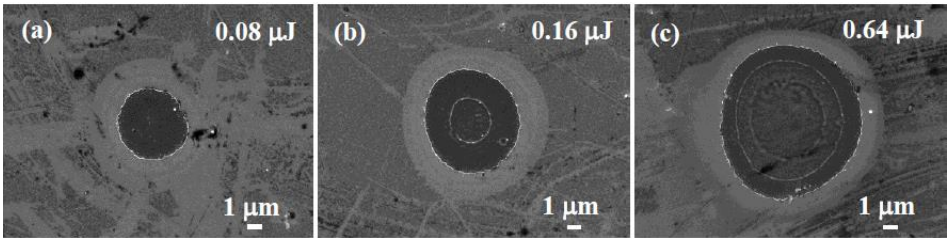

Figure 2. SEM micrographs of the 5x(Ni/Ti)/Si system after 200 fs single-pulse. Corresponding pulse energies are written in the upper right corners.

Quantitative examinations of ablated areas/craters were done by both profilometry and EDX (not presented here). One step and two step ablations are presented in Fig.3(a-c). The ablation depths were ~ 30 nm and ~ 10 nm in the cases of Ti(5x(Al/Ti)) and 5x(Ni/Ti) systems, respectively. Complete first layers, in both systems, were ablated, which was confirmed by EDX investigation. One step ablation was typical for the used Gaussian beam shape, either at the whole spot region or at the edges of the spots, as the pulse energy was increasing.

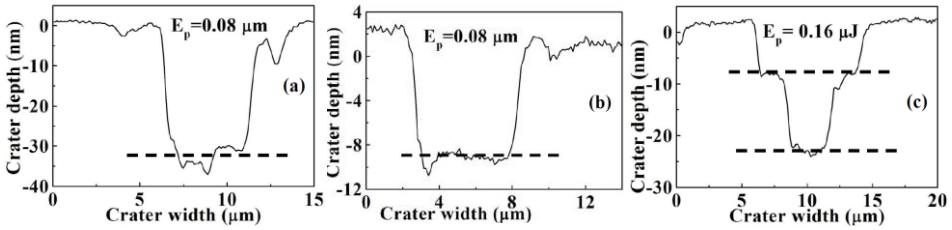

Figure 3. Profilometry of the Ti(5x(Al/Ti)) and 5x(Ni/Ti) systems after single-pulses. a), b) and c) correspond to spots presented on Fig.1 b and Figs.2 a and b.

CONCLUSION

In this work, it is shown that the single fs laser pulses, at certain values of applied pulse energies, are able to remove the whole first nano-layer from the RNLTFs. Physical mechanisms, leading to this specific form of ablation, can be identified from both the spots/craters morphology and their compositions. The flat crater's bottom and constant depth after irradiation by single fs pulse of specific value of pulse energy are the result of spallation [4]. Effect of higher pulse energies can be attributed to mixed ablation-spallation of the craters edge and explosive decomposition in the central areas [5].

Acknowledgement

To the Ministry for Science of Republic of Serbia (III 45016; ON 171023) and Government of the Russian Federation (Grants: 074-U01; 16-32-00880).

REFERENCES

[1] C. P. Yashar, W. D. Sproul, Vacuum, 1999, **55**, 179-190
[2] D.P. Adams, Thin Solid Films, 2015, **576**, 98–128
[3] Y.N. Picard, D.P. Adams, J.A. Palmer, S.M. Yalisove, App. Phys. Lett., 2006, 88, 144102-1
[4] A. A. Ionin, S. I. Kudryashov, A. A Samokhin, Physics-Uspekhi, 2017, **60**, 149-160
[5] S.I. Kudryashov, B. Gaković, P.A. Danilov, S. Petrović, D. Milovanović, A.A. Rudenko, A.A Ionin, Applied Physics Letters, 2018, **112**, 023103.

GREEN SYNTHESIS OF L-METHIONINE CAPPED SILVER AND GOLD NANOPARTICLES

D. Sejdinović [1], B. Laban [2], M. M. Marković[3], U. Ralević[3], A. Badnjević[1], E. Omanović Miklićanin[1], A. Jokić[2] and V. Vasić [4]

[1]*Department of Genetics and Bioengineering, Faculty of Engineering and IT, International Burch University, Francuske revolucije bb, Sarajevo, Bosnia and Herzegovina*
[2]*Faculty of Natural Science and Mathematics, University of Priština, Lole Ribara 29, 38220 Kosovska Mitrovica, Serbia (bojana.laban@pr.ac.rs)*
[3]*Center for Solid State Physics and New Materials, Institute of Physics, University of Belgrade 11080 Belgrade, Serbia*
[4]*Vinča Institute of Nuclear Sciences, University of Belgrade, P.O. Box 522, Belgrade, Serbia*

ABSTRACT

In this work, we present a simple green method for Ag and Au nanoparticles (NPs) synthesis in an aqueous medium. Ag and Au NPs were synthesized by chemical reduction method, using amino acid L-Methionine as reducing as well as a stabilizing agent. The size of Ag and Au NPs was controlled by changing the pH values of the reaction mixture. They were characterized by UV-Vis spectroscopy, FTIR spectroscopy, and measurement of electrophoretic properties. The size of NPs was determined by atomic force microscopy (AFM) and dynamic light scattering (DLS) measurement.

INTRODUCTION

Noble metal nanoparticles (NPs) have attracted attention due to their unique optical properties, and because of their application in different areas, such as electronics, catalysis, optoelectronic devices, biosensing, drug delivery, nanomedicine, etc., they are the subject of substantial and continuous study. There are many different methods for noble metal NPs synthesis, but the most frequently used method is a chemical reduction of metal ions in solutions. Recently, amino acids, peptides, and enzymes were used in order to develop a green method of NPs synthesis with an aim to obtain biologically compatible NPs [1, 2, 3].

The silver NPs have wide use because of their good conductivity, chemical stability, and antimicrobial activity. Gold NPs also have good physical and chemical properties and they are widely used in the biomedical field. Ag and Au NPs are the most frequently synthesized among metal NPs

because of their well-defined surface plasmon resonance, attractive chemical and physical properties, and their good biocompatibility [4].

Here we report a simple environmentally friendly method for synthesis of Ag and Au NPs using amino acid L-methionine (L-Met) as reducing as well as a capping agent. The influence of pH of solutions and molar ratio between the metal ion and L-met on NPs synthesis and stability were studied.

EXPERIMENTAL

Chemicals. Silver Nitrate ($AgNO_3$), Hydrogen tetrachloroaurate trihydrate ($HAuCl_4 \times 3H_2O$), L-Methionine, and Potassium hydroxide (KOH) from Aldrich and Merck, were used as received. Water purified with a Millipore Milli-Q system was used in all cases.

Apparatus. Absorption spectra were measured by Perkin Elmer Lambda 35 UV – Vis spectrophotometer. FTIR spectra were recorded on Nicolet IS 50 FTIR Spectrometer. Atomic Force Microscopy (AFM) measurements were performed using commercial NTegra Spectra system from NT-MDT. Dynamic Light Scattering (DLS) and zeta potential (ZP) measurements were performed using a Nano ZS zetasizer system with 633 nm He-Ne laser (Malvern Instruments, UK) and data were analyzed by the Zetasizer Software Version 6.20.

Synthesis of silver and gold colloids. The synthesis of silver and gold colloids was followed by chemical reduction of Ag^+ and Au^{3+} ions by L-Met while the reaction mixture was heated. For AgNPs@LM synthesis, 1 ml of 10^{-3} M $AgNO_3$ and 0.5 ml of 10^{-2} M L-Met were mixed, and water was added to the final volume 10 ml, then the reaction mixture was heated. When mixture started to boil, the transparent color became dark yellow, indicating NPs formation. The heating was stopped and the solution was cooled by tap water. For AuNPs@LM synthesis, 10 ml of 10^{-3} M $HAuCl_4$ was heated to boiling, 5 ml of 10^{-2} M L-Met and water were added to the 20 ml final volume. The yellow color of tetrachloroaurate became blue due to the formation of NPs. The alkalinity of solutions was adjusted by adding a proper amount of 1 M KOH for both colloids.

RESULTS AND DISCUSSION

The influence of pH on Ag and Au NPs synthesis was examined in the range from pH 4 to pH 11 for Ag NPs synthesis, the narrow absorption band of the reaction mixture at 413 nm (pH 11) was blue shifted with increasing pH, indicating the narrow distribution and small size of Ag NPs. However, for Au NPs synthesis, the absorption band at 600 nm (pH 9) is red shifted with increasing pH, due to increasing the size of NPs. It was found that obtained

colloid dispersions were stable in alkaline medium (pH ~10) for long period of time, in both cases. Further studies lead to the conclusion that the highest peak intensities of surface plasmon bands at 413 nm and 600 nm for Ag and Au NPs, respectively, were observed by increasing molar ratio metal/L-met to 1:5 in an alkaline environment, at pH ~10.

Absorption spectra of Ag and Au colloid dispersions are given in Figure 1. It is well known that surface plasmon resonance comes from the collective oscillations of free electrons of NPs induced by incident electromagnetic radiation.

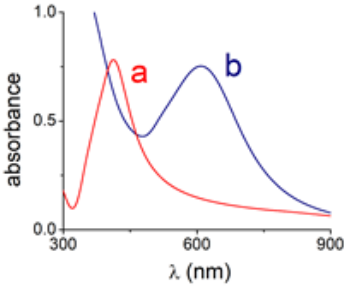

Figure 1. Absorption spectra of Ag a) and Au b) colloids.

The FTIR spectroscopy measurements (Fig.2) were performed with an aim to confirm the presence of L-met on the surface of Ag and Au NPs. As can be seen, FTIR spectra of both Ag and Au NPs are very similar and possess intense peaks in the range from 600 cm^{-1} to 1650 cm^{-1}. The bands around 1600 cm^{-1}, 1560 cm^{-1} and 1410 cm^{-1} are due C = O stretching from carboxyl group. The weak band around 2600 cm^{-1} corresponds to N – H stretching. Positions of peaks of NPs correspond to peaks characteristic for L-Met, but they are slightly shifted compared to peaks characteristic for bare L-Met. These findings confirm that molecules of L-Met are adsorbed on the surface of NPs.

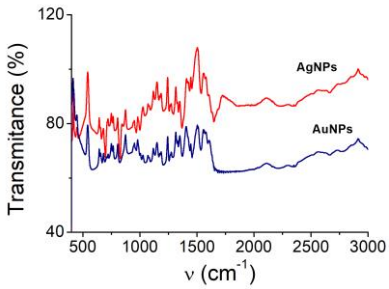

Figure 2. FTIR spectra of Ag (red line) and Au (blue line) NPs@LM.

The size of Ag and Au NPs was determined by AFM and DLS measurements (Table 1). AFM measurements suggest that prepared Ag and Au NPs are nearly spherical in shape and have the average particle diameter (d_{av}) 30 nm for Ag NPs, and 40 nm for Au NPs. Further, the size and surface charge of Ag and Au NPs were determined by DLS measurements. Obtained results show higher particle size diameter, both for Ag and Au NPs. This findings are in accordance with the fact that the size of NPs measured by these method represents the hydrodynamic sphere surrounding the NPs. The charge of Ag and Au NPs was determined by zeta potential measurements and shows that surface of NPs are negatively charged. The obtained values of mean particle

size (d_{av}) by AFM and DLS measurements, along with zeta potential and pH values for Ag and Au colloids are given in Table 1.

Table 1. pH, d_{av}, and zeta potential of silver and gold colloids.

Colloids	pH	d_{av} (nm) AFM	d_{av} (nm) DLS	ζ (mV) zeta
AgNPsLM	11	30±3	55±0.7	-40.2
AuNPsLM	9.4	40±5	70±0.9	-41.9

CONCLUSION

In this work, we presented a simple green method for Ag and Au NPs synthesis using amino acid L-Methionine as a reducing and as a stabilizing agent. The influence of pH and molar ratio of Ag or Au ions and L-Met on the optical properties and stability of NPs was studied. It was found that NPs are stable in alkaline medium and that the high amount of NPs can be obtained using a higher concentration of L-Met, ie. with increasing molar ratio of metal/L-Met. FTIR spectra confirmed that L-Met molecules are adsorbed on the surface of NPs, and AFM and DLS measurements confirmed that spherical NPs were obtained and evaluated the particles size diameters (30 nm for Ag NPs and 40 nm for AuNPs).

Acknowledgement

This work was partially supported by the Ministry for Science of the Republic of Serbia (Grants no. 172023).

REFERENCES

[1] A. Mikalauskaitė, R. Kondrotas, G. Niaura, A. Jagminas, J. Phys. Chem. C, 2015, 119, 17398−17407.
[2] K. L. Roth, X. Geng, T. Z. Grove, J. Phys. Chem. C, 2016, 120, 10951−10960.
[3] L. Zou, W. Qi, R. Huang, R. Su, M. Wang, Z. He, ACS Sustainable Chem. Eng. 2013, 1, 1398−1404.
[4] T. Shanmugasundaram, M. Radhakrishnan, V. Gopikrishnan, K. Kadirvelu, R. Balagurunatha, Nanoscale, 2017, 9, 16773 – 16790.

SYNTHESIS AND CHARACTERIZATION OF QUERCETIN-CONJUGATED GOLD NANOPARTICLES

T. Momić[1], T. Lazarević-Pašti[1], B. Laban[2], M. M. Marković[1] and V. Vasić[1]

[1]Institute of Nuclear Sciences Vinča, University of Belgrade (momict@vin.bg.ac.rs)
[2]University of Priština - Kosovska Mitrovica, Faculty of Natural Science and Mathematics, Mitrovica, Serbia

ABSTRACT
Gold nanoparticles and quercetin-conjugated gold nanoparticles complex were synthesized using trisodium citrate as reducing agent. Both kinds of nanoparticles were characterized using spectrophotometry, dynamic light scattering and zeta potential measurements. Comparison of the results confirmed successful synthesis of quercetin-conjugated gold nanoparticles complex.

INTRODUCTION
In recent years, considerable attention has been paid to the synthesis and characterization of gold nanoparticles (GNPs). Gold nanoparticles are renowned for their promising therapeutic possibilities, due to their significant properties such as biocompatibility, high surface reactivity, resistance to oxidation and plasmon resonance [1].

Quercetin (Q) (Fig.1) is the most abundantly consumed bioflavonoid with high concentrations in tea, apple, and onion. This flavonoid exhibits antioxidant, anti-inflammatory, antiglycating, anti-allergic properties.

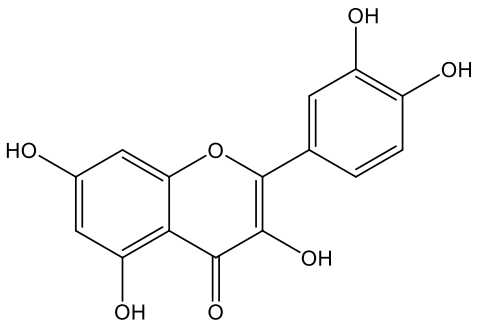

Figure 1. Quercetin structure

Although the mechanism of action is not fully known, quercetin is considered as a drug which helps protecting against various kinds of heart diseases and cancer [2]. Since flavonoids are easily metabolized and removed from the biological systems, nanoparticle-mediated delivery may enhance their activities by decelerating their metabolism [3]. To enhance the efficacy of a therapeutic agent, use of nanoparticle-based drug formulation is an important aspect of nanomedicine, for which the first step is the preparation of a stable nanoparticle-drug complex.

Previously, stable quercetin-gold nanoparticle complex (QGNP) was synthesized and characterized [4]. We have undertaken the present study to synthesize different quercetin-gold nanoparticle formulation and to characterize the complex for further study of its antioxidant effect.

EXPERIMENTAL

Gold nanoparticles were synthesized by reducing chloroauric acid by trisodium citrate in the boiling condition according to the method of Turkvitch [5]. To synthesize free gold nanoparticles, 1 mL of 1% trisodium citrate was added to 15 ml of 0.025 % (6×10^{-4} M) tetrachloroauric acid under boiling condition. After few minutes the color changed to wine red. The solution was boiled for 15 min. Quercetin was coated onto the nanoparticles during synthesis of GNP [4]. For preparation of quercetin-conjugated gold nanoparticle, 2 mg/ml of quercetin in DMSO was added to the chloroauric acid and trisodium citrate mixture to get 6×10^{-4} M quercetin, at the boiling condition prior to the formation of the wine red color. Absorption spectra were recorded by Lambda 35 UV-Vis Spectrometer, Perkin Elmer, Inc., Waltham, MA, USA). The measurements of particles size and zeta potential measurements were performed using a Zeta-sizer Nano ZS with 633 nm He-Ne laser (Malvern, UK), and the data were analyzed by the Zetasizer Software Version 6.20 (Malvern, UK).

RESULTS AND DISCUSSION

GNP and QGNP were synthesized and their absorption spectra were recorded and presented in Fig. 2. As can be seen from the spectra, surface plasmon resonance (SPR) band of citrate-capped gold nanospheres (bare) showed absorption maximum at 522 nm (Fig. 2A) while the absorption maximum of QGNP (quercetin coated) was red-shifted to 554 nm (Fig. 2B). The values of absorption maxima of GNP and QGNP suggest that the

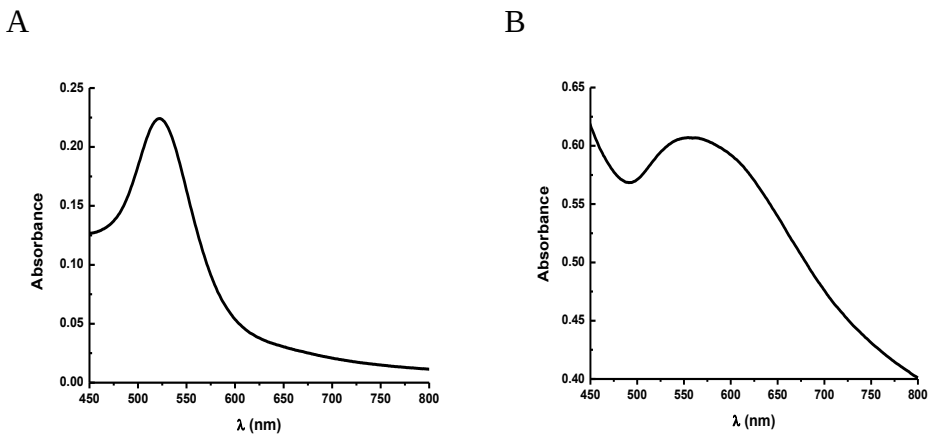

Figure 2. UV-Vis absorption spectra of A) GNP and B) QGNP.

diameters of the particles are around 20 nm and 80 nm, respectively. The diameter of GNPs measured by dynamic light scattering (DLS) was found to be approximately 30 nm, while QGNP appeared to be approximately 94 nm. The size appeared larger in DLS studies because of hydrodynamic factor also contributed to the observed diameter by this method. Also, one gold nanoparticle may attach with several molecules of quercetin. Enlarged size of flavonoid-coated GNP in comparison with bare NP was also reported by other authors [4,6].

We observed that surface charge present on GNP was -45 mV, as measured by zeta potential. Since gold atoms should not contain any negative charge on their surface, the presence of negative surface charge suggests a citrate capping on the surface of the particle. The reduction of surface charge to -13 mV in case of QGNP further indicates the attachment of quercetin on the citrate coated GNP surface [4,6].

CONCLUSION

In this work, results obtained from different experiments suggested successful formation of quercetin-conjugated gold nanoparticles. These conjugates can be proposed as potential therapeutic for an emerging nanomedicine application.

Acknowledgement
This work was financially supported by the Ministry of Education, Science and technological Development of the Republic of Serbia, Project no. 172023.

REFERENCES

[1] R. Guo, Y. Song, G. Wang, R.W. Murray, J. Am. Chem. Soc., 2005, **127**, 2752-2757.
[2] A.V.A. David, A. Radhakrishnan, S. Parasurman, Pharmacogn Rev., 2016, **10**, 84–89.
[3] F.Y. Kong, J.W. Zhang, R.F. Li, Z.X. Wang, W.J. Wang, W. Wang, Molecules, 2017, **22**, 1445 (13 pages).
[4] R. Pal, S. Panigrahi, D. Bhattacharyya, A.S. Chakraborti, J. Mol. Struct., 2013, **1046**, 153–163.
[5] J. Turkevich, G. Kim, Science, 1970, **169**, 873–879.
[6] A.Halder, S. Das, T.y Bera and A. Mukherjee, RSC Adv., 2017, **7**, 14159- 14167.

SYNTHESIS OF CALCIUM DOPED PHOSPHATE TUNGSTEN BRONZE

T.V. Maksimović[1], J.P. Maksimović[2], S.Đ.Stojadinović[3], P.I. Tančić[4] and Z.P. Nedić[2]

[1]Faculty of Science, Department of Chemistry, University of Kragujevac, Radoja Domanovića 12, 34000 Kragujevac, Serbia.
[2]Faculty of Physical Chemistry, University of Belgrade, Studentski trg 12-16, 11000 Belgrade, Serbia. (jelena.maksimovic@ffh.bg.ac.rs)
[3]Faculty of Physics, University of Belgrade, Studentski trg 12, 11000 Belgrade, Serbia.
[4]Geological Survey of Serbia, Rovinjska 12, 11000 Belgrade, Serbia.

ABSTRACT

A study is presented of phase transitions of acid $CaHPW_{12}O_{40}\cdot 6H_2O$ salt of 12-tungstophosphoric acid and characterized in the temperature range from room temperature to 1093 K. The structure and its phase transformations were characterized by thermal analysis (TGA and DSC), X-ray powder diffraction (XRPD) and Fourier-transform infrared spectra (FTIR). Dehydration processes are finished at about 770 K. Keggin's anions are transformed by solid-solid recrystallization at about 873 K in calcium doped phosphate tungsten bronze.

INTRODUCTION

Heteropoly acids Keggin's type with general formula $H_{3-x}XM_{12}O_{40}\cdot nH_2O$ (x=0-1; $X=P^{5+}$, Si^{4+}, As^{5+}, Ge^{4+}, Ce^{4+}, Th^{4+}; M=Mo, W, V, Nb; n=31-6) belong to new materials, primarily interesting because of their high protonic conductivity at room temperature [1-3]. Our investigations at high temperature of 12-tungstophosphoric acid calcium salt 6-hydrate show that this heteropoly compound could be used as a precursor for the synthesis of calcium doped phosphate tungsten bronze [4,5]. The potential application of tungsten bronzes is in their installation in batteries and fuel cellsand as catalysts for electroreduction of oxygen [6]. Numerous structural studies concerning adaptability of the PO_4 tetrahedra to an ReO_3 type framework of corner-sharing WO_6 octahedra showed the existence three families of such intercalated compounds: monophosphate tungsten bronzes with pentagonal tunnels ($MPTB_p$) or with hexagonal tunnels ($MPTB_h$), and diphosphate tungsten bronzes with hexagonal tunnels ($DPTB_h$) [7]. The physical properties of monophosphate tungsten bronzes yielded interesting

correlations between their electromagnetic properties and crystal structure [8]. The present paper deals with the synthesis and characterizations of calcium doped phosphate tungsten bronze, obtained in the process of high-temperature transformation of 12-tungstenphosphoric acid calcium salt.

EXPERIMENTAL

The 12-tungstenphosphoric acid ($H_3PW_{12}O_{40} \cdot 29H_2O$) was synthesized by the procedure described in detail in [9]. The salt acid $CaHPW_{12}O_{40} \cdot 6H_2O$ prepared ionic exchange H^+ in heteropoly acid with calcium ion. Thermal investigation were performed using TA Instruments STD 2960 Simultaneous DSC-TGA scanning rate 10 K/min. X-ray powder diffraction (XRPD) patterns were obtained using a Rigaku Ultima4 automated diffractometer with a Cu tube operated at 40 kV and 40 mA. The instrument was equipped with a curved graphite monochromatic diffraction beam, and Xe-filled proportional counter. The diffraction data were collected in the 2θ Bragg angle ranges from 10° to 90°, counting for 2 deg/min at every 0.05° steps. The divergence and receiving slits were fixed at 0.5° and 0.15 mm, respectively. The XRPD measurements were performed *ex situ* at room temperature in a stationary sample holder. Diffractometer alignment was checked by means of a standard Si powder material. FTIR spectra were recorded on a Thermo Scientific Nicolet 6700, using KBr technique with 64 scan and 2 cm^{-1} resolution.

RESULTS AND DISCUSSION

The results of thermal analysis of $CaHPW_{12}O_{40} \cdot 6H_2O$ from room temperature to 1100 K are presented in Fig.1. The DSC curve for the sample

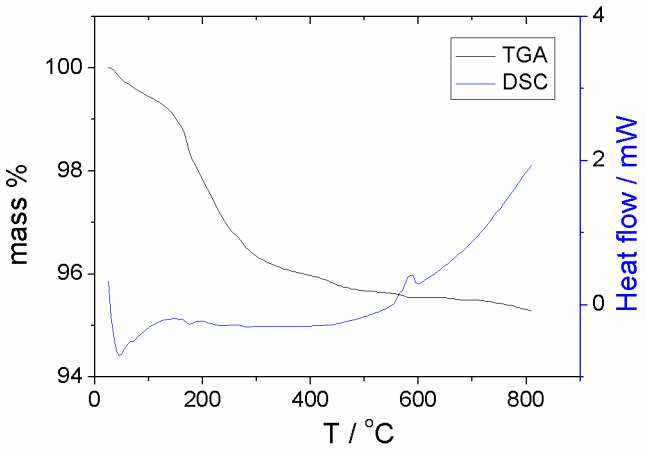

Figure 1. DSC and TGA curves of $CaHPW_{12}O_{40} \cdot 6H_2O$.

in Fig.1. show two endothermic peaks (at 323 K and 443 K) and one exothermic (at about 863 K). The sample loss molecules water and anhydrous phase of $CaHPW_{12}O_{40}$ isformed. The exothermal process correspond to solid-solid transformations of Keggin's anions and to bronze formation.

XRPD patterns of Ca-WPA and Ca-WPB are shown in Fig.2. and Table 1. The obtained data indicate that these two studied samples are obviously very different. The main reason is in their structure differences, and that there was phase temperature transition occurred. Namely, the data for Ca-WPA are very similar to those obtained for cubic stable phase determined as 6-WPA which was calcined at 443 K [4].

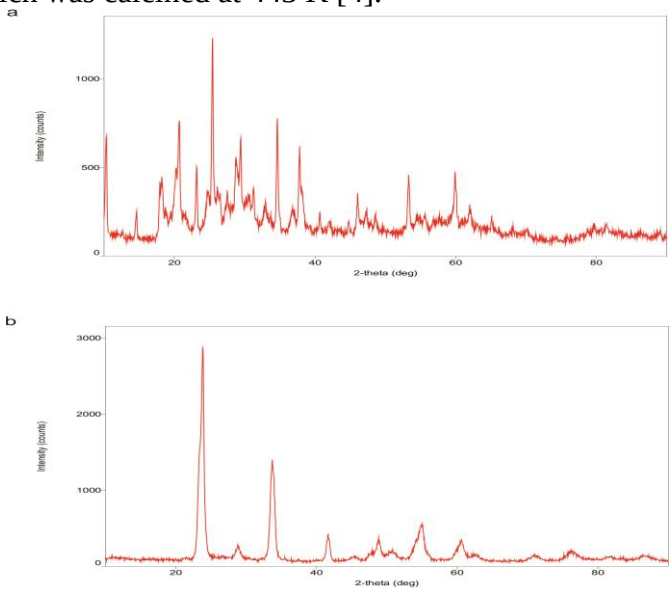

Figure 2. XRPD patterns of: (a) Ca-WPA; and (b) Ca-WPB.

On the other hand, the data for Ca-WPB are very similar to those obtained for WPB crystallized as monoclinic at temperature conditions of 1023 K [4]. It should be also mentioned that this calcium derivative also significantly differs from its Li analog synthetized at the same temperature of 923 K, which is most probably orthorhombic or triclinic [10]. The investigations about their structures are in progress, and it will be published later.

FTIR spectra of polycrystalline Ca-WPA and Ca-WPB at room temperature are shown Fig.3. In the spectrum Ca-WPA there are band characteristic of PO_4 tetrahedral and WO_6 octahedral. In the process of calcination, definite changes are evident, the destruction of Keggin's ions bronze is formed (Ca-WPB).

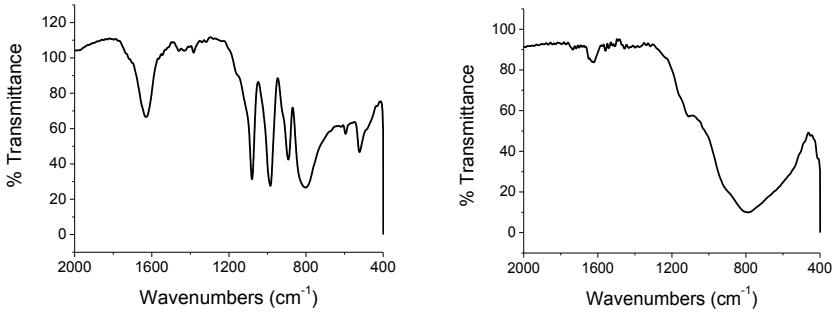

Figure 3. FTIR spectra of: (a) Ca-WPA; and (b) Ca-WPB.

CONCLUSION

In this work thermally phase transformation of acid calcium salts of 12-tungstenphosphoric acid in the temperature range from room temperature to 1100 K is presented and characterized. The dehydration processes are finished at 843 K. Increasing the temperature above 860 K new material synthesized from Keggin's anion framework as precursor was formed by solid-solid recrystallization.

Acknowledgement

This work was partially supported by the Ministry for Science of the Republic of Serbia Project III 45014, III 45001 and 172015.

REFERENCES

[1] O. Nakamura, T. Kodama, J. Ogino, I. Miyake, Chem. Lett., 1979, 1, 17-18.
[2] R. C. T. Slade, H. A. Pressman, E. Skou, Solid State Ionics, 1990, 38, 207-211.
[3] K. D. Kreuer, M. Hampele, K. Dolde, A. Rabenau, Solid State Ionics, 1988, 28-30, 589-593.
[4] U. B. Mioč, R. Ž. Dimitrijević, M. Davidović, Z. P. Nedić, M. M. Mitrović, Ph. Colomban, J. Mater. Sci. 1994, 29, 3705-3718.
[5] R. Ž. Dimitrijević, Ph. Colomban, U. B. Mioč, Z. Nedić, M. R. Todorović, N. Tjapkin, M. Davidović, Solid State Ionics, 1995, 77, 250-256.
[6] B. Broyde, J. Catal. 1968, 10, 13-18.
[7] P. Roussel, O. Perez, Ph. Labbe, ActaCryst., 2001, B57, 603-632.
[8] Z. S. Teweldemedhin, K. V. Ramanujachary, M. Greenblatt, J. Solid State Chem., 1991, 95, 21-28.
[9] U. B. Mioč, Ph. Colomban, A. Novak, J. Mol. Struct., 1990, 218, 123-128.
[10] M. Vujković, Z. Nedić, P. Tančić, O. S. Aleksić, M. V. Nikolić, U. Mioč, S. Mentus, J. Mater. Sci., 2016, 51, 2481-2489.

SOME PROPERTIES OF ALUMINA/ZIRCONIA COMPOSITE CERAMICS

N. D. Abazović [1], M. I. Čomor [1], T. D. Savić [1] and T. B. Novaković [2]

[1] *University of Belgrade, Vinča Institute of Nuclear Sciences, P.O. Box 522, 11000 Begrade, Serbia*
[2] *University of Belgrade, IChTM- Department of Catalysis and Chemical Engineering, Njegoševa12, 11000 Belgrade, Serbia (tnovak@nanosys.ihtm.bg.ac.rs)*

ABSTRACT

The mesoporous alumina/zirconia composites were synthesized via sol-gel method, followed by heat treatment at 500°C, for 5h. The effect of Al/Zr ratio on the structure and textural properties of the obtained composites was explored. Sorption analysis has confirmed that all samples have a mesoporous structure whose parameters (S_{BET}, V_p and D_{max}) strongly depend on Al/Zr ratio. The XRD pattern of composite 1Al-0.5Zr has shown that even the smallest addition of zirconia disrupts the crystallinity of alumina. The composites with higher zirconia content (1Al:1Zr and 1Al:2Zr) are characterized with peaks related only to zirconia phase.

INTRODUCTION

Porous materials possess attractive properties, such as high surface areas, tunable pore size and shapes, various structures, and a multitude of compositions, which endow them with potential applications in catalysis, adsorption, sensors, lithium-ion batteries, drug delivery, and nanodevices [1]. Among these, porous zirconia-based materials have been the subjects of intense research because the materials promise extensive use in various areas of science and technology. A variety of approaches have been developed for the preparation of porous Zr-based materials, such as sol-gel, hydrothermal and precipitation method [1]. However, like other porous metal oxides, porous zirconia cannot resist high temperatures in most cases. The mesostructure of the zirconia tends to disappear when the sample is heated above 400°C [2]. It was shown that not only thermal stability, but also structure and porosity, can be improved by adding different metal oxides, like an Al_2O_3 [1, 3-5].

This paper presents the results of studies on the influence of different Al/Zr ratio on the structural and textural properties of alumina/zirconia composites.

EXPERIMENTAL

Boehmite sol was prepared by the hydrolysis of aluminium isopropoxide according to the procedure given by Yoldas [6]. In order to obtain a Al/Zr-composite samples (atomic ratios 1/0.5, 1/1 and 1/2), appropriate concentrations of zirconium nitrate solution was mixed with freshly prepared boehmite sol; after that mixtures were gelled at 40 °C and thermally treated at 500 °C, during 5h. The nitrogen sorption was performed at -196 ^{o}C and relative pressure interval between 0.05 and 0.98 in automatic sorption apparatus (Sorptomatic 1990 Thermo Finningen). The specific surface areas, S_{BET} and C (the parameter exponentially related to E1-the first -layer adsorption energy) were calculated by the BET method [7, 8] from nitrogen adsorption-desorption isotherms, using data up to p/p_o= 0.3, and the pore size distribution have been computed from desorption branch of the isotherms [9]. The X-ray powder diffraction measurements were performed on a PHILIPS 1050 X-ray diffractometer using Ni-filtered Cu Kα radiation and Bragg-Brentano focusing geometry. The patterns were taken in the 10–70^{o} 2θ range with the step length of 0.05^{o} and exposure time of 5 s per step.

RESULTS AND DISCUSSION

Nitrogen adsorption-desorption isotherms (not shown) were used to determine textural properties of obtained samples. Type of isotherms, hysteresis loop, specific surface areas (S_{BET}), pore volumes (total, $V_{p0.98}$, and micro, $V_{pmicro)}$ and pore sizes are summarized in Table 1.

Table 1. Textural properties of the pure γ-alumina (A-500), ZrO_2 and alumina/zirconia composites with different Al/Zr ratio (1Al-0.5Zr, 1Al-1Zr, 1Al-2Zr)

Sample	S_{BET} ($m^{-2}g^{-1}$)	$V_{p0.98}$ ($cm^{-3}g^{-1}$)	$V_{p\ micro}$ ($cm^{-3}g^{-1}$)	D_{max1} (nm)	D_{max2} (nm)	Type of isotherm and hysteresis loop
A - 500	280	0.441	0.104	4.9		IVa, H2
1 A l-0.5 Zr	171	0.124	0.056	3.2	6.3	IVa, H2
1 Al – 1 Zr	145	0.154	0.044	3.2	6.4	IVa, H2
1 Al - 2 Zr	90	0.167	0.037	3.8	7.2	IVa, H2
ZrO_2	55	0.228	0.019	10.9		IVa, H2

The isotherms of all samples can be classified as IUPAC type IVa with H2hysteresis loop, characteristic for mesoporous materials. Pure γ-alumina (A 500) has large S_{BET} and pore volume and narrow pore size distribution with mean pore diameter of 4.9 nm. Increasing amount of zirconia in nanocomposites induced the reduction of S_{BET}, V_p and changes in pore size

distribution, i.e. the occurrence of bimodal distribution with two predominating pore diameter (Table 1). Changes in porous structure of alumina/zirconia composites are dependent to the amount of present zirconia.

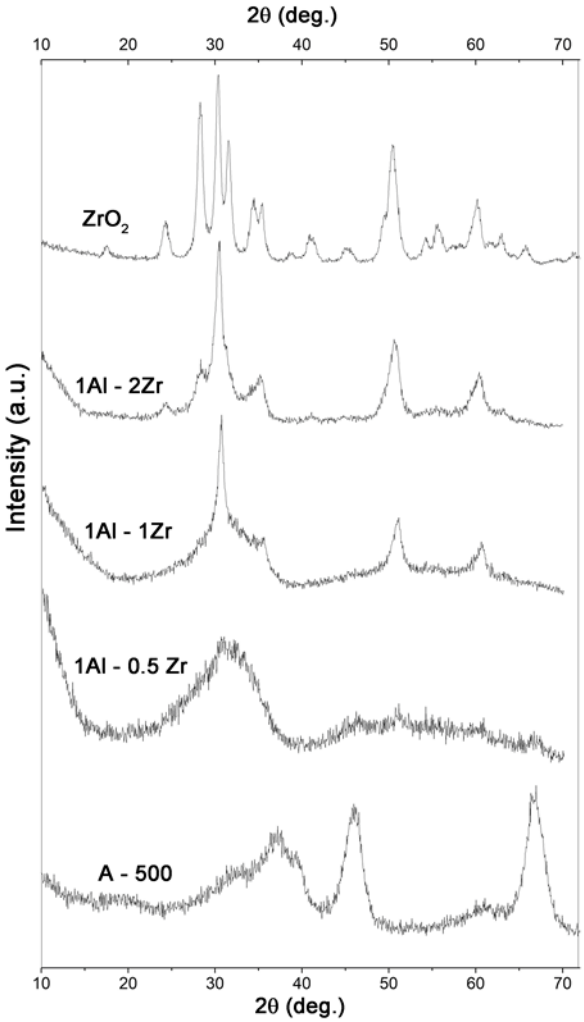

Figure 1. XRD patterns of the pure γ-alumina (A-500), ZrO2 and alumina/zirconia composites with different Al/Zr ratio (1Al-0.5Zr, 1Al-

XRD pattern of sample A-500 (Fig.1.) is characterized by diffractions characteristic for cubic γ-alumina (γ-Al2.144O3.2, PDF No. 79-1558), which has spinel-type lattice that contains cation vacancies. Broad diffraction peaks indicate nanocrystalline nature of alumina. Pure ZrO2 mainly crystalizes in a metastable tetragonal crystal form ((JCPDS 81-1544), but low-intensity peaks that originate from monoclinic (JCPDS 65-1025) crystalline structure can also be seen. X-ray diffractions of composite with the lowest amount of zirconia indicate that crystallization of alumina is suppressed even for that Al/Zr ratio. XRD patterns of the other two composites are dominated by peaks related to tetragonal zirconia.

CONCLUSION

Alumina/zirconia composites with different Al/Zr ratio were synthesized in order to obtain materials with improved textural properties compared to pure zirconia. The nitrogen sorption data confirmed mesoporosity of obtained composites and that the Al/Zr ratio strongly affects the texture, as well as the crystalline phase composition of the samples. Since the porous zirconia-based materials are promising for use in various areas of science and technology, these results will serve as a basis for future studies of the possible application of alumina/zirconia composites in the field of photocatalysis.

Acknowledgement

This work was partially supported by the Ministry for Science of the Republic of Serbia (Grants no. OI 172056 and OI 172015).

REFERENCES

[1] J. Su, Y. Li, B. Fan, F. Yu, R. Li, Micropor. Mesopor. Mat., 2016, 233, 87-92.
[2] S. G. Liu, H. Wang, J.P. Li, N. Zhao, W. Wei, Y. H. Sun, Mater. Res. Bull. 2007, 42, 171-176.
[3] R. Liu, Y. Li, Ch.-An Wang, Sh. Tie, Mater. Design., 2014, 63, 1-5.
[4] H. L. Calambás Pulgarin, M. P. Albano, Ceram. Int., 2014, 40, 5289-5298.
[5] K. R. Nemade, R. V. Barde, S. A. Waghuley, Ceram. Int., 2015, 41, 4836-4840.
[6] B.E. Yoldas, Am. Ceram. Soc. Bull. 54 (1975) 286-289.
[7] F. Rouquerol, J. Rouquerol, K.S.W. Sing, P. Llewellyn, G. Maurin, Adsorption by Powders and Porous Solids, Principles, Methodology and Applications, Academic Press, New York, 2012
[8] B.C. Lippens, B.G. Linsen, J.H. De Boer, Studies on pore systems in catalysts I The adsorption of nitrogen; apparatus and calculation, J Catal 1 (1964) 32-37.
[9] K.S. Sing, Reporting physisorption data for gas/solid systems with special reference to the determination of surface area and porosity (Recommendations 1984), Pure Appl Chem 4 (1985) 603-619.

SORPTION OF Pb(II) IONS FROM AQUEOUS SOLUTIONS BY CHEMICALLY MODIFIED CORN COB

M. Kostić, M. D. Radović, M. Petrović, S. Najdanović, N. Velinov, D. Bojić and A. Bojić

University of Niš, Department of Chemistry, Faculty of Science and Mathematics, Višegradska 33, 18 000 Niš, Serbia. (mk484475@gmail.com)

ABSTRACT

In this study, the sorption removal of Pb(II) ions from aqueous solution, using xanthated corn cob (xCC) was investigated in batch mode. The sorption equilibrium was reached after 40 minutes of contact time. The pseudo-second order and Chrastil kinetic model the best describe the Pb(II) ions removal process and thus supports the assumption behind the models. The experimental sorption capacity of xCC was 25.71 mg g^{-1}.

INTRODUCTION

Heavy metals are one of the major contaminates and the concentration levels of heavy metals in the environment are continually changing due to human's activities [1]. The heavy metals are stable, not degradable and show a high tendency toward reaching the food chain [2]. Exposure to heavy metals, even at trace levels, is high risk to human health and the environment. The typical heavy metal, such as lead, is widely used in industry of batteries, mining, paint and pigments, ceramics, petroleum and weapon industries. Lead is considered the most toxic, due to its cumulative nature can do serious harm to humans and animals mainly affecting the nervous system, blood circulation, reproductive system and kidney [3]. The maximum permissible level of lead in drinking water, according to WHO standards, is less than 0.1 mg dm^{-3} [4]. Hence, removal of lead from aqueous environment is of the utmost importance. Different methods can be used for removing metals, such as chemical precipitation, ion exchange, membrane filtration, photoreduction, reduction, reverse osmosis biological treatment, electrocoagulation and sorption. However, the most interesting method is sorption process because of its simplicity and efficiency.

The purpose of this study is to investigate the xanthated corn cob (xCC) as a biosorbent for the removal of Pb(II) ions from aqueous solutions. The sorption properties of Pb(II) ions on xCC using contact time and kinetics study were evaluated. In order to investigate the sorption mechanism, confirm the efficiency of the sorption process and predict the rate, a kinetics

investigation was conducted. Linear regression was used to determine the best fitting correlation coefficients.

EXPERIMENTAL

Reagents

All chemicals were of analytical reagent grade. HNO_3, NaOH, CS_2, $Pb(NO_3)_2$ were purchased from Merck (Germany). All solutions were prepared with deionized water. Standard stock solution of Pb(II) ions (1000 mg dm^{-3}) was used to prepare appropriate concentrations for the sorption studies. The pH of the solutions was adjusted pH-metrically to the required value with HNO_3 or NaOH (0.01 mol dm^{-3}). pH of solutions was determined by a pH meter (H260G, HACH, USA).

Preparation of biosorbent

Corn cob (*Zea mays*) used in the synthesis of the xanthated corn cob (xCC) was cultivated and collected from a farm in south Serbia (near the city of Niš). Corn cob (seedless) was roughly crushed, washed with deionized water, and grounded by laboratory mill (Waring, Germany). Corn cob was initially treated with diluted nitric acid and sodium hydroxide, producing a basic corn cob. Dried basic corn cob biomass was fractionized using standard sieves (Endecotts, England) and xanthation was carried out by process of alkalization and esterification with CS_2. The process of synthesis of xCC, used as a sorbent in this study, has been in detail described in our previous study [5].

The sorption experiments

Sorption of Pb(II) ions was done in a batch system. The effects of contact time and kinetic study were conducted by xCC dose of 0.5 g which added in 125 cm^{-3} Pb(II) ions solutions of known concentrations (10, 20, 50, 100 and 200 mg dm^{-3}) in 250 cm^3 flasks with stirring at pH 5.0 and at 20 °C. Rate of metal sorption by xCC was determined by analyzing residual of Pb(II) ions in the filtered solutions after contact periods of 0, 1, 5, 10, 20, 40, 90, 120, and 180 min. The amounts of sorbed Pb(II) ions were determined using spectrometer model AAnalyst 400 (Perkin-Elmer, USA).

RESULTS AND DISCUSSION

Effect of contact time

The effect of contact time (0–180 min) on the sorption of Pb(II) ions by xCC was studied and the obtained results are shown in Fig. 1. The removal efficiency of Pb(II) ions increases considerably until the contact time reaches 40 min (equilibrium). A further increase in the contact time has a negligible effect on the removal efficiency of Pb(II) ions.

Kinetic study

In order to examine the mechanism of sorption process onto xCC, pseudo-first and pseudo-second order and Chrastil kinetics models were used to test the experimental data (Table 1).

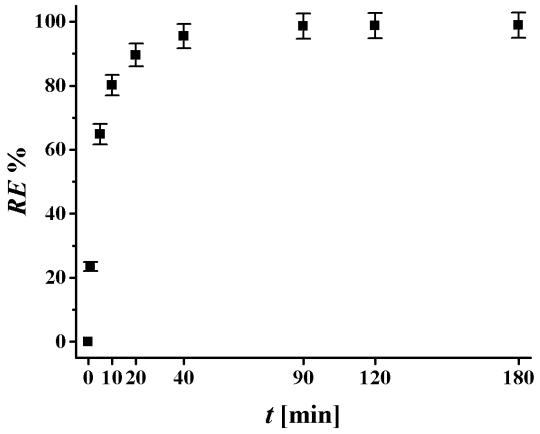

Figure 1. Results of effects of contact time on the sorption of Pb(II) ions by xCC. Initial dye concentration 50.0 mg dm^{-3}, sorbent dose 4.0 g dm^{-3}, pH 5.

The determination coefficient values for sorption Pb(II) ions on xCC were in the range from 0.926 to 0.993, while calculated $q_{e,cal}$ values were not approximate to experimental $q_{e,exp}$ values for pseudo-first order. This showed that results do not fit the pseudo-first order kinetic model.

Based on r^2 and calculated $q_{e,cal}$ values that are approximate to experimental $q_{e,exp}$ values shown in Table 1, it is revealed that the best fitted model are the pseudo-second order kinetic model.

This suggests that the rate-controlling step in the sorption process is the

Table 1. Parameters of kinetics modelling for sorption of Pb(II) ions by xCC.

Parameters	10 [mg dm^{-3}]	20 [mg dm^{-3}]	50 [mg dm^{-3}]	100 [mg dm^{-3}]	200 [mg dm^{-3}]
$q_{e,exp}$	2.47	4.94	12.36	21.60	25.12
Pseudo-first order					
$q_{e,cal}$	1.76	3.57	5.84	12.57	13.57
k_1	0.0535	0.0599	0.0527	0.0483	0.0371
r^2	0.975	0.993	0.947	0.959	0.926
Pseudo-second order					
$q_{e,cal}$	2.56	5.10	12.58	22.24	25.71
k_2	0.019	0.0434	0.0307	0.0105	0.0096
r^2	0.999	0.999	0.999	0.999	0.999
Chrastil model					
$q_{e,cal}$	2.49	4.90	12.17	21.36	24.95
k_c	0.0093	0.0176	0.0350	0.0240	0.0132
n	0.413	0.566	0.663	0.713	0.425
r^2	0.998	0.995	0.995	0.998	0.998

chemical interaction between functional groups (xanthate, carboxylic, hydroxyl etc.) of xCC and Pb(II) ions in the solution [6].
The values of determination coefficient (0.995-0.998) for Chrastil's diffusion model were very high. The values of diffusion resistance coefficient (*n*) were in the range from 0.413 to 0.713, which indicates that the sorption process was limited by diffusion resistance [7].

CONCLUSION

The ability of xanthated biosorbent based on corn cob for Pb(II) ions sorption from aqueous solution was investigated in batch conditions. The operating parameters such as contact time and initial Pb(II) ions concentration described the sorption efficiency and kinetics of sorption process. The obtained results showed that the maximum removal efficiency of Pb(II) ions attained at pH 5, after 40 min of contact time and with 4.0 g dm^{-3} of sorbent dose. The sorption capacity of xCC obtained from kinetic study was 25.71 mg g^{-1}. Xanthated corn cob have been successfully used as low-cost sorbent for the removal of Pb(II) ions from aqueous solutions.

Acknowledgement
This work was partially supported by the Ministry of Education, Science and Technological Development of the Republic of Serbia (Grants no. TR 34008).

REFERENCES

[1] B. G. Manju, S. Swaminathan, M. K. Uma, B. B. R. John, Sensors and Actuators B: Chemical, 2015, 213, 515–533.
[2] R. A. Wuana, F. E. Okieimen, International Scholarly Research Notices Ecology, 2011, 1–20.
[3] A. A. Edathil, I. Shittu, J. H. Zain, F. Banat, M. A. Haija. Journal of Environmental Chemical Engineering, 2018, 6(2), 2390–2400.
[4] W. H. Organization, Guidelines for drinking-water quality, 4th edition, incorporating the 1st addendum, 2008. Available: http://apps.who.int/iris/bitstream/handle/10665/254637/9789241549950-eng.pdf?sequence=1
[5] M. Kostić, M. Đorđević, J. Mitrović, N. Velinov, D. Bojić, M. Antonijević, A. Bojić, Environmental Science and Pollution Research, 2017, 24 (21), 17790–17804.
[6] W. K. A. W. M. Khalir, M. A. K. M. Hanafiah, S. Z. M. So'ad, W. S. W. Ngah, Polish Journal of Chemical Technology, 2012, 13(4), 84–88.
[7] A. Witek-Krowiak, Chemical Engineering Journal, 2012, 192,13–20.

THERMOMECHANICAL BEHAVIOR OF EPOXY RESINS MODIFIED WITH ORGANOCLAY NANOPARTICLES

M. Jovičić[1], V. Teofilović[1], R. Poreba[2], J. Pavličević[1], O. Bera[1], S. Sinadinović-Fišer[1] and M. Janković[1]

[1] University of Novi Sad, Faculty of Technology, Novi Sad, Serbia
[2] Institute of Macromolecular Chemistry AS CR v.v.i., Prague, Czech Republic

ABSTRACT

Epoxy-based hybrid materials were obtained by mixing diglycidyl ether bisphenol A and 5 wt% of organolayer silicate (montmorillonite and bentonite). The films of epoxy resin modified with organoclay nanoparticles were obtained using the curing agent poly (oxypropylene) diamine, at 120 °C for half hour. The thermomechanical behaviour of prepared samples was investigated using dynamic mechanical analysis (DMA) in the temperature range from 25 to 150 °C. Obtained DMA data were used to estimate the crosslink density, elastically effective chain length between crosslinks (M_c) and the glass transition temperature.

INTRODUCTION

The properties of hybrid materials containing silicate with layered structure mostly depend on the clay stratification degree determined by the nature of the used components, the type of polymer matrix and organoclay, as well as preparation method. Epoxy resins are very common and important type of matrix systems for composite materials. Reasons for this popularity include low melt viscosity, good filer dispersion, and relatively low processing temperatures. There is a great interest in the dispersion of clay to epoxy/amine systems, since the addition of organically modified clay achieves the preservation of thermal stability, improves mechanical properties, and increases the glass transition temperature [1, 2]. The clay exfoliation depends on the polarity and viscosity of the epoxy/hardener mixture. The incorporation of clay leads to a significant increase in storage modulus and a modest increase in *Tg* of the nanocomposites. The increase in modulus is more prominent in case of a soft matrix than a hard matrix. [3]. The incorporation of 7 wt% of montmorillonite clay resulted in a 60 % of increase in the dynamic storage modulus and an increase of 14 °C in the heat distortion temperature of epoxy network cured with p,p'-diaminodiphenyl sulfone [4].

The aim of this paper was to monitor the influence of organoclay nanoparticles type (montmorillonite and bentonite) on the thermomechanical behavior of the epoxy/amine mixture.

EXPERIMENTAL

For the preparation of hybrid materials with an epoxy matrix, the following raw materials were used: diglycidyl ether bisphenol A (DGEBA, Sigma-Aldrich Chemie GmbH), poly (oxypropylene) diamine (Jeffamine D-230, Huntsman International LLC), organically modified montmorillonite (MMT, Cloisite 15A, Southern Clai Products, Inc., Texas) or organically modified bentonite (Bentonite for organic systems, BO, Fluka). A hybrid with an epoxy matrix and organolayer silicate was prepared by in situ polymerization. Firstly, the organoclay was mixed in liquid DGEBA at temperature of 45 °C in an ultrasonic bath twice per 10 minutes, in order to obtain a homogeneous solution. Then, the curing agent, Jeffamine D-230, was added in a stoichiometric ration to DGEBA. The sample films were obtained by curing in an oven at 120 °C for 30 min. The content of organolayer silicate was 5 wt % in regard to the total mass of the DGEBA /Jeffamin D-230 system.

Dynamic mechanical properties were carried out on ARES-LS2 from Rheometrics Scientific (now TA instruments). The DMA spectra of samples were recorded in tensile mode in the temperature range from 25 to 150 °C, at a frequency of 1 Hz and with a heating rate of 3 °C/min. The glass transition temperatures, T_g, were determined as the maxima of tanδ and maxima of E'' in DMA spectra of coatings. The crosslink density (υ_e), the number of moles of elastically effective network chains per cubic centimeter of sample, can be calculated from the DMA data using the kinetic theory of rubber elasticity, eq. 1 [5]:

$$\nu_e = \frac{E'_{\min}}{RT} \tag{1}$$

where E'_{min} is E' values in rubbery region at $T>T_g$ (E'_{min}), R is the gas constant (8.314 J/molK) and T (in K) is the temperature at E'_{min}. The weight of sample in grams which contains 1 mol of elastically effective network chain (M_c), can be calculated using eq. 2:

$$M_C = \frac{\rho}{\nu_e} \tag{2}$$

where ρ is the density of coating films.

RESULTS AND DISCUSSION

The dynamic spectra of E', E'' and tanδ versus temperature for epoxy/amine/bentonite film is shown in Fig. 1. The temperature scan covers the full range of polymer behavior from glassy (left) to transition (center) to rubbery plateau (right), Fig 1. From tensile storage module (E'), it is evident that the sample is very stiff in the glass region, softens throughout the transition region, and levels out at a low value in the rubbery plateau. The breadth and shape of the tanδ, detected for all samples, indicate the heterogeneity of the components used in the coating formulation [6]. The glass transition temperatures, T_g, which were determined as the maxima of tanδ and maxima of E'' in DMA spectra of coatings, are reported in Table 1.

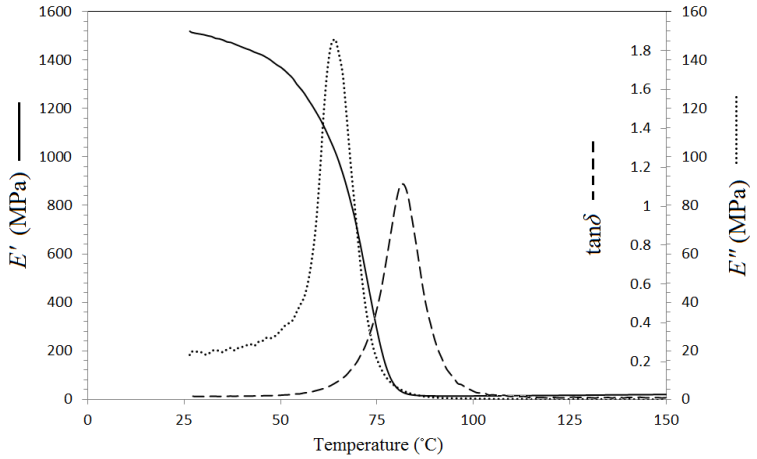

Figure 1. Storage modulus (E'), loss modulus (E'') and the loss factor (tanδ) versus the temperature for the cured film epoxy/amine/bentonite.

The values of ρ were determined experimentally and found to be in the range of 1.01-1.11 g/cm^3 for the all prepared films. The values of υ_e and M_c are summarized in Table 1.

Table 1. The values of T_g (on the basis of E''_{max} and tanδ_{max}), E'_{min}, ν_e, and M_c of coating films.

Film	T_g(°C)		E'_{min} (Pa) at 110°C	ν_e (mol/m^3)	M_c(g/mol)
	E''_{max}	tanδ_{max}			
epoxy/amin	60	70	$4.59 \cdot 10^6$	1480	710
epoxy/amin/montmorillonite	67	76	$9.9 \cdot 10^6$	3192	348
epoxy/amin/bentonite	72	81	$10.8 \cdot 10^6$	3482	320

The mixtures containing organoclay nanoparticles (montmorillonite or bentonite) show higher values of the crosslink density than those based on pure epoxy/amine, which can be attributed to the confinement of polymer chains as a result of intercalation into the interlayer gallery of the clay [3]. The data obtained for υ_e indicate that a tighter network in the structure of epoxy/amine/bentonite mixture is formed in regard to epoxy/amine/montmorillonite, due to the interaction of the epoxy matrix with the external surfaces of the micro-particles of the bentonite [7]. The above observation is confirmed with the observed values of M_c that is found to be the highest for the epoxy/amine/bentonite crosslinked film. As it is expected, with the increase of crosslinking density, the glass transition temperature of prepared sample is increasing (Table 1).

CONCLUSION

Thermomechanical behavior of epoxy resins modified with organoclay nanoparticles (montmorillonite and bentonite) was studied, in order to obtain detailed information on network structure, necessary for the calculation of crosslink density, elastically effective chain length between crosslinks and the glass transition temperature. The samples with organoclay nanoparticles show higher values of the crosslink density of pure epoxy/amine. With the increase in crosslinking density, the glass transition temperature of prepared material increases.

Acknowledgement

This work was supported by the Ministry of Education, Science and Technological Development of Serbia (Grant no. III45022).

REFERENCES

[1] T. D. Ngo, M. T. Ton-That, S. V. Hoa, K. C. Cole, J. Appl. Polym. Sci., 2008, **107**, 1154−1162.
[2] E. Kaya, M. T. Lu, S. Okur, J. Appl. Polym. Sci., 2008, **109**, 834−840.
[3] D. Ratna, N. R. Manoj, R. Varley, R. K. Singh Raman, G. P. Simon, Polym. Int., 2003, **52**, 1403–1407.
[4] P. B. Messersmith, E. P. Giannelis, Chem. Mater., 1994, **6**, 1719-1725.
[5] L. W. Hill, Prog. Org. Coat., 1997, **31**, 235-243.
[6] M. Johansson, T. Glauser, G. Rospo, and A. Hult, J. Appl. Polym. Sci., 2000, **75**, 612-618.
[7] P. I. Xidas, K. S. Triantafyllidis, Eur. Polym. J., 2010, **46**, 404–417.

THE EFFECTS OF NaA ZEOLITE WEIGHT FRACTION ON THERMAL PROPERTIES OF LDPE/NaA ZEOLITE COMPOSITES

F. Marinković [1] and B. Stanković [2]

[1] *University of Belgrade, Faculty of Physics, Studentski trg 12-16, 11000 Belgrade, Serbia.*
[2] *University of Belgrade, Faculty of Physical Chemistry, Studentski trg 12-16, 11000 Belgrade, Serbia. (branislav@ffh.bg.ac.rs)*

ABSTRACT

The effects of weight fraction of NaA zeolite (0-30 % wt) on the thermo-physical properties (density, specific heat capacity, thermal diffusivity and heat conductivity) of the low density polyethylene (LDPE) and NaA zeolite composite has been studied. The samples of LDPE/NaA zeolite composites were prepared by the compression molding procedure. Based on the obtained results it was concluded that the increase in the NaA zeolite weight fraction in the composite leads the increase in the values of thermal diffusivity, density, thermal conductivity, and on the contrary to decrease in the composite specific heat capacity. Model by which thermo-physical properties changes with increase in weight fraction of NaA zeolite has been proposed.

INTRODUCTION

Polyethylene is the most commonly used polymer with widely applications in many areas such as industry of packaging, industry of cables, housewares etc. As other polymers, polyethylene has low thermal conductivity because of relative low atomic density, weak interactions and high anharmonicity in their molecular vibrations [1]. In literature is well known, that fillers can improve thermal properties of polymers [2]. Weidenffeler et al. [3] was investigated thermal conductivity of polypropylene with different types and amount of fillers. They concluded that thermal conductivity increased with increasing of fillers amount. Zeolites are inorganic materials with higher thermal conductivity than polymers, so they can be good fillers for polymer matrix. Structurally the zeolites are framework aluminosilicates which are based on an infinitely extending three-dimensional network of AlO_4 and SiO_4 thetrahedra linked to each other by sharing all oxygens [4]. Scetar et al. [5] investigated thermal properties of low density polyethylene (LDPE) nanocomposites modified with zeolite and clay. They found that the

presence of zeolite tend to reduce thermal stability of LDPE/zeolite in comparison to the polyethylene. In the present work we investigated influence of zeolite weight fraction in LDPE matrix on thermal properties.

EXPERIMENTAL

Materials

The commercially LDPE (PE552, HIP Pančevo, Serbia) (M_w = 110 000 g/mol, ρ = 0.922 g/cm^3) was used as the polymer matrix. The NaA zeolite (Alumina factory, Birač, Bosnia and Herzegovina) with mean particle size 4μm and density ρ = 2.07 g/cm^3 was dried at 400 °C for 24 h in order to ensure completely removal of water, and then used as fillers.

Composite sample preparation

Predetermined quantity of granulated LDPE was placed in Brabender rheometer at 160 °C for 3 min and different weight fraction (*w*) from 0 wt % to 30 wt % of zeolite fillers was added in polymer matrix thereafter. Mixing process was continued in the additional 9minat constant temperature. The composite plates were prepared by compression molding for 7 min at the constant pressure and temperature (4.5 MPa, 170 °C).

Specific density

The specific density ρ_c of the composite materials was determined using pycnometer and following equation:

$$\rho_c = \frac{m\rho_t}{m_1+m-m_2} \quad (1)$$

where, m is mass of sample, m_1 is mass of pycnometer filled with isopropanol (ρ_t = 0.87 g/cm^{-1}) which is used as nonpolar solvent, m_2 is mass of pycnometer filled with isopropanol and with sample.

Differential scanning calorimetry (DSC)

Specific heat capacities were determined by DSC measurements, which have been performed on TA Instruments DSC Q1000 , under air flow of 50 ml/min. DSC was calibrated with a high-purity indium standard.

Thermal diffusivity

The thermal diffusivity of samples was measured by laser-flash method using instrument DLF-1200 TA Instruments. The results of thermal diffusivity were used to calculate thermal conductivity by using the equation: $K=\alpha\rho C_p$, where K is thermal conductivity of samples, α is thermal diffusivity of samples, ρ is density and C_p is specific heat capacity. All samples were measured at room temperature.

RESULTS AND DISCUSSION

Values of density, specific heat capacity and thermal conductivity of the LDPE/NaA zeolite composites with different weight fraction of NaA zolite are presented in Table 1.

Table 1. Thermo-physical properties of LDPE/NaA composites

w%	Density (kg/m^3)	Specific heat capacity (kJ/kg*K)	Thermal diffusivity ($m^2/s \cdot 10^{-7}$)	Thermal conductivity (W/m·K)
0	922	2300	2.18	0.462
5	942	2263	2.21	0.472
10	961	2227	2.31	0.496
15	1024	2192	2.35	0.529
20	1039	2156	2.49	0.560
25	1087	2112	2.55	0.588
30	1121	2093	2.58	0.602

As it can been seen with the increase in the NaA zeolite weight fraction in the composite leads the increase in the values of thermal diffusivity, density, thermal conductivity, whereas the specific heat capacity of composite decreases. All of the thermo-physical properties changes by the serial
model [6].

CONCLUSION

The NaA zeolite weight fraction has significant effect on the thermo-physical properties of LDPE/NaA zeolite composite. The increase in NaA zeolite content leads to the increase of all investigated properties except specific heat capacity. Changes in the investigated thermo-physical properties can be described by the serial model.

Acknowledgement

This work was partially supported by the Ministry for Science of the Republic of Serbia (Grants no. 172015 and 171029).

REFERENCES

[1] I.A. Tsekmes, R. Kochetov, P.H.F. Morshuis, J.J Smit, 2013 IEEE International Conference on Solid Dielectrics, 2013,678-681.

[2] S. Yhang, X.Y. Cao, Y.M. Ma, Y.C. Ke, J.K. Zhang, F.S. Wang, eXPRESS Polymer Letters, 2001, 5, 581-590.
[3] B. Weidenfeller, M. Hofer, F. Schilling, Copmosites: Part A, 2002, 33, 1041-1053.
[4] S. Suresh, S. Sundaramoorthy, Green Chemical Engineering: An Introduction to Catalysis, Kinetics, and Chemical Processes, CRC Press, Boca Raton, 2015.
[5] M. Scetar, A.Pticek-Sirocic, Z. Hrnjak-Murgic, K. Galic, Polymer-Plastics Technology and Engineering, 2013, 52, 1611-1620.
[6] R.C. Progelhof, J.L. Throne, R.R. Ruetsch, Polymer Engineering and Science, 1976, 16, 615-625.

XRD METHOD FOR QUANTITATIVE DETERMINATION OF FILLER WEIGHT FRACTION IN POLYMERS COMPOSITES

F. Marinković [1], B. Stanković [2] and N. Tadić [1]

[1] *University of Belgrade, Faculty of Physics, Studentski trg 12-16, 11000 Belgrade, Serbia.*
[2] *University of Belgrade, Faculty of Physical Chemistry, Studentski trg 12-16, 11000 Belgrade, Serbia. (branislav@ffh.bg.ac.rs)*

ABSTRACT

New method for the determination of filler weight fraction in polymer composite based on measurement of integral area of XRD diffraction peak has been established. Powdery calibration mixtures of low density polyethylene (LDPE) and zeolite NaA were prepared with the certain weight fraction of zeolite from 5 wt % to 30 wt % and there's XRD patterns were recorded. The effect of zeolite weight fraction on the integral area of the diffraction peaks of the zeolite NaA was investigated. The composite samples in the form of plates which contains 5–30 wt % of zeolite were prepared. Determination of the weight fraction of zeolite in the composite is based on the measurement of the area of the selected diffraction peak of zeolite.

INTRODUCTION

It is well-known that the physicochemical properties and performances of composite materials depend not only on the physicochemical properties of the constituents, but rather on the composite microstructure, i.e. on the dispersion and orientation of the filler and on the filler–filler and filler–matrix interactions [1]. Having this in mind, for the production of polymeric composite materials, it is important to develop new methods that enable complete dispersion of filler particles in the polymer matrix. On the other side, in order to verify methods, it is extremely important to have simple, accessible and reliable procedures by which one can determine the dispersion degree of filler particles within the composite material. Novel method for determination of crystalline filler weight fraction and dispersion degree based on XRD analysis are developed and applied on the LDPE/NaA zeolite composite.

EXPERIMENTAL

Materials

The commercially LDPE (PE552, HIP Pančevo, Serbia) (M_w =110 000 g/mol, ρ=0.922 g/cm^3) was used as the polymer matrix. The NaA zeolite (Alumina factory, Birač, Bosnia and Herzegovina) with mean particle size 4 μm and density ρ = 2.07 g/cm^3 was dried at 400 °C for 24 h in order to ensure completely removal of water, and then used as the fillers.

Composite sample preparation

Predetermined quantity of granule LDPE was placed in Brabender rheometer at 160°C for 3min and different weight fraction (w) from 0 wt % to 30 wt % of zeolite fillers was added in polymer matrix thereafter. Mixing process was continued in the additional 9 min at constant temperature. The composite plates were prepared by compression molding for 7 min at the constant pressure and temperature (4.5 MPa, 170 °C).

Preparation of powdery calibration mixtures

Predetermined quantities of powdery LDPE were added to the predetermined quantities of zeolite in order to achieve desired weigh fraction of zeolite in composite (0 wt % to 30 wt %) and homogenized at Perkin-Elmer Vibrating mill.

X-ray diffraction (XRD)

The X-ray patterns of all powdered calibration samples and samples taken from the composite plates were recorded by X–ray diffractometer, Rigaku Ultima IV, in Bragg–Brentano configuration using Ni-filtered CuK$_\alpha$ radiation (λ = 1.54178 Å).

RESULTS AND DISCUSSION

The XRD patterns of powdery NaA zeolite and LDPE are presented in Fig. 1a and b, respectively. XRD patterns are in well agreement with JSPDS cards of NaA zeolite (No. 71-1557) and LDPE (No. 11-0834).

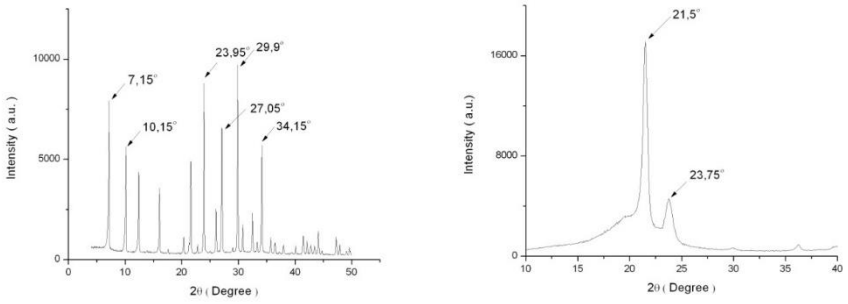

Figure 1. XRD patterns of powdery NaA zeolite (a) and LDPE (b).

In order to develop a method for determination of zeolite weight fraction in the composite, the X–ray patterns of powdery calibration mixtures with given zeolite *w* in the range from 5 wt % to 30 wt % were recorded. The area (*A*) of zeolite peaks linearly increase with increasing of zeolite weight fraction and the best linearly dependence is found for the peak at 2θ = 29.9 ° (correlation degree *R* = 0.9987):

$$A = 206.92 + 5.89w \quad (1)$$

which has been chosen for the determination of the zeolite weight fraction in the LDPE/NaA composite. The XRD patterns of the LDPE /NaA zeolite composites taken from the central part of the composite plate are shown in Fig. 2.

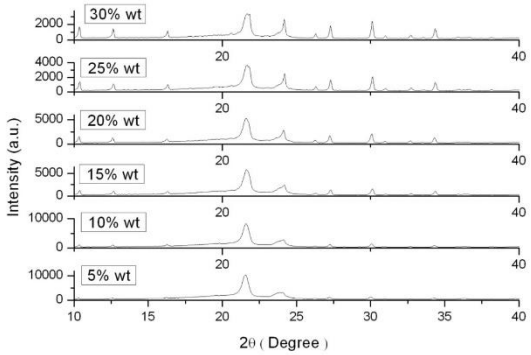

Figure 2. The XRD patterns of the LDPE /NaA zeolite composites.

Table 1. Values of: calculated *w*, relative and absolute errors, $\overline{w_{i,j}}$ and *DD* for different composites.

$(w_{o,j})$ (%)	Calculated *w* (%)	Abs. error (%)	Rel. error (%)	$(\overline{w_{i,j}})$ (%)	*DD* (%)
5	4.87	0.13	2.6	4.82	96.4
10	9.76	0.24	2.4	9.74	97.4
15	14.63	0.37	2.5	14.69	97.9
20	19.66	0.34	1.7	19.74	98.7
25	24.64	0.36	1.4	24.58	98.3
30	29.38	0.62	2.1	29.34	97.8

The zeolite weight fraction taken from the central part of composite plate was calculated by Eq. 1 and results are presented in the Table 1. In order to determine the dispersion degree of NaA zeolite in LDPE/NaA zeolite

composite, the 25 differently positioned samples were taken from each of the plate of different zeolite weight fraction. Out of these 25 samples, the 5 randomly selected samples were analyzed. Dispersion degree (*DD*) is calculated from value of average weight fraction of zeolite ($\overline{w_{t,J}}$) as $DD = \overline{w_{t,J}} / w_{o,\,j}$

CONCLUSION

XRD patterns were recorded for the samples of powdery calibration mixtures and for samples taken from different locations on LDPE/NaA composite plates. Areas of diffraction peaks with highest intensities linearly increase with weight fraction of NaA zeolite in both calibration mixtures and composites. Procedure for the calculation of NaA zeolite weight fraction in composite was developed. It was shown that relative error for the determination of weight fraction of NaA zeolite in composite is in the interval of 1.2–2.3 %. Method for the determination of dispersion degree of NaA zeolite in composite was established. By the XRD method, it was shown that all composite samples have high dispersion degree of NaA zeolite in composite.

Acknowledgement

This work was partially supported by the Ministry of Education, Science and Technological Development of Serbia (Grants no. 172015, 171029, and 171035).

REFERENCES

[1] M.-J. Wang, Rubber Chemistry and Technology, 1998, 71, 520-589.

ANALYSES OF ISOTHERMAL DEHYDRATION KINETICS OF PAAG HYDROGEL BY MAXWELL-BOLTZMANN DISTRIBUTION OF ACTIVATION ENERGIES

B. Stanković[1] and F. Marinković[2]

[1] University of Belgrade, Faculty of Physical Chemistry, Studentski trg 12-16, 11000 Belgrade, Serbia. (branislav@ffh.bg.ac.rs)
[2] University of Belgrade, Faculty of Physics, Studentski trg 12-16, 11000 Belgrade, Serbia.

ABSTRACT
The possibility of applying the Skrdla's and Robertson's semi-empirical disperse kinetics model to describe the isothermal dehydration kinetics of poly(acrylic acid)-g-gelatin (PAAG) hydrogel was investigated. The isothermal thermogravimetric curves of PAAG hydrogel dehydration were measured at temperature range from 313 K to 353 K. The kinetics conversion curves were fitted by model equations from Skrdla's and Robertson's semi-empirical model. It was found that the isothermal thermogravimetric conversion curves can be completely described by acceleratory model equation. The values of model equation parameters (*a* and *b*) were calculated. The mechanism of PAAG hydrogel dehydration was discussed.

INTRODUCTION
Hydrogels can be represented as a three-dimensional network of hydrophilic polymers, which are able to reversibly absorb (swelling) and release (dehydrate) large fraction of aqueous solvent without dissolving or losing their structural integrity. As such, hydrogels are important class of so-called "smart" and "stimuli-sensitive" materials and have wide practical application [1]. Due to the fluctuating structure of hydrogel, dehydratation kinetics should be described by the some of the dispersion kinetics models. Therefore, the aim of this of this work is to examined the possibility of mathematical description of the PAAG hydrogel isothermal kinetics by Skrdla's and Robertson's semi-empirical dispersive kinetics model in which distribution of activation energies is described in form of Maxwell-Boltzmann distribution [2].

EXPERIMENTAL

Synthesis of poly(acrylic acid)-g-gelatine hydrogels

The PAAG hydrogel was synthetized by the procedure of free radical crosslinking grafting polymerisation described in previous work [3].

Thermogravimetric measurements

The kinetics of hydrogel dehydration was analyzed by isothermal thermogravimetric (TG) analysis at four temperatures, 313, 323, 343 and 353 K. Mass losses of 20 ± 1 mg equilibrium swollen hydrogel samples were measured in platinum pans under nitrogen atmosphere at a gas flow rate of 10 ml min^{-1} by TG Analyser, TA Instruments, Model Q500, USA.

Calculation of the dehydration degree

The dehydration degree, α, was calculated as:

$$\alpha = \frac{m_0 - m}{m_0 - m_f} \quad (1)$$

where m_0, m, and m_f refer to the initial, actual, and final mass of the sample, respectively.

Experimental data fitting

The conversion curves were fitted with deceleratory (Eq. 2) and acceleratory (Eq. 3) model equations of Skrdla's and Robertson's dispersive kinetics model:

$$\alpha = 1 - e^{at(e^{-bt^2}-1)} \quad (2)$$

$$\alpha = 1 - e^{-\frac{a}{t}(e^{bt^2}-1)} \quad (3)$$

where α represents conversion degree at time t, while a and b are the first and the second order reaction rate constant.

RESULTS AND DISCUSSION

Thermogravimetric curves showing dehydration process of equilibrium swollen PAAG hydrogel at different temperatures are presented in Fig. 1.

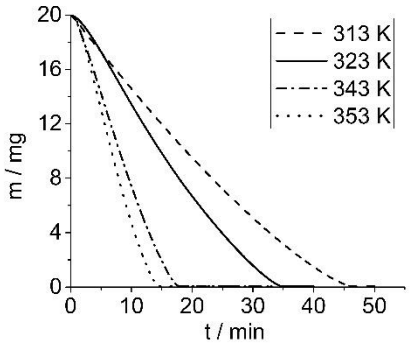

Figure 1. The isothermal TG curves of PAAG hydrogel dehydration at different temperatures.

Fitting of experimental data was firstly done by both deceleratory and acceleratory model (Fig 2). It has been found that kinetics of dehydration process can be described by acceleratory equation along the entire interval of time. From a closer look on Table 1, where parameters of Eq. 3 are presented, one can see that for all sets of experimental data, values of R^2 very high.

Table 1. Parameters of acceleratory model equation which fit PAAG hydrogel isothermal dehydration kinetics

T / K	313	323	343	353
a / min	35.9±0,2	21.1±0,2	8.6±0.1	5.7±0.1
b / min^{-2}	$(8.55\pm0,04)\cdot10^{-4}$	$(1.74\pm0.02)\cdot10^{-3}$	$(7.46\pm0.06)\cdot10^{-3}$	$(1.26\pm0.01)\cdot10^{-2}$
R^2	0.996	0.994	0.994	0.999

Values of E_a^0 are ln$A$ were estimated from curve ln(a*b) versus 1/T. Value of ln$A$ is intercept of this linear dependence, whereas E_a^0 can be calculated as as a product of gas constant, R, and the slope [37]. It was found that E_a^0≈20.8±0.2 kJ mol^{-1} and A≈ 89±1 min^{-1}. Activation energies were calculated using Eq. 4 (Fig 3.):

$$Ea = E_a^0 - RTbt^2 \quad (4)$$

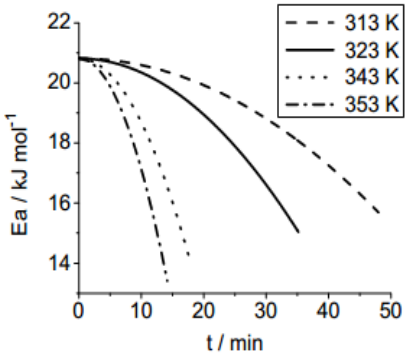

Figure 2. Dependence of PAAG dehydration activation energy on time.

CONCLUSION

PAAG isothermal dehydration can be mathematically described by the acceleratory equation that Skrdla and Robertson derived. The established results can be correlated with different structures of the absorbed water. In the case of PAAG hydrogel dehydration that means that dehydration leads to continual changes in the structure of absorbed water, as well as in hydrogel itself. Relaxation of fluctuating structures in absorbed phases and polymer network occurs in the time scales that are shorter or comparable to the one

of dehydration process. Due to that specific rate of dehydration become a time-dependent parameter.

Acknowledgement
This work was partially supported by the Ministry for Science of the Republic of Serbia (Grants no. 172015 and 171029).

REFERENCES

[1] E. M. Ahmed, Journal of Advanced Research, 2015, 6, 105-121.
[2] P.J. Skrdla, R. T. Robertson, RT, Thermochim Acta, 2007, 453,14–20.
[3] B. Potkonjak, J. Jovanović, B. Stanković, B. Adnađević, Chemical Engineering Research and Design, 2015, 100, 323–330.

SYNTHESIS OF ZnO-Ag NANOPARTICLES BY SOLVENT FREE METHOD AND THEIR CHARACTERIZATION

S. Janković[1], D. Milisavić[1], P. Schlender[2] and D. Jelić[3]

[1]University of Banja Luka, Faculty of Natural Sciences and Mathematics, Chemistry Department, Mladena Stojanovića 2, Banja Luka, Bosnia and Herzegovina (savka.jankovic@pmf.unibl.org)
[2]University of Dresden, Faculty of Chemistry and Food Chemistry, Chair of Inorganic Chemistry II, Bergstrasse 66, D-01187 Dresden, Germany.
[3]University of Banja Luka, Faculty of Medicine, Pharmacy, Department, Bulevar vojvode Bojovića 1a, Banja Luka, Bosnia and Herzegovina.

ABSTRACT

ZnO is well known nanomaterial mostly due to its good physical and chemical characteristics, wide spectrum of energy band gap, high index of refraction, thermal conductivity, non-toxicity, antibacterial activity etc. Based on these properties ZnO material can be used as gas and bio-sensor, the solar cell, light emitter (LED diode) or transparency conducting material. In order to improve the properties of material, different doping agent can be incorporated in structure. Incorporation of Ag^{+} ions into Zn^{2+} sites within the ZnO crystal can affect particle size. The aim of this paper is synthesis of silver doped zinc oxide (ZnO-Ag) nanoparticles using relatively novel solvent free method. Zinc nitrate, glycerol and silver nitrate were used as precursors. Glycerol had a role to overcome process of nanoparticles agglomeration. Obtained samples of undoped ZnO and doped ZnO-Ag were submitted to characterization by FTIR, XRD, SEM and EDX. Results showed the presence of silver nanoparticles in doped samples. Size of particle showed to be dependent of glycerol amount added.

INTRODUCTION

Investigations of metal nanoparticles with specific properties are continuously growing. Properties of metallic nanoparticles depend very much on synthesis method and there are several synthesis methods proposed in the literature, such as: chemical vapor condensation, arc discharge, hydrogen plasma-metal reaction, hydrothermal, sol-gel or ball milling [1] are some of them. Zinc oxide belongs to the group of the *n*-semiconductor

materials type II^b –VI, with energy band gap (≈3.4eV), high bond energy (≈60 meV) and high thermal and mechanical stability at room temperature. Zink oxide can be used for emitters of ultraviolet radiation, the varistor, the piezoelectric converters, the aeriform sensors. Also, thanks to its non-toxic, antibacterial properties and protection of UV light, is often ingredient of many pharmaceutical and cosmetic products [2]. In order to improve the properties of material, different doping agent can be incorporated in structure and hence in its physical and especially optical properties. In this paper we use silver as doping agent. Present investigation deals with synthesis of Ag doped ZnO nanoparticles by relatively new way of synthesis, a solvent free method. This method of synthesis is very simple, eco-friendly and low cost.

EXPERIMENTAL

Zinc nitrate hexahydrate ($Zn(NO_3)_2 \cdot 6H_2O$ Sygma Aldrich), glycerol ≥85% (Merck) and silver nitrate ($AgNO_3$, Sygma Aldrich) were used for the synthesis of ZnO-Ag by solvent free method. 6.5 g of zinc nitrate hexahydrate and 100 μL (165 μL) of glycerol was constantly mixed for 30 minutes until pasta consistency was achieved. The mixture was then transferred into the muffle furnace and calcinated for 3h at 300 ^oC. The obtained ZnO nanopowder was later dispersed in 10 mL of deionized water and stirred on a magnetic stirrer for 2h. 0.014 g $AgNO_3$ was added to the solution and the solution was constantly stirred vigorously for 4h, to get the doping effect. After stirring, the sample was dried for 5 hours at 70 ^oC and again calcinated 3h at 300 °C to predict eventual impurities. Samples were characterized by following techniques: FTIR spectroscopy (Bruker Tensor 27). X-Ray structure analysis (Philips PW-1050 with CuKα radiation, λ = 1.5148 Å). SEM – JEOL JSM-6390 LV was used for morphology and particles size determination. EDX was used of determination of the presence of silver nanoparticles on the surface of zinc oxide.

RESULTS AND DISCUSSION

Figure 1. shows the FTIR spectra of undoped and doped zinc oxide synthesized by the solvent free method in the range 400 - 4000 cm^{-1}. A deformed stretched vibration band, which is characteristic for zinc oxide, appeared on 530.41 cm^{-1}. Both IC spectra, for doped and undoped ZnO, gave quite similar vibration bands. Besides this characteristic peak, which belongs to zinc oxide nanoparticles, three additional different vibration peaks are also pronounced. The vibration peak, on 814 cm^{-1} originates from carbonate group, while vibration stretched band on 1323 cm^{-1} belongs to nitrate.

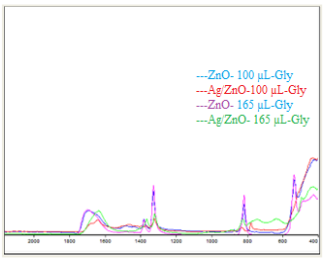

Figure 1. FTIR spectra of ZnO and Ag/ZnO nanoparticles

Also, the wide-stretched peak in the range from 1600 to 1800 cm^{-1} is attributed to bending OH^- group [3]. Phase analysis and morphology of powdery samples were examined by XRD and SEM techniques.

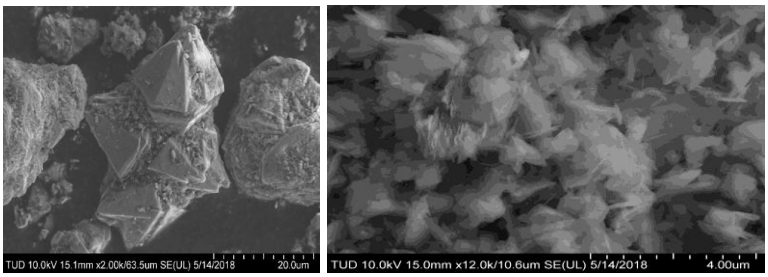

Figure 2. SEM microphotograph of ZnO nanoparticles synthesized by using 100 µL glycerol (left), and 150 µL glycerol (right)

The average grain size for samples with 100 µL glycerol (Sample 1) added was around 25 µm (Figure 2, left), while particles size obtained by SEM was around 600 nm. Samples with 165 µL glycerol (Sample 2) showed thegrain size of 1 µm with particle size of 500 nm (Figure 2, right). Based on EDX results we calculated the size of silver nanoparticles on the sample surface. In the case of Sample 1 (100 µL of glycerol) the size of the silver nanoparticles was around 150 nm. A higher amount of glycerol has caused a decrease in the size of silver nanoparticles on the ZnO surface and as shown in Figure 3 (right) the size was around 100 nm.

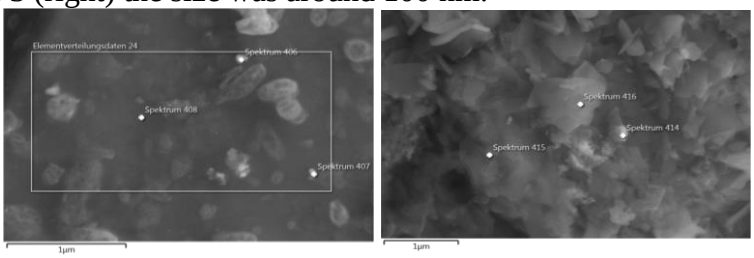

Figure 3. EDX microphotograph with marked spots which presents silver ions on surface of the ZnO nanoparticles synthesized by using 100 µL glycerol (left), and 150 µL glycerol (right)

Based on XRD the most intense lines at 2θ of 31.775, 34.430, 36.275, 47.540, 56.600, 62.855, 66.380, 67.955, 69.080 and 72.590 degrees in XRD pattern are in a good agreement with the angles (31.770, 34.420, 36.253, 47.540, 56.604, 62.865, 66.383, 67.967, 69.103 and 72.564) in JCPDS card of ZnO No.36-1451 (Figure 4) [4].

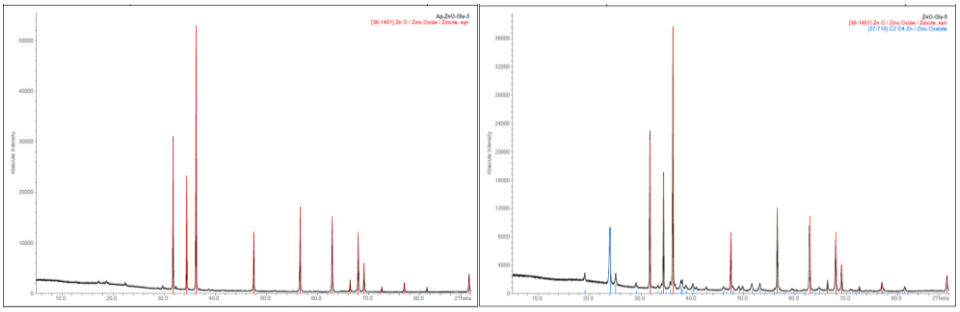

Figure 4. XRD patterns of ZnO (a) Ag/ZnO nanoparticles (100 μL-Gly), b) undoped ZnO NPs (165 μL-Gly)

CONCLUSION

The silver doped ZnO nanoparticles were synthesized successively by solvent free method. Incorporation of silver ions attributes to various particle sizes when different amount of glycerol, as a dispersing agent, was used. With a higher content of glycerol, ZnO nanoparticles become smaller. Incorporation of silver ions was detected by EDX technique.

Acknowledgement

This work was done within the framework of the research project no. 19/06-020/961-26/15 supported by the Ministry of Science and Technology of Republic of Srpska.

REFERENCES

[1] Khalaf A. A. et al., Synthesis of ZnO Nanopowders By Using Sol-Gel and Studying Their Structural and Electrical Properties at Different Temperature, Energy Procedia, Vol. 119 (2017) pp. 565-570.

[2] Huang M. H. et al, Room-Temperature Ultraviolet Nanowire Nanolasers, Science, Vol. 292, Issue 5523, (2001) pp. 1897-1899.

[3] Pholnak C. et al., Effects of precursor concentration and reaction time on sonochemically synthesized ZnO nanoparticles, Materisals resarch, Ibero-american Journal of Materials, Vol.17 (2013) pp. 405−411.

[4] Chauhan J et al.,Synthesis and Characterization of Ni and Cu Doped ZnO, J Nanomed Nanotechnol Vol. 8 (2017) pp. 429.

INTERACTION BETWEEN GOLD NANOPARTICLES AND SELECTED ANTITUMOR GOLD COMPLEXES

A. Bondžić[1], A. Vujačić Nikezić[1], B. Kalska[2], U. Klekota[2], B. Laban[3], V. Vodnik[1] and V. M. Vasić[1]

[1]Vinča Institute of Nuclear Sciences, University of Belgrade, P.O. Box 522, 11000 Belgrade, Serbia (aleksandrab@vin.bg.ac.rs, anavu@vin.bg.ac.rs)
[2]Institute of Chemistry, University of Bialystok, Hurtowa 1, 15-399 Bialystok, Poland
[3]Faculty of Natural Science and Mathematics, University of Priština, Lole Ribara 29, 38220 Kosovska Mitrovica, Serbia

ABSTRACT

The paper presents the results of study of interaction between citrate capped gold nanoparticles (AuNPs) and some antitumor gold complexes with pyridine ligands (AubipyC, AubipyOH and AupyOAc), in order to elucidate the possibility for their tracking in physiological fluids using NPs. The surface plasmon absorption band of AuNPs at 524 nm decreased in the presence of selected complexes, while the new broad band appeared at ~ 640 nm, which showed the increase in intensity with time upon the addition of complex. The spectral changes were followed by its red shift of to 750 nm and could be ascribed to aggregation and precipitation of AuNPs caused by the adsorption of selected gold complexes. Transmission electron microscopy (TEM) images showed that prepared AuNPs were monodisperse spheres with the average size of ~ 27 nm before and after the addition of selected gold complexes. Dynamic light scattering (DLS) and zeta potential measurements also confirmed the adsorption of complexes on the surface of AuNPs.

INTRODUCTION

Citrate capped AuNPs are nearly monodisperse spheres with a negative surface charge which size is controlled due to their preparation [**1**]. Interesting properties of AuNPs associated with their surface plasmon, located around 520 nm allow their use and application in many different fields, especially in biology and medicine **[2]**. Surface plasmon resonance (SPR) is very sensitive to changes in size, shape, surface capping and interparticle distance between AuNPs **[3]**. Compounds capable of causing changes in their initial absorption spectra can be used for the development of a SPR as sensing platform to follow their destiny in many different fields.

The aim of this work was to elucidate the interaction of some antitumor gold complexes, AubipyOH, $Aupy(OAc)_2$ and AubipyC **(Scheme 1,** complexes 1, 2, 3, respectively) with citrate-stabilized AuNPs in order to investigate the possibility of using AuNPs for their tracking after application in biological and physiological fluids.

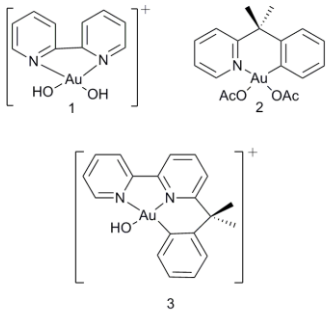

Scheme 1. Structures of the investigated gold (III) complexes: (1) $[Au(OH)_2(bipy)][PF_6]$; (2) $[Au(CH_3COO)_2(py^{dmb\text{-}H})]$ and (3) $Au(bipy^{dmb\text{-}H})(OH)][PF_6]$.

EXPERIMENTAL

Chemicals. Gold (III) chloride trihydrate ($HAuCl_4 \times 3H_2O$), trisodium citrate dihydrate ($C_6H_5Na_3O_7 \times 2H_2O$), all from Aldrich, were of analytical grade and used without further purification. Gold(III) complexes (structures shown in Scheme 1.) were synthesized as described in the literature [4].

Apparatus. UV-Vis spectra were recorded on Lambda 35 UV-Vis Spectrometer, Perkin Elmer, Inc., Waltham, MA, USA. TEM measurements were performed on a Tecnai™ G2 X-TWIN type from FEI (Hillsboro, OR, USA). DLS and zeta potential measurements were done on Nano ZS zetasizer system with 633 nm He−Ne laser (Malvern Instruments, U.K.) and data were analyzed by the Zetasizer Software Version 6.20 (Malvern Instruments, U.K.).

Synthesis of AuNPs. Colloid dispersion of spherical AuNPs was prepared using sodium citrate as a reducing and a loosely bound capping agent, as described earlier in the literature **[5]**.

RESULTS AND DISCUSSION

TEM images (Figure 1A) showed that prepared citrate-capped AuNPs are monodisperse spheres with the average size of ~ 27 nm. After the addition of selected gold complexes in AuNPs solution the size and shape of NPs generally remained the same (Figure 1B). UV/VIS spectra of AuNPs have characteristic SPR band

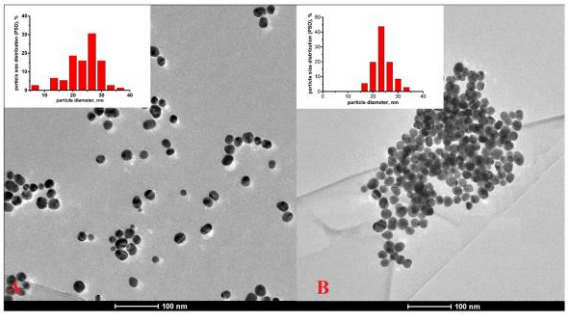

Figure 1. TEM micrographs of A) 2×10^{-10} M AuNPs and B)obtained flocs after the addition of 2×10^{-6} $Aupy(OAc)_2$ (final concentration).

with one single peak at ~ 524 nm pointing out on dispersed AuNPs with diameter of about 25 - 30 nm. After the addition of complexes the absorption intensity of NPs – complex assemblies decreased accompanied with the simultaneous appearance and rise of a new broad band at about 640 nm (Figure 2). The intensity of this new band reached the maximum at 725 nm within 60 min. The red shift of this band to 750 nm was observed, indicating the changes of interspacing distance between AuNPs and their aggregation. Moreover, the intensity decay of the absorbance suggested the precipitation of formed aggregates. In addition, in the presence of these complexes a slight red shift (2-5 nm) of the plasmon absorption band was observed, due to increased hydrodynamic radii in the presence of these complexes on the surface of NPs. The application of DLS measurements on the same assemblies confirmed the results obtained using UV-Vis and TEM measurements. DLS measurements pointed out the time dependent increase of hydrodynamic radii and confirmed aggregation of NPs in the presence of metal complexes. The average sizes of hydrodynamic diameter of AuNPs in the presence and absence of complexes and their electrophoretic mobility are presented in Table 1. The negative value of surface potential indicated a stable dispersion system in all cases followed by the significant change in conductivity. The obtained results confirmed the adsorption of complexes on the surface of NPs. The values of zeta potential indicated that the adsorption of neutrally charged complex led to additional stabilization of the system while positively charged complexes trigger its destabilization. Significant increase in conductivity of AuNPs-complex dispersion, indicated the replacement of citrate ions from the surface of NPs.

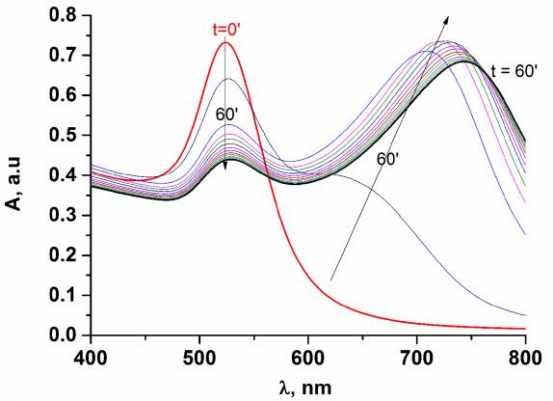

Figure 2. UV/VIS spectra of 2×10^{-10} M AuNPs in the presence of 2×10^{-6} M AubipyC as a function of time.

Table 1. Values of hydrodynamic diameter, surface potential and conductivity obtained by DLS and zeta potential measurements.

	Surface potential (mV)	Hydrodynamic diameter (nm)		Conductivity (mS/cm)
		after 15'	after 60'	
AuNPs	-30.90	30	30	0.093
AuNPs+AupyOAc	-66.78	61	148	0.118
AuNPs+AubipyOH	-6.86	297	640	0.150
AuNPs+AubipyC	-18.00	40	517	0.140

CONCLUSION

In this work we investigated interaction between citrate stabilized AuNPs and some potential antitumor gold complexes using different experimental techniques. The obtained results indicated that investigated complexes adsorb on the surface of AuNPs and that obtained assemblies have the potential to be applied for the tracking of Au(III) complexes in physiological liquids.

Acknowledgement

Authors would like to thank dr Mirjana Marković, from Vinča Institute of Nuclear Sciences, University of Belgrade, Serbia for her assistance with Malvern Zetasizer Nano ZS acquisition.

This work was supported by the Ministry for Science of the Republic of Serbia (Grant no. 172023) and COST action MP1302.

REFERENCES

[1] A. N. Shipway, E. Katz, I. Willner, Chem.Phys.Chem. 2000, 1, 18-52.
[2] E. Katz, I. Willner, Angew.Chem. Int. Ed. 2004, 43, 6042-6108.
[3] K. Saha, S. S. Agasti, C. Kim, X. N. Li, V. M. Rotello, Chem. Rev., 2012, 112, 2739-2779.
[4] A. M. Bondžić, G. V. Janjić, M. D. Dramićanin, L. Messori, L. Massai, T. N. Parac Vogtd, V. M. Vasić, Metallomics, 2017, 9, 292-300.
[5] A. Vujačić, V. Vasić, M. Dramićanin, S. P. Sovilj, N. Bibić, S. Milonjić, V. Vodnik, J. Phys. Chem. C, 2013, 117, 6567−6577.

I – Physical Chemistry of Condensed Phases, Solid State and Fluids

DENSITY ANOMALY AS A FUNCTION OF TETRAHEDRALITY AND BOND ANGLE IN STILLINGER-WEBER POTENTIAL

D. Fijan and M. Wilson

University of Oxford, Department of Chemistry, Physical and Theoretical Chemistry Laboratory,
South Parks Road, OX1 3QZ, Oxford, United Kingdom.
(domagoj.fijan@chem.ox.ac.uk)

ABSTRACT

Thermodynamic anomalies have been highly-debated topics over the last decades, especially in the water community. However, the anomalies appear in many systems of broad technological or biological interest that are constructed from tetrahedral building blocks. In this work we use molecular dynamics to study thermodynamic anomalies in Stillinger-Weber (SW) liquids. We employ a systematic approach to explore how the structure of the liquid changes the anomalous behaviour. We change the liquid structure continuously by varying specific parameters of the SW model in order to produce parametrisations that correspond to different real liquids (such as germanium, silicon, water or carbon). We monitor the progression of the anomalies and give an explanation for their progression.

INTRODUCTION

The density anomaly in water is probably the most famous of the thermodynamic anomalies. This magnificent phenomenon enables ice to float on water and by doing so has a massive impact on life on Earth as we know it. Anomalous behaviour in liquids is, however, widespread, spanning systems like water, but also tetrahedral monatomic liquids such as silicon, germanium or carbon. All these liquids have basic building blocks in the form of interconnected tetrahedral units.

Thermodynamic interpretations of the anomalous behaviour in liquids (particularly in water) have received significant attention starting with Speedy's first attempt to explain them[1]. Today several scenarios are considered[2] but most of them are overshadowed by water's most likely candidate - the second liquid-liquid critical point (LLCP) scenario[3]. However, alternative approaches to studying the origin of anomalous behavoiur through the structure of the liquid have gained traction over the last couple of years[4], [5].

One of the main model candidates used for studying anomalous behaviour is the Stillinger-Weber (SW) potential[6]. The main reason for this is its very simple and physically-transparent set of parameters, easily relatable to structure of the liquid whose change enables simulation of different real systems such as silicon[6], germanium[7], carbon[8] and even water[9]. There have been several attempts now to elucidate change in thermodynamic anomalies as a function of tetrahedrality in the SW potential[10], [11]. These attempts, however, did not scan the full parameter range in which the density anomaly appears or consider different parametrisations for different real systems thus changing more then just the tetrahedrality parameter. Another way to change the structure of the liquid that hasn't been explored so far is to vary the ideal bond angle (the angle between two bonds on a single atom favored by the potential model). In this paper we scan the full range of tetrahedrality for the SW potential for which the density anomaly appears. We also scan the ideal bond angle parameter starting from the lowest value for which the density anomaly appears.

EXPERIMENTAL

A density anomaly is defined by temperature of maximum density (TMD) line. Density maxima are calculated for different isobars and then connected by a single line we refer to as the TMD line. In practice one can also calculate TMD lines by connecting the minima in isochores. We use NVT ensemble molecular dynamics (MD) to calculate the required thermodynamic data using the LAMMPS[12] implementation of the Nose-Hoover thermostat. In order to calculate isochores the volume and number of atoms (512) is kept constant while the temperature of each run is changed systematically. MD is used to calculate the pressures corresponding to the starting temperature and density (volume). Several densities (volumes) are used in order to obtain the full TMD profile including upper and lower pressure limits. Thermodynamic data is analyzed in Python using NumPy and SciPy packages. Points on an isochore are filtered using a second order Butterworth filter with a cutoff of 0.2. The 4th order univariate spline is fitted to filtered data, it's first derivative calculated and zeros obtained. Zeros are confirmed to be maxima by calculating the sign of the second derivative at that point. These points correspond to points on the TMD line.

The potential used is the original Stillinger-Weber (SW) potential parametrised for silicon[6]. The potential reads:

$$U = \sum_i \sum_{j>i} \phi_2(r_{ij}) + \sum_i \sum_{j\neq i} \sum_{k>j} \phi_3(r_{ij}, r_{ik}, \Theta_{ijk})$$

$$\phi_3(r_{ij}, r_{ik}, \Theta_{ijk}) = \lambda\varepsilon\left(cos\Theta_{ijk} - cos\Theta_0\right)^2 e^{\left(\frac{\gamma\sigma}{r_{ij}-a\sigma}\right)} e^{\left(\frac{\gamma\sigma}{r_{ik}-a\sigma}\right)}$$

$$\phi_2(r_{ij}) = A\varepsilon\left[B\left(\frac{\sigma}{r_{ij}}\right)^p - \left(\frac{\sigma}{r_{ij}}\right)^q\right]e^{\left(\frac{\sigma}{r_{ij}-a\sigma}\right)}$$

This potential is most famous for it's silicon parametrisation (λ = 21)[6], but was also parameterised for germanium (λ = 20)[7], carbon (λ = 26.2)[8] and even water (λ = 23.15)[9] while keeping ideal bond angle (Θ_0 in ϕ_3) tetrahedral. In this work we use the original silicon parametrisation and scan the range of λ starting at 17 and ending at 28 in increments of 1 while keeping ideal bond angle tetrahedral (Θ_0=Θ_{td}≈109.45°). We also scan the range of Θ_0 starting at 102° all the way to 128° in increments of 2° while keeping λ constant at 21 (which corresponds to silicon parametrisation).

RESULTS AND DISCUSSION

The range of λ values for which the density anomaly was found is 18 to 27. The lowest value of Θ_0 for which the density anomaly could be detected was 104° and the upper value was not located but it is higher then 128°. Increasing λ pushes the density anomaly to higher pressures and temperatures. Similarly, an increase in Θ_0 also pushes the anomalies to higher temperatures and pressures, however, above 122° the temperature dependence is reversed (see Figure 1.). The origin of this behaviour can be understood by considering the influence of the λ and Θ_0 parameters on the network structure of liquids. Lowering of the λ parameter increases the importance of pairwise (Lennard-Jones like) term. This will favor close packed structures and increase in local coordination number. High values of λ will favor a 4-coordinated tetrahedral environment. Similarly, at Θ_0=90° the 6-coordinated octahedral coordination is favored. By increasing Θ_0 we go away from a more close packed structures towards the ideal tetrahedral angle Θ_0≈109.45°. Further increase in the ideal bond angle forces coordination number to reduce further. This could be the origin of the deviation of the temperature dependence upon increase of Θ_0 for very high values of Θ_0.

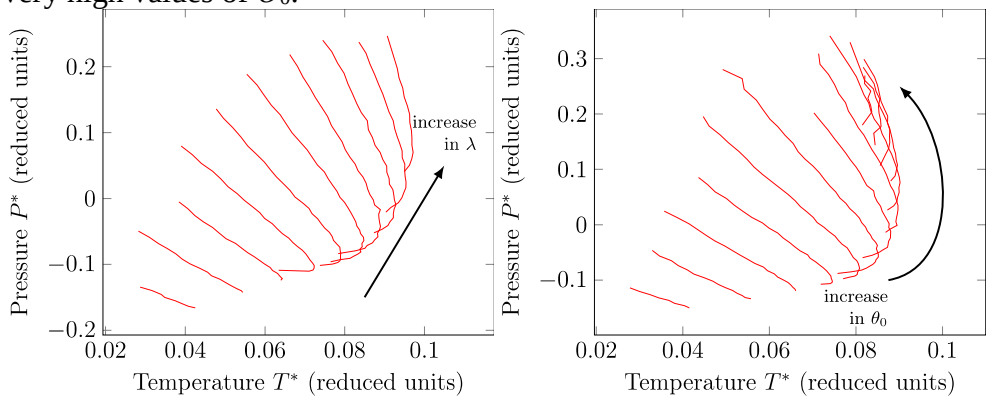

Figure 1. Progression of the density anomaly for λ progression (left) and Θ_0 progression (right) in temperature and pressure space.

Another interesting observation is the change in shape of the TMD line for values of λ larger then 20 and Θ_0 larger then 108°. Above these values the TMD lines start retracting to lower temperatures at low pressure. This behaviour is often associated with different thermodynamic scenarios that govern anomalous behaviour of thermodynamic quantities in liquids. Retracting behaviour is necessary in order to have the LLCP or singularity free interpretation[13] scenarios. Thus it could be possible that at lower values of Θ_0 (below 110°) and λ (below 21) we have a realization of Speedy's stability limit conjecture scenario.

CONCLUSIONS

We calculated the progression of density anomalies with respect to two parameters in the SW potential over ranges in which they appear. The density anomalies are pushed to higher pressure and temperature with an increase in strength of the three body term (λ) and ideal bonding angle term (Θ_0) with change in temperature dependence at high values of Θ_0. The similarity in progression of the anomalies between the two parameters can be rationalized by considering the influence of these parameters on the coordination of the liquid environment. We also note possible implications of shape of TMD lines on thermodynamic scenarios.

Acknowledgement

This work was supported by the TMCS CDT EPSRC grant (EP/L015722/1) and Clarendon scholarship.

REFERENCES

[1] R. J. Speedy, *J. Phys. Chem.*, 86, 6, 982–991, 1982.
[2] P. Gallo *et al.*, *Chem. Rev.*, 116, 13, 7463–7500, 2016.
[3] P. H. Poole, *et al.*, *Nature*, 360, 6402, 324–328, 1992.
[4] J. Russo, H. Tanaka, *Nat. Commun.*, 5, 3556, 2014.
[5] A. Nilsson, L. G. M. Pettersson, *Nat. Commun.*, 6, 1–11, 2015.
[6] F. H. Stillinger, T. A. Weber, *Phys. Rev. B*, 31, 8, 5262–5271, 1985.
[7] M. H. Bhat *et al.*, *Nature*, 448, 7155, 787–90, 2007.
[8] A. S. Barnard, S. P. Russo, *Mol. Phys.*, 100, 10,1517–1525, 2002.
[9] V. Molinero, E. Moore, *J. Phys. Chem. B*, 113, 13, 4008–4016, 2009.
[10]D. Dhabal *et al.*, *J. Chem. Phys.*, 145, 21, 214502, 2016.
[11]J. Russo, K. Akahane, H. Tanaka, *Proc. Natl. Acad. Sci.*, 201722339, 2018.
[12]S. Plimpton, *J. Comput. Phys.*, 117, June 1994, 1–19, 1995.
[13]S. Sastry, P. G. Debenedetti, F. Sciortino, H. E. Stanley, *Phys. Rev. E*, 53, 6, 6144–6154, Jun. 1996.

CHARACTERIZATION OF THE EPOXIDIZED FLAXSEED OIL AS AN RAW MATERIAL FOR THE POLYMER INDUSTRY

O. Govedarica, M. Janković, S. Sinadinović-Fišer, V. Teofilović, J. Budinski-Simendić and N. Vukić

University of Novi Sad, Faculty of Technology, Bul. Cara Lazara 1, 21000 Novi Sad, Serbia. (ogovedarica@uns.ac.rs)

ABSTRACT

Epoxidized flaxseed oil with high epoxy oxygen content of 8.27% and low residual iodine number of 4 was obtained by the epoxidation of flaxseed oil with peracetic acid formed *in situ* from acetic acid and hydrogen peroxide in the presence of an acidic ion exchange resin as a catalyst. Physico-chemical properties important for the production and processing of this vegetable oil derivative were determined. The molecular mass of the obtained epoxidized flaxseed oil is 1001 g/mol. In the temperature range from 20 to 90ºC, the density of the epoxidized flaxseed oil decreased from 1022.9 to 973.87 g/L, while the kinematic viscosity decreased from 663.9 to 27.05 mm^2/s.

INTRODUCTION

The development of biobased products is one of the major concerns in the chemical and polymer industry. Among renewable raw materials, vegetable oils have attracted the most attention [1]. Since the double bonds of vegetable oils` triglycerides are not reactive enough for typical free radical polymerization, they are usually converted into more reactive functional groups, such as epoxy group, in order to produce polymeric materials [1]. In industry, vegetable oils are epoxidized with percarboxylic acid formed *in situ* from corresponding carboxylic acid and hydrogen peroxide in the presence of a mineral acid or an acidic ion exchange resin as a catalyst [2].

Epoxidized flaxseed oil (EFO) is commonly used as a stabilizer and plasticizer for polyvinyl chloride. It is also used as a component for the production of epoxy resins [3-5]. The aim of the present work was to determine the molecular mass, as well as temperature dependencies of density and viscosity of epoxidized flaxseed oil, since these properties are of great importance for the production and processing of this flaxseed oil (FO) derivative.

EXPERIMENTAL

Epoxidation procedure. The FO was epoxidized with peracetic acid formed *in situ* in the presence of the catalyst Amberlite IR120-H at the temperature of 71°C over the reaction time of 7 h. The catalyst was applied in the amount of 20 wt% of acetic acid and 30% hydrogen peroxide weights. The molar ratio of FO unsaturation:acetic acid:hydrogen peroxide was 1:0.5:1.5. The initial unsaturation of FO was 0.6757 mol/100 g oil. The FO, acetic acid and hydrogen peroxide were added into a reactor. When the stirred mixture reached 71°C, the catalyst was added. The process was conducted approximately isothermally under the constant stirring speed of 2000 rpm. At the end, the reaction mixture was cooled and centrifuged. The separated oil layer was washed with water until pH 7. Further, water was evaporated from the oil layer under 300 mbar at 60°C. The obtained EFO was then characterized.

Characterization of FO and EFO. Iodine number and epoxy oxygen content were determined in triplicate by Hanush method and AOCS Cd 9-57 method, respectively. Fatty acid composition of the FO was determined according to the method given in the literature [6]. Thermo Nicolet 5700 spectrometer with attenuated total reflection (ATR) accessory was used to collect infrared spectra in the range of 400-4000 cm^{-1}. The density was measured in the range of 20-90°C using Anton Paar DMA 4500M densitometer. The kinetic viscosity was measured in the same temperature range using Cannon-Fenske capillary viscosimeter.

RESULTS AND DISCUSSION

The epoxidation of FO was conducted at the conditions which were previously determined as the optimal for reaching the maximal epoxy yield in the following process conditions ranges: temperature 65-75°C, hydrogen peroxide-to-oil unsaturation molar ratio 1.1-1.5, catalyst amount 10-20 wt% and reaction time 5-13 h, when acetic acid-to-oil unsaturation molar ratio was 0.5:1 [7]. The obtained EFO was characterized with high epoxy oxygen content of 8.27% and low iodine number of 4, which corresponds to the unsaturation level of 0.0157 mol/100 g oil. Due to high conversion of double bonds, the residual unsaturation of EFO is 97.7% lower that the initial unsaturation of FO.

Infrared spectra of the FO and EFO are given in Figure 1. The appearance of doublet band with maxima at 823 and 847 cm^{-1} in the EFO spectrum confirmed the formation of epoxy group. The disappearance of the band

corresponding to the double bond (3009 cm^{-1}) confirmed that the residual unsaturation of EFO is low.

The molecular mass of EFO is calculated based on expression given in the literature [8], using the values of the iodine number of FO and EFO, epoxy oxygen content of EFO and molecular mass of FO. The later mass was calculated based on FO fatty acid composition using the expression given in the literature [7]. According to the determined fatty acid composition (palmitic 5.2%, stearic 4.1%, oleic 19.8%, linoleic 16.0%, linolenic 54.8% and arahidic 0.1%), the molecular mass of FO is 874 g/mol. The corresponding molecular mass of EFO is 1001 g/mol.

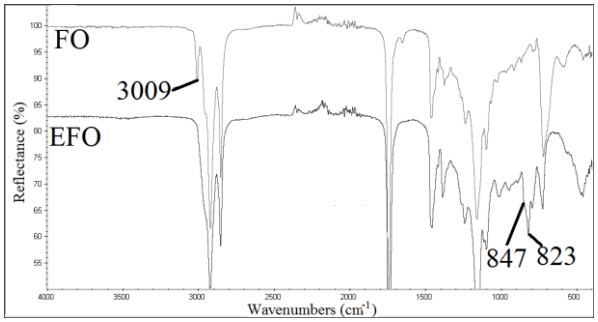

Figure 1. FTIR spectra of the flaxseed oil (FO) and epoxidized flaxseed oil (EFO).

Decrease of the oil unsaturation and formation of the epoxy group changed the physico-chemical properties of the oil. The EFO has both density and viscosity higher than the FO. With temperature increase from 20 to 90ºC, the densities of both oils decrease linearly with temperature (Figure 2). The density of EFO decreased from 1022.9 to 973.87 g/L, whereas the density of FO decreased from 927.91 to 880.76 g/L. At each temperature, the density of EFO was higher 10.24 to 10.57% than the density of FO.

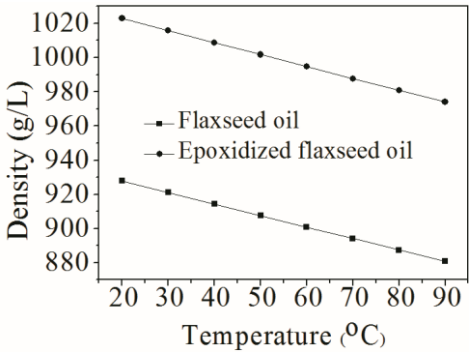

Figure 2. Temperature dependence of the densities of the flaxseed oil and epoxidized flaxseed oil.

With temperature increase from 20 to 90ºC, the viscosity of EFO decreased from 663.9 to 27.05 mm^2/s, whereas the viscosity of FO decreased from 45.56 to 9.637 mm^2/s (Figure 3). At the lowest measured temperature (20ºC), the viscosity of EFO is 14.6 times higher compared to the untreated oil. At the highest measured temperature (90ºC), the viscosity of EFO is 2.8 times higher compared to the untreated oil.

Decrease of both density and viscosity of EFO with an increase in temperature is important for the production stages of separation and stabilization of the epoxidized derivative. Additionally, an increase of the density and viscosity of the oil during the epoxidation process influences the mass transfer phenomena in the reaction system. This should be taken into consideration when developing a mechanistic model of the FO epoxidation reaction system.

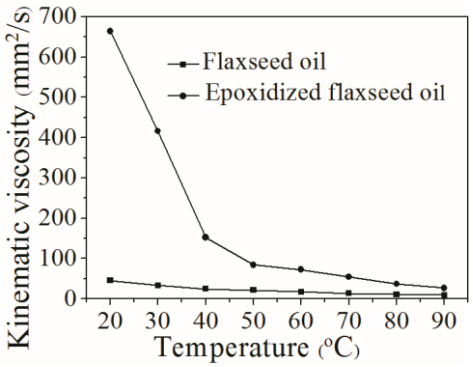

Figure 3. Temperature dependence of the viscosity of the flaxseed oil and epoxidized flaxseed.

CONCLUSION

Physico-chemical properties of EFO were determined and compared with the properties of FO. Molecular mass of the oil increased for 14.5% during the epoxidation process as a result of the epoxy group formation. Also, both density and viscosity of the oil increased due to significantly lower unsaturation level of the derived oil and epoxy group formation. The change in these physico-chemical properties is of great importance for the production and processing of EFO.

Acknowledgement

This work was supported by the Ministry of Education, Science and Technological Development of Serbia (Grant no. III45022).

REFERENCES

[1] J. Lu, R.P. Wool, J. Appl. Polym. Sci., 2006, **99**, 2481-2488.
[2] S. Chua, X. Xu, Z. Guo, Process Biochem., 2012, **47**, 1439-1451.
[3] N. Supanchaiyamat, P. Shuttleworth, A. Hunt, J. Clark, A. Matharu, Green Chem., 2012, **14,** 1759-1765.
[4] C. Ding, P. Shuttleworth, S. Makin, J. Clark, A. Matharu, Green Chem., 2015, **17**, 4000-4008.
[5] JM. Pon, N. Sbirrazzuoli, A. Mija, ChemSusChem., 2015, **8**, 1232-1243.
[6] M. Srbinoska, N. Hrabovski, V. Rafajlovski, S. Sinadinović-Fišer, Maced. J. Chem. Chem. Eng., 2012, 31, 65-78.
[7] O. Govedarica, Ph.D. dissertation, University of Novi Sad, 2017.
[8] M. Janković, O. Govedarica, S. Sinadinović-Fišer, J. Pavličević, V. Teofilović, N. Vukić, Hem. Ind., 2016, **70**, 165-175.

CLASTER FORMATION IN ORGANIC LIQUIDS

I.I. Grinvald, I.Yu. Kalagaev and R.V. Kapustin

R.A. Alekseev State Technical University
Minin str. 24, 603950 Nizhniy Novgorod, Russia. (grinwald@mts-nn.ru)

ABSTRACT
The IR data confirming the stabilization of liquid phase by the formation of cluster shapes under different mechanisms of molecule interaction are presented.

INTRODUCTION
Weak Coulomb interaction, arising between dipoles is taken as the nature of condensed state formation. For organic liquids the hydrogen or dihydrogen bonding is in some cases a reason of phase stability. But in terms of this interpretation it is not clear, why non-polar and hydrogen bondless compounds, such as alkanes or alkenes, benzene and many others can have a boiling temperature, i.e. the destruction energy of liquid phase, higher than polar organic compounds or systems with hydrogen or dihydrogen bond. A bright example of similar ambiguous behavior is also demonstrated by the methyl substituted species (CH_3X), the stability of condensed state of which has a tendency opposite to the power of dipole-dipole coupling.

At the same time the IR bands of organic fluids, which can be assigned to the vibrations of clusters species, are observed in the spectra [1-3]. This phenomenon could be involved for explanation of molecular arrangement in organic bulk.

In this work the IR spectroscopic findings, obtained for organic liquids, namely, tetrachlorides of carbon, silicon and germanium, benzene, as well as for methyl species (CH_3I, CH_3CN) at ambient condition also for their vapours and solid films at low temperature are presented in order to discuss the mechanism of molecular interaction in condensed state.

EXPERIMENTAL
Vapor spectra were measured using stainless steel optical cells with the 60 and 100 mm distances between optical windows and a system of vapor puffing (Fig. 1). The unit allows to provide effective heating of the cell on the whole as well as its optical windows.

A liquid sample was placed in a glass ampoule, degassed, connected with an evacuated system and then evaporated at room temperature in the gas cell.

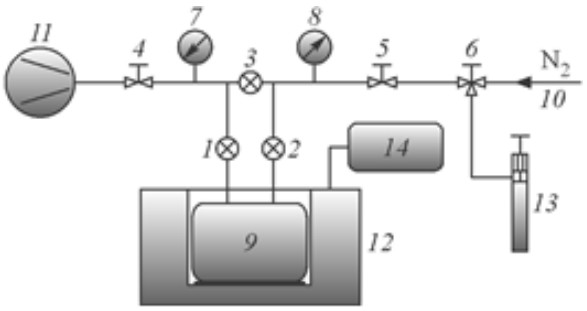

Figure 1. Experimental setup: general adjustment valves (*1, 2, 3*); fine adjustment valves (*4, 5, 6*); manovacuumeters (*7, 8*); gas cell (*9*); nitrogen or argon supply line (*10*); high-vacuum system (*11*); Fourier-IR spectrometer (*12*); ampoule with a sample (*13*); temperature controller (*14*)

Low-temperature films were studied by a closed cycle helium optical refrigerator DISPLEX CSE-202A (Advanced Research Systems Inc., USA) with the accessories for sample depositing on an optical window.

The experiments were accomplished using FTIR spectrometers IRAffinity-1 (Shimadzu, Japan) and FSM 1202 (Infraspek, Russia). The purity of samples was controlled with a chromato-mass spectrometer GCMS-QP2010 Plus (Shimadzu, Japan) to be at least 99 %.

RESULTS AND DISCUSSION

In this section the cluster formation in organic liquids with different mechanisms of interaction is considered. The selected compounds have either negligible total and bond dipole moments, strong bond dipole moment only, or considerable bond and total dipole moments.

Benzene

Benzene in the singular shape is a planar molecule corresponding to D_{6h} symmetry point group. In accordance with selection rules in IR spectra only one stretching CH band (E-specie) for similar molecule should be active. However in real spectra of liquid benzene three bands are observed (Fig, 2). The picture in CH stretching region can be coursed by the existence of clusters. For this system the mechanism of intermolecular interaction under H-bond was discussed. Similar binding should have led to the additional splitting of stretching CH bands, but this was not revealed. Therefore in this case the cluster formation can be assigned to the carbon-carbon binding between parallel placed rings.

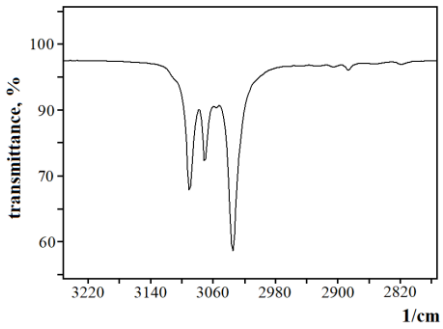

Figure 2. FTIR spectrum of liquid benzene

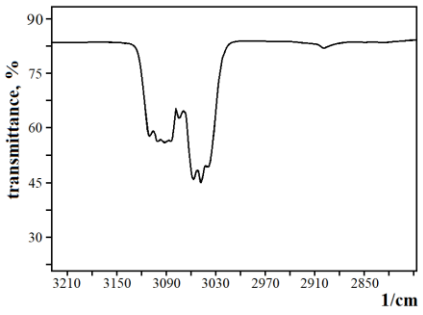

Figure 3. FTIR spectrum of benzene vapour

This assignment is confirmed by the spectra of benzene vapour at ambient conditions (Fig.3). The complicated view of absorption with the manifestation of rotational structure is the display of low-symmetrical shape with several bonded molecules. At heating up to 473K the vapour spectra are simplified.

Tetraclorides

The molecules of tetraclorides (ECl_4, where E=C, Si, Ge) attribute to high symmetry point group Td. The selection rules require the occurring of only one stretching ECl band in IR spectra. However carbon tetrachloride in liquid state (Fig.4,*a*) and in solid film at 25K (Fig.4,*b*) has two bands at 786 and 761 cm^{-1} with approximately equal intensities. The second component disappears at heating the sample up to 423K (Fig.5,*b)* and 473K (Fig.5,*c)* compared to initial vapour spectra of CCl_4 recorded at room temperature (Fig 5,*a*). At the same time for silicon and germanium tetrachlorides only one E-Cl stretching band was found.

Therefore the appearance of two bands in CCl_4 spectrum cannot be assigned to the CCl stretching of chlorine isotopes and is the manifestation of cluster formation, for example of (··C-Cl···C-Cl) bonded chains.

Unlike CCl_4 in tetraclorides of silicon and germanium the clusters exist due to the d-d orbitals interaction of central atoms. It does not lead to the sufficient distortion of initial molecular symmetry.

Methyl compounds CH_3X

The IR spectra of methyl iodide in different states are presented in Fig.6 (spectrum *a* - liquid phase at ambient conditions, spectrum *b* - solid film at 25K). They demonstrate the transition of molecular structure from initial C_{3V}

to D_{3h} symmetry. It can be coursed due to the shift of I-atom to neighboring molecule and formation of almost planar (CH_3) fragment.

The IR stretching of CN bond in acetonitrile has two components instead of an expected one (Fig.7). This effect justifies the interaction between molecules under CN group. In the diluted solution the second component disappears.

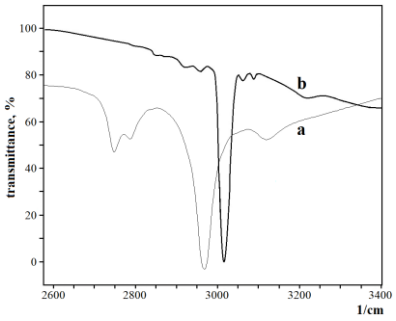

Figure 6. FTIR spectrum of liquid (a) and solid (b) methyl iodide

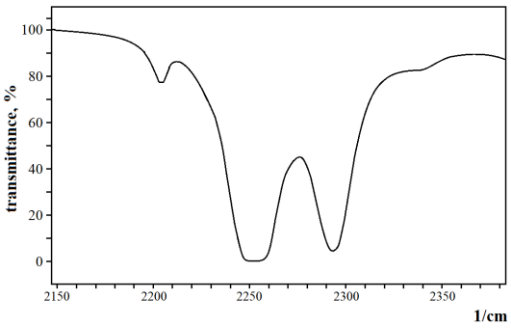

Figure 7. FTIR spectrum of liquid acetonitrile

CONCLUSION

The presented data can be taken as reliable evidence of existence in condensed phase of the interaction between molecules, different from Coulomb and H-bonding mechanism, leading to formation of cluster shapes.

REFERENCES

[1] Ivan Yu. Kalagaev and Iosif I.Greenwald, Pure Appl. Chem. 2013, 85, 135-148

[2] I.I. Grinvald, G.A. Domrachev, I.Yu. Kalagaev, Doklady Physical Chemistry, 2011, 440, 168-170

[3] I.I. Grinvald, I.Yu. Kalagaev, A.N. Petukhov, A.I. Grushevskaya, R.V. Kapustin , Zhurnal Structurnoi Khimii, 2018, 59, 326-333

METHOD OF DETERMINATION VISCOSITY INDEX IMPROVERS FOR MULTI-GRADE OIL OF COPOLYMER HYDROGENATED POLY (ISOPRENE-CO-STYRENE)

I. Stanciu

University of Bucharest, Faculty of Chemistry, Department of Physical Chemistry, 4-12 Elisabeta Blvd, 030018, Bucharest, Romania (istanciu75@yahoo.com)

ABSTRACT

To establish the ability of copolymer hydrogenated poly (isoprene-co-styrene) solutions in SAE 10W mineral oil as solvent to perform at low and high temperatures in a vehicle's engine that is their capacity to improve the oil viscosity index of their 3 % solutions were determined two methods. Viscosity index is determined using the formula much higher than that determined by the software.Viscosity index of the solution copolymer of 3 % is 67.04 units lower than that one obtained with formula (1) according to ASTM standard.

INTRODUCTION

With the development of modern technology, manufacturing technology and transmits engine oil would be impossible without the use of a lubricant additive. Industry producing additives for oil lubricants worked in partnership with the automotive industry to enhance durability and performance systems and creating a suitable lubricant engine [1-3]. Additives are synthetic chemicals that added oil based lubricants can improve performance. Some additives give new and useful properties of the lubricant; others can enhance properties already present, while some acts to reduce engine life. The most important types of additives are viscosity index improvers such as viscosity modifiers known [2-5]. Viscosity index is an indicator of viscosity change with temperature. A higher viscosity index indicates that oil viscosity changes very little with increasing temperature. Improvement of viscosity limits change viscosity with temperature. These enhancers have little effect on oil viscosity at low temperatures. However, when these heated oil viscosity improvers allow growth in a limited premise of the type and concentration of the additive. This quality is most evident in the implementation of engine oils several degrees.

Viscosity index depends on oil viscosity and temperature [4-5]. This results in changing the configuration of the polymer in the solvent with increasing temperature. The polymer molecule in solution exists as a coil, which is swollen by a solvent of the lubricating oil.
The volume of this molecule increases the lubricating oil viscosity. At low temperatures, the polymer molecules adopt a spiral configuration, so their effect on viscosity is minimized. At high temperatures, molecules tend to straighten and the interaction of these molecules long oil increases in volume and she produces a thickening effect, which in turn increases the viscosity index of the oil.

An ideal lubricant is possessing the same viscosity at all temperatures and for all purposes [6-9].

Viscosity index modifiers add lubricating oils to make them conform more ideal lubricant. Suitable polymers exert a greater thickening effect (percent increase in oil viscosity based on unit weight of polymer) at high temperatures than at low temperatures [10-12] and thus improve the viscosity index of the lubricating oil [13-15].

The purpose of this study was the determination of the viscosity of the solutions in two ways copolymer of styrene-hydrogenated polyisoprene one concentration 3% .

EXPERIMENTAL

The kinematic viscosities of the concentrated copolymer hydrogenated poly (isoprene-co-styrene) solutions 3 % were determined using a set of Schott Ubbelohde-type viscometers selected according to the values of their constants and viscosities of solutions, so that the margins of the uncertainty, inherent in the Hagebach-Couette correction, does not exceed the error allowed for the measurements. The measurements were carried out at 40 ± 0.1 and 100 ± 0.1^{o}C, according to the recommandation of ASTM D2270 [6]. They were possible only for 3 % solutions with the available set of viscometers.

RESULTS AND DISCUSSION

Multi-grade oils which have a viscosity index greater than 100 and viscosity index occur equation parameters U and H, and N, where U is the viscosity of the multi-grade oil at a temperature of 40^{o}C.

The IV is defined by a new parameter N, calculated from H and Y rather than H and L:

$$IV = 100 + 140((\text{antilog } N) - 1 \quad (1)$$

$$N = (\log H - \log U)/\log Y \quad (2)$$

All logarithms are to base 10. Y is the value of kinematic viscosity multi-grade oil at 100 ^{o}C. Values of L and H for higher viscosities are calculated from two equations:

$$L = 0.8385Y^2 + 14.67Y - 216 \quad (3)$$

$$H = 0.1684Y^2 + 11.85Y - 97 \quad (4)$$

For Y >70.

The viscosity index for solutions copolymer hydrogenated poly (isoprene-co-styrene) of 3 % concentrations calculation was performed with a computer program developed by INCERP SA, created in Visual Basic using kinematics viscosity at 40^{o}C and 100^{o}C [7].

The kinematic viscosities of 3 % copolymer solutions Infineum SV 260 in SAE 10W as solvent were measured at 40 and 100^{o}C, according to ASTM D2270 [7].

Viscosity index of the solution copolymer hydrogenated poly (isoprene-co-styrene) of 3 % concentration obtained with equation (1) is 67.04 units lower than that obtained with the software but is still at the standard ASTM 2270.

CONCLUSION

The viscosity indices of 3 % solutions of copolymer hydrogenated poly (isoprene-co-styrene), recommended as viscosity index improvers, in SAE 10W mineral oil as solvent were determined using the ASTM 2270-93 diagram and two methods according to the recommandation of ASTM D2270.

Viscosity index of the solution copolymer hydrogenated poly (isoprene-co-styrene) of 3 % is 67.04 units lower than that one obtained with formula (1) according to ASTM standard.

REFERENCES

[1] M. Smeeth, H. Spikes, S. Gunsel, 1996, Tribology transactions, 39(3), 726-734.
[2] W. V. Horne, Industrial & Engineering Chemistry, 1949, 41(5), 952-959.
[3] R. J. A.Eckert, D. F. Covey, 1988, Lubrication Science, 1(1), 65-80.
[4] H. G.Mueller, 1978,TRIBOLOGY international, 11(3), 189-192.
[5] A. Jukic, E. Vidovic, Z. Janovic, 2007, Chemistry and Technology of Fuels and Oils, 43(5), 386-394.

[6] H. H. Horowitz, 1958, Lubricants. Industrial & Engineering Chemistry, 50(7), 1089-1094.
[7] J. Fan, M. Müller, T.Stöhr, H. A. Spikes, 2007, Tribology Letters, 28(3), 287-298.
[8] M. Smeeth, H. Spikes, & S. Gunsel, 1996, Langmuir, 12(19), 4594-4598.
[9] A. A. Azim, A. M. Nasser, N. S. Ahmed, A. F. El Kafrawy & R. S. Kamal, 2009, Petroleum Science and Technology, 27(1), 20-32.
[10]E. F. Jordan, S. Smith, R. E. Koos, W. E. Parker, B. Artymyshyn & A. N. Wrigley, 1978, Journal of Applied Polymer Science, 22(6), 1509-1528.
[11]R. L. Stambaugh, 1994, InChemistry and technology of lubricants (pp. 124-159). Springer US.
[12]M. M. Mohamed, A. El Naga, H. Hamdi, & M. F. El Meneir, 1994, Journal of Chemical Technology and Biotechnology, 60(3), 283-289.
[13]A. M. Nassar & N. S. Ahmed, 2003, International Journal of Polymeric Materials, 52(9), 821-832.
[14]S. Morgan, Z. Ye, R. Subramanian & S. Zhu, 2010, Polymer Engineering & Science, 50(5), 911-918.
[15]D. Lariviere, A. F. A. Asfour, A. Hage, & J. Z. Gao, 2000, Lubrication Science, 12(2), 133-143.

ABSORPTION SPECTRUM OF A SATURATED DIPHENYLAMINE SOLUTION IN THE MAGNETICALLY TREATED WATER

Z. Velikić [1] and D. Veselinović [2]

[1] *Institute of Physics, University of Belgrade, P.O. Box 68, Pregrevica 118 11080, Zemun, Serbia.*
[2] *Faculty of Physical Chemistry, University of Belgrade, P.O. Box 276, 11001 Belgrade, Studentski trg 12-16, Serbia.*

ABSTRACT
Magnetic water treatment leads to alterations in the absorption spectrum of diphenylamine originating in the processed water. The extent of the alteration is a consequence of changes in the solution components influenced by the magnetic field.

INTRODUCTION
In literature, there are a number of papers presenting data on the influence of magnetic, electromagnetic and electric fields on the tested systems, i.e. processes. Our paper [1] determines the influence of electromagnetic field on the measurement of solution pH using glass electrode, indicating that it is possible for the field to act upon the solution, as well as upon a glass electrode. The paper investigates and discovers the influence of the magnetic field on the lime dissolution, i.e. calcium carbonate, by processing the water, i.e. distilled water [2], [3], [4], [5], [6]. There is no evidence on the impact of the radio frequency electromagnetic field on the oscillatory reaction [7]. Likewise, it is a well-known fact that water running perpendicular in relation to the lines of the magnetic field is subject to change, i.e. magnetically treated water occurs [8].

EXPERIMENT
For the experiment presented in the paper, the following was used: spectrophotometer DU720 Beckman Coulter, pH meter Adwa AD8000 and magnets $Nd_2Fe_{14}B$ (sintered).

Chemicals: diphenylamine p.a. "Kemika", ultrapure water, filter paper Macherey-Nagel.

Magnetic water treatment was performed in the system depicted in Figure 1. The determined water volume (10 ml) was let passing through the glass funnel consecutively for 25 times, where a pass lasted for approximately two seconds. The length of the funnel pipe was 50 mm and the diameter was 4 mm. After that, the distance between magnets was adjusted, the intensity of the magnetic field was measured, and the entire procedure was repeated. As a result, four samples of magnetically treated water were obtained, each with the different field intensity: sample 1 - 0 mT, sample 2 - 375 mT, sample 3 - 570 mT, sample 4 - 750 mT, sample 5 - 900 mT, presented at Figure 2 . Solutions of the diphenylamine in the magnetically treated water were made to be saturated at this way. In the glass with a measured amount of magnetically treated water, sturdy diphenylamine of approximately 50 mg was added. After that, occasional stirring was performed in every glass, for about 15 minutes, using individual glass rods. Prepared saturated solutions were separated from the insoluble diphenylamine by filtering through a funnel with a filter paper. The filtered solution was let passing through the same funnel with the same filter paper and insoluble diphenylamine two more times, for better solution balance prior to spectrum processing.

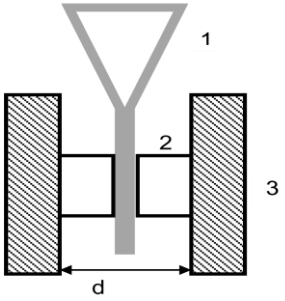

Figure 1. The system for magnetic water treatment. 1. funnel; 2. funnel and magnet holder; 3. magnets; d-spacing between magnets.

The previously described manner was used to prepare a series of five solutions; one of those, the first solution, was made in the magnetically untreated water, while the rest were processed in the magnetically treated water with different magnetic field intensity.

The temperatures in the laboratory during the preparation and measurements were not altered over 0.1°C.

RESULTS AND DISCUSSION

The absorption spectra of a series of saturated solutions of diphenylamine, in the magnetically untreated water and magnetically treated waters with

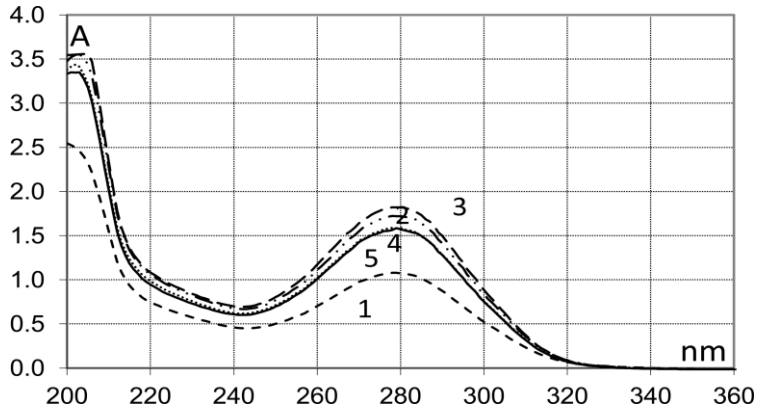

Figure 2. Solutions absorption spectra in the magnetically treated water with different magnetic field intensity.

varying magnetic field intensity are presented at Figure 2. From the obtained spectra, it can be concluded that the magnetic water treatment influences the absorption spectrum of the diphenylamine solution; i.e. the field intensity in water treatment contributes to alterations in the absorption spectrum, as a consequence of the corresponding water modifications. This preliminary results can be observed in Figure 3, where the resizing of the maximum to 279 nm with the magnetic field intensity is presented. Analogue results were

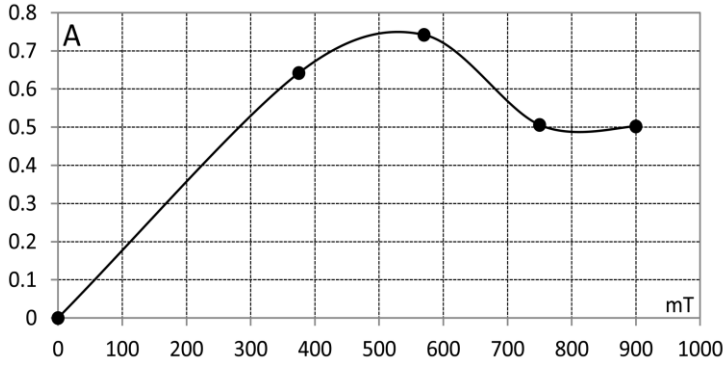

Figure 3. Solution absorption modification to 279 nm with the magnetic field intensity.

obtained from several experiments. It is need evaluated equation for quantitative dependence of the solution absorbance, i.e. concentration of diphenylamine on magnetic field intensity.

CONCLUSION

Based on the presented results, it can be concluded that the magnetic field has a certain influence on chemical and physical-chemical processes, as well as on the biochemical processes. Indirect confirmation for this conclusion can be obtained from the magneto therapy in Chinese medicine, since it is established on the impact of magnetic fields onto processes in living organisms, i.e. in biochemical systems.

REFERENCES

[1] D. Veselinović, Z. Velikić, Sixth International Congress "Ecology, Health, Work, Sport", Banja Luka, 2013, Association "Health for All", Book of abstracts, 211-214.
[2] D. Veselinović, D. Ilić, II Regional Syposium "The Chemistry and the Enviroment" 18-21 June, Kruševac, SCG, Proceedings, 223-224, Serb. Chem. Soc. Belgrade.
[3] D. Ilić, D. Veselinović, M. Vukić, 6th International Conference of Fundamental and Applied Aspects of Physical Chemistry, 26-28 Sept. 2002, Belgrade, Society of Phys. Chem. Proceedings, 645-647.
[4] Ilić D.; Vukić M.; Veselinović D.; Vukić Đ., Societies on Chemical Sciences for Sustainable Development, June 6-9, 2000, Halkidiky (Greece) Book of Abstracts, vol. II, 289.
[5] D. Veselinović, J.B.Krstić, "XXXIX Savetovanje Srpskog hemijskog društva", Begrad, 15-17, 10, 1999, Knjiga izvoda, 131.
[6] D.T. Ilić, M.R.Vukić, D.S. Veselinović "XXXIX Savetovanje Srpskog hemijskog društva", Begrad, 15-17, 10, 1999, Knjiga izvoda, 131.
[7] D.R. Stanisavljev, Z. Velikić, D.S. Veselinović, N.V. Jacić, M.C. Milenković, Chemical Physics 2014, **441,** 1.
[8] I.Otsuka, S.Ozeki, J. Phys. Chem. B, Vol. 110, No. 4, 2006

J *– Macromolecular Physical Chemistry*

INFLUENCE OF THE CROSS-LINK DENSITY ON THE RATE OF CRYSTALLIZATION OF CROSS-LINKED POLY(ε-CAPROLACTONE)

I. Sedov

Kazan Federal University, Chemical Institute, Kremlevskaya 18, 420008 Kazan, Russia. (igor_sedov@inbox.ru)

ABSTRACT

Kinetics of crystallization of cross-linked poly(ε-caprolactone) (PCL) was studied for the first time. Samples of polymer with different cross-link density were synthesized. Dependence of the degree of crystallinity on the preceding cooling rate for each sample was studied by following their heats of melting determined using fast differential scanning calorimetry technique. The cooling rate required to keep the cooled sample amorphous decreases with increasing cross-link density, and the crystallization half-time grows up monotonically. It is shown that covalent bonds between PCL chains impede crystallization process.

INTRODUCTION

Poly(ε-caprolactone) (PCL) is an industrially produced biocompatible and biodegradable polymer with good mechanical properties. Its low melting point (around 60°C) make PCL a convenient material for 3D printing and rapid prototyping. Prospective biomedical applications of PCL include implant manufacturing and encapsulation of pharmaceuticals in micro- and nanospheres made up of this polymer. In addition, it is capable of cross-linking when treated with radical initiators. Cross-linked PCL has greater mechanical strength, does not flow even at high temperatures and has slower biodegradation rate, which may be useful for controlling the rate of drug release from encapsulated forms. Cross-linked PCL exhibits two-way shape memory effect. It can remember one shape at low temperature and another shape at high temperature and recover them after deformation on both heating and cooling, which can find its use in creating programmable matter.

The studies of crystallization of polymers are important in order to control the degree of crystallinity in polymer processing. The rate of crystallization of PCL with various molecular masses was studied previously [1]. However, according to our knowledge, no data on crystallization kinetics of cross-linked PCL was reported up to now. Our goal was to study the influence of

the spatial density of the cross-links between PCL linear chains on the minimum cooling rate of the melt at which amorphous polymer is formed.

EXPERIMENTAL

The samples of commercial PCL (average Mn = 45000 g/mol) and benzoyl peroxide in different proportions were dissolved in dichloromethane. The solvent was evaporated, and the mixture was heated up to 180°C and kept for 30 minutes at this temperature. The degree of cross-linking grows up with the amount of radical initiator taken. It was measured using an equilibrium swelling method.

Phase transitions of cross-linked samples and initial PCL were studied using a combination of conventional differential scanning calorimetry (DSC) at 5 – 100 K/min scanning rates and fast differential scanning calorimetry (FDSC) using Mettler Toledo Flash DSC 1 instrument at 0.5 – 5000 K/s heating and cooling rates. Huge scanning rates in FDSC experiments are possible due to very low masses of the samples (10–50 ng) which are put directly onto the chip sensor as shown in Figure 1.

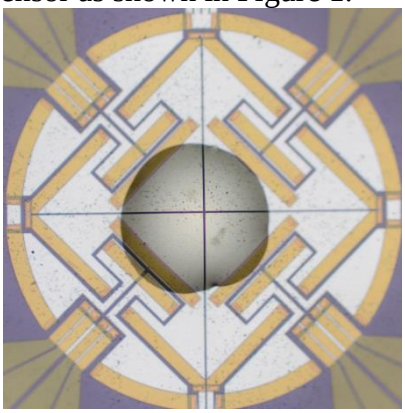

Figure 1. Sample of polymer on FDSC chip sensor

RESULTS AND DISCUSSION

Using conventional DSC experiments, we determined the enthalpies of melting of the studied samples with the highest possible degree of crystallization after slow cooling. These values were used to calculate the masses of the samples in FDSC experiments, which cannot be done by direct weighing.

With increasing scan rate, the crystallization peak position moves to lower temperatures and its area decreases. The temperature corresponding to the peak maximum changes almost linearly with the logarithm of the cooling rate until it reaches certain critical value when the sample has not enough time to crystallize and the peak disappears. This rate equals about 400 K/s for pure

PCL and decreases with increasing degree of cross-linking. However, it is difficult to determine this critical rate precisely from the cooling curves, especially when it has low values at which the signal is very noisy.

Thus, to characterize crystallization kinetics, we made a number of cooling scans with different rates from 0.5 to 5000 K/s succeeded by reheating scans with the same scanning rate (which varied from 100 to 5000 K/s). Heating with not too high rates results in the curves having the peak of cold crystallization. The difference in the areas of the melting peak and cold crystallization peak equals to the overall latent heat (OLH) of melting, which characterizes the total amount of crystalline phase in the polymer after cooling. The values of OLH are decreasing with increasing preceding cooling rates and reach zero at the same rate when the crystallization peak disappears in the cooling curves (Figure 2). Nevertheless, it is more precise and convenient to determine the cooling rate v_c at which the OLH reaches half of its maximum value measured at the slowest preceding cooling rate. The reciprocal of this rate corresponds to the crystallization half-time τ_c.

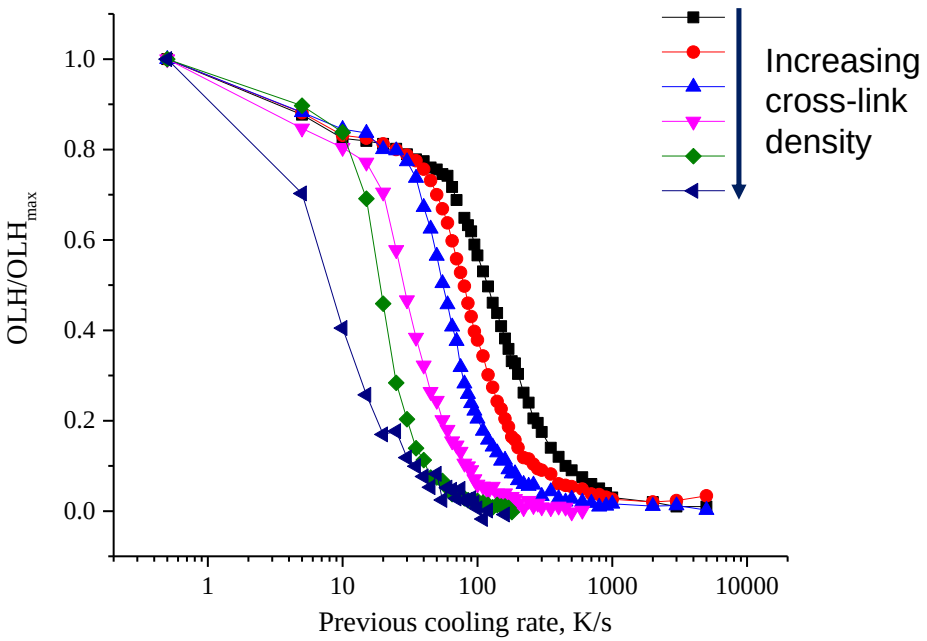

Figure 2. Dependence of the overall latent heat (OLH) of melting on the previous cooling rate for PCL with different cross-link density

The values of v_c are found to decrease monotonically with increasing cross-link density (Figure 3). The results were reproduced with several samples of polymer for each cross-link density. Covalent bonds between PCL

chains seem to impede crystallization process. This is similar to some other cross-linked polymers [2].

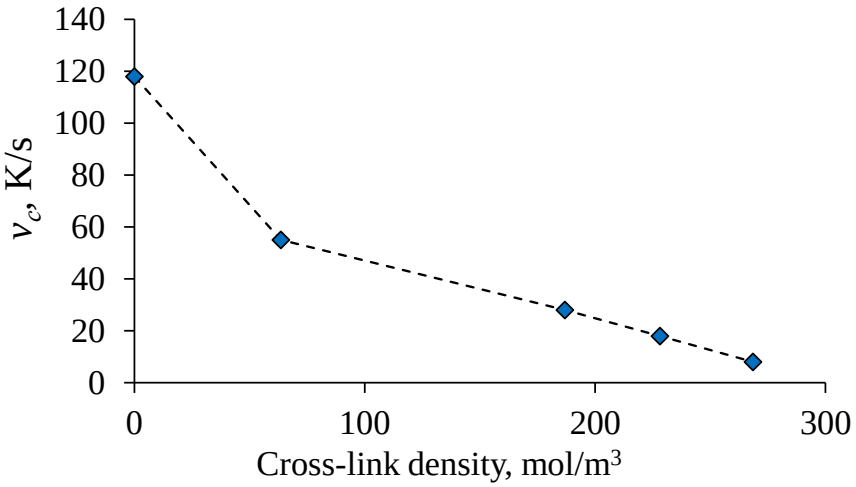

Figure 3. Dependence of the half-crystallization cooling rate v_c on the cross-link density of PCL

CONCLUSION

The crystallization kinetics of a cross-linked polymer was studied for the first time by means of fast scanning calorimetry. It is shown that crystallization half-time grows up with increase in the cross-link density.

Acknowledgement

This work was supported by the Russian Federation President Grant MK-6547.2018.3.

REFERENCES

[1] A. Wurm, E. Zhuravlev, K. Eckstein, D. Jehnichen, D. Pospiech, R. Androsch, B. Wunderlich, C. Schick, Macromolecules, 2012, 45, 3816-3828.

[2] C. Jiao, Z. Wang, X. Liang, Y. Hu, Polymer Testing. 2005, 24, 71–80.

OXIDATIVE TRANSFORMATION OF LEVAN PRODUCED BY BACILLUS LICHENIFORMIS STRAIN

B. D. Lončarević[1], G. Dj. Gojgić-Cvijović[1], D. M. Jakovljević[1], V. P. Beškoski[2] and M. M. Vrvić[2]

[1] *University of Belgrade, Institute of Chemistry, Technology and Metallurgy, 11000 Belgrade, Njegoševa 12, Serbia (djakovlj@chem.bg.ac.rs);*
[2] *University of Belgrade, Faculty of Chemistry, 11158 Belgrade, Studentski trg 12-16, Serbia.*

ABSTRACT
In this work, microbial polysaccharide levan produced by *Bacillus licheniformis* NS032 was functionalized by introducing aldehyde groups into glycan chain. Resulting polyaldehyde polymer was characterized by FT-IR spectral analyses and content of aldehyde groups was determined titrimetrically.

INTRODUCTION
Levan is microbial polysaccharide produced by broad range of microorganisms [1]. This glycan consisting of β-(2,6)-fructose units with a terminal D-glucose residue (Fig.1). Branching that occurs through β-(2,1)-bonds are often short and sometimes consisting of a single fructose residue. Bacterial levans have the broad spectrum of applications in many fields like food, health care, pharmacy, medical, cosmetic and others [1]. Levan is also successfully subjected to many reactions including grafting reaction with polystyrene [2].

This paper describes the formation of polyaldehyde polymers of partially oxidized levan with the aim of obtaining a suitable reactive derivative enbling covalent coupling with different amino compounds. The presence of aldehyde groups was evidenced by FT-IR spectroscopy data of polyaldehyde polymers.

EXPERIMENTAL
Levan used in this work was produced by the *B. licheniformis* NS032 [3]. Samples of aldehyde-functionalized levans (1.0 g) were obtained with periodate salts (0.5 g-2.0 g) in aqueous solution at room temperature for 24 h. The aldehyde content in polymers was varied over a broad range by changing the reaction conditions. Excess periodate was removed by ethylene glycol and

resulting polyaldehyde glycan was purified by dialysis (MWCO 14,000). Obtained products were lyophilized. The aldehyde content was determined titrimetrically by hydroxylamine hydrochloride method. Characterization of resulting polyaldehyde polymers was performed by FT-IR data (Thermo Nicolet 6700 FT-IR Spectrophotometer in ATR mode).

RESULTS AND DISCUSSION

Polyaldehyde derivatives of levan are obtained by reaction with periodate salts in aqueous solution. The aldehyde content in obtained levan samples was in range 24.4%-69.5%. Levan contains two monomer units in the polysaccharide chain, depending of their linkages in the molecule. However, it contains same types of vicinal diol groups and periodate oxidation results in the same types of dialdehyde structures (Fig. 1). In the molecule of this glycan predominate fructofuranosyl residues, because the glucopyranose unit is located only at the nonreducing end of the polymer chain.

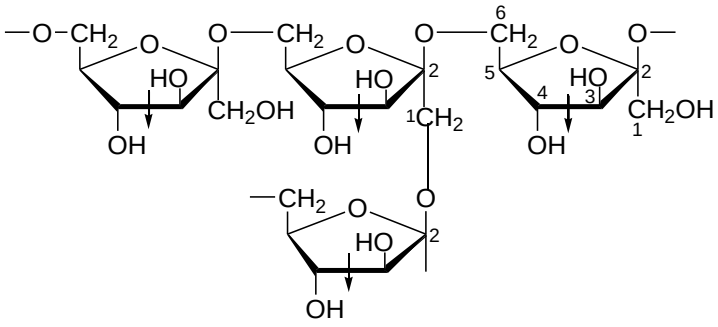

Fig. 1. Sites of oxidation in a periodate-oxidized levan (denoted by arrows)

The aldehyde-functionalized levan can react with various amine-containing compounds, e.g. some drugs or polymers to form Schiff base structures (Fig. 2) or alkylamines if coupling occurs in the presence of a reducing agent. Some periodate oxidized polysaccharides were successfully coupled with various amino compounds that can potentially have many of the uses in many fields, especially in medicine and pharmacy [4]. Polyaldehyde levan, because of its nontoxicity and solubility in water also can have great potential applications.

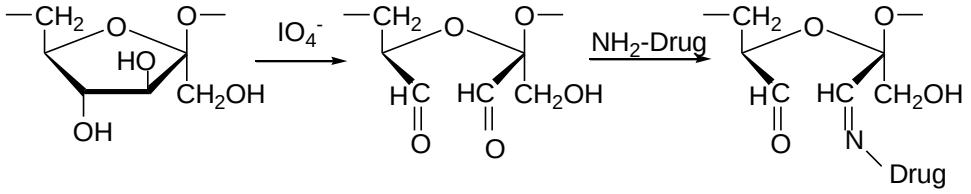

Fig. 2. Schematic representation of coupling reaction of aldehyde-functionalized levan with amine-containing drug

FTIR spectra were used to determine structural changes in the native and the oxidized levan. The FT-IR spectrum of native levan (Fig.3.) revealed characteristic absorption bands for polysaccharide, namely a strong broad band at 3000-3400 cm^{-1} as well as band at 2936 cm^{-1}; they were assigned to the OH stretching vibration and CH stretching, respectively [5]. Strong narrow bands between 1128 cm^{-1} and 1014 cm^{-1} corresponded to C-O-C and C-O-H stretching. The absorption bands arising from C-H deformation vibration were observed in the wavenumber region 1200-1500 cm^{-1}, while absorption band at 1645 cm^{-1} (H-O-H bending) was arising due to bound water. The vibration of C1-H bond in the IR anomeric region (950-700 cm^{-1}) near 891 cm^{-1} is specific for the β-configuration of the glycosidic linkages that are typical for levan.

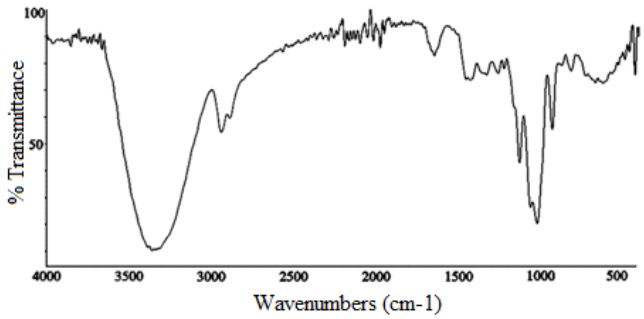

Fig. 3. FTIR spectrum of native levan produced by *B. licheniformis*

After oxidation, the FTIR spectrum (Fig. 4.) showed change in the carbonyl stretching region, while maintaining the general appearance. The new peak of low intensity for C=O groups at 1730 cm^{-1} appeared, which has been attributed to carbonyls in periodate-oxidized polysaccharides in different glycans [6].

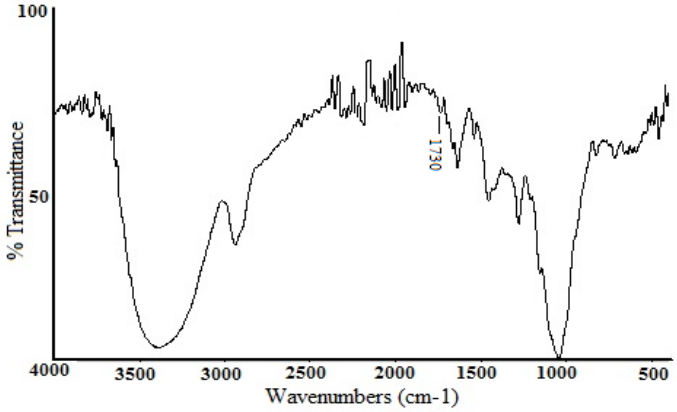

Figure 4. FT-IR spectrum of aldehyde-functionalized levan

CONCLUSION

Polyaldehyde polymers with different carbonyl contents were prepared by the oxidation of native levan using periodate ions in aqueous solution. The presence of aldehyde groups was confirmed by the FT-IR data. Aldehyde-functionalized levan can have potential application in many areas, due to enabling covalent coupling with different amino compounds.

Acknowledgement

This work was supported by the Ministry of Education, Science and Technological Development of the Republic of Serbia through Project III 43004.

REFERENCES

[1] E. T. Öner, L. Hernández, J. Combie, Biotechnol. Adv., 2016, **34**, 827-844.

[2] B. Kekez, G. Gojgić-Cvijović, D. Jakovljević, V. Pavlović, V. Beškoski, A. Popović, M. Vrvić, V. Nikolić, Carb. Polym., 2016, **154**, 20-29.

[3] B. Kekez, G. Gojgić-Cvijović, D. Jakovljević, J. Stefanović Kojić, M. Marković, V. Beškoski, M.Vrvić, Appl. Biochem.Biotech., 2015, **175**, 3068-3083.

[4] J. Stefanović, D. Jakovljević, G. Gojgić-Cvijović, M. Lazić, M. Vrvić, J. Appl. Polym. Sci., **2013**, 127, 4736-4743.

[5] M. Mathlouthi, J. L. Koenig, Adv. Carbohydr. Chem. Biochem., 1987, **44,** 7–89.

[6] S. D. Zhang, X. L. Wang, Y. R. Zhang, K. K. Yang,Y. Z. Wang, J. Polym. Res., 2010, **17**, 439–446.

SILVER-POLYANILINE-POLYVINYLPYRROLIDONE NANOCOMPOSITES: IN SITU SYNTHESIS AND CHARACTERIZATION

U. Stamenović,[1] V. Vodnik,[1] M. Otoničar,[2] S. D. Škapin[2] and M. Mitrić,[1]
[1]*Vinča Institute of Nuclear Sciences, University of Belgrade, P. O. Box 522, 11001 Belgrade, Serbia (una.bogdanovic@gmail.com)*
[2]*Jožef Štefan Institute, Department of Advanced Materials, Jamova 39, 1000 Ljubljana, Slovenia*

ABSTRACT
A simple, fast and cost-effective *in situ* chemical oxidative polymerization of aniline by silver ions was used as a method for the preparation of silver-polyaniline-polyvinylpyrrolidone (Ag-PANI-PVP) nanocomposites. Varying experimental conditions (pH and PVP concentration) prompted the formation of three different nanocomposites, considering their morphological properties and weight content of Ag. Within PVP presence as an accelerator and stabilizer, Ag nanoparticles (nanospheres and polyhedral particles) and PANI chains (granular morphology and nanosheets) were simultaneously formed, without any additional reducing/oxidizing and capping agents. Their optical and structural characteristics together with electrical conductivity were examined by using different analytical techniques. The simplicity of their synthesis combined with physicochemical characteristics and large-scale availability makes them attractive as Pt-free electrocatalysts, biosensors and antimicrobial agents.

INTRODUCTION
There is a constant need for the development of new functional materials, cheap, but with appreciable features that could easily replace some common materials in various fields [1]. Based on the well-known features of polyaniline (PANI) as a representative π-conjugated conductive polymer and silver nanoparticles (AgNPs) there was an opportunity to combine their unique properties, as well as the appearance of new ones, through the charge transfer at the regions of their contact in the nanocomposites [2,3]. The investigation of their physicochemical characteristics (optical and structural) before their further applications in various fields was presented here. The nanocomposites denoted as Ag-PANI-PVP were prepared in water in the presence of PVP as an accelerator of oxido-reduction reaction between Ag^+ ions and aniline monomer. Thus, we managed to synthesize them faster than can be found in the literature (regarding the Ag-PANI nanocomposites). The

aim of the work was to optimize the experimental conditions, gaining stable and conductive nanocomposites with a certain amount of Ag incorporated, in order to investigate their possible applications in two fields, as electrocatalytic and antimicrobial agents.

EXPERIMENTAL

Varying the molar ratios of only three reactants ($AgNO_3$, aniline and PVP) that participate in these polymerization processes and the initial pH of the reaction mixtures (from 2 to 11), led to the formation of three seemingly similar Ag-PANI-PVP nanocomposites' water dispersions [4]. After washing and drying precipitates, their powders denoted as Ag-PANI-PVP1, Ag-PANI-PVP2 and Ag-PANI-PVP3 contain 3.4, 43.8 and 22.5 wt% of Ag, respectively, determined by ICP–AES. Their further characterizations were done using TEM, FESEM, UV-Vis, FTIR and XRD analysis [4].

RESULTS AND DISCUSSION

Nanocomposites' formation was firstly visualized by the color changes of the reaction mixtures, from light yellow to dark green olive, indicating aniline polymerization to doped, emeraldine salt PANI form (PANI-ES) [1] that was also confirmed by UV-Vis and structural analysis by FTIR (results not presented here, see Ref. 4).

The surface of powdered nanocomposites and their morphology were observed in greater detail by FESEM and TEM analysis (Figure 1). Ag-PANI-PVP1 and Ag-PANI-PVP2 (Figure 1a,b) have granular morphology, while Ag-PANI-PVP3 (Figure 1c) is mostly formed in the shape of nanosheets. The differences in the morphologies as well imply the influence of PVP concentration on the nanocomposites' features. Namely, the development of the oxido-reduction reaction between Ag^+ ions and aniline in the presence of PVP is dependent on the reactants' concentrations, their oxidation potentials and pH. As a steric stabilizer, PVP affects AgNPs' size and shape, and together with the initial pH will influence their preferential growth. For example, in acidic conditions when PVP concentration is reduced, relative to Ag concentration, as within Ag-PANI-PVP3, its particle-shape controller role is decreased enabling particles' growth in different crystallographic orientations to polyhedron nanostructures, 140 nm in size (Figure 1f). When there is PVP excess in acidic solution (Ag-PANI-PVP2), the speed of nucleus formation is greater than the speed of their further growth, and 7 nm small AgNPs are obtained (Figure 1e). Also, PVP chains adsorbed on the particles surface prevent particles' mutual interactions, and therefore their aggregation to larger structures. Besides, PVP concentration influences the final nanocomposites' morphologies. When PVP is in a large excess relative to

aniline concentration, as in the case of Ag-PANI-PVP1 and Ag-PANI-PVP2, granular morphology is obtained. Lowering its concentration, as in Ag-PANI-PVP3, reduces the growth of granular PANI chains and the formation of PANI nanosheets through multiple point attachment to PVP chains is favored.

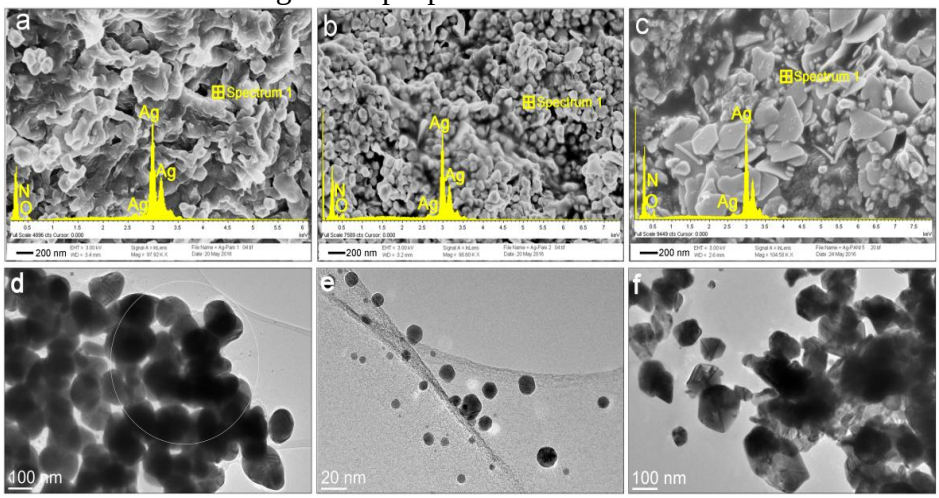

Figure 1. FESEM and TEM images of (a,d) Ag-PANI-PVP1, (b,e) Ag-PANI-PVP2, and (c,f) Ag-PANI-PVP3 nanocomposites.

In addition to being a steric stabilizator and accelerator of the simultaneous formation of AgNPs and PANI chains into nanocomposites, PVP represents a bridge between AgNPs and PANI chains. There is a coordination bonding to AgNPs surface through oxygen and nitrogen atoms from pyrollidone ring on one side, and hydrogen bonding between PVP and PANI chains on the other [4]. These interactions restrict AgNPs growth and prevent PANI aggregation. However, the lack of PVP presence is the formation of non-conductive islands between AgNPs and PANI in acidic conditions, when PVP chains are protonated, forming PVP cations. PVP-PVP interactions become dominant over PANI-PANI interactions, hindering the formation of 3D PANI conducting network in nanocomposite, as in the case of Ag-PANI-PVP2 and Ag-PANI-PVP3 that were synthesized at initial pH of 2. Even though, Ag amount in these composites is several times higher than in Ag-PANI-PVP1 (synthesized without adjusting initial pH), their conductivities are significantly lower - 1.50×10^{-6} and 4.40×10^{-7} S cm^{-1} for Ag-PANI-PVP2 and Ag-PANI-PVP3, over 0.56 S cm^{-1} for Ag-PANI-PVP1, due to the presence of a non-conducting polymeric component – PVP.

Presented nanocomposites were the subject of the electrocatalytic activity testing toward oxygen reduction reaction (ORR), where they showed high electrocatalytic efficacy and suggested to us to conclude that the Ag-PANI-

PVP composites are promising Pt-free electrocatalysts [4]. Moreover, since AgNPs and PANI have proven to be good antibacterial and antifungal agents, our future research considering these nanocomposites is focused on an examination of their antimicrobial activity.

CONCLUSION

Fast and simple synthetic procedure for Ag-PANI-PVP nanocomposites preparation was presented. Varying its initial setup, the molar ratio of the reactants and pH led to the formation of nanocomposites with different features. Determining and adjusting experimental conditions is crucial for the characteristics of nanocomposite as the final product and consequently its further applications in different areas.

Acknowledgment

This work was supported by grants from the Ministry of Education, Science and Technological Development of the Republic of Serbia (172056 and 45020).

REFERENCES

[1] G. Ćirić-Marjanović, Synthetic Metals, 2013, 177, 1–47.
[2] U. Bogdanović, I. A. Pašti, G. Ćirić-Marjanović, M. Mitrić, S. P. Ahrenkiel, V. V. Vodnik, ACS Applied Materials & Interfaces, 2015, 7, 28393–28403.
[3] U. Bogdanović, V. Vodnik, M. Mitrić, S. Dimitrijević, S.D. Škapin, V. Žunič, M. Budimir, M. Stoiljković, ACS Applied Materials & Interfaces, 2015, 7, 1955−1966.
[4] U. Stamenović, N. Gavrilov, I.A. Pašti, M. Otoničar, G. Ćirić-Marjanović, S.D. Škapin, M. Mitrić, V. Vodnik, Electrochimica Acta, 2018, DOI:10.1016/j.electacta.2018.05.2020013-4686.

SURFACE CHARACTERISTICS OF POLYURETHANE NETWORKS BASED ON POLYCAPROLACTONE

J. V. Džunuzović [1], E. S. Džunuzović [2], B. M. Marković [1], A. B. Nastasović [1] and I. S. Stefanović [1]

[1] *University of Belgrade, Institute of Chemistry, Technology and Metallurgy, Njegoševa 12, 11000 Belgrade, Serbia. (ivanstefanovic.com8@gmail.com)*
[2] *University of Belgrade, Faculty of Technology and Metallurgy, Karnegijeva 4, 11120 Belgrade, Serbia.*

ABSTRACT

A series of polyurethane networks (PUN) having different soft segment content (SSC) was synthesized by the prepolymer method in solution, using polycaprolactone diol as soft segment, and hyperbranched polyester and isophorone diisocyanate (IPDI) as components of hard segments. FTIR spectroscopy confirmed the structure of the prepared PUN. Furthermore, it has been shown that swelling degree of PUN in tetrahydrofuran (THF) and molecular weight of polymer chains between crosslinks (M_c) increase with increasing SSC, while the opposite was observed for the crosslinking density (v) and percent of the water absorption.

INTRODUCTION

Polyurethanes (PU) have been utilized as engineering materials in a broad range of applications, due to the possibility to easily tailor their properties by altering PU components [1,2]. However, in order to prepare novel PU with desired end-use properties, the structure-property relationship must be well understood. In segmented polyurethanes, which represent multiblock copolymers composed of alternating soft and hard segments, extent of the phase separation and, consequently, properties of PU, strongly depend on the chemical structure and molecular weights of the soft and hard segments, their content and interactions between them. Polycaprolactone (PCL) is synthetic, aliphatic, semicrystalline biodegradable polyester with very low glass transition and melting temperature, which has been progressively used for drug delivery and tissue engineering, in manufacturing biomedical devices, as a soft segment in the synthesis of environmentally-friendly PU coatings, etc. [3,4]. Aliphatic hydroxy-functional Boltorn® hyperbranched polyesters are due to the presence of numerous end functional groups and their three-dimensional and compact structure, often applied as crosslinkers in the synthesis of PUN [5]. In this work, Boltorn® hyperbranched polyester of the

second pseudo generation (BH-20) was, together with PCL diol and IPDI applied for the synthesis of novel PUN. The morphology, swelling behavior and water absorption of the prepared PUN was examined in order to investigate surface properties of these networks for their possible application in coatings.

EXPERIMENTAL

Five PUN with different SSC (presented in wt.% as last two numbers in the name of PUN) were synthesized by catalyzed two-step polymerization in solution (DMAc/THF), from PCL (Sigma-Aldrich, M_n = 2000 g/mol), BH-20 (Perstorp Specialty Chemicals AB, M_n = 1340 g/mol, 12 end –OH groups) and IPDI (Sigma-Aldrich), keeping the molar NCO/OH ratio at 1.05. In the first step of the synthesis, prepolymer was prepared by reacting PCL and excess of IPDI for 3h, at 80 ^oC in argon atmosphere, while in the second step, BH-20 was added. After short stirring, the reaction mixture was transferred into the Teflon® dishes and the crosslinking reaction was continued in the air oven first at 60 ^oC for 24 h and then at 80 ^oC for 3 h, and finally at 50 ^oC for 24 h in a vacuum oven.

FTIR spectra of PUN were obtained using ATR NICOLET 6700 FTIR spectrometer. Scanning electron microscopy (SEM) images of samples were recorded on a JEOL JSM-6460LV scanning electron microscope. Prior to scanning, samples were prepared by gold sputtering and cryo-fracturing. Swelling behavior of square PUN samples was examined in THF at room temperature. Water absorption of PUN was investigated by their immersion in distilled water for 48 h at room temperature.

RESULTS AND DISCUSSION

FTIR spectra of PCL, BH-20 and synthesized PUN_{IPDI}-30 are given in Figure 1a. In the FTIR spectrum of PCL the following absorption bands characteristic for different groups can be observed: hydroxyl groups (around 3500 cm^{-1}), stretching of symmetric and asymmetric CH_2 groups (2868 and 2950 cm^{-1}, respectively), stretching vibrations of ester carbonyl groups (1726 cm^{-1}) and stretching of asymmetric and symmetric C-O-C (1242 and 1186 cm^{-1}, respectively). FTIR spectrum of BH-20 shows bands characteristic for the hydroxyl groups (3300 cm^{-1}), $–CH_2–$ and $–CH_3$ groups (2900-3000 cm^{-1}), carbonyl ester groups (1723 cm^{-1}), C-O linkage of ester groups (1040-1210 cm^{-1}) and ether groups (1010-1120 cm^{-1}). The absence of peak at 2260 cm^{-1} in the FTIR spectrum of PUN_{IPDI}-30 indicates complete reaction of NCO groups and formation of urethane bonds. Furthermore, bands characteristic for the N-H stretching of urethane group (3365 cm^{-1}), amide II vibrations (1538 cm^{-1}), symmetric and asymmetric CH_2 groups (2867 and 2952 cm^{-1},

respectively), free carbonyl groups (1733 cm^{-1}) and hydrogen bonded carbonyl groups from ester bonds (1646 cm^{-1}) can also be observed in the FTIR spectrum of PUN_{IPDI}-30 [4].

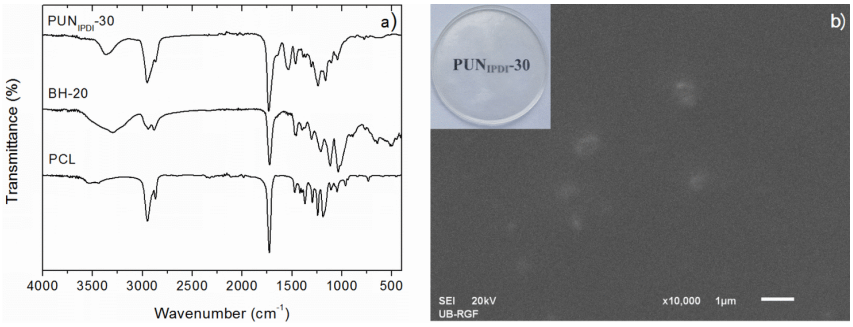

Figure 1. a) FTIR spectra of PUN_{IPDI}-30, BH-20 and PCL and b) SEM image of PUN_{IPDI}-30 (photo of PUN_{IPDI}-30 sample is given as inset).

The surface morphology of the prepared PUN was examined using SEM analysis (Figure 1b). It can be seen that PUN_{IPDI}-30 has certain surface homogeneity and smoothness with small surface roughness, indicating possible application in coatings. Similar was obtained for other PUN, showing lack of influence of SSC on the surface morphology of these PUN.

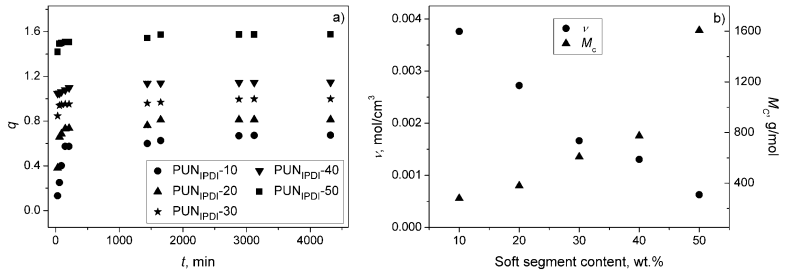

Figure 2. a) Change of the swelling degree (q) with time and b) dependence of the crosslinking density (ν) and molecular weight of polymer chains between crosslinks (M_c) on the SSC.

The change of swelling degree of PUN in THF, calculated using conventional gravimetric method, with time is shown in Figure 2a. It has been found that equilibrium swelling degree of PUN was reached after 48 h of networks immersion in THF, and that it increases from 0.6 to 1.6 with SSC increasing, indicating higher crosslinking density of samples with lower SSC. This was confirmed from the values of crosslinking density, calculated using Flory-Rehner equation, and M_c presented as a function of SSC in Figure 2b [5]. As expected, the presence of higher amount of crosslinker BH-20 during

the PUN synthesis led to the formation of networks with higher v and smaller M_c.

The dependence of the water absorption of PUN on SSC is given in Figure 3. The weight percent of the absorbed water decreased with increasing SSC, due to the increased amount of the hydrophobic PCL in the structure of prepared PUN.

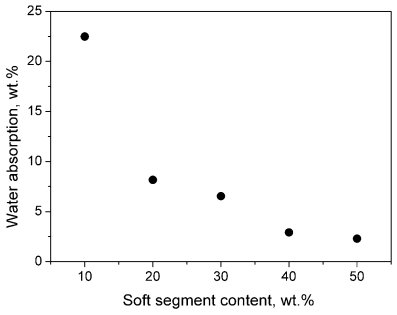

Figure 3. Dependence of the water absorption of PUN on the SSC.

CONCLUSION

Five PUN with different SSC was synthesized from PCL, BH-20 and IPDI. FTIR spectroscopy confirmed the structure of the prepared networks. The swelling ability of PUN in THF increased with increasing SSC, due to the decrease of the crosslinking density. PUN with higher content of hydrophobic PCL showed better water resistance.

Acknowledgement

This work was supported by the Ministry of Education, Science and Technological Development of the Republic of Serbia (Grants no. 172062 and III43009).

REFERENCES

[1] Z. S. Petrović, J. Ferguson, Prog. Polym. Sci., 1991, **16**, 695-836.
[2] D. K. Chattopadhyay, K. V. S. N. Raju, Prog. Polym. Sci., 2007, **32**, 352-418.
[3] T. K. Dash, V. B. Konkimalla, J. Control. Release, 2012, **158**, 15-33.
[4] A. Santamaria-Echart, A. Arbelaiz, A. Saralegi, B. Fernandez-d'Arlas, A. Eceiza, M. A Corcuera, Colloids and Surfaces A: Physicochem. Eng. Aspects, 2015, **482**, 554–561.
[5] J. V. Džunuzović, M. V. Pergal, R. Poręba, V. V. Vodnik, B. R. Simonović, M. Špírková, S. Jovanović, J. Non Cryst. Solids, 2012, **358**, 3161-3169.

SYNTHESIS OF HIGH MOLCULAR WEIGHT POLYACRYLAMIDE

I. Ristić[1], J.Tanasić[1], M. Janković[1], A.Aroguz[2], S. Cakić[3], N. Vukić[1] and J. Budinski-Simendić[1] .

[1]*University of Novi Sad, Faculty of Technology, Bul. Cara Lazara 1, 11000 Belgrade, Serbia.(ivan.ristic@uns.ac.rs)*
[2]*Istanbul University, Faculty of Engineering, Deparment of Chemistry, Avcilar, Istanbul 34320, Turkey.*
[3]*University of Niš, Faculty of Technology, Bul. Oslobođenja 124, 16000 Leskovac, Serbia*

ABSTRACT

In this work polyacrylamide was synthesized via radical polymerization, using two different initiators (potassium persulfate and ammonium persulfate) and iron(II)sulfate as catalyst in waterborne systems. Molecular structure of synthesized polymers was confirmed by Fourier transmission infrared spectroscopy. Thermal properties of obtained polymers were analyzed by differential scanning calorimetry, while average molecular weights were analyzed by gel permeation chromatography. It was shown that the types of initiator have not affect molecular weight of polyacrylamide. Thermal properties of synthesized polymer depend on molecular weight, increasing glass transition and melting temperatures with molecular weights increasing.

INTRODUCTION

Pure water is one of the basic requirements for a normal human life and one of the main conditions for survival. In order to meet the requirements that must be fulfilled by drinking water, there is a constant need for wastewater treatment, which can contain dissolved and dispersed impurities, which are undesirable in drinking water [1]. Water purification can be achieved in several ways by gravity (long lasting), coagulation and flocculation. Flocculation refers to a successful collision that occurs when destabilized particles are guessing one another with the help of a hydraulic shear in rapid mixing and a fluctuating pool. It agglomerates several colloids, and then quickly bridges together to form microplates that convert to visible mass. The polymers used in the water treatment are soluble in water and depend on their ionic nature, whether cationic, anionic, and non- ionic [2]. Many of synthetic polymers can be adapted as flocculant, but molecular weight, weight

distribution, structure, and nature and percentage of ionic groups must be controlled. One of the most commonly used polymers in the flocculation process is polyacrylamide [3] due to solubility in water and great mechanical properties. By choosing appropriate polymerization method it is possible to control a molecular weight, molecular mass distribution, pH, solubility, the degree of crosslinking of polyacrylamide. For this variety of reasons, in this work were investigated the influence of the type of initiators and catalyst on the molecular weight and thermal properties of polyacrylamide.

EXPERIMENTAL

Acrylamide (98.5 %) purchased from Acros Organics, SAD, potassium persulfate, ammonium persulfate and iron(II) sulfate pentahydrate were purchased from Centrohem Serbia. Two series of polyacrylamide were synthesized in waterborne system by radical polymerization using potassium persulfate or ammonium persulfate as initiator and iron(II) sulfate pentahydrate as catalysis. Distilled water was used as reaction medium and concentration of the acrylamide in the system was 25 wt%. Concentration of initiators (potassium persulfate and ammonium persulfate) was 0.1 wt%, 0.2 wt% and 1 wt% and concentration of catalyst was 1 wt%. Synthesis was done at 65 °C for 1.5 h at magnetic stirrer. For the characterization of the polyacrylamide samples differential scanning spectroscopy (DSC), gel permeation chromatography (GPC) and Fourier transmission infrared spectroscopy (FTIR) were used. DSC measurements were done on TA Instruments Q200, from -50 °C to 250° C ratio 10 °C min^{-1}. Average molecular weights (*Mn*, *Mw*) and polydispersity index (PDI) were determined by gel permeation chromatography GPC Agilent 1100Series with RID detector 1200. Measurements on FTIR were performed in the range from 4000 to 400 cm^{-1} using FTIR spectrophotometer Shimadzu IRAffinity-1S.

RESULTS AND DISCUSSION

The FTIR spectra of synthesized polyacrylamide with different initiators are shown in Fig. 1. The bands at 3410-3421 cm^{-1} (ν_{as} NH_2), 3190-3194 cm^{-1} (ν_s NH_2) and 1682-1685 cm^{-1} (νC=O) are characteristics of the acrylamide unit. The bands from 2930 and 2850 cm^{-1} correspond to C-H stretching vibration of polymer backbone. Two close lower intensive bands from 1450 and 1400 cm^{-1} are from C-N stretching vibration. Sharper band in acrylamide IR spectrum at 1426 cm^{-1} corresponds to C-N vibrations is detected. Bands from 1200 to 1100 cm^{-1} are from OH groups. In polyacrylamide, the vibrations of C-N are manifested as two small bands at 1350 and 1320cm^{-1} [4,5]. Band at 644 cm^{-1} attributed to the wagging C-O (ωC-O) vibrations [6].

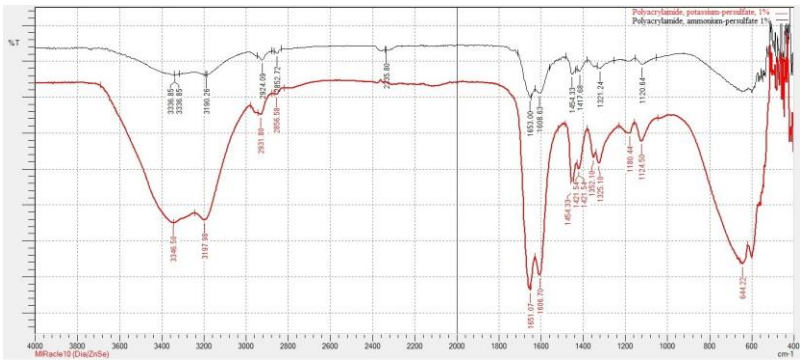

Figure 1. FTIR spectrum of synthesis samples polyacrylamide

The results obtained by GPC measurements are given in the Table 1. While the values of M_n are similar for all samples, the higher difference is obvious for M_w values and it is influenced by the concentration of chain length regulator. Good control of molecular weights was achieved using iron sulfate as chain length regulator.

Table 1. Average molecular weights of synthesized polyacrylamide

Sample	$\overline{M}_n$, g mol^{-1}	$\overline{M}_w$, g mol^{-1}	PDI	Tg, °C	Tm, °C
PAA-AP1	$5.41 \cdot 10^5$	$1.57 \cdot 10^6$	2.9	56	149
PAA-AP2	$7.12 \cdot 10^5$	$1.99 \cdot 10^6$	2.8	54	153
PAA-AP3	$9.73 \cdot 10^5$	$2.43 \cdot 10^6$	2.5	60	162
PAA-PP1	$5.51 \cdot 10^5$	$1.59 \cdot 10^6$	2.9	59	153; 205
PAA-PP2	$8.51 \cdot 10^5$	$2.64 \cdot 10^6$	3.1	62	154; 209
PAA-PP 3	$10.36 \cdot 10^5$	$3.42 \cdot 10^6$	3.3	62	212

*PAA-AP(PP)2 – sample of polyacrylamide with 0.2 wt% of ammonium persulfate (potassium persulfate)

DCS thermograms of polyacrylamide are shown in Figure 2.

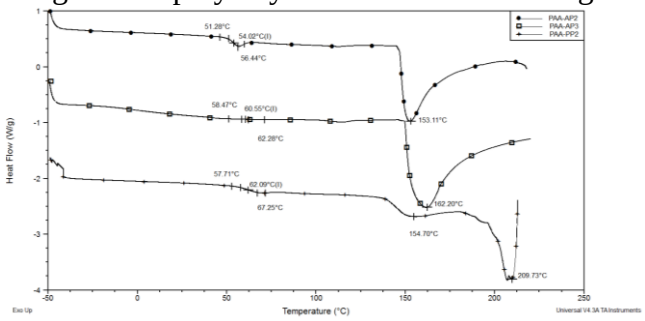

Figure 2. DSC termograms for synthesised polyacrylamide PAA-AP1

Temperature of glass transition (Tg) is similar for both series, with different initiators. While the melting temperature differs, the samples with ammonium

persulfate have higher values (above 200 °C), while in potassium persulfate samples there are melting values below 200 °C.

CONCLUSION

Waterborne system for synthesis of polyacrylamide was developed using the regulator of polymer chain length. It has been assessed that polymer molecular weights can be successfully controlled by proposed initiator system and iron(II) sulfate for synthesis of polyacrylamide. Polyacrylamide synthesized by this procedure has possible application in water purification systems.

Acknowledgement

This work was partially supported by the Ministry of Education, Science and Technological Development of the Republic of Serbia (Grants no. III45022).

REFERENCES

[1] R. S. Shatat, S. K. Niazi, A. Ariffin, IOSR Journal of Applied Chemistry, 2017, 10(4), 67-73.
[2] G. Craciuna, D. Ighigeanua, E. Manaila, M. D. Stelescu, Materials Research, 2015, 18 (5), 984-993.
[3] J. K. Inman, H. M. Dintzis, Biochemistry, 1969, 8 (10), 4074–4082.
[4] T. Erceg, I. Ristić, S. Cakić, J. Budinski-Simendić, Zaštita Materijala, 2017, 58 (4), 433 – 444.
[5] P. Kumar, Y. E. Choonara, L. C. Toit, G. Modi, D. Naidoo, V. Pillay, International Journal of of Molecular Sciences, 2012, 13, 13966-13984.
[6] R. Murugan, S. Mohan, A. Bigotto, Journal of the Korean Physical Society, 1998, 32(4), 505-512.

KINETICS AND THERMODYNAMICS OF Mo(VI) AND Re(VII) SORPTION ON AMINO-FUNCTIONALIZED MAGNETIC POLYMER

B. M. Marković[1], I. S. Stefanović[1], J. V. Džunuzović[1], Z. P. Sandić[2], Lj. T. Suručić[3], A.E. Onjia[4] and A. B. Nastasović[1]

[1]University of Belgrade, Institute of Chemistry, Technology and Metallurgy, Njegoševa 12, 11000 Belgrade, Serbia. (ekmescicbojana@gmail.com)
[2]University of Banja Luka, Faculty of Science, 78000 Banja Luka, Mladena Stojanovića 2, BiH, Republic of Srpska.
[3]University of Banja Luka, Faculty of Medicine, 78000 Banja Luka, Save Mrkalja 14, BiH, Republic of Srpska.
[4]University of Belgrade, Faculty of Technology and Metallurgy, Karnegijeva 4, 11120 Belgrade, Serbia.

ABSTRACT

Kinetics and thermodynamics of Mo(VI) and Re(VII) sorption onto amino functionalized magnetic poly(glycidyl methacrylate-*co*-ethylene glycol dimethacrylate) [mPGME-deta] at 298 K and pH=4.0 were investigated. It was shown that Mo(VI) and Re(VII) sorption obeys the pseudo-second-order model with evident influence of pore diffusion. The maximum sorption capacity of 60 mg/g for Mo(VI) and 47 mg/g for Re(VII) were observed. Thermodynamic studies implied an endothermic and spontaneous process in nature.

INTRODUCTION

Molybdenum (Mo) is an essential element to all species. However, it can be highly toxic at larger doses and cause serious health problems, like anemia, liver and kidney abnormalities, sterility, etc. [1]. Typical industrial sources of waste molybdenum include pigments, lubricants, catalysts, fertilizer, and corrosion control chemicals. In aqueous environment, Mo exists mainly as molybdate and/or other molybdenum polyanions, depending on the solution pH and the initial metal concentration [2]. Rhenium (Re) does not occur freely in nature. It is mainly obtained as a by-product of the extraction and refinement of molybdenum and copper ores. Re is widely used for high temperature superalloy productions, in chemical and petrochemical industry, etc. So far, various mineral substances, natural materials, polymers and bioadsorbents have been studied as Mo(VI) and Re(VII) adsorbents [3-5].

EXPERIMENTAL

Magnetic macroporous mPGME nanocomposite of glycidyl methacrylate (GMA) and ethylene glycol dimethacrylate (EGDMA) was prepared by suspension copolymerization in the presence of suspended magnetite nanoparticles and functionalized with diethylene triamine (V_s=0.99 cm^3/g, S_{Hg}=59 m^2/g, $D_{V/2}$=104 nm), as described elsewhere [5]. The Mo(VI) and Re(VII) sorption kinetics was tested in batch non-competitive experiments (T=298 K, pH=4.0). In each experiment, 0.3 g of mPGME-deta was added into 30 ml of aqueous solutions containing Mo(VI) (C_i= 0.01) or Re (VII) (C_i= 0.005). Sample aliquots were withdrawn at the predetermined time intervals and analyzed with ICP-OES.

RESULTS AND DISCUSSION

Sorption kinetic data were analyzed using the surface-reaction (pseudo-first-order, PFO and pseudo-second-order, PSO) and particle diffusion-based (intraparticle diffusion, IPD) [6] kinetic models to investigate the controlling mechanism of Mo(VI) and Re(VII) sorption by mPGME-deta.

The plots for the PSO and IPD models are shown in Figure 1.

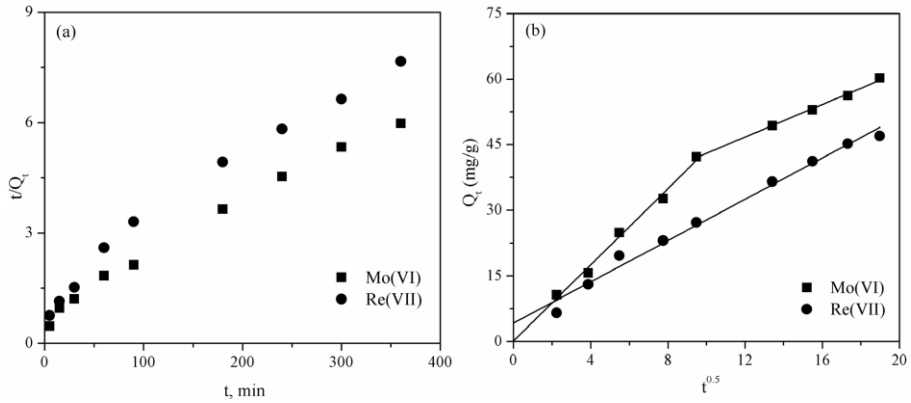

Figure 1. (a) PSO and (b) IPD kinetics for Mo(VI) and Re(VII) sorption on mPGME-deta (pH = 4, T = 298 K).

Kinetic parameters calculated from these models are presented in Table 1, where: Q_t-amount of sorbed metal ions at time t, Q_e-amount of sorbed metal ions at equilibrium, k_1-PFO rate constant, k_2-PSO rate constant, k_{id}-IPD coefficient, C_{id}-intercept of IPD plot, S-rate parameter.

Table 1. The kinetic parameters for Mo(VI) and Re(VII) sorption on *m*PGME-deta (pH=4.0, *T*=298K)

	Mo(VI)	Re(VII)
Q_e^{exp}, mg/g	60	47
pseudo-first-order		
$k_1 \cdot 10^3$, 1/min	8.06	9.21
Q_e^{calc}, mg/g	46.4	42.2
R^2	0.987	0.960
pseudo-second-order		
$k_2 \cdot 10^3$, g/(mg min)	0.32	0.32
Q_e^{calc}, mg/g	65.8	52.6
R^2	0.992	0.982
intraparticle diffusion		
k_{1id}, mg/(g min$^{0.5}$)	4.35	2.35
C_{1id}, mg/g	0.14	4.22
R_1^2	0.991	0.987
k_{2id}, mg/(g min$^{0.5}$)	1.86	/
C_{2id}, mg/g	24.3	/
R_2^2	0.997	/

As it can be seen from Table 1, the Q_e values predicted by the PSO model agree very well with experimental Q_e values with rather high R^2 values. According to the IPD model, if a Q_t–$t_{1/2}$ plot is a straight line, IPD is the only rate-controlling step. If the data exhibit multi-linear plots, two or more steps influence the sorption process. The IPD plot for Mo(VI) sorption on *m*PGME-deta has two straight lines with different slopes with high R^2 (>0.99) indicating that two diffusion steps are involved in the sorption process. The first stage (the sharper portion) represents the fast sorption over the outer surface and in the macropores, while the second one could be attributed to the IPD through mesopores. The IPD plot for Re(VII) sorption gives a straight line, indicating the IPD influence.

Table 2. Thermodynamic parameters for Mo(VI) and Re(VII) sorption onto mPGME-deta.

	Mo(VI)				Re(VII)			
T, K	$-\Delta G°$, kJ mol^{-1}	E_a, kJ mol^{-1}	$T\Delta S°$, kJ mol^{-1}	$\Delta H°$, kJ mol^{-1}	$-\Delta G°$, kJ mol^{-1}	E_a, kJ mol^{-1}	$T\Delta S°$, kJ mol^{-1}	$\Delta H°$, kJ mol^{-1}
298	7.50	35.1	104.5	97.0	4.38	43.1	17.3	12.9
313	12.8		109.8		5.25		18.1	
328	18.0		115.0		6.12		19.0	
343	23.3		120.3		6.99		19.9	

Thermodynamic parameters ($\Delta G°$- free energy of adsorption, $\Delta H°$-enthalpy change and $\Delta S°$-entropy change) were determined from Van't Hoff equation. The activation energy, E_a, was calculated from the linearized

Arrhenius equation. The positive $\Delta H°$ values (Table 2) implies endothermic nature of Mo(VI) and Re(VII) sorption, characteristic for the chemical sorption. Also, the calculated E_a values for Mo(VI) and Re(VII) are outside the range of values of 8–22 kJ mol^{-1} for diffusion-controlled processes [7]. The negative $\Delta G°$ values indicate that Mo(VI) and Re(VII) sorption is spontaneous, while the positive $\Delta S°$ values suggest an increased randomness at the solid–solution interface.

CONCLUSION

The rate-controlling mechanisms of Mo(VI) and Re(VII) sorption onto mPGME-deta was analyzed using PFO, PSO and IPD kinetic models. The sorption kinetics for both anions adhered to the PSO model, implying an important role of chemisorption in the sorption process, with the evident influence of the intraparticle diffusion. Thermodynamic parameters revealed spontaneous and endothermic nature of Mo(VI) and Re(VII) adsorption with increased randomness in the system.

Acknowledgement

The work was supported by the Ministry of Education, Science and Technological Development of the Republic of Serbia (Grants no.172062 and III43009).

REFERENCES

[1] C. Namasivayam, D. Sangeetha, Bioresour. Technol., 2006, **97**, 1194-1200.
[2] R. Navarro, J. Guzmán, I. Saucedo, J. Revilla, E. Guibal, 2003, **3**, Macromol. Biosci., 552-561.
[3] Z. Lou, L. Wan, C. Guo, S. Zhang, W. Shan, Y. Xiong, Ind. Eng. Chem. Res., 2015, **54**, 1333–1341.
[4] S. Hassanpour, M. Taghizadeh, RSC Adv., 2016, **6**, 100248–10026.
[5] B. M. Marković, Z. M.Vuković, V. V. Spasojević, V. B. Kusigerski, V. B. Pavlović, A. E. Onjia, A. B. Nastasović, J. Alloy. Compd., 2017, **705**, 38-50.
[6] B. M. Ekmeščić, D. D. Maksin, J. P. Marković, Z. M. Vuković, R. V.Hercigonja, A. B. Nastasović, A. E.Onjia, Arab. J. Chem., DOI: 10.1016/j.arabjc.2015.11.010.
[7] S. Glasston, K.J. Laidler, H. Eyring, The Theory of Rate Processes, McGraw-Hill, New York, 1941.

XRD AND TGA STUDY OF POLYMER/MAGNETITE NANOCOMPOSITE

B. M. Marković[1], I. S. Stefanović[1], J. V. Džunuzović[1], E. S. Džunuzović[2], A. Dapčević[2] and A. B. Nastasović[1]

[1]*University of Belgrade, Institute of Chemistry, Technology and Metallurgy, Njegoševa 12, 11000 Belgrade, Serbia. (ekmescicbojana@gmail.com)*
[2]*University of Belgrade, Faculty of Technology and Metallurgy, Karnegijeva 4, 11120 Belgrade, Serbia.*

ABSTRACT
Two samples of poly(glycidyl methacrylate-*co*-ethylene glycol dimethacrylate)/magnetite nanocomposite (mPGME) with different magnetite content were prepared by suspension copolymerization. The samples were characterized by X-ray powder diffractometry (XRD) and thermogravimetric analysis (TGA).

INTRODUCTION
Polymer/magnetite nanocomposites (PMNC) combine the advantages of both their components, magnetic nanoparticles (MNPs) and polymer [1]. The magnetic NPs enable the rapid and easy separation of magnetic polymer by an external magnetic field, while the polymer stabilizes the MNPs and suppress their aggregation. Also, the functionalization of the surface of PMNC by specific ligands makes them applicable in microfluidics and microelectronics, wastewater treatment, biomedical sensing, etc. Due to the presence of highly reactive epoxy groups on the side chain, GMA polymers can be modified by chemical reaction and grafting and used as sorbents selective towards targeted cations or oxyanions [2, 3], nonlinear optical materials [4], for enzymes immobilization [5], pre-concentration, chemical and biological separations [6], etc. In this study, two samples of mPGME with different magnetite content were synthesized by suspension copolymerization and characterized by X-ray powder diffractometry (XRD) and thermogravimetric analysis (TGA).

EXPERIMENTAL
Two PMNC samples with different magnetite content (2 and 10 wt. %) in the reaction mixture, labeled as 2MAG-SGE60 and 10MAG-SGE60, respectively were prepared by a radical suspension copolymerization as reported elsewhere in details [2]. Reaction mixtures consisted of the monomer

phase suspended in the aqueous phase (1 wt. % of poly(N-vinyl pyrrolidone) solution). The monomer phase contained monomer mixture of glycidyl methacrylate (60 wt. %) and EGDMA, 2,2'-azobisiso-butyronitrile (AIBN) as an initiator (1 wt. %), magnetite (Fe_3O_4) nanoparticles in different proportions, as well as inert component, i.e. mixture of cyclohexanol (80 wt. %) and tetradecanol. The copolymerization was carried out under nitrogen atmosphere at 75 °C for 2 h and at 80 °C for 2 h with a stirring rate of 250 rpm. After the reaction, the magnetic copolymer particles were washed with water and ethanol, kept in ethanol for 12 h and dried in vacuum oven at 50 °C. The fraction with particles with diameter in range from 0.15 to 0.30 nm was further characterized.

The crystallographic characterization of the magnetic copolymer samples was done by a powder X-ray diffraction (XRD) spectrometer (Ital Structure APD 2000) using Cu *K*α radiation (λ = 1.5418 Å) over a 2θ range of 10–80° with a step-width of 0.02° and a counting time of 1.0 s per step. The PowderCell software was used for the crystallite size determination. Thermogravimetry was carried out on a TA Instruments SDT Q600 analyzer in N_2 atmosphere (flow rate: 100 cm^3/min; heating rate: 20 °C/min), ranging from room temperature to 700 °C.

RESULTS AND DISCUSSION

Due to the low Fe_3O_4 concentration, the reflections originated from magnetite were not observed in 2MAG-SGE60. For that reason, Figure 1 displays only the results of X-ray diffraction analysis of 10MAG-SGE60 nanoparticles.

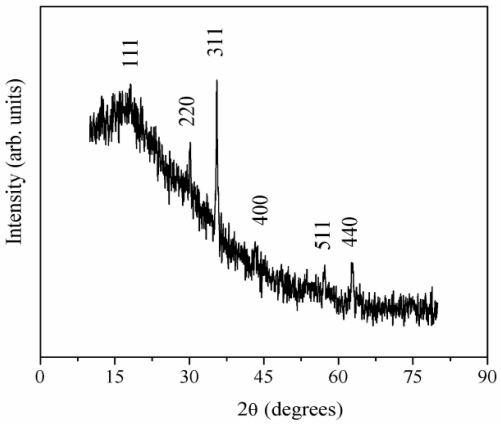

Figure 1. The X-ray diffraction pattern of 10MAG-SGE60 with the indices showing reflections of Fe_3O_4.

The diffraction peaks at 2θ = 18.10, 30.20, 35.50, 43.50, 57.3 and 62.9 are assigned to the (111), (220), (311), (400), (511) and (440), respectively. These reflections are in accordance with the standard JCPDS card (reference code: 89-0950) of magnetite and matched crystal planes of magnetite Fe_3O_4 with a cubic crystal structure. The crystallite size was estimated by XRD diffraction pattern from measurement of the half-height width of the strongest reflection (311) plane, using the well-known

Scherrer formula [7]. The average crystalline size of 10MAG-SGE60 particles was approximately 21.8 nm.

The obtained TG and DTG curves for 2MAG-SGE60 and 10MAG-SGE60 are shown in Figure 2.

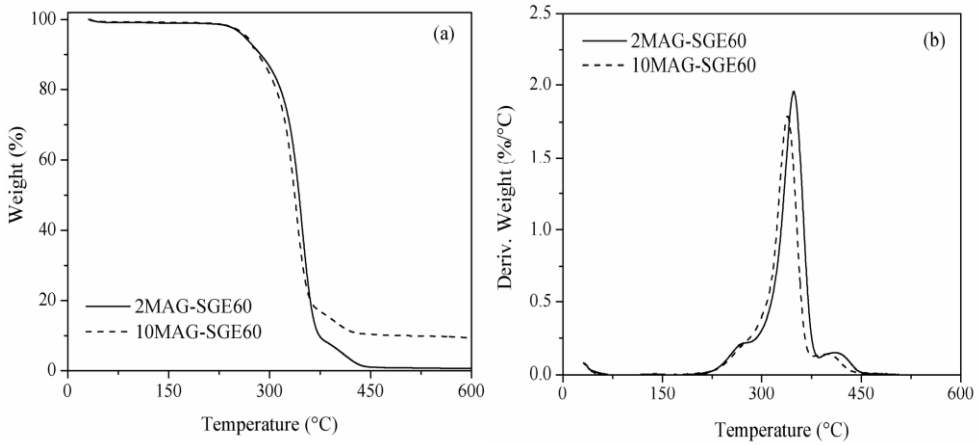

Figure 2. (a) TG analysis and (b) DTG curves of 2MAG-SGE60 and 10MAG-SGE60.

The thermal decomposition of the samples proceeds by depolymerization and ester decomposition and involves three degradation steps (Table 1). The first step could be associated with the decomposition initiated at weak bonds in backbone pendant groups (epoxy groups). The second step could be attributed to the random chain end scission, while the third one represents the total degradation of copolymers by random chain scission. The major loss for both samples was observed during the second degradation step.

Table 1. The results of TG analysis for investigated samples.

Sample	Degradation steps, T (°C)			T_{max}[a] (°C)	Residue at 500 °C (wt. %)
	I	II	III		
2MAG-SGE60	210-285	285-385	385-450	265/350/415	0.7
10MAG-SGE60	210-270	270-375	375-435	260/340/440	9.3

[a]The maxima values for observed degradation steps.

The initial decomposition temperature (T_0) for both samples is 210 °C. The incorporation of magnetite slightly increased the thermal stability of both magnetic samples in comparison to the initial non-magnetic macroporous copolymer (T_0=200 °C). The residues of ca. 0.7 and 9.3 wt. % found for

2MAG-SGE60 and 10MAG-SGE60, respectively, are in agreement with the magnetite content incorporated in these two samples.

CONCLUSION

In this study, poly(glycidyl methacrylate-*co*-ethylene glycol dimethacrylate)/magnetite nanocomposite (mPGME) with different magnetite content (2 and 10 wt. %) was prepared by suspension copolymerization. The samples were characterized by X-ray powder diffractometry (XRD) and thermogravimetric analysis (TGA). The XRD analysis confirmed the existence of magnetite in mPGME sample. Polymer/magnetite nanocomposites degradation mechanism of investigated samples involves depolymerization to monomers and oligomers initiated by scission of weak linkages and ester decomposition that simultaneously occur.

Acknowledgement

This work was supported by the Ministry of Education, Science and Technological Development of the Republic of Serbia (Grants no. 172062 and III43009).

REFERENCES

[1] O. Philippova, A. Barabanova, V. Molchanov, A. Khokhlov, Eur. Polym. J., 2011, **47**, 542-459.
[2] B. M. Marković, Z. M.Vuković,V. V.Spasojević, V. B. Kusigerski, V. B. Pavlović, A. E. Onjia, A. B. Nastasović, J. Alloy. Compd., 2017, **705**, 38-50.
[3] K. Z. Elwakeel, E. Guibal, J. Environ. Chem. Eng., 2016, **4**, 3632-3645.
[4] A. Sousani, P. N. Moghadam, R. Hasanzadeh, H. Motiei, M. Bagheri, Opt. Mater., 2016, **51**, 232-240.
[5] N. Miletić, A. Nastasović, K. Loos, Bioresource Technol., 2012, **115**, 126-135.
[6] R. J. Groarke, D. Brabazon, Materials., 2016, **9**, 446 doi:10.3390/ma9060446
[7] B. D. Cullity, Elements of X-ray Diffraction, Addison-Wesley, Reading, MA, 1967.

K *– Environmental Protection,*
Forensic Sciences,
Geophysical Chemistry,
Radiochemistry,
Nuclear Chemistry

SPECTRA AND ORIGIN OF BIOMOLECULES ON EARTH-LIKE EXOPLANET WITH REDUCING ATMOSPHERES UNDERGOING LATE HEAVY BOMBARDMENT

M. Ferus [1], P. B. Rimmer [2,3], I.P. Waldmann[4], O.Ivanek[1], P. Kubelík[1], S. N. Yurchenko[4], A. Knížek[1], T. Burian[5], J. Dostál[5], L. Juha[5,6], R. Dudzak[5], M. Krůs[5], J.Tennyson[4] and S. Civiš[1]

[1] J. Heyrovsky Institute of Physical Chemistry, Czech Academy of Sciences, Dolejškova 2155/3, 182 23 Prague, Czech Republic. (martin.ferus@jh-inst.cas.cz)
[2]University of Cambridge, Cavendish Astrophysics, JJ Thomson Ave, Cambridge CB3 0HE.
[3]MRC Laboratory of Molecular Biology, Francis Crick Ave, Cambridge CB2 OQH.
[4]Department of Physics & Astronomy, University College London, Gower Street, London, WC1E 6BT.
[5]Institute of plasma physics, Czech Academy of Sciences, Za Slovankou 1782/3, 182 00 Prague Czech Republic.
[6]Institute of Physics, Czech Academy of Sciences, Na Slovance 1999/2, 182 21 Prague, Czech Republic.

ABSTRACT
The chemical environments of young planets are assumed to be largely influenced by impacts of bodies lingering after the dissolution of the protoplanetary disk. We explore the chemical consequences of impacts by these bodies within the context of reducing planetary atmospheres dominated by carbon monoxide, methane and molecular nitrogen. The impact is simulated using a terawatt high-power laser. We provide simulated transit spectra for an Earth-like exoplanet with this reducing atmosphere during and shortly after eras of intense impacts. We predict that acetylene is as observable as other molecular features on exoplanets with reducing atmospheres that have recently gone through their own `Late Heavy Bombardments'.

INTRODUCTION
Chemical evolution of the Earth and subsequent origin of the first living structures are one of the most fascinating and most controversial questions of contemporary science. Direct geological records revealing chemical

conditions and their evolution during Hadean eon (>4 Gya) of the early Earth are very sporadic. Informations on the Hadean are very sparse, and the evidence is indirect, e.g. studies of ancient zircons from Jack Hills in Australia, providing the strongest evidence at present for the existence of liquid water oceans and supracrustal, placing them at approximately 4.2 Gya[1]. Additionally, trace-element analysis of igneous zircon of crustal origin shows that the Hadean continental crust was probably more reduced than its modern counterpart [2], i.e. the atmosphere likely contained a higher volume of reducing gases such as NH_3, CH_4, CO, H_2S, HCN etc. than assumed before. Measurements of the age of craters on the Moon[3] and the recent NICE model[4] of the evolution of planetary orbits have both independently pointed to periods of heavy bombardment, [5], [6] estimated to be between 4.5-3.85±0.05 Gyr ago.[5] We can assume that the impact-degassed or transformed atmosphere led to a reduced chemical composition [7]. However, the degree to which the atmosphere was reducing is still uncertain and the exact composition of the reducing mixture remains unknown. It is very complicated to unify these diverse results into one picture that would show in detail conditions on early Earth, nor do they answer the fundamental question: which chemical environment was behind the initial prebiotic synthesis and the subsequent origin of life. A key component to finding an answer should be detailed information on the initial chemical composition of the early environment.

Upcoming observations of exoplanets afford a unique opportunity to solve this fundamental problem by studying other planetary systems with similar initial conditions.

Universe is possibly full of young planets in early stages of their chemical evolution. As soon as we will be able to detect chemical composition of Earth's young sisters, we will be able to say, how environment on early Earth evolved and how it was like.

In the current paper, we explore complete transformation starting from re-ducing atmosphere containing methane, carbon monoxide, water and nitrogen, leading to synthesis of HCN as a precursor of biomolecules and ending with formation of fundamental RNA nucleobases. We apply the chemical yields from laser experiments to a photochemistry/diffusion model in order to predict the atmospheric signatures of impacts. We then calculate synthetic transmission spectra for these planets, to investigate how feasible observing these signatures will be on rocky exoplanets. We finish by discussing the next steps for impact chemistry, both chemically and observationally.

EXPERIMENTAL

Simulation of impact plasmas using large kJ-class laser PALS. Although laser−induced dielectric breakdown (LIDB, also called laser spark) in gases has been studied extensively since 1963, only our group performs this kind of research with a single sub−nanosecond laser pulse with energies achieving hundreds of Joules. Similarly with our previous studies[8]–[22], the plasma impact plasma induced by the impact of an extraterrestrial body was simulated using the high−power laser PALS (Prague Asterix Laser System). The laser beam (pulse length ≈300 ps, wavelength ≈1.315 μm) focused in the center of the sample cell containing a model atmosphere of an equimolar mixture CH4:CO:N2 saturated with water wapour in presence of montmorillonite clay simulating surface alterated by water. Laser pulse caused the dielectric breakdown in a gas phase (LIDB) and all processes connected with a high energy density took place: shock rises in temperature to several thousand K, the formation of an impact plasma and the generation of secondary short-wavelength radiation (UV−VUV, XUV, X−Ray). The dielectric gas represented an atmosphere in which relatively hot, dense impact plasma is formed, and a solid sample represented the surface. During the irradiation, plasma was studied in situ using OES, the gas phase was be analyzed using HR FTIR spectroscopy and, after filtration and drying under vacuum, biomolecules were detected in the solid residua.

Optical emission spectroscopy (OES) of laser induced breakdown plasma was performed using a High Resolution Echelle Spectra Analyzer ESA 4000 (LLA Instruments GmbH, Germany), complex spectra within the entire UV / VIS –range were recorded. The optical analyzer unit enabled a spatial and temporal resolved image of lowest spectral intensities. The resolution was a few pm in the range 200 – 780 nm with resolution of 0.005 nm (200 nm) to 0.019 nm (780 nm). The signal from the diagnostic window was focused using an LLA collimator.

FTIR Spectroscopy. The composition of the gas phase in all the experiments was monitored using Fourier transform high resolution Bruker IFS 125 HR spectrometer (Bruker Optics, Germany) equipped with a KBr beam splitter and a nitrogen cooled MCT and InSb detectors over the spectral range of 650 to 8000 cm^{-1}. Spectra are standardly measured with a resolution of 0.01 cm^{-1} using the Blackmann−Harris apodization function. Concentrations are determined by independent calibration using pure gases. To enhance detection limit of the instrument, the analysis was performed in a White multi pass cell with an optical beam length of 100 m by accumulation of 400 signals from the detector (scans).

GC−MS analysis of the non-volatile part of the sample. Methanol or water extracts (200 μL) of solid residue was transferred from the

experimental cell to 1.5 mL vials, filtered and dried under vacuum at ambient temperature. Subsequently, the samples were derivatized. The derivatization process was applied in order to detect glycine, purine, hypoxanthine and basic RNA nucleobases. The derivatization procedure was beperformed as follows: 50 µL of the derivatization agent N−(tert−butyldimethylsilyl)−N−methyl−trifluoroacetamide (Sigma Aldrich; 99 % (wt/wt) MTBSTFA, CAS 77377−52−7) and 150 µL of pyridine aprotic solvent (Scharlau; 99.5 % (wt/wt) anhydrous) was added to the dried remainder of the sample. The vial was then heated to 110 °C for 2 h, and 1 µL of the liquid sample was injected into the split injector and heated to 250 °C. The measurement was performed using a column temperature range of 180 °C to 280 °C with a temperature gradient of 10 °C·min^{-1}. In case of detection of sugars, 17 µL of hexamethyldisilazane (99% HMDS, CAS 999−97−3, Sigma Aldrich), 6µL of chlorotrimethylsilane (99% TMCS, CAS 75−77−4, Sigma Aldrich), and 52 µL of pyridine (99.5% anhydrous, Scharlau) were added to the residue as derivatization agents and aprotic solvent, respectively.

RESULTS AND DISCUSSION

The effect of impacts is determined not simply by the frequency of impacts, but also by the initial atmospheric composition. An atmosphere composed only of CO_2 and N_2 will have very different chemical tracers of impact history than a planet with a more reducing atmosphere, typically in the form of $CO/CH_4/C_2H_2$. Since the more reducing atmospheres result greater yields of life's building blocks from impacts, and since these atmospheres also produce chemical signatures of impacts, or 'impact signatures' that will be easier to observe, we concentrate our analysis on planets with reducing atmospheres. Our spectroscopic analysis pointed that the model atmosphere containing CO, CH_4 a N_2 studied in this work is reprocessed in presence of water excess in several products, among them dominate hydrogen cyanide (HCN), acetylene (C_2H_2) and cyanoacetylene (HC-CCN), in mutual ratio approximately 3:2:2, accompanied with a few percent of ethylene, carbon dioxide and ammonia. We have estimated, that large amount of methane, about 72 %, is decomposed, while more stable gases such as carbon monoxide and nitrogen are transformed from 28 % and 13 % respectively.

In presence of montmorillonite catalytic surface, GC-MS analysis of the non-volatile parts of the sample show that canonical nucleic bases are formed along-side with gas phase molecules such as HCN, C_2H_2, HCCCN, C_2H_2 and NH_3. Using this method, we detected 7 ppmV of adenine, 4 ppmV of guanine, 0.5 ppmV of cytosine and uracile, together with 0.1 ppmV of urea and 60 ppmV of glycine. Our results show that formamide is not

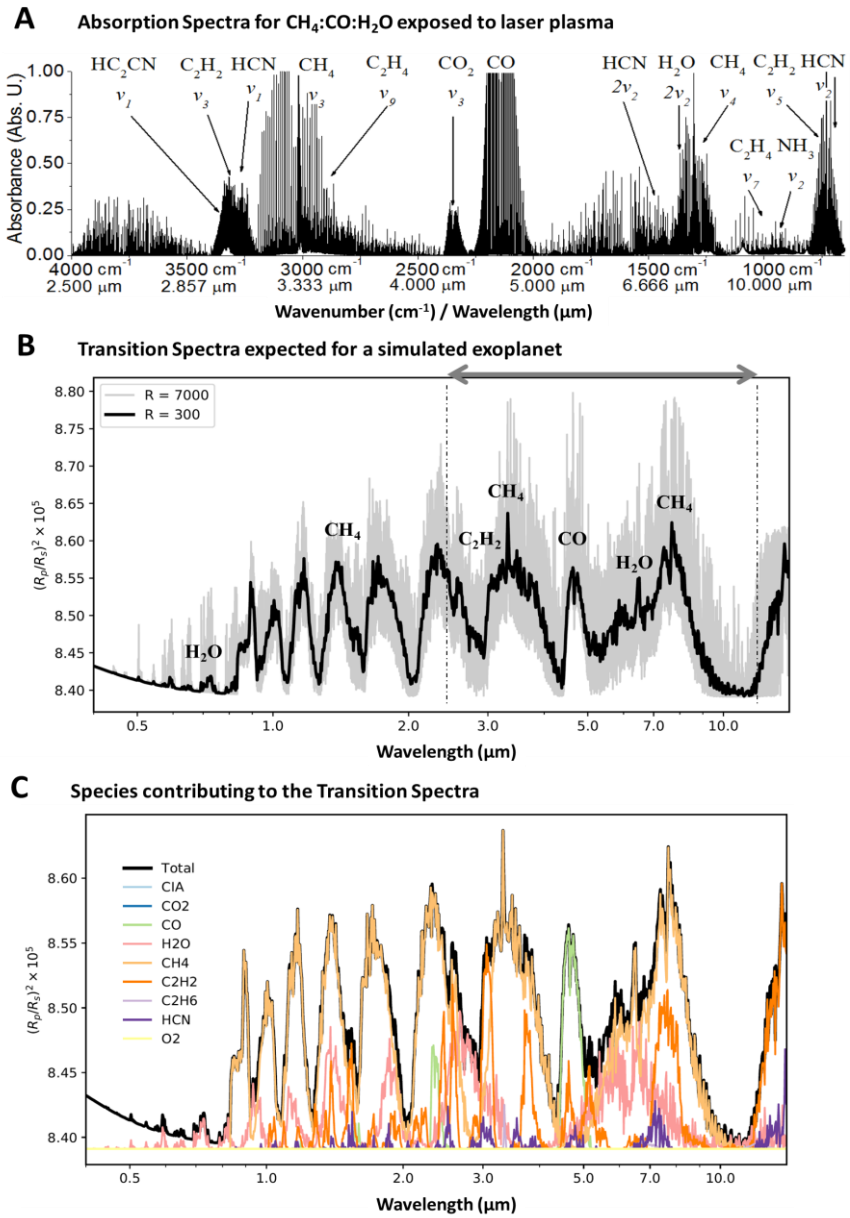

Figure 1. Panel A shows gas phase spectrum after LIDB. Panel B the simulated transition spectrum of an exoplanet. Panel C contribution of particular atmospheric constituents.

exclusive prebiotic parent or feedstock molecule for one pot synthesis of nucleobases, but also simple atmosphere producing hydrogen cyanide can become direct source for one pot synthesis of all the canonical nucleobases.

Finally, we simulated reprocessing of the atmosphere exposed to series of impacts considering the yields also as a function of the composition of the bulk atmosphere. The outgassing rates are placed as part of the lower boundary conditions for, ARGO, a Lagrangian photochemistry/cosmic-ray atmospheric chemistry model, that takes a prescribed temperature and high resolution (1 Angstrom) UV field estimated for a variety of stars, including the sun and all the stars observed as part of the MUSCLES survey, and a comprehensive chemical network, STAND, valid between 300 K and 30000 K incorporating H/C/N/O ion and neutral chemistry including complex hydrocarbons and amines. Finally, we simulated the transition spectra of particular exoplanet taking the line lists from the ExoMol62, 63, HITRAN, HITEMP and ASD-100060 databases. We used an adaptive wavenumber grid ranging from $2x10^4$ cm^{-1} at the longest wavelength (15 μm) and 0.01 at the shortest wavelength (0.5 μm). The results are shown in the Figure 1. What is interesting, the visible marker of impact driven chemistry is acetylene and not the main product of impact chemistry, the HCN molecule.

CONCLUSION

Our results show that in the system containing CO + CH_4 + N_2 + H_2O, one pot synthesis of all the canonical nucleobases, glycine and urea can occur in presence of montmorillonite initiated by a laser spark induced by focused 150-J pulses from the terawatt laser system PALS. In the first step, atmosphere is reprocessed by 4500 K high temperature plasma mainly to HCN, C_2H_2 and HCCCN. In the subsequent steps on acidic montmorillonite surface, these molecules react forming several intermediates and finally, nucleobases and glycine. Oxygen is introduced to the structure of biomolecules by hydrolysis of CN groups in several intermediates (except of uracil formed by direct hydrolysis of cytosine NH_2 group). This HCN-based scenario does not require synthesis of formamide feed-stock molecule containing all the macroelements. On the other hand, HCN-rich atmosphere was indicated as plausible source of formamide formed by HCN hydrolysis in water. However, direct scenario describing formation of all the RNA canonical nucleobases is simple, elegant and very likely explanation for the ob-servation of the one pot creation of nucleobases created by shock waves induced in reducing atmosphere of CO + CH_4 + N_2 + H_2O.

Acknowledgement

This work is a part of a research series funded by the Czech Science Foundation grant no. 17-05076S. Our thanks go to Jiří Skála, Miroslav Pfeifer, Pavel Prchal and Jakub Mareš for a valuable technical assistance at the PALS facility. The work at the PALS facility was financially supported

by the Czech Ministry of Education (Grants LTT17015, CZ.02.1.01/0.0/0.0/16_013/0001552 and LM2015083). Part of this project was also financially supported by project GAUK 1674218. S. N. Y. thanks the support of the UK Science and Technology Research Council (STFC) No. ST/M001334/1. This project has received funding from the European Research Council (ERC) under the European Union's Horizon 2020 research and innovation programme (grant agreement No. 758892, ExoAI).

REFERENCES

[1] A. J. Cavosie, J. W. Valley, and S. A. Wilde, "Magmatic delta O-18 in 4400-3900 Ma detrital zircons: A record of the alteration and recycling of crust in the Early Archean," *Earth Planet. Sci. Lett.*, vol. 235, no. 3–4, pp. 663–681, 2005.

[2] X. Yang, F. Gaillard, and B. Scaillet, "A relatively reduced Hadean continental crust and implications for the early atmosphere and crustal rheology," *Earth Planet. Sci. Lett.*, vol. 393, pp. 210–219, May 2014.

[3] J. Geiss and A. P. Rossi, "On the chronology of lunar origin and evolution Implications for Earth, Mars and the Solar System as a whole," *Astron. Astrophys. Rev.*, vol. 21, no. 68, pp. 1–54, 2013.

[4] D. de Niem, E. Kuehrt, A. Morbidelli, and U. Motschmann, "Atmospheric erosion and replenishment induced by impacts upon the Earth and Mars during a heavy bombardment," *Icarus*, vol. 221, no. 2, pp. 495–507, 2012.

[5] C. Koeberl, W. U. Reimold, I. McDonald, and M. Rosing, "Search for petrographic and geochemical evidence for the late heavy bombardment on Earth in early Archean rocks from Isua, Greenland," in *Impacts and the Early Earth*, 2000, vol. 91, pp. 73–97.

[6] C. Koeberl, "Impact processes on the early Earth," *Elements*, vol. 2, no. 4, pp. 211–216, 2006.

[7] G. L. Hashimoto, Y. Abe, and S. Sugita, "The chemical composition of the early terrestrial atmosphere: Formation of a reducing atmosphere from CI-like material," *J. Geophys. Res.*, vol. 112, no. E5, p. E05010, May 2007.

[8] M. Ferus, S. Civis, A. Mladek, J. Sponer, L. Juha, and J. E. Sponer, "On the Road from Formamide Ices to Nucleobases: IR-Spectroscopic Observation of a Direct Reaction between Cyano Radicals and Formamide in a High-Energy Impact Event," *J. Am. Chem. Soc.*, vol. 134, no. 51, pp. 20788–20796, 2012.

[9] M. Ferus, A. Knizek, S. Civiš, A. Knížek, and S. Civiš, "Meteorite catalyzed synthesis of nucleosides and other prebiotic compounds," *Proc. Natl. Acad. Sci. U. S. A.*, vol. 112, no. 23, pp. 7109–7110, 2015.

[10]M. Ferus, A. Knizek, J. Sponer, J. E. Sponer, and S. Civis, "RADICAL SYNTHESIS OF NUCLEIC ACID BASES FROM FORMAMIDE IN IMPACT PLASMA," *Chem. List.*, vol. 109, no. 6, pp. 406–414, 2015.
[11]M. Ferus, I. Matulkova, L. Juha, and S. Civis, "Investigation of laser-plasma chemistry in CO-N-2-H2O mixtures using O-18 labeled water," *Chem. Phys. Lett.*, vol. 472, no. 1–3, pp. 14–18, 2009.
[12]M. Ferus, R. Michalčíková, V. Shestivská, J. J. E. Šponer, S. Civiš, and S. Civis, "High-Energy Chemistry of Formamide: A Simpler Way for Nucleobase Formatione," *J. Phys. Chem.*, vol. 118, pp. 719–736, 2014.
[13]M. Ferus, D. Nesvorný, J. Šponer, P. Kubelík, R. Michalčíková, V. Shestivská, J. E. Šponer, and S. Civiš, "High-energy chemistry of formamide: A unified mechanism of nucleobase formation," *Proc. Natl. Acad. Sci.*, vol. 112, no. 3, pp. 657–662, 2015.
[14]J. E. Šponer, R. Szabla, R. W. Góra, A. M. Saitta, F. Pietrucci, F. Saija, E. Di Mauro, R. Saladino, M. Ferus, S. Civiš, and J. Šponer, "Prebiotic synthesis of nucleic acids and their building blocks at the atomic level - merging models and mechanisms from advanced computations and experiments," *Phys. Chem. Chem. Phys.*, vol. 18, no. 30, p. 20047—20066, 2016.
[15]M. Civis, M. Ferus, A. Knížek, P. Kubelík, M. Kamas, P. Španěl, K. Dryahina, V. Shestivska, L. Juha, P. Skřehot, V. Laitl, and S. Civiš, "Spectroscopic investigations of high-density-energy plasma transformations in a simulated early reducing atmosphere containing methane, nitrogen and water," *Phys. Chem. Chem. Phys.*, vol. 18, no. 39, pp. 27317–27325, 2016.
[16]M. Ferus, F. Pietrucci, A. M. Saitta, A. Knížek, P. Kubelik, O. Ivanek, V. Shestivská, and S. Civiš, "Formation of Nucleobases in a Miller-Urey Reducing Atmosphere," *Proc. Natl. Acad. Sci.*, vol. Will be pu, 2017.
[17]M. Davidkova, L. Juha, M. Bittner, S. Koptyaev, V. Hajkova, J. Krasa, M. Pfeifer, V. Stisova, A. Bartnik, H. Fiedorowicz, J. Mikolajczyk, L. Ryc, L. Pina, M. Horvath, D. Babankova, J. Cihelka, and S. Civis, "A high-power laser-driven source of sub-nanosecond soft X-ray pulses for single-shot radiobiology experiments," *Radiat. Res.*, vol. 168, no. 3, pp. 382–387, 2007.
[18]S. Civis, D. Babankova, J. Cihelkat, P. Sazama, and L. Juha, "Spectroscopic investigations of high-power laser-induced dielectric breakdown in gas mixtures containing carbon monoxide," *J. Phys. Chem. A*, vol. 112, no. 31, pp. 7162–7169, 2008.
[19]D. Babankova, S. Civis, and L. Juha, "Chemical consequences of laser-induced breakdown in molecular gases," *Prog. Quantum Electron.*, vol.

30, no. 2–3, pp. 75–88, 2006.
[20]D. Babankova, S. Civis, and L. Juha, “Chemical consequences of laser-induced dielectric breakdown in molecular gases,” *Chem. List.*, vol. 99, no. 2, pp. 109–115, 2005.
[21] S. Civis, L. Juha, D. Babankova, J. Cvacka, O. Frank, J. Jehlicka, B. Kralikova, J. Krasa, P. Kubat, A. Muck, M. Pfeifer, J. Skala, and J. Ullschmied, “Amino acid formation induced by high-power laser in CO2/CO-N-2-H2O gas mixtures,” *Chem. Phys. Lett.*, vol. 386, no. 1–3, pp. 169–173, 2004.
[22]D. Babankova, S. Civis, L. Juha, M. Bittner, J. Cihelka, M. Pfeifer, J. Skala, A. Bartnik, H. Fiedorowicz, J. Mikolajczyk, L. Ryc, and T. Sedivcova, “Optical and X-ray emission spectroscopy of high-power laser-induced dielectric breakdown in molecular gases and their mixtures,” *J. Phys. Chem. A*, vol. 110, no. 44, pp. 12113–12120, 2006.

SORPTION AND DEGRADATION OF 4-NITROPHENOL USING OIL SHALE AND ITS COMPOSITE FORMS

M. Molnár [1], O. Horváth [2] and R. Földényi [1]

[1]*Soós Ernő Water Technology Research Center, University of Pannonia Faculty of Engineering, Egyetem u. 10, 8200 Veszprém, Hungary. (foldenyi@almos.uni-pannon.hu)*
[2]*Institute of Chemistry, University of Pannonia, Egyetem u. 10, 8200 Veszprém, Hungary.*

ABSTRACT
Oil shale can be used as a pollutants remover material because of its sorption ability and microorganisms' activity. Adsorption and desorption of 4-nitrophenol were investigated on oil shale, which is easily crumbling. In order to find more manageable and efficient form of oil shale, two types of oil shale composites were produced, and their sorption nature was compared to those of oil shale powder. Catalytic effect of this oil shale was also studied in the decomposition of 4-nitrophenol in different parallel experiments with different model systems containing 4-nitrophenol and oil shale powder alone or oil shale powder pretreated with sodium azide of various concentrations. Decomposition process of 4-nitrophenol was faster, when sodium azide was absent. This result can be assigned to the importance of microorganisms' activity.

INTRODUCTION
Oil shale is a unique rock, it has natural origin, containing no artificial chemicals, which is present in a large amount in the world, also in Hungary. Oil shale originates from the biomass, thus contains high amounts of organic matter (5–50%). It is widely used as a fuel material as well as a soil-ameliorating agent because of its microelement and organic contents and low price [1]. Oil shale has already been used as a sorption material and its detoxification effect has already been utilized [1-3]. Unfortunately, oil shale is easily crumbling, which inhibits its easy and routine applicability as a sorbent. Therefore, it should be used in a special form containing suitable additives, e.g., alginate and agar.

Alginate is an anionic polysaccharide, a copolymer, it is an extraction from brown algae. It consists of 1,4-linked β-D-mannuronic acid and α-L-guluronic acid residues in different sequences. The ratio of mannuronic acid and guluronic acid fractions depends on the source of the alginate, thus the

physical and chemical properties of alginate vary in wide ranges. Some divalent cations (such as Ca^{2+}, Sr^{2+}, Ba^{2+}) crosslink the alginate chains, so the linear copolymer chains change to gel form [4].

Agar is also a natural polysaccharide, a biopolymer, it derives from cell wall of red algae. Agar can be fractionated into two components: agarose and agaropectin. Agarose fraction has greater gelling capability, also at very low concentration. It consists of 1,3-linked β-D-galactopyranose and 1,4-linked 3,6-anhydro-α-L-galactopyranose. These repeating units form long chains. Agaropectin has essentially the same backbone structure, but with various amounts of the residues replaced by pyruvic acid ketal and other sugar units. The gel liquefies when heated and it binds when cooled. The random coils in solution change to bundles of double helices in the gelation process [4-5]. Agar and alginate has already been used as a sorption material for removing environmental pollutants [6-7].

4-nitrophenol is a potential hazardous material, since it is a persistent intermediate and precursor of several pharmaceutical, explosive, dye and agrochemical products. 4-nitrophenol can accumulate in the soil and natural waters [8]. Therefore, this compound was used in the present work in order to investigate the applicability of oil shale as a natural medium for its removal from contaminated nature.

EXPERIMENTAL

Oil shale sample originated from Pula (Hungary), which was milled to the size of $\varnothing < 0.8$ mm. Sodium alginate, agar, 4-nitrophenol and calcium chloride were obtained from Sigma-Aldrich Co., Naturtrade Hungary Kft., Reanal Laborvegyszer Kft. and Lach-Ner, s.r.o., respectively. All chemicals were used without further purification. Concentration of 4-nitrophenol was determined by Merck Hitachi HPLC with UV detector at 317 nm. The eluent was a mixture of 30% methanol and 70% water, pH=4.6, flow rate: 1 mL/min.

Sorption experiments were performed in stoppered Erlenmeyer flasks and crystallizing dishes. 5 g of oil shale powder or composite forms, which contained 5 g of oil shale were weighed. Oil shale powder was left to swell in 5 mL water or solution of sodium azide (10 g/L) overnight. Different concentrations of 4-nitrophenol (from 10 μmol/L to 20 mmol/L) solutions were prepared with 0.01 mol/L $CaCl_2$ (pH=7.6). 50-50 mL of these solutions were transferred to the swollen oil shale powder or composite forms. Then these were shaken and left to stand for 24 hours for equilibration at room temperature, in the case of oil shale–agar composite the equilibration time was 48 hours.

At the degradation experiments, 25 g of oil shale powder was weighed

into stoppered glass flasks and pretreated by 25 mL sodium azide or water, then 4-nitrophenol solution (500 µmol/L) with 0.01 mol/L $CaCl_2$ was transferred to the swollen oil shale powder. After equilibration, samples were periodically taken and the concentration of 4-nitrophenol was measured by HPLC. All samples were in triplicate, in every case blank samples were used.

RESULTS AND DISCUSSION

The adsorption isotherms were analyzed in terms of Langmuir or Freundlich isotherm equation, which ever fits on the data better. The adsorption isotherms of 4-nitrophenol can be seen in Figure 1.

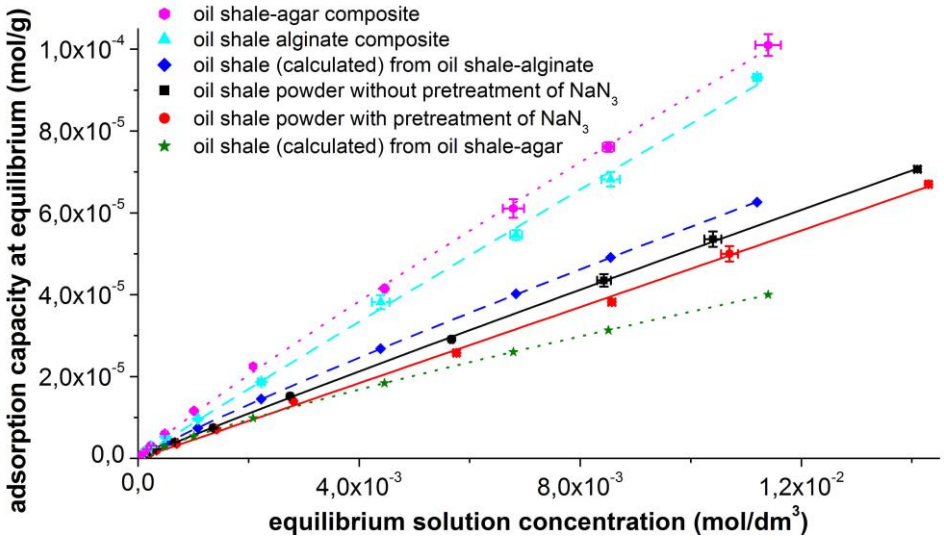

Figure 1. Adsorption isotherms of 4-nitrophenol.

The adsorption isotherm of 4-nitrophenol on oil shale alone is slightly higher than on oil shale powder pretreated by sodium azide. Consequently, after the 24-hour equilibration, not only sorption, but also small degree of degradation took place in the presence of living microorganisms. The amount sorbed by oil shale calculated from the oil shale–agar composite is lower than by oil shale alone. It can be caused by the apolar-apolar interaction between 4-nitrophenol and agar, which hinders the solute to reach the oil shale in the composite. The amount sorbed by oil shale calculated from oil shale–alginate composite is higher than by oil shale alone. It can be caused by the difference of liquid-solid ratio compared the powder to the composite. Thus, the repulsion between the dissociated 4-

nitrophenol and the anionic surface-charged oil shale powder is more significant. The adsorption–desorption isotherms represent hysteresis between sorption and desorption, which may ascribe to the interaction (e.g. absorption) between solute and kerogen content of oil shale, which has a zigzag-like nanopore structure.

Degradation experiments were also performed. The results show that 4-nitrophenol disappeared from the solution in the presence of oil shale within 29 days, which was much faster compared to the powder pretreated by sodium azide.

CONCLUSION

Sorption and degradation are two satisfactory solutions for eliminating environmental pollutants, such as 4-nitrophenol. Oil shale has a good sorption ability and because of its microbial content, the presence of oil shale dramatically enhanced the rate of degradation of chemicals, even if these compounds are persistent. Two types of forming agents were used, which were alginate and agar, creating two different sorbent materials, in which the oil shale preserves its sorption ability.

Acknowledgement

We are grateful to Judit Szauer for her valuable work.

REFERENCES

[1] R. Rauch, R. Földényi, Journal of Environmental Science and Health, Part B, 2012, 47, 670-676.
[2] E.T. Acar, S. Ortaboy, G. Atun, Chemical Engineering Journal, 2015, 276, 340-348.
[3] N. Ayar, B. Bilgin, G. Atun, Chemical Engineering Journal, 2008, 138, 239-248.
[4] P. de Vos, H.A. Lazarjani, D. Poncelet, M.M. Faas, Advanced Drug Delivery Reviews, 2014, 67-68, 15-34.
[5] S. Arnott, A. Fulmer, W.E. Scott, Journal of Molecular Biology, 1974, 90, 269-284.
[6] B. Gupta, Z. Begum I, G. Rajput, Chemical Engineering Communication, 2008, 195, 1200-1212.
[7] S. Peretz, O. Cinteza, Colloids and Surfaces A, 2008, 319, 165-172.
[8] S. Zhang, W. Sun, L. Xu, X. Zheng, X. Chu, J. Tian, N. Wu, Y. Fan, BMC Microbiology, 2012, 12, 27.

DEHP LEACHING FROM PVC PARTS OF TRANSFUSION SET AFTER UV TREATMENT

T. Anđelković[1], I. Kostić[1], D. Anđelković[1], T. Cvetković[2] and D. Pavlović[2]

[1] *University of Niš, Faculty of Sciences and Mathematics, Višegradska 33, 18000 Niš, Serbia (ivana.kostic83@gmail.com)*
[2] *University of Niš, Faculty of Medicine, Bul. Zorana Đinđića 80, 18000 Niš, Serbia*

ABSTRACT

Leaching of di-(2-ethylhexyl) phthalate (DEHP) from 3 different parts of transfusion set (Quadruple blood bag, SAG-M transfer bag and Transfer bag) made from polyvinyl chloride (PVC) after UV treatment was investigated. Plastic bags were irradiated with UV-A light, using UV-A lamps at 365 nm. All samples were extracted for 6, 15 and 30 days. By comparing of obtained results after 6 and 30 days, DEHP leached amount from investigated samples was more than 77% compare to DEHP leached amount after 30 days, except for SAG-M transfer bag which is about 41%. Results obtained from post-hoc test, Tukey's test, showed that there is a significant difference in leached amount of DEHP between 6 and 30 days for Quadruple blood bag and SAG-M transfer bag, while in case of Transfer bag, there was no significant difference between any extraction time. After 30 days of leaching just 6.06; 6.78 and 7.34% of total DEHP content was leached from investigated samples.

INTRODUCTION

Phthalates are substances that are widely used as plasticizers for many industrial products made of polyvinyl chloride (PVC). They are added to PVC to increase their physical properties such as flexibility and softness [1]. Due to their widespread use, relatively large amounts of these compounds could be released into the environment [2].

Many investigations showed that PVC medical devices contain up to 40% of plasticizers by weight. The most abundant plasticizer is di-(2-ethylhexyl) phthalate (DEHP) [3,4].

PVC plastic material is often used for producing of various types of medical devices: blood bags and tube systems for blood cell separation, parenteral nutritional tubing, infusion and transfusion tubings. Bearing in mind that phthalates can released to surrounding media from PVC parts, patients can be exposure to DEHP. In humans, phthalates are rapidly

hydrolyzed to the monoesters and then further metabolized, and they can be detected in urine, breast milk, faeces, *etc* [5]. DEHP is compound that is listed as one of potentially endocrine disruptors and some of health outcomes may be the result of phthalate-induced increases in oxidative stress or inflammation, which have been demonstrated in animal studies [6].

Because of phthalates are not bound to plastic material, phthalates can migrate, and various conditions may enhance the migration of phthalates from PVC. Content and transfer properties of phthalates may be influenced by optical radiation and temperature change during storage [7].

EXPERIMENTAL

Transfusion set was taken from the local Clinical Center Niš, Serbia. Set was consisted of three bags and coupled tubing (TIANHE Pharmaceutical, China). All bags were full filled with appropriate solutions.

All used chemicals (DEHP, DBA - dibuthyl adipate and hexane) were purchased from Sigma Aldrich, USA. Hexane was HPLC grade and screened to determine the DEHP background. Amount of DEHP standard was accurately weighted out by analytical balance with precision at ±0.0001 g (Kern, Germany) and diluted with *n*-hexane to 5 mL. Working standard solutions were at the concentration range from 0.25 to 10 μg mL^{-1} and obtained by diluting of stock solution. During the experiment, any contact with plastic equipment was avoided and special care was taken to avoid the contamination of solvents with DEHP.

Analysis was carried out by gas chromatography coupled to mass spectrometer (Hewlett Packard 6890 series GC System with autosampler connected with Agilent 5973 Mass Selective Detector (Electron Ionization MSD-EI, single quadrupole). The separation was achieved with 30 m × 0.25 mm × 0.25 μm a non-polar AGILENT DB-5MS column coated with 5% phenyl, 95% dimethylpolysiloxane. The MSD was used in the single ion-monitoring (SIM) mode. The identification of target compound was based on the relative retention time, the presence of target ion and its relative abundance. The most abundant ion *m/z* 149 was chosen for quantification of DEHP, with no qualifier ions, due to the simplicity of the matrix. Ion *m/z* 185 was chosen as representative ion of DBA internal standard. The dwell time was 100 ms.

Plastic bags from transfusion set were kept in the shade and at room temperature before UV treatment. Certain parts of plastic bags were irradiated with UV-A light, using UV-A lamps at 365 nm (PHILIPS, 18w/10 BL, 25 W, G 13), at the distance of 10 cm for 12 hours. After radiation treatment, the samples were stored in shade. Plastic samples that were exposed to UV treatment were cut into pieces with area of about 1

cm^2. All samples were extracted for 6, 15 and 30 days with 5 ml of *n*-hexane in glass vials.

RESULTS AND DISCUSSION

The analytical curve obtained for DEHP within concentration range 0.25 – 10 μg mL^{-1} was linear with determination coefficient $R^2 = 0.99853$ and linear equation $y = (2.94352 \pm 0.03017)\ x - 0.18073 \pm 0.15241$. Limit of quantitation (LOQ) was determined using signal to noise ratio of 10 to 1, for repeated measurements with RSD less than 20%. The obtained LOQ value was 0.05 μg mL^{-1}.

Obtained results of DEHP leached amount after different extraction times are presented in Table 1.

Table 1. Amount of leached DEHP (mg) from PVC parts of transfusion set determined for different extraction times (6, 15 and 30 days) after exposure to UV-A radiation (compared to 1 g of sample)

Sample*	Amount of DEHP leached by time (mg)		
	6 days	15 days	30 days
Quadruple blood bag	9.07±0.87 [a]	9.93±0.89 [a, b]	11.46±0.49 [b]
SAG-M transfer bag	1.14±0.09 [a]	1.14±0.07 [a]	2.73±0.51 [b]
Transfer bag	11.78±1.06 [a]	12.67±0.64 [a]	13.75±0.43 [a]

*SD – standard deviation (n = 3). [a,b] Values with the same letter within a row are not statistically significant different at the $p < 0.05$ level (Tukey's HSD test)

Obtained results show that after 6 days of leaching, DEHP leached amount from investigated samples was more than 77% compare to DEHP leached amount after 30 days, except for SAG-M transfer bag which is about 41%. Obtained results after 15 days of leaching showed that DEHP leached amount is increased for all samples except SAG-M transfer bag, and that is more than 86%. For samples of SAG-M transfer bag results presented the same value as for 6 days, 41%.

Difference between values of DEHP leached amount obtained for different extraction times were compared to a critical value to see if the difference is significant. The post-hoc test, Tukey's test, was performed and the test compares the difference between each pair of mean values with appropriate adjustment for the multiple testing. Values of HSD (honest significant difference) for each pair were computed by Origin© program. Comparing was performed in case $p < 0.05$.

Obtained results by Tukey's test, showed that samples of Transfer bag did not show significant difference between any periods of leaching, while

in case of two other samples, Quadruple blood bag and SAG-M transfer bag, there is a significant difference between leached amount of DEHP after 6 and 30 days.

By comparing these results with previous published results of total content of DEHP in parts from transfusion set after the same UV treatment, it can be concluded that after 30 days of leaching just 6.06; 6.78 and 7.34% of total DEHP content was leached from Quadruple blood bag, SAG-M transfer bag and Transfer bag, respectively [8].

CONCLUSION

Leaching of DEHP from 3 different parts of transfusion set (Quadruple blood bag, SAG-M transfer bag and Transfer bag) for 3 different extraction times (6, 15 and 30 days) after UV treatment was investigated. Obtained results show that after 6 days of leaching, DEHP leached amount from samples of Quadruple blood bag and Transfer bag were more than 77% compare to DEHP leached amount after 30 days, except for SAG-M transfer bag which is about 41%. After 30 days of leaching just 6.06; 6.78 and 7.34% of total DEHP content was leached from investigated samples.

Acknowledgement

This work was partially supported by the Ministry for Education, Science and Technological Development of the Republic of Serbia (Grant no. III 41018).

REFERENCES

[1] N. Nanni, K. Fiselier, K. Grob, M. Di Pasquale, L. Fabrizi, E. Coni, P. Aureli, Food Control, 2011, 22, 209-214.
[2] S. Pradeep, S. Benjamin, J Hazard Mater, 2012, 235-236, 69-77.
[3] H. Luo, G. Sun, Y, Shen, K. Xu, Springer Plus, 2014, 3, 58-60.
[4] F. Marcella, C. Federica, P. Giorgio, G. Luca, E. T. Florio, P. Stefania, C. Francesco, L. Giuseppe, Int J Pharm, 2012, 430, 86-88.
[5] S. Hildenbrand, R. Wodarz, T. Gabrio, G. Volland, Int J Hyg Envir Heal, 2009, 212, 679-684.
[6] S. Benjamin, S. Pradeep, M. S. Josh, S. Kumar, J Hazard Mater, 2015, 298, 58-72.
[7] P. D. Zygoura, E. K. Paleologos, M. G. Kontominas, Food Chem., 2011, 128, 106-113.
[8] I. Kostić, T. Anđelković, D. Anđelković, T. Cvetković, D. Pavlović, Physical Chemistry 2016, Proceedings, 2016. 499-502.

SEASONAL VARIATIONS OF NO_2, O_3 AND PM_{10} IN MOSTAR, BOSNIA AND HERZEGOVINA

S. Talić [1], A. Martinović Bevanda[1], M. Ćurlin [2] and T. Kraljević[1]

[1] University of Mostar, Faculty of Science and Education, Department of Chemistry, Matice hrvatske bb, 88000 Mostar, Bosnia and Herzegovina (*stanislava.talic@fpmoz.sum.ba*)
[2]Department of Laboratory Medicine, University Clinical Hospital Mostar, Mostar, Bosnia and Herzegovina

ABSTRACT

This paper shows seasonal variations of pollutants in the air of city of Mostar. NO_2, O_3 and PM_{10} represent the biggest threat for human health in this climate zone. Their concentrations were continuously measured by methods based on chemiluminescence, UV photometry and absorption of beta radiation during a three-year period. Mean monthly values of NO_2 (7-26 $\mu g/m^3$) and PM_{10} (9 -38 $\mu g/m^3$) did not exceed limit values. The concentrations of O_3 are higher in spring and summer (69-183 $\mu g/m^3$) but lower in winter (31-110 $\mu g/m^3$) while the concentrations of NO_2 are lower in summer. Multiple exceedings of limit values of O_3 warn of a need for reducing emission of pollutants.

INTRODUCTION

Urban environments with developed industry and intensive traffic are mostly affected by polluted air. The reduction of emission of pollutants from various anthropogenic sources is a subject of many discussions and legal regulations on national and global level. Improving air quality in urban environments is an important ecological challenge [1]. Monitoring of air quality on a local level is the first step in air quality management.

This paper shows seasonal and yearly variations of pollutants in Mostar, which is the biggest urban center of Herzegovina (111,000 inhabitants). Mostar is the warmest city in Bosnia and Herzegovina with a moderate Mediterranean climate and a high number of sunny days. The main pollutants in these climate conditions are nitrogen dioxide (NO_2), suspended particles ($PM_{2,5}$ and PM_{10}) and tropospheric ozone (O_3) [2]. NO_2 is the primary atmosphere pollutant which is formed from fossil fuel burning, decomposition of biomass and from households. Tropospheric ozone is generated by photochemical reactions with the presence of nitrous oxide sunlight (NO_x) and volatile organic compounds (VOC) [3]. Ozone is

detrimental to human health, vegetation and materials because of its highly reactive chemical properties [4]. Ozone is also a very effective greenhouse gas in the troposphere. In order to reduce the concentrations of tropospheric ozone, it is necessary to reduce emissions of polluting oxides in the environment [5]. Suspended particles can cause various health issues such as premature death, lung cancer, cardiovascular diseases and asthma attacks [6]. Limit values of pollutants are regulated by Regulations on limit values.

Table 1. Limit and tolerable values of pollutants-National standards [7].

Pollutant	Averaging period	Limit value ($\mu g/m^3$)	Tolerant value ($\mu g/m^3$)
NO_2	24 hour	85	105
NO_2	1 year	40	50
PM_{10}	24 hour	50	65
PM_{10}	1 year	40	44
O_3	8 hour	120	-

EXPERIMENTAL

The measurements were performed in the period from January 2012 to December 2014 at a station for air quality monitoring „Mostar 1“ (coordinates; N 43º 20’ 42,6’’ / E 017º 45’ 34,7’’ and altitude 64 m).

Concentrations of NO_2 were measured with NO_x-Analyzer (Horiba Model, APNA–370). The measurement was based on a combination of the dual cross flow modulation type chemiluminescence principle and the referential calculation method. The method ensured high stability and extraordinary sensitivity. O_3-Analyzer (Horiba Model APOA-370) was used for measuring concentrations of O_3. The O_3-Analyzer is using the non-dispersive ultraviolet absorption (NDUV) method as its operating principle. The ultra-violet absorption method works on the principle that ozone absorbs ultra-violet rays in the area of 254 nm [8]. PM_{10} was measured by the method of beta radiation absorption (Verewa Beta-Dust Monitor F-701-20). Instrument measures the dust concentration in µg dust/cubic meters of gas. The sample gas is drawn through a glass fiber filter tape and the volumetric flow of the gas is recorded by the system. The dust particles are then trapped on the filter tape and radiometrically measured. The radiometric measurement is achieved using a Betaemitter (C-14) and a Geiger-Müller counter [8]. The mean monthly values were derived from average 24-hours measurements for NO_2 and PM_{10}, and from 8-hours measurements for O_3. All results were processed in „Extended Reports, Version 1“ software.

RESULTS AND DISCUSSION

Mean yearly values of NO_2 for 2012/13/14. were: 15, 13 and 12 µg/m^3, respectively. The lowest mean values were reported in the summer period (min. 7 µg/m^3) while the increase was reported in the winter period (max. 19 µg/m^3). The exception is a high mean value (26 µg/m^3) for September 2012,

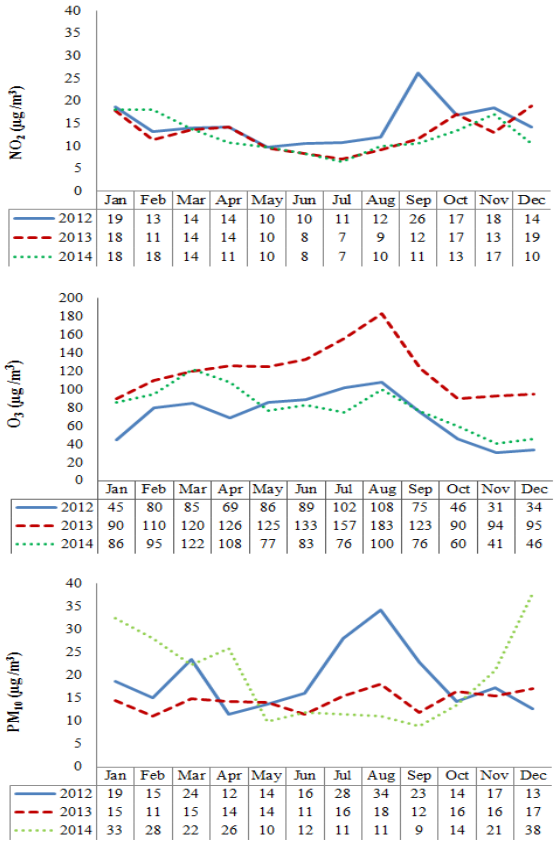

NO_2 (µg/m^3)	Jan	Feb	Mar	Apr	May	Jun	Jul	Aug	Sep	Oct	Nov	Dec
2012	19	13	14	14	10	10	11	12	26	17	18	14
2013	18	11	14	14	10	8	7	9	12	17	13	19
2014	18	18	14	11	10	8	7	10	11	13	17	10

O_3 (µg/m^3)	Jan	Feb	Mar	Apr	May	Jun	Jul	Aug	Sep	Oct	Nov	Dec
2012	45	80	85	69	86	89	102	108	75	46	31	34
2013	90	110	120	126	125	133	157	183	123	90	94	95
2014	86	95	122	108	77	83	76	100	76	60	41	46

PM_{10} (µg/m^3)	Jan	Feb	Mar	Apr	May	Jun	Jul	Aug	Sep	Oct	Nov	Dec
2012	19	15	24	12	14	16	28	34	23	14	17	13
2013	15	11	15	14	14	11	16	18	12	16	16	17
2014	33	28	22	26	10	12	11	11	9	14	21	38

Figure 1. Mean monthly concentrations of NO_2, O_3 and PM_{10} (µg/m^3) from 2012-2014 in Mostar (Bosnia and Herzegovina)

possibly because of a local fire. Conversely, higher mean values of O_3 were observed in spring and summer periods for all monitored years (max. 183 µg/m^3) and lower in winter periods (min. 31 µg/m^3). Multiple exceedings of limit values for O_3 were reported in 2013, with highest temperature values being reported in the same year (max. 41^{0}C). Mean yearly values of O_3 for 2012/13/14 were 71, 121 and 81 µg/m^3 respectively. It is known that O_3 forms from NO_x in presence of sunlight, so when the concentrations of O_3 are high, concentrations of NO_2 are low [4,5], which is also confirmed by

these measurements. Mean yearly values of PM_{10} for 2012/13/14 were 19, 15 and 20 $\mu g/m^3$, respectively. The lowest monthly value (9 $\mu g/m^3$) was reported in September 2014, and the highest (38 $\mu g/m^3$) was reported in December 2014. Earlier researches (2011) on seasonal, daily and hourly variations of PM_{10}, NO_2, NO and O_3 for city of Mostar showed a relation of pollutant levels with traffic intensity and seasonal conditions, but did not exceed limit values [8].

CONCLUSION

Results presented in this paper show seasonal variability for all monitored pollutants. Mean monthly values and mean yearly values for NO_2 and PM_{10} did not exceed limit values during the three-year period of air quality monitoring. However, high concentrations of ozone indicate the presence of pollutants, and their emissions from anthropogenic sources should reduce in accordance with EU regulations.

Acknowledgement

This work was partially supported by the Federal Ministry of Education and Science, FBIH (Grants no. 05-39-2379-1/17).

REFERENCES

[1] J.M. Baldasano, E. Valera, P. Jimenez, Scie. of the Tot. Env, 2003, 307, 141-165.
[2] M. Goncalves, P.J. Guerrero, J.M. Baldasano, Hrvatski meteorološki časopis, 2008, 43(43/1), 119-123. (https://hrcak.srce.hr/64189).
[3] EEA, Air quality in Europe -2017 report, Publications Office of the European Union, Luxembourg, 2017. (http://europa.eu).
[4] M. Amann, D. Derwent, B. Forsberg, O. Hanninen, F. Hurley, M. Krzyzanowski, F. de Leeuw, S.J. Lui, C. Mandin, J. Schneider, P. Schwarze, D. Simpson, Health risks of ozone from long-range transboundary air pollution,WHO, 2008.
[5] WHO, Air quality guidelines for particulate matter, ozone, nitrogen dioxide and sulfur dioxide, global update 2005: summary of risk assessment, Geneva,2006. (http://www.who.int/iris/handle/10665/69477).
[6] K.-H. Kim, E. Kabir, S. Kabir, Environ. Int. 2015, 74, 136-143.
[7] Službene novine FBiH (01/12) (http://www.sluzbenilist.ba/)
[8] N. Buntić, T. Kraljević, S.Talić, *Glas. hem. tehnol. Bosne Herceg., 2012, 39, 7-10.*

MONTE CARLO SIMULATION AS AN ALTERNATIVE APPROACH FOR ESTIMATION OF UNCERTAINTY MEASUREMENT OF 2,4-DIMETHYLPHENOL

B. Savić [1], T. Brdarić [1], I. Mihajlović [2], S. Milutinović [1], M. Pijović [1], J. Georgijević [1] and G. Tasić [1]

[1]*Vinča Institute of Nuclear Sciences, University of Belgrade, Department of Physical Chemistry, Mike Petrovića Alasa 12-14, 11351 Vinča, Belgrade, Serbia (branislava@vin.bg.ac.rs)*
[2]*University of Novi Sad, Faculty of Technical Sciences, Department of Environmental Engineering, Trg Dositeja Obradovića 6, 21000 Novi Sad, Serbia*

ABSTRACT
The estimation of uncertainty measurement using different approaches is increasingly applied to assess the reliability of results generated by applied analytical methods. This paper presents the Monte Carlo simulation model (MCS) for calculating the uncertainty of the measurement associated with the result of the analysis. The results of MCS were compared with the commonly used a standard method (GUM). The calculations of the measurement uncertainty were demonstrated in the case of the determination of 2,4-dimethylphenol by gas chromatography in concrete samples.

INTRODUCTION
The estimation of measurement uncertainty is an important aspect in evaluating measurement results. The International Standardization Organization (ISO) was published the Guide to Expression of Uncertainty in Measurement (GUM) in 1993 [1].

This approach to estimating measurement uncertainty is based on theoretical principles but exhibit some important limitations that are mainly derived from the use of the law of uncertainty propagation and from the application of the central limit theorem. To avoid these limitations, the joint committee for guides in Metrology (JCGM) presents a methodology that uses Monte Carlo method (MCS) for propagation of distributions, which is described in JCGM 101 [2, 3]. Monte Carlo approach for evaluation of uncertainty is a reliable tool when GUM framework is not adequate [3]. In analytical chemistry, uncertainty estimation is crucial, since it determines

conformance or non-conformance with a referent level, thus affecting risk management directly related to human health.

2,4-dimethylphenol (DMP) is used in the manufacture of commercial products for industry and agriculture. The presence of DMP in manufacture of numerous products, shows the potential for water, soil, air or building materials contamination [4]. DMP is termed as "toxic" in all regulatory resources listed by the EPA. It is estimated that the total annual discharge of DMP is around 72640 kg per year of which about 95% is slated for onsite disposals (air, water, land, underground injection, surface water discharge) [5]. In our previous research, we validated gas chromatography-mass spectrometry (GC-MS) method for the analysis of phenol compound in solid-solid concrete [6]. In the present work the uncertainty estimation for DMP in a concrete sample, using the Monte-Carlo simulated method, is studied. The results are compared to the ones obtained using the GUM method.

EXPERIMENTAL

Uncertainty estimation

Input data for calculating measurement uncertainty were taken from our previously presented validation study [6].

C++ programming language was used for estimation of measurement uncertainty by Monte-Carlo simulated method.

RESULTS AND DISCUSSION

Information about uncertainty is summarized in Table 1. The results obtained by processing the set of available information by GUM uncertainty approach and corresponding statistical parameters obtained by Monte Carlo simulation for the DMP are presented in Table 2.

Table 1. Uncertainty sources and associated distributions with their respective parameters for the estimation of uncertainty for the 2,4-dimethylphenol compound

Uncertainty source	Distribution	Parameters of a distribution
Volume (V)	Normal	Mean: 75 ml; SD: 2.55 ml
Mass (m)	Normal	Mean: 10 g; SD: 0.22g
Recovery (R)	Student's t Location-Scale	Mean: 33.71%; SD: 3.47 %; DF: 3
The peak area (y)	Student's t Location-Scale	Mean: 73259; SD: 4000; DF: 3
Slope (a)	Student's t Location-Scale	Mean: -10495; SD: 7726; DF: 3
Intercept (b)	Student's t Location-Scale	Mean: 50044/mg; SD: 15007l/mg; DF: 3
Purity of standard	Uniform	Min: -0.0193 mg/kg; Max: 0.0193 mg/kg

*SD – Standard Deviation; DF – Degrees of Freedom

Table 2: Results obtained using the GUM and Monte Carlo uncertainty approach for uncertainty estimation for the 2,4-dimethylphenol compound

Parameter (GUM)	Value	Parameter (MC)	Value
Mean	3.72 mg/kg	Median	3.72 mg/kg
Combined standard uncertainty	0.58 mg/kg	*Low endpoint for 95%	1.99 mg/kg
Expanded uncertainty for 95%	1.30 mg/kg	*High endpoint for 95%	5.83 mg/kg

*The values represent the limits of the shortest-length 95 % confidence intervals

Deviation of PDF (probability density function) of the output estimated by Monte Carlo simulation from distribution assigned to measurand through GUM analysis is shown in Figure 1. It can be seen that these two ways of expressing measurement results are in disagreement.

Since these disagreements came from the assumptions and approximation included in GUM Uncertainty Framework, for analysis of this kind of uncertainty the Monte Carlo method described in JCGM 101:2008 is proposed.

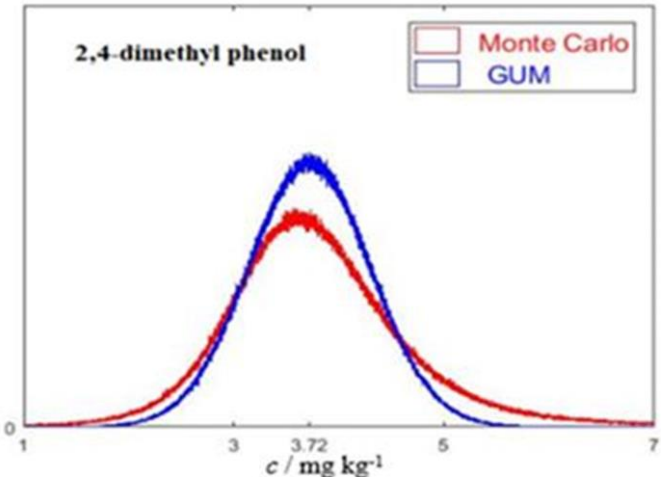

Figure 1. Comparison of PDFs obtained with GUM and Monte Carlo method for the 2,4-dimethylphenol compound

CONCLUSION

Two alternative approaches approved nowadays for estimation of combined measurement uncertainty in case of DMP were evaluated and demonstrated in the presented study. It has been shown that there is disagreement in the estimation of combined uncertainty of measurement using GUM recommendations and Monte-Carlo simulated method.

Monte Carlo method for uncertainty estimation should be encouraged, since the MCS does not require the evaluation of partial derivatives as the GUM method.

Acknowledgement
This study was financially supported by Ministry of Education, Science and Technological Development of the Republic of Serbia, project no. TR 37021.

REFERENCES

[1] ISO/IEC 98: Uncertainty of measurement — Part 3: Guide to the expression of uncertainty in measurement (GUM:1995), 2008.
[2] JCGM 101: Evaluation of measurement data — Supplement 1 to the "Guide to the expression of uncertainty in measurement" — Propagation of distributions using a Monte Carlo method, 2008.
[3] B. Savić, S. Milutinović, T. Brdarić, M. Seović, Ž. Nikolić, M. Tošić, A. Šutulović, Monte Carlo simulation for the evaluation of measurement uncertainty of phenolic compouns in concrete, International Conference Ecological Truth & Environmental Research, 26th June, 2018, 212.
[4] EPA, US Environmental Protection Agency. Ambient water qualitycriteria for 2,4-dimethylphenol. Environmental Protection Agency Office of Water Regulations and Standards Criteria and Standards Division. Washington, DC, 1990.
[5] EPA, US Environmental Protection Agency. Toxics release inventory (TRI), Washington, DC, 2002-2004.
[6] B. Savić, I. Mihajlović, T. Brdarić, N. Krivokapić, M. Seović, Ž. Nikolić, Determination of the phenol compounds in concrete using GC-MS, Proceedings of the 23rd International Symposium on Analytical and Environmental Problems, Szeged, Hungary, 09th September, 2017, 313-316.

COMPETITIVE REMOVAL OF DIVALENT Pb, Zn, Cu AND Sr IONS BY ARAGONITE SEASHELL WASTE

M. Egerić, I. Smičiklas, A. Mraković, M. Jović and M. Šljivić-Ivanović

University of Belgrade, Vinča Institute of Nuclear Sciences, P.O. Box 522, Belgrade, Serbia (egericmarija@vin.bg.ac.rs)

ABSTRACT

Biogenic calcium carbonate obtained from waste seashells can efficiently remove a variety of metal cations from single component solutions. In this study, the concurrent removal of divalent Pb, Zn, Cu and Sr ions from their equimolar mixtures by aragonite based seashell material was investigated in batch conditions. With en exception of Sr^{2+} ions, which removal was completely suppressed, the shells were effective in the removal of Cu^{2+}, Zn^{2+} and Pb^{2+} ions from $5 \cdot 10^{-4}$ mol/L mixture. The increase in the initial metal concentration have provoked dominant Pb^{2+} removal, which was found to be a result of the formation of cerussite coating and reduced surface reactivity towards other cations in the mixture.

INTRODUCTION

The seashells represent a significant source of calcium carbonate, therefore, application of this waste material as a substitution to natural limestone, especially in neutralization [1] and metal immobilization processes [2] is an interesting scientific and practical topic. Depending on the species, carbonate phase in seashells is in the form of aragonite, calcite, or both polymorphs may by present in different proportions [3]. Mineral composition affects the sorption capacity and selectivity, nevertheless, seashells generally exhibit high capacity for a range of metal cations [4–7].

Using single component solutions, the maximum sorption capacity of aragonite seashell waste (SW) was found to decrease in the order Zn^{2+} (4.77 mmol/g) > Pb^{2+} (1.55 mmol/g) ≈ Sr^{2+} (1.53 mmol/g) > Cu^{2+} (0.21 mmol/g) [8]. Removal of cations was followed by precipitation of new crystalline phase (strontianite ($SrCO_3$), hydrozincite ($Zn_5(CO_3)_2(OH)_6$) and cerussite ($PbCO_3$)), except in the case of Cu^{2+} [8].

The aim of this study was to investigate the sorption properties of SW in multicomponent Cu^{2+}, Zn^{2+}, Pb^{2+} and Sr^{2+} solutions, in order to assess the effect of competition and evaluate SW selectivity towards certain cations.

EXPERIMENTAL

The details on SW collection, preparation and characterization are described in the previous study [8]. The effect of initial metal concentration onto concurrent sorption of Pb^{2+}, Zn^{2+}, Cu^{2+}, and Sr^{2+} ions was studied using equimolar mixture solutions with total concentration in the range $5 \cdot 10^{-4}$ - 10^{-2} mol/L, and initial pH 5.0. Working solutions were prepared by dissolving nitrate salts of investigated cations in deionized water. 0.100 g of SW was equilibrated on the orbital laboratory shaker with 20.0 mL of appropriate mixtures, for 24 h at room temperature (21±2°C). After centrifugation the residual metal concentrations were measured using Atomic Absorption Spectrophotometer Perkin Elmer 3100. X-ray diffraction analysis of SW after interaction with 10^{-2} mol/L mixture was performed on Rigaku Smartlab SAXS diffractometer.

RESULTS AND DISCUSSION

Removal efficiency of cations from equimolar four-component solutions by SW is presented in Fig. 1a. In contrast to effective Sr^{2+} sorption from single component solutions [8], its removal was completely suppressed by coexisting ions. At the mixture concentration of $5 \cdot 10^{-4}$ mol/L, SW has removed 93% Pb^{2+}, 97% Cu^{2+} and 93% Zn^{2+}. With the increase of metal concentrations, process efficiency commonly decreased. Considering the entire concentration range, Pb^{2+} removal was reduced to 85%, while Cu^{2+} removal decreased to 15%. The presence of competitive species affected Zn^{2+} removal significantly, i.e. at mixture concentrations $\geq 5 \cdot 10^{-3}$ mol/L Zn^{2+} practically remained in the liquid phase.

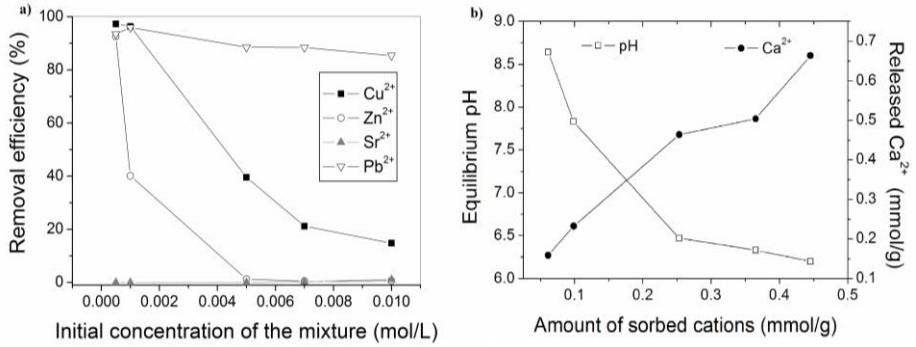

Figure 1. (a) Competitive removal of Zn^{2+}, Pb^{2+}, Cu^{2+} and Sr^{2+} ions by SW from equimolar four-component solutions. (b) Dependencies between total amounts of sorbed cations, equilibrium pH values and amounts of released Ca^{2+} ions.

The addition of SW in mixed metal solutions has caused the increase in pH relative to the initial value (5.0) (Fig. 1b). However, with the increase in the total amount of cations sorbed by SW, the decrease in equilibrium pH from 8.6 to 6.2 was detected, as well as the increase in the amounts of Ca^{2+} ions released from SW surface to the solution phase (Fig. 1b). These results are the indication of the specific cation sorption in cooperation with the ion-exchange and/or dissolution of aragonite and precipitation of metal carbonates.

Competition has provoked reduced metal removal in comparison with single component systems [8], and furthermore, the order of SW selectivity towards investigated cations has been completely reversed. Removal of metals from a mixture can be linked to the kinetic parameters, as the rate constants of Pb^{2+} and Cu^{2+} sorption were found to be much higher in respect to Zn^{2+} and Sr^{2+} [8]. The obtained results may be interpreted as cation competition for limited complexation and ion-exchangeable sites, but also as competition for lattice sites in the scope of precipitation reactions.

XRD analysis of solid phase after interaction of SW with 10^{-2} mol/L mixture solution of metals have confirmed the presence of initial aragonite phase and appearance of the cerussite ($PbCO_3$) diffraction maximums (Fig. 2). Although 15% of Cu^{2+} was also removed under the given conditions, formation of Cu-bearing crystalline phases was not detected, which suggests that Cu^{2+} ions were incorporated in the aragonite and/or specifically sorbed at the SW surface.

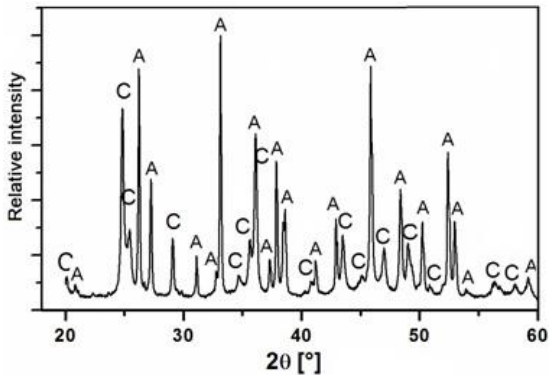

Figure 2. Powder XRD patterns of SW after interaction with 10^{-2} mol/L equimolar mixture of Cu^{2+}, Pb^{2+}, Zn^{2+} and Sr^{2+} ions. The crystalline phases are indicated as: aragonite (A - $CaCO_3$) and cerussite (C - $PbCO_3$).

The solubility product of aragonite is $K_{sp}=6.0\cdot10^{-9}$, while the solubility of metal carbonates increases in the order: $PbCO_3$ ($7.4\cdot10^{-14}$) < $CuCO_3$ ($1.4\cdot10^{-}$

^{10}) < $SrCO_3$ ($5.6\cdot10^{-10}$) < $Zn_5(CO_3)_2(OH)_6$ ($1.9\cdot10^{-9}$). Therefore, the lowest solubility product of $PbCO_3$ may explain the prevalent selectivity of the SW towards Pb^{2+} in the mixture.

CONCLUSION

Given that the waste waters are commonly mixtures of various pollutants with a wide range of concentrations, examining the effects of competition on treatment efficiency is of a particular significance. In comparison to the performance of seashell waste as a cation removal agent in single-component solutions, the capacity and selectivity has been radically changed by metal competition. From the mixtures of divalent Pb, Zn, Cu and Sr, Sr sorption was completely suppressed, while Pb ions were removed most effectively. Formation of $PbCO_3$ precipitate coating reduced the reactivity of the surface towards Zn^{2+} and Cu^{2+} at higher metal concentrations. Optimization of process conditions or multi-stage processes may be necessary to effectively reduce the concentration of all pollutants.

Acknowledgement

This work was supported by the Ministry of Education Science and Technological Development of the Republic of Serbia (Project III43009).

REFERENCES

[1] K. K. Kefeni, T. A. M. Msagati, B. B. Mamba, J. Clean. Prod., 2017, 151, 475–493.
[2] I. Moodley, C. M. Sheridan, U. Kappelmeyer, A. Akcil, Miner. Eng., 2017, in press.
[3] D. Fernández-Calviño, L. Pérez-Armada, L. Cutillas-Barreiro, R. Paradelo-Núñez, A. Núñez-Delgado, M. J. Fernández-Sanjurjo, E. Álvarez-Rodriguez, M. Arias-Estévez, L. Degrad. Dev., 2016, 27, 1276–1285.
[4] Y. Du, F. Lian, L. Zhu, Environ. Pollut., 2011, 7, 1763–1768.
[5] Q. Wu, J. Chen, M. Clark, Y. Yu, Appl. Surf. Sci., 311, 264–272.
[6] S. K. Bozbas, Y. Boz, Process Saf. Environ. Prot., 2016, 103, 144–152.
[7] C. A. Papadimitriou, G. Krey, N. Kallianiotis, S. Argyris, J. Chem. Technol. Biotechnol., 2017, 92, 1943–1947.
[8] M. Egerić, I. Smičiklas, A. Mraković, M. Jović, M. Šljivić-Ivanović, D. Antanasijević, M. Ristić, J. Chem. Technol. Biotechnol., 2018, 93, 1477-1487.

OPTIMIZATION STUDY OF THE AZAMETHIPHOS DEGRADATION USING CHLORINE DIOXIDE

M. V. Pergal[1], D. M. Kuč[2], I. D. Kodranov[2], M. M. Pergal[2], D. M. Stanković[3], B. B. Petković[4] and D. D. Manojlović[2]

[1]Institute of Chemistry, Technology and Metallurgy, University of Belgrade, Njegoševa 12, Belgrade, Serbia. (marijav@chem.bg.ac.rs)
[2]Faculty of Chemistry, University of Belgrade, Studentski trg 12-16, Belgrade, Serbia.
[3]The Vinca Institute of Nuclear Sciences, University of Belgrade, POB 522, Belgrade, Serbia.
[4]Depatment of Chemistry, Faculty of Natural Science and Mathematics, University of Priština, Lole Ribara 29, Kosovska Mitrovica, Serbia.

ABSTRACT

In the present study, the degradation of azamethiphos using chlorine dioxide was studied. The optimization of the azamethiphos degradation in terms of chlorine dioxide dosage, different time of degradation and at different pH values, was performed in system with deionized water. The degradation was monitored using high performance liquid chromatography (HPLC-DAD) analysis. It was found that complete degradation was achieved with optimal concentration of 5 mg/dm^3 chlorine dioxide at concentration of azamethiphos solution of 10 mg/dm^3 under light after 1 h treatment and also at pH 9.00 after 30 min treatment at the same concentration of chlorine dioxide. Gas chromatography coupled with triple quadrupole mass detector (GC-QQQ) was also used to identify degradation products of azamethiphos.

INTRODUCTION

Organophosphorous pesticides have been intensively applied worldwide in agriculture as an alternative to organochlorides. Azamethiphos is a systemic organothiophosphorous pesticide that is widely used to kill mites and insects on contact. Pesticide removal from wastewater is today one of the major environmental problems [1-3]. To minimize the risk of pesticide pollution, it is advisable to develop new technologies that would promote easy degradation pesticides. This is the first study on degradation of azamethiphos with chlorine dioxide. Chlorine dioxide is a strong oxidizing agent, bactericide, fungicide, algaecide, and antiseptic. It is a powerful oxidant which can remove pesticides and is effectively used as a disinfecting/oxidizing agent in the treatment of drinking water. The aim of

this study was to investigate and optimize degradation of azamethiphos with chlorine dioxide in deionized water and identify degradation products of pesticide using GC-QQQ analysis.

EXPERIMENTAL

Azamethiphos was supplied from Sigma-Aldrich. The pure stock solution of chlorine dioxide (3 g/dm^3) was prepared by mixing sodium chlorite (Superior Water Disinfection Power, TwinOxide®) and sodium bisulphate (Superior Water Disinfection Power, TwinOxide®), in 1 dm^3 of distilled water. The exact concentration of chlorine dioxide in the stock solution was quantified using 4500-ClO_2 DPD method according to the Standard Method. Sodium-thiosulfate ($Na_2S_2O_3$, p.a., Merck) was used as received.

Degradation of azamethiphos solution by chlorine dioxide was performed in a 200 mL closed flasks on rotary shaker. Different dosage of ClO_2 stock solution (5 mg/dm^3 and 10 mg/dm^3) was added in pesticide solution (10 mg/dm^3) to initiate the reaction at room temperature. In different time intervals (30 min, 1 h, 2 h, 3 h, 6 h and 24 h) 10 mL of reaction mixture was taken and chlorine dioxide residues were quenched with $Na_2S_2O_3$ prior to HPLC analysis, which was used to evaluate degradation efficiency. Light conditions were provided using Osram Ultra-Vitalux (300 W) which was used for sunlight simulation and which has radiated power from 315 – 400 nm (UVA) of 13.6 W and from 280 – 350 nm (UVB) of 3.0 W, and dark conditions were provided by placing reaction vessels into enclosed space without any light during reaction period.

Degradation efficiency of pesticide was monitored using high-performance liquid chromatograph (HPLC; Thermo Ultimate 3000 RS) with photodiode array detection (DAD) on Hypersil Gold aQ C18 analytical column (150 mm x 3 mm, 3 µm) at 40 °C. Mobile phase consisted of 0.1% formic acid water solution (Fluka analytical HPLC grade) as component A and acetonitrile (> 99.9%, Sigma-Aldrich HPLC grade) as component B. The chromatographic elution was conducted at flow rate of 0.6 mL/min in gradient mode: 0.0-0.5 min 5% B, 0.5-6.0 min from 5% to 45% B, 6.0-8.0 min from 45% to 95 % B, 8.0-8.1 min from 95% to 5% B, then 5% B for 6 min. Injection volume was 25 µL. Detector was set at 195 nm.

Major degradation products of azamethiphos were analyzed by Agilent Technologies gas chromatograph with triple quadrupole mass detector (GC-QQQ; 7890B/7010). Samples for GC-QQQ analysis were prepared by extraction with methylene chloride (>99.5 %; LGC) and concentrating the organic extract to 1 mL.

RESULTS AND DISCUSSION

This paper studies the reactivity of azamethiphos with chlorine dioxide under conditions that have relevance in the water treatment. In this study, optimization of chlorine dioxide dosage (5 and 10 mg/dm^3), different time of degradation (30 min, 1 h, 2 h, 3 h, 6 h and 24 h) and at different pH values (3.00, 7.00 and 9.00) were performed in system with deionized water. Chlorine dioxide was added in deionized water solution of pesticide. Concentration of pesticide was 10 mg/dm^3.

The percentage of degradation was monitored by HPLC analysis on the basis of the pesticide peak area reduction after degradation compared to the peak area of the pesticides prior to degradation. The HPLC results showed that chlorine dioxide was effectively used for degradation of azamethiphos. The high degradation efficiency (88-100%) was achieved under different experimental conditions.

The results of HPLC analysis for azamethiphos showed that at a concentration of 5 mg/dm^3 ClO_2, high efficiency of degradation was achieved in the light and in the dark (in the light, after 1 h, 100%, after 24 h, 98.90% and in the dark, after 24 h, 97.77%;) (Fig. 1 a). Moreover, at concentration of 10 mg/dm^3 ClO_2 somewhat lower, but good efficiency of degradation also was achieved in the light (99.56% after 3 h). Good degradation efficiency was achieved in the dark, but slightly lower than for that in the light (after 24 h, 97.44% at a concentration of 10 mg/dm^3 ClO_2) (Fig. 1 a). The results showed that the best degradation efficiency of 100% was achieved after 1 h under light condition, at concentration of 5 mg/dm^3 ClO_2, and after 30 min at pH 9.00 at the same concentration of ClO_2. On the other pH values (Fig. 1 b), at pH 3.00 and 7.00 and at concentration of 5 mg/dm^3, satisfactory degradation efficiency was observed (at pH 3.00, after 24 h, 94.92%; at pH 7.00, after 24 h, 94.63%) (Fig. 1 b), but at concentration of 10 mg/dm^3 ClO_2, at pH 3.00 and 7.00 similar degradation efficiency was achieved (at pH 3.00, after 24 h, 93.57%; at pH 7.00, after 24 h, 95.76%) (Fig. 1 b).

The degradation products of azamethiphos obtained under optimal conditions (i.e. 10 mg/dm^3 azamethiphos with 5 mg/dm^3 ClO_2 under light and after 1 h) were analyzed by GC-QQQ. They were identified according to the corresponding spectral characteristics: mass spectra, accurate mass and characteristic fragmentation. Chromatogram has showed four degradation products of azamethiphos: O,O,S-trimethyl phosphorothioate (m/z 155; retention time 5.33 min), 6-chlorooxazolo[4,5-b]pyridin-2(3H)-one (m/z 169; retention time 10.237 min), S-(aminomethyl) O,O-dimethyl phosphorothioate (m/z 169; retention time 11.325 min), 6-chloro-3-(mercaptomethyl)oxazolo[4,5-b]pyridin-2(3H)-one (m/z 215; retention time 13.033 min).

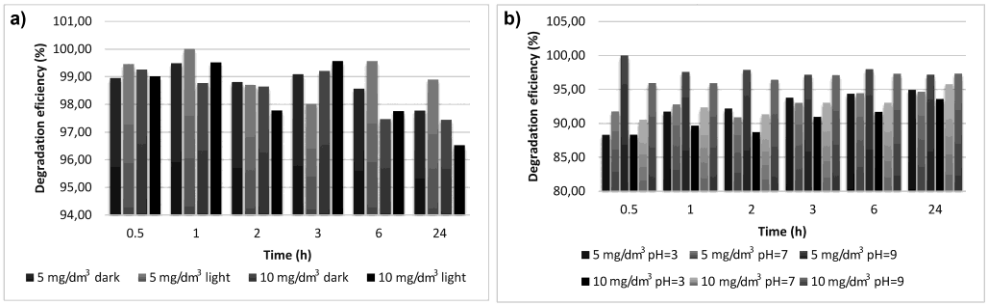

Figure 1. Degradation efficiency of azamethiphos: at concentrations 5 and 10 mg/dm^3 ClO_2 under (a) light and dark conditions and (b) at different pH values

CONCLUSION

This study reports the results for the degradation of organophosphorous pesticide, such as azamethiphos by chlorine dioxide in deionized water under light and dark conditions with different dosage of chlorine dioxide, at different time of degradation and at different pH values. The most efficient degradation (100%) of azamethiphos was obtained in the light at a concentration of 5 mg/dm^3 ClO_2, and also at concentration of 5 mg/dm^3 ClO_2, pH 9.00. Under other conditions, degradation efficiency was also high and was in the range from 88 to 99%. After treatment with chlorine dioxide four degradation products were identified. It was concluded that chlorine dioxide was effectively used for degradation of azamethiphos and these results made the application of chlorine dioxide for degrading organic pollutants from aqueous solution more practical.

Acknowledgement

Financial support for this study was granted by the Ministry of Science and Technological Development of the Republic of Serbia. Authors would like to thank TwinOxide-RS d.o.o. for providing "TWINS" preparation.

REFERENCES

[1] F.-X. Tian, B. Xu, T.-Y. Zhang, N.-Y. Gao, Chem. Eng. J., 2014, **258**, 210–217.

[2] D. N. Priya, J. M. Modak, P. Trebše, R. Žabar, A. M. Raichur, J. Hazard. Mater., 2011, **195**, 214-222.

[3] F. Tian, Z. Qiang, C. Liu, T. Zhang, B. Dong, Chemosphere 2010, **79**, 646–651.

SAFECAST BGEIGIE NANO FOR ENVIRONMENTAL RADIATION MONITORING: CASE STUDY FOR BELGRADE, REPUBLIC OF SERBIA

M. Ćujić, J. Petrović, Lj. Janković Mandić, M. Đolić and S. Dragović

University of Belgrade, Vinča Institute of Nuclear Sciences,Belgrade, Serbia (cujicm@vinca.rs)

ABSTRACT

The Safecast, an international volunteer-based organization devoted to monitoring of environmental radiation, was start up a day after the accident in Fukushima nuclear power plant. The bGeigie Nano is a solid-state, fully digital device, and the key components are the iRover high-voltage supply and the LND 7317 pancake Geiger Muller tube. In bGeigie Nano device, data were recorded and reported as raw counts per minute (cpm) data, and dose rate (μSv h^{-1}) conversion was done at the visualization stage. Radiation measurements using bGeigie Nano, hand-held sensor, was carried out in Belgrade, the capital of Republic of Serbia city and radiation dose rates assessment was evaluated and geographically mapped. The benefits of the Safecast bGeigie nano device have been recognized by international organizations and experts worldwide. Open data creates new opportunities for innovation increases awareness and coordination, and strengthens inclusion participation and human well-being. The case of Safecast gave a new dimension to the radiation protection by pioneering the citizen participatory.

INTRODUCTION

The European Parliament pointed out the Environmental Citizenship as a key factor in European Union's Environment Action Programme. Main aim of the radiation protection is to protect the environment, equally human and non-human biota, thus the concept of societal innovations into the framework of the radiation protection was expected. In the light of the nuclear accidents, certainly the biggest ones occurred in the Chernobyl (1986) and the Fukushima (2011) nuclear power plants. The population usually waits for several years for the official results of the consequences of the hazards to be published. Two years after Fukushima accident World Health Organization published report based on preliminary dose estimation to the health risk assessment from nuclear accident [1], while International Atomic Energy Agency published summary report four years after the accident [2]. The hazards associated with the accidents have never been transparent completely.

Few weeks after the Fukushima accident, citizens had lack of information regarding the actual radiation levels, and publicly available data were incomplete. Initially, the aim of the Safecast organization was to aggregate publicly available radiation data for Japan and makes it available in the form of online maps. From the start open-source and open-data methodologies were the key components of the Safecast project [3].

Citizen environmental monitoring and engagement during peaceful and hazard situation is very useful and important for progress of the society. The data that citizens record and produce are usually shared via internet platforms. The challenge is it to make that social data become trustworthy and meaningful.

In this work radiation dose rates for Belgrade, Republic of Serbia, recorded using Safecast bGeigie nano device are presented.

EXPERIMENTAL

The Safecast bGeigie Nano is a Geiger counter developed as a cost effective device for ionized radiation monitoring [4]. The bGeigie Nano is a solid-state, fully digital device, and the key components are the iRover high-voltage supply and the LND 7317 pancake Geiger Muller tube. In bGeigie nano device, data are recorded every 5 s and reported as raw counts per minute (cpm) data, and dose rate ($\mu Sv\ h^{-1}$) conversion was done at the visualization stage. In order to record the location bGeigie device poses a receiver to connect to the Global Positioning System (GPS) and an SD card memory to log observations. In general the data are measured via on-ground methods, e.g. device attached to moving vehicles, carried by foot, or placed as a static sensor.

RESULTS AND DISCUSSION

Until now, applying the Safecast bGeigie Nano device, about 95 million radiation measurements worldwide were performed, predominantly in Japan [5]. In order to validate Safecast measurements Colletti et al. compared Safecast data with authoritative data collected by the U. S. Department of Energy (DOE) and the U. S. National Nuclear Security Administration (NNSA). These two data sets were highly correlated, though the DOE/NNSA observations were generally higher [6].

In this work radiation dose rates ($\mu Sv\ h^{-1}$) for Belgrade, Republic of Serbia, recorded via Safecast bGeigie nano device are geographically visualized (Figure 1.). It could be noticed that average radiation dose rate was 0.12 $\mu Sv\ h^{-1}$. Data visualization could be difficult task, and for radiation measurements in the light of the citizen science it needs to be done in a meaningful way that

is understandable to the population through the use of comparative radiation values in the legend.

For Belgrade area the estimated annual effective doses were in the range of 0.41-17.5 nSv, with a mean value of 4.67 nSv [7]. Detailed research works devoted to experimentally radiation measurements for Belgrade city could be found elsewhere [7-9].

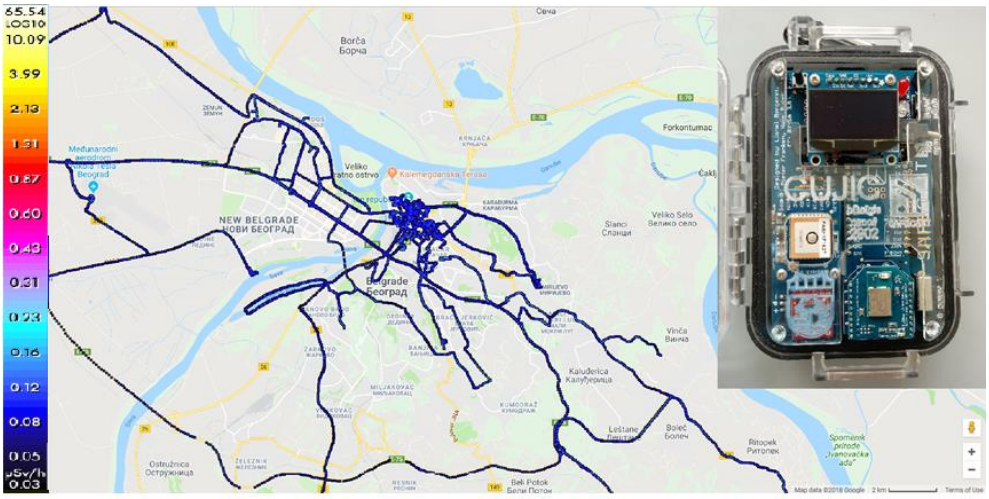

Figure 1. Safecast measurements, screenshot from the Safecast web site of log adjusted radiation observations in μSv h^{-1} for Belgrade, Republic of Serbia [5] (in the right corner the front of the bGeigie Nano is shown)

CONCLUSION

Radiation dose rates for Belgrade area recorded by Safecast bGeigie Nano device were found to be in the radiation safe level. Users of these handheld sensors collect radiation measurements that are later freely shared with the public via internet platform. Environmental citizen science is in growing movement, but trustworthy and meaningful of collect data is always questionable, because of the varying technical ability of devices end-users.

Acknowledgement

Authors acknowledge the Ministry of Education, Science and Technological Development of the Republic of Serbia (Project no. III43009). M. Ćujić gratefully acknowledges the Safecast, International Atomic Energy Agency and International Centre for Theoretical Physics (smr2858) and CA16229.

REFERENCES

[1] WHO (World Health Organization) Health risk assessment from the nuclear accident after the 2011 Great East Japan earthquake and tsunami, based on a preliminary dose estimation, 2013.
[2] IAEA (International Atomic Energy Agency) Fukushima Daiichi Accident, Summary Report by the Director General, Board of Governors, Vienna, 2015.
[3] A. Brown1, P. Franken, S. Bonner, N. Dolezal, J. Moross, J. Radiol. Prot., 2016, **36** S82.
[4] https://blog.safecast.org/the-safecast-report/
[5] https://safecast.org/tilemap/
[6] M. Coletti, C. Hultquist, W.G. Kennedy, G. Cervone, J. Environ. Radioact. 2017, **171**, 9-20.
[7] V. Spasić-Jokić, Lj. Županski, Lj. Janković Mandić, V. Gordanić, Environ. Sci. Pollut. Res. 2011, **18**, 708-715.
[8] M. Ćujić, S. Dragović, Đorđević, R. Dragović, B Gajić, Š Miljanić, Environ. Sci. Pollut. Res., 2015, **22**, 10317-10330.
[9] J. Petrović, M. Ćujić, M. Đorđević, R. Dragović, B. Gajić, Š. Miljanić, S. Dragović, Environ. Sci. Proc. Impa., 2013, **15(6)**, 1279-1289.

REUSABILITY OF ALGINATE BEADS WITH IMMOBILIZED AMINATED HRP FOR PHENOL REMOVAL FROM WATER

D. Spasojević [1], M. Prokopijević [1], O. Prodanović [1], K. Radotić [1] and R. Prodanović [2]

[1] *University of Belgrade, Institute for multidisciplinary research, Kneza Višeslava 1, 11000 Belgrade, Serbia. (dragica@imsi.rs)*
[2]*University of Belgrade, Faculty of Chemistry, Studenstski trg 12-16, 11000 Belgrade, Serbia.*

ABSTRACT

Phenols are hazardous substances that enter into the environment as by-products of various industries. The immobilizate of aminated horseradish peroxidase (HRP) onto oxidized alginate beads was tested for reusability in the removal of aqueous phenol. In the present study, the possibility of continuous phenol removal using immobilized aminated HRP on alginate beads was shown to be promising. After five repeated cycles, the efficiency of HRP immobilizate for phenol removal has decreased by 46%.

INTRODUCTION

Phenols are toxic and mutagenic organic compounds that are found in wastewaters from petroleum, plastics and chemical industries. In European Union (EU) and the United States (USA) phenolic compounds are listed as pollutants of priority concern because of their severe impacts on both humans and animals [1]. Enzymatic removal of phenols from water using peroxidase and hydrogen peroxide has been extensively investigated since the 1980s [2]. Horseradish peroxidase (HRP, E.C.1.11.1.7) is the most known peroxidase from plants that belongs to the ferroprotoporphyrin group of peroxidases [3]. By enzymatic polymerization, phenolic compounds are converted into non-soluble, high molecular weight products that can be easily removed from the aqueous phase [4].

The use of enzymes is limited due to their high cost, instability and inhibition by end products. These limitations can be overcome by enzyme immobilization on solid supports. The enzyme can be immobilized through weak interactions with support by physical methods, but for stable attachment the formation of covalent bonds can be achieved by chemical methods of immobilization [5]. Among different types of support materials, alginate is one of the most widely used. It is abundant natural and nontoxic algal

polymer, but due to its porous structure enzyme can easily diffuse from alginate matrix, so different types of chemical modifications of alginate and/or enzyme and covalent immobilization techniques have been used.

In our previous work, we have developed a novel method for HRP immobilization within alginate beads by chemically modifying enzyme and introducing new functional groups into alginate through periodate oxidation [6]. In this study, we tested the obtained immobilizate for reusability and removal of phenol from a synthetic wastewater.

EXPERIMENTAL

Phenol assay

The concentration of phenol was determined by colorimetric assay with 2.08 mM 4-aminoantipyrine (4-AAP) and 8.34 mM potassium ferricyanide ($K_3Fe(CN)_6$) in bicarbonate buffer pH 8,0. After 10 minutes phenol fully reacted with 4-aminoantipyrine to form a stable reddish-brown colored antipyrine dye with maximum absorbance at 510 nm. Phenol concentrations were calculated using a calibration curve, with a series of aqueous standards of phenol.

Experimental procedure

The immobilization method was carried out according to the procedure described by Spasojević et al. [6]. 200 mg oxidized alginate beads with aminated HRP (specific activity 0.43 U/g) were added in 3 mL 2mM phenol solution. The reaction was started with addition of H_2O_2 (2.4 mM) and then placed on magnetic stirrer. At predefined time intervals, aliquots were taken and concentration of remaining phenol was determined using 4-AAP method. The removal efficiencies of phenol were calculated using the initial and residual concentrations. Each cycle lasted 2 hours, after which the beads were filtered and washed. This procedure was repeated five times.

RESULTS AND DISCUSSION

The immobilized aminated HRP on oxidized alginate beads showed the ability to remove phenol from aqueous solution. The reusability of the immobilized system was investigated as one of the main advantages for industrial application. The phenol content was calculated from the standard curve, shown in Figure 1.

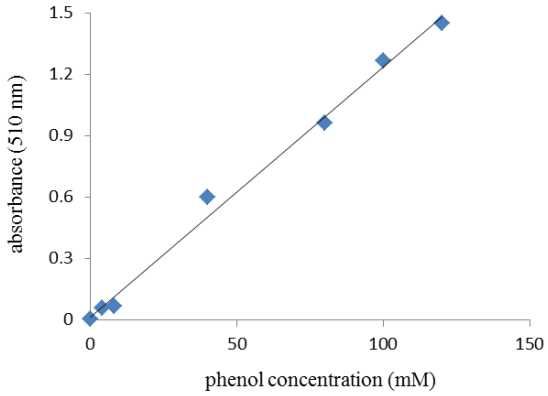

Figure 1. Calibration curve for phenol.

The beads with HRP were tested for five cycles in the batch reactor at 25 °C with constant stirring. After the 5th cycle, the immobilizate retained 54% of its original activity (Figure 2.) This result was better than some previously reported studies for immobilized HRP [7,8]. The loss of enzyme activity is probably a result of the accumulation of polymerized phenol products onto alginate beads, that become dark brown upon the utilization. A possible solution to this problem would be washing the beads with organic solvents.

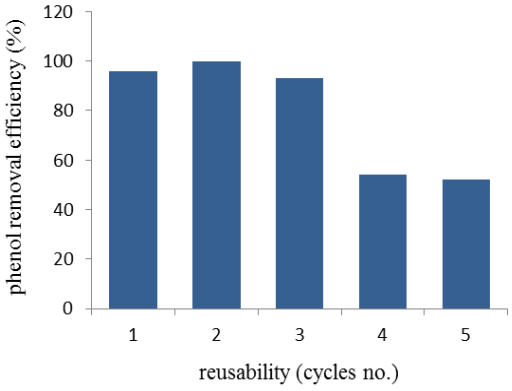

Figure 2. Reusability of HRP-alginate beads.

CONCLUSION

The results obtained in the present work showed that aminated HRP within oxidized alginate has good potential for phenol removal from aqueous solutions. The reusability experiment revealed that prepared immobilizate did not lose its activity in the first 3 cycles and that after 5 cycles 54 % of

activity is retained. Therefore, immobilized aminated HRP is a suitable candidate for industrial wastewater treatment and pollution control.

Acknowledgment
This work was supported by the Ministry of Education, Science and Technological Development of Serbia (Grants no.173017).

REFERENCES

[1] W. W. Anku, M. A. Mamo, P. P. Govender in: Phenolic Compounds, M. Soto-Hernández (Ed.), InTechOpen, 2017.
[2] S. Hejri, A. Saboora, JUST, 2009, 35 (1), 13-19.
[3] O. Prodanović, M. Prokopijević, D. Spasojević, Ž. Stojanović, K. Radotić, Z. Knežević-Jugović, R. Prodanović, Appl Biochem Biotechnol, 2012, 168, 1288–1301.
[4] I.Alemzadeha, S. Nejatib, M. Vossoughi, Engineering Letters, 2009, 17 (4), 297-300.
[5] A. A. Homaei, R. Sariri, F. Vianello, R. Stevanato, J Chem Biol, 2013, 6, 185–205.
[6] D. Spasojević, M. Prokopijević, O. Prodanović, M. G. Pirtea, K. Radotić, R. Prodanović, Hem. Ind., 2014, 68 (1), 117–122.
[7] F. Zhang et al., J. Phys. Chem. C, 2010, 114, 8469–8473.
[8] Y.-M. Lu et al., Clean – Soil, Air, Water, 2017, 45 (2), 1600077.

REMOVAL OF DIURON FROM WASTE WATERS BY HYDRODYNAMIC CAVITATION

B. Adnađević[1], J. Jovanović[1], D. Ranković[1], S. Salvestrini[2] and S. Petković[3]

[1] *Faculty of Physical Chemistry, University of Belgrade, Studentski trg 12-16, 11001 Belgrade, Serbia. (bora@ffh.bg.ac.rs)*
[2]*Università degli Studi della Campania "Luigi Vanvitelli", Department of Environmental, Biological and Pharmaceutical Science and Technologies, Caserta, Italy*
[3]*Mining Institute Ltd., Batajnički put 2, 11080 Belgrade, Serbia*

ABSTRACT
The possibility to remove diuron from waste waters without using chemicals by a novel hydrodynamic cavitation method was investigated. Hydrodynamic cavitation device for waste waters purification was constructed and its operating parameters were determined. The effects of inlet pressure, time, temperature and pH of solution on the degree of diuron reduction were determined. The optimal parameters of novel hydrodynamic cavitation method for diuron removal from water were determined. Model of mechanism for diuron removal by hydrocavitation method was suggested.

INTRODUCTION
Herbicides are extensively used throughout the world to control weeds in order to increase the agricultural production. Conventionally, for more effective use, herbicides are applied in excess in the fields causing serious problems for the environment and human health. During their application they may affect non-target organisms and can lead to loss of biodiversity.

Depending on their chemical properties, herbicides can be easily transformed through biotic/abiotic degradation pathways or persist in soil in an adsorbate state and leach to groundwater and surface water.

One of the most widely used herbicides is diuron, which is a systematic phenylurea herbicide [1]. Diuron is easily taken up from soil solution by the root system of plants and rapidly translocated into stems and leaves by the transpiration system, moving primary via the xylem.

Among the most representative methods aimed to remove diuron from water are oxidation, nanofiltration, photodegradation coupled with biodegradation and adsorption [2]. Hydrodynamic cavitation is a new, low cost and energy efficient method for waste water treatment and has been

proven to be able to generate conditions for organic pollutant removal. The ability to remove diuron from water solutions by hydrodynamic cavitation without use of any additional chemicals was investigated in this work.

EXPERIMENTAL

Diuron was supplied by Sigma Aldrich, Germany. Diuron solutions in water were prepared in range from 0-10 mg/L. Diuron concentration in water was performed by HPLC method.

Hydrodynamic cavitator, Ventury type was used for hydrodynamic treatment. The construction and principle of working is described in details [3]. The effects of inlet pressure, time, temperature and pH on the degree of diuron reduction from water solution were determined.

RESULTS AND DISCUSSION

Fig 1. shows the effects of inlet pressure on the diuron concentration after cavitation treatment.

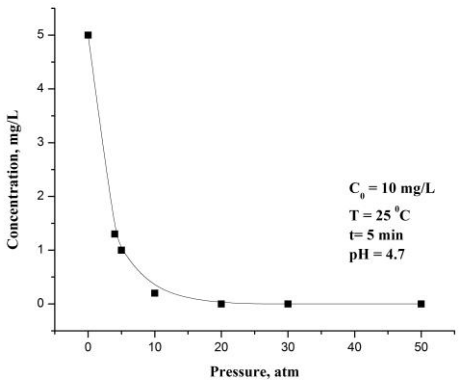

Figure 1. The effects of inlet pressure on the diuron concentration after cavitation treatment

Diuron concentration after cavitation treatment decreases abruptly, almost linearly, from 10 mg/L to 1 mg/L, when the inlet pressure increases from 1 atm to 5 atm. Further increase in inlet pressure leads to entire disappearance of diuron from water solution.

The decrease in diuron concentration with the increase in inlet pressure is a consequence of the increased cavitational activity and collapse of pressure of the cavity, which all leads to the OH radicals concentration increase in the reaction system.

Table 1. presents the effects of cavitation time and temperature on the diuron concentration after cavitation treatment.

Table 1. The effects of cavitation time and temperature on the diuron concentration after cavitation treatment. (Co- 10, p1-20 atm, pH 4.7)

t (min)	Concentration (mg/L)		
	T=15°C	T=15°C	T=15°C
1	1.6	1.3	1.0
2	1	0.6	0.08
3	0.5	0.25	0.01
5	0.35	0.10	0.01

At all of the investigated temperatures, the increase in duration of cavitation leads to the rapid decrease in diuron concentration.
The effect of pH solution on the residual diuron concentration is shown in Fig 2.

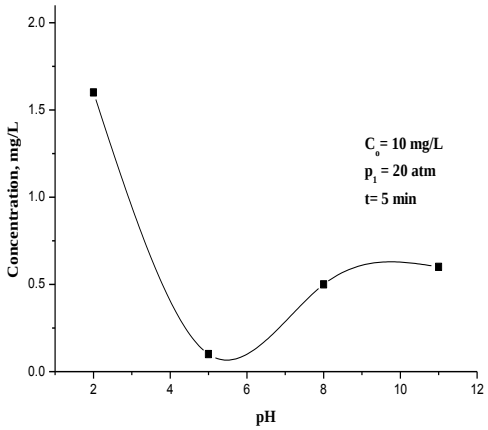

Figure 2. The effect of pH solution on the residual diuron concentration

For the pH >2 and <5, the increase in pH leads to the decrease in diuron concentration from 1.6 mg/L to 0.1 mg/L. Further increase in pH does not lead to the significant decrease in diuron concentration.

CONCLUSION

Novel hydrodynamic cavitation method is highly efficiency method for diuron removal from water without using any chemicals. For the inlet power values higher than 5 atm, diuron concentration is decreased to lower than 1mg/L. The increase in temperature and time leads to the decrease in diuron concentration in solution. The optimal pH value for diuron removal is 4.7 mg/L.

Acknowledgement

The presented investigations were supported by The Ministry of Education, Science and Technological Development of the Republic of Serbia, under Project 172015.

REFERENCES

[1] R. Dragone, R. Cheng, G. Grasso, C. Frazzoli, Diuron in water: Functional toxicity and intracellular detoxification patterns of active concentrations assayed in tandem by a yeast-based probe, Int. J. Environ. Res. Public Health 2015, **12,** 3731-3740.

[2] O.S. Bello, I.A. Bello, K.A. Adegoke, Adsorption of dyes using different types of sand: A review, S. Afr. J. Chem. 2013, **66**, 117-129.

[3] J.Jovanović, S.Petković,M.Gigov, B.Adnađević, The effects of H_2O_2 on cavitation purification of waste, waters from phenol, Mining and Geology today, Belgrade, 2017, doi 10.25075/SI.2017.30

USING THE WASTE SLUDGE FROM Ni/Cr PLATING PROCESS AS A RAW MATERIAL FOR INORGANIC PIGMENTS OBTAINING

A. Devečerski, K. Kumrić, J. Ilić, R. Vujasin, M. Omerašević, L. Slavković-Beškoski and Lj. Matović

Vinča Institute of Nuclear Sciences, University of Belgrade, 11001 Belgrade, Serbia. (kkumric@vinca.rs)

ABSTRACT

Hazardous industrial waste is the most common source of environmental pollution. Waters originating from unregulated landfills and places of inadequate disposal of this type of waste can pollute the sources of water beverages and affect the health of the population. As a starting material for the synthesis of inorganic pigments, galvanic waste sludge from "PPT - TMO" AD Trstenik company was used. Color of the obtained inorganic pigments vary from green through brown to black, which can be attributed to the existence of Cr and Fe chromophore ions, as dominant components in the composition of sludge. However, only black $Cr_{1.3}Fe_{0.7}O_3$ pigment possesses promising properties required for use as an inorganic pigment.

INTRODUCTION

Inorganic pigments are widely applied due to their many advantages: high chemical and temperature stability, non-toxicity, they are not degraded under the influence of UV radiation, and as such, can be used for external uses: facades, roofs, wall and floor tiles [1-4]. The sludge studied in this paper comes from an electroplating plant (nickel, chromium, zinc, etc.) and belongs to toxic industrial wastes. It has been used as a raw material to obtain a non-toxic and potentially commercial product i.e. an inorganic pigment. The dark brown and black colour of the pigments can be attributed mainly to the existence of Cr and Fe as chromophore ions. Despite expectations that a spinel ($FeCr_2O_4$) black pigment will be obtained, by analyzing the diffractograms of the product, it was found that a mixed Fe/Cr oxide ($Cr_{1.3}Fe_{0.7}O_3$) was obtained instead.

EXPERIMENTAL

Characterization of the Cr/Ni plating sludge and products obtained from it, included determination of chemical composition (XRF), main crystalline phases (XRD), color of the samples (UV/VIS, NIR) expressed in L*a*b*

values and toxicity level (leaching test, performed according to DIN-38414-S4, to determine the metals mobility under the neutral conditions [5]).

RESULTS AND DISCUSSION

The sludge in liquid form was taken from a basin at three different depths: Sample 1 - taken from the bottom of the basin; Sample 2 - taken from the middle of the basin; Sample 3 - taken from the surface of the basin. Samples were dried at 110^{o}C and the mass of the dry residue was measured. It was found that water content in sludges is about 91 – 92.5 wt%. Chemical composition of the samples is shown in Table 1.

Table 1. Chemical composition of dried sludges

Element (%)	Sample 1	Sample 2	Sample 3
Pb	1.75	1.73	1.45
Zn	6.51	7.39	3.44
Cu	2.62	1.14	1.23
Ni	3.58	3.15	2.66
Fe	11.79	15.15	17.77
Cr	62.93	59.16	63.36
Si	1.36	1.23	0
P	9.20	10.78	9.81

Considering the chemical composition of the sludge and that black pigments are commercially the most attractive ones, synthesis of spinel ($FeCr_2O_4$) black pigment was tried, by adding the appropriate amount of Fe into the dried sludges and calcinating them at 1000^{o}C. However, by analyzing the diffractograms (Fig.1) of the products, it was found that a black mixed Fe/Cr oxide ($Cr_{1.3}Fe_{0.7}O_3$) is obtained instead.

Colour of the pigments was estimated by UV/VIS spectroscopy and Table 2 shows the colorimetric coordinates of some pigments. As one can see, values for L*a*b* coordinates are in accordance with the literature, or even better. (L = 100 = white colour; L = 0 = black colour).

Level of toxicity, i. e. the leaching test, was conducted according to DIN-38414-S4 standard, which is most commonly found in the literature regarding the synthesis of pigments from waste materials. The DIN-38414-S4 test is used for determination of the mobility of metals in neutral conditions, using distilled water for leaching (24 h, weight ratio H_2O/pigment = 10/1). The metal concentrations in eluates were determined by the AAS method (Atomic Absorption Spectroscopy) and the results are

shown in Table 3. It can be seen that thermal treatment of sludge at 1000ºC is sufficient to stabilize all the metals, except Cr, against the water leaching. However, addition of Fe is crucial for the stabilization of Cr, which is considered as highly toxic, when found in water/soil. According to the classification of materials (EU Council Decision 2003/33/EC), black pigments can be considered as "inert", which is quite opposite to the leaching stability of the dried sludge.

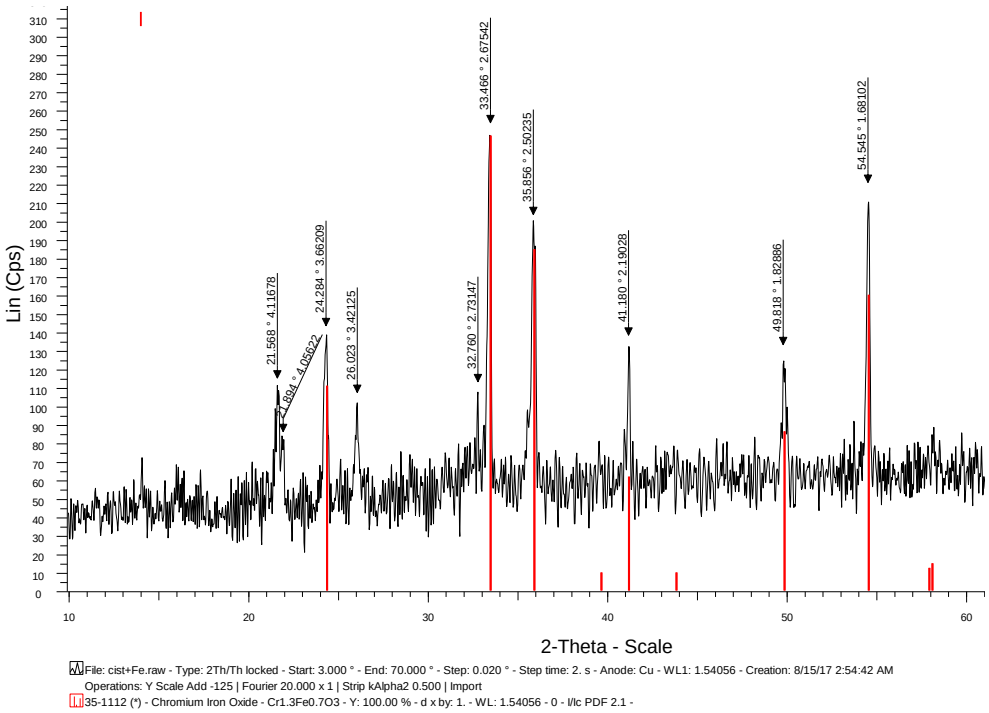

Figure 1. XRD pattern of the black $Cr_{1.3}Fe_{0.7}O_3$ pigment obtained

Table 2. The colourimetric coordinates of some pigments

	L*	**a***	**b***
Brown pigment, obtained from sample 3 at 1000ºC, *without* the addition of Fe	35.4	3.5	14.0
Black pigment, obtained from sample 3 at 1000ºC, *with* the addition of Fe	23.8	1.6	0
Commercial black pigment	33.0	1	0
Commercial black pigment	28.8	-1.2	0.7

Table 3. Metal concentrations (mg/dm^3) in eluates obtained after the leaching test

	Cr	**Ni**	**Pb**	**Zn**	**Fe**	**Cu**
Brown pigment, obtained from sample 3 at 1000^{o}C, *without* the addition of Fe	7.3	0.02	0.02	0.11	0.28	<0.01
Black pigment, obtained from sample 3 at 1000^{o}C, *with* the addition of Fe	0.01	0.02	0.02	0.05	0.31	<0.01
Sludge dried at 110 ^{o}C	10.5	75	0.1	194	69	9.1
Allowed concentrations*	***0.05 - 1***	***0.04 - 1***	***0.05 - 1***	***0.4 - 5***	*/*	***0.2 - 5***

*** -** EU Council Decision 2003/33/EC; first value refers to the ***"Inert"*** and second to the ***"Non-hazardous"*** classification of materials

CONCLUSIONS

Products obtained from Cr/Ni waste, are of much less volume and weight, comparing to the starting sludge. They are also environmentally acceptable since they are stable against the water leaching. Addition of Fe into the waste sludge, followed by a thermal treatment, is essential both to obtain the black coloured pigments and to stabilize them against the water leaching.

Acknowledgments

This research was supported by the Serbian Ministry of Education, Science and Technological Development under Grants III 45012 and III 45006.

REFERENCES

[1] W. Hajjaji, M. P. Seabra, J. A. Labrincha, J. Hazard. Mater., 2011, **185**, 619 - 625.
[2] G. Costa, M. J. Ribeiro, T. Trindade, J. A. Labrincha, Bol. Soc. Esp. Ceram. V., 2007, **46**, 7 - 13.
[3] G. Costa, V. P. Della, M. J. Ribeiro, A. P. N. Oliveira, G. Monros, J. A. Labrincha, Dyes and Pigments, 2008, **77**, 137 - 144.
[4] J.M. Magalhaes, J. E. Silva, F. P. Castro, J. A. Labrincha, J. Envir. Manag., 2005, **75**, 157 - 166.
[5] A.P. Galvin, J. Ayuso, J. R. Jimenez, F. Agrela, Waste Management, 2012, **32**, 88 - 95.

PRECONCENTRATION OF TARGETED PESTICIDES FROM AQUEOUS SOLUTIONS BY THE SOLID PHASE EXTRACTION ON ACTIVATED CARBON DERIVED FROM COCONUT SHELL

K. Kumrić, R. Vujasin, M. Egerić, M. Omerašević, A. Devečerski and Lj. Matović

Vinča Institute of Nuclear Sciences, University of Belgrade, 11001 Belgrade, Serbia. (kkumric@vinca.rs)

ABSTRACT

A solid phase extraction (SPE) method for preconcentration of five varying polarity pesticides on activated carbon (AC) derived from coconut shell prior to their determination by high performance liquid chromatography with diode array detector (HPLC-DAD) was investigated. The adsorption was achieved quantitatively on AC column at the pH range 2.0 – 8.0, then the retained pesticides content was eluted with dichloromethane. The effects of the solution pH, eluent type, eluent volume and flow rate were investigated for optimization of the presented procedure. The detection limit was found to be 29.3 - 121.4 ng/dm^3, depending on the pesticide. The obtained results indicated that the proposed method could be used for the simultaneous determination of the varying polarity pesticides in environmental water samples at trace levels.

INTRODUCTION

Pesticides released from agricultural practices are an important class of pollutants due to their widespread use, toxicity, persistence, polar nature and water solubility. Due to washing and leaching processes, these substances pass to surface and ground waters together with their transport by the wind and their propagation through biological chains, and present a potential risk on human health and environmental safety [1]. Monitoring of the pesticides comprises a sample preparation step for separation and enrichment, and high performance techniques for quantifications [2]. SPE has been proved to be an effective sample pretreatment method due to high enrichment efficiency, low consumption of organic solvents, simplicity and easy operation. The choice of appropriate adsorbent is a crucial factor to obtain high recoveries and high enrichment factors in SPE procedure.

Over recent years there has been considerable interest in using low-cost waste materials as adsorbents of pesticides and many other contaminants

from environmental samples. Adsorption of contaminants by activated carbons has been identified as one of the most effective and feasible technologies owing to activated carbons' microporous nature, favorable pore size distribution, high surface reactivity, large adsorption capacity, versatility and easy availability. Activated carbon may be prepared using a variety of raw materials. However, there has been an increasing interest in using lignocellulosic by-products including agricultural residues and coconut shells as raw materials [3 - 5].

The aim of this study was to investigate the possibility of using activated carbon derived from coconut shell as the SPE packing material for the preconcentration of the selected pesticides (imidacloprid (Imi), acetamiprid (Ace), carbendazim (Car), simazine (Sim) and linuron (Lin)) from aqueous solutions before determination by HPLC-DAD. The factors that may influence the preconcentration such as the type of eluent, pH of the sample solution, volume of the eluent and flow rates of the sample and eluent were optimised. The performance of the proposed SPE column for determination trace level of the pesticides in water samples was discussed.

EXPERIMENTAL

Coconut shell activated carbon was obtained from Trayal corporation (Kruševac, Serbia), while pesticides Imi, Ace, Car, Sim and Lin were obtained from Fitofarmacija (Zemun, Serbia). Methanol (MeOH), acetonitrile (ACN) and dichloromethane (DCM) were purchased from Sigma-Aldrich (St. Louis, USA). Stock solutions of the pesticides (100 mg/L) were prepared in methanol and stored in the dark at -18°C. Working solutions were prepared before each experiment by appropriate dilution of the stock solutions with deionized water.

50 mg of AC was packed into the empty cartridge. The polypropylene upper and lower frits were placed at each end of the cartridge to hold the sorbent packing in place. The column was connected to a peristaltic pump (Perkin-Elmer, USA). Prior to use, methanol and water were passed through the column in order to clean it. Then, an appropriate volume of the sample solutions spiked with the selected pesticides was passed through the column at a controlled flow rate. Subsequently, the pesticides retained on the column were eluted with an adequate eluent. The concentrations of pesticides were determined with an Agilent 1100 liquid chromatograph (Agilent Technologies, USA) with Zorbax XDB-C_{18} column (4.6 x 250 mm, 3.5 μm particle size) and DAD detector at 220 nm for Sim, 254 nm for Lin and 270 nm for Imi, Ace and Car. The mobile phase consisted of methanol (A) and deionized water (B), applying the following gradient profile: 0.0 min 43% A and 57% B, 7 min 60% A and 40% B, 10 min 70% A and 30%

B, 14 min 72% A and 28% B, and 20 min returned to the initial composition. Flow rate and sample volume were 0.7 cm^3/min and 20 μL.

RESULTS AND DISCUSSION

Columns prepared with AC filling and in combination with three different eluents were tested. Adsorption efficiencies were 100% for all pesticides, while recovery depended on applied eluent. Figure 1 shows the effect of the organic solvents of different polarity on the recovery of the selected pesticides from the prepared column. The most acceptable recoveries were obtained by using DCM. For all pesticides, except carbendazim, the recoveries were in the range 57.9 – 100%. According to these results, DCM was chosen as the optimal SPE elution solvent for simultaneous determination of the selected pesticides.

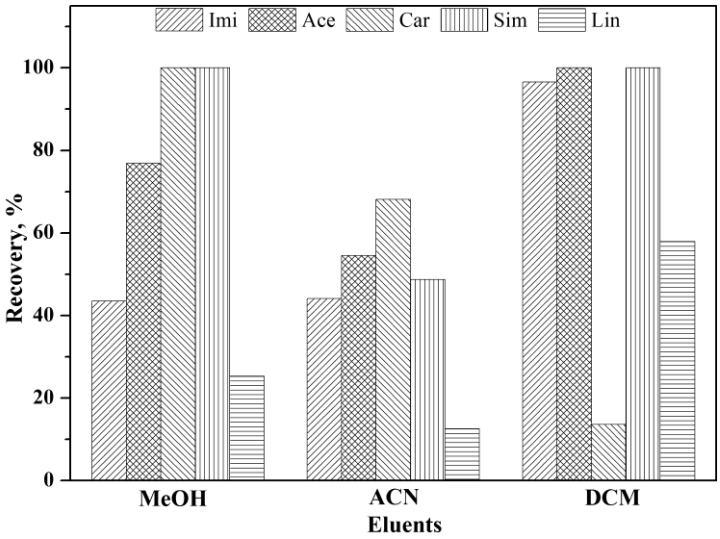

Figure 1. Effect of eluent on the recovery of the selected pesticides using SPE column packed with activated carbon derived from coconut shell

The next step in optimization of SPE procedure was the selection of optimal aqueous solution pH. The effect of pH on the adsorption and recovery of the pesticides was investigated in the pH range from 2.0 to 6.0. It was found that the best recoveries were obtained at the pH 6.0, therefore this pH was selected as optimal for recovery of the selected pesticides.

The effect of the eluent volume on the recovery of the pesticides was studied by using six fractions of 1 mL DCM. Recovery of Imi, Ace, Sim and Lin increases with increasing eluent volume from 1 to 5 mL, while further increase had no significant influence on the recovery of pesticides. Elution

of Car was slower and incompleted. Further, adsorption efficiencies and recoveries of all tested pesticides were not affected by the flow rates neither the aqueous solution nor eluent.

The features of the investigated sample preparation method in terms of linearity and detection limits (LODs) were evaluated under the optimal conditions and the results are presented in Table 1. Due to low recovery determination of Car was not accomplished in this concentration range.

Table 1. Linear ranges and detection limits of the proposed method

Pesticide	Linear range (ng/dm^3)	R^2	RSD (%) n = 3	LOD (ng/dm^3)
Imi	25 – 250	0.998	3.8	29.3
Ace	25 – 250	0.996	4.7	34.1
Sim	25 – 250	0.998	3.4	30.7
Lin	100 - 250	0.992	8.9	121.4

CONCLUSION

In the present work, activated carbon derived from coconut shell was successfully applied for preconcentration of selected pesticides of varying polarity in water samples. Under the optimized conditions, satisfied recoveries, wide linear ranges and low detection limits were observed. The obtained results indicate that the activated carbon derived from coconut shell could be successfully applied as a solid phase sorbent for pesticides analysis in water samples.

Acknowledgement

We acknowledge the support to this work provided by the Ministry of Education, Science and Technological Development of Serbia through the projects III 45006, III 45012 and III 43009.

REFERENCES

[1] Q. Zhou, Y. Ding, J. Xiao, Chromatographia, 2007, 65, 25-30.
[2] J. J. Villaverde, B. Sevilla-Morán, C. López-Goti, J. L. Alonso-Prados, P. Sandín-España, Trends in Analytical Chemistry, 2016, 80, 568-580.
[3] M. Kilic, E. Apaydin-Varol, A. E. Pütün, Journal of Hazardous Materials, 2011, 189, 397-403.
[4] Y. Zhu, P. Kolar, Journal of Environmental Chemical Engineering, 2014, 2, 2050-2058.
[5] A. Mohd Din, B. Hameed, A. Ahmad, Journal of Hazardous Materials, 2009, 161, 1522-1529.

CARBON CRYOGEL AS AN ADSORBENT FOR REMOVAL OF DRUGS AND PESTICIDES FROM WATER

M. Vukčević[1], M. Maletić[2], A. Kalijadis[3], B. Babić[4], T. Đurkić[1] and M. Laušević[1]

[1]University of Belgrade, Faculty of Technology and Metallurgy, Karnegijeva 4, 11000 Belgrade, Serbia.
[2]Innovation Center of the Faculty of Technology and Metallurgy,Karnegijeva 4, 11000 Belgrade, Serbia. (mvukasinovic@tmf.bg.ac.rs)
[3]University of Belgrade, Vinča Institute of Nuclear Sciences, P.O.Box 522, 11000 Belgrade, Serbia.
[4]University of Belgrade, Institute of Physics,Pregrevica 118, 11000 Belgrade, Serbia.

ABSTRACT
Carbon cryogel (CC), obtained by pyrolysis of resorcinol–formaldehyde cryogels, was chemically modified and used for adsorption of drugs and pesticides from water. FTIR analysis and point of zero charge determination showed that applied chemical treatments affect the surface chemistry of carbon cryogel by changing the acidity of the surface as well as the nature and amount of surface oxygen groups. Generally, the chemical modification has no influence on drugs adsorption, while both chemical treatments increase the adsorption of pesticides onto carbon cryogel surface.

INTRODUCTION
Carbon cryogels (CC) represent a class of carbon materials that draw attention due to their developed and controllable mesoporosity. Since adsorption characteristics of carbon materials depend not only on surface porosity, but also on surface chemistry, adsorption properties of CC, obtained by pyrolysis of resorcinol–formaldehyde cryogels [1, 2], was altered by applying chemical modification with various agents. Alteration of surface chemistry, i.e. amount and nature of surface oxygen groups, can change the wettability of CC surfaces, and consequently make it more hydrophilic and suitable for the adsorption of relatively low molecular weight and polar compounds. On the other hand, functional groups may increase diffusion resistance and reduce the accessibility and affinity of CC surfaces for organic chemicals. Therefore, finding the optimal method of surface modification is crucial for improving CC adsorption properties toward the selected pesticides and drugs.

EXPERIMENTAL

CC was modified by 4 M KOH or 4 M HNO_3. 5 g of pristine CC was suspended in 25 mL of reagent and stirred at 80°C for 4 h. Then, the suspension was filtered and washed with deionized water until neutral pH. The obtained materials were labeled CC/KOH and CC/HNO_3, which refers to samples treated with potassium hydroxide and nitric acid, respectively.

The point of zero charge (PZC) was determined by mass titration, by placing various amounts (0.05, 0.1, 0.5, 1 and 10% by weight) of material in 10 cm^3 of 0.1 M KCl solution. The beakers were shaken overnight, and the limiting pH value was taken as the PZC.

Fourier Transform Infrared Spectroscopy (FTIR) measurements were used for characterization of functional groups. FTIR spectra were recorded in the range from 400–4000cm^{-1} on Bomem MB-Series, Hartmann Braun.

Adsorption of selected pesticides (imidacloprid (Im) and acetamiprid (Ac)) and drugs (sulfamethoxazole (S), diclofenac (D) and erythromycin (E)) by unmodified and modified CC samples were performed from aqueous solutions, in the batch system at 25°C. Initial concentration per each compound was 20 mg/dm^3. 0.05 g of CC samples were immersed in 50 cm^3 of pesticides/drugs solution and constantly shaken for three hours. To determine the optimal pH value of the aqueous solution, the effect of pH on CC samples adsorption capacities was studied. The concentration of selected pesticides and drugs in the solution were measured by high-performance liquid chromatography-tandem mass spectrometry (LTQ XL, Thermo Scientific).

RESULTS AND DISCUSSION

FTIR spectra, for both unmodified and modified CC samples are shown in Fig. 1a. The wide band between 3300 and 3700 cm^{-1} is assignable to the stretching vibrations of O-H bond, whereas the bands around 2922 and 2850 cm^{-1} are to be ascribed to asymmetric and symmetric C-H stretching vibrations, respectively. The peak at 1637 cm^{-1} is assigned to OH bending vibration [3, 4], while the band at 1620 cm^{-1} can be attributed to the aromatic C=C bond. The band at 1384 cm^{-1} can be attributed to carboxyl O-H deformation vibrations. Bands in the range 1500-1000 cm^{-1} can be assigned to the C-O stretching and O-H bending vibrations, which imply the existence of hydroxyl, ester or ether groups.For all samples, FTIR spectra are similar and show a presence of oxygen groups on CC surface. Applied chemical treatments alter the surface chemistry, especially in the case of HNO_3 treatment, which enhances the amount of surface oxygen groups. These changes in the surface chemistry, induced by chemical modification, also reflect on the values of the pH_{PZC} (Fig. 1b.).

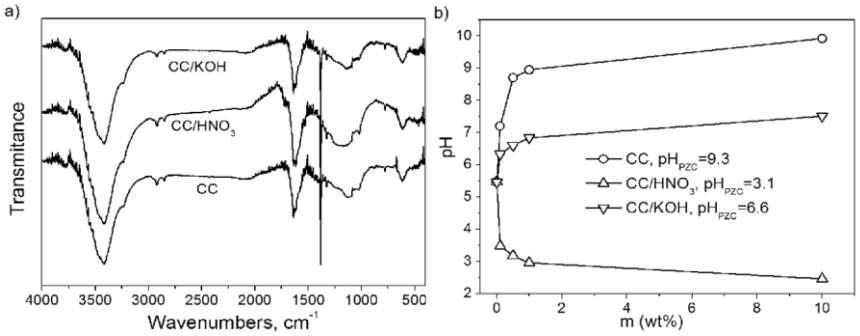

Figure 1. Characterization of CC samples: a) FTIR spectra and b) PZC

Adsorption properties of CC samples tested through the pesticides and drugs adsorption are presented in Fig. 2. Although the pesticides adsorption equilibrium onto modified CC samples has not been achieved after 180 minutes, applied chemical treatments improve pesticide adsorption (Fig. 2a). The influence of chemical modification on drugs adsorption on CC (Fig. 2b) surface primarily depends on particular drug. Chemical modification has no influence on adsorption of sulfamethoxazole, while decreases the adsorption of erythromycin. Adsorption of diclofenac is slightly increased by chemical modification with KOH, while HNO_3 modification of CC decreases diclofenac adsorption.

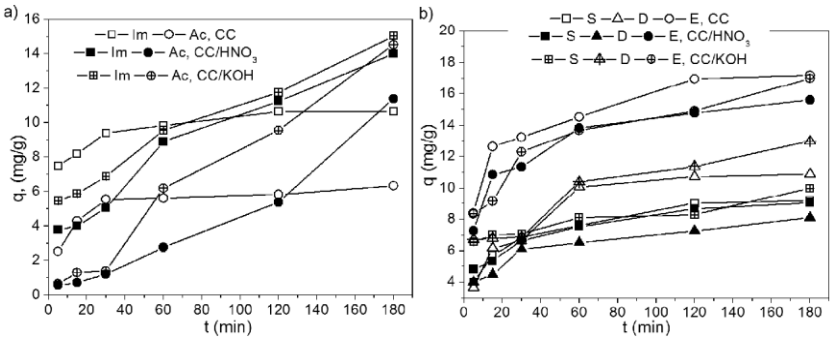

Figure 2. Amount of the pesticides (a) and drugs (b) adsorbed at the surface of CC samples

Effect of initial pH on the pesticides and drugs adsorption on unmodified and modified CC samples is shown in Fig. 3. It was found that optimal pH value of the aqueous solution for pesticides adsorption was pH=4 on CC and CC/HNO_3, while for CC/KOH maximal adsorption was achieved at pH=2 (Fig. 3a). For all tested materials optimal pH value of the aqueous solution for drugs adsorption was pH=8 (Fig. 3b).

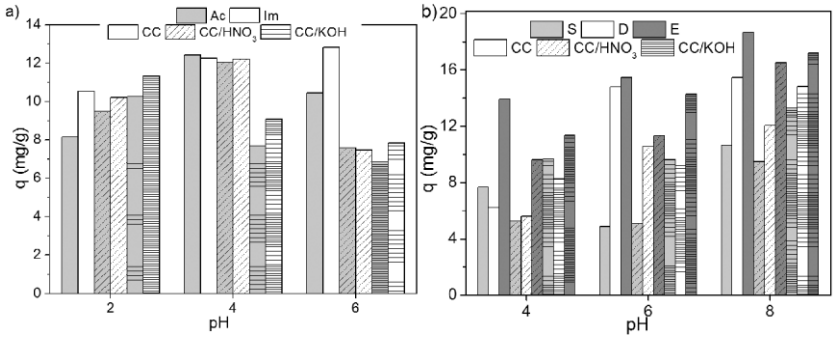

Figure 3. Effect of initial pH on the pesticides (a) and drugs (b) adsorption on unmodified and modified CC samples

CONCLUSION

Applied chemical treatments affect the surface chemistry of carbon cryogel by changing the acidity of the surface as well as the nature and amount of surface oxygen groups. Chemical modification generally has no influence, or deteriorate the drugs adsorption onto carbon cryogel. On the other hand, both chemical treatments increase the adsorption of pesticides onto carbon cryogel surface.

Acknowledgement

This work was supported by Ministry of Education, Science and Technological Development Republic of Serbia through the project No 172007.

REFERENCES

[1] T.Z. Minović, J.J. Gulicovski, M.M. Stoiljković, B.M. Jokić, Lj.S. Živković, B.Z. Matović, B.M. Babić, Micropor. Mesopor. Mat., 2015, **201**, 271 – 276.

[2] B. Babić, B. Kaluđerović, Lj. Vračar, N. Krstajić, Carbon, 2004, **42**, 2617 –2624.

[3] M. Maletić, M. Vukčević, A. Kalijadis, I. Janković-Častvan, A. Dapčević, Z. Laušević, M. Laušević, Arab. J. Chem., http://dx.doi.org/10.1016/j.arabjc.2016.06.020

[4] Y. Du, L. Wang, J. Wang, G. Zheng, J. Wu, H. Dai, J. Environ. Sci., 2015, **29**, 71 – 81.

RADIOACTIVITY IN SOIL AND MOSSES FROM NP DJERDAP IN 2017

A. Čučulović [1], R. Čučulović [2], S. Nestorović [3], N. Radaković [3] and D. Veselinović [4]

[1]University of Belgrade, INEP- Institute for the Application of Nuclear Energy, Banatska 31b, 11080 Zemun-Belgrade, Serbia. (anas@inep.co.rs).
[2]Higher Business School, Vlade Jovanovića 8, 16000 Leskovac, Serbia
[3]Public Company Djerdap Nationalni Park, Kralja Petra I 14a, 19220 Donji Milanovac, Serbia.
[4]University of Belgrade, Faculty of Physical Chemistry, Studentski trg 12-16, P. Fax 47, 11158 Belgrade, Serbia.

ABSTRACT

In June 2017, 9 soil samples and 16 moss samples were collected from 9 locations on the territory of National Park Djerdap. The radionuclide content (Bq/kg) in soil (moss) was: ^{137}Cs 105-746 (16.0-183), ^{40}K 68.8-611 (31.4-452), ^{226}Ra 5.6-39.2 (2.8-28.6), ^{232}Th 5.3-43.7 (2.1-24.7), ^{238}U 4.4-37.5 (0.8-29.6) and ^{7}Be 26.1-170 (58.7-557). The external gamma dose rate originating from the activity of radionuclides in the soil and the annual effective dose were determined. Values of the external gamma dose and the annual effective dose from external gamma dose rate radiation based on the content of natural radionuclides in soil were in the range of the expected values and close to the average values in the world.

INTRODUCTION

The NP Djerdap is located in Southeast Europe in the Northeast part of the Republic of Serbia with an area of 93.968 ha, while the protected zone is 63.608 ha. Primordial radionuclides are the most significant source of ionizing radiation in the environment. Uranium, thorium and their decay products in the Earth core are the most significant radionuclides. Potassium-40 is the essential natural radionuclide that enters the composition of the human organism. Cosmogenic radionuclides (^{7}Be) are not very significant in the total population irradiation. Anthropogenic radionuclides are enhanced or created due to human activity. Pollution with these radionuclides generally has a regional character, but it can have wider implications in the case of strong nuclear explosions [1]. ^{137}Cs is a toxic element and is an active participant of the human and animal food chain through plants as it metabolitically replaces potassium. Monitoring

radioactivity is necessary and significant to realize protection of the environment and radiological protection of the population of a certain region.

EXPERIMENTAL

Investigations performed on the territory of NP Djerdap in the last few years have shown that the radionuclide content in moss and its substrate is not homogenous and this is the reason why mosses and substrates were collected from previously defined locations. In June 2017 9 soil samples and 16 moss samples were collected from 9 locations in NP Djerdap: Kožica, 38a (**1**); Đerdap, 75/b (**2**); Crni vrh (**3**); Crni vrh, 17 (**4**); Crni vrh, 45 (**5**); Đerdap, 48b (**6**); Ploče, 57a (**7**); Porečke šume (**8**); Boljetinska reka, 9 (**9**). Moss samples were: 1. *Hypnum cupressiforme* Hedw. (**M1**) 2. *Polytrichum formosum* Hedw. (**M2**); 3. *Plagiomnium rostratum* (Schlad.) t. Kop. (**M3**); 4. *Homalothecium sericeum* (Hedw.) Schimp (**M4**). In the laboratory the samples were cleaned from visible impurities dried, homogenized and packed in Marinelli vessels with a volume of 0.5 and 1L. They were sealed with paraffin and left for at least four weeks to ensure equilibrium between ^{226}Ra and its decay products prior to radioactivity measurements. A semiconducting germanium high purity detector of the n-type produced by ORTEC - AMETEK, USA, with 8192 channels, resolution 1.65 keV and relative efficiency of 34% at 1.33 MeV for ^{60}Co was used for detection. All samples were measured for 60000 s. The ^{238}U content was determined based on gamma lines: ^{234}Th and ^{234}Pa; ^{226}Ra: ^{214}Bi and ^{214}Pb; and ^{232}Th: ^{228}Ac. The ^{40}K content was determined based on the gamma line at 1460 keV, ^{7}Be at 477 keV and ^{137}Cs at 661.6 keV. Spectra were analyzed using the Gamma Vision 32 software package. The total uncertainty of the activity measurements was typically in the range of 3% to 10%.

RESULTS AND DISCUSSION

The results obtained from measuring the content of radionuclides in investigated soil and moss samples collected in 2017 on the territory of NP Djerdap, including values of the external gamma dose rate D (nGy/h) and annual effective dose D_E (10^{-5} Sv) are given in Table 1. The average value (Bq/kg) of the radionuclide content in soil collected in 2017 was: ^{137}Cs 255, ^{40}K 384, ^{226}Ra 28.3, ^{232}Th 27.7, ^{238}U 29.8 and ^{7}Be 80.9 that is within the range of average values in soil in the world [2]. In moss it was: ^{137}Cs 85.1, ^{40}K 174, ^{226}Ra 13.0, ^{232}Th 11.3, ^{238}U 15.1 and ^{7}Be 295 that is in the range determined in our previous research [3]. The measured values for the content of radionuclides with a natural origin are within the world average content range.

Table 1. Radionuclide content (Bq/kg) in soil and moss samples collected in 2017 in NP Djerdap and also values of the external gamma dose rate D (nGy/h) and annual effective dose D_E (10^{-5} Sv)
(**L**-Locality, **S**-Sample, **M**-Moss, **Soil**-Soil)

		^{137}Cs	^{40}K	^{226}Ra	^{232}Th	^{238}U	^{7}Be	D	D_E
L	**S**	(Bq/kg)						(nGy/h)	(10^{-5} Sv)
1	**M2**	183	179	16.1	9.1	15.2	243	---	---
	Soil	746	257	39.2	32.6	36.9	170	48.5	5.95
2	**M1**	103	127	22.8	6.7	14.8	---	---	---
	M2	104	219	13.9	12.8	5.9	289	---	---
	Soil	290	312	32.1	36.2	34.8	34.2	49.7	6.10
3	**M2**	68.5	246	10.8	10.1	10.9	261	---	---
	Soil	163	529	35.9	22.0	35.2	26.1	51.9	6.37
4	**M1**	154	144	10.4	8.3	14.9	549	---	---
	M1	120	83.6	9.5	10.9	22.6	---	---	---
	Soil	145	68.8	5.6	5.3	4.4	131	8.7	1.07
5	**M1**	80.2	183	2.8	4.8	8.3	215	---	---
	Soil	269	436	30.1	28.2	31.5	---	49.1	6.02
6	**M2**	90.1	189	17.6	17.6	8.4	---	---	---
	Soil	285	161	37.3	42.7	37.5	---	49.7	6.10
7	**M1**	59.8	172	28.6	16.3	15.3	58.7	---	---
	M4	30.1	86.4	6.9	6.3	2.8	268	---	---
	Soil	133	573	31.4	43.7	34.8	---	64.8	7.95
8	**M1**	97.5	68.0	3.0	6.4	18.1	---	---	---
	M1	31.5	76.2	13.5	17.3	23.1	557	---	---
	M1	64.4	198	19.2	16.0	23.8	269	---	---
	M1	16.0	31.4	2.8	2.1	0.8	---	---	---
	M2	50.4	328	17.2	24.7	29.6	273	---	---
	Soil	105	611	20.4	19.8	27.7	43	46.9	5.75
9	**M3**	109	452	12.1	10.8	27.0	267	---	---
	Soil	155	507	22.9	18.4	25.3	---	42.8	5.25

The external gamma dose rate in the air at 1m above ground level was calculated from the measured activity concentrations of the ^{226}Ra, ^{232}Th and ^{40}K in the soil assuming that others radionuclides, such as ^{137}Cs, can be neglected as they contribute very little to the total dose from environmental background. The calculations were performed according to the following equation: $D(nGy/h) = 0.462C_{Ra} + 0.604C_{Th} + 0.0417C_K$ where C_{Ra}, C_{Th}, C_K are the radionuclide content in soil, while according to recommendations of UNSCEAR, corresponding conversion coefficients nGy/h/(Bq/kg), are: 0.462, 0.604, 0.0417, respectively [2]. The external gamma dose rate (nGy/h) in 2017 on the territory of NP Djerdap is in the range from 8.7 to 64.8. The annual effective dose was determined as:

D_E (10^{-5} Sv) = D×0.7×0.2×365×24. The annual effective dose (10^{-5} Sv) in 2017 was from 1.07 to 7.95, and they are the same order of magnitude as values determined on other locations in our country [4]. The transfer factor (TF) is defined as the ratio between the content of a given radionuclide in a plant (Bq/kg) and the content of the given radionuclide in soil (Bq/kg) for dried plant and soil samples. Transfer of radionuclides from the soil to plants depends on physical, chemical and biological factors. TF for ^{137}Cs is 0.15-1.06, ^{40}K 0.05-2.09, ^{226}Ra 0.09-1.86, ^{232}Th 0.11-3.74, ^{238}U 0.03-5.14.

CONCLUSION

Radionuclides belonging to the radioactive series of uranium ^{238}U, ^{226}Ra and ^{232}Th, natural isotope ^{40}K, and also the artificially produced radionuclide ^{137}Cs were detected and measured in all investigated samples. The average values of radionuclide content in soil collected in 2017 were in the range of average values of radionuclide content in soil in the world, and in moss it was in the range of our previous research. The content of ^{137}Cs in soil and moss indicates that there was no new pollution with this radionuclide on the investigated territory.

Acknowledgement

This work was financed by the Ministry of Education, Science and Technological Development of the Republic of Serbia (Project: III 43009)

REFERENCES

[1] D. Veselinović, I.A. Gržetić, Š.A. Đarmati, D. Marković, Stanja i procesi u životnoj sredini, Fizičkohemijski osnovi zaštite životne sredine, knjiga I, Udžbenici Fizičke hemije, Fakultet za fizičku hemiju, Univerzitet u Beogradu, Beograd,1995.

[2] UNSCEAR Sources and Effects of Ionizing Radiation. Annex B: Exposure from natural radiation sources. United Nations, New York, 2000.

[3] A. Čučulović, R. Čučulović, M. Sabovljević, D. Veselinović, Arch. Biol. Sci., 2012, **64**(3), 917-925.

[4] Republika Srbija, Agencija za zaštitu od jonizujućih zračenja i nuklearnu sigurnost Srbije, Izveštaj o sistematskom ispitivanju sadržaja radionuklida u zemljištu u 2014 godini, Beograd, 2015.

PRINCIPAL COMPONENT ANALYSIS OF THE SELECTED TECHNOLOGY-CRITICAL ELEMENTS IN THE DANUBE SEDIMETS

T. Trtić-Petrović[1], R. Balvanović[1], A. Dimitrijević[1], O. Culicov[2,3] and A. Petković[4]

[1]*University of Belgrade, Vinča Institute of Nuclear Sciences, Laboratory of Physics, Belgrade (daleksandra@vinca.rs).*
[2]*Frank Laboratory of Neutron Physics, Joint Institute for Nuclear Research, Dubna, Russian Federation.*
[3]*National Institute for R&D in Electrical Engineering ICPE-CA, Bucharest, Romania.*
[4]*Institute for the Development of Water "Jaroslav Černi", Belgrade*

ABSTRACT

In this work, the concentration of the selected technology-critical elements were analysed in the Danube sediments with aspect of possible anthropogenic influence. The principal component analysis was applied due to high variability of the samples in the sense of elements, concentration range and sampling places. The significant variability was obtained for the following TCEs: Dy, Gd, La, Eu and Nd, and for the samples placed within Iron gate I and II.

INTRODUCTION

The aquatic sediments absorb and accumulate the organic and inorganic pollutants in higher level comparing with their concentration in corresponding water sample. The adsorption of pollutants depends on both the particle size and composition of sediments. The pollution of the European rivers and their sediments with heavy metal ions have been well investigated and mainly focused on determination of heavy metals such as Hg, As, Ni, Zn, Cu, Cr, Pb and Cd [1].

Technology-critical elements (TCEs) are of the great relevance in the development of modern technologies such as information, telecommunications and optic/photonic, semiconductors, electronic displays, etc. [2]. TCEs include Nb, Ta, Ga, In, Ge, Tl, Te, the platinum group elements (Pt, Os, Ru, Rh, Pd and Ir), and most of the rare earth elements (Y, La, Ce, Pr, Nd, Sm, Eu, Gd, Tb, Dy, Yb, Lu). Application of TCEs rapidly increases in last decade, and their presence in the environment start to be detectable.

Gd (from the contrast agents for MR imaging) was the first detected TCE in river water which is anthropogenic originated [3]. The increasing amount of Sm and La was detected in the Rhine River derived from the industrial effluent from a facility producing catalyst for petroleum refining [4]. Recently, increasing concentration of REE were found in agricultural soils as well as human samples in the area of the REE mining and smelting [5].

The Danube is the second longest river in Europe. The building of the biggest hydropower dam and reservoir system along the Danube River (Iron gate, 117 km long) has been influenced on both hydrological regime of the surface and ground waters, and amount of sediments [6]. Although, the Danube River has been well examined in a sense of heavy metal pollution, investigation of the presence of TCEs has not been investigated yet. The aim of this study is determination of the selected TCEs in the Danube River sediments by Neutron Activation Analysis (NAA) and data analysis by applying principal component analysis.

EXPERIMENTAL

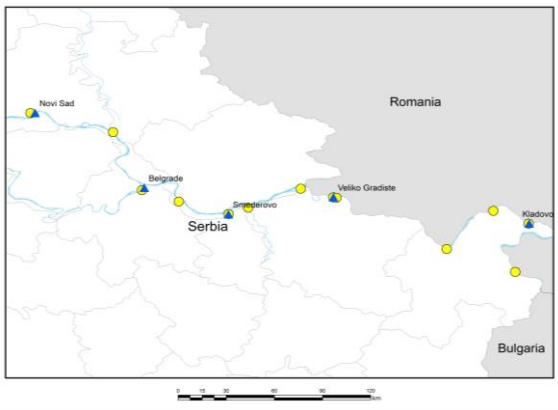

Figure 1. Map of sampling sites

The surface river sediments were collected using an Ekman grab sampler at 11 locations which are shown in Fig.1 and Table 1. A deep river sediment and river bad were collected at 1112 km of the Danube. The samples were mixed and dried at 40 ± 1 °C. Then, the samples were homogenized and sieved through a 1-mm sieve.

NAA was used to quantify selected REE: La, Ce, Nd, Sm, Eu, Gd, Tb, Dy, Tm and Yb. The analytical procedure based on NAA has been described in detail elsewhere [7]. The results were analyzed using Principal Component Analysis (PCA). Power transformation was used as the data pretreatment method, in order to reduce data heteroscedasticity.

RESULTS AND DISCUSSION

The experimentally determined concentrations of the selected REEs (normalized to upper continental crust, UCC [8]) are shown in Fig. 2. It can be seen the pattern of the normalized concentration values of the bad river

Table 1. Properties of the sample locations.

Nº	River	*km	Place	Features
1	Danube	1141	Ritopek	Upper stream from Iron gate I
2	Danube	1112	Smederevo	
3	Danube	1072	Ram	Iron gate I
4	Danube	1059	V. Gradiste	
5	Danube	991	D. Milanovac	
6	Danube	956	Tekija	
7	Danube	934	Kladovo	Iron gate II
8	Danube	864	Kusjak	
9	Sava	5	Belgrade	Tributaries
10	V. Morava	2	-	
11	Pek	0	-	
12	Deep sed.	1112	Smederevo	1.5 m deep
13	Bad river	1112	Smederevo	7.2 m deep

sample and the deep sediment sample is smooth and close to 1, and slightly lower for the bad river sample. It can be assumed that the bad river sample is without anthropogenic influence. The results of surface sediments show increasing concentrations of Nd, Eu and Dy comparing to UCC.

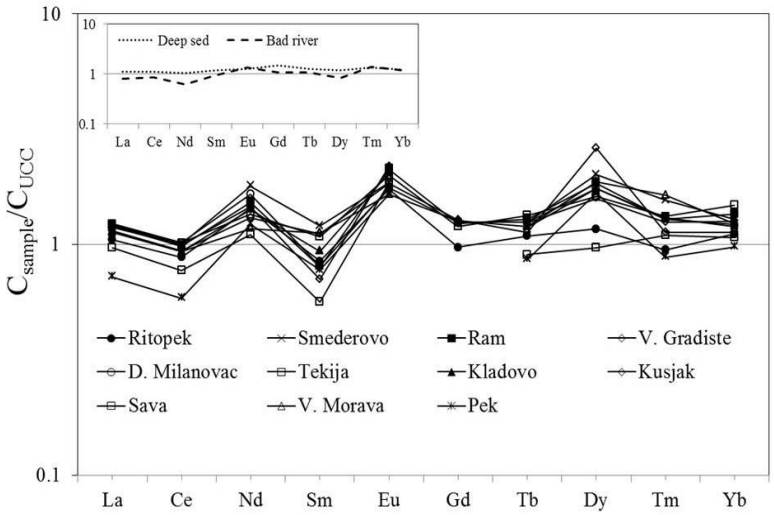

Figure 2. The normalized REE at various sample places.
Insert: Normalized REE in deep sediments and river bad samples.

In order to deeply analyse quantified REEs at different sampling places, PCA was chosen as statistical method (Fig. 3) due to high variability of the samples (various elements, concentrations and sample places). The obtained results show the highest variability for following elements: Dy, Gd and La for samples which are placed in Iron gate I. Also, the significant variability can be seen for Eu and Nd in the sampling places at Iron gate II. It should be

mentioned that the deep sediment and bad river samples are out-layers e.g. the variability in these samples is very low.

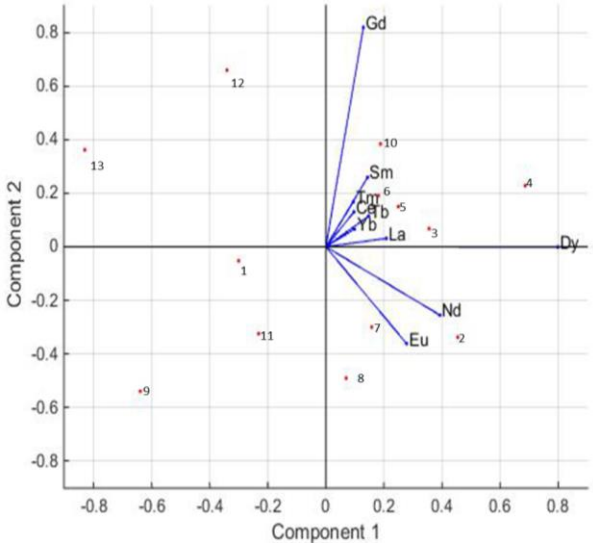

Figure 3. Principal component analysis of the REEs. Numbered points denote measurements, vectors directions and intensities of concentrations increase in the

CONCLUSION

The analysis of the Danube sediments with the aspect of the selected TCE was presented for the first time. Due to high variability of the samples PCA was applied as the statistical methods. The quantified REEs (Dy, Gd, La, Eu and Nd) show significant variability in the area of Iron gate I and II and related to increasing quantity of sediments.

Acknowledgement

This work was supported by the Ministry of Education, Science and Technological Development of Serbia (Grants no. III45006). The authors would like to acknowledge the contribution of the COST Action TD 1407.

REFERENCES

[1] P. Woitke, J. Wellmitz, D. Helm, P. Kube, P. Lepom, P. Litheraty, Chemosphere, 2003, 51, 633–642.
[2] B. Karn, Journal of Environmental Monitoring, 2011, 13 1184–1189.
[3] M. Bau, P. Dulski, Earth. Planet. Sci. Lett. 1966, 66, 245-255.
[4] S. Kulaksiz, M. Bau, Earth. Planet. Sci. Lett. 2013, 362, 43-50.
[5] B. Meryem, J.I. Hongbing, G.A.O. Yang, D. Huajian, L. Cai, Journal of Rare Earths, 2016, 34, 1156-1167.
[6] M. Babic Mladenovic, V. Kolarov, V. Damjanovic, Int. J. Sediment Res., 2013, 28, 470–485.
[7] M.V. Frontasyeva, Phys. Particles Nuclei, 2011, 2, 332–378.
[8] Taylor SR, McLennan SM, The continental crust: its composition and evolution, Blackwell Scientific Publication, Carlton, 1985.

ANALYSIS OF TAP WATER FOR GROSS ALPHA/BETA ACTIVITY

M. M. Janković[1], S. Jokanović[2], N. Sarap[1] and K. Stevanović[2]

[1]University of Belgrade, Radiation and Environmental Protection Department, Vinča Institute of Nuclear Sciences, Mike Petrovića Alasa 12-14, 11000 Belgrade, Serbia
[2]University of Belgrade, Faculty of Physical Chemistry, Studentski trg 12-16, 11000 Belgrade, Serbia (kristina@ffh.bg.ac.rs)

ABSTRACT

This paper describes determination of gross alpha and beta activity in tap waters used for drinking in Serbia. 19 samples from different cities were investigated. Method used for sample preparation was EPA 900.0 and activity was determined by proportional counter. Obtained gross alpha activity was in range MDA-0.318 Bq/l, while gross beta activity was in range MDA-0.370 Bq/l. With these values individual dose criterion of 0.1 mSv/year will not be exceeded. Based on the fact that all investigated samples met the criteria given in Serbian rule book, further analyzes were not conducted.

INTRODUCTION

Drinking water may contain different radionuclides that could present a risk to human health. Naturally occurring radionuclides (^{40}K, ^{226}Ra, ^{238}U…) and artificial radionuclides (^{137}Cs, ^{90}Sr, ^{241}Am…) are present in environment. Different amount of radionuclides can be found in water, soil, sediment, indoor air, outdoor air, plant. Determination of gross alpha and beta activity presents screening technique for radioactivity measurement. Drinking water should be analyzed first for gross alpha/beta activity according to national and international standards and screening levels for drinking water below which no further action is required are 0,5 Bq/l for gross alpha and 1 Bq/l for gross beta activity [1] (Figure 1). These recommendations do not make a difference between natural and artificial radionuclides. Radionuclides with low beta energy (tritium and iodine) can not be detected with standard gross alpha beta measurement. If there is any reason to believe that these radionuclides may be present in water samples, some techniques must be performed such as liquid scintillation techniques or gamma spectrometry analysis to identify these radionuclides.

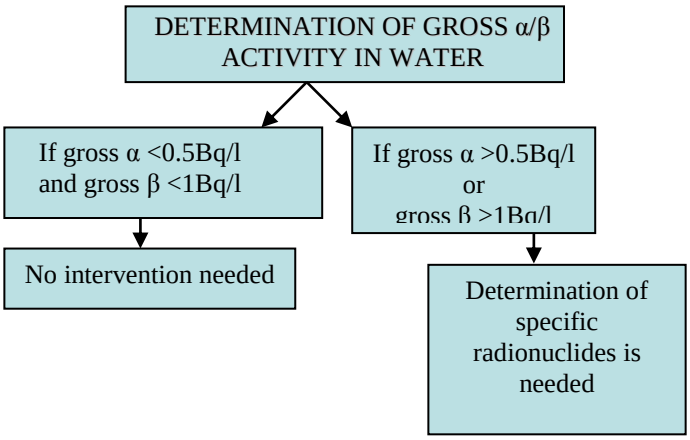

Figure 1. Application of guidance level for gross alpha/beta activity in drinking water

EXPERIMENTAL

19 tap water samples from cities in Serbia: Belgrade (Vinča), Belgrade (Zvezdara), Čačak, Kragujevac, Ivanjica, Bujanovac, Ruma, Kučevo, Smederevo, Smederevska Palanka, Inđija, Kikinda, Šabac, Obrenovac, Lazarevac, Kovin, Pančevo, Požarevac and Vršac were investigated for gross alpha and beta activity. Some chemical parameters were also determined. Sammpling was performed in April 2018.

Total dissolved solids (TDS) was determined after evaporation of small volume of sample (40 ml), dried for at least 2 h in an oven at 105°C, cooled and weighted. The pH was measured by InoLab pH meter WTW using glass electrode SenTix 81. Calibration of the instrument was carried out by 4, 7 and 10 pH standard solutions. The conductivity of the samples was measured by Conductometer InoLab WTW Cond7110 at 22°C.

Preparation of tap water samples for gross alpha and beta determination was performed according to EPA method [2]. Initial volume of each sample was 3 l and preparation includes evaporation to complete dryness and ashing. A certain amount of ash sample was transferred to aluminum planchet and measured by proportional counter ThermoEberline FHT 770 T. Calibration of counter was performed using standard sources of ^{90}Sr (EM145, Prague) and ^{241}Am (EM445, Prague). The counting gas was a mixture of 90% argon and 10% methane and the counting efficiencies for the system are 28% for alpha and 34% for beta.

RESULTS AND DISCUSSION

All samples belongs to poor basal water or poorly acidic. Four investigated waters belong to the medium mineral class (residue > 500 mg/l) and the others

belong to the low mineral class (residue 50–500 mg/l). Generally, good correlation exists between TDS and conductivity. Gross alpha activity in investigated samples range from minimum detectable activity to 0.318 Bq/l, until gross beta activity range from minimum detectable activity to 0.370 Bq/l. Based on these results it can be concluded that further investigation is not necessary. Because of gross alpha and beta activities are below the 0.5 and 1 Bq/l, it is assumed that the indicative dose of the parameter values is 0.1 mSv. The gross alpha radioactivity is mainly due to uranium and radium isotope, and the gross beta is due to natural long-lived isotopes ^{40}K, ^{210}Pb and ^{228}Ra or artificial isotopes, such as ^{90}Sr and ^{137}Cs.

Table 1. Results of chemical parameters and gross alpha/beta activity of investigated tap water samples

Sample origin	pH	TDS (mg/l)	Conductivity (µS/cm)	Gross alpha (Bq/l)	Gross beta (Bq/l)
Čačak	7,44	470	444	< 0.055	< 0.121
Kragujevac	6,67	738	1066	< 0.105	< 0.165
Belgrade (Vinča)	6,97	285	385	0.068±0.023	0.071±0.032
Kikinda	8,29	535	745	0.318±0.063	0.370±0.078
Ivanjica	7,97	160	365	0.120±0.031	0.143±0.033
Bujanovac	7,22	383	564	0.230±0.060	0.249±0.065
Belgrade (Zvezdara)	7,83	190	451	0.088±0.033	0.143±0.037
Ruma	8,21	618	348	< 0.105	0.189±0.076
Kučevo	7,08	363	594	< 0.062	< 0.095
Smederevska Palanka	7,32	603	953	0.219±0.072	0.292±0.081
Šabac	6,77	320	451	0.148±0.038	0.200±0.051
Obrenovac	8,41	130	428	< 0.050	< 0.070
Lazarevac	7,94	50	558	0.271±0.057	0.370±0.074
Smederevo	7,04	295	607	0.152±0.046	0.233±0.057
Pančevo	7,71	398	487	0.224±0.052	0.244±0.059
Inđija	7,09	425	388	0.222±0.057	0.259±0.058
Kovin	7,85	275	739	< 0.081	< 0.125
Požarevac	6,93	485	714	0.107±0.043	0.118±0.053
Vršac	6,97	340	537	< 0.051	< 0.079

Measurement uncertainty presented in Table 1 is expressed as an expanded measurement uncertainty for the factor k = 2 which corresponds to a normal distribution with a confidence level of 95%.

CONCLUSION

Determination of gross alpha/beta activity in drinking water samples from Serbia was performed. Results for all investigated tap water samples are below the limits defined by rule book and can be used for drinking if a radiological examination is observed. Activities obtained in this study are the same order of magnitude as the data present in the world literature [3-6].

Acknowledgement

This paper was realized as a part of the project III43009 financed by the Ministry of Education, Science and Technological Development of the Republic of Serbia.

REFERENCES

[1] Official Gazette of the Republic of Serbia, Regulation on limits of radionuclide content in drinking water, foodstuffs, feeding stuffs, drugs, items of general use, building materials and other goods to be placed on the market, 86/11.

[2] EPA (Environmental Protection Agency), Prescribed Procedures for Measurement of Radioactivity in Drinking Water, EPA−600/4−80−032; Method 900.0, 1980.

[3] L. Currivan, K. Kelleher, E. Solodovnik, C. McMahon, Radioactivity in Bottled Water Produced in Ireland, Radiological Protection Institute of Ireland RPII 13/05, Ireland 2013.

[4] X. Xiang Miao, Y. Ji, X. Zhang Shao, H. Wang, Q. Fu Sun, X. Su, International Journal of Environmental Research and Public Health, 2013, **10(12)**, 6863–6872.

[5] R. Amin, Advances in Applied Science Research, 2017, **8(1)**, 62-69.

[6] N.Todorović, J.Nikolov, B.Tenjović, I.Bikit, M.Veskov, Radiation Measurements, 2012, **47**, 1053-1059.

CHARACTERIZATION OF THE FINE AIR PARTICULATE MATTER FRACTION BY PROTON INDUCED X-RAY EMISSION TECHNIQUE (PIXE)

M. Radenković[1], M. Todorović[2], J. Marković[1] and A. Onjia[3]

[1]University of Belgrade, Vinča Institute of Nuclear Sciences, Mike Petrovića Alasa 12-14, 11000 Belgrade, Serbia
[2]University of Belgrade, Institute of Physics, Pregrevica 118, 11000 Belgrade, Serbia
[3]University of Belgrade, Faculty of Technology and Metallurgy, Karnegijeva 2, 11000 Belgrade, Serbia
(mirar@vin.bg.ac.rs)

ABSTRACT

In the study are presented the possibilities of PIXE technique as multi-elemental, non destructive and very sensitive nuclear analytical technique for characterization of the fine fraction of air particulate matter collected at suburban monitoring site in Belgrade. The reliable database was provided adequate for application of receptor source apportionment modeling as well as other numerical and statistical analysis of data for air pollution assessment.

INTRODUCTION

The air quality has become a matter of global concern due to its evident harmful effects to environment and consequently to human health. Very complex in composition, atmospheric particulate matter (APM) has certainly the most significant contribution to the air pollution, especially in urban areas. Airborne particulates may be coarse, fine and ultrafine according to their aerodynamic diameter, less than 10 μm, less than 2.5 μm and less than 1 μm, respectively. Usually, the regulations oblige states, including Serbia, to have regularly monitoring of PM10 and PM2.5 mass concentrations including Pb, Mn, Ni and As concentrations in PM10 aerosol fraction. But, complete physical-chemical characterization of APM aerosol fractions would include determination of macro and micro elements content, hydrocarbon compounds, anions, cations, specific tracers, etc. It is a demanding requirement to share and analyze daily aerosol deposit by several different techniques in order to complete PM mass concentration closure, increasing thus the uncertainty and the cost of analysis. On the other side stand nuclear analytical techniques such as neutron activation

analysis (NAA), particle induced X ray emission (PIXE) and energy dispersive X ray emission (EDXRF) with the advantage of non destructive, multi-elemental, highly sensitive and not time-consuming procedures. Here will be presented the PIXE nuclear analytical technique capabilities to provide a database adequate for fingerprinting and apportioning of air pollution sources by mathematical modeling and statistical analysis.

EXPERIMENTAL

The PM 2.5 aerosol samples have been collected at Zeleno Brdo suburban background area on daily basis during both heating and non heating seasons, 2014. Sampling was done according to EN12341 standard operating procedure described elsewhere in detail [1] but using PTFE instead of quartz filters. PIXE analysis of aerosol deposit was done in the Atomki Institute for Nuclear Research, Laboratory of Ion Beam Applications, Debrecen, with support of IAEA regional project on the air quality management for Europe. The measurement set-up was the PIXE chamber installed at the 45^0 beam line of the Van de Graaf accelerator with the 1.8 MeV H^+ ions irradiating beam, 0.5cm in diameter. [2] The homogeneity during the measurement was insured by beam passing through a thin scattering Ni foil. Punched PTFE filter circles 1.2 cm in diameter have been fixed on the disc holder and placed into vacuum chamber without any previous treatment. The obtained X-ray spectra were fitted by the PIXECOM program code, for „thin" samples. The quality assurance was carried out using NIST SRM2783 and NIST SRM610.[3] Source apportionment was done based on the obtained PIXE dataset of 90 samples, by the application of Positive Matrix Factorization software (EPA 5.0) developed by US EPA, publicly available.

RESULTS AND DISCUSSION

The concentrations of following elements: Al (37,8), As, Ba (21,3), Ca (26,4), Co, Cr (2,3), Cu (2,1), Fe (55,3), K (3,1), Mn (3,2), Ni (1,8), Pb (7,5), Ti (2,7), V (3,2), Zn (1,9), Si (62,7), S (4,1), P (4,2), Cl, Br and Sr, have been obtained by PIXE analysis with minimum detectable concentration (MDC) per filter surface (ng/cm2) in certain experimental setup given in parenthesis. Light elements with Z below 12 cannot be determined by this technique. Considering the sampling site situated in suburban background area, obtained elemental concentrations in whole are expectably very low and represent a small portion of the PM2.5 mass due to the lack of other data, especially water content, secondary ions, large hydrocarbons content etc. The pollution roses of trace elements in non-heating and heating seasons may lead to the origin of the element. In Figure 1 are presented pollution

roses for K, showing maximum concentrations in the heating period and for S, the product of combustion in the heating units but also present in fine aerosol fraction as result of traffic pollution during non-heating season. Based on the relations of measurements and their uncertainties, with recognition of the missing concentration values and values below the MDC, known Pearson correlation coefficients, with seasonality of peak concentrations but also with a subjective decision on the weight of the certain species (bad/weak/strong) a positive matrix factorization had recognized 5 dominant factors/pollution sources: mixed traffic and soil resuspension (Al), wood burning (Cl, K, Zn, Pb), soil resuspension (Si, Ca, Ti, Mn, Fe), heavy oil combustion (PM2.5, V, Ni), and mixed fossil fuels combustion (S, Ti, Cu, Pb), respectively. If we slightly increase the number of factors, recognized sources might become more distinguished, especially if data for black carbon (BC) and secondary ions concentrations are available. Considering that non destructive PIXE analysis gives data on about 20 elements and BC analysis is based on the light absorption, in this case, the only chemical sample treatment prior to ion chromatography analysis may be necessary. Besides PIXE, the EDXRF may be equally used as multi-elemental non-destructive analytical technique for PM2.5 analysis. The limitation of these two techniques may be lack of necessary installations or devices that might be got over in research community by sharing the regional infrastructure. The meteorological parameters should be available for further analysis having the significant role in the explanation of the modeling results.

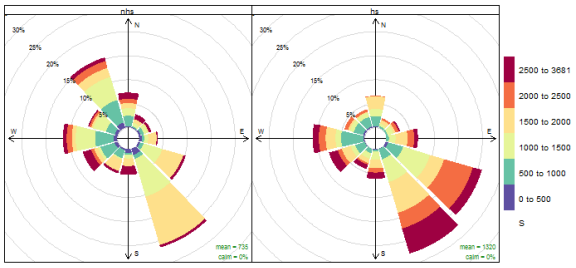

Figure 1. The pollution roses of potassium and sulfur in heating and non-heating seasons

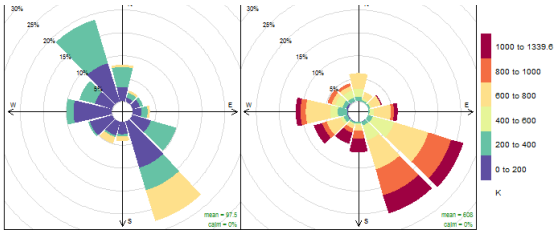

CONCLUSION

Here is demonstrated that PIXE, as non destructive, multielemental and highly sensitive nuclear analytical technique may be a basis for apportioning

of air pollution sources by mathematical modeling and statistical analysis especially for PM2.5 aerosol samples coming from suburban and rural areas where low levels of trace elements are expected. For additional considerations, meteorological data and complementary analysis such as BC and secondary ion analysis would improve the air pollution assessment.

Acknowledgement
This study was supported by the Serbian Ministry of Education, Science and Technological Development by funding III43009 project and by IAEA RER1013 regional project. The authors are grateful for PIXE measurements done at the installation in the ATOMKI Nuclear Research Institute, Debrecen, Hungary, under supervision of Dr.Zsofia Kertesz.

REFERENCES

[1] J.D.Joksić, M.Jovašević-Stojanović, A.Bartonova, M.B.Radenković, K-E.Yttri, S.Matić-Besarabić, Physico-chemical characterization of particulate matter suspended in aerosols from urban Belgrade area, Journal of the Serbian Chemical Society, 2009, 74(10):
[2] Borbély-Kiss I. et al. Experimental and theoretical calibration of a PIXE setup for K and L X-rays. Nuclear Instruments and Methods in Physics Research Section B: Beam Interactions with Materials and Atoms 1985 (12) 496-504.
[3] Zsofia Kertesz, PIXE elemental analysis on atmospheric aerosol samples, Research Report for IAEA RER1013 project, 2015. Debrecen, Hungary.

HUMAN/ANIMAL AND PLANT STEROLS IN SUSPENDED MATTER OF MUNICIPAL WASTEWATER

I. Matić Bujagić, Z. Jauković, S. Grujić and M. Laušević

University of Belgrade, Faculty of Technology and Metallurgy, Karnegijeva 4, 11000 Belgrade, Serbia. (imatic@tmf.bg.ac.rs)

ABSTRACT

The aim of this paper was determination of human/animal and plant sterols in suspended matter of untreated wastewater. Wastewater samples were filtered and the obtained suspended particulates were extracted using ultrasonic extraction and analyzed by liquid chromatography-linear ion trap-tandem mass spectrometry with atmospheric pressure chemical ionization of analytes. In the investigated samples, coprostanol and cholesterol were detected at the highest concentrations, up to 1755 μg g^{-1} and 1958 μg g^{-1}, respectively.

INTRODUCTION

Municipal wastewater represents significant source of a growing variety of pollutants (steroids, pesticides, domestic and industrial chemicals, pharmaceuticals, personal care products, etc.). So far, the main focus of scientific papers was the analysis of dissolved phase of wastewater. However, the hydrophobic nature and limited solubility of some compounds, such as sterols, indicates that the suspended fraction of wastewater should be considered, as well [1, 2]. Namely, hydrophobic, and lipophilic contaminants are predominantly associated with particulate matter or biota [1]. Suspended particulate matter plays a controlling role in the exposure and fate of different organic pollutants in aquatic environments though the processes of sorption and desorption. That way, suspended matter can act as both the source and sink of pollutants in the water compartment and even influence sediment quality through sedimentation and resuspension [3]. Therefore, identification and quantification of organic contaminants in suspended matter of wastewater is necessary to understand pollution status, possible migration and transformation of pollutants in the aquatic environment. Human/animal and plant sterols are a class of steroids that have received considerable attention in the recent years due to its successful application as chemical markers of sewage contamination [4, 5].

Since particle-associated contaminants mainly accumulate in fine-grained and organic-rich fractions, a proper sampling and isolation of suspended

fraction is essential. Filtration allows complete separation of the solid phase, including fine particles, from the water phase. Commonly, 0.7 μm pore-sized filters are used to separate analytes present in the suspended phase of water samples [1, 4, 6–7]. The sample preparation involves extraction, preconcentration and clean up, usually by ultrasound extraction [2], accelerated solvent extraction [5] or Soxhlet extraction [8].

The aim of this work was development of simple, time, cost, labor efficient and quantitative method for the analysis of human/animal and plant sterols in the suspended phase of wastewater. Five composite samples of wastewater were used for the analysis of wastewater suspended matter.

EXPERIMENTAL

High purity (> 99%) analytical standards of human/animal (coprostanol, epicoprostanol, cholestanol, epicholestanol, cholesterol and cholestanone) and plant sterols (desmosterol, stigmasterol, campesterol, β-sitosterol and sitostanol) were obtained from Steraloids Inc. (Newport, USA). To isolate suspended fraction of wastewater, samples were filtrated through a glass fiber filters (pore size <0.7 μm, LLG Labware, France) and filters were afterwards dried. The filters were weighted before and after filtration, and then extracted. These filters were treated as solid samples and extracted using ultrasound extraction. Briefly, filter with suspended matter was extracted using 10 ml of methanol in the ultrasonic bath for 10 min. The sample was then centrifuged (for 10 min, at 4000 rpm) and supernatant was separated. Ultrasonic extraction was repeated once more. Obtained extract (20 ml) was evaporated to the dryness under a gentle nitrogen stream and reconstituted with methanol to the volume of 0.5 ml. The extract was filtered through 0.45 mm polyvinylidene difluoride (PVDF) filter, acquired from Roth (Karlsruhe, Germany) and analyzed using previously developed method [9]. Liquid chromatographic analysis was performed on Dionex UltiMate 3000 LC system (Thermo Fisher Scientific, USA) and for the separation of analytes, Zorbax Eclipse® XDB-C8 reverse-phase column was used (150 mm × 3.0 mm with 3.5 μm particle size, Agilent Technologies, USA). The detection and quantification of sterols was carried out using LTQ XL linear ion trap (Thermo Fisher Scientific, USA) and the ionization technique used was atmospheric pressure chemical ionization. Mobile phase consisted of deionized water, acetonitrile and 10% (v/v) acetic acid.

RESULTS AND DISCUSSION

Seven sterols were detected in the suspended fraction of the investigated wastewater samples, including two human/animal sterol and five plant sterols (Table 1).

Table 1. Concentrations of detected sterols in suspended matter of wastewater samples.

Wastewater sample	1	2	3	4	5
Sterols	c, μg g^{-1} (RSD, %)	c, μg g^{-1} (RSD, %)	c, μg g^{-1} (RSD, %)	c, μg g^{-1} (RSD, %)	c, μg g^{-1} (RSD, %)
Coprostanol	57 (4)	368 (4)	622 (20)	1755 (0,3)	1595 (6)
Desmosterol	12 (1)	15 (1)	18 (8)	18 (26)	16 (5)
Cholesterol	106 (13)	803 (21)	489 (16)	689 (19)	1958 (9)
Stigmasterol	24 (10)	81 (9)	104 (11)	74 (7)	91 (7)
Campesterol	21 (5)	44 (4)	35 (1)	30 (6)	34 (3)
β-Sitosterol	467 (8)	331 (12)	398 (6)	175 (9)	116 (11)
Sitostanol	117 (11)	485 (5)	161 (6)	844 (18)	43 (14)

Human/animal sterols, coprostanol and cholesterol, were detected at highest concentrations, up to 1755 μg g^{-1} and 1958 μg g^{-1}, respectively. These results can be explained by the fact that previous study of raw sewage showed that coprostanol and cholesterol constitute 37–48 and 23–38% of the particulate sterols [4]. Sitostanol was the most prominent plant sterol, detected in the concentration range 43–844 ng g^{-1}. Similar findings were obtained by the analysis of suspended particles from the Mediterranean Sea [10]. Sitostanol represent reduction product derived from phytosterol β-sitosterol [11], which is a component of vegetable oils used for cooking.

The amount of sterols in suspended phase is usually defined as analyte mass (in mg or μg) per mass of dried suspended material (in g), without any correlation with the volume of water samples they have been prepared from. However, to define the distribution of pollutants between the dissolved and suspended phases of water samples, it is necessary to express concentration in ng L^{-1} or μg L^{-1} values to be comparable with their corresponding parts in dissolved fraction. Table 2 shows the concentration range of sterols detected in suspended fraction of wastewater, expressed in μg L^{-1}.

Table 2. Concentration of sterols detected in suspended matter of Serbian wastewater (in μg L^{-1}) and comparison with data from other countries.

Location/ Analyte	Serbia	Hungary[2]	France[4]	Spain[12]
Coprostanol	7.3–381	8.6–36	19–220	630
Desmosterol	1.5–3.9	–	–	–
Cholesterol	14–365	0.79–22	24–200	300
Stigmasterol	3.1–19	0.17–8.8	1.9–20	–
Campesterol	2.7–8.9	–	–	–
β-Sitosterol	38–74	0.42–9.2	8.5–70	50
Sitostanol	8.0–183	–	–	–

High concentrations of human sterols coprostanol (up to 381 μg L^{-1}) and cholesterol (up to 365 μg L^{-1}) observed in suspended matter of Serbian untreated wastewater, were similar to those in effluents in France and Spain. The wastewater plants in Hungary are more efficient in reducing coprostanol and cholesterol in effluents. Concentrations of stigmasterol and β-sitosterol detected in Serbia were comparable to treated effluents in France and lower than sterol concentrations in treated wastewater from Hungary.

CONCLUSION

Results confirmed that the sterol content in the suspended phase of wastewater samples need to be considered as well, since these compounds are preferably bound to the solid phase. Therefore, the analysis limited to the water phase results in an underestimation of the concentration of sterols.

Acknowledgement

This work was financially supported by the Ministry of Education, Science and Technological Development of the Republic of Serbia (Project No. 172007).

REFERENCES

[1] B. Schubert, P. Heininger, M. Keller, M. Ricking, E. Claus, TrAC, 2012, 36, 58–70
[2] N. Andrási, B. Molnár, B. Dobos,A. Vasanits-Zsigrai,G. Záray, I. Molnár-Perl, Talanta, 2013, 115, 367–373.
[3] Q.-S. He, Q.-M. Wang, Y. Wang, W. He, N. Qin, X.-Z. Kong, W.-X. Liu, B. Yang, F.-L. Xu, Ecol. Eng., 2015, 80, 214–222.
[4] M. Quèmèneur, Y. Marty, Water. Res., 1994, 28, 1217–1226.
[5] M. Le Meur, L. Mansuy-Huault, C. Lorgeoux, A. Bauer, R. Gley, D. Vantelon, E. Montargès-Pelletier, Org. Geochem., 2017, 110, 45–56.
[6] D. He, R. N. Mead, L. Belicka, O. Pisani, R. Jaffé, Org. Geochem., 2014, 75, 129–139.
[7] M-A. Sicre, R. C. Tian, A. Saliot, Org. Geochem., 1994, 21, 1–10.
[8] M. Kim et al., Mar. Pollut. Bull., 2016, 108, 281–288.
[9] Z. D. Jauković, S. D. Grujić, I. V. Matić Bujagić, M. D. Laušević, Microchem. J., 2017, 135, 39–47.
[10]I. Tolosa, N. LeBlond, C. Copin-Montégut, J.-C. Marty,S. de Mora, L. Prieur, Mar. Chem., 2003, 82, 161–183.
[11]M. Gourmelon et al., Water Res., 2010, 44, 4812–4824.
[12]J. 0. Grimalt, P. Ferninder, J. M. Bayona, J. Albaigés, Environ. Sci. Technol., 1990, 24, 357–363.

INVESTIGATION ON STABILITY OF COMMERCIAL PESTICIDE SOLUTION MIXTURE

M. Branković [1], D. Anđelković [1], G. Kocić[2], T. Anđelković[1] and I. Kostić[1]

[1] University of Niš, Faculty of Science and Mathematics, Department of Chemistry, Višegradska 33, 18000 Niš, Serbia (milica.chem@outlook.com(
[2] University of Niš, Faculty of Medicine, Bulevar dr Zorana Đinđića 81, 18000 Niš Serbia

ABSTRACT

Stability of pesticide stock solutions used in pesticide residue analysis is crucial for accomplishing reliable data on pesticide presence and quantification in the environment. This study was conducted to determine pesticide solution stability during a period. Investigation was done with the five-pesticide mixture solution (trifloxystrobin, kresoxim-methyl, chlorpyrifos, pendimethalin, boscalid) made of commercial pesticides and stored in refrigerator at 4 °C. Data collection was performed every 7 days, over 35 days. During this period, decline in pesticide response was observed. The most visible decline was observed after first 15 days of storage, after which the decline was less evident. Stability of pesticide stock solutions appeared affected even after short period of time, leading to a conclusion that in pesticide analysis is better to use freshly prepared stock solutions.

INTRODUCTION

Pesticide residue analysis is essential in the evaluation of the human and environmental exposure to pesticides. To achieve the reliable data on pesticide in the environment, laboratories have to check continuously the stability of stock standard solutions and replace them, which is time-consuming. Factors that can affect pesticide storage stability include temperature, storage period, physical and chemical properties of pesticides and in particular, matrix properties [1]. In pesticide residue analysis, i.e. in the step of recovery determination, commercial-pesticide solutions are more desirable to use than pure pesticide standards, since the commercial pesticides are those that are applied to crops. On the other hand, active ingredients in these solutions are more susceptible to degradation due to the presence of ballast materials. The aim of this study was to investigate the stability of multi-pesticide solution derived from commercially available pesticide formulations.

EXPERIMENTAL

Individual stock solutions of each pesticide were prepared at concentration of 1000 μg mL^{-1} (Table 1) by dissolving in appropriate solvents the following formulations: Signum® (BASF, Germany), Zato® 50 WG (Bayer Crop Science AG, Germany), Konzul® (Galenika Fitofarmacija AD, Serbia), Stroby® (Bayer Crop Science AG, Germany), Stomp® 330E (Bayer Crop Science AG, Germany). A mixed stock solution of pesticides (working solution) was prepared at concentration of 10 μg mL^{-1} for each pesticide in HPLC grade hexane by mixing individual stock solutions and it was kept at 4 °C. Internal standard solution was prepared by dissolving pure quinoline in HPLC grade ethanol to concentration of 10 μg mL^{-1}. Injection solutions were prepared by mixing internal standard with the aliquot of working solution and subsequent diluting with HPLC grade hexane to the final concentration of 1 μg/mL of each component. Pesticide quantification was performed with 5-level calibration method (linear regression). Individual solutions were made of high purity pesticide standards obtained from AccuStandard® (boscalid, kresoxim-methyl, trifloxystrobin, pendimethalin) and Sigma-Aldrich® (chlorpyrifos) at concentration of 50 μg mL^{-1} in HPLC grade hexane and were stored in freezer. Mixed solutions used for calibration were prepared freshly each time, prior to analysis from the stock standards at concentration range 0.25 – 5.0 μg mL^{-1}. Data acquisition was accomplished by injection of three replicates.

Table 1. Properties and qualification parameters of tested pesticides (quantifier ion is given in bold).

Pesticide	Class/Structure	Source	Molecular mass	Retention time (min)	Characteristic ions
Boscalid	Fungicide/Pyridine	Signum®	343.2	21.98	**140,** 281,342
Chlorpyrifos	Insecticide/Organothiophosphate	Konzul®	350.5	11.68	97, 199, **197**
Kresoxim-methyl	Fungicide/Strobiluri n	Stroby®	313.35	13.97	131, 207, **116**
Trifloxystrobin	Fungicide/Strobiluri n	Zato® 50 WG	408.37	15.56	131, 207, **116**
Pendimethalin	Herbicide/Dinitroaniline	Stomp® 330E	281.31	12.33	281, **252**

Agilent 6890 gas chromatograph equipped with 5973 Mass Selective Detector and 7683 autosampler was employed with following parameters of data acquisition method: splitless injector with 1 µL of injection volume, Agilent DB-5ms capillary column (0.25µm×250µm×30m) with initial helium flow of 1 mL/min and quadrupole mass filter with a transfer line temperature set at 280°C. Oven temperature ramps were: (1) initial temp. 60°C, hold 1 min; (2) 60-220°C, 20°C/min, hold 1 min; (3) 220-280°C, 5°C/min, hold 4 min). The mass spectrometer was used in electronic ionization (70 eV) operating full-scan acquisition mode. Both data acquisition and processing were accomplished by Agilent Chemstation® software.

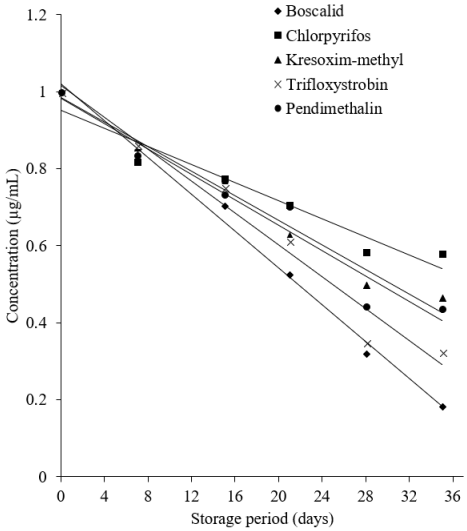

Figure 1. Changes in pesticides concentration over 35 days.

RESULTS AND DISCUSSION

Trend lines showing pesticide stability, were obtained by plotting the pesticide concentration against period of storage. All tested pesticides showed slow decline in concentration (Figure 1).

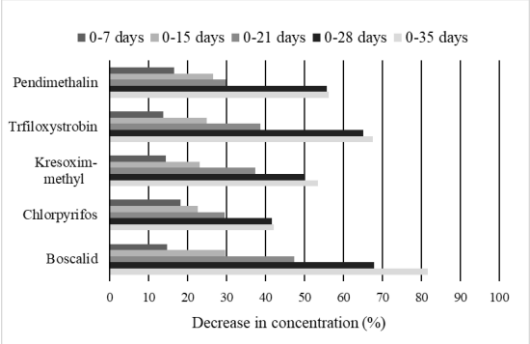

Figure 2. Loss in pesticides concentration in percentage of initial concentration (100%), over 35 days.

For stability of pesticide residues in stored commodities, OECD suggested that if the loss of a pesticide after storage is less than 30%, it is defined as stable and its corresponding storage period is considered as stable period

[2]. Obtained results showed that, after 7 days storage, decrease in pesticide concentration ranged from 13.79% for trifloxystrobin to 18.16% for chlorpyrifos. At the end of survey, decrease ranged from 42.06% for chlorpyrifos to 81.03% for boscalid (Figure 2).

The linear relationship (R^2>0.9) between storage period and ln (C_T/C_O), where C_O and C_T present pesticide concentration at the beginning of experiment and at intervals of 7 days, respectively (Figure 3), indicated that dissipation followed a pseudo-first order kinetics. Chlorpyrifos with $t_{1/2}$ value of 42.56 days was the most stable and boscalid with $t_{1/2}$ value of 17.85 days was the most unstable pesticide under the given conditions.

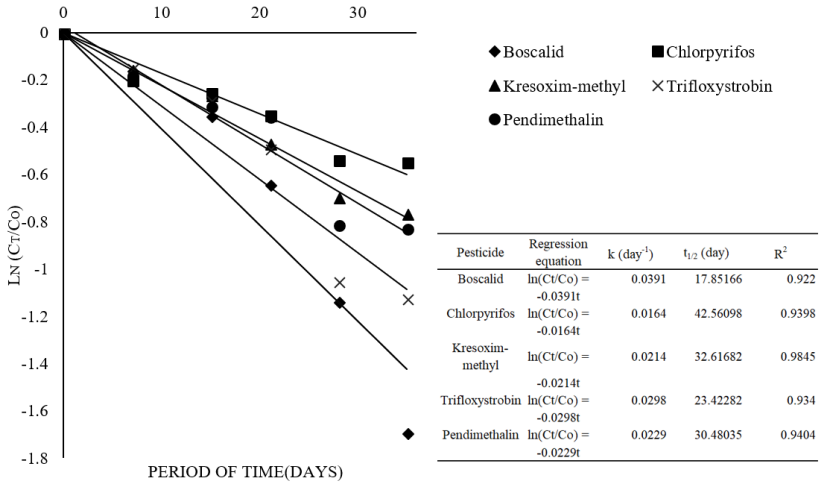

Pesticide	Regression equation	k (day^{-1})	$t_{1/2}$ (day)	R^2
Boscalid	ln(Ct/Co) = -0.0391t	0.0391	17.85166	0.922
Chlorpyrifos	ln(Ct/Co) = -0.0164t	0.0164	42.56098	0.9398
Kresoxim-methyl	ln(Ct/Co) = -0.0214t	0.0214	32.61682	0.9845
Trifloxystrobin	ln(Ct/Co) = -0.0298t	0.0298	23.42282	0.934
Pendimethalin	ln(Ct/Co) = -0.0229t	0.0229	30.48035	0.9404

Figure 3. Pseudo-first order kinetics model fitted to the stability of pesticides with deduced parameters.

CONCLUSION

The investigation demonstrated limited stability of a mixture of commercial pesticides. Monitoring of pesticide concentration showed pseudo-first order dissipation kinetics with different $t_{1/2}$ values. Therefore, in pesticide residue quantification, preparing fresh stock solutions is preferable.

Acknowledgement

This work was partially supported by the Ministry for Education, Science and Technological Development of the Republic of Serbia (Grant no. TR 31060).

REFERENCES

[1] B. Yanli, L. Fengmao, C. Fei, S. Pan, Food Chemistry, 2018, (250), 230-235.
[2] OECD, OECD Guidelines for the Testing of Chemicals, 2007, 1(7), 1-12.

SMALL-SCALE DEPTH DISTRIBUTION OF ^{40}K, ^{226}RA AND ^{232}TH IN UNCULTIVATED SOILS OF SOUTHEASTERN SERBIA

J. Petrović [1], R. Dragović [2], M. Đorđević [2], M. Đokić [2], M. Ćujić [1] Lj. Janković Mandić [1] and S. Dragović [1]

[1] University of Belgrade, Vinča Institute of Nuclear Sciences, Mike Petrovića Alasa 12- 14, 11000 Belgrade, Serbia. (petrovicj@vin.bg.ac.rs)
[2] University of Niš, Faculty of Sciences and Mathematics, Department of Geography, Višegradska 33, 18000 Niš, Serbia.

ABSTRACT
In this study, ^{40}K, ^{226}Ra and ^{232}Th activity concentrations were measured in soil profiles collected from five different locations in southeastern Serbia. The mean values of the ^{40}K, ^{226}Ra and ^{232}Th activity concentrations were found to be 674, 35.2, 43.5 Bq kg^{-1}, respectively. Homogeneous depth distribution of ^{40}K, ^{226}Ra and ^{232}Th in all analyzed soil profiles was observed and positive correlations between them were found. Based on ^{40}K, ^{226}Ra and ^{232}Th activity concentrations in the 0-5 cm soil layer, the mean value of total absorbed gamma dose rate was found to be 73.9 nGy h^{-1}.

INTRODUCTION
Soil is the main reservoir of long-lived radionuclides and the concentrations of the primordial radionuclides in soil are related to the radioactivity of the rock from which the soils originate. Gamma-emitting radionuclides present in soil, mainly uranium-238 and thorium-232 families and potassium-40, are the main sources of external radiation exposure. The world average activity concentrations of the ^{40}K, ^{226}Ra and ^{232}Th in soils were reported to be 412, 32 and 45 Bq kg^{-1}, respectively, and appear at different levels in the soils of each region in the world [1]. According to extensive study conducted by Dragović et al. (2012) the average activity concentrations of the ^{40}K, ^{226}Ra and ^{232}Th in surface soil from Serbia were 508 (range: 45-900), 33 (range: 8-88) and 36 (range: 9.5-84) Bq kg^{-1}, respectively [2]. Dragović et al. (2014) indicated that concentrations of primordial radionuclides in soils of Serbia are similar to those reported in neighbouring countries, since they belong to the same geological and metallogenical provinces (Carpatho-Balkanides, Dinarides, Serbian-Macedonian Mass) [3]. The aim of this study is to (1) determine the ^{40}K, ^{232}Th and ^{226}Ra activity concentrations in five uncultivated soil profiles, (2) assess the relationships between radionuclides

activity concentrations in soil profiles, (3) calculate the absorbed gamma dose rate based on ^{40}K, ^{226}Ra and ^{232}Th activity concentrations in the 0-5 cm soil layer and (4) compare results of the present study with corresponding values reported worldwide and in the country.

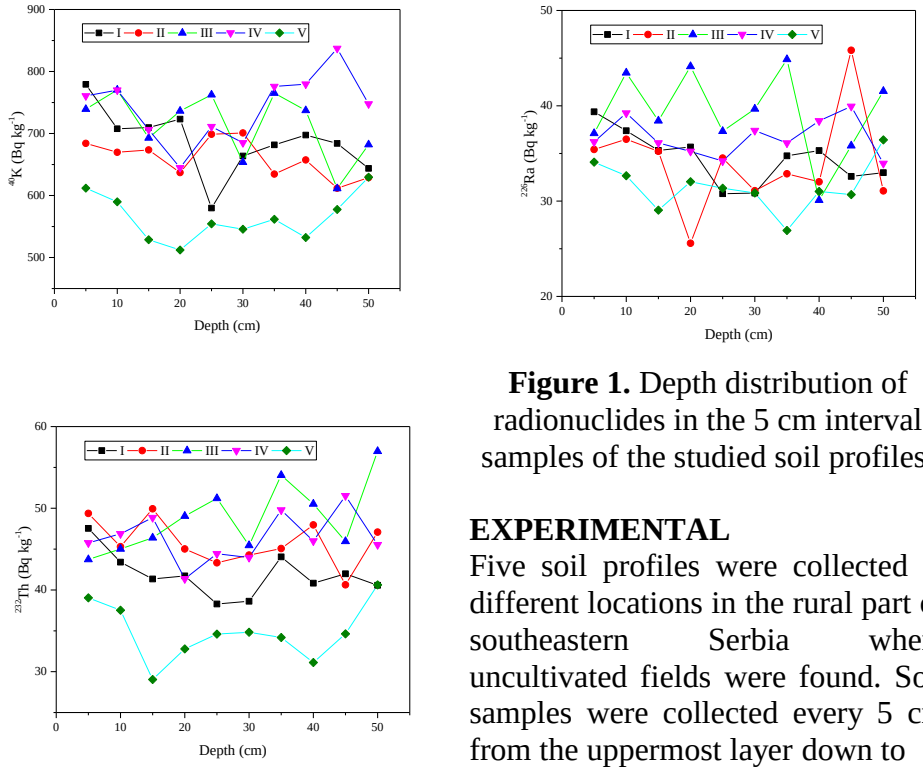

Figure 1. Depth distribution of radionuclides in the 5 cm interval samples of the studied soil profiles.

EXPERIMENTAL

Five soil profiles were collected at different locations in the rural part of southeastern Serbia where uncultivated fields were found. Soil samples were collected every 5 cm from the uppermost layer down to 0.5 m depth at each location, obtaining a total of 50 soil samples. The collected soil samples were dried, homogenized and passed through 2 mm sieve prior to radioactivity measurements on HPGe γ-ray spectrometer ORTEC-AMETEK. The calibration of the HPGe γ-ray spectrometer was carried out using a 0.5 L Marinelli calibration source MBSS2, and the calibration was checked using standard reference materials. The activities of ^{40}K, ^{226}Ra and ^{232}Th were determined from their gamma-ray lines. Gamma Vision 32 MCA emulation software was used to analyze gamma-ray spectra [4].

RESULTS AND DISCUSSION

Basic statistics of the ^{40}K, ^{226}Ra and ^{232}Th activity concentrations for each depth interval are presented in Table 1. The mean values of the ^{40}K, ^{226}Ra and ^{232}Th activity concentrations obtained in the study area (Table 1) fell

within the range of corresponding values reported for Serbian soils [2]. Studies conducted in the country indicated that variations in natural radionuclides concentrations can be associated to the differences in radioactivity levels of parent rocks [2, 3]. The depth distribution of ^{40}K, ^{226}Ra and ^{232}Th activity concentrations in soil profiles are presented in Fig. 1. Homogeneous depth distribution of radionuclides were observed, which is in accordance with results obtained in similar studies [5, 6]. Pearson correlation coefficients between ^{40}K, ^{226}Ra and ^{232}Th activity concentrations in soils are presented in Table 2. Significant positive correlations between radionuclides were found (Table 2), which indicates a common source.

The mean value of total absorbed gamma dose rate was found to be 73.9 (range: 64.8-79.3) nGy h^{-1}, std. deviation (SD): 5.4 nGy h^{-1}, which is higher than the worldwide average value of 58 nGy h^{-1} [1] but is close to the Serbian average value of 66.8 nGy h^{-1} [7]. The contribution of ^{40}K, ^{226}Ra and ^{232}Th to the total absorbed gamma dose rate varied with sampling locations (Fig. 2.).

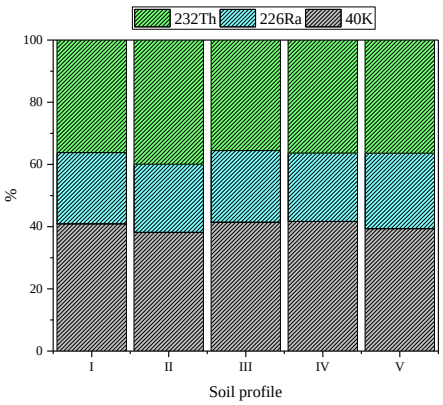

Figure 2. Relative contribution to the total gamma dose rate due to ^{40}K, ^{226}Ra and ^{232}Th.

CONCLUSION

Naturally occurring radionuclides (i.e. ^{40}K, ^{226}Ra and ^{232}Th) in studied soils exhibit a homogenous distribution with depth. To enable better understanding of the complex behaviour of these radionuclides in the soils further investigations should include analysis of vertical distribution of primordial radionuclides in different soil types as well as influence of biological and physicochemical soil properties on their spatial and vertical distribution.

Acknowledgement

This work was supported by the Ministry of Education, Science and Technological Development of the Republic of Serbia (Project no. III 43009).

Table 1. Basic statistics of the ^{40}K, ^{226}Ra and ^{232}Th activity concentration for each depth interval.

Soil depth	^{40}K (Bq kg^{-1})		^{226}Ra (Bq kg^{-1})		^{232}Th (Bq kg^{-1})	
(cm)	Mean	SD	Mean	SD	Mean	SD
0-5	715	67.7	36.4	2.0	45.1	4.0
5-10	702	75.7	37.8	3.9	43.6	3.6
10-15	662	75.9	34.8	3.5	43.1	8.5
15-20	651	89.5	34.5	6.7	42.0	6.0
20-25	661	89.7	33.6	2.7	42.4	6.3
25-30	650	61.0	34.0	4.2	41.4	4.5
30-35	684	90.0	35.1	6.5	45.4	7.4
35-40	681	94.6	33.4	3.4	43.3	7.7
40-45	664	104.2	37.0	6.1	42.9	6.3
45-50	666	50.3	35.2	4.0	46.2	6.7
0-50	674	76.4	35.2	4.4	43.5	5.9

Table 2. Pearson correlation coefficients between the radionuclides in soil.

	^{40}K (Bq kg^{-1})	^{226}Ra (Bq kg^{-1})	^{232}Th (Bq kg^{-1})
^{40}K (Bq kg^{-1})	1		
^{226}Ra (Bq kg^{-1})	0.573**	1	
^{232}Th (Bq kg^{-1})	0.772**	0.551**	1

**. Correlation is significant at the 0.01 level (2-tailed).

REFERENCES

[1] UNSCEAR (United Nations Scientific Committee on the Effects of Atomic Radiation), New York, United Nation, 2010.

[2] S. Dragović, Lj. Janković-Mandić, R. Dragović, M. Đorđević, in Radiation Exposure: Sources, Impacts and Reduction Strategies. D. Balenovic, E. Stimac (Eds.), Nova Science Publishers, Inc., New York, 2012.

[3] S. Dragović, Lj. Janković-Mandić, R. Dragović, M. Đorđević, M. Đokić, J.Kovačević,Journal of Geochemical Exploration 2014, **142**,4-10.

[4] ORTEC, 2001. Gamma Vision 32, Gamma-Ray Spectrum Analysis and MCA Emulation. Oak Ridge, Version 5.3.

[5] A. Navas, J. Soto, J. Machin, Applied Radiation and Isotopes 2002, **57**, 579-589.

[6] S. Dragović, B. Gajić, R. Dragović, Lj. Janković-Mandić, L. Slavković-Beškoski, N. Mihailović, M. Momčilović, M. Ćujić, Journal of Environmental Monitoring 2012, **14**, 127-137.

[7] S. Dragović, Lj. Janković, A. Onjia, Radiation Protection Dosimetry 2006, **121**, 297-302.

DETERMINATION OF RADIONUCLIDES IN CIGARETTES IN SERBIA AND THEIR ESTIMATED EFFECTIVE DOSES DUE TO THE SMOKING

Lj. Janković Mandić [1], M. Đolić [1], M. Ćujić [1], J. Petrović [1], A. Onjia [2] and S. Dragović [1]

[1] University of Belgrade, Vinča Institute of Nuclear Sciences, PO Box 552, 11001 Belgrade, Serbia (ljmandic@vin.bg.ac.rs)
[2]University of Belgrade, Faculty of Technology and Metallurgy, Karnegijeva 4, 11000 Belgrade, Serbia

ABSTRACT

In this work, the radionuclide activity concentrations (^{40}K, ^{137}Cs, ^{210}Pb, ^{226}Ra, ^{228}Ra) of 166 different cigarette samples, selected in 23 brands available on the Serbian market and corresponding effective doses due to smoke inhalation are reported. The average estimated annual effective dose: 4.6 μSv y^{-1} for ^{40}K, 203 μSv y^{-1} for ^{210}Po, 64 μSv y^{-1} for ^{226}Ra and 47 μSv y^{-1} ^{228}Ra due to the smoking exposure (8 cigarettes/day).

INTRODUCTION

Tobacco is a plant of the genus *Nicotiana* whose leaves are mostly used for smoking [1]. The cigarette is the most popular and worldwide consumed tobacco product. Tobacco products e.g. cigarettes contains small amounts of radioactive materials. Among the radionuclides which are found in cigarette tobacco, ^{210}Pb, ^{210}Po, ^{226}Ra, ^{228}Ra are characterized as a very high radiotoxic, ^{137}Cs as a high radiotoxic, ^{235}U and ^{238}U as a low radiotoxic, and ^{40}K has no classification [2]. The World Health Organization estimated that smoking will be fatal for 10 million people per year globally by the 2020 [3]. In Serbia, the average prevalence of tobacco use in 2016 was 38% (39% of the men and 37% of the women), with 2924 cigarettes per person per year (average 8 cigarettes per day) [4].

The aim of this paper is to determine the content of natural radionuclides (^{40}K, ^{210}Po, ^{226}Ra and ^{228}Ra) in cigarette tobacco of the most frequently used brands of cigarettes in Serbia and to estimate the annual effective dose due to radionuclides inhalation on adults.

EXPERIMENTAL

Radionuclide concentrations were determined in 166 samples of 23 brands of cigarettes frequently consumed in Serbia. The tobacco of each cigarette

was carefully separated from wrapping paper and filter. The content of cigarette packages was homogenized together and dried samples transferred to polyethylene containers of 100 cm^3 capacity, sealed and kept aside at least for four weeks to ensure equilibrium between ^{226}Ra and its daughters prior to being taken for gamma spectrometric analysis.

Radioactivity measurements were performed using coaxial HPGe detector (ORTEC-AMETEK, GEM 50195-P, 8192 channels) with an energy resolution of 1.95 keV at the 1.33 MeV of ^{60}Co and the relative efficiency of 46%. Gamma Vision 32 MCA emulation software was used to analyse gamma-ray spectra.The gamma-ray lines used for calculations of activity concentration were 352.9 (^{214}Pb), 609.3, 1120.3 and 1764.5 keV (^{214}Bi) for ^{226}Ra, 338.4, 911.1 and 968.9 keV (^{228}Ac) for ^{228}Ra, 1460.7 keV for ^{40}K, 661.6 keV for ^{137}Cs, and 46.5 keV for ^{210}Pb.

The activity concentration of ^{210}Po (A_{Po}) was estimated from that of its parent ^{210}Pb (A_{Pb}). It usually takes 24-30 months from the harvesting of tobacco leaves to their availability in the market. This means that six to seven half-lives of ^{210}Po are completed during this period and ^{210}Pb approaches the secular equilibrium in cigarette tobacco [5-6]. As it can be concluded that the radioactive equilibrium between ^{210}Pb and ^{210}Po was well accomplished at the time when measurements were conducted, the activity concentrations of ^{210}Po (A_{Po}) were calculated from the activity concentration of ^{210}Pb (A_{Pb}) as follows:

$$A_{Po}=1.02A_{Pb} \quad (1)$$

The annual effective dose, H_E (Sv y^{-1}), due to inhalation for smokers, was calculated according to the following equation:

$$H_E = 0.75 \times M_T \times Ci \times F \quad (2)$$

where M_T (kg y^{-1}) refers to the annual mass of tobacco consumed, (considering the average mass 0.8 g of tobacco per cigarette and assuming adults smoking 8 cigarettes (6.4 g of tobacco) per day, the annual consumption of tobacco in Serbia is estimated to be 2.34 kg y^{-1});

Ci (Bq kg^{-1}) refers to the activity concentration of the *i*-th radionuclide;
F (Sv Bq^{-1}) refers to the dose conversion factor: 2.1×10^{-9} Sv Bq^{-1} for ^{40}K, 3.3×10^{-6} Sv Bq^{-1} for ^{210}Po, 3.5×10^{-6} Sv Bq^{-1} for ^{226}Ra, 2.6×10^{-6} for ^{228}Ra; 0.75 is the fraction of the radionuclide activity concentration that is recovered from cigarette tobacco to cigarette smoke, as on the average, i.e. 75 % of the radioisotope in the cigarette tobacco was contained in the

cigarette smoke, which is partially inhaled and deposited in the lung tissues and 25 % was retained in the cigarette filter and ash [7-8].

RESULTS AND DISCUSSION

The activity concentrations of radionuclides in cigarette tobacco of commonly used brands in Serbia are presented in Table 1.

Table 1. The activity concentrations of radionuclides in cigarrete tobacco of commonly used brands in Serbia

BREND (number of samples)	Activity concentration (Bq kg^{-1} d.w.)				
	^{40}K	^{137}Cs	^{210}Po	^{226}Ra	^{228}Ra
T1 (4)	1250	<1.0	31	6.2	6.8
T2 (8)	1100	<0.8	23	4.5	5.0
T3 (7)	1180	<1.0	38	7.0	7.8
T4 (6)	1320	<1.0	44	7.2	7.6
T5 (8)	1450	<1.0	58	12.0	12.5
T6 (8)	1120	<1.0	45	9.0	8.0
T7 (9)	980	<1.0	31	5.0	6.3
T8 (11)	1100	<1.0	35	4.4	6.2
T9 (4)	1540	<1.0	28	5.7	7.3
T10 (8)	1210	<1.0	36	7.5	6.4
T11 (10)	1330	<0.6	23	10.2	9.2
T12 (5)	1480	<1.0	45	15.6	13.8
T13 (8)	1200	<1.0	18	14.2	16.5
T14 (7)	1630	<1.0	75	18.8	20.2
T15 (4)	1160	<1.0	42	12.4	10.0
T16 (12)	1000	<0.8	22	7.7	9.3
T17 (10)	970	<1.0	17	6.6	6.8
T18 (4)	1350	<1.0	39	15.5	17.5
T19 (8)	1270	<1.0	32	18.2	15.3
T20 (5)	1150	<1.0	28	11.4	9.2
T21 (6)	1410	<1.0	48	17.3	16.4
T22 (8)	1080	<1.0	24	10.6	8.3
T23 (6)	1260	<0.8	20	12.2	9.8
Mean	1240	<1.0	35	10.4	10.3
St.dev.	165	-	15	3.5	4.3
Annual effective dose H_E (μSv y^{-1})	4.6	-	203	64	47

Activity concentrations of ^{40}K in the tobacco leaves ranged from 970 to 1630 Bq kg^{-1} (average 1240 Bq kg^{-1}). The activity concentration of ^{210}Po ranges from 17 to 75 Bq kg^{-1} (average 35 Bq kg^{-1}). The activity

concentration of ^{226}Ra ranges from 4.4 to 18 Bq kg^{-1}(average 10.4 Bq kg^{-1}), while that of ^{228}Ra ranged 5.0 to 20.2 Bq kg^{-1} (average 10.3 Bq kg^{-1}). In all samples the activity concentrations of ^{137}Cs were below minimum detectable activity.

The annual effective dose to ^{40}K varied from 3.6 to 6.0 μSv y^{-1} (average 4.6 μSv y^{-1}). The highest contribution to the annual effective dose rate is derived from ^{210}Po (average 203 μSv y^{-1}), while for ^{210}Po varied from 98.5 to 434 μSv y^{-1}.The annual effective dose due to ^{226}Ra from 27 to 115 μSv y^{-1} (average 64 μSv y^{-1}) and to ^{228}Ra from 22.8 to 91.3 μSv y^{-1} (average 47 μSv y^{-1}).

CONCLUSION

The results obtained in this study pointed out that high contribution of the annual effective dose due to the inhalation of cigarette smoke to the total inhalation exposure due to natural radionuclides of 1.26 mSv [9]. Among analyzed radionuclides, the highest effective dose rate arises from ^{210}Po with 64%, ^{226}Ra (20%),^{228}Ra (15%) and ^{40}K (1%).

Acknowledgement

This work was supported by the Ministry of Education, Science and Technological Development of the Republic of Serbia (project number III 43009).

REFERENCES

[1] W.S. Godwin, V.R. Subha, K.M. Feroz, Curr. Sci., 2010, **98**, 681-686.
[2] ISO 2919. Radiation Protection Geneva, Switzerland, 1999.
[3] WHO. Tobacco Free Initiative., Oslo, Norway, WHO, 2000
[4] B. Kilibarda, N. Nikolić, The Results of Research on the Effects and Attitudes regarding the Law on Protection from Exposure to Tobacco Smoke, Institute of Public Health of Serbia, Dr Milan Jovanović Batut", Belgrade, 2016.
[5] A.E.M. Khater,. J. Environ. Radioactiv., 2004, **71**, 33-41.
[6] A. Sakoda, K. Fukao, A. Kawabe, T. Kataoka, K. Hanamoto, K. Yamaoka, Radiat. Prot. Dosim., 2012, **150**, 109-113.
[7] H.A. Shousha, F. Ahmad, Radiat. Prot. Dosim., 2012,**150**, 91-95.
[8] Lj. Janković Mandić, M. Đolić, D. Marković, D.Todorović, A. Onjia, S. Dragović, Radiat. Prot. Dosim., 2016, **168**, 111-115.
[9] UNSCEAR, Sources and Effects of Ionizing Radiation, New York, 2010.

POSSIBILITIES OF APPLYING NATURAL EXTRACTS AS ACID-BASE INDICATORS

A. Ivanković [1], A. Martinović Bevanda [2], M. Martinović [1], D. Peteović [1], M. I. Perić [1], F. Drmać [1] and S. Talić [2]

[1] Faculty of Agronomy and Food technology, University of Mostar, Biskupa Čule bb, 88000 Mostar, Bosnia and Herzegovina. (anitaivankovic@gmail.com)
[2] Department of Chemistry, Faculty of Science and Education, University of Mostar, Bosnia and Herzegovina, Matice hrvatske bb, 88000 Mostar, Bosnia and Herzegovina

ABSTRACT

The paper explores the possibility of using natural extracts as acid-base indicators. In addition to the standard pH indicators, the natural pH indicators may be used, such as red cabbage, beets, onions, chicory and spices curry and turmeric. They all have in common that in contact with acids and bases they change color, because they contain a compound that belongs to a group of plant pigments anthocyanins. In this paper were prepared water extracts of anthocyanins from above mentioned plants and their reaction on pH change is tested. The best results were obtained by the red cabbage extract. It gave the whole spectrum of colors depending on the pH change and its practical application was made in volumetric determination of citric acid comparing with standard indicators. The values of citric acid content in lemon, orange, grapefruit and lime juices volumetrically obtained using the red cabbage extract and phenolphthalein as a standard indicator show a high positive correlation (R^2 = 0.9983). Concluding that, the red cabbage extract can be used for some simple volumetric determinations.

INTRODUCTION

Some natural compounds react with color change in the presence of other substances. Most commonly we associate them with the acidity and the solubility of the solution. For example, when lemon juice (acid) is added to slice or barley tea, the tea color changes. Also, if you take red cabbage juice and add a bit of this extra to vinegar or solution of baking soda it will change the color again [1].

Many plants or parts of plants contain naturally colored chemicals from the group of anthocyanin compounds. They are red in acidic solutions and

blue in alkaline solutions. Anthocyanins are quite reactive and unstable compounds. They suffer reversible structural transformation with changing the pH and that has the greatest impact on the color. pH is defined as the cause of the greatest instability of anthocyanins, and their pigmentation mostly depends on the pH. The anthocyanins can be extracted with water or other solvents from a number of colored plants or plant parts, such as roots of golden beets [2], leaves (red cabbage) [1], cherry juice [3] and flowers [4, 5]. Red cabbage has potential to be used as a visual indicator of pH variations during storage of packaged food [6].

The aim of this paper is to show that extracts of some plants containing anthocyanins can be used as acid-base indicators.

EXPERIMENTAL

In this experiment, the extraction of anthocyanin from minced red cabbage, radish, cycles, purple port, curry and curcuma was carried out. Anthocyanin extraction from each of the above mentioned samples was performed using hot water. To determine the possibility of using natural extracts as a pH indicator, eight different solutions were used, which were used as reference and had different pH values. These solutions were then used in experiment to observe color change after mixing with plant extracts. For the success of the experiment it was necessary to determine the exact pH of the individual solutions.

The prepared lemon, grapefruit, orange and lime juice samples were titrated with a standardized solution of 0.1 mol dm^{-3} NaOH using aqueous red cabbage extract as indicator and then using phenolphthalein as a standard indicator to compare the results.

RESULTS AND DISCUSSION

In each of the experiments, the color difference between the first tube containing the lowest pH and the last one containing the highest pH solution was clearly seen. There were 12 experiments carried out with different plant extracts. The red cabbage extract proved to be the best natural pH indicator. The color spectra obtained by adding the red cabbage extract to each of the eight solutions of the known pH values can be clearly seen (Table 1). There is no clear difference only between the lowest and the highest pH values, i.e. strong acids and strong bases, but the change in color varies at other pH values. In an aqueous red cabbage extract, pigment anthocyanin is released. The anthocyanin molecule alters its color depending on the pH value of the used reference solution. The aqueous red cabbage extract was used as an indicator for volumetric determination of citric acid content in the juices of different citrus fruits (Table 2).

Table 1. Data on the reference solutions and color changes by adding an aqueous red cabbage extract

Solution	pH	Color before adding indicator	Color after adding indicator
HCl	1.54	colorless	red
CH_3COOH	3.30	colorless	dark pink
NaCl	7.97	colorless	light purple
KCl	8.07	colorless	purple
$NaHCO_3$	8.15	colorless	dark blue
Dishes detergent	8.71	colorless	light green
Laundry detergent	10.56	white	green
NaOH	12.73	colorless	olive green

Table 2. Content of citric acid in different juice samples (expressed in %) obtained volumetrically in the presence of red cabbage extract (ERC) and phenolphthalein (FF)

	Indicator	Citric acid (%)			Mean value	SD
Lemon	ERC	6.72	6.60	6.60	6.64	0.069282
	FF	6.60	6.66	6.60	6.62	0.034641
Grapefruit	ERC	2.63	2.69	2.69	2.67	0.034641
	FF	2.63	2.82	2.69	2.71	0.097125
Orange	ERC	0.83	0.83	0.90	0.85	0.040415
	FF	0.87	0.81	0.81	0.83	0.034641
Lime	ERC	6.02	6.08	5.95	6.02	0.065064
	FF	6.21	6.27	6.14	6.21	0.065064

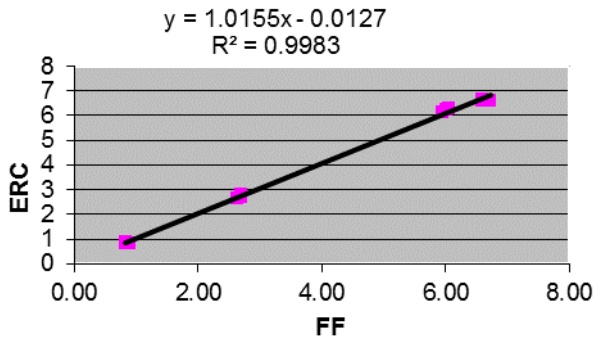

Figure 1. Correlation between the values of citric acid content in the citrus juices obtained by red cabbage extract (ERC) and phenolphthalein (FF) as indicators

The values of citric acid content in lemon, orange, grapefruit and lime juices volumetrically obtained using the red cabbage extract and phenolphthalein as a standard indicator show a high positive correlation (R^2 = 0.9983) (Figure 1). In this case it is a simple experiment that is applicable in laboratory chemistry teaching.

CONCLUSION

Among all the extracts tested, only the red cabbage extract can be used as a pH indicator. He showed the clearest spectrum of color at different pH values used, from acid to alkaline.

The application of the red cabbage extract water proved to be applicable in a specific experiment. This simple experiment is recommended to be performed in the laboratory chemistry teaching.

Acknowledgement

This work was supported by the Federal Ministry of Education and Science of the Federation of Bosnia and Herzegovina (Grants No. 05-39-2389-1/17, November 6th 2017).

REFERENCES

[1] A. Munmai and E. Somsook, The Determination of the pKa of Red Cabbage Anthocyanin by the Spectrophotometric Method and Nonlinear Curve Fitting, Chem. Educator 2011, 16: 1–3.

[2] P. Thote, Green chemistry: study of acid-base indicator property of golden beet root, Social Issues and Environmental Problems, 2015, 3 (9).

[3] P. M. A. Khan and M. Farooqui, Analytical Applications of Plant Extract as Natural pH Indicator: A Review, J Adv Scient Res, 2011, 2(4): 20-27.

[4] G. Kavitha, V. Aswathi, S. G. Chinju, R. Rakhi and A. Elessy, Flowers as natural indicators, World Journal of Pharmaceutical Research, 2017, 6(7): 1217-1221.

[5] T. R. Doctor and RA. P. Cababat, Blood leaf (*Iresine herbstii*) extract used as an indicator of soil pH, nternational Journal of Scientific and Research Publications, 2014, 4(10).

[6] S. Pourjavaher, H. Almasi, S. Meshkini, S. Pirsa and E. Parandi, Development of a colorimetric pH indicator based on bacterial cellulose nanofibers and red cabbage (*Brassica oleraceae*) extract, Carbohydrate Polymers, 2017, 156(20): 193-201.

L *– Phase Boundaries, Colloids, Liquid Crystals, Surface-Active Substances*

TUNING THE PROPERTIES OF AQUEOUS BIPHASIC SYSTEM BASED ON BLOCK COPOLIMER FOR THE EXTRACTION OF SELECTED ALKALOIDS

A.Dimitrijević, A.Jocić, N.Zdolšek and T.Trtić-Petrović

Vinča Institute of Nuclear Science, University of Belgrade, Mike Petrovića Alasa 12-14, 11351, Vinča, Belgrade, Serbia. (daleksandra@vinca.rs)

ABSTRACT

In this work the novel aqueous biphasic systems (ABSs) based on Pluronic® PE6200 (PL6200), low-foaming, nonionic triblock copolymer, were studied and their abilities to extract caffeine and nicotine from aqueous solution were assessed. Aqueous solutions of cholinium-based ionic liquids (ILs) were used to induce phase separation as the second phase-former. The obtained results indicate that investigated systems are able to induce two aqueous phases and to extract selected alkaloids with high efficiencies.

INTRODUCTION

The advantages of aqueous biphasic systems based on ionic liquids (IL-ABSs) over other liquid−liquid extraction systems are well known. IL-ABSs allow to develop adequate extraction platforms for many biomolecules through the wise selection of the phase-forming components and to finely tune their lipophilic−hydrophilic nature.[1] Cholinium-based ILs are bio-based, low-toxic, high biodegradable and biocompatible. They have proved to be a good option for purification and extraction of added-value biomolecules such as proteins, antibodies, pharmaceuticals etc. [2]. As the second phase-forming component Pluronic PE6200 (trademark registered from BASF) with a molecular weight of 2450 g/mol was used. The introduction of copolymers in the cholinium IL-based ABSs gives "more tunable" and selective systems comparing to traditional ABSs. Pluronics are triblock copolymers (Figure 1) that are currently used, among others, as a pharmaceutical excipients [3]. Their backbones are formed by ethylene oxide (EO) blocks at both terminals and propylene oxide (PO) blocks in the middle

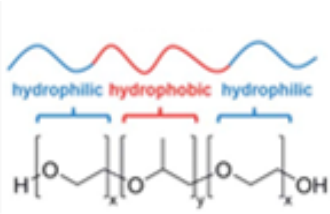

Figure 1. Molecular structure of a Pluronic® triblock copolymer

with distinct EO/PO ratios. Pluronics are often labeled as $(EO)_x$- $(PO)_y$-$(EO)_x$. Pluronics may be either highly lipophilic or hydrophilic depending on their EO/PO composition. They are very suitable for ABS formulations given that they present convenient properties (a) their amphiphilic nature allows the solubilization of hydrophobic molecules, (b) thermo-sensitivity facilitating recovery, (c) capacity to be designed with intermediate degrees of hydrophobicity and (d) pronounced biocompatible nature [4]. After addressing the potential of PL6200 to induce ABS with cholinium based ILs, these systems will be investigated for the extraction of alkaloids (caffeine and nicotine) from aqueous solutions.

EXPERIMENTAL

Materials. The copolymer used is a poly(ethylene glycol)-block-poly(propylene glycol)-block-poly(ethylene glycol) with an average molecular weight of 2450 g mol^{-1} containing 20 percentage of polyethylene glycol (Pluronic PE6200, BASF, Germany). Cholinium chloride, [Ch][Cl] cholinium dihydrogencitrate, [Ch][DHCit], cholinium bitartrate, [Ch][Bit], caffeine and niacin were supplied by Sigma-Aldrich. Cholinium dihydrogen phosphate, [Ch][DHP] and cholinium acetate, [Ch][Ac] were purchased from Iolitec.

Determination of Phase Diagrams. The ternary phase diagrams were determined by the cloud point titration method at 25 °C and atmospheric pressure [1].

Partitioning of alkaloids. The extraction abilities of the studied ABS were carried out by fixing mixture point at the biphasic zone of the ternary phase diagram. Taking into account the distinct aptitudes to undergo phase separation, the following ternary mixture compositions were selected: 25% PL6200 + 25% IL + 50% of aqueous solution of alkaloid. Vigorous agitation was used, and at least 12 h of equilibration time was allowed. After separating the phases, they were weighed and the alkaloids content in each phase assayed by UV spectroscopy using a Shimadzu UV-1800 spectrophotometer at wavelengths of λ_{caf} = 275 nm and λ_{nic} = 282 nm. The partition coefficients of caffeine, K_{caf} and nicotine, K_{nic} were determined as the ratio of its concentration in the PL6200-rich and IL-rich phases.

RESULTS AND DISCUSSION

Ternary phase diagrams were determined for each PL6200 based ABS {IL + PL6200 + H_2O} at 25 °C under atmospheric pressure (Figure 2). For a fixed concentration of copolimer (25%), the tendency of the ILs to form ABS follows the order: [Ch][DHP] > [Ch][Ac] > [Ch][Bit] > [Ch][Cl]. In fact, the behaviour of the higher melting cholinium-based ILs such as studied

[Ch][DHP], [Ch][Ac], [Ch][Bit] and [Ch][Cl] with melting temperatures 392, 358, 422 and 575 K, respectively, are governed mainly by solvation in water and their specific affinity for water [5]. This pattern is a direct consequence of the ILs that act as the salting-out species.

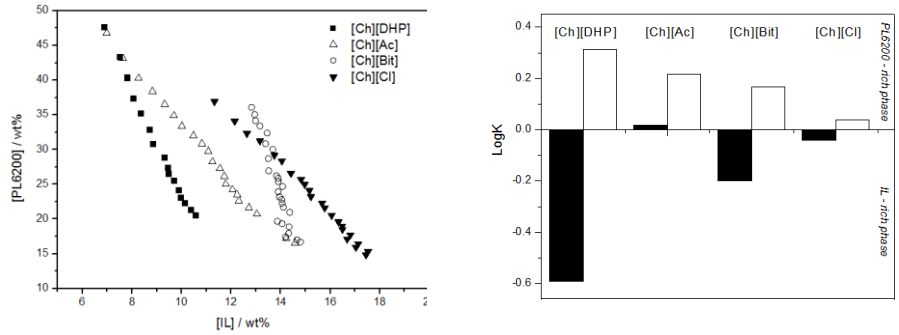

Figure 2. (a) Phase diagrams for the ABSs { IL + PL6200 + H_2O} at 25 °C and atmospheric pressure; (b) partition coefficients of caffeine (open bars) and nicotine (solid bars)

After the characterization of the studied ABS by the determination of their phase diagrams they were additionally evaluated in their ability to extract the alkaloids. Figure 2 depicts the results obtained for the partition coefficients of caffeine and nicotine in the several cholinium IL-based ABS. Caffeine preferentially partitioned to the PL6200-rich phase ($K_{caf} > 1$). The results also show that the K_{caf} values increase with increasing hydrophylic character of cholinium based ILs in order: [Ch][DHP] > [Ch][Ac] > [Ch][Bit] > [Ch][Cl]. Caffeine does not suffer speciation in a large range of pH values (pK_{a1}/pK_{a2} = 0.12 / 10.5) which means that electrostatic interactions between the IL ions and charged solutes do not play a significant role in the partition trend. Caffeine is only moderately hydrophilic ($logK_{ow}$ = –0.63, where K_{ow} is partition coefficient in the octanol/water system) so its partitioning is directly related with the relative hydrophobicity of phases. Nicotine presents lower affinity for water-rich phases ($logK_{ow}$ = -0.04) but unlike caffeine, is positively charged in the pH range of phases. This supports the fact that electrostatic interactions play the important role in nicotine partitioning. The results show that nicotine preferentially migrated to the IL-rich phase ($K_{nic} < 1$) except for the ABS based on [Ch][Ac] where nicotine preferentially migrates to the PL6200-rich phase. This difference can be attributed to the intrinsic nature of IL anions.

Table 1. The extraction efficiencies of caffeine (EE_{caf}) and nicotine (EE_{nic}) for the studied ABS {IL+PL6200+water} based on cholinium ILs

IL	EE_{nic}, %	EE_{caf}, %
[Ch][DHP]	33,88	82,15
[Ch][Ac]	59,38	67,36
[Ch][Bit]	50,51	78,58
[Ch][Cl]	42,11	39,63

In the Table 1, the extraction efficiencies (EE) of caffeine and nicotine in PL6200-rich phase are presented. It can be seen that EE of caffeine and nicotine are the highest for [Ch][DHP] based ABS. But it should be noted that alkaloids migrate to the different phases, caffeine in PL6200-rich phase while nicotine goes to IL-rich phase. So this fact can be used for the efficient separation of these alkaloids.

CONCLUSION

The novel ABSs based on Pluronic® PE6200 and cholinium ILs were investigated and their abilities to extract caffeine and nicotine from aqueous solution were studied. It can be concluded that studied biocompatible aqueous biphasic platform has great potential for selective extraction of alkaloids.

Acknowledgement

This work was supported by the Ministry of Education, Science and Technological Development of Serbia under project contracts III 45006.

REFERENCES

[1] M.G. Freire, A.F.M. Cláudio, J.M.M. Araújo, J.A.P. Coutinho, I.M. Marrucho, J.N.C. Lopes, L.P.N. Rebelo, Chemical Society Reviews, 2012, 41, 4966-4995.

[2] M. Petkovic, J.L. Ferguson, H.Q.N. Gunaratne, R. Ferreira, M.C. Leitão, K.R. Seddon, L.P.N. Rebelo, C.S. Pereira, Green Chemistry, 2010, 12, 643-649.

[3] A. Pitto-Barry, N.P.E. Barry, Polymer Chemisty, 2014, 5, 3291–3297.

[4] F.A. E Silva, R.M.C. Carmo, A.P.M. Fernandes, M. Kholany, J.A.P. Coutinho, S.P.M. Ventura, ACS Sustainable Chemistry and Engineering, 2017, 5, 6409–6419.

[5] J.F.B. Pereira, K.A. Kurnia, O.A. Cojocaru, G. Gurau, L.P.N. Rebelo, R.D. Rogers, M.G. Freire, J. A. P. Coutinho, Physical Chemistry Chemical Physics, 2014, 16, 5723–5731.

PROTIC IONIC LIQUIDS AS TAILORS OF POLYMER/INORGANIC SALT BASED AQUEOUS BIPHASIC SYSTEMS PERFORMANCES

A. Jocić[1], A. Dimitrijević[1], M. Vraneš[2], S. Gadžurić[2] and T.Trtić-Petrović[1]

[1] Laboratory of Physics, Vinča Institute of Nuclear Sciences, University of Belgrade, Belgrade, Serbia (daleksandra@vinca.rs)
[2] Department of Chemistry, Biochemistry and Environmental Protection, Faculty of Sciences, University of Novi Sad, Trg Dositeja Obradovića 3, 21000 Novi Sad, Serbia

ABSTRACT
In this work, the application of newly synthesized protic ionic liquids as adjuvant in building aqueous biphasic systems based on polymer and inorganic salt, as well as their effect on the extraction of selected dyes is studied. The obtained results show that the addition of small amount of PIL reduces the biphasic region, modifies the polarity of the polymer-rich phase and change the extraction performance of the ABS.

INTRODUCTION
Protic ionic liquids (PILs) are a subset of ionic liquids. The key characteristic of PILs is possibility to build up a hydrogen-bonded network due to presence of a proton on the cation [1]. The main advantages of PILs comparing to aprotic ILs are the low cost and simplicity of their synthesis [1]. Aqueous biphasic system (ABS) is a green alternative to classic organic-aqueous extraction and can be formed by mixing aqueous solutions of two polymers, polymer and salt or two salts at appropriate concentrations or at a particular temperature. The two phases are mostly composed of water and enriched in one of the solutes.

Polyethylene glycol (PEG) is a polymer commonly used in the preparation of ABS, due to its favorable characteristics in terms of biodegradability, toxicity and cost-effectiveness [2]. Their application has been limited by the low polarity range between coexisting phases [3] and low selectivity [4]. Recently, it has been shown that the use of ILs as adjuvants permits the fine tuning of the characteristics of either the salt- or polymer-rich phase in a conventional ABS [5]. This allows an efficient and tailored control of the partition coefficients and high extraction efficiency [3].

The aims of this study are investigation of the newly synthetized PILs as the adjuvant in classical polymer-salt ABS in order to develop an alternative

technique to modify PEG-rich phase characteristics. The influence of seven hydroxypropilamonium based PILs on ABSs {H_2O + PEG + K_2CO_3} was addressed. The effect of the PIL chemical structure on the partition coefficients and extraction efficiencies of different polarity dyes (Rhodamine B, RB; Orange II, OII; Remazol brilliant blue R, RBBR; Congo red, CR) as model molecules were evaluated and compared with the results where no PIL was added.

EXPERIMENTAL

Materials. PEG 2000 (2000 g mol^{-1}) and K_2CO_3 acquired from Sigma Aldrich. The synthesized PILs contain the same 2-hydroxypropilamonium ([2OHC3NH_3]) cation and following anions: formate ([Fo]), chloroacetate ([ClAc]), trichloroacetate ([TClAc]), trifluoro-acetate ([TFAc]), trichloropropanoate ([ClPr]), hydroxyl(phenyl)acetate ([MA]) and hydroxybutanoate ([OHBu]). The purity of the PILs was confirmed by NMR.

Experimental procedure. The phase diagrams for the ternary {PEG2000 + K_2CO_3 + H_2O} and the pseudo-ternary ABSs {PEG2000 + K_2CO_3 + H_2O + 5% PIL} were constructed at 296.15 K and atmospheric pressure by cloud point titration method [3]. The experimental data were fitted using Merchuk equation [6]. For the partition studies a mixture point was selected into the biphasic region composed of 26% PEG 2000, 10% K_2CO_3, 59% H_2O and 5% PIL. The partition coefficient of each dye, K_{dye}, is defined as the ratio of the dye concentration in the PEG2000-rich and salt-rich phase.

RESULTS AND DISCUSSION

Initially, the phase behavior of {PEG2000 + K_2CO_3 + H_2O} ABS in the presence of newly synthesized PILs used as adjuvants ([2OHC_3NH_3][Fo], [2OHC_3NH_3][ClAc], [2OHC_3NH_3][TClAc], [2OHC_3NH_3][TFo], [2OHC_3NH_3][ClPr], [2OHC_3NH_3][MA] and [2OHC_3NH_3][OHBu]) was studied.

The experimentally obtained solubility curves are reported in Fig. 1, showing the impact of the PIL anion on the ABS formation. In all investigated systems, the presence of 5% PIL reduce the biphasic region i.e. the binodal curves of the PIL-containing ABS {PEG2000 + K_2CO_3 + H_2O + 5% PIL} are always further from the axis origin comparing to the conventional ABS {PEG2000 + K_2CO_3 + H_2O}. The addition of PILs decrease hydrophobicity of the PEG-reach phase, and consequently more inorganic salt is needed to induce two phases. The influence of the PIL anion nature on building ABS

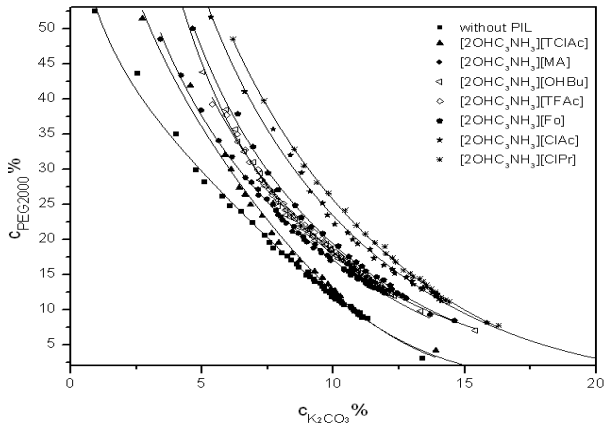

Figure 1. The phase diagrams of the ABSs {PEG-2000 + K_2CO_3 + H_2O + 5% PIL} at 296.15 K and atmospheric pressure.

follows the order: [TClAc] > [MA] > [OHBu] ≈ [TFAc] > [Fo] > [ClAc] > [ClPr].

Also, the effect of PIL's addition as the adjuvant in extraction of the selected dyes was investigated hereby. Four dyes RB, OII, RBBR and CR with different polarity from highly hydrophilic (RBBR: log D = -2.95, where log D is partition coefficient in the octanol-water system)) to hydrophobic (RB: log D= 2.81) were chosen for the study. The results of the partition experiments are shown in Fig. 2. It is clear from the figure that all dyes preferentially migrate to the PEG-rich phase. In all studied ABS highly hydrophilic dyes, RBBR and CR (logD = -2.22) are completely extracted in PEG-reach phase, it means that addition of PILs does not influence on partitioning. The slightly lower partitioning was obtained in the case of less hydrophilic dye OII (logD = -1.47) comparing to RBBR and CR, and should be mentioned that addition of PILs increase partitioning of OII comparing to system without PIL. The partitioning of the hydrophobic dye, RB, is significantly lower comparing to other targeted dyes. Also, all studied PILs decrease partitioning of RB e.g. but in different degree e.g. addition of [2OHC3NH_3] [ClPr] ten times decrease partition comparing to ABS without adjuvant. These

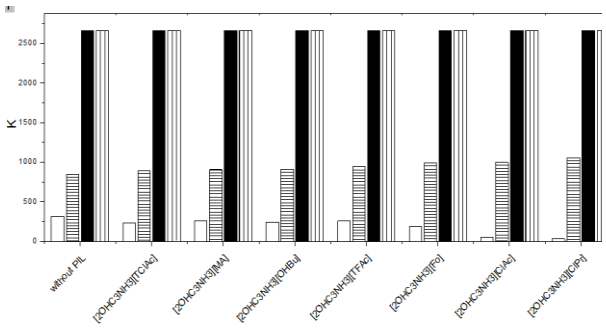

Figure 2. The effect of PILs as the adjuvant in ABS {PEG-2000 + K_2CO_3 + H_2O + 5% PIL} on partitioning (K) of the targeted dyes. Legend: RB – open bar, O II – horizontal pattern bar, RBBR – solid bar and CR – vertical pattern bar.

results represent a platform for application of ABS with PILs as an adjuvant for selective separation of different polarity dyes.

CONCLUSION

The effect of PILs as adjuvants in the ABS {PEG-2000 + K_2CO_3 + H_2O + 5% PIL} on building ABS and partitioning of the selected dyes was investigated. It is shown that all PILs increase the miscibility of polymer phase compared to the system without PIL i.e. increase polarity of the PEG-reach phase. The addition of the PILs as adjuvants in ABS was modified characteristics of the PEG-rich phase by increasing its polarity and extraction efficiency of hydrophilic dyes. It is shown that addition of PILs could improve selectivity of ABS.

Acknowledgement

This work was supported by the Ministry of Education, Science and Technological Development of Serbia under project contracts III 45006 and ON 172012.

REFERENCES

[1] T. L. Greaves, C. J. Drummond, Chemical Reviews, 2015, 115, 11379–11448.
[2] J. H. P. M. Santos, F. A. E Silva, J. A. P. Coutinho, S. P. M. Ventura, A. Pessoa, Process Biochemistry, 2015, 4, 661–668.
[3] M. G. Freire, J. F. B. Pereira, M. Francisco, H. Rodríguez, L. P. N. Rebelo, R. D. Rogers, J. A. P. Coutinho, Chemistry A European Journal, 2012, 18, 1831–1839.
[4] A. F. Cláudio, J. F. B. Pereira, P. D. McCrary, M. G. Freire, J. A. P. Coutinho, R. D. Rogers, Physical Chemistry Chemical Physics, 2016, 18, 30009–30019.
[5] J. F. B. Pereira, Á. S. Lima, M. G. Freire, J. A. P. Coutinho, Green Chemistry, 2010, 12, 1661.
[6] J. C. Merchuk, B. A. Andrews, J. A. Asenjo, Journal of Chromatography B: Biomedical Sciences and Applications, 1998, 711, 285–293.

FLUORIMETRIC STUDIES OF MICELLAR PROPERTIES OF CETYLTRIMETHYLAMMONIUM BROMIDE IN ACETONITRILE-WATER MIXTURE

A. Janošević Ležaić[1], L. Pavun[1], D. Đikanović[2], J. Goronja[1], A. Malenović[1] and N. Pejić[1]

[1]*University of Belgrade-Faculty of Pharmacy, Vojvode Stepe 450, 11000 Belgrade, Serbia*
[2]*University of Belgrade - Institute for Multidisciplinary Researches, Kneza Višeslava 1, 11030 Belgrade, Serbia*

ABSTRACT

Aggregation of the cationic surfactant cetyltrimethylammonium bromide (CTAB) in water (W) and acetonitrile–water (ACN–W) mixtures of different composition (10–20% (v/v) of ACN) was studied through fluorescence measurements. The CTAB critical micellar concentration (CMC) and the micelle aggregation number (N_{agg}) were determined at T = 22.0 °C. It was found that for increasing volume ratios of ACN to W, the CMC value attains a minimum (1.22 mM) at 15% (v/v) ACN while N_{agg} is continuously decreasing as ACN content in the ACN–W mixture increases. The effect of this dipolar aprotic solvent on the CTAB micelle formation can be interpreted in terms of its considerably hydrogen bonding ability and influence on balk-phase properties (solvophobic effect).

INTRODUCTION

When dissolved in a solvent (polar or nonpolar), CTAB, as other surfactants, under certain conditions (solvent, temperature, etc.) undergoes self-aggregation (micellization) forming at a specific surfactant concentration, the so-called critical micelle concentration (CMC), microheterogeneous supramolecular structures (micelles) that exist in equilibrium with the surfactant monomers from which it is formed. The average number of surfactant monomers in a micelle is referred to as micellar aggregation number (N_{agg}). These characteristic surfactant properties, CMC and N_{agg}, depend on the hydrocarbon tail length of the surfactant, the nature of counter-ion and on the ionic strength of the bulk.

aleksandra.janosevic@pharmacy.bg.ac.rs

As known, the very presence of even extremely small amounts of organic solvents in aqueous micellar solution, affects various micellar parameters (CMC, degree of counterion dissociation, N_{agg}, etc.). A particular organic solvent can be incorporated to some degree into the micelles, which causes changes in the surfactant aggregates characteristics either by solvent incorporation into the micellar aggregates or by modifying the bulk-phase properties (solvophobic effect). Changing solvent characteristics, allows us to examining the role of the aforementioned solvophobic effect and provides the increasing use of surfactants in applications which require water-free or water-poor media (as lubricants or cleaners).

In this work, the influence of ACN on micellar properties of CTAB, was studied using steady-state fluorescence. Recently, we have investigated the effects of this co-solvent on the micellization of CTAB, by conductometry [1]. In the present work our study is extended to ACN–W mixtures with different co-solvent composition (10–20 % (v/v)) at T = 22.0 °C. For those different ACN contents, the CMC and N_{agg} were determined in order to clarify the effect of ACN on CTAB micellization.

EXPERIMENTAL

Cetyltrimethylammonium bromide (Sigma-Aldrich), acetonitrile (J.T. Baker), pyrene (Sigma-Aldrich) and cetylpyridinium chloride (CPC, Krka) were used without any pretreatment.

Both the CMC and N_{agg} of CTAB in different media were determined by performing steady-state fluorescence measurements (using pyrene as the fluorescent probe) and static quenching method (using cetylpyridinium chloride, CPC as the quencher). The Fl3-221 P spectrofluorimeter (JobinYvon, Horiba, France), equipped with a 450W Xe lamp as an excitation source and a photomultiplier tube as detector, was used. The slits on the excitation and emission beams were both set at 1 nm. All measurements were performed at 22.0 ± 0.1 °C using a Peltier element. The excitation wavelength was 335 nm. The fluorescence emission spectra were recorded in the range of 350–500 nm.

For CMC determinations, fluorescence spectra of solutions with different CTAB concentrations (0.2–5.6 mM) and constant pyrene concentration (1 μM) in both W and ACN–W mixtures were recorded. For the N_{agg} determinations, solutions with constant concentrations of both pyrene (2 μM) and CTAB (20 mM) were prepared. Then, fluorescence quenching was done by the addition of CPC, the concentration of which varied in the range 0 – 100 μM.

The CMC values of CTAB in different systems were determined with the pyrene emission vibrational fine structure method, the so-called pyrene 1:3 ratio method [2]. So, the pyrene (1 μM) fluorescence emission intensities of the first (I_1) and third (I_3) vibrational peaks ratio (I_1/I_3) with respect to the CTAB concentration in both, W and ACN–W mixtures at T = 22.0 °C were identified as typical Boltzmann type sigmoidal functions.

RESULTS ANS DISCUSSION

The CMC values were obtained fitting the pyrene 1:3 ratio data versus the total surfactant concentration to the sigmoid of the Boltzman type. Thus, the CTAB concentrations corresponding to the interception point of the horizontal and the steep parts of the 1:3 ratio plots, the CMC values, are listed in Table 1. To calculate the N_{agg}, steady-state fluorescence quenching measurements were used [3]. Briefly, the ratio of the logarithm of emission fluorescence intensity for surfactant solutions in the absence of quencher (I_0) and in the presence of the quencher (I_Q) was related to the total concentration of surfactant ([C]) as well as to the concentration of the quencher [Q]:

$$ln\frac{I_0}{I_Q} = \frac{N_{agg}\,[\mathrm{Q}]}{[\mathrm{C}]-\mathrm{CMC}}$$

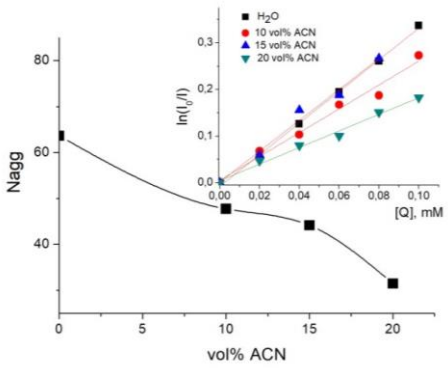

Figure 1. The N_{agg} versus the volume fraction of ACN in ACN–W mixtures. Insert: Plots of $\ln(I_0/I_Q)$ at 335 nm versus concentration of quencher [Q]; concentration of CTAB is 20 mM

The values of N_{agg} calculated from the slopes of the obtained linear plots $\ln(I_0/I_Q) = f([Q])$ (see the insert in Fig. 1.), are all summarized in Table 1.

In the mixed ACN–W solutions, N_{agg} decreases with ACN content increasing (Fig. 1). A similar type of decrease was obtained for CTAB by addition of some other polar organic solvents, such as ethanol [4]. The obtained ″regular″ behavior of ACN can be explained by the fact that ACN could break the ordered structure of water molecules around the micelles and replace those molecules in the micelle solvent shell [5].

Table 1. The CMC and Nagg of CTAB in W as well as in ACN–W mixtures

Vol% of ACN	CMC (mM)	N_{agg}
0	1.20	64
10	1.30	48
15	1.22	44
20	2.30	32

CONCLUSION

Micellar properties of CTAB in W and ACN–W mixtures were determined at constant temperature, T = 22.0 °C, using steady-state fluorescence measurements. In the examined range of ACN content in aqueous mixtures, the CMC values have a minimum at intermediate ACN concentration, while N_{agg} decreases for increasing ACN content in ACN–W mixtures. The effect of this co-solvent on the CTAB micelle formation can be interpreted in terms of ACN interaction with W and its possible influence on solvophobic interactions related to micellization.

Acknowledgement

This work was partially supported by the Ministry for Education, Science and Technological Development of the Republic of Serbia (Grants no. 172015, 172052, 172016, 173017).

REFERENCES

[1] Goronja J., Janošević Ležaić A., Dimitrijević B., Malenović A., Stanisavljev D., Pejić N., Hem. Ind., 2016, **70**(4), 485-492.
[2] Aguiar J., Carpena P., Molina-Bolivar J.A., Carnero Ruiz C., J. Colloid Interface Sci., 2013, **258**, 116-122.
[3] Kabir-ud-Din, Koya P.A., J. Mol. Liq., 2011, **158**, 111-118
[4] Li W., Han Y.-C., Zhang J.-L., Wang B.-G., Coll. J., 2005, **67**, 186-191.
[5] Kabir-ud-Din, Siddiqui U.S., Kumar S., Dar A.A., Colloid. Polym. Sci., 2006, 284, 807-812.

MICELLIZATION OF MIXTURES CONTAINING SODIUM-LAURETH SULPHATE AND POLYSORBATE SURFACTANTS

S.M.Blagojević[1], N. Erić[2] and M. Nešović[3]

[1]*University of Belgrade–Faculty of Pharmacy, Department of Physical Chemistry and Instrumental Methods, Vojvode Stepe 450, Belgrade, Serbia*
[2]*Miter International d.o.o, Resavska 16, Belgrade, Serbia*
[3]*Institute of General and Physical Chemistry, Studentski trg 12/V, Belgrade*

ABSTRACT

The micellization behavior of anionic surfactant sodium–laureth sulphate (SLES) and a nonionic homologous polysorbate surfactants (Tween 20, Tween 40, Tween 60 and Tween 80) in aqueous solution were studied by using a conductometric titration at 25 °C. The negative deviation of the experimentally determined values of critical micellar concentration (CMC^{exp}) from theoretical values for ideal surfactant mixtures (CMC^{id}) indicate nonideal mixing behavior due to synergism or favorable attractive interaction between the individual surfactants in formed mixed micelles. The synergism enlarges with both the increase the mole fraction and lenght of hydrophobic tail of examined Tween in SLES/Tween mixtures.

INTRODUCTION

The mixed surfactant systems form mixed micelles at a solution concentration called critical micelle concentration (CMC). The aqueous solutions of binary surfactant mixtures can have CMC either lower or higher than CMC of each individual surfactant due to of specific attractive (synergism) and repulsive interactions (antagonism) between surfactants within micelles [1]. These interactions as well as the surfactant composition strongly affect the mixed behavior of different anionic/nonionic surfactant mixtures. [2]. Attractive and repulsive interactions in mixed micelles are conventionally studied by CMC measurements and were analyzed using Clint's ideal models [3]. In order to analyze the nonideal mixing behavior of anionic/nonionic SLES–Tween series surfactant mixtures and possible synergism, according to Clint's ideal theory, CMC of ideal anionic/nonionic surfactant mixtures (CMC^{id}) [3] were calculated using following equation:

$$\frac{1}{CMC^{id}} = \frac{\alpha_1}{CMC_1} + \frac{1-\alpha_1}{CMC_2} \qquad (1)$$

where CMC_1 and CMC_2 are the experimentally obtained CMC of individual nonionic surfactant in the ideal mixed micelle (more hydrophobic surfactant) and of individual anionic surfactant, respectively, and α_i is mole fraction in the solution of nonionic surfactant. Any negative or positive deviation of the CMC^{exp} from CMC^{id} suggests synergism (attractive interactions) and antagonism (repulsive interactions) respectively, and indicate nonideal mixing behaviour of binary surfactant mixtures. The most commonly used polysorbates are Tween series which have the same hydrophilic head (sorbitan ring with polyethylene oxide) and a hydrophobic fatty acid tail which can vary in the fatty acid chains length and hence hydrophobity. In this study, conductometric analysis of the micellization behavior of anionic SLES and nonionic Tween surfactants was presented, in order to explain the influence of various nonionic Tween surfactants on the CMC and the synergism in the SLES/polysorbate binary systems.

EXPERIMENTAL

Materials: Anionic surfactant is sodium laureth sulfate (SLES) (Cosmacol). Nonionic surfactants are polyoxyethylene sorbitan monolaurate (Tween 20), polyoxyethylene sorbitan monopalmitate (Tween 40), polyoxyethylene sorbitan monostearate (Tween 60) and polyoxyethylene sorbitan monooleate (Tween 80) (Alfa Aesar). Surfactant mixtures with different mole fractions of nonionic surfactant (α) were prepared by dissolving of the surfactants in deionised water (Resistivity 18 MΩ cm, MilliQ, Millipore). The conductometric titration method was used for determination of CMC values of SLES and surfactant mixtures. The CMC values of individual nonionic Tween surfactants at the same temperature are obtained from the literature [4]. The measurements of specific conductivity (κ) were carried out with digital conductivity meter SensION 5 (Hach) with the conductivity probe 51975 that uses the 4–ring method. Those measurements were carried out at 25.0 ± 0.1 °C, by adding 0.2 mL aliquots of titrant to 50 mL of deionized water. The CMC values of surfactant mixtures were determined from the intersection of the fitting lines of the κ versus c plots above and below the break point, according to the Williams' method [5].

RESULTS AND DISCUSSION

For examined SLES–Tween mixtures two breaks in conductivity against surfactant mixture concentration were noticed, for all investigated mole fractions of nonionic surfactant (α). The presence of these two breaks suggests the formation of two types of mixed micelles, where each break

corresponds to one CMC (CMC_I^{exp} and CMC_{II}^{exp}). Both CMC^{exp} for selected SLES–Tween 20 mixture are presented in Figure 1.

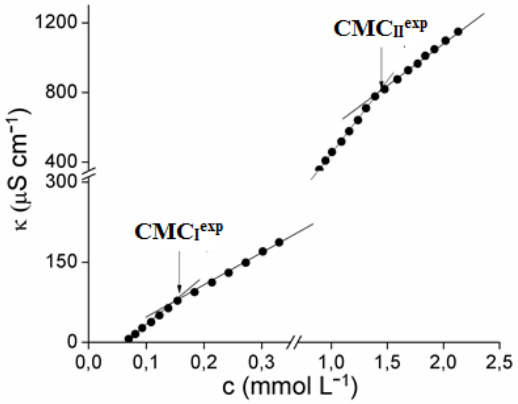

Figure 1. Representative plots of specific conductivity vs. concentration of SLES/Tween 20 surfactant mixture from which both CMC_I^{exp} and CMC_{II}^{exp} are determined. The mole ratio of Tween 20 in mixture is $\alpha = 0.3$.

The summarized CMC^{id} and both CMC^{exp} values for selected SLES/Tween 80 mixtures with various mole fraction of Tween 80 are presented in Table 1. It can be concluded that CMC_I^{exp} values decrease with the increase of α and that are significantly closer to the CMC values of individual nonionic surfactant. Generally, for all examined surfactant mixtures the first break at low surfactants concentration corresponds to mixed micelles richer in nonionic surfactant, as found by Munoz *et al*. [2]. The second break at higher concentrations of surfactant mixture, represents another type of mixed micelles with unknown mole fractions of the surfactants and indicats mixed micelles richer in anionic surfactant. Deviation of the both CMC_I^{exp} and CMC_{II}^{exp} of mixed micelles (Table 1 and 2) values from those CMC^{id} calculated using equation 1 indicatis nonideal behavior of examined mixtures and existence of both type of interactions between components in the micelles. The lowering of the CMC_I^{exp} when surfactants form mixed micelles arises from attractive interactions between the surfactants and indicating strong synergism between surfactants in mixture.

In case of the Tween series, with the same mole fraction (α) of homologous Tween surfactants in mixtures, length of hydrophobic chain decides micellization concentration. The longer and more hydrophobic tails of nonionic surfactants show stronger interactions with hydrophobic part of SLES, thus expressing stronger synergism in the mixed micelles and lower is the CMC of mixture. In SLES/Tween binary surfactant mixtures with same mole fraction (α) of homologous Tween surfactants, SDS–Tween 20 (shortest the chain length, C12) showed the weakest synergistic effect, while SLES/Tween 80 expressed the strongest synergistic effect, due to both the largest tail length (C18) and the presence of a double bond in tail which in certain extent

influence the formation of micelles with polysorbate compounds. All obtained results are in accordance with results found previously for different anionic/nonionic binary mixtures [2].

CMC_{SLES} = 8.214; $CMC_{Tween\ 80}$ = 0.012			
α	CMC^{id}	CMC_I^{exp}	CMC_{II}^{exp}
0.1	0.118	0.073	2.287
0.3	0.040	0.017	1.463
0.5	0.024	0.011	0.839

Table 1. CMC values (in mmol L^{-1}) of SLES/Tween 80 mixture with different mole ratio of Tween 80 surfactant in mixtures.

Table 2. CMC (in mmol L^{-1}) of individual surfactants and comparison of CMC^{id} and both CMC^{exp} values of the SLES/Tweens mixtures (α = 0.1)

CMC of individual nonionic surfactant[1]		Anionic/nonionic surfactant mixture	CMC of surfactant mixture		
			CMC^{id}	CMC_I^{exp}	CMC_{II}^{exp}
Tween 20	0.060	SLES/Tween 20	0.563	0.440	2.785
Tween 40	0.027	SLES/Tween 40	0.262	0.209	1.642
Tween 60	0.021	SLES/Tween 60	0.205	0.179	1.377
Tween 80	0.012	SLES/Tween 80	0.118	0.073	2.287

[1]The CMC of anionic surfactant SLES determined in this study is 8.214 mmol L^{-1}

CONCLUSION

The two types of mixed micelles are formed between anionic SLES and the selected nonionic surfactants polysorbates at all compositions. For the presented SLES/Tween series mixtures, the experimentally determined CMC values came out to be lower than their ideal values, suggesting nonideal mixing behavior. With the increase of the mole fraction and the length of the hydrophobic tail of polysorbates, examined mixtures deviate from the ideal, due to the appearance of synergism in all examined mixtures. It is evident that nonionic surfactants with longer and more hydrophobic tail express stronger synergism in mixed micelles.

Acknowledgement

The present investigations were supported by the Ministry of Education, Science and Technological Development of the Republic of Serbia, Grants no. 172015.

REFERENCES

[1] P. M. Holland, D. N. J. Rubingh, Phys. Chem. 1983, 87, 1984−1990.
[2] M. Munoz et all., Langmuir 2004, 20, 10858–10867.
[3] J. H. Clint, J. Chem. Soc., Faraday Trans. 1 1975, 71, 1327−1334. [5] J.
[4] www.sigmaaldrich.com/catalog/product/sigma/p2287/p1504/p1629/470
[5] R. Williams et all., Trans. Faraday Soc., 1955, 51, 728−737.

FOAMABILITY OF MIXTURES CONTAINING ANIONIC AND DIFFERENT POLYSORBATE SURFACTANTS

S.M. Blagojević[1], N. Erić[2], M. Nešović[3] and S.N. Blagojević[3]

[1]University of Belgrade–Faculty of Pharmacy, Department of Physical Chemistry and Instrumental Methods, Vojvode Stepe 450, Belgrade, Serbia
[2]Miter International d.o.o, Resavska 16, Belgrade, Serbia
[3]Institute of General and Physical Chemistry, Studentski trg 12/V, Belgrade

ABSTRACT

The goal of the present study is to evaluate influence of nonionic polysorbate surfactants with commercial names Tween 20, Tween 40, Tween 60 and Tween 80 which, due to the high stability and low irritability are used in cosmetic and pharmaceutical formulations, on the foamability (foam height and foam stability) of anionic surfactant sodium–laureth sulphate (SLES). Various homologous polysorbates with an identical polar head and a different structure of the hydrophobic tail significantly affect foamability of anionic surfactant. Foam *height* and stability significantly decrease with increasing length of the hydrophobic chain of Tween surfactants and their mole fractions in the binary mixture. The obtained results are important for the application of the investigated surfactants in formulations which require low foaming.

INTRODUCTION

Although known as strong irritants, anionic surfactants such as sodium laureth sulfate (SLES) is often used in the formulation of cosmetic and pharmaceutical preparations, primarily due to good foaming properties [1]. In order to reduce the irritant potential of anionic surfactants, nonionic surfactants are often used as poor irritants in pharmaceutical and cosmetic formulations. Nonionic surfactants (amine oxides, ethoxylates, etc.) have a lower foaming performance and are also highly synergistic, owing to their lack of a charged headgroup [1]. Nonionic surfactants polysorbates (commercial names Tweens), which play important roles in various cosmetic and food products, are a series of polyoxyethylenated sorbitan esters that are different with respect to the number of polymerized oxyethylene subunits and the number and type of fatty acid moieties present. The Tween series is comprised of polysorbate with identical polar head (polyoxyethylene (20) sorbitan) and difference in the length of the fatty acid chains (hydrophobic tail).

Foamability is the property of the solution to form foam of certain characteristics and is measured by the height (volume) and foam stability that is formed under certain conditions and at a certain time. Foam is a thermodynamically unstable system and without the presence of a stabilizer rapidly decreases in a short time interval. The foam stability is estimated based on the value of the foam volume ratio at a certain time after the formation and at the time of formation. Depending on the characteristics and purposes of the investigated surfactant system, foam is considered stable if this ratio is above 75% [2]. The foamability is influenced by the structure of the surfactant molecules, their concentration and temperature [1,3].

In order to analyze the foamability of binary anionic/nonionic surfactant mixtures, the influence of the mole fraction and structure of the hydrophobic part of the polysorbate commercially named Tween 20, Tween 40, Tween 60, and Tween 80 on the foam height and foam stability of anionic surfactant SLES was examined.

EXPERIMENTAL

***Materials*:** Anionic surfactant is sodium laureth sulfate (SLES) (Cosmacol). Nonionic surfactants are series of polyoxyethylenated sorbitan esters with different fatty acid moieties: monolaurate (Tween 20), monopalmitate (Tween 40), monostearate (Tween 60) and monooleate (Tween 80). All surfactant solutions with different mole fraction of nonionic surfactant in mixture (α) were prepared by dissolving of the surfactants in deionised water (Resistivity 18 MΩ cm, MilliQ, Millipore).

Experimental procedure: For foamability determination, aqueous solution of SLES concentration 2.60×10^{-1} mol L^{-1} and various binary mixtures of SLES and different Tween surfactants with same mole fraction of Tweens in the mixture (α = 0.1) and mixture SLES/Tween 20 with different mole fraction of Tween 20 (0.1, 0.3 and 0.5) in mixture, were prepared. Foamability was tested using the standard procedure of Ross–Miles [4]. The stability of the foam was assessed by measuring its volume at 23 ºC room temperature, both at the time of formation and after specific periods of time.

RESULTS AND DISCUSSION

The results of determining the foam height expressed as the foam volume at the time of formation and 60, 180 and 300 seconds after foam formation are shown in Figures 1a and 1b. The values of the stability of the SLES foam and the mixture of SLES and Tweens, which represents the ratio of the volume of the foam at specific time after formation and at the moment of formation, are shown in Table 1.

In the investigated time interval of 300 seconds, the foam content of the test mixture of SLES and Tween surfactants with a molar fraction of polysorbate in the mixture $\alpha = 0.1$ (Fig. 1a) decreased significantly with the change in the structure of the hydrophobic part of the homologous polysorbate. After 60 seconds of foam formation, only SLES solutions and SLES/Tween 20 mixtures with $\alpha = 0.1$ and $\alpha = 0.3$ show stable foam [2].

Compared with the aqueous solution of anionic surfactant SLES that exhibits the best foam, the foam content of the SLES/Tween 20 mixture at the time of formation decreases with the increase in the molar fraction of Tween 20 in the mixture (Fig. 1b). Over time, the effect of degradation of foam (height and stability of foam) with an increase of α is more pronounced (Fig. 1b and Table 2).

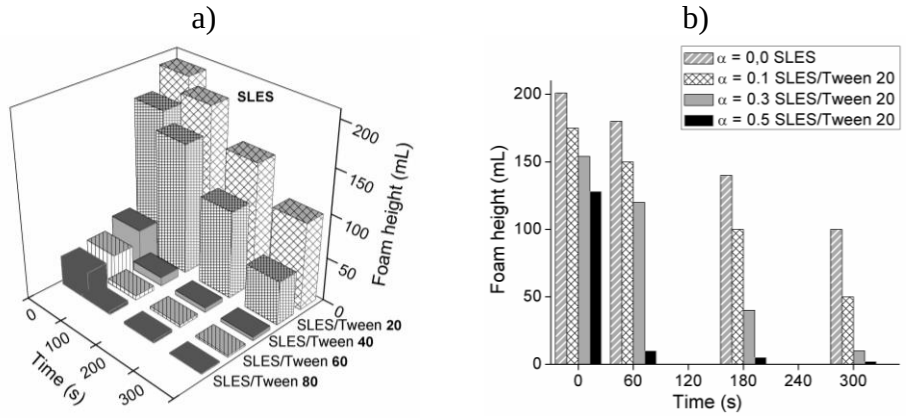

Figure 1. Foam height of SLES and mixtures of SLES and different Tweens: a) influence of Tween chain length on foam height ($\alpha = 0,1$); b) influence of mole fraction of Tween 20 in SLES/Tween 20 mixture on foam height.

Based on the results shown, it can be concluded that the presence of polysorbate affects the foamability of the anionic surfactant of SLES, and that the study of the structure of the hydrophobic tail (the length of the hydrophobic chain) of the nonionic surfactants significantly reduce and destabilizes the foam. Regarding the influence of the structure of the hydrophobic part of the polysorbate molecule, the increase in the molar fraction of the polysorbate on the foaming of the solution of the mixture is more pronounced. A significant decrease in the height and stability of the foam with an increase in the molar fraction of the nonionic surfactant in the test mixture can be explained by the decrease in the proportion of anionic

surfactant, which due to its properties is producer and carrier of foam stability [1,2].

Table 1. Foam stability of SLES, SLES/Tween series mixture (α = 0.1) and SLES/Tween 20 mixtures with different mole fraction of Tween 20.

α = 0.1	Foam stability (%)	
	Time (s)	
	60	300
SLES	88.2	49.0
SLES/Tween 20	85.7	28.5
SLES/Tween 40	19.3	9.6
SLES/Tween 60	13.1	5.3
SLES/Tween 80	12.1	3.0

Time (s)	Foam stability (%)			
	SLES	SLES/Tween 20 α of Tween 20		
		0.1	0.3	0.5
60	88.2	85.7	77.9	7.8
180	68.6	57.1	25.9	3.9
300	49.0	28.5	6.5	1.6

CONCLUSION

The results of determining the foamability of anionic SLES surfactant,t and mixtures of SLES and nonionic Tween surfactants show that all examined nonionic formulated surfactant mixtures are more efficient foamers, because the interactions between SLES and Tween surfactants affect the height and stability of foam in examined binary systems. The increase of length of the hydrophobic chain of the polysorbate, as well as the molar fraction of the polysorbate in mixtures decrease height and stability of the foam, leading to a low foam formation ability.

Acknowledgement

This work was partially supported by the Ministry of Education, Science and Technological Development of the Republic of Serbia (Grant no. 172015).

REFERENCES

[1] J. Falbe, Surfactants in consumer products: Theory, Technology and Application, Springer–Verlag, Berlin, 1987.

[2] L. Schramm, F. Wassmuth, Foams: Fundamentals and Applications in the Petroleum Industry, American Chemical Soc.,Washington, 1994.

[3] S. N. Blagojević, S. M. Blagojević, N. D. Pejić, J. Surfact. Deterg., 2016, 19, 363–372.

[4] SRPS ISO 696:2000 Surface active agents–Measurement of foaming power–Modified Ross-Miles method, Institute for standardization of Serbia.

M *– Complex Compounds*

THEORETICAL TECHNIQUES FOR CLARIFICATION OF STRUCTURAL AND FUNCTIONAL FEATURES OF METAL COMPLEXES

G. V. Janjić [1], N. R. Filipović [2], M. V. Rodić [3], P. Ristić [4], M. Donnard [5], M. Gulea [5] and T. Todorović [4]

[1] *Institute of Chemistry, Technology and Metallurgy, University of Belgrade, Njegoševa 12, 11000 Belgrade, Serbia. (janjic_goran@chem.bg.ac.rs)*
[2] *Faculty of Agriculture, University of Belgrade, Nemanjina 6, Belgrade, Serbia.*
[3] *Department of Chemistry, Faculty of Sciences, University of Novi Sad, Trg Dositeja Obradovića 4, Novi Sad, Serbia.*
[4] *Faculty of Chemistry, University of Belgrade, Studentski trg 12-16, Belgrade, Serbia.*
[5] *Université de Strasbourg, CNRS, Laboratoire d'Innovation Thérapeutique, LIT UMR 7200, 67000 Strasbourg, France.*

ABSTRACT

The structural characterization of *trans*-[MCl_2(tm-CN)$_2$] complexes of Pd(II) and Pt(II) (tm-CN is N-carbonitrile-substituted thiomorpholine) was made by combining the quantum chemical calculations with X-ray structural data. In crystal structures tm-CN ligands are coordinated *via* S atom to Pt(II) and Pd(II), where M–S bonds have an equatorial position in *trans*-[$PdCl_2$(tm-CN)$_2$] complex, while in *trans*-[$PtCl_2$(tm-CN)$_2$] complex they have an axial position. The calculations estimated that the coordination of the S atoms at axial position is slightly favourable than at equatorial position, while the coordination *via* N atom is thermodynamically unfavourable. The quantum chemical calculations also predicted that the interactions of these complexes with the species from environment (crystal packaging) are responsible for the positions of M–S bonds in crystal structures.

INTRODUCTION

Thiomorpholines have a variety of pharmacological activities, such as analgesic [1], antibacterial [2], antimycobacterial [3] and anti-inflammatory [4]. However, the information on coordination of ligands, such as a thiomorpholine and its derivatives, is relatively scarce [5, 6], because it includes a range of aspects that complicate their chemistry, such as coordination modes, conformations as well as a range of isomers and stereoisomers. Thiomorpholine (tm) contains two different coordination sites

to cyclohexane ring (hard N-donor and soft S-donor), with preference of ring to the low-energy chair conformation for monodentate and bidentate coordination, while the boat conformation is required for the chelating coordination mode. In crystal structures extracted from Cambridge Structural Database (CSD), tm ligand and its derivatives are mainly coordinated with monodentate binding by the N ligator atom, while the excess of metal ions leads in buildings of metal complexes with tm as a bidentate ligand in a bridging coordination mode [7] or in a chelate coordination mode [6].

The importance and relatively scarce number of studies with thiomorpholine derivatives motivated us to extend the studies of thiomorpholine based complexes. Accordingly, the Pd(II) and Pt(II) complexes with N-carbonitrile-substituted thiomorpholine ligand (tm-CN ligand) has been examined.

EXPERIMENTAL

The complexes were obtained by reaction of tm-CN with $K_2[MCl_4]$ (M=Pt or Pd) in water as a solvent and in tm-CN : metal salt = 2 : 1 molar ratio. Pale yellow (Pt complex) and orange (Pd complex) single crystals, suitable for X-ray diffraction (XRD) analysis, were obtained by vapor diffusion of EtOH in DMSO solutions of crude products.

The quantum chemical calculations for optimization, prediction of interaction energies and for prediction of reaction pathways were done in *Gaussian09* program, by using the wb97xd method, 6-31+g** basis set for non-metals and lanl2dz for metal ions (Pd and Pt). The geometries of species along reaction pathways are optimized with the SMD solvation model.

The crystallographic analysis is based on the crystal structures archived in the Cambridge Structural Database (CSD, November 2016 release, version 5.38).

RESULTS AND DISCUSSION

By analysing the crystal structures of complexes with tm ligand, extracted from CSD, it is shown that tm is mostly coordinated to central metal as monodentate ligand, *via* the N atom. There are only two structures with tm ligand as N coordinating bridging ligand and one structure with tridentate bridging behaviour of tm ligand. Monodentate bonding through the sulphur atom and crystal structures with tm-CN ligand were not found in the CSD.

The S-monodentate coordination mode of tm-CN ligand has been confirmed in crystal structures of *trans*-$[PtCl_2(tm\text{-}CN)_2]$ and *trans*-$[PdCl_2(tm\text{-}CN)_2]$ complexes. The coordination mode of tm-CN ligand is in accordance with previous studies which showed that N-substituted thiomorpholine coordinates mainly *via* N atoms [6], except if the nitrogen

atom is a part of the fragment with resonance ability [8]. The binding of CN group to tm leads to extending of resonance area, which includes N atom of ring, and consequently results in a reduced coordination ability of this N atom.

To determine whether the geometries and conformations of *trans*-$[MCl_2(tm\text{-}CN)_2]$ complexes in the crystal structures are the result of intermolecular interactions (determined by crystal packaging) or intramolecular interactions (determined by their stability), the structures of tree possible isomers of investigated complexes have been optimized. In Pt(II) and Pd(II) systems, the axial conformer is more stable than the equatorial, while the complexes in which ligands are coordinated to metal *via* N atom from carbonitrile group are the least stable (Table 1).

Table 1. The energy differences between the optimized isomers of *trans*-$[MCl_2(tm\text{-}CN)_2]$ complexes.

Structure of metal complex	S-axial coordination 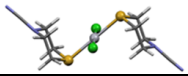	S-equatorial coordination 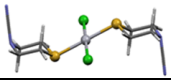	N-nitrile coordination 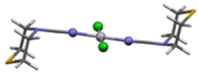
The relative stability of complexes (in kcal/mol)			
M=Pt(II)	-15.1	-7.6	0.0
M=Pd(II)	-15.5	-8.9	0.0

Despite the fact that the equatorial conformer of Pd complex is less stable, this conformer occurs in the crystal structure, not the axial one. Possible reason for this phenomenon could be found in the mechanism of tm-CN complexes formation, taking into account all isomers of complexes. Bearing in mind the stability of reactants, the energy barriers and stability of the products, it can be concluded that the axial conformers are slightly favored than the equatorial ones, while the coordination of tm-CN ligand *via* N atom leads to the least stable products (Figure 1). Taking into account the stability of optimized isomers of *trans*-$[MCl_2(tm\text{-}CN)_2]$ complexes, the mechanism of $[MCl_3(tm\text{-}CN)]^-$ complexes formation and the interconversion of tm-CN ligand in $[MCl_3(tm\text{-}CN)]^-$ complexes, it should be expected that axial and equatorial conformers will occur in aqueous solution.

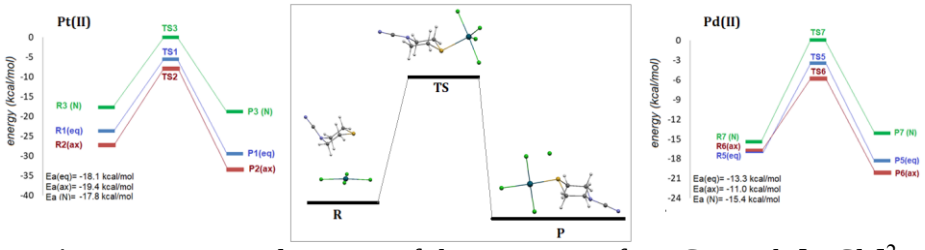

Figure 1. Energy diagrams of the reactions of tm-CN with $[PtCl_4]^{2-}$ complex (left) and $[PdCl_4]^{2-}$ complex (right), in 1:1 molar ratio. Relative free energies were computed at wb97xd/6-31+g** +lanl2dz level, and compared with respect to the most unstable transition state. The reaction pathway is the following: $[MCl_4]^{2-}$ + tm-CN (R, reactant) → Transition state x (TS) → $[MCl_3(tm\text{-}CN)]^-$ + Cl^- (P, product).

Based on the results of calculations one can conclude that the conformations of the studied complexes in the crystal structures are determined by intermolecular interactions with the species from the environment (Figure 2).

Intermolecular non-covalent interactions are calculated in both crystal structures. Due to the absence of classical hydrogen bond donors and acceptors, the crystal packings in both complexes are based on weak hydrogen bonds (C-H/Cl-M, C-H/S-M and C-H/M interactions).

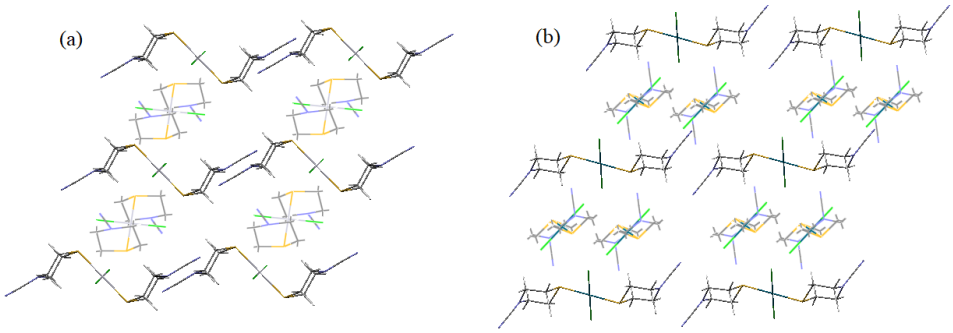

Figure 2. The packing in the crystal structure of Pt complex (a) and Pd complex (b).

The maps of the electrostatic potential of studied complexes (Figure 3) showed that the potential above Cl, S and metal atoms is close to electro-neutral, regardless the nature of central metal ions. Hence, it should be expected that C-H/Cl-M, C-H/S-M and C-H/M interactions have a similar strength. The quantum chemical calculations for prediction of the strength of C-H/Cl-M, C-H/S-M and C-H/M interactions were performed on the model

systems (Figure 3), containing methane molecule, as a donor for hydrogen bonding, and metal complex as an acceptor. However, the results of calculations (Figure 3) show that the C-H/Cl-M and C-H/S-M interactions are weaker, with the values of energy less than 1.0 kcal/mol for both Pd(II) and Pt(II) complexes, compared to C-H/M interactions (energies are larger than 2.0 kcal/mol). The hydrogen bonds in which the metal ions have a role of an acceptor were intensively studied in the last decade. It was shown that Pt (II) complexes form a slightly stronger hydrogen bonds in comparison to Pd(II) complexes [9], and that the strength of those hydrogen bonds strongly depends on the nature of the ligands. Noncovalent C-H/M interactions in this study are considerably stronger, with a maximum value of -2.95 kcal/mol for Pt (II) complex, and -2.84 kcal/mol for Pd(II) complex.

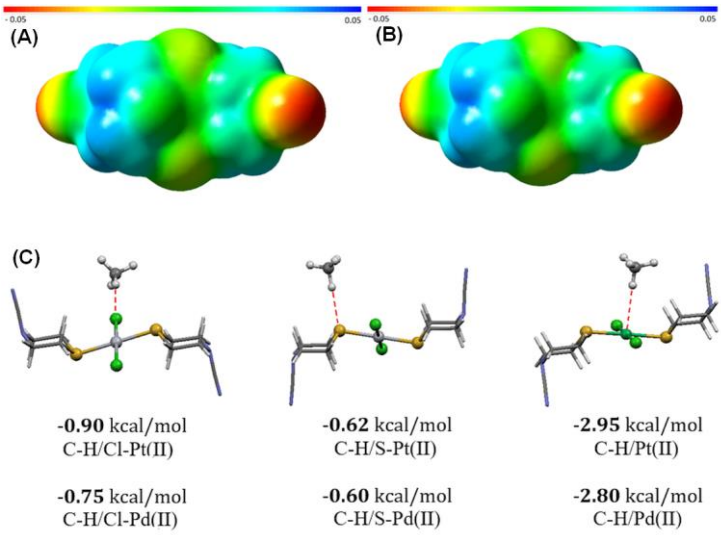

Figure 3. Map of the electrostatic potential for equatorial $[PdCl_2(tm\text{-}CN)_2]$ (A) and equatorial $[PtCl_2(tm\text{-}CN)_2]$ complex (B). Model systems and calculated interaction energies for C-H/Cl-M, C-H/S-M and C-H/M interactions (M= Pd(II) or Pt(II)) (C).

CONCLUSION

Based on the crystallographic and quantum chemical data, it was shown that the coordination mode of tm-CN in *trans*-$[MCl_2(tm\text{-}CN)_2]$ complexes (M=Pt(II) or Pd(II)), is caused by the crystal packing, defined by intermolecular interactions of the metal complexes with the species from environment (C-H/Cl-M, C-H/S-M and C-H/M interactions).

The presented results are important in many aspects: to the best of our knowledge, first crystal structures with tm-CN as a ligand were determined. In addition, the results show that the combination of crystallographic analysis and quantum chemical calculations could be used successfully in prediction of the mechanism of formation of metal complexes and their structural characterization, and also in the design of related compounds.

Acknowledgement
This work was supported by the Ministry for Science of the Republic of Serbia (Project no. OI 172023 and OI 172055).

REFERENCES

[1] A.H. Abadi, G.H. Hegazy, Bioorganic & Medicinal Chemistry, 2005, 13, 5759–5765.
[2] J.W. Kim, H. B. Park, B. Y. Chung, Bulletin of the Korean Chemical Society, 2006, 27, 1164–1172.
[3] Y. Baran, H. Ozay, H. Esener, M. Turkyilmaz, Spectrochimica Acta A, 2011, 81, 99– 103.
[4] G. Kucukguzel, A. Mazi, F. Sahin, S. Ozturk, J. Stables, European Journal of Medicinal Chemistry, 2003, 38, 1005–1013.
[5] E. J. Tierney, A. D. Sabatelli, J. E. Sarneski, Inorganic Chemistry, 1987, 26, 617-620.
[6] Y. Li, Y. H. Lai, K. F. Mok, M. G. B. Drew, Inorganica Chimica Acta, 1999, 285, 31-38.
[7] D. Britton, F. B. Stocker, T. P. Staeva, Acta Crystallographica, 1999, C55, 2014-2016.
[8] T. H. Kim, Y. W. Shin, J. H. Jung, J. S. Kim, J. Kim, Angewandte Chemie International Edition, 2008, 47, 685-688.
[9] G. V. Janjić, M. D. Milosavljević, D. Ž. Veljković, S. D. Zarić, Physical Chemistry Chemical Physics, 2017, 19, 8657-8660.

NEW ADDUCTS OF RARE EARTH 3,5-DINITROBENZOATES AND AMINOBENZENES: CORRELATION BETWEEN CHARGE TRANSFER DEGREE AND IONIZATION POTENTIALS OF THE DONORS

P.S. Koroteev, N.N. Efimov, A.B. Ilyukhin, V.V. Minin, Zh.V. Dobrokhotov and V.M. Novotortsev

N.S. Kurnakov Institute of General and Inorganic Chemistry of Russian Academy of Sciences, 119991, Leninskyprosp., 31, Moscow, Russia. (pskoroteev@list.ru)

ABSTRACT

Two novel series of charge transfer complexes (CTCs) of rare earth 3,5-dinitrobenzoates as acceptor molecules and aminobenzene derivatives (diaminodurene and 1,2-phenylenediamine) as donors were prepared and studied. Due to charge transfer between the aromatic rings, stacking interactions that determine the supramolecular structure of complexes take place. Optical spectra of the complexes indicate the presence of significant charge transfer while EPR and magnetic studies testify to an impact of ion radical structure in case of diaminodurene adducts. A correlation between the degree of CT in the complexes, and the ionization potentials of the donor molecules was found for the two new series of similar CTCs and two previously obtained ones. Magnetic properties of the complexes correspond to the prevalence of antiferromagnetic interactions in all of the cases.

INTRODUCTION

The problems in the development of the magnetic materials on a basis of the lanthanides are the low possibility of the Ln ions to exchange interactions and the presence of the diamagnetic ligands, the “spin ballast” in the complexes. Conversion of diamagnetic ligands into magnetically active fragments is possible when a charge transfer complex (CTC) [1] is formed between a molecule that can serve as an efficient electron density donor, and a ligand if it is electron-deficient. Recently we have obtained and studied CT complexes containing binuclear lanthanide 3,5-dinitrobenzoates and *N*,*N*-dimethylaniline ($[Ln_2(DNBZ)_6(DMSO)_4]\cdot x$DMA; DMA = Me_2NPh; x = 3, 4, 5; DNBZ = 3,5-$(NO_2)_2C_6H_3CO_2^-$) [2] or *N*,*N*,*N′*,*N′*-tetramethylphenylenediamine ($[Ln_2(DNBZ)_6(DMSO)_4]\cdot x$TMPD; TMPD = 1,4-$(Me_2N)_2C_6H_4\cdot y$MeCN;$x$ = 1 or 3; y = 1 or 0) [3] which represent an

original type of hybrid compounds. Supramolecular structures of those complexes are formed due to stacking interactions between donor aromatic amine molecules and acceptor 3,5-dinitrobenzoate fragments. With use of *p*-diaminotetramethylbenzene (diaminodurene, DAD), and 1,2-phenylenediamine (PDA), two new series of CT adducts of rare earth 3,5-dinitrobenzoates, $[Ln_2(DNBZ)_6(DMSO)_4]\cdot 4DAD$ and $[Ln_2(DNBZ)_6(DMSO)_2]_2\cdot PDA\cdot 4MeCN$, were prepared and studied.

EXPERIMENTAL

Commercial reagents and solvents were used for the syntheses (from Alfa Aesar and Aldrich). The solvents were purified by conventional methods.

The adducts $[Ln_2(DNBZ)_6(DMSO)_4]\cdot 4DAD$ and $[Ln_2(DNBZ)_6(DMSO)_2]_2\cdot PDA\cdot 4MeCN$ were obtained by crystallization of the products of exchange reaction between $LnCl_3\cdot 6H_2O$ and potassium salt of 3,5-dinitrobenzoic acid from CH_3CN/DMSO media in the presence of the corresponding amine similarly to the adducts with DMA [2] and TMPD [3]. The yields were 40-45%.

RESULTS AND DISCUSSION

Novel compounds $[Ln_2(DNBZ)_6(DMSO)_4]\cdot 4DAD$ (Ln = Sm(**1**), Gd(**2**), Tb(**3**), Dy(**4**), Ho(**5**), Er(**6**),Y(**7**); DAD = 1,4-$(H_2N)_2C_6Me_4$) and $[Ln_2(DNBZ)_6(DMSO)_2]_2\cdot PDA\cdot 4MeCN$ (Ln = Tb(**8**), Ho(**9**), Dy(**10**), Er(**11**)) were obtained in moderate yields. The complexes precipitate from the reaction mixture as black (**1**-**7**) or brown (**8**-**11**) crystals. The complexes within each series are isostructural.

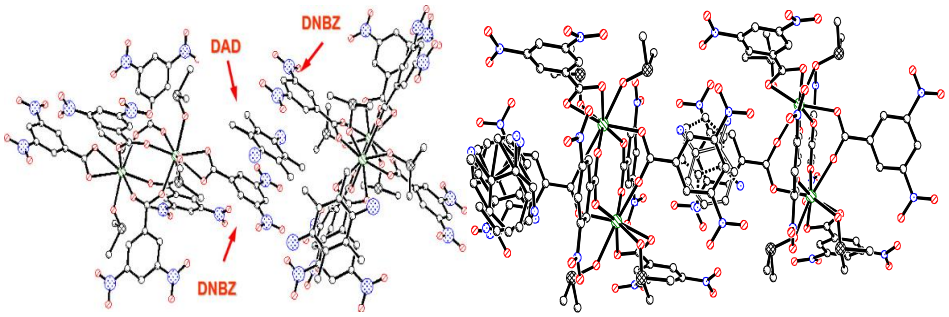

Figure 1. Fragments of the structures of CT complexes with DAD (left) and with PDA (right).

The self-assembly process of formation of the structures **1**-**11** takes place due to the CT between aromatic amine molecules and DNBZ fragments. In

case of absence or lack of the amines the crystallization brings about the colorless polymers $[Ln(DNBZ)_3(DMSO)_2]_n$ which we have described earlier [3]. Supramolecular structures of compounds **1-11** are built of the typical of the lanthanide carboxylates binuclear complexes $[Ln_2(DNBZ)_6(DMSO)_4]$ and donor DAD or PDA molecules (Fig. 1); 3D-structures in case of the first series and 1D-chains in case of the complexes with PDA are formed due to stacking between donor and DNBZ aromatic rings.

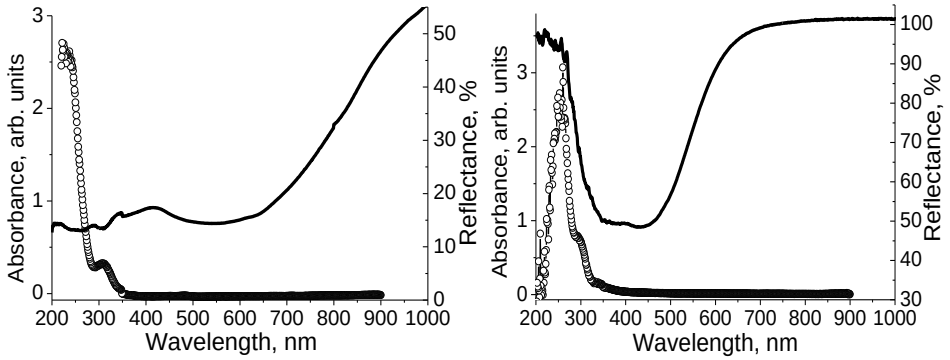

Figure 2. Absorption UV–Vis spectra of 10^{-4} M THF solutions (-○-) and solid-state reflectance spectra (solid lines) of complexes **7** and **8**.

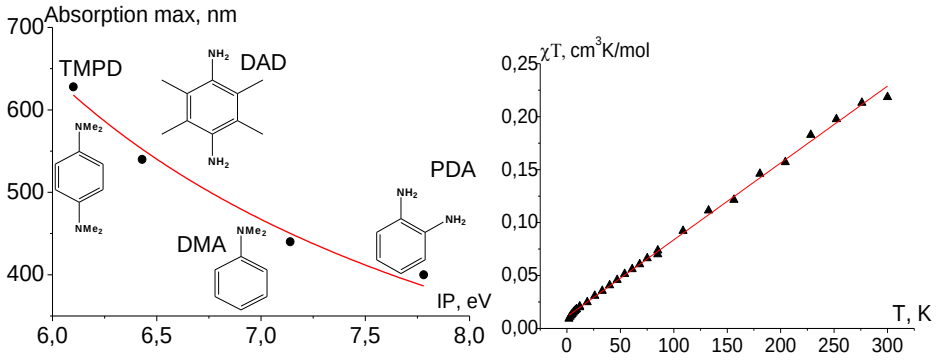

Figure 3. Correlation between ionization potentials (IP) of the donors and CT bands maxima in reflectance spectra of CT complexes with different aminobenzene derivatives as donors (left); temperature dependence of $\chi_M T$ for compound **7**; solid line is the linear approximation (right).

The electron spectra of CTCs are characterized by a "CT band" corresponding to a CT transition, the position of this band being determined

by the difference in the energies of the excited (ion-radical) and ground (molecular complex) state of CT complex, which, in turn, determines the degree of charge transfer. In case of weaker CT, the energy gap between the ground state and excited state increases, so higher-energy quanta are required for a transition to the excited state [2]. In our case the CT bands are manifested in reflectance spectra and are lost in solution due to dissociation of the complexes (Fig. 2). For complex **7**, λ_{max}(CT band) ≈ 540 nm; for complex **8**, λ_{max}(CT band) ≈ 400 nm (the minimum of reflectance is the maximum of absorbance). Among the studied series of CT complexes with DNBZ as acceptors, the weakest donor is PDA while the strongest one is TMPD. The correlation between the ionization potentials (IPs) of the donors (literature data) and λ_{max} values of the CT bands was approximated by a hyperbolic function suggested in the work [4] (R^2 = 0.974; Fig. 3, left). For the complex **7** containing diamagnetic Y, a high level of CT was also proved by direct magnetic measurements (Fig. 3, right) and EPR studies.

CONCLUSION

In summary, we have obtained two new families of the adducts of rare earth 3,5-dinitrobenzoates with diaminodurene and 1,2-phenylenediamine, which have a nature of charge transfer complexes. The supramolecular structures of those hybrid compounds are formed due to charge transfer between 3,5-dinitrobenzoate fragments and aromatic amine molecules. For the yttrium complex with DAD, the paramagnetic contribution of the charge-transfer fragments was characterized by the EPR method and quantitatively estimated by direct measurement of the magnetic susceptibility. According to UV-vis spectra, the complexes completely dissociate into constituents in THF solution. In the absence of amines, the coordination polymers are formed, thus, charge transfer has a cardinal effect on composition and structure of the reaction products. A correlation between the level of charge transfer and the ionization potentials of the aromatic amines is shown.

Acknowledgement

The work was supported by the Russian Science Foundation (grant 16-13-10407).

REFERENCES

[1] V. P. Parini, Russ. Chem. Rev., 1962, **31 (7)**, 408-417.
[2] P. S. Koroteev, A. B. Ilyukhin et al., Polyhedron, 2015, **89**, 238-249.
[3] P. S. Koroteev, A. B. Ilyukhin et al., Inorg. Chim. Acta, 2016, **442**, 86-96.
[4] B. S. Pryalkin, Russ. J. Gen. Chem., 2009, **79 (11)**, 2359-2366.

XRD AND SEM-EDX CHARACTERIZATION OF COBALT(II) COMPLEXES WITH REDUCED LOW-MOLAR DEXTRAN

Ž. Mitić [1], G. M. Nikolić [1], M. Cakić [2], S. M. Mitić [2], G. S. Nikolić [2], S. Najman [1] and M. Trajanović [3]

[1]*Faculty of Medicine, University of Niš, RS-18000 Niš, Serbia (zak_chem2001@yahoo.com)*
[2]*Faculty of Technology, University of Niš, RS-16000 Leskovac, Serbia*
[3]*Faculty of Mechanical Engineering, University of Niš, RS-18000 Niš, Serbia*

ABSTRACT
Co(II)-RLMD complexes were characterized by XRD analysis and SEM-EDX spectroscopy. XRD analysis was used for the investigation of changes in crystallinity/amorphicity of Co(II)-RLMD complexes, and results show a predominantly amorphous structure of Co(II)-RLMD complexes. The EDX spectra confirmed the presence of cobalt (strong peak at ~7 keV) and absence of impurities in Co(II)-RLMD complexes.

INTRODUCTION
Polysaccharide type complexes have scientific and practical interest because of their application in pharmacy and medicine. Biometal based complexes on polysaccharides are important in treatment of biometal deficiency, as well as in metal ion transporting in organism [1]. Complexes of iron and copper with polysaccharides have a great significance, and they have been described in details [2,3]. Cobalt complexes, based on polysaccharides and its derivatives, are used in both human and veterinary medicine [4]. The aim of this work is to use X-ray diffraction (XRD) analysis and scanning electron microscopy – energy dispersive X-ray (SEM-EDX) spectroscopy as the main tools for characterization of Co(II)-RLMD complexes.

EXPERIMENTAL
Details of the Co(II)-RLMD complex synthesis, UV-Vis and FTIR spectroscopic characterization have already been described elsewhere by Mitić et al. [5,6].
XRD analysis. The XRD diffractograms were recorded on *θ:θ* Bruker Axs D8 Advance vertical scan diffractometer in the 2θ range of 5–50° using Cu (K_α, 1.5418 Å) as X-ray source.

SEM analysis. The morphology Co(II)-RLMD samples, previously dried and gold-coated by cathode sputtering in JPC JEOL-1100 apparatus, was analyzed on scanning electron microscope (SEM) JEOL JSM 5300.
EDX spectroscopy. The qualitative analysis of Co(II)-RLMD samples was performed by EDX spectroscopy. The EDX spectra were recorded using a Link-Analytical QX-2000 microprobe, mounted on scanning electron microscope (SEM, JEOL JSM-5300), operating at 20 kV. The EDX spectra were analyzed by using EDS analyzer v2© software.

RESULTS AND DISCUSSION

XRD analysis was used for the investigation of changes in crystallinity/amorphicity caused by the complexation of reduced low-molar dextran (RLMD) with Co(II) ions. The XRD patterns of RLMD and Co(II)-RLMD complexes are shown in Fig. 1.

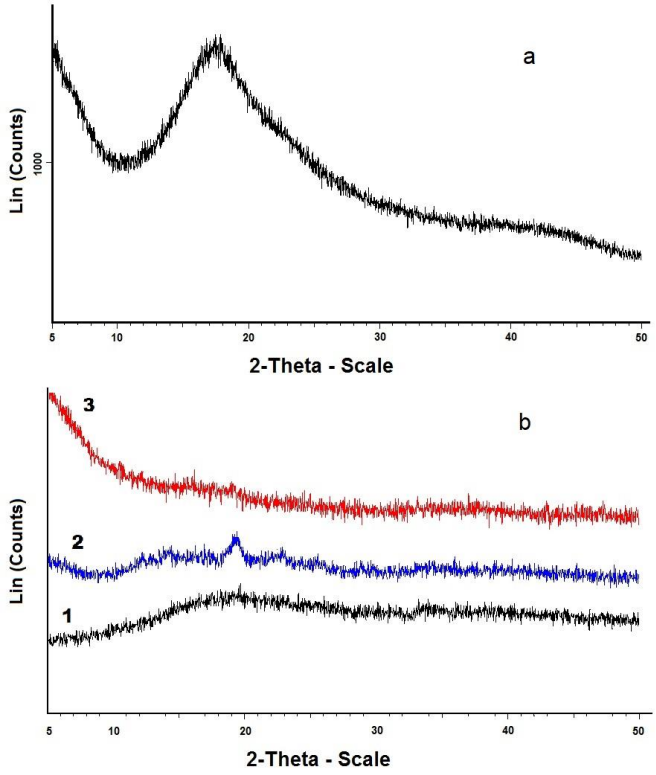

Figure 1. XRD patterns of RLMD (a) and Co(II)-RLMD complexes (b) synthesized at different pH values: pH=8.5 (**1**); pH=11.0 (**2**); pH=13.5 (**3**).

XRD. The broad peak between 15° and 20° is due to the amorphous polysaccharide phase [7], used as the complexing agent (Fig. 1a). XRD patterns in Fig. 1b clearly showed that Co(II)-RLMD complexes synthesized

under preparation conditions used in this work were completely amorphous. The differences observed in the XRD patterns of the ligand RLMD (Fig. 1a) and the Co(II)-RLMD (Fig. 1b) samples indicated the total loss of crystalline structure of RLMD as the complexation progressed. Crystalline polysaccharide complexes were found not suitable for the dissolution experiments due to the non-reproducible results [8].

SEM. The size and shape of Co(II)-RLMD particles were characterized by SEM analysis. SEM image (Fig. 2), showed a number of aggregates, size of about 50–500 μm. Ridged shapes that are visible on the surface of some granules are larger and flatter for synthesized Co(II)-RLMD complexes. This may be attributed to the stabilization of the particles by RLMD, as capping agents. Aggregated particles with larger irregular structure and no well-defined morphology were also found (Fig. 2).

EDX. Elemental analysis of Co(II)-RLMD complexes was performed by using the EDX analysis which proved to be very convenient method for the analysis of this type of samples [9]. Typical EDX spectrum of Co(II)-RLMD complexes is shown in Fig. 2. The peaks in the EDX spectra indicate the presence of following elements: C (Kα 0.277 keV), O (Kα 0.525 keV), and Co (Kα 6.924, Lα 0.776 keV). Strong peak at ~7 keV confirmed the presence of cobalt in the synthesized Co(II)-RLMD complexes. Moreover, the signal intensities for O and C atoms were very similar. No other peaks were detected throughout the scanning range of binding energies thus indicating that synthesized Co(II)-RLMD complexes are free of impurities (like Na^+ from NaOH or Cl^- from $CoCl_2$ used during the synthesis).

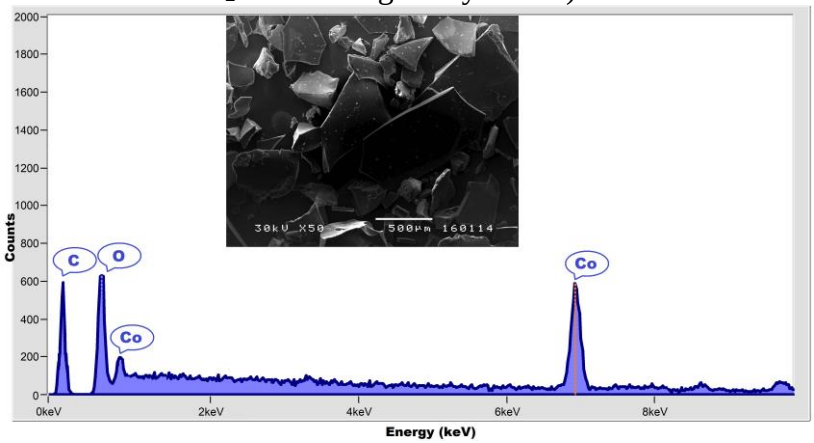

Figure 2. The EDX spectrum with related SEM image of Co(II)-RLMD complex synthesized at pH 13.5.

CONCLUSION

XRD results pointed out to a predominantly amorphous structure of Co(II)-RLMD complexes. The differences observed in the XRD patterns of the ligand RLMD and Co(II)-RLMD complexes indicated the total loss of crystalline structure of RLMD as the complexation progressed. SEM results were showed a number of aggregates, size of about 50–500 μm. The presence of cobalt (strong peak at ~7 keV) and absence of impurities in Co(II)-RLMD complexes was confirmed by EDX spectroscopy.

Acknowledgement

This work was partially supported by the Faculty of Medicine, University of Niš, Republic of Serbia (Grant no. **11-14629-4/16**) and the Ministry for Science of the Republic of Serbia (Grant no. **OI 172044**)

REFERENCES

[1] Ž. Mitić, M. Cakić, Acta Med. Median. 2014, 53, 54–63.
[2] G. Nikolić, M. Cakić, Lj. Ilić, S. Ristić, Ž. Cakić, Die Pharmazie, 2002, 57, 155–158.
[3] Ž. Mitić, M. Cakić, G.M. Nikolić, R. Nikolić, G.S. Nikolić, R. Pavlović, E. Santaniello, Carbohydr. Res. 2011, 346, 434–441.
[4] G. Nikolić, M. Cakić, S. Glišić, D. Cvetković, Ž. Mitić, D. Marković, In: Fourier Transforms - High-tech Application and Current Trend, InTech, 2017, 149–174.
[5] Ž. Mitić, M. Cakić, G. Nikolić, Spectroscopy, 2010, 24, 269–275.
[6] Ž. Mitić, G.M. Nikolić, M. Cakić, S. Mitić, G.S. Nikolić, S. Najman, Acta Fac. Med. Naiss. 2018, 35, 37–48.
[7] K.P. Bankura, D. Maity, M.M.R. Mollick, D. Mondal, B., Bhowmick, M.K. Bain, A. Chakraborty, J. Sarkar, K. Aharya, D. Chattopadhyay, Carbohydr. Polym. 2012, 89, 1159–1165.
[8] E. Somsook, D. Hinsin, P. Buakhrong, R. Teanchai, N. Mophan, M. Pohmakotr, J. Shiowatana, Carbohydr. Polym. 2005, 61, 281–287.
[9] M. Cakić, S. Glišić, G. Nikolić, G.M. Nikolić, K. Cakić, M. Cvetinov, J. Mol. Struct. 2016, 1110, 156–161.

PREPARATION AND STUDY OF TWO NEW Cu(II) OCTAAZAMACROCYCLIC COMPLEXES WITH β- ARYL -β- HYDROXY PROPANOIC ACID

B. Dražić[1], S. B. Tanasković[1] and M. Antonijević Nikolić[2]

[1] University of Belgrade, Faculty of Pharmacy, Vojvode Stepe 450, 11000 Belgrade, Serbia. (bdrazic@pharmacy.bg.ac.rs)
[2] Higher Medical and Business-technological School of Applied Studies, Hajduk Veljkova 10, 15000 Šabac, Serbia

ABSTRACT

Novel binuclear Cu(II) complexes with general formula $[Cu_2(L)tpmc](ClO_4)_2 \cdot Y$ (LH: 3-(3-methylphenyl)-3-hydroxy-3-phenylpropanoic acid**,** Y= $2NaClO_4 \cdot 4H_2O$; LH 3-(3-(trifluoromethyl)phenyl)-3-hydroxy-3-phenylpropanoic acid, Y= $2NaClO_4 \cdot 5H_2O$; tpmc = *N,N′,N″,N‴*-tetrakis(2-pyridylmethyl)-1,4,8,11-tetraazacyclotetradecane), were synthesized and their composition proposed by: elemental analysis (C, H, N), conductometric measurements, IR and UV/Vis spectroscopy. It is assumed that all complexes are binuclear with an *exo* coordination mode of the octaazamacrocyclic pendant ligand in *boat* conformation. Besides two -N-$(CH_2)_2$-N- portions of cyclam ring within tpmc ligand, Cu(II) ions are the most probable bridged engaging oxygen atoms from carboxylate anion.

INTRODUCTION

Mixed ligand complexes of some transition metals (Cu(II), Co(II,III), Zn(II), Mn(II), Ni(II)) with aromatic or aliphatic carboxylates and N-donor ligands (tpmc) are of interest due to their specific structural, physical and medical properties. Tpmc with pendant N-donor arms can accommodate to different additional ligands in a variety of coordination mode giving stable complexes. A great variety of coordination modes of carboxylate ligands with transition metals depending on the reaction conditions and selection of central metal ion. β-Aryl-β-hydroxy_acids and their derivatives belong to the aryl-propanoic acid class of compounds, structurally similar to the commercially available non-steroidal anti-inflammatory drugs (NSAIDs). This class of drugs are used to treat fever, pain and inflammation and belong to one of the most prescribed class of compounds. Here we report the preparation of two new mixed ligand Cu(II) complexes with tpmc and β-aryl-β-hydroxy propanoic acid, their physical and chemical properties and proposed coordination mode of the ligand systems.

EXPERIMENTAL

Ligand tpmc [1], complex $[Cu_2tpmc](ClO_4)_4$ [2] and ligands β-aryl-β-hydroxy propanoic acids [3] were prepared and purified as described in the literature. The other chemicals: CH_3CN, NaOH as *p.a.* commercial products were provided by Sigma Aldrich, USA.

$[Cu_2(L)tpmc](ClO_4)_2xY$ (L1 = 3-(3-methylphenyl)-3-hydroxy-3-phenyl-propanoic acid; L2=3-(3-(trifluoromethyl)phenyl)-3-hydroxy-3-phenylpropa-noic acid; Y= $2NaClO_4 \cdot 4H_2O$; $2NaClO_4 \cdot 5H_2O$)

General procedure. $[Cu_2tpmc](ClO_4)_4$ (0.5 mmol) was dissolved in minimum amount (5 ml) of CH_3CN and refluxed on water bath (80° C) for 30 min with stirring. After that, 3-(3-methylphenyl)-3-hydroxy-3-phenylpropanoic acid/ 3-(3-(trifluoromethyl)phenyl)-3-hydroxy-3-phenylpropanoic acid (0.75 mmol) saturated solution in mixture of CH_3CN/H_2O (3:1) (previously neutralized with 0.1M aqueous NaOH to pH=6) was slowly added dropwise. Reaction mixture was continuously stirred and refluxed on water bath (80°C) for the next 2 h, concentrated to 1/4 of initial volume and cooling in refrigerator overnight and a blue product appeared. The final microcrystals were separated by vacuum filtration and left in a desiccator (over CaO). **$[Cu_2Ltpmc](ClO_4)_2 \cdot 2NaClO_4 \cdot 4H_2O$ (LH = $C_{16}H_{15}O_3$) (1).** Yield: 52%; Anal. Calcd. for $C_{50}H_{66}N_8O_{23}Cu_2Na_2Cl_4$ (FW = 1461): C, 41.07; H, 4.52; N, 7.67. Found: C, 41.66; H, 4.45; N, 7.10.

$[Cu_2Ltpmc](ClO_4)_2 \cdot 2NaClO_4 \cdot 5H_2O$ (LH = $C_{16}H_{13}F_3O_3$) (2) Yield: 64%; Anal. Calcd. for $C_{50}H_{66}N_8O_{24}Cu_2Na_2F_3Cl_4$ (FW = 1534): C,39,11; H, 4.30; N, 7,30. Found: C, 40,35; H, 4,42; N, 7,54

Analytical methods: Elemental analysis were performed on a Elementar Vario EL III elemental analyzer. Electronic absorption spectra of complex solution in CH_3CN ($C=1x10^{-3}$ M) were recorded on GBC UV/Vis spectrophotometer Cintra 20. IR spectra were recorded on NICOLET 6700 FTIR (ATR technique) in the range 400-4000 cm^{-1}. Molar conductivities were measured on conductometer HANNA instruments HI 8820N (at 20 ± 2ºC) in CH_3CN ($c=1x10^{-3}$ M).

RESULTS AND DISCUSSION

Both new synthesized complexes are insoluble in CH_3OH and cold distilled water. Molar electrical conductivity in CH_3CN of 1131 S cm^2 mol^{-1}(1); 1068 S cm^2 mol^{-1} (2) is very high, corresponding to an electrolyte type 1:6 but they are consistent with the results of the elemental analysis. The large value obtained for complexes could be a consequence of the crystal bonded molecules of H_2O in this compound. The molar conductivity of $NaClO_4$ (in the crystal lattice of the complex) is 135 S cm^2 mol^{-1}, which contributes a

great deal to the total molar conductivity. In the literature there is no precise data for such an electrolyte type.

UV/VIS spectra of complexes in CH_3CN exhibiting maxima at 675 nm (ε=393 $dm^3\ mol^{-1}\ cm^{-1}$) (1) and 680 nm (ε=317 $dm^3\ mol^{-1}\ cm^{-1}$) (2). The position of the absorption peaks corresponded to d–d transitions in Cu(II) complexes. Approximately the same absorption values, similar form and intensity of absorption maxima indicate that complexes have the same geometries, which means that in both complexes, ligands are bound in the same mode.

In the IR spectra of the complexes, can observed following characteristic bands belonging to: ν(O-H) in the range 3600-3300 cm^{-1} (broad, medium) from the crystal bonded molecules of H_2O at 1609 cm^{-1} (sharp, medium) of skeletal ν(C-N) of pyridine ring from macrocyclic ligand. In the spectra of complexes there is a band around 466 cm^{-1} which is origin from ν(C–N) and a band about 416 cm^{-1} from ν(Cu–O).

The comparison of the spectra of the complexes and corresponding ligands β-aryl-β-hydroxy propanoic acids, in the range 1700–1350 cm^{-1}, can observed the change of the $\Delta\nu$ value ($\nu_{asym} - \nu_{sym}$) of the complex which confirms that the ligand is coordinated to the metal through COO^- groups. The proposed coordination mode of the ligands in complexes: oxygen atoms of COO^- are engaged in coordination thus forming a bridge between two Cu(II) from the same tpmc unit. Also $\nu(ClO_4^-)$ at 1092 cm^{-1} (strong, sharp) and 628 cm^{-1} the presence of ClO_4^- as counter ion. From all presented data proposed geometry for both new complexes are shown in Scheme 1.

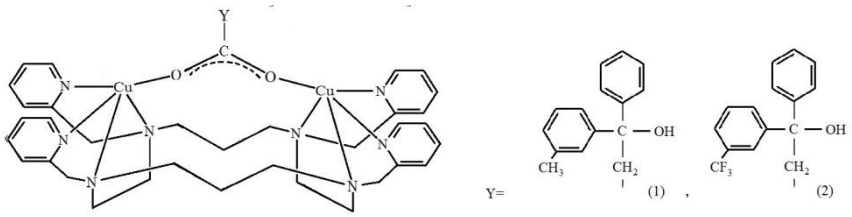

Scheme 1. Proposed structures of the complex cation $[Cu_2(L)tpmc]^{2+}$ (L1= 3-(3-methylphenyl)-3-hydroxy-3-phenylpropanoic acid (1); L2= 3-(3-(trifluoromethyl) phenyl)-3-hydroxy-3-phenylpropanoic acid (2))

CONCLUSION

Two new binuclear cationic Cu(II) complexes with octaazamacrocyclic ligand tpmc and β-aryl-β-hydroxy propanoic acids were prepared Their composition and geometries were assumed based on elemental analysis,

electrical conductivity and spectral properties, as well as by comparison with previously published results of related complexes. It is proposed that the complexes are binuclear, same exo coordination of each Cu(II) ion with azamacrocyclic ligand engaging two pyridine nitrogens and two cyclam's N atoms, and μ- O,O' coordinated COO^- group from β-aryl-β-hydroxy propanoic acids.

Acknowledgement
This work was partially supported by the Ministry for Science of the Republic of Serbia (Grants no. 172014).

REFERENCES

[1] S. Chandrasekhar, W. L. Waltz, L. Prasad, J. W. Quail, Can. J. Chem., 1997, **75**, 1363 – 1374
[2] E. Asato, H. Toftlund, S. Kida, M. Mikuriya, K. S. Murray, Inorg. Chim. Acta, 1989, **165**, 207 – 214
[3] J.Savić, S.Dilber, M. Milenković, J. Kotur-Stevuljević, B. Marković, S. Vladimirov, J. Brborić, Medicinal Chemistry, 2017, **13**(2), 186-195

TETRANUCLEAR *CR-REE*-FERROCENECARBOXYLATES WITH DEFECT-DICUBANE STRUCTURE

P.S. Koroteev, N.N. Efimov, A.B. Ilyukhin, A.V. Gavrikov, Zh.V. Dobrokhotova and V.M. Novotortsev

N.S. Kurnakov Institute of General and Inorganic Chemistry of Russian Academy of Sciences, 119991, Leninskyprosp., 31, Moscow, Russia. (pskoroteev@list.ru)

ABSTRACT

Using ferrocenecarboxylic acid and triethanolamine as core-forming ligands, a series of isostructural *Ln-Cr-Fe*-trimetallic complexes having defect-dicubane structure was obtained. In all of the complexes, doubly deprotonated triethanolamine chelates the chromium ion, however, for Tb an isomeric complex in which Tb^{3+} is chelated by triethanolamine as a tetradentate ligand, was also isolated. DC magnetic studies revealed ferromagnetic interactions in the metal core of Dy and Ho complexes at $T \approx 25$ K, and in Y complex below 25 K. Complexes of heavy lanthanides display the properties of single-molecule magnets. Thermolysis of the complexes was studied by means of TG and DSC; the products obtained under air contain trimetallic oxide phases.

INTRODUCTION

The preparation and investigation of polynuclear *3d-4f*-heterometallic complexes is an extensive and intensively developing field of modern coordination chemistry. A special type among heterometallic complexes is represented by carboxylates and diketonates containing transition metal in an organometallic fragment. In recent years, we have obtained and studied a variety of complexes based on REE and organometallic acids [1]. The obtained complexes can serve as precursors for valuable complex oxides of a specified composition [2]. It was of interest to obtain complexes containing atoms of three different metals. One of the most common types of ligands used to construct *3d-4f*-complexes are the polynuclear aminoalcohols. Here we report on the synthesis and studies of new *3d-3d'-4f*-trimetallic complexes based on ferrocenecarboxylic acid ($FcCO_2H$) and triethanolamine (H_3tea) as core-forming ligands.

EXPERIMENTAL

Commercial reagents and solvents were used for the syntheses. All experiments with the solutions were carried out in foil-wrapped vessels to prevent photolysis. The solvents were purified by conventional methods.

Complexes $[Ln_2Cr_2(OH)_2(FcCO_2)_4(NO_3)_2(Htea)_2]\cdot 2MePh\cdot 2THF$ (Ln = Tb (**1** and **1a**), Dy (**2**), Ho (**3**), Er (**4**), and Y (**5**)) were obtained by interaction of $Cr(NO_3)_3\cdot 9H_2O$, $Ln(NO_3)_3\cdot nH_2O$, $FcCO_2H$, triethanolamine and triethylamine in the CH_3OH/THF mixture with the following evaporation in vacuum, extraction of the residue with the THF/EtOH/toluene mixture, and the following slow evaporation during 10 days. The yields were 40-45%. For the case of Tb, in one of the syntheses, several crystals of the isomeric complex **1a** appeared on the third day.

RESULTS AND DISCUSSION

Structure of isomorphous compounds will be considered taking complex **1** as an example. The central fragment of the centrosymmetric complex $[Tb^{III}_2Cr^{III}_2(OH)_2(FcCO_2)_4(NO_3)_2(Htea)_2]$ (Fig. 1, left) is formed by two cubes built of metal atoms, μ_3-O atoms and O atoms of the coordinated Htea. Each cube is lacking one vertex and sharing a common facet $Tb_2\mu_3\text{-}O_2$. Coordination number of Tb atom is 8, and the polyhedron is a strongly distorted trigonal dodecahedron. Htea ligand is coordinated by the Cr atom; the ligand branch that bears hydroxyl, is not coordinated.

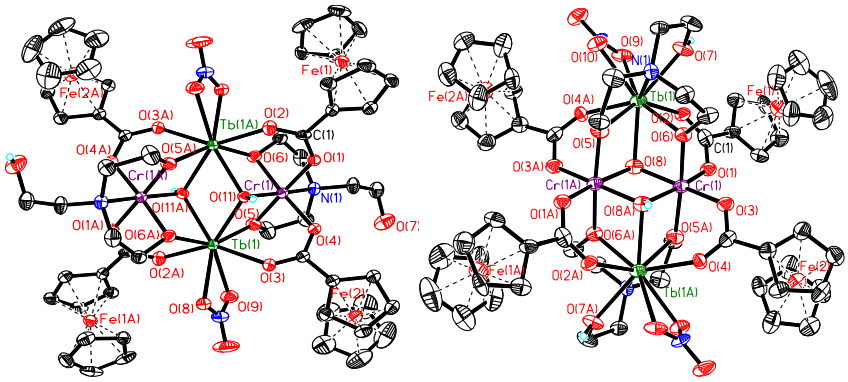

Figure 1. Structure of complexes **1** (left) and **1a** (right).

The structure of complex **1a** (Fig. 1, right), which is isoformular with **1**, is also based on the defect-dicubane motif. However, in **1a** Htea chelates the Tb atom, unlike in compound **1**. Two deprotonated Htea oxygen atoms unite the Tb and Cr atoms, the third OH group of the Htea also coordinates Tb, so that CN (Tb) is 9 and the polyhedron is the three-capped trigonal prism.

Thermolysis of complexes **1** - **5** was studied in atmospheres of argon and air. In both cases, the thermal decomposition of complexes occurs stepwise, and the main characteristics of the process are independent of the nature of the REE ion. The results of the study of the Ho complex **3** are taken as an example (Fig. 2). The first step of the decomposition both in air and in the inert atmosphere in the temperature range of 60 – 160°C is the removal of lattice THF and toluene. The desolvated compound is stable under Ar up to 270°C. At higher temperature, in case of the Ar atmosphere, the exothermic intramolecular reduction of NO_3^- groups starts (Fig. 2). In the range of 320 – 370°C the mass loss is insignificant; the further temperature rise leads to a start of the third stage (370 - 520°C) during which the weight loss accompanied with a complex-shaped endotherm is observed. This stage corresponds to a further destruction of organic parts of the molecule with a partial elimination of ferrocene (b.p. = 249°C). At higher temperatures, the weight loss process substantially slows down and is not completed at 950°C. The products of the decay under Ar are amorphous.

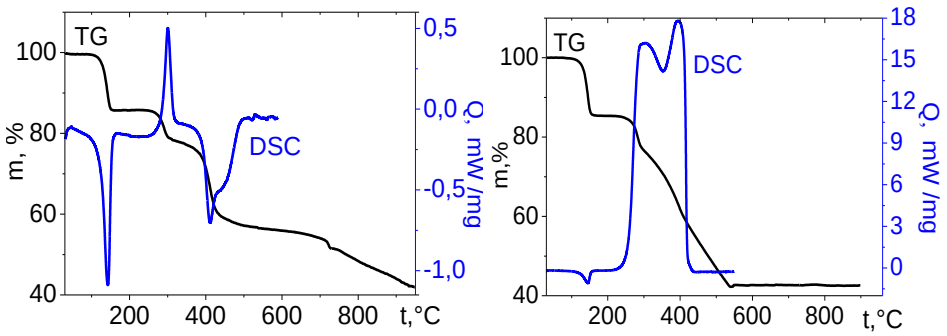

Figure 2. Thermolysis of complex **3** under Ar (left) and in air (right).

To obtain well-crystallized products, thermolysis of the complexes under air with the following annealing at 850°C during one hour was performed. According to the data of powder X-ray analyses, the products contained perovskite phases $LnMO_3$ (M = Cr/Fe) and a mixed oxide $Cr_{0.75}Fe_{1.25}O_3$. According to energy dispersive X-ray microanalyses, the gross composition of the thermolysis products approximately corresponds to the formula $LnCrFe_2O_6$. Since the second phase in the mixture is $Cr_{0.75}Fe_{1.25}O_3$, the estimated formula for the trimetallic perovskite phase is $LnCr_{0.25}Fe_{0.75}O_3$. Such phases are interesting as multiferroic materials.

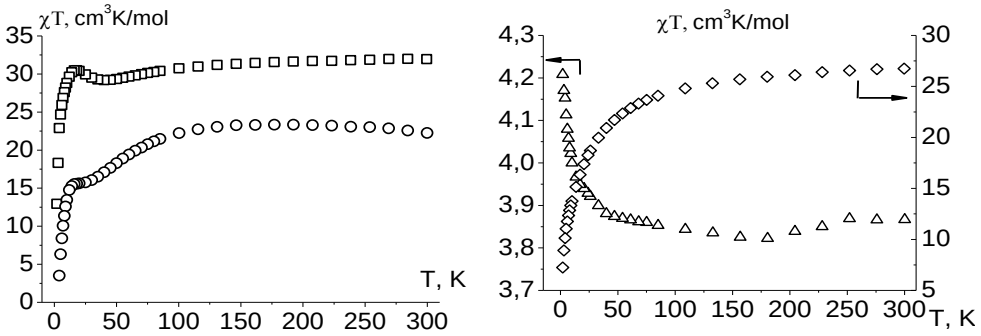

Figure 3. $\chi_M T(T)$ depenences for complexes **1** (○), **2** (□), **4** (◊), **5** (Δ).

The $\chi_M T$ values experimentally determined at 300 K for the newly studied complexes **1 - 5** are close to the theoretical summary values for two isolated Ln^{3+} and two Cr^{3+} ions. The magnetic behavior of complexes **1** – **3** is somewhat similar; it reveals ferromagnetic interactions in the cores of them at T ≈ 25K. Such effect is suppressed in case of **4**, however, in complex **5** containing diamagnetic Y, ferromagnetic interactions between Cr^{3+} ions appear below 25 K and are noted down to 2K (Fig. 3). The results of AC magnetic studies allowed to characterize complexes **1 - 4** as SMMs.

CONCLUSION

In summary, we obtained a family of new *3d-3d´-4f*-trimetallic complexes containing an organometallic ferrocene fragment, $[Ln_2Cr_2(OH)_2(FcCO_2)_4(NO_3)_2(Htea)_2]\cdot 2MePh\cdot 2THF$ (Ln = Tb, Dy, Ho, Er, and Y). Metal core of the complexes belongs to the defect-dicubane type. The presence of ferromagnetic interactions in the cores of Tb, Dy, Ho and Y complexes was shown. Complexes **1**, **2**, **3**, and **4** display the properties of SMMs with magnetization reversal barriers Δ_{eff}/k_B of 56, 80, 48 and 14 K, respectively. Thermolysis of complexes in air leads to the mixture of $Cr_{0.75}Fe_{1.25}O_3$ and trimetallic perovskite phases $LnCr_{1-x}Fe_xO_3$ ($x \approx 0.75$).

Acknowledgement

The work was supported by the Russian Science Foundation (grant 14-13-00938).

REFERENCES

[1] N. N. Efimov, P. S. Koroteev, A. V. Gavrikov et al., Magnetochemistry, 2016, **2 (4)**, 38, DOI: 10.3390/magnetochemistry2040038.

[2] P. S. Koroteev, Zh. V. Dobrokhotova, A. B. Ilyukhin et al., Rus. J. Coord. Chem., 2016, **42 (9)**, 591–603.

SYNTHESIS AND CHARACTERIZATION OF NEW MIXED LIGAND COMPLEXES Cu(II) WITH MACROCYCLICE AND VALINE/NORVALINE

M. Antonijević-Nikolić[1], S. Tanasković [2], B. Dražić[2] and V. Živković-Radovanović[3]

[1]*Higher Medical and Business-technological School of Applied Studies, Hajduk Veljkova 10, 15000 Šabac, Serbia,(nikanto@ptt.rs),*
[2]*Faculty of Pharmacy, University of Belgrade, Vojvode Stepe 450, 11000 Belgrade, Serbia,*
[3] *Faculty of Chemistry, University of Belgrade, P.O.Box 118, 11158, Serbia*

ABSTRACT

The new mixed ligand binuclear complexes of Cu(II) with amino acids, L-valine (2-amino-3-methylbutanoic acid) and L-norvaline (2-aminopentanoic acid) and tpmc (*N*,*N´*,*N´´*,*N´´´*-tetrakis-(2-pyridylmethyl)-1,4,8,11-tetraazacyclotetra-decane) were synthesized and characterized by elemental analysis, molar conductivity, FTIR and electronic spectroscopy. In these complexes, the macrocyclic ligand tpmc is coordinated through all eight nitrogens to two Cu(II) ions. Based on the results of applied methods we proposed that the complexes with the general formula: $[Cu_2(L)(tpmc)](ClO_4)_4 \cdot xH_2O$, L=valine, x=1; L=norvaline, x=0, are binuclear with five-coordinate square pyramidal geometries around Cu(II) ions. The spectroscopic measurements suggested that the aminocarboxylate ligands are coordinated via their carboxylate group.

INTRODUCTION

Macrocyclic structures are favourable for metal complexation and, thus, a large number of macrocyclic ligands have been synthesized because of their importance in coordination chemistry. Among the various ligands, the 1,4,8,11-tetraazacyclotetradecane (cyclam) is one of the most studied azamacrocycle [1]. Most of these studies have been focused on macrocycle bearing additional coordinating pendant groups as octaazamacrocycle *N*,*N´*,*N´´*,*N´´´*-tetrakis-(2-pyridylmethyl)-1,4,8,11-tetraazacyclotetradecane (tpmc) [2], Fig. 1.

The field of investigation concerning azamacrocyclic and/or aminocarboxylic transition metal complexes is widely explored with regard to their properties: some of them are models for the active centres of

metalloenzymes, potentially bioactive and could be used as drugs, catalysts or new materials with specific electrical and magnetic properties [3, 4].
Previously we have described copper(II) complexes with octaazamacrocycle *N*,*N*´,*N*´´,*N*´´´-tetrakis-(2-pyridylmethyl)-1,4,8,11-tetraazacyclotetradecane and μ-coordinated aminocarboxylate, L-glycine and L-alanine [5]. Continuing our research in this paper we described the synthesis and properties of two new dinuclear copper(II) complexes with L-valine and L-norvaline (Fig. 1).

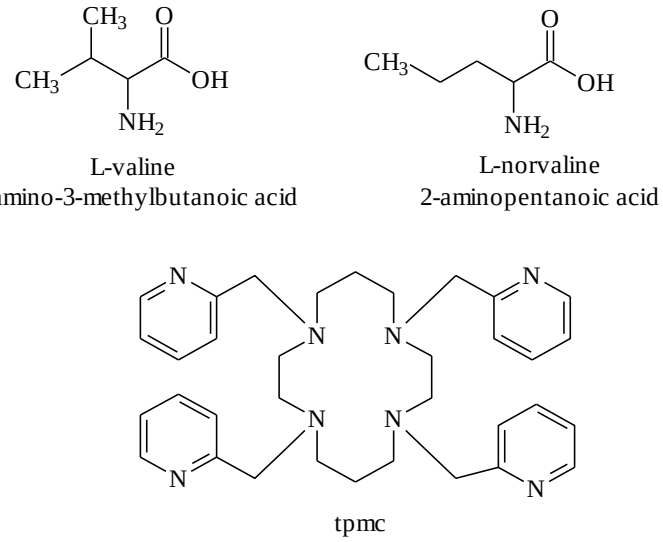

Figure 1. Structure of ligands.

EXPERIMENTAL

Preparation

The ligand and complex $[Cu_2tpmc](ClO_4)_4$ were prepared according to a previously reported procedure [1, 2].

The complexes were synthesized by the reaction of $[Cu_2tpmc](ClO_4)_4$ and aminoacids: valine or norvaline in 1:1.5 molar ratio. The complexes with general formula $[Cu_2(L)(tpmc)](ClO_4)_4 \cdot xH_2O$, L=valine, x=1; L=norvaline, x=0 were prepared by the addition of ligand aqueous solution (17 mg, 0.14 mmol valine or norvaline) to a solution of the complex $[Cu_2tpmc](ClO_4)_4$ (100 mg, 0.09 mmol) in CH_3CN. The mixture was then refluxed on a water bath for 2 h with stirring. The blue products obtained were filtered and dried at room temperature.

Measurements

Elemental analysis (C, H, N) were performed by standard micromethods in the Centre for Instrumental Analysis, Faculty of Chemistry, Belgrade. The

conductivity of the complexes in CH_3CN ($1\cdot10^{-3}$ M) was measured at room temperature using a Hanna instruments HI 8820N conductometer. Electronic absorption spectra of the complexes in CH_3CN ($1\cdot10^{-3}$ M) were recorded on spectrophotometer GBC UV/Vis Cintra 20 in the range 200-700 nm. FTIR spectra (ATR technique) were recorded using NICOLET 6700 FTIR spectrophotometer in the range 400- 4000 cm^{-1}.

RESULTS AND DISCUSSION

The results of elemental analysis are consistent with a proposed general formula $[Cu_2(L)(tpmc)](ClO_4)_4\cdot xH_2O$, L=valine, x=1; L=norvaline, x=0. The analytical data are in Table 1.

Table 1. Analytical data of the complexes.

complex	FW	Found (Calculated) (%) C	H	N	Yield (%)	Λ_M (S cm^2 mol^{-1})
$[Cu_2(val)(tpmc)](ClO_4)_4\cdot H_2O$	1248.59	37.97 (38,22)	4.84 (4.69)	10.23 (10.29)	80	600
$[Cu_2(norval)(tpmc)](ClO_4)_4$	1207.54	38.71 (38,78)	4.32 (4.59)	10.49 (10.69)	76	401

The molar conductivity of the complexes in CH_3CN (Table 1) showing that they are 1:4 electrolyte type. The electronic spectra of Cu(II) complexes exhibited bands at 651 nm and 681 nm for valine or norvaline complexes respectively, assigned to the d-d transitions. It is expected for five-coordinated Cu(II). The appearance and position of the maxima correspond to CuN_4O chromophores. This indicates that the aminocarboxylates are coordinated through OCO^- group to Cu(II) [3]. In the FTIR spectra of the complexes some common characteristic bands are observed: a strong band ~1610 cm^{-1} is typical for the skeletal vibration of coordinated pyridine from tpmc; at 1100 cm^{-1} the strongest band in the spectra belongs to the $\nu(ClO_4^-)$ and sharp, medium intensity band at ~620 cm^{-1} to $\delta(ClO_4^-)$. In free aminocarboxylate ligands and complexes there are amine bands $\nu(NH_3^+)$ in the range 2630-3149 cm^{-1} and bands at about 1600 $cm^{-1}$from $\delta_{as}(NH_3^+)$ overlapped the $\nu_{asym}(OCO^-)$. The FTIR spectral assignments for the complexes were achieved by comparing their vibration frequencies with those of the free ligands in the region of carboxylic group (Table 2).

Table 2. Some FTIR data of OCO^- group from free aminocarboxylate ligands and the corresponding complexes.

compounds	$\nu_{asym\ (OCO^-)}$	$\nu_{sym(OCO^-)}$	$\Delta\nu$ $(\nu_{asym}-\nu_{sym})$
$[Cu_2(val)(tpmc)](ClO_4)_4 \cdot H_2O$	1600	1402	198
Valine	1589	1395	194
$[Cu_2(norval)(tpmc)](ClO_4)_4$	1573	1415	158
Norvaline	1583	1410	173

The asymmetric and symmetric stretching vibration for the carboxylate group was shifted with the complexes, confirming coordination via this functional group. In accordance with that is Δν value of complex compared with Δν of valine/norvaline. In complexes OCO^- group formed a bridge between two Cu(II) from the same tpmc [3].

CONCLUSION

In this article we reported the synthesis and characterization of two new Cu(II) mixed ligand complexes with octaazamacrocyclic ligand tpmc and aminocarboxylate: L-valine and L-norvaline. The complexes are binuclear in which the five coordination sites around the Cu(II) are occupied by four nitrogen atoms from the macrocyclic ligand tpmc and one oxygen atom from valine/norvaline. Aminocarboxylate ligands are coordinated via carboxylic group whereas amino group do not participate in the coordination to Cu(II).

Acknowledgement

This work was partially supported by the Ministry for Science of the Republic of Serbia (Grant no. 172014).

REFERENCES

[1] S. Chandrasekhar, W. L. Waltz, L. Prasad, J. W. Quail, Can. J. Chem.,1997, **75**, 1363 – 1374.

[2] E. Asato, H. Toftlund, S. Kida, M. Mikuriya, K. S. Murray, Inorg. Chim.Acta, 1989, **165**, 207 – 214.

[3] G. Vučković, M. Antonijević Nikolić, S. B. Tanasković, V. Živanović Radovanović, J. Serb. Chem. Soc., 2011, **76**, 719–731 (and references cited therein).

[4] S. Anbu, M. Kandaswamy, P.S. Moorthy, N. Balasubramanian, M.N. Ponnuswamy, Polyhedron, 2009, **28**, 49-56.

[5] M. Antonijević Nikolić, S. B. Tanasković, V. Živković Radovanović, 13th International Conference on Fundamental and Applied Aspects of Physical Chemistry, Belgrade, September 26-30, 2016, Proceedings Vol II, 771-774.

N *– General Physical Chemistry*

IONIZATION ENERGIES OF K_nI (n = 2, 3) CLUSTERS THEORETICAL AND EXPERIMENTAL EVALUATION

B.Milovanović [1] M. Milovanović [1], S. Veličković [2], F.Veljković [2], A. Perić-Grujić [3] and S. Jerosimić [1]

[1)] University of Belgrade, Faculty of Physical Chemistry, Studentski trg 12-16, P.O.Box 47, PAC 105305, 11158 Belgrade, Republic of Serbia
[2)] University of Belgrade, Vinča Institute of Nuclear Sciences P. O. Box 522, 11001 Belgrade, Republic of Serbia (vsuzana@vin.bg.ac.rs)
[3)] University of Belgrade, Faculty of Technology and Metallurgy, Karnegijeva 4, 11120 Belgrade, Serbia

ABSTRACT

In the present study, we report the results of experimental observations of ionization energies for K_nI (n = 2 and 3) clusters along with the results of theoretical investigations. Experiments were done using a Knudsen effusion cell as a chemical reactor with thermal or surface ionization, and selected by a magnetic sector mass spectrometer which provided simultaneous generating of all clusters at once. Theoretical adiabatic ionization energies for K_nI (n = 2 and 3) are close to experimental values. The results have shown that this experimental setup provides efficient way for determining of the ionization energies of the type K_nI clusters.

INTRODUCTION

The non-stoichiometric potassium iodide clusters of the form K_nI_{n-1} (n=2 and 3) were detected with many mass spectrometric techniques [1-9]. For example, mass spectrometric analysis of the ionic sublimation of KI crystals in the interval of 670-900 K showed the presence of positive ions K^+ (100), K_2^+ (5.5), K_2I^+ (6.4), $K_3I_2^+$ (7.1×10^{-2}), and negative ions I^- (2.9×10^{-3}), K_2I^- (7.6×10^{-2}) [1]. Also, thermal emission of molecules and ions from the $CsAg_4I_5$ (I) and KAg_4I_5 (II) solid electrolytes was investigated by mass spectrometer over temperature range 500-760 K, and K_2I^+ was identified [2]. By mass spectroscopy ion species, K^+, K_2^+, K^+, KI^+, K_2I^+, I_2^+, $K_2I_2^+$, and $K_3I_2^+$ were recorded in the vapors over KI [3, 4]. During the studies of KI and KOH mixture, the ions K_2I^- and $K_2I_3^-$ were also identified [4]. Potassium halide adducts of the form K_2X^+ desorbed from neutral salts by high power pulsed infrared laser radiation are detected by Fourier transform ion cyclotron resonance mass spectrometry (FT-ICR). Among the potassium halides, KI generates the highest ratio of detected K_2I^+ to K^+, so is therefore

best suited for cation-transfer reactions in infrared laser desorption ionization FT-ICR [5]. The K_2I^+ ions are produced from solution of potassium iodide salt in methanol by electrospray ionization (ESI). This cluster data are of importance in protein analysis by ESIMS [6-8]. The K_2I ion was formed by the surface ionization mass spectrometry (SIMS) using triple filament technique [9].

However, experimental and theoretical data about ionization energies of K_nI clusters are very scarce. Hence the main purpose of this work is to provide data about the conditions for measuring the ionization energies of iodine–doped potassium clusters and compare these results with corresponding theoretical values.

EXPERIMENTAL

The experimental method has been previously described [10]. Briefly, the rhenium (Re) filament was placed in the centre of the Knudsen effusion cell's base. The sample, KI salt, was pressed as a ring and placed on the inner wall of the Knudsen effusion cell. The ions emitted from the surface of Re filament were extracted to a mass analyzer, a 12-inch radius, 90° magnetic sector.

The ionization energies of the clusters were calculated by the Ionov equation: $\ln (I(K^+)/I(cluster^+))= (IE(cluster^+)-IE(K^+))/kT$.

RESULTS AND DISCUSSION

In this work K_2I^+ and K_3I^+ clusters were obtained in the vapor of KI salt, using the Knudsen effusion method in the temperature range from 1100-1500 K. To determine ionization energies of the clusters produced, the ion currents of K_nI^+ (n = 2, 3) clusters were measured as a function of the Re filament temperature. Plots of $\ln I_i^+$ (I_i^+ - ion intensity of positive ions**)** versus 1/T for K_2I^+ and K_3I^+ clusters is presented in Fig. 1a and 1b.

Using 4.34 eV as the ionization energy of K^+, and the values of the slopes of the plots $\ln (I(K^+)/I(cluster^+)) = 1/T$ by Ionov equation, the ionization energy of clusters were obtained.

In order to calculate the ionization energies for the K_nI (n = 2 and 3) clusters, single-point RCCSD(T)/ECP10MDF(K), cc-pVQZ-PP(I) calculations were performed at the B3P86-optimized geometries, for most stable isomers. Experimental values together with the adiabatic (AIE) and vertical (VIE) ionization energies for the most stable K_nI (n = 2 and 3) species, obtained at the B3P86/ECP10MDF(K),cc-pVTZ-PP(I) (marked with *a*) and RCCSD(T)/ECP10MDF(K),cc-pVQZ-PP(I)//B3P86/ ECP10MDF(K), cc-pVTZ-PP(I) (marked with *b*), are presented in Table 1. One can see that DFT values is higher up to 0.7 eV than RCCSD(T) values.

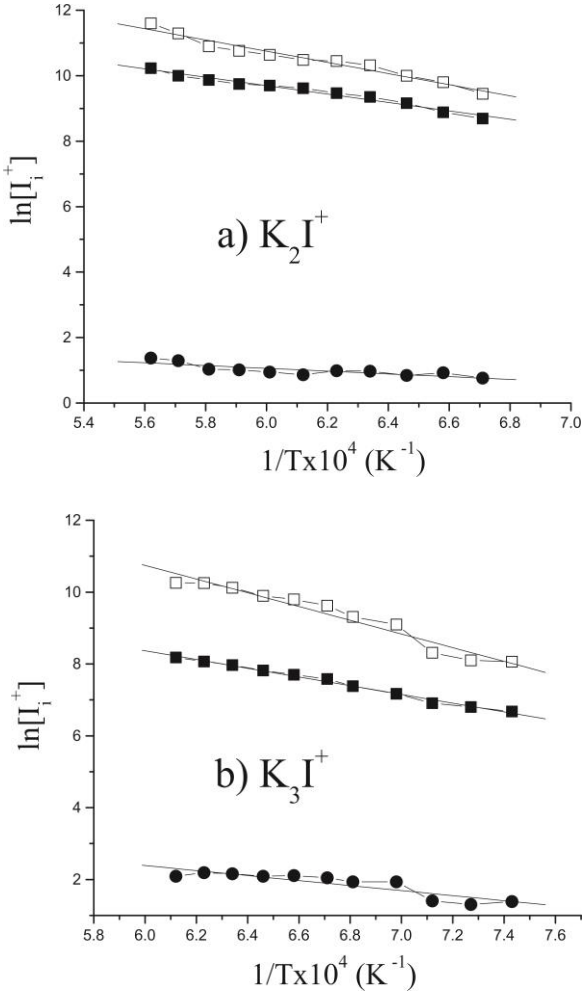

Figure 1. Plots of ln I_i^+ (I_i^+ - ion intensity of positive ions**)** versus 1/T for K_2I^+ (a) and K_3I^+ (b) cluster, where white square is ln($I(K^+)$, black square is ln($I(K_2I^+)$ (a) and ln($I(K_3I^+)$ (b), black circle is ln($I(K^+)/I(K_2I^+)$) (a) and ln($I(K^+)/I(K_3I^+)$) (b).

Table 1. Experimental and computed adiabatic (AIE) and vertical (VIE) ionization energies (in eV) for potassium-iodide K_2I and K_3I clusters.

	AIE	VIE	Exp.
K_2I	3.98[a] 3.39[b]	4.61[a] 4.09[b]	3.92±0.10[7] 3.98±0.20
K_3I	4.28[a] 3.80[b]	4.72[a] 4.32[b]	3.74±0.20

CONCLUSION

Comparing theoretical ionization energies with experimental values, it can be seen that for K_nI (n = 2 and 3) clusters adiabatic ionization energies are

close to experimental values. These experimental results showed that the Knudsen effusion cell, as chemical reactor, combined with thermal or surface ionization, is a suitable method for determination of the ionization energies for obtained clusters.

Acknowledgement
This work was supported by the Ministry of Education, Science and Technological development of the Republic of Serbia (Project No. 172019 and 172040).

REFERENCES

[1] M. F. Butman, L. S. Kudin. *Zh. Fiz. Khim*. 2003, **77**, 997.
[2] A. M. Pogrebnoi, L. S. Kudin, K. V. Rakov. *Zh. Fiz. Khim*. 2001, **75**, 825.
[3] T. A. DeMercurio, R. T. Grimley. *ECS-Proceedings*. 1986, **86**, 59.
[4] G. G. Burdukovskaya, L. S Kudin, M. F. Butman, K. S. Krasnov. *Zh. Neorg. Khim*. 1984, **29**, 3020.
[5] J. D. Hogan, D. A. Laude. *J. Am. Soc. Mass Spectrom*. 1992, **3**, 301-310.
[6] A. T. Blades, M. Pescahke, U. H. Verkerk, P. Kebarle. *J.Am. Chem. Soc*. 2004**, 126**, 11995–12003.
[7] S. R. Veličković, F. M. Veljković, A. A. Perić-Grujić, B. B. Radak, F. M. Veljković. *Rapid Commun. Mass Spectrom.* 2011, **25**, 2327-2332.
[8] G.D. Wang, R.B. Cole. *Anal. Chim. Acta.* 2000, 406, 53-65.
[9] R. Juraschek, T. Dulcks, M. Karas, *J. Am. Soc. Mass Spectrom*. 1999**, 10**, 300-308.
[10] S. R. Veličković, J. B. Đustebek, F. M. Veljković, M. V. Veljković. *J. Mass Spectrom*. 2012, **47**, 627-631.

EXPERIMENTAL EVALUATION OF $Li_3Cl_2^+$, $Li_4Cl_3^+$ AND $Li_5Cl_4^+$ CLUSTERS' IONIZATION ENERGIES

F. Veljković, B. Vurdelja, B. Rajčić and S. Veličković

University of Belgrade, VINČA Institute of Nuclear Sciences, Department of physical chemistry, P. O. Box 522, Belgrade, Republic of Serbia,
(vsuzana@vinca.rs)

ABSTRACT

In current study, a non-stoichiometric lithium chloride clusters of the type Li_nCl_{n-1} (n = 3 - 5) are generated by combining a Knudsen effusion cell and surface ionization, and selected by a magnetic sector mass spectrometer. Ionization energies determined by Saha - Langmuir equation for $Li_3Cl_2^+$, $Li_4Cl_3^+$ and $Li_5Cl_4^+$ clusters were 4.51 ± 0.2 eV, 4.18 ± 0.2 eV and 5.05 ±0.2 eV, respectively. These values are in consistence with theoretically gained ionizations energies.

INTRODUCTION

Clusters of lithium halides attract attention of scientists, both, experimental and theoretical, since they can be intermediates between atoms and bulk materials. Clusters consisting of lithium metal along with high electronegative element such as chlorine, exhibit unique physical and chemical phenomena which have fundamental and technological significance [1].

Current study of lithium chloride clusters is an extension of our previous studies on the heterogeneous lithium clusters. Earlier, clusters Li_nCl (n = 2 and 3) were formed by the surface (thermal) ionization mass spectrometry using triple filament technique, where the side filaments were used to evaporate the sample while the central filament was used for ionization of the neutral species. In this case sample was the mixture of lithium chloride, lithium iodide, and fullerene (C_{60}) [2]. It was noted that arrangement of the triple filament ion sources has an important role in obtaining this kind of clusters. By modifying sources for surface ionization the clusters of the type Li_nCl (n ≥3) were obtained. The thermal ionization source of modified design allows detection Li_nCl (n = 2 - 6) clusters simultaneously, in one set of measurements, which makes it possible to monitor the stability of ions of these clusters [3]. Previous studies have shown that the cluster ions of the

type $Li_nCl_m^+$ ($n \geq m$, n = 1–6, m = 1–3) were obtained by the same experimental setup in the temperature range between 1800 and 2700 K [4].

Given the lack of experimental data about ionization energies (IE) for $Li_nCl_{n-1}^+$ ($n \geq 3$) clusters, the aim of the current study was to get data about conditions for the measurement of the IE of these clusters, and to compare them with the theoretical results, where possible.

EXPERIMENTAL

The experiment is performed using the Knudsen cell which was placed into ionization chamber of a magnetic sector mass spectrometer. The filament of tungsten is placed in the center of the Knudsen effusion cell. The experimental conditions allowed direct identification of positive charge ionic. For this reason the ionization energies of the Li_nCl_{n-1} (n = 3 – 5) clusters can be obtained by the Saha-Langumuir equation [2, 3]:

$$I_i^+ = A\exp[(\Phi - IE_i)/kT] \quad (1)$$

where I^+ is the ion current (*i* are Li^+ or $Li_nCl_{n-1}^+$); A is the term containing reflection coefficients and statistical weighting factors (constant with temperature); Φ is the work function of the ionization filament, IE*i* are the ionization energies of clusters or atoms; k is the Boltzman's constant, T is the temperature of the tungsten filament. The slope of the plotting $\ln(I(Li^+)$ versus 1/T gives the values of work (Φ)function for this experimental conditions. Using the slope of the plotting $\ln(I(Li_nCl_{n-1}^+)$ versus 1/T and the values of work function obtained in the previous step the ionization energy of $Li_nCl_{n-1}^+$ clusters was obtained.

In the second case Ionov equation is gained by dividing the equation for Li^+ and $Li_nCl_{n-1}^+$:

$$\ln (I(Li^+)/I(Li_nCl_{n-1}^+)) = (IE(Li_nCl_{n-1}^+) - IE(Li^+))/kT \quad (2)$$

The slope of the plotting $\ln(I(Li^+)/I(Li_nCl_{n-1}^+))$ versus 1/T gives the difference between the ionization energies of $Li_nCl_{n-1}^+$ and the IE of Li^+. Using 5.39eV as the ionization energy of lithium, and the values of the slopes of the plots $\ln (I(Li^+)/I(Li_nCl_{n-1}^+)) = 1/T$ by equation 2, the ionization energy of $Li_nCl_{n-1}^+$ clusters was obtained.

RESULTS AND DISCUSSION

In this study clusters $Li_nCl_{n-1}^+$ (n = 3, 4, and 5), such as $Li_3Cl_2^+$, $Li_4Cl_3^+$, $Li_5Cl_4^+$, were obtained by the evaporation solid lithium chloride salt from the Knudsen effusion cell. The conditions for producing the non-stoichiometric lithium chloride clusters were optimized by adjustments of

temperatures of the filament of tungsten. The ion intensities of $Li_nCl_{n-1}^+$ clusters as a function of this filament temperature were measured. The natural logarithm of the ion intensities of the most abundant isotopes for $Li_3Cl_2^+$, and $Li_5Cl_4^+$ together with the ion intensities of Li^+ are plotted in Fig. 1 as a function of the inverse of the filament temperature (1/T). Using Saha-Langumuir equation is obtained results for IE of these clusters.

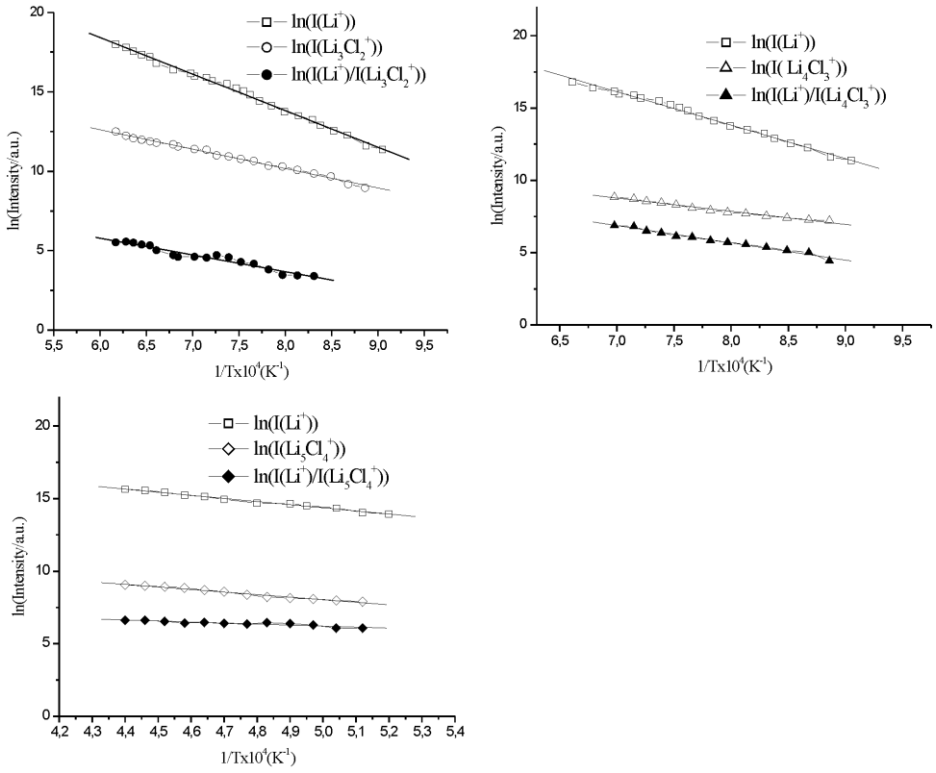

Figure 1. Plots of ln(Intensity) versus 1/T for $Li_nCl_{n-1}^+$ (n = 3, 4, and 5): white square is natural logarithm of the ion intensities for lithium, white circle is $ln(I(Li_3Cl_2^+))$; white up triangle is $ln(I(Li_4Cl_3^+))$; white diamond is $ln(I(Li_5Cl_4^+))$; black circle is $ln(I(Li^+)/I(Li_3Cl_2^+))$; black up triangle is $ln(I(Li^+)/I(Li_4Cl_3^+))$; black diamond is $ln(I(Li^+)/I(Li_5Cl_4^+))$; T is filament temperature.

It needs to be pointed out that the signals detected at *m*/z 133, 132, 134, 135, 136, 137 indicate the presence of $Li_4Cl_3^+$. However, according to obtained results the most abundant isotopes for $Li_4Cl_3^+$ and Cs^+ ions are characterized by a same mass number (*m*/z 133). Hence for $Li_4Cl_3^+$ the ion

intensity of the isotope at *m/z* 135 as a function of filament temperature were measured. In the same Figure is shown the plots $\ln(I(Li^+)/I(cluster^+))$ versus 1/T. The IE for each cluster was determined by Ionov equation 2. In Table 1 are summarized the experimental and theoretical values of the IEs for Li_nCl_{n-1} (n = 3, 4, and 5) clusters.

Table 1. The experimental and theoretical values of the ionization energies for Li_nCl_{n-1} (n = 3, 4, and 5) clusters

Clusters	Ionization energies **(Saha-Langmuir equation) (eV)**	Ionization energies **(Ionova equation) (eV)**	Ionization energies (**Theoretical values**) (**eV**)
Li_3Cl_2	4.51 ± 0.20	4 86 ± 0.20	4.50[4]
Li_4Cl_3	4.18 ± 0.20	4.37 ± 0.20	4.09[4]
Li_5Cl_4	5.05 ± 0.20	4.79 ± 0.20	/

CONCLUSION

The experimentally obtained IEs using Saha-Langmuir equation are in better agreement than Ionova equation with the theoretically calculated adiabatic ionization energies. Being in accordance with theoretically obtained data for $Li_3Cl_2^+$, $Li_4Cl_3^+$ and $Li_5Cl_4^+$ clusters' ionization energies, the obtained experimental results show that using the modified surface ionization source installed in the magnetic sector mass spectrometer might be a suitable method for generation of investigated clusters.

Acknowledgement

Supported by the Ministry of Education, Science and Technological Development of the Republic of Serbia, grant No OI 172019.

REFERENCES

[1] P. G. Reinhard, E. Suraud, Introduction to Cluster Dynamics, Wiley-VCH, Weinheim, 2004.

[2] S. Veličković, V. Đorđević, J. Cvetićanin, J. Đustebek, M. Veljković, O. Nešković, Rapid Commun. Mass Spectrom, 2006, **20**, 3151-3153.

[3] S. R. Veličković, J. B. Djustebek, F. M. Veljković, B. B. Radak, M. V. Veljković, Rapid Commun. Mass Spectrom. 2012, **26**, 443-448.

[4] M. Milovanović, S. Veličković, F. Veljković, S. Jerosimić, Structure and stability of small lithium-chloride $Li_nCl_m^{(0,1+)}$ ($n \geq m$, n = 1–6, m = 1–3) clusters, Phys. Chem. Chem. Phys., 2017, **19**, 30481–30497.

INFLUENCE OF DIMETHYL SULFOXIDE ON THE UNFOLDING MECHANISM OF HEN EGG-WHITE LYSOZYME: A THEORETICAL STUDY

T. Magsumov and I. Sedov

Kazan Federal University, Chemical Institute,
Kremlevskaya 18, 420008 Kazan, Russian Federation. (timomax@mail.ru)

ABSTRACT

Influence of dimethyl sulfoxide (DMSO) on the unfolding rate and mechanism of hen egg-white lysozyme was studied by molecular dynamics. Average unfolding times were determined using different structural parameters and are shown to be in good agreement with each other. In the presence of ≥ 5 molar percent of DMSO, the protein loses its secondary and globular tertiary structure within 30 ns of simulation at 450 K. In pure water, even after 130 ns of simulation at the same temperature the protein remains in the globule-like state, despite many of its native contacts become disrupted. The unfolding times decrease with increasing DMSO content. Analysis of the temperature dependence of unfolding times yields the activation energy of unfolding, which is, however, much less than the experimental one.

INTRODUCTION

Disruption of the native structure of proteins lead to a loss in biological activity, aggregation, and precipitation. It is well-known that stability of the native protein is influenced by various factors such as temperature, pH, ionic strength, and presence of various organic compounds, which can act as denaturants promoting denaturation or stabilizers preventing it. Of particular interest is the effect of addition of common organic solvents on the protein stability. Organic and aqueous-organic media are suggested to use for some enzyme-catalyzed reactions because they can enhance the solubility of organic substrates, reduce the rate of side reactions, and improve the selectivity. Moreover, organic solvents are used as penetrating cryoprotectants for long-term storage of cellular and protein preparations. In such systems, proteins should not be denatured or their denaturation should be completely reversible.

Experimental methods such as differential scanning calorimetry, fluorescence, circular dichroism, and IR spectroscopy can be used to study the stability and changes in the native protein structure under the influence

of various factors, but they unfortunately cannot provide a detailed molecular mechanism of unfolding. Thus, we appeal to molecular dynamics simulations which allow to monitor the structural changes at molecular level in the nanosecond to microsecond timescale.

In the present work, we studied the effect of addition of dimethyl sulfoxide (DMSO) on the rate and mechanism of unfolding of a model protein, hen egg-white lysozyme (HEWL), using molecular dynamics [1].

EXPERIMENTAL

We performed molecular dynamics simulations using Gromacs 5.1 software. OPLS force field for protein and SPC/E model for water were used. DMSO was modeled using united atom approach (OPLS-UA) [2]. The combination of selected models of water and DMSO reproduces properties of mixtures such as densities, self-diffusion coefficients, and enthalpies of mixing in the full concentration range. The mixture does not separate into organic and aqueous phases at any of the concentrations and temperatures considered.

The initial structure of HEWL was taken from the Protein Data Bank (193L). HEWL was pre-equilibrated in water at T=298 K and p=1 bar for 1 ns. After that, the cell consisting of protein and 10000 molecules of solvent with a mole fraction of DMSO x_1 ranging from 0 to 1 was minimized with fixed protein atoms. After minimization, the cell was heated to 400 K at constant pressure 1 bar for a short time (200 ps). Then the cell was heated in the NVT-ensemble to desired temperature and equilibrated for 1 ns. Finally, position restraints were turned off, and production runs were performed for 30 ns in the solvent mixtures and for 130 ns in pure water. For each concentration, the simulations were repeated 10 times.

RESULTS AND DISCUSSION

Transition from the native to the unfolded state goes continuously, and it is difficult to say at which moment the protein becomes unfolded. We can assume that the time at which some structural parameter reaches certain critical value and the changes in protein structure become prominent and irreversible is the unfolding time t_u. To assess the time of disruption of the tertiary structure, we used several different parameters: RMSD, radius of gyration (Rg), solvent-accessible surface area (SASA), fraction of native contacts (FNC), and distance between two α-helices in lysozyme molecule (D). Dependences of the unfolding times at 450 K obtained using each of these parameters from the composition of solvent mixture is shown in Figure 1.

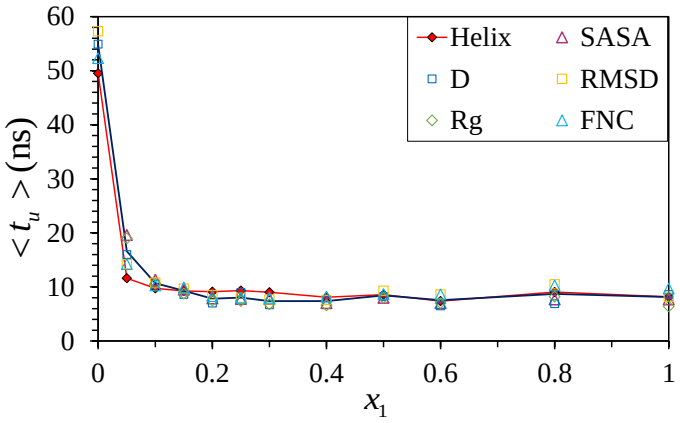

Figure 1. Dependences of $<t_u>$ on the mole fraction of DMSO x_1 in simulations at 450 K. Solid line connects the average of $<t_u>$ values from five different unfolding criteria for each concentration.

The values of unfolding times obtained using different parameters are in general agreement with each other. Unfolding of lysozyme is accelerated with increasing DMSO concentration up to 30-40%, which is in good agreement with experimental observations. At higher concentrations, unfolding times remain approximately constant. In pure water, the protein remains in a compact globule-like state within entire simulation time. However, many of the native contacts become disrupted in this globule. The difference in the unfolding mechanism in pure water and its mixtures with DMSO is clearly manifested in the two-dimensional property space histograms. These histograms can be obtained by plotting the negative

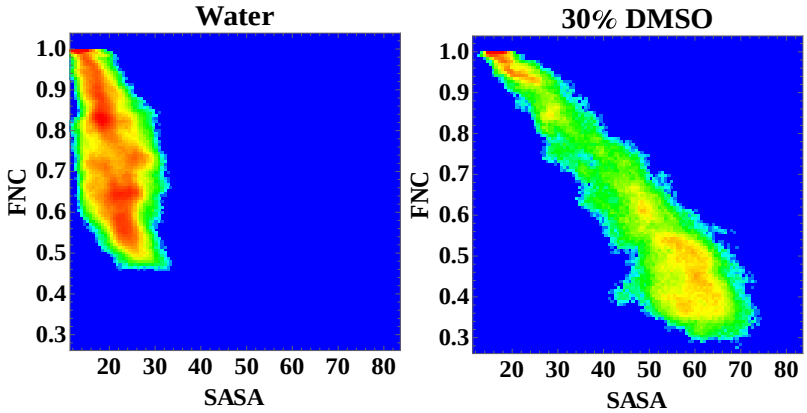

Figure 2. 2D property space histograms for the process of unfolding of HEWL at 450 K in pure water and in mixture with 30 molar percent of DMSO. The most populated areas are colored with red, zero population is indicated with blue.

logarithm of the number of frames $-\ln N(p_1,..,p_i)$ within a simulation trajectory(-ies) for which certain structural parameters $p_1,..,p_i$ of the protein lie in the range $[p_1, p_1+\Delta p_1;...; p_i, p_i+\Delta p_i]$, where $\Delta p_1,...,\Delta p_i$ are parameter bin sizes, against the values of parameters $p_1,..,p_i$, resulting in an i+1-dimensional histogram. We binned the values of FNC and SASA parameters taken each 2ps from all the simulations at the same concentration of DMSO. The resulting plots with the values of $-\ln N$ are shown in color scale (Fig. 2).

Using the values of unfolding times at different temperatures from 373 to 500 K for the mixture of water with 30 molar percent of DMSO, we determined the activation energy of the unfolding process. The plot of $\ln(1/\langle t_u \rangle)$ against 1/T is linear (Fig. 3), which is consistent with Arrhenius equation. The activation energy equals 40±5 kJ·mol^{-1}, which is much less than the experimental value determined by fluorescence spectroscopy (230±20 kJ·mol^{-1}). A similar result was obtained in previous attempts to determine the activation energy of unfolding of various proteins using molecular dynamics [3].

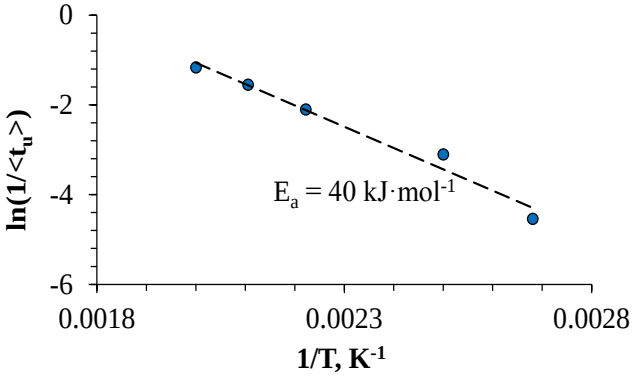

Figure 3. Correlation of $\ln(1/\langle t_u \rangle)$ with 1/T

CONCLUSION

Using molecular dynamics simulations, it is shown that addition of even a small amount of DMSO leads to increase of the rate and change in the mechanism of unfolding. In mixtures, a compact globule-like state is rapidly disrupted, while in water it can be retained for quite a long time.

Acknowledgement

This work was supported by grant 14.Y26.31.0019 from the Ministry of Education and Science of Russian Federation..

REFERENCES

[1] I.A. Sedov, T.I. Magsumov, J. Mol. Graph. Model. 76 (2017) 466–474.
[2] Y.-J. Zheng, R.L. Ornstein, J. Am. Chem. Soc. 118 (1996) 4175–4180.
[3] C. Yan et al.. Mol. Graph. Model. 29 (2010) 2–12.

O *– Pharmaceutical Physical Chemistry*

RATIONAL DESIGN OF SELECTIVE HISTONE DEACETYLASE INHIBITORS

D. Ruzić[1], N. Djoković[1], M. Petković[2], D. Agbaba[1], M. Lahtela-Kakkonen[3], A. Ganesan[4] and K. Nikolić[1]

[1] Department of Pharmaceutical Chemistry, Faculty of Pharmacy, University of Belgrade, Vojvode Stepe 450, 11000 Belgrade, Serbia (knikolic@pharmacy.bg.ac.rs)
[2] Department of Organic Chemistry, Faculty of Pharmacy, University of Belgrade, Vojvode Stepe 450, 11000 Belgrade, Serbia
[3] School of Pharmacy (Pharmaceutical Chemistry) University of Eastern Finland, Kuopio, Finland
[4] School of Pharmacy, University of East Anglia, Norwich Research Park, NR4 7TJ Norwich, United Kingdom

ABSTRACT

The concept of gene expression is continuously explained with epigenetic modifications. One of the most studied enzymes which have an influence on histone posttranslational modifications are histone deacetylases (HDACs). The overexpression and alterations in the structure of HDACs isoforms are described in the pathogenesis of cancer, inflammation and neurodegeneration. With different cellular function and tissue distribution of HDACs, scientists introduced them as attractive targets used in novel drug discovery protocols. Rational drug design of novel small molecules is usually guided by computational approaches. In our laboratory, we use ligand-based (pharmacophore modeling and virtual screening) and structure-based (molecular docking and molecular dynamics) drug design methodologies. The main focus in our drug design project is identification of selective HDAC6 and SIRT2 inhibitors. With respect to all published data, very small number of selective HDAC modulators has been reported so far. Here, we present rational design of novel selective HDAC6 and SIRT2 inhibitors as promising drug candidates for further development and structure optimization.

INTRODUCTION

Histone modifications such as histone acetylation, deacetylation, methylation, demethylation, phosphorylation, and deamination, are defined as epigenetic hallmarks with crucial influence on regulation of gene expression and chromatin organization [1, 2]. The chromatin condensation

and gene expression are mainly regulated by level of activities of Histone Acetyl Transferases (HATs) and Histone Deacetylases (HDACs), which catalyzes acetylation of ε-amino group of particular lysine residues and hydrolysis of acetyl-lysine residues of the histone tails, respectively [3].
Histone deacetylases are clinically confirmed drug targets for cancer, neurological diseases and immune disorders, with four FDA approved HDAC inhibitors (HDACi) for clinical use as antineoplastic drugs [4, 5]. One of the main goals in current epigenetic research is to rationally design selective HDACi for specific isoform as drug candidates with increased efficacy and safety.

The HDAC enzyme family is divided into four classes, where classes I, II and IV are zinc-dependent hydrolases and class III (sirtuins) are NAD+-dependent enzymes [6].

Histone deacetylase 6 (HDAC6) is mainly cytoplasmatic enzyme with two catalytic domains. In the study was used crystal structure of the trichostatin A in complex with second catalytic domain of human HDAC6 (PDB code - 5EDU). HDAC6 is involved in regulation of activity of cytoplasmatic proteins and therefore play a crucial role in cytoskeleton remodelling, dynamics of microtubule and triggering of apoptosis [5]. Inhibition of HDAC6 is confirmed to strongly influence on migration and viability of the cancer cells. Recent discovery of hydroxamic acid derivatives as potent and selective HDAC6 inhibitors [7], indicated on severe cardiotoxicity, mutagenicity, and poor solubility, as crucial problems for clinical use of the agents.

In our study were developed 3D-QSAR (Quantitative Structure Activity Relationship) models for HDAC1 and HDAC6 inhibitors in order to define specific molecular determinants for selective HDAC6 inhibition. The HDAC6 and HDAC1 enzymes significantly differ in structure, function, and localization and therefore present optimal pair for the rational design of selective HDAC6 inhibitors.

Sirtuin 2 (SIRT2), another cytoplasmatic NAD-dependent histon deacetylase, is recently confirmed as promising drug target for the treatment cancers, depression and Parkinson's disease. Until today none of SIRT2 inhibitors has been approved for the clinical use. Some of the main problems with current SIRT2 inhibitors are poor potency, selectivity and pharmacokinetic.

Therefore in our study was examined conformational space of sirtuin2-inhibitor complexes, further refinement of crystallographic structures, and development of more efficient virtual screening (VS) protocol.

EXPERIMENTAL

The 3D-QSAR data sets of 36 HDAC1 and 32 HDAC6 inhibitors (hydroxamic acid derivatives) were selected from ChEMBL database (https://www.ebi.ac.uk/chembl/). Negative logarithm of the inhibitory constant pKi = -log (Ki) was further used as dependent variable in 3D-QSAR modeling. The wide range of pKi values (pKi = -log (Ki)), as dependent variable in the HDAC1 (pKi: 6.486-9.699) and HDAC6 (pKi: 6.548-9.602) data sets, provide wide applicability domain of the formed 3D-QSAR models.

The HDAC1 and HDAC6 data sets contain more than 80% of common compounds.

Dominant forms of the HDAC1 and HDAC6 inhibitors at the physiological pH=7.4 were defined by use of Marvin Sketch 6.1.0 program (Chem Axon 2013). Conformations of the ligands for 3D-QSAR modelling were generated by virtual docking of data set ligands into the crystal structures of HDAC1 (PDB: 5ICN) and HDAC6 (PDB: 5EDU). Molecular docking was performed by use of GOLD Software 5.6.0 [8].

Calculation of GRIND molecular descriptors and development of 3D-QSAR models was performed by Pentacle program 1.07 [http://www.moldiscovery.com/software/pentacle/].

The data set compounds used for 3D-QSAR modelling were divided into training and test set.

The General Fragment Library (40142 fragments) and Epigenetic Targeted Library (7019 fragments), from Life Chemicals Inc. (http://www.lifechemicals.com/), were used for fragment-based design of novel HDAC6 inhibitors.

The ADMET Predictor Software v.8.5.0 [http://www.simulations-plus.com/] was used to predict physico-chemical parameters, pharmacokinetic properties and toxicity of the examined and designed HDAC6 inhibitors.

The SIRT2 study has started from five different crystallographic structures of SIRT2 with inhibitors. Molecular dynamics (MD) simulations in explicit solvent has been done for 1.5 μs. Structure based virtual screening was performed by use of GRID-based 3D descriptors and linear discriminant analysis.

RESULTS AND DISCUSSION

The developed and validated 3D-QSAR models for HDAC1 and HDAC6 inhibitors were successfully used to define specific GRIND variables as molecular determinants for inhibiting activity on HDAC6. For the comparative GRIND analysis were used HDAC6 selective inhibitors such as scriptaid and tubacin.

Based on the comparative study and novel drug design protocols is hypothesized that hydrophobic and steric interactions of the CAP group should be potentiated, distance between the CAP and zinc binding groups should be optimized, and diversity in linker chemistry should be applied in order to improve the selectivity for the HDAC6 isoform.

The employed design strategies were based on the replacement of the 1.8-naphthalimide CAP group of scriptaid, while retaining the aliphatic linkers of six or eight carbon atoms.

The Epigenetic Targeted Library and General Fragment Library were used for fragments selection based on similar McGowan Volume (Vx) and total surface area (SAtot) values to 1.8-naphthalimide (**Table 1**).

Table 1. Selected fragments for design of novel HDAC6 inhibitors.

Fragment Epigenetic Targeted Library	**Total Surface Area**	**McGowan Volume**
1.8-naphthalimide	191.659	205.864
F1957-0054	191.012	190.864
F1956-0006	207.766	206.03
G3000-0080	191.38	196.113

The selected CAP groups were further used in fragment based design of novel selective HDAC6 inhibitors. Based on the 3D-QSAR predicted pKi values against HDAC1 and HDAC6 enzymes (**Table 2**) and *in silico* ADMET parameters of the designed ligands were selected group of the most promising candidates for further study.

Table 2. Designed HDAC inhibitors with improved HDAC6 selectivity.

Designed compound	Pred. pKi_{HDAC1}	Pred. pKi_{HDAC6}	ΔpKi
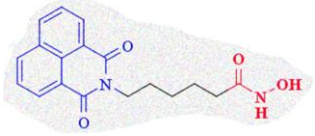 Scriptaid CHEMBL96051	8.824 (exp.)	9.602 (exp.)	**-0.778**
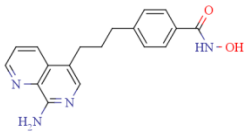 D1-3	7.796	8.879	-1.083
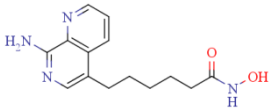 D1-5	7.380	9.175	-1.795
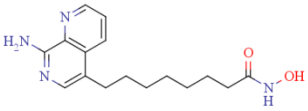 D1-6	7.895	8.974	-1.079
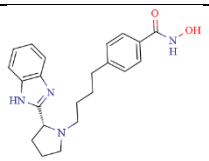 D3-4	7.834	8.896	-1.062
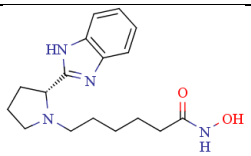 D3-5	7.911	9.004	-1.093

Specific binding modes and ChemScore docking scoring functions of selected designed HDAC6 inhibitors and scriptaid (CHEMBL96051) were further examined by virtual docking in crystal structures of human HDAC1 (5ICN) and HDAC6 (5EDU) (**Figure 1, Table 3**).

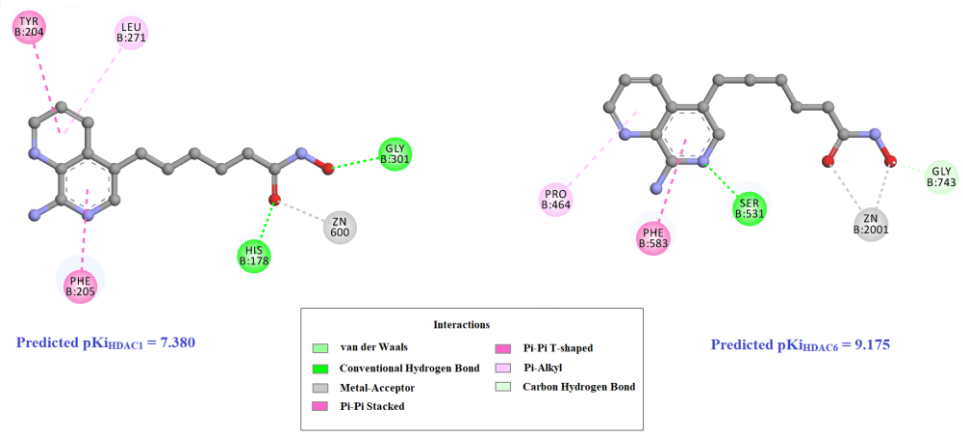

Figure 1. Binding mode of designed **D1-5** obtained by virtual docking on HDAC1 (left) and HDAC6 (right).

Table 3. The ChemScore docking of designed HDAC inhibitors.

	ChemScore	
Compound	HDAC1	HDAC6
Scriptaid	**25.432**	**30.6137**
D1-3	32.9064	35.1829
D1-5	27.1201	31.1112
D1-6	28.3858	30.9245
D3-4	34.0629	37.5489
D3-5	29.1502	31.1169

The binding modes and ChemScore docking scoring functions of the selected designed compounds have confirmed potent and selective binding with HDAC6 enzyme.

Molecular dynamic simulation of SIRT2-inhibitor complexes has indicated on significant conformational flexibility of the system, flexibility of binding site and multiple binding modes of inhibitors. Structure-based VS models, generated from three extracted molecular dynamic SIRT2-inhibitor complexes, were significantly improved related to VS models created from crystallographic structures and to published virtual screening studies. These VS results clearly indicate on significance of considering flexibility of binding site in rational design of SIRT2 inhibitors. The

developed VS models were successfully applied for screening of commercial databases of compounds and several types of novel SIRT2 inhibitors have been identified.

CONCLUSION

The 3D-QSAR models for HDAC1 and HDAC6 inhibition were developed with the conformers generated by virtual docking study.
Based on the 3D-QSAR study and GRIND analysis were defined molecular determinants for design of selective HDAC6 inhibitors.
Based on the 3D-QSAR predicted activities against HDAC1 and HDAC6 enzymes, *in silico* ADMET parameters, and virtual docking results of the designed ligands were selected group of the most promising candidates for further study.

Refined atomistic models of SIRT2-inhibitor complexes have been created. Significant progress in the virtual screening performance will be applied in rationalize design of SIRT2 inhibitors with improved selectivity and potency.

Acknowledgement
This work was supported by the Ministry of Education, Science and Technological Development of the Republic of Serbia (Grant No 172033). Authors kindly acknowledge COST action CM1406.

REFERENCES

[1] A.J. Bannister, T. Kouzarides, Cell Res, 2011, Regulation of chromatin by histone modifications. 21, 381-395.
[2] E. Bártová, J. Krejčí, A. Harničarová, G. Galiová, S. Kozubek, J Histochem. Cytochem, 2008, Histone modifications and nuclear architecture: a review 56, 711-721.
[3] Verdin, E, Ott, M (2015) 50 years of protein acetylation: from gene regulation to epigenetics, metabolism and beyond Nat. Rev. Mol. Cell Biol, 16(4); 258
[4] A. Ganesan, ChemMedChem, 2016, Multitarget drugs: an epigenetic epiphany.11(12), 1227-1241.
[5] K.J. Falkenberg, R.W. Johnstone, Nat Rev Drug Discov, 2014, Histone deacetylases and their inhibitors in cancer, neurological diseases and immune disorders 13(9), 673.
[6] C.H. Arrowsmith, C. Bountra, P.V. Fish, K. Lee, M. Schapira, Nat Rev Drug Discovery, 2012, Epigenetic protein families: a new frontier for drug discovery 11(5), 384.

[7] X.X. Wang, R.Z. Wan, Z.P. Liu, Eur J Med Chem, 2017, Recent advances in the discovery of potent and selective HDAC6 inhibitors 143, 1406-1418.
[8] G. Jones , P. Willett, R.C. Glen, A.R. Leach, R. Taylor, J Mol Biol, 1997, Development and validation of a genetic algorithm for flexible docking, 267, 727-748.

THE EFFECT OF DIFFERENTLY CHARGED MICELLES ON PROTOLYTIC EQUILIBRIA OF MALEIC AND FUMARIC ACID

M. Popović-Nikolić [1], G. Popović [2], K. Stojilković [2], M. Dobrosavljević [2] and D. Agbaba [1]

[1] *Department of Pharmaceutical Chemistry, (majap@pharmacy.bg.ac.rs)*
[2] *Department of General and Inorganic Chemistry, Faculty of Pharmacy, University of Belgrade, Vojvode Stepe 450, 11000 Belgrade, Serbia*

ABSTRACT

The pK_a values of maleic and fumaric acid have been determined potentiometrically in the presence and in the absence of differently charged micelles. The ionization of maleic acid has been significantly affected (ΔpK_a up to 1.91) by the presence of micelles, unlike the ionization of fumaric acid (ΔpK_a up to +0.30). Observed shift in equilibrium forms is most expressed in pH range 2 – 6.

INTRODUCTION

Maleic and fumaric acid are diastereoisomers that contain the same number and kinds of atoms, the same arrangement of bonds but differ in three-dimensional arrangement of atoms in space (Figure 1). Due to the presence of double bond, these organic diacids represent geometric isomers of ethylene dicarboxylic acid and exhibit different physico-chemical properties [1]. Maleic and fumaric acid are among the most frequently used acids as salt formers in drug compounds, such as enalapril maleate, pheniramine maleate, domperidone maleate, bisoprolol fumarate, rupatadin fumarate, quetiapine fumarate, etc. Various pharmaceutical dosage forms are formulated to administer drug substances by different routs whereas the dosage form and the applicable technology depend on the physico-chemical properties profile of the chosen salt. One of the most important physico-chemical properties is pK_a value which allows us to calculate the relative percentages of ionized and unionized form of the compound for any given pH. In the solutions of

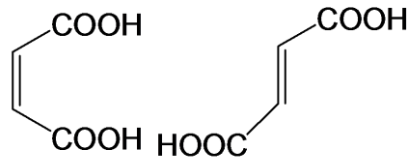

Figure 1. Chemical structures of examined compounds.

ionizable drugs formulated as salts with organic diacid, complex protoliytic equilibria are established. Determination of the pK_a values of organic diacids helps in defining the ionization profile of the corresponding ionizable drug.

The aim of this study was the determination of the pK_a values of maleic and fumaric acid in "pure" water, as surfactant free media, and in micellar solutions of differently charged surfactants. Micelles express a solubilizing effect on the compounds sparingly soluble in water, but may influence protolytic equilibria, reaction rates, products, and stereochemistry that may be different from those observed in the surfactant free solutions [2]. The results obtained in this study provide a better insight into the behavior of investigated compounds in experimental conditions especially in analytical procedures important for drug compounds containing maleic and fumaric acid as salt formers.

EXPERIMENTAL

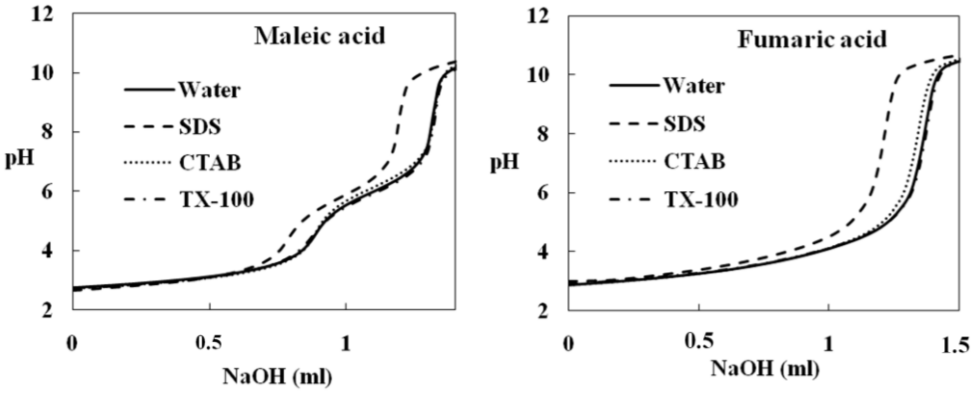

Figure 2. Potentiometric curves of maleic and fumaric acid solutions in the absence and in the presence of 10^{-2} M surfactant titrated with standard NaOH solution. I = 0.1 M (NaCl), t = 25 °C.

The pK_a values were determined potentiometrically on Automatic titrator 798 MPT Titrino (Metrohm, Switzerland) with a combined electrode LL unitrode Pt 1000 (Metrohm, Switzerland). Maleic and fumaric acid were kindly donated from Medicines and Medical Devices Agency of Serbia (Belgrade, Serbia). The surfactants, anionic, sodium dodecylsulphate - SDS (J.T. Baker); cationic, cetyltrimethylammonium bromide - CTAB (Acros Organic); and nonionic, 4-octylphenol polyethoxylate – TX-100 (Acros Organic) were used for the preparation of micellar solutions. All solutions

were prepared in double distilled water. Standard solutions of HCl and carbonate-free NaOH were standardized potentiometrically.

All solutions (10^{-3} M) of investigated compounds with and without the presence of 10^{-2} M surfactants (SDS, CTAB, and TX-100) were titrated with 0.0997 M NaOH at a 25°C and a constant ionic strength (0.1 M NaCl) (Figure 2). Surfactants were used at a concentration higher than their critical micellar concentrations. Experimental data obtained by potentiometric titration were analyzed by the program Hyperquad.

RESULTS AND DISCUSSION

The ionization profiles are defined for surfactant free media and obtained pK_a values are pK_{a1}=2.32 and pK_{a2}=6.03 for maleic acid and pK_{a1}=2.86 and pK_{a2}=4.26 for fumaric acid. The intramolecular hydrogen bond in maleic acid facilitates the ionization of the first carboxyl group by the stabilization of carboxylic anion (lower pK_{a1}) but e^--e^- repulsion between carboxylic groups, when are both deprotonated, hinders the ionization of the second group (higher pK_{a2}). The carboxylic groups are too far from each other to form hydrogen bond in fumaric acid and there are no e^--e^- repulsions between carboxylic anions.

Table 1. The pK_a values obtained potentiometrically in the presence of 10^{-2} M surfactants. ΔpK_a - differences in relation to pK_a values obtained in surfactant-free media. MA-maleic acid; FA-fumaric acid.

Acid	pK_a	SDS	ΔpK_a	CTAB	ΔpK_a	TX-100	ΔpK_a
MA	pK_{a1}	1.23±0.05	-1.09	1.11±0.06	-1.21	1.88±0.02	-0.44
	pK_{a2}	6.25±0.05	+0.22	5.81±0.06	-0.22	5.97±0.02	-0.06
FA	pK_{a1}	2.87±0.04	+0.01	2.74±0.02	-0.12	2.93±0.01	+0.07
	pK_{a2}	4.56±0.04	+0.30	4.28±0.02	+0.02	4.25±0.01	-0.01

On the basis of the values obtained in the presence of micelles (Table 1), the shift in protolytic equilibria (ΔpK_a) can be noticed. More pronounced effect is observed for maleic acid, ΔpK_a from -1.21 for pK_{a1} in the presence of CTAB, to +0.22 for pK_{a2} in the presence of SDS. The pK_a values of fumaric acid are not significantly affected by the presence of micelles, whereas ΔpK_a range from -0.12 for pK_{a1} in the presence of CTAB to +0.30 for pK_{a2} in the presence of SDS. Electrostatic and nonspecific hydrophobic interactions could be dominant in interaction with ionic SDS and CTAB micelles. The

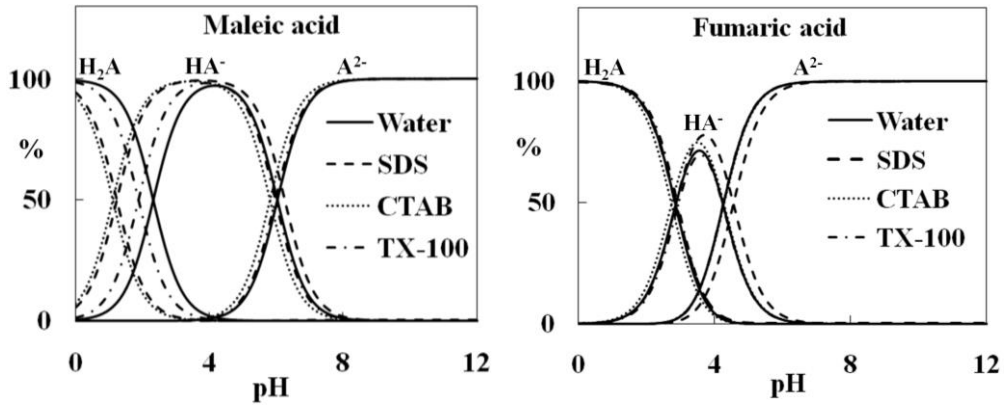

Figure 3. Distribution of maleic and fumaric acid equilibrium forms as function of pH.

nonionic micelles are not charged, but contain hydrophilic surface layer in which hydrogen bond forming and dipole interactions with carboxylic groups of examined diacids are possible (ΔpK_a up to -0.44).

The effect of micelles on protolytic equilibria can be clearly seen on the distribution diagrams of equilibrium forms as function of pH (Figure 3). Obtained shift in distribution of the equilibrium forms is the most expressed in a pH range 2 – 6.

CONCLUSION

The difference in pK_a values has been observed for geometric isomers, maleic and fumaric acid. The protolytic equilibria of maleic acid is shifted in the presence of micelles, especially anionic and cationic. The presence of differently charged micelles does not significantly affect the ionization of fumaric acid. Obtained results could be observed together with corresponding drug molecules under the different experimental conditions.

Acknowledgement

This work was supported by the Ministry of Education, Science and Technological Development of the Republic of Serbia, Contract No. 172033.

REFERENCES

[1] Lemke T. L., Williams D. A., Roche V. F., Zito S. W., Foye's Principles of Medicinal Chemistry, Lippincott Williams & Wilkins: Philadelphia, 2013.

[2] Fendler, J. H. Chem. Rev. 1987, 87, 877−899.

THE USAGE OF DIFFERENT POLYOLS AS AUXILIARY REAGENTS FOR BORIC ACID DETERMINATION

V. Radulović [1], B. Marković [2], S. Vladimirov [2] and K. Karljiković-Rajić [1]

[1] Department of Analytical Chemistry and [2]Department of Pharmaceutical Chemistry, University of Belgrade, Faculty of Pharmacy, Vojvode Stepe 450 11000 Belgrade, Serbia. (valentina.radulovic@pharmacy.bg.ac.rs)

ABSTRACT

The application of different polyols (mannitol, sorbitol, glycerol) in diverse excess, used as the auxiliary reagents for volumetric assay of boric acid, prescribed in three pharmacopoeias: Ph.Eur.9., JP XVII and USP 35-NF 30, gave 99.82%, 99.66% and 100.01%, respectively. Significant difference between mean values (Ph.Eur.9., JP XVII) pointed out the importance of phenolphthalein concentrations 0.1% and 1%, as monochrome indicator, as well as the diverse initial boric acid concentrations of approximately 0.16 M and 0.48 M, respectively. The results of pH-metric analysis of prepared initial solutions before titrations according to prescribed procedures; modifications concerning the excess of polyols or initial H_3BO_3 concentrations, as well as the calculated pH values for mannitol usage, indicated the agreement of solid polyols usage and lower excess of sorbitol.

INTRODUCTION

Boric acid is used as an active component (antiseptic, antimicotic) or an excipient in pharmaceutical preparations for external usage. Boric acid is absorbed from gastrointestinal tract, through damaged skin, from wounds as well as through mucous membranes causing toxic effects [1].

The aim of these investigations was to establish resemblances and differences of various polyols' application, as auxiliary reagents, for boric acid volumetric analysis according to procedures of three pharmacopoeias: European (Ph.Eur.9. [2]), Japanese (JP XVII [3], and American (USP 35-NF 30 [4], with mannitol, sorbitol and glycerol, respectively. Additionally, the correlations of the obtained results were carried out with pH-metric analysis of prepared initial solutions before the titrations.

EXPERIMENTAL

Listed chemicals were used: Boric acid, "Zdravlje", Leskovac, Serbia (99.5-100.5% assay acidimetric); Mannitol bacteriological, (98-101.5%) Biolife,

Milano, Italy; Sorbitol (Ph.Eur., BP), "Zdravlje", Leskovac, Serbia (98.0-101.0% iodimetric assay); Glycerol anhydrous G.R. Lacn-Ner, Neratovice, Czech Republic, (assay min 99% ;1L ~ 1.26 kg); Phenolphthalein, indicator ACS, pH 8.2-9.8, Merck, Germany; Ethanol 96% , REAHEM, Novi Sad, Serbia. As titrant Sodium Hydroxide Analytical Volumetric Solution, Reagecon Certificate of Analysis 1,002 M, Reagecon, Shannon Free Zone, Ireland was used. The indicator solutions were prepared according to procedures as 0.1% Phenolphthalein solution R (Ph.Eur.9) or 1% Phenolphthalein TS (JP XVII, USP 35-NF 30). Assay procedures for boric acid were carried out according to pharmacopoeias. pH-meter HI 9017 and combined pH electrode HI 1131 (HANNA Instruments, Inc. USA) were employed with standard buffer solutions (pH 4.00; 7.00) (*KEFO*, Slovenia).

RESULTS AND DISCUSSION

Boric acid as a very weak monoprotic acid (values of pK_{a1} in the range 9.14 - 9.24) can be titrated accurately, to a phenolphthalein end point, with standard alkali, but only in the presence of certain organic polyhydroxy compounds: mannitol, glucose, sorbitol or glycerol, whereby forming a

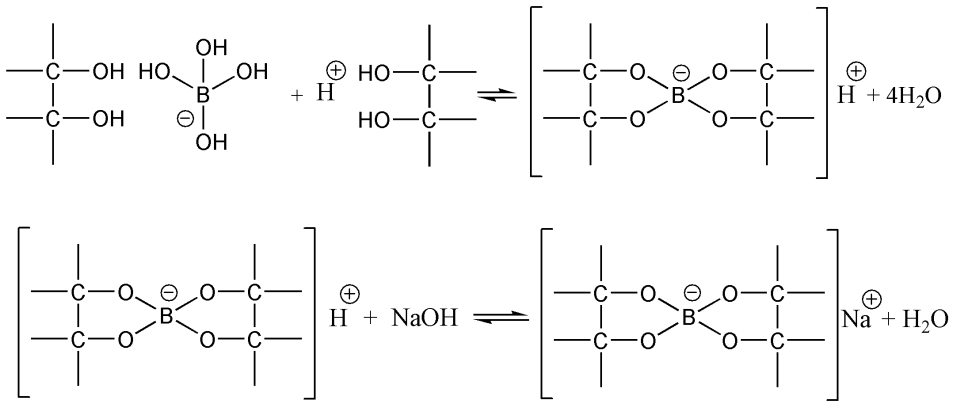

Figure 1. Formation and titration of complex acid produced between tetrahedral $B(OH)_4^-$ anion and polyols in 1:2 mole ratio

much stronger acid (for mannitol $K_a \approx 1.5 \cdot 10^{-4}$ [5]) (Fig.1.). The obtained results for volumetric analysis of boric acid according to all three pharmacopoeias are presented in Table 1. Due to the highest standard deviation (*s*) value for applied USP 35-NF 30 procedure, the significant difference in precision was established, in comparison with other two procedures, by applying F-test.

Table 1. Pharmacopoeias' volumetric assay of boric acid

Data H_3BO_3 (%)	Ph.Eur.9. [a]ratio (1:5.08) mannitol 0.1% Ind[b]	JP XVII [a]ratio (1:3.38) sorbitol 1% Ind[b]	USP 35-NF 30 [a]ratio total (1:42.4) (1:21.2 first aliquot) glycerol 1% Ind[b]
$\bar{x}$	99.82 (n=5)	99.66 (n=6)	100.01 (n=6)
s	0.095	0.1134	0.2630
RSD(%)	0.10	0.11	0.26

[a] prescribed ratio of quantities - H_3BO_3 : polyol; [b] Ind-Phenolphthalein

The statistically significant difference between mean values ($t_{cal} = 2.503 > t_{tab} = 2.262$; P = 0.05) was obtained for the comparison of Ph.Eur.9. and JP XVII as the result of diverse initial phenolphthalein's concentrations as monochrome indicator.

Table 2. The pH-metric data of prepared solutions for titrations according to Pharmacopoeias' monographs or denoted modifications

$m_{H_3BO_3}$ (g)	m_{polyol} (g)	V_{H_2O} (mL)	$\approx c_{H_3BO_3}$ (M)	pH (pH)[a]	Ratio[b]
1.5	15.0 sorbitol **JP XVII**[c]	50	0.48	2.01	1 : 3.38
1.5	22.5 sorbitol JP XVII[d]	50	0.48	1.87	1 : 5.08
1.0	15.0 mannitol **Ph.Eur.9.**[c]	100	0.16	2.62 (2.31)[a]	1 : 5.08
1.5	15.0 mannitol Ph.Eur.9.[d]	50	0.48	2.05 (2.07)[a]	1 : 3.38
1.5	15.0 mannitol Ph.Eur.9.[d]	100	0.24	2.39 (2.22)[a]	1 : 3.38
2.0	50 mL glycerol +50 mL water neutralized to indicator **USP 35-NF 30**[c]		0.32	2.95	1: 21.2

[a]Calculated pH values using $K_a \approx 1.5 \cdot 10^{-4}$ (for complex acid with mannitol [5]); [b]Ratio- H_3BO_3: polyol; [c]Original procedure; [d]Modification

The additional modified set of titrations (n=5) according to Ph.Eur.9. with 1% phenolphthalein, also showed significant difference in comparison with JP XVII ($t_{cal} = 2.675 > t_{tab} = 2.262$; P = 0.05). This result indicated the importance of used initial H_3BO_3 concentration in these procedures.

The results of pH-metric analysis were carried out to indicate the relationship between the excess/selection of polyols and initial concentration of H_3BO_3 on strength of formed complex acid (Table 2.). Some modifications in relation to initial boric acid concentration or the excess of polyol, were checked. Some pH values were calculated using literature data $K_a \approx 1.5 \cdot 10^{-4}$ (for complex acid with mannitol [5]). As expected the highest pH value was measured using glycerol. The lowest pH was obtained using sorbitol and also due to the highest initial concentration of H_3BO_3 prescribed [3]. The calculated pH values for the different initial H_3BO_3 concentrations indicated very good accordance with measured values using mannitol. The best agreement was obtained for the highest concentration ≈0.48 M, which also pointed out the insignificant difference between usage of mannitol and sorbitol.

CONCLUSION

The initial concentration of H_3BO_3 is higher in JP XVII regulation (comparing with Ph.Eur.9.) and allows the usage of lower sorbitol excess thus causing cost-effectiveness of procedure. It was pointed out that the initial phenolphthalein's concentration, as monochrome indicator, was crucial for evaluation of mean values accordance.

Acknowledgement

This work was partially supported by the Ministry of education science and technological development of the Republic of Serbia (Project TR34031).

REFERENCES

[1] S.C. Sweetman editor, Martindale: The Complete Drug Reference, 36th edition London:Pharmaceutical Press, 2009.
[2] European pharmacopoeia 9th ed., European Directorate for the Quality of Medicines (EDQM), Council of Europe, Strasbourg, France, 2017.
[3] Japanese Pharmacopoeia 17th ed., JP XVII The Pharmaceuticals and Medical Devices Agency, Tokyo, Japan, 2016.
[4] United States Pharmacopeia (USP) USP35-NF30: United States Pharmacopoeia National Formulary, Rockville, Maryland, USA, 2012.
[5] Vogel's Textbook of Quantitative Chemical Analysis, sixth edition Revised by Mendham M, Denney RC, Barnes JD, Thomas M, Prentice Hall, Pearson Education Limited, Harlow, England, 2000.

SYNTHESIS AND CHEMILUMINOGENIC PROPERTIES OF A NEW CHEMILUMINOGEN BASED ON ACRIDINIUM DERIVATIVES

A. Romanowska, M. Pieńkos and B. Zadykowicz

University of Gdansk, Faculty of Chemistry, Laboratory of Luminescence Research, Wita Stwosza 63, Gdansk, Poland
anna.romanowska@phdstud.ug.edu.pl

ABSTRACT

In this paper we will present our research on synthesis, physicochemical and chemiluminescent properties of 9-[[(4-methoxy-4-oxobutyl)-[(4-methylphenyl)sulphonyl]amino]carbonyl-10-methyl-acridinium trifloromethanesulphonate.

INTRODUCTION

Chemiluminogenic features of acridines have been investigated since 1970's. Until then these derivatives were only analyzed for medicinal purposes because of their bactericidal or tumoricidal properties [1–2].

The chemiluminescent markers are highly sensitive tools in medical diagnostic (limit of detection at the level of 10^{-19} M of an analyte or below). Acridinium derivatives are used in chemiluminescent markers as chemiluminogen, a group which transforms into an electronically excited molecule which returns to the ground state via light emission.

The possibility that acridinium derivatives undergo oxidation by H_2O_2 or other oxidants (in alkaline media) and then transform to electronically excited 10-methylacridinone was the reason to begin our research on their chemiluminogenic properties. Acridinium esters bounded to the active group can affect the identification of antigens, hormones, antibodies, nucleic acids and other biological molecules. This is the cause for their application in medical diagnostic. A phenomenon of chemiluminescence has been the subject of thorough investigation and has found numerous applications in clinical, pharmaceutical, chemical, biochemical and environmental analysis [3].

EXPERIMENTAL

Synthesis

The solution of the dehydrated acridine-9-carboxylic acid derivative in excess of thionyl chloride was refluxed for 3h (Scheme 1). $SOCl_2$ was evaporated and the crude product was washed with dry toluene.

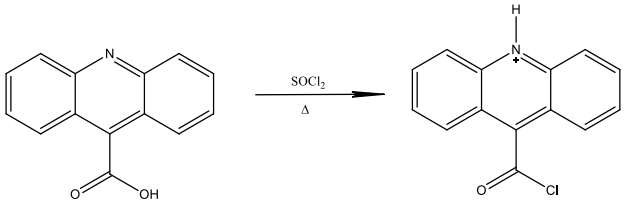

Scheme 1. Synthesis procedure of 9-(chlorocarbonyl)acridinium chloride

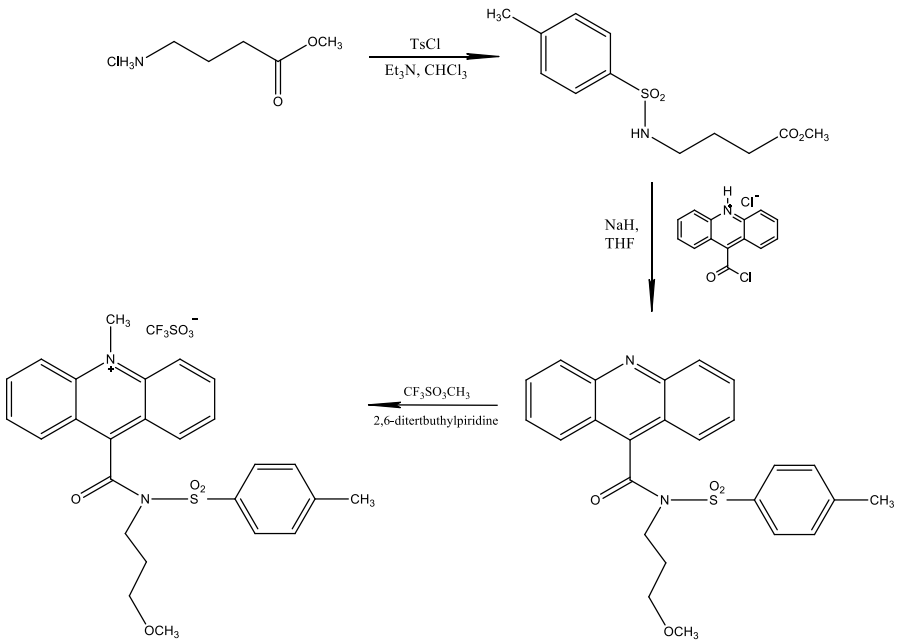

Scheme 2. Synthesis procedure of 9–[[(4–methoxy–4–oxobutyl)–[(4–metyhylphenyl)sulphonyl]amino] carbonyl-10-methyl-acridinium trifloromethanesulphonate

The titled compound was synthesized according to the modification of a procedure described in literature [4] and shown in scheme 2. A portion of 4-aminobutyrate hydrochloride (1 mM) was stirred with a stoichiometric

quantity of *p*-toluenesulphonylchloride in chloroform (6 mL) in the presence of *N*,*N*-dimethylamine under argon. The reaction mixture was cooled in ice bath (ice + NaCl) while *p*-toluensulphonylchloride was added. The reaction mixture was stirred for 24h at room temperature. The product was purified by extraction with 5% aqueous solution of sodium hydrogen carbonate. Organic extract was dried over anhydrous magnesium sulphate and purified by gravitational LC chromatography (stationary phase: SiO_2, mobile phase: methanol/chloroform (1/19 *v*/*v*). Yield: 50%. Next, 1 mM of methyl *N*-tosyl-4-aminobutyrate was stirred with sodium hydride (2 mM) and 9-(chlorocarbonyl)acridinium chloride (1 mM) in tetrahydrofuran and presence of *N*,*N*-dimethylamine under argon. The reaction mixture was cooled in ice bath (ice + NaCl) and a new portion of sodium hydride (2 mM) was added. Reaction mixture was stirred for 3h at room temperature. Product was dissolved in chloroform (100 mL) and extracted with water. The organic extract was dried over anhydrous magnesium sulphate and purified by gravitational LC chromatography (stationary phase: SiO_2, mobile phase: ethyl acetate/cyclohexane (3/7 *v*/*v*). Yield: 51%. Pure 9-[[(4-methoxy-4-oxobutyl)-[(4-methylphenyl)sulphonyl]amino]carbonyl]acridine was converted to 10-methylacridinium derivative with using methyl trifluoromethanesulphonate and 2,6-di-tert-buthylpyridyne as catalyst. Yield: 78 %. Confirmation of receiving and purity of 9-[[(4-methoxy-4-oxobutyl)-[(4-metyhylphenyl)sulphonyl]amino]carbonyl-10-methyl-acridinium trifloromethanesulphonate: R_T = 2.24, m.p. = 457,2 K, m/z(M^+) = 491.16, ^{1}H NMR (CD_3CN), δ, ppm (J, Hz): 1.7 and 2.4 (2H, m), 1.9 and 2.7 (2H, m), 2.2 and 2.5 (3H, s), 3.2 and 3.8 (3H, s), 3.5 and 4.3 (2H, m), 4.2 (3H, s), 6.8 (2H, d, J = 7.7), 7.2 (2H, d, J = 7.7), 7.4 (2H, d, J = 11.8), 7.6 (2H, m), 7.8 (2H, m), 8.2 (2H, d, J = 11.8).

Chemiluminescence measurements

Chemiluminescence measurements were conducted using Ascent FL plate luminometer (Labsystems-Thermo) with 300 mV sensitivity of the detector. A stock solution of acridinium salt was 5 mM was diluted with 0.001 M hydrochloric acid to 8 concentrations between 2×10^{-5} and 1×10^{-8} M. The solutions were dispensed over a 96-well plate. Next, portion of 0.06% H_2O_2 in 0.01 M HNO_3 was added to every acridinium solution and incubated for 30 seconds. The emission of light was triggered by adding 0.2 M sodium hydroxide solutions.

RESULTS AND DISCUSSION

The synthesis of 9–[[(4–methoxy–4–oxobutyl)–[(4–metyhylphenyl)sulphonyl]amino]carbonyl-10-methyl-acridinium trifluoromethanesulphonate was founded on the method described by

Adamczyk [4]. However, some modification were made to receive a pure product with an acceptable yield. Receiving a novel compound was confirmed by mass spectrometry, high liquid chromatography and nuclear magnetic resonance. The chemiluminescence measurements show that the luminescent properties of the sulphonamide acridinium derivative are comperable to the well known 10-methyl-9-(phenoxycarbonyl)acridinium trifluoromethanosulphonates [3], but the sulphonamide has a longer chemiluminescence reaction decay time. On the other hand, 9–[[(4–methoxy–4–oxobutyl)–[(4–metyhylphenyl)sulphonyl]amino]carbonyl-10-methyl-acridinium trifluoromethanesulphonate is characterized by the lowest intensity of light, it might be a caused by properties of the leaving group. A sulphonamide group is a weaker nucleophile and has a stronger steric effect than a phenoxy group. These properties cause a longer chemiluminescence reaction.

CONCLUSION

The synthesis procedure of new chemiluminogen has been modified to obtain the purer product with higher yield [4]. 9–[[(4–methoxy–4–oxobutyl)–[(4–metyhylphenyl)sulphonyl]amino]carbonyl-10-methyl-acridinium triflоromethanesulphonate has similar chemiluminogenic properties to 10-methyl-9-(phenoxycarbonyl)-acridinium trifluoromethanosulfonates, which are commercially used in medical, environmental and chemical analysis as chemiluminogens in chemiluminescent labels.

Acknowledgement

This study was financed from the Research of Young Scientists grant no. 538-8220-B782-17.

REFERENCES

[1] F. McCapra, Pure Appl. Chem., 1970, 24, 611–629.
[2] A. Roda, M.Guardigli, E. Michelini, M. Mirasoli, P. Pasini, Anal. Chem., 2003, 1, 462A–470A.
[3] J. Czechowska, A. Kawecka, A. Romanowska, M. Marczak, P. Wityk, K. Krzymiński, B. Zadykowicz, J. Luminescence, 2017, 187, 102-112.
[4] M. Adamczyk, Y.-Y. Chen, P.G. Mattinly, J.A. Moore, Tetrahedron, 1999, 55, 10899-10914.

A KINETIC STUDY OF THE ISOTHERMAL MICROWAVE ASSISTED EXTRACTION OF HYPERICIN FROM THE FLOWERING TOPS OF HYPERICUM PERFORATUM

B.Koturević[1], B. Adnađević[2] and J. Jovanović[2]

[1]*The Academy of Criminalistic and Police Studies, Cara Dusana 196, 11080 Belgrade, Zemun, Serbia*
[2]*Faculty of Physical Chemistry, Studentski trg 12-16, 11001 Belgrade, Serbia (bora@ffh.bg.ac.rs)*

ABSTRACT
The kinetics of the isothermal microwave assisted extraction (MAE) of total hypericin from the *H. perforatum* at temperature range from 313 to 328 K, was investigated. The concentrations of the total hypericins in ethanolic extracts were determined by UV-VIS spectrophotometry. Model fitting method was used to conform the kinetic model of MAE of hypericin. It was found that the kinetics of hypericin extraction can be modeled by Ginstling-Brounshtein theoretical kinetic model. The kinetic parameters, activation energy and pre-exponential factor were also determined. By applying the isoconversional method, it was established that the kinetics of the MAE of hypericin from *H. perforatum* is a single-step kinetic process.

INTRODUCTION
Hypericum perforatum, also known as St. John's Wort, is an aromatic perennial plant which is native to Europe, Western Asia, North Africa, and South America. Traditionally, it has been used in herbal remedies for the treatment of excitability, neuralgia, anxiety, depression and for the treatment of wounds [1]. Plant leaves, bright yellow-orange flowers and stalks are characterized by the presence of oil glands which contain a group of reddish naphthodianthrones pigments, namely hypericin and pseudohypericin [2]. Extraction of hypericin and pseudohypericin (expressed as total hypericins) are usually carried out using conventional extraction technique, such as Soxhlet extraction [3]. Recently, more advanced methods have been used for extraction of total hypericins from *H. perforatum*.

Since to our knowledge, there is no report on the kinetics of the isothermal microwave assisted extraction of hypericin, the aim of this paper is to examine the isothermal MAE of hypericin from *H. perforatum* flower.

EXPERIMENTAL

Materials and methods: The top aerial parts of *H.perforatum* (St.John worth) were harvested by hand in summer, during the period of full blooming (National Park, Kopaonik, Serbia). The plant material was dried immediately after harvesting in a dark and well ventilated space. Before extraction, the plant material was ground in an electrical mill until powder were obtained ($d_p \leq 500$ μm). Ethanol, p.a. purchased from Zorka Pharma, Serbia, was used as solvent.

Extraction procedure: The MAE was carried out in a commercially single-mode microwave device (Discover, CEM Corporation, Matthews, USA), operating at 2.45 GHz with adjustable microwave power output (from 0 to 300 W). In typical experiment, the 50 mL of absolute ethanol was placed in a borosilicate vessel and 1.0 g of powdered *H.perforatum* was added. The suspension was stirred continuously maintaining constant temperature at 313 K, 318 K, and 328 K (± 1 K) in a microwave reactor. At predominated time intervals, aliquots were taken from the reaction mixture. The concentration of hypericin (C g/L) was determined by spectrophotometric method using Beer's law and refers to sum of all derivatives of hypericin, expressed as hypericin. The UV-VIS absorption spectrum of ethanolic extracts was recorded using spectrophotometer Agilent technologies, USA. The kinetic model of hypericin extraction was evaluated applying model fitting method [4]. The kinetics complexity of extraction was established by the Friedman isoconversional method [5]. For each temperature, the degree of extraction (α) was determined by the equation: $\alpha = C/C_{max,}$ where C (g/L) is the hypericin concentration in extract in the time interval t, and C_{max} is the maximal concentration of hypericin achieved during the extraction process at a particular temperature.

RESULTS AND DISCUSSION

The obtained isothermal kinetic curves of the total hypericins MAE (dependence of C vs. time), at different temperatures are shown in Fig. 1. The kinetic curves at all of the investigated temperatures have the same shape. Initially, the concentration of the hypericin increases rapidly with time, so high initial slope can be observed. Further increase of the extraction time leads to a convex-like shape which is followed by the plateau.

Concentration of hypericin increases with increasing temperature, which indicate that this is thermally activated process. By applying the model fitting method it was determined that the kinetics of isothermal MAE of total hypericins can be kinetically modeled by Ginstling-Brounshtein theoretical kinetic model (D4 model). This type of three-dimensional model is given

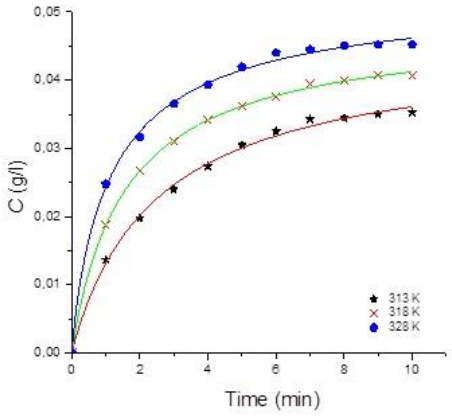

Figure 1. The isothermal kinetic curves of extracted hypericin from *H. parforatum*

by the following equation: $[(1-(2/3)\cdot\alpha-(1-\alpha)^{2/3}]=k_M\cdot t$, where k_M is the model rate constant of hypericin extraction from *H.perforatum*.

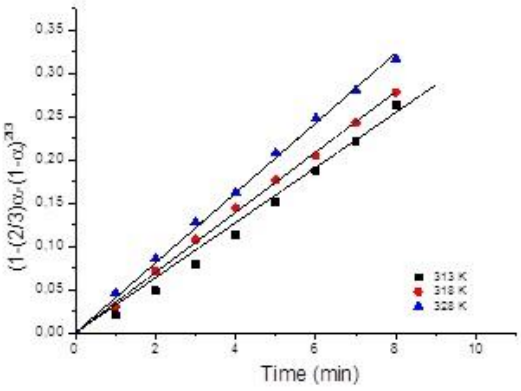

Figure 2. The dependence of $[(1-(2/3)\cdot\alpha-(1-\alpha)^{2/3}]$ vs. time of MAE of hypericin

The dependence of $[(1-(2/3)\cdot\alpha-(1-\alpha)^{2/3}]$ on time at all investigated temperatures gives straight lines which allows calculation of the model rate constant (k_M) and kinetic parameters of extraction, namely, the activation energy (E_a) and preexponential factor (A).

Since k_M values increase with the temperature increase, the model parameters of hypericin extraction (E_a and ln$A$) were determined by applying the Arrhenius equation. These results are given in Table 1.

By applying Friedman's isoconversional method it was established that E_a is independent on the degree of total hypericins extraction (Fig. 3) which indicates that the kinetic of MAE of hypericins from H. perforatum is single-step kinetic process.

Table 1. The influence of temperature on model rate constant and kinetic parameters of MAE of total hypericins

T (K)	k_M (min-1)	R^2	E_a (kJ/mol)	A (min^{-1})
313	0.03186	0.996		
318	0.03484	0.999	15.16 ± 2.0	2.37 ± 0.02
328	0.04044	0.999		

CONCLUSION

Microwave assisted extraction of total hypericins from flowering tops of *Hypericum perforatum* under isothermal conditions is process that takes place in a single elementary step. It was found that the kinetic of MAE extraction can be modeled by Ginstling-Brounshtein theoretical kinetic model. The values of the kinetic parameters are: E_a=15.16 kJ/mol and A=2,37 min^{-1}.

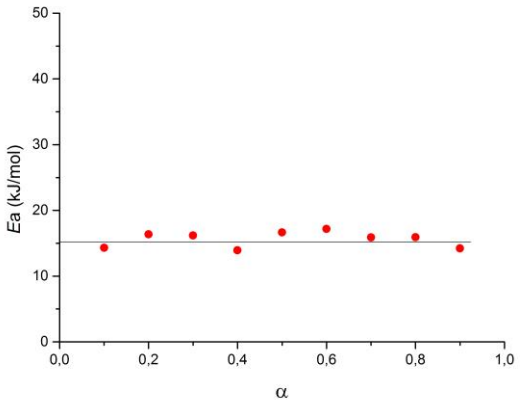

Figure 3. Dependence of E_a on degree of extraction

Acknowledgement

This investigation was supported by the Ministry of Science and Technical Development of the Republic of Serbia, through Project No.142025G.

REFERENCES

[1] J. Barnes, L.A. Anderson, J.D Phillipson, Journal of pharmacy and pharmacology, 2001, **53(5)**, 583-600.
[2] The ABC Clinical Guide to Herbs, Herbal Gram (Eds.), 2002.
[3] F.B. Williams, L.C. Sander, S.A. Wise, J. Girard, Journal of Chromatography A, 2006, **1115(1)**, 93-102.
[4] S. Vyazovkin, C.A Wight, Thermochim. Acta, 1999, **340/341**, 53-68.
[5] H. Friedman, J. Polym. Sci., 1964, **C 6**, 183–195.

MICROSPHERICAL PARTICLES OF ALBUMIN-BASED DRUG FOR INHALATION ADMINISTRATION

A.E. Boldyrev, A.V. Gerasimov, M.A. Ziganshin and A.A. Osipov

Kazan Federal University, A.M. Butlerov Institute of Chemistry, Kremlevskaya 18, 420008 Kazan, Russia. (boldyrev25@gmail.com)

ABSTRACT

Inhalation administration is a promising alternative to invasive drug administration. One of the most important factors is the particle size, which should be in a narrow range of 1-3 μm. Equally important factor is carrier material, which must be biocompatible and provide sufficient drug release rate. Protein materials can be used in the development of inhalation delivery systems due to its structure providing good binding of drugs and low toxicity. The possibility of obtaining microspherical particles of a model hydrophobic drug phenacetin with bovine serum albumin using the spray drying method was shown in the present work. Obtained particles were characterized by set of physic-chemical methods. The release kinetic of drug and composite was researched. Obtained results can be useful in the development of the drug delivery systems with rapid action and increased bioavailability.

INTRODUCTION

The drugs bioavailability increasing is one of the most important problems of modern pharmacology. There are two main ways to solve this problem – the increasing of active pharmaceutical ingredient solubility and using the alternative drug delivery methods [1].

The usage of inhalation administration of the drugs provide fast increasing of API concentration in blood. The inhaled substances do not undergo changes with this method of administration similar to those observed when administered through the gastrointestinal tract, since there is no reduction in the activity of the drug in the liver [2]. Furthermore, inhalation administration can be non-invasive alternative to injection drug administration.

One of the main criteria determining the possibility of using drug in the inhalation administration, besides good solubility, is particle size, which should be in 1-3 μm range [3].

Proteins are attractive macromolecular drug carriers because a significant amount of the drug can be included into the matrix due to different drug binding sites present in protein molecule [4].

In present work submicron composite particles of model drug phenacetin [5] with bovine serum albumin was obtained using spray drying method.

EXPERIMENTAL

Phenacetin (PHE) 98% (Aldrich, Lot #BCBD7322V), bovine serum albumin (BSA) (Fisher Sci., Lot 62-1397) were used as received. Bidistilled water and absolute ethanol were used as solvents. Physical mixtures (PM) obtained by mechanically mixing two components whose ratio is equivalent to their content in the composites was obtained

Composite of protein with drug particles (SD) were prepared by Nano spray dryer B90 (Buchi, Switzerland) operated in the open mode with inlet temperature of 95 °C.

Powder X-ray diffraction (PXRD) studies of BSA, phenacetin and its composites were made using a MiniFlex 600 diffractometer (Rigaku, Japan) equipped with a D/teX Ultra detector. Cu Kα radiation (40 kV, 15 mA) was used and data were collected at room temperature in the range of 2θ from 3 to 50° with a step of 0.02° and exposure time at each point of 0.24 s without sample rotation.

The total drug content in the spray dried particles was analyzed by Cary 100 UV-Vis Spectrophotometer (Agilent Technologies, Germany) at 245 nm with suitable dilutions.

Thermophysical properties of PHE and BSA, as well as their physical mixtures in the temperature range of -60-160 °C were determined using differential scanning calorimeter DSC 204 F1 Phoenix (Netzsch, Germany). Measurements were carried out on samples weighing 7.7-10.7 mg, at heating rate of 5 °C/min (cooling 10 °C/min), in a dynamic atmosphere of argon (150 ml/min).

Simultaneous thermogravimetry and differential scanning calorimetry (TG/DSC) analysis of solid samples was performed using thermoanalyzer STA 449F1 Jupiter (Netzsch, Germany) at the temperature range of 40-200 °C. In each experiment, the temperature rate was 5 °C/min, and an argon atmosphere with a total flow rate of 75 ml/min was used.

Sample morphology studies were performed on Zeiss EVO 50 XVP scanning electron microscope (Carl Zeiss, Germany) in variable pressure mode. For image acquisition, tetrasolid-state BSE detector was used. Samples were visualized using an acceleration voltage of 20.0 kV.

PHE dissolution kinetics from composites and physical mixtures was assayed with Dissotest CE1 (Sotax, Switzerland) (USP IV) in a closed loop. Phosphate buffer with pH = 6.86 was used as dissolution medium.

RESULTS AND DISCUSSION

Average product yields of spray drying were 55 ± 3. Dried sample has the appearance of white powder and was analyzed using several physicochemical methods.

Residual solvent content in microspherical particles was investigated using TG/DSC. The mass loss between 40-140 °C is below 4.5%. This loss of mass is related to water. The solvent loss is accompanied by the endo effect on DSC curves. The majority of water is lost below 100 °C. The low residual water content at the resulting composites indicates that the spray drying method allows to obtain microparticles with a relatively low residual solvent content.

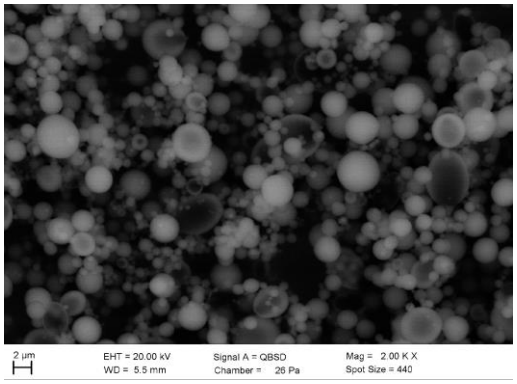

Figure 1. Results of scanning electron microscopy.

Phenacetin content at obtained composites was determined by UV-spectrophotometry method. Drug content was 7.4 ± 0.6%.

Results of PXRD analysis shows, that degree of crystallinity of drug decreases, which manifested in characteristic peaks absence on curves that match to obtained composites of drug with protein. It should be noted, that characteristic reflections of the drug are recorded on the diffractograms for physical mixtures (PM) with PHE content 7.4%.

DSC analysis showed that the melting peaks of the drug in the composites are not observed, which indicates the absence of the crystalline component of the drug in the spray dried composites. While for the physical mixture obtained by mechanically mixing two components whose ratio is equivalent to their content in the composites was obtained, the endothermic effect of the melting of the drug is recorded on the DSC curve. This suggests that using the spray drying method, it is possible to produce composites in which the drug is included in the

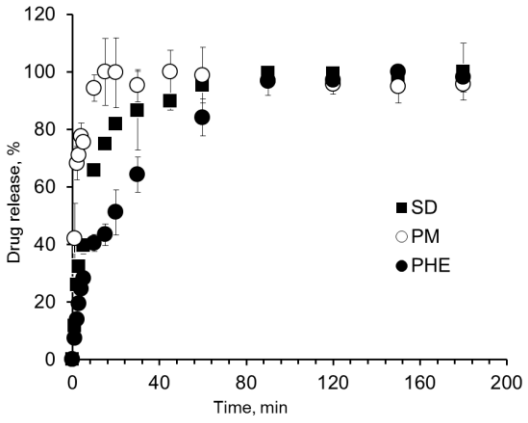

Figure 2. Results of dissolution kinetics analysis.

protein matrix and is unable to form crystallites. Data obtained using the DSC method is in good agreement with the results of X-ray powder diffractometry.

The distribution of the obtained particles by size was studied by scanning electron microscopy (Figure 1). Average diameter of particles was 1,5 μm. The obtained particles have spherical shape, which, together with the absence of agglomeration, should serve as the basis for good aerodynamic properties.

One of the important parameters in the use of drugs is dissolution kinetics, which has been studied in accordance with the USP IV standard. It has been found that the rate of release of the drug from the physical mixture (PM) and the composite prepared using spray drying method (SD) exceeds the rate of dissolution of the pure crystalline drug (Figure 2).

CONCLUSION

In present work composites of albumin with model drug phenacetin were prepared by using spray drying method.

The obtained particles were characterized by complex of physicochemical methods. It was shown that the obtained particles have a size suitable for the use in the inhalation form.

It was shown that using albumin as protein matrix provides significantly increasing of PHE dissolution rate.

The results obtained in this work can find their application in the development of modern dosage forms, the introduction of which will reduce the time to reach maximum concentration, side effects and increase the effectiveness of active pharmaceutical ingredient.

Acknowledgement

The reported study was funded by RFBR according to the research project № 18-015-00267.

REFERENCES

[1] B. Vraníková, J. Gajdziok, Ceska Slov Farm, 2015, 64, 159-172.
[2] W.H. Lee, C.Y. Loo, D. Traini, P.M. Young, Asian Journal of Pharmaceutical Sciences, 2015, 10, 481-489.
[3] J.S. Patton, C.S. Fishburn, J.G. Weers, Proc Am Thorac Soc., 2004, **1**, 338 – 344.
[4] A.O. Elzoghby, W.M. Samy, N.A. Elgindy, J. Control. Release, 2012, 161, 38-49.
[5] N. Ono, F. Hirayama, H. Arima, K. Uekama, and J. H. Rytting, J Incl Phenom Macrocycl Chem, 2002, 44, 93–96.

RP-HPLC EVALUATION OF LIPOPHILICITY OF 17β-CARBOXAMIDE GLUCOCORTICOIDS

V. Dobričić, S. Vladimirov and O. Čudina

University of Belgrade-Faculty of Pharmacy, Department of Pharmaceutical chemistry,
Vojvode Stepe 450, 11000 Belgrade, Serbia. (vladimir@pharmacy.bg.ac.rs)

ABSTRACT

Retention behaviour of eight selected 17β-carboxamide glucocorticoids was tested in six RP-HPLC systems, chromatography parameters (*logKw*, *a* and φ_0) were calculated and correlation between these parameters and previously determined *logPo/w* values was tested. RP-HPLC system with the highest values of correlation coefficients was selected (cyano column and methanol/water mobile phases) and in this system chromatography behaviour of remaining 17β-carboxamide glucocorticoids was examined. Compounds with the highest values of calculated chromatography parameters were HF, PF, MPF and DF and with the lowest value was HG.

INTRODUCTION

Soft drugs are compounds that possess metabolically sensitive functional groups and undergo predictable biotransformation to inactive and non-toxic metabolites. The first and second generations of soft glucocorticoids are derivatives of cortienic acid, which is an inactive glucocorticoid metabolite. Additionally, other glucocorticoids readily metabolized to non-toxic and inactive products could also be considered soft (antedrug) derivatives [1,2].

Twenty-two amides of cortienic acids (synthesized by oxidation of hydrocortisone, prednisolone, methylprednisolone, dexamethasone and betamethasone) and esterified amino acids (methyl and ethyl esters of glycine, L-alanine, β-alanine and L-phenylalanine) were synthesized in our laboratory. These compounds are potentially new soft glucocorticoids with local anti-inflammatory activity and fewer side effects than traditional glucocorticoids [3,4]. Their skin retention and permeability were evaluated *in vitro* and quantitative structure - permeability relationships (QSPR) analyses showed that lipophilicity is a significant factor influencing skin permeability [3].

The shake-flask method is considered standard method for *logPo/w* determination [5]. This method has been successfully replaced by reversed-phase thin-layer chromatography (RP-TLC) and reversed-phase high

performance liquid chromatography (RP-HPLC) for simple and fast lipophilicity evaluation of several groups of drugs [6,7]. Retention parameters obtained using these chromatographic techniques are usually well correlated with *logPo/w*.

The aim of this study was to develop a RP-HPLC method that could be used for fast, simple and reliable evaluation of lipophilicity of novel 17β-carboxamide glucocorticoid derivatives.

EXPERIMENTAL

RP-HPLC analysis was performed using C8 (Zorbax Eclipse XDB-C8 150 × 4.6 mm; 5 µm particle size), cyano (Zorbax SB-CN 150 × 4.6 mm, 5 µm particle size) and phenyl column (Zorbax Eclipse XDB-phenyl 150 × 4.6 mm; 5 µm particle size) and mobile phases consisted of methanol/water and acetonitrile/water. Applied chromatography systems were presented in Table 1. For each compound in each system retention factors (*k*) and their logarithmic values (*logk*) were calculated. *logk* values (y-axis) were plotted with the percentage of organic solvent in the mobile phase (x-axis) and $logk_w$ was determined by extrapolation of this line to the y-axis. Parameter *a* is slope of this curve and φ_0 is negative quotient of $logk_w$ and *a*.

Table 1. RP-HPLC systems used in this study

RP-HPLC system	Column	Mobile phase composition
A	C8	acetonitrile/water = 30:70, 40:60, 50:50 and 60:40, v/v
B	C8	methanol/water = 50:50, 60:40, 70:30 and 80:20, v/v
C	cyano	acetonitrile/water = 30:70, 40:60, 50:50 and 60:40, v/v
D	cyano	methanol/water = 50:50, 60:40, 70:30 and 80:20, v/v
E	phenyl	acetonitrile/water = 40:60, 50:50, 60:40 and 70:30, v/v
F	phenyl	methanol/water = 60:40, 70:30, 80:20 and 90:10, v/v

Chemical structures of 17β-carboxamide glucocorticoids tested in this study are presented in Figure 1.

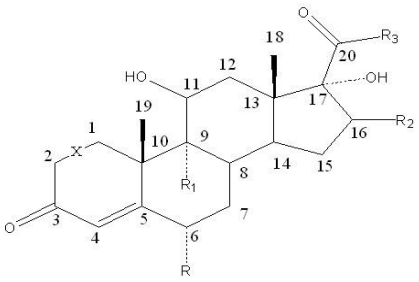

Compound	X	R	R_1	R_2	R_3	$logk_w$	a	φ_0
HG	-C-C-	-H	-H	-H	$-NHCH_2COOCH_3$	1.61	-0.027	60.16
HA	-C-C-	-H	-H	-H	$-NH(CH)CH_3COOCH_3$	1.87	-0.031	61.07
HEG	-C-C-	-H	-H	-H	$-NHCH_2COOCH_2CH_3$	1.88	-0.031	61.15
HEA	-C-C-	-H	-H	-H	$-NHCH_2CH_2COOCH_2CH_3$	2.05	-0.032	64.52
HF	-C-C-	-H	-H	-H	$-NH(CH)C_6H_5COOCH_3$	2.95	-0.043	69.23
PG	-C=C-	-H	-H	-H	$-NHCH_2COOCH_3$	1.84	-0.030	61.09
PA	-C=C-	-H	-H	-H	$-NH(CH)CH_3COOCH_3$	2.04	-0.032	63.32
PEG	-C=C-	-H	-H	-H	$-NHCH_2COOCH_2CH_3$	2.09	-0.033	63.39
PEA	-C=C-	-H	-H	-H	$-NHCH_2CH_2COOCH_2CH_3$	2.23	-0.034	64.83
PF	-C=C-	-H	-H	-H	$-NH(CH)C_6H_5COOCH_3$	3.01	-0.042	71.84
MPG	-C=C-	$-CH_3$	-H	-H	$-NHCH_2COOCH_3$	2.05	-0.032	62.97
MPA	-C=C-	$-CH_3$	-H	-H	$-NH(CH)CH_3COOCH_3$	2.25	-0.035	65.06
MPEG	-C=C-	$-CH_3$	-H	-H	$-NHCH_2COOCH_2CH_3$	2.29	-0.035	65.32
MPEA	-C=C-	$-CH_3$	-H	-H	$-NHCH_2CH_2COOCH_2CH_3$	2.47	-0.037	66.46
MPF	-C=C-	$-CH_3$	-H	-H	$-NH(CH)C_6H_5COOCH_3$	3.46	-0.047	73.09
DG	-C=C-	-H	-F	CH_3	$-NHCH_2COOCH_3$	1.98	-0.031	63.94
DA	-C=C-	-H	-F	CH_3	$-NH(CH)CH_3COOCH_3$	2.31	-0.036	64.76
DEG	-C=C-	-H	-F	CH_3	$-NHCH_2COOCH_2CH_3$	2.27	-0.034	66.04
DEA	-C=C-	-H	-F	CH_3	$-NHCH_2CH_2COOCH_2CH_3$	2.52	-0.038	66.25
DF	-C=C-	-H	-F	CH_3	$-NH(CH)C_6H_5COOCH_3$	3.40	-0.047	72.51
BG	-C=C-	-H	-F	CH_3	$-NHCH_2COOCH_3$	2.08	-0.033	62.19
BEG	-C=C-	-H	-F	CH_3	$-NHCH_2COOCH_2CH_3$	2.33	-0.035	66.36

Figure 1. Chemical structures of tested compounds

RESULTS AND DISCUSSION

Suitability of applied RP-HPLC systems (A, B, C, D, E and F) for the evaluation of lipophilicity was tested on the set of eight 17β-carboxamide glucocorticoids (HG, DG, HEA, DEG, BEG, PF, MPF and DF). Correlation between calculated chromatography parameters ($logk_w$, a and φ_0) and previously determined *logPo/w* values of these compounds [8] was tested. System B was the least reliable, with the lowest values of correlation coefficients (*logPo/w* and $logk_w$: 0.90, *logPo/w* and a: 0.73, *logPo/w* and φ_0: 0.99). RP-HPLC system with the highest values of correlation coefficients was D (*logPo/w* and $logk_w$: 0.98, *logPo/w* and a: 0.98, *logPo/w* and φ_0: 0.98). Using this system, retention behaviour of remaining 17β-carboxamide glucocorticoids was also tested and chromatography parameters $logk_w$, a and

φ_0 were calculated (Figure 1). Correlation coefficients for all compounds were 0.94 (*logPo/w* and $logk_w$ and *logPo/w* and *a*) and 0.93 (*logPo/w* and φ_0). Compounds with the highest values of chromatography parameters and highest lipophilicity were methyl ester L-phenylalanine derivatives (HF, PF, MPF and DF). Compound with the lowest values of chromatography parameters and lowest lipophilicity was HG.

CONCLUSION

Retention behaviour of eight selected 17β-carboxamide glucocorticoids was tested in six RP-HPLC systems, chromatography parameters $logk_w$, *a* and φ_0 were calculated and the most suitable system was selected according to the correlation between these chromatography parameters and previously determined *logPo/w* values. Selected RP-HPLC system was used for the investigation of retention behaviour of remaining 17β-carboxamide glucocorticoids. Derivatives with the highest values of chromatography parameters and lipophilicity were HF, PF, MPF and DF, whereas the derivative with the lowest value of chromatography parameters and lipophilicity was HG.

Acknowledgement

This work was partially supported by the Ministry of Education, Science and Technological Development of the Republic of Serbia (Grant no. 172041).

REFERENCES

[1] N. Bodor, P. Buchwald, Curr. Pharm.Des., 2006, **12,** 3241-3260.
[2] M.O.F Khan, H.J. Lee, Chem. Rev., 2008, **108,** 5131-5145.
[3] V. Dobričić, B. Marković, K. Nikolic, V. Savić, S. Vladimirov, O. Čudina, Eur. J. Pharm. Sci., 2014, **52,** 95-108.
[4] V. Dobričić, V. Jaćević, J. Vučićević, K. Nikolic, S. Vladimirov, O. Čudina, Arch. Pharm., 2017, **350,** e1600383.
[5] A. Leo, C, Hansch, D. Elkins, Chem. Rev., 1971, **71**, 525-616.
[6] M. Starek, Ł. Komsta, J. Krzek, J. Pharm. Biomed. Anal., 2013, **85**, 132–137.
[7] P. Maes, P. Formstecher, P. Lustenberger, M. Dautrevaux, J. Chromatogr., 1988, **445,** 409-416.
[8] V. Dobričić, A. Stanišić, S. Vladimirov, O. Čudina, JPC-J.Planar.Chromatogr., 2018, **31,** 250-256

CHEMICAL COMPOSITION AND ANTIMICROBIAL ACTIVITY OF FENNEL SEEDS ESSENTIAL OIL

M.P.Petrović[1], T.Šolević-Knudsen [2], M.Pantić [3], M.Nikšić[3] and S. Pecić[1]

[1]*Institute of General and Physical Chemistry, Studenstki trg 12-16, Belgrade, Serbia* (marijapetrovic52@gmail.com)
[2]*Scientific Institution ICTM, University of Belgrade, Njegoševa 12, 11000 Belgrade, Serbia*
[3]*Faculty of Agriculture, University of Belgrade, Nemanjina 6, Zemun, 11080 Belgrade, Serbia*

ABSTRACT

Chemical composition of the essential oil (EO), obtained by hydrodistillation of fennel (*Foeniculum vulgare* Mill.) seeds, was analyzed by GC-MS technique. Nine compounds were identified in this oil, representing 94.66% of the total oil. The minimum inhibitory concentrations (MIC), as well as minimum lethal concentrations (MLC) of the plant EO, were determined by broth microdilution assay against selected food-borne pathogenic microorganisms.

INTRODUCTION

Food poisoning caused by food-borne microorganisms is serious problem affecting general human health, even in developed countries [1]. Since many pathogenic microorganisms have developed resistance against some conventionally used antibiotics, natural antimicrobial substances, such as herbs, spices and their isolates, may have increasing importance in therapeutic purposes [2]. In addition, it is well known nowadays that herbal isolates, such as essential oils, can enhance the shelf life of unprocessed or processed foods, thus representing potential substitution to artificial preservatives in food industry [3].

Fennel is well known for its aromatic properties, making it appropriate flavouring agent in food products. Fennel fruit,consisting of the hundreds of small seeds, is rich in volatile oil, whose amount reaches up to 7% [4]. The most abundant compounds in fennel oil are trans-anethole, fenchone, anisaldehyde, estragole, d-limonene and many others [1, 2, 5, 6, 7, 8]. Antimicrobial properties of the fennel isolates, including essential oil, have been reported earlier [1, 2, 6, 9]. Essential oil of the fennel has been widely used in the food industry, mainly in production of spirits and beverages, candies and other confectioneries, bread, pickles, pastries and cheese [8].

This study was aimed to evaluate chemical composition and antimicrobial activity of essential oil obtained from fennel seeds.

EXPERIMENTAL

Dried fennel seeds, donated from the "Bilje Borča" company, Belgrade, Serbia, was finely grinded and about 40 g was subjected to hydrodistillation for 2 h using a Clevenger type apparatus. Chemical composition of oil was analysed by gas chromatograph Agilent 7890N fitted with HP5-MS capilar column, and coupled with Hewlett-Packard 5972 mass selective detector. Helium was the carrier gas (flow rate 1.5 cm^3/ min). Components of the volatile oil were identified based on their retention indices and their mass spectra using the Wiley and NIST Mass Spectral Libraries or literature data.

Broth microdilution method was used to determine the antimicrobial activity of EO in concentrations 0.47 mg/mL –7.50 mg/mL [10]. The following strains were tested: Gram (+) bacteria (*Listeria monocytogenes* ATCC 19111, *Rhodococcus equi* ATCC 6939, *Staphylococcus aureus* ATCC 25923, *Bacillus subtilis subsp. spizizenii* ATCC 6633 and *Bacillus cereus ATCC* 11778), Gram (-) bacteria (*Proteus mirabilis* ATCC 12453, *Proteus hauseri* ATCC 13315, *Shigella sonnei* ATCC 29930, *Yersinia enterolitica* ATCC 27729, *Salmonella enteritidis* ATCC 13076) and one standard strain of yeast *Candida albicans* ATCC 10259. Minimal lethal concentration was determined by sub-culturing content of the wells with no visible growth on agar plates followed by incubation. No growth on the agar plate was reported as MLC. The MIC and MLC procedures were done in triplicates.

RESULTS AND DISCUSSION

Phenylpropanoid trans-anethole (56.64%) was found as the main component of the fennel oil with more than half of the total characterized compounds. Monoterpene limonene (22.65%) was the second major compound detected, followed by fenchone (5.81%), alpha-pinene (3.07%), estragole (3.05%) and others as the minor components in the essential oil of fennel seeds (Table 1.).

Table 1. Chemical composition of fennel (*Foeniculum vulgare* Mill.) seeds essential oil

№	Compound	Percentage in oil (%)
1.	alpha-Pinene	3.07
2.	beta-Pinene	1.00
3.	beta-Myrcene	0.74
4.	alpha-Phellandrene	0.26
5.	Limonene	22.65
6.	β-Ocimene	1.44
7.	Fenchone	5.81
8.	trans-Anethole	56.64
9.	Estragole	3.05
Σ	Total identified	94.66

Fennel seeds EO exhibited inhibitory and lethal effect against *Bacillus spizizeni* with the same MIC and MLC values (0.47 mg/mL). The growth of *Bacillus cereus* and *Staphylococcus aureus* was inhibited by 0.47 mg/mL of EO, whereas lethal effect was not observed in the tested range of concentrations. Inhibitory and lethal concentrations against strain *Rhodococcus equi* were 0.94 mg/mL and 1.87 mg/mL, respectively. *Listeria monocytogenes* was the most resistant among tested G (+) bacteria, since the highest tested concentration had no effect on its growth.

Volatile oil of fennel seeds displayed inhibitory and lethal effect on Gram (-) bacteria at concentration of 7.50 mg/mL, with exception of *Salmonella enteritidis* and *Proteus mirabilis*, that were resistant on the tested range of concentrations.

The growth of the yeast *Candida albicans* was inhibited by MIC= 1.87 mg/mL, whereas lethal concentration was 3.75 mg/mL.

Generally, Gram (+) bacteria showed more sensitivity to the presence of fennel seeds EO. It can be explained by the different cell structure of Gram (+) and Gram (-) bacteria. Gram (-) bacteria possess a double membrane surrounding cell wall, which exclude certain antimicrobial agents from penetrating the cell [3].

CONCLUSION

Chemical composition of the fennel (*Foeniculum vulgare* Mill.) seeds essential oil was characterized by GC-MS analysis. The predominant compounds in this oil were trans-anethole and limonene. It was observed by broth microdilution method that the growth of the majority of the selected

food-borne pathogens were inhibited or killed by the range of EO concentrations tested. Therefore, considering fennel EO application in the food industry, as natural preservative agent, might be of great significance.

Acknowledgement
This study was financial supported by Ministry of Education, Science and Technological Development of the Republic of Serbia, project no.TR 31055.

REFERENCES

[2] F. Anwar, M. Ali, A. I. Hussain, M. Shahid, Flavour and Fragrance Journal 2009, **24(4)**, 170-176.
[2] M. H. H. Roby, M. A. Sarhan, K.A.H. Selim, Khalel, K. I. Industrial Crops and Products 2013, **44**, 437–445.
[3] B. Speranza, M. R. Corbo, Application of Alternative Food-Preservation Technologies to Enhance Food Safety & Stability 2010, **23**, 35-57.
[4] J. Tucakov, Lečenje biljem; fitoterapija; Kultura: Beograd, 1971.
[5] E. Miraldi, Flavour and Fragrance Journal 1999, **14 (6)**, 379–382.
[6] N. Mimica-Dukić, S. Kujundžić, M. Soković, M. Couladis, Phytotherapy Research 2003, **17 (4)**, 368–371.
[7] A. C. Aprotosoaie, A. Şpac, M. Hăncianu, A. Miron, V. F. Tănăsescu, V. Dorneanu, U. Stănescu, Farmacia 2010, **58(1)**, 46-53.
[8] S. B. Badgujar, V. V. Patel, A. H. Bandivdekar, BioMed Research International 2014, 1-32.
[9] M. Gulfraz, S. Mehmood, N. Minhas, N. Jabeen, R. Kausar, K. Jabeen, G. Arshad, African Journal of Biotechnology 2008, **7 (24)**, 4364–4368.
[10] A. Klačnik, S. Piskernik, B. Jeršek, S. S. Možina, Journal of Microbiological Methods 2010, **81 (2)**, 121–126.

CHEMICAL COMPOSITION AND ANTIMICROBIAL PROPERTIES OF *Lavandula officinalis* ESSENTIAL OIL

P.M.Petrović[1], M.Pantić [2], M.Nikšić[2], T.Šolević-Knudsen[3], S.Pecić[1] and M.Antić[2]

[1]*Institute of General and Physical Chemistry, Studenstki trg 12-16, Belgrade, Serbia* (marijapetrovic52@gmail.com)
[2]*Faculty of Agriculture, University of Belgrade, Nemanjina 6, Zemun, 11080 Belgrade, Serbia*
[3]*Scientific Institution ICTM, University of Belgrade, Njegoševa 12, 11000 Belgrade, Serbia*

ABSTRACT

Essential oil (EO) obtained from dried flowers of *Lavandula officinalis* was investigated for its chemical composition and antimicrobial properties against some common food-born pathogens. Forty-eight compounds were characterized in this oil, representing 90.40% of the total oil. The minimum inhibitory concentration (MIC), as well as minimum lethal concentration (MLC) of the plant EO were determined by broth microdilution assay against five G (+) bacteria, five G (-) bacteria strains and one yeast.

INTRODUCTION

Lavandula officinalis and its preparations have traditionally been used for carminative, antispasmodic, antidepressant, expectorant, anti-rheumatic, relaxant, sedative, anti-inflammatory and tonic properties [1,2]. Lavander flowers are rich in volatile oil, with average amount 1-3% [3]. The most abundant compounds in lavender oil are linalool (25 – 38%) and linalool acetate (25 – 45%) [4]. In addition to its widespread uses in medicinal and cosmetic purposes, lavender oil has found application in the food industry, as natural flavorings in baked goods, alcoholic and nonalcoholic beverages, puddings, confectioneries etc [1].

Essential oils of medicinal plants have been increasingly researched in terms of their potential application in food industry, especially as promising antimicrobial agents. In addition, medicinal plants isolates have been reported as more effective in some cases in comparison with conventional antimicrobial drugs [5, 6]. Lavender EO was reported to show antibacterial activity [7, 8, 9], as well as antifungal effect [10, 11].

This research was conducted to investigate chemical composition and antimicrobial properties of EO obtained from *L. officinalis* flowers.

EXPERIMENTAL

Dried flowers of *L. officinalis,* donated from the "Bilje Borča" company, Belgrade, Serbia, were powdered and subjected to hydrodistillation in a Clevenger type apparatus. Obtained oil was injected in HP5-MS capilar column of gas chromatogram Agilent 7890N, coupled with Hewlett-Packard 5972 mass. Helium was the carrier gas (flow rate 1.5 cm^3/ min). Components of the volatile oil were identified based on their retention indices and their mass spectra using the Wiley and NIST Mass Spectral Libraries or literature data.

Broth microdilution method was used to determine the antimicrobial activity of EO *in vitro* [12]. Concentrations of EO in range of 0.47 mg/mL – 7.50 mg/mL were tested. Minimal lethal concentration was determined by sub-culturing content of the wells with no visible growth on agar plates. After incubation, no growth on the agar plate was reported as minimum lethal concentration MLC. The MIC and MLC procedures were done in triplicates.

RESULTS AND DISCUSSION

The most of the identified compounds in lavander EO belong to the class of monoterpenes and sesquiterpenes. The predominant components were linalool (26.88%), linalool acetate (12.50%), lavandulol (5.74%), lavandulol acetate (5.27%), α-terpineol (5.25%), caryophyllene (5.06%) and caryophyllene oxide (3.52%). Also, significant amount (more than 1%) of terpinen-4-ol, geranyl acetate, neryl acetate, 1,8-cineole, cis-linalool oxide, trans-linalool oxide, cis-β-ocimene, trans-β-ocimene, β-myrcene i nerol was detected (not shown).

Gram (+) bacteria were more suspectible to EO (MIC and MLC values ranging from concentrations lower than 0.47 mg/mL to 3.75 mg/mL) than Gram (-) bacteria (with inhibitory and lethal concentration ranging from 3.75 mg/mL to 7.50 mg/mL). Essential oil inhibited the growth of the yeast *Candida albicans* with MIC= 3.75 mg/mL, whereas lethal concentration was 7.50 mg/mL (Table 1.). Generally higher resistance among Gram (-) bacteria is associated with the presence of the outer membrane, surrounding the cell wall, which restricts diffusion of hydrophobic compounds through its lipopolysaccharide covering [13].

Table 1. MIC and MLC values of *L. officinalis* EO against some common food-borne pathogens

Test bacteria		*L.officinalis* EO (mg/mL)[a]
G (+)		
Listeria monocytogenes ATCC 19111	MIC	3.75±0.00
	MLC	3.75±0.00
Bacillus spizizeni ATCC 6633	MIC	0.47±0.00
	MLC	0.47±0.00
Bacillus cereus ATCC 11778	MIC	*
	MLC	*
Staphylococcus aureus ATCC 25923	MIC	*
	MLC	*
Rhodococcus equi ATCC 6939	MIC	*
	MLC	*
G (-)		
Salmonella enteritidis ATCC 13076	MIC	7.50±0.00
	MLC	7.50±0.00
Shigella sonnei ATCC 29930	MIC	7.50±0.00
	MLC	7.50±0.00
Proteus mirabilis ATCC 12453	MIC	3.75±0.00
	MLC	7.50±0.00
Proteus hauseri ATCC 13315	MIC	3.75±0.00
	MLC	7.50±0.00
Yersinia enterocolitica ATCC 27729	MIC	3.75±0.00
	MLC	7.50±0.00
Yeast		
Candida albicans ATCC 10259	MIC	3.75±0.00
	MLC	7.50±0.00

[a] Data are expressed as mean of three replicates ± standard deviation (n = 3).
*Tested samples showed antibacterial activity in concentration lower than 0.47 mg/mL.

CONCLUSION

Volatile fraction of *L.officinalis* flowers was characterized by GC-MS analysis. The compounds present with the greatest percentage of all identified compounds were linalool and linalool acetate. According to the results, obtained EO has shown promising antimicrobial properties, thus it can be

considered as a potential alternative to chemical preservatives in the food industry.

Acknowledgement
This study was financial supported by *Ministry* of Education, *Science and Technological* Development of the Republic of *Serbia*, project no. TR 31055.

REFERENCES

[1] M. Lis-Balchin, Lavender: the genus Lavandula; Taylor & Francis: London, 2002.
[2] M. B. Hassanpour-Aghdam, A.Hassani, L. Vojodi, B. Hajisamadi, A. Rostami, Chemija, 2011, **22(3)**, 167–171.
[3] J. Tucakov, Lečenje biljem; fitoterapija; Kultura: Beograd, 1971.
[4] ISO 3515:2002. Oil of lavender (Lavandula angustifolia Mill.).
[5] G. G. Nascimento, J. Locatelli, P. C. Freitas, G. L. Silva, Brazilian Journal of Microbiology, 2000, **31(4)**, 247-256.
[6] H. C. Voon, R. Bhat, G. Rusul, Comprehensive Reviews in Food Science and Food Safety, 2012, **11(1)**, 34-55.
[7] G. Gabbrielli, F. Loggini, P. L. Cioni, B. Giannaccini, E. Mancuso, Pharmacological Research Communications, 1988, **20**, 37-40.
[8] F. V. Romeo, S. De Luca, A. Piscopo, M. Poiana, Journal of Essential Oil Research, 2008, **20(4)**, 373-379.
[9] C. Jianu, G. Pop, A. T. Gruia, F. G. Horhat, International Journal of Agriculture and Biology, 2013, **15(4)**, 772-776.
[10]F. D. D'auria, M. Tecca, V. Strippoli, G. Salvatore, L. Battinelli, G. Mazzanti, Medical mycology, 2005, **43(5)**, 391-396.
[11]F. Behmanesh, H. Pasha, A. A. Sefidgar, M. Taghizadeh, A. A. Moghadamnia, H. Adib Rad, L. Shirkhani, Scientifica, 2015, Article ID 261397, 1-5.
[12]Klačnik, A., Piskernik, S., Jeršek, B., Možina, S.S., Journal of Microbiological Methods, 2010, **81**, 121-126.
[13]B. Speranza, M. R. Corbo, Application of Alternative Food-Preservation Technologies to Enhance Food Safety & Stability, 2010, **23**, 35-57.

BIOACTIVE PULLULAN BASED EDIBLE FILMS WITH MEDICINAL HERBAL EXTRACTS

D. Jakovljević[1], B. Lončarević[1], G. Gojgić-Cvijović[1], A. Žeradjanin[1], N. Lugonja[1], K. Joksimović[3] and V. P. Beškoski[2]

[1]*University of Belgrade, Institute of Chemistry, Technology and Metallurgy, Njegoševa 12, 11000 Belgrade, Serbia (djakovlj@chem.bg.ac.rs)*
[2]*University of Belgrade, Faculty of Chemistry, Studentski trg 12-16, 11000 Belgrade, Serbia.*
[3]*University of Belgrade, Innovation center of the Faculty of Chemistry, 11000 Belgrade, Studentski trg 12-16, Serbia.*

ABSTRACT

In this work, pullulan based films with water extracts of medicinal herbs, thyme and sage, were prepared. Resulting films were characterized by FTIR spectroscopy and their antioxidant properties and antimicrobial activity were evaluated. These products have potential use in food applications, as a supplement to functional food and/or as coatings for food packaging material.

INTRODUCTION

The field of bioactive edible films is in significant development as a result of wide application in food and other industries. In the last decades, the use of some microbial polysaccharides in preparing films greatly increased due to their non-toxicity and biocompatibility [1]. In this context, microbial glycan pullulan has a commercial use for decades as edible film and coating for food applications because this glycan is tasteless and odorless, soluble in water, and impermeable to oxygen [2]. It is widely accepted that pullulan is a linear polysaccharide consisting mainly of 1,6-linked maltotriosyl repeating units that connected mutually by α-(1,6)-glycosidic linkages (Fig. 1.).

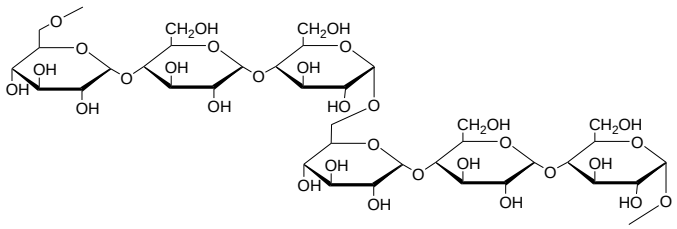

Figure 1. Structure of pullulan

Medicinal plants have traditional and important role in the maintenance of human health. They

are recognizing as source of natural antioxidants and antimicrobial agents due to their biologically active components. In relations to that, the different extracts of medicinal herbs were used for improving functional properties of some polysaccharide based films to find novel promising materials for application in food industry [3].

This paper reports the preparation of pullulan based films containing separately two water extracts of medicinal plant, thyme (*Thymus serpyllum*) and sage (*Salvia officinalis*) as an active ingredients, with aim of obtaining potentially applicable films in food industry as tasty additive or packaging wrap.

EXPERIMENTAL

Pullulan used in this work was produced by the *A. pullulans*, strain CH-1 (IChTM, Collection of Microorganisms) [4]. Medicinal plants *S. officinalis* and *T. serpyllum* were purchased at a local pharmacy. All other reagents and solvents were purchased from commercial sources and used as supplied.

Pullulan powder (3.5 g) was dissolved into distilled water (50 mL) by continuous stirring. Film-forming solutions were prepared with and without addition of two different medical herbal plants, sage and thyme. Water extracts of these plants were prepared separately, by extraction of each plant (6 g) in water (50 mL) with stirring and heating (100 ^{o}C, 30 min). After centrifugation (3000 rpm, 20 min), supernatant solutions separately were mixed with aqueous solution of pululan in a ratio of 1: 1 (vol/vol), and poured (per 5 mL each) into Petri dishes (9x50 mm). The solutions were dried at 60 ^{o}C for 24 h. After that the thin, transparent films were obtained. Characterization of prepared films was performed using FTIR spectroscopy. Antioxidant and antimicrobial activity were also evaluated [5].

RESULTS AND DISCUSSION

The FTIR spectra of the films containing aqueous extracts shows some significant changes in the peak intensity in the range of 900–1600 cm^{-1} related to pure pullulan. Water extracts of sage and thyme have similar FT-IR profil due to their polyphenolic compounds which are often found in glycosidic form [**6**]. FT-IR spectrum of pullulan (Fig. 2.) shows characteristic absorption bands typical for glycans [7]. However the intensity of the peaks at 1600, 1412, 1280, and 1020 cm^{-1} in the spectrum of pullulan raises after adding the water extracts of thyme (Fig. 3.) and sage (Fig. 4.). This is attributed to the presence of extract compounds which show sharp peaks at the same wavelengths in the FTIR spectrum. These peaks can be assigned as follow: aromatic ring vibrations at 1400–1600 cm^{-1}, OH groups of phenolic

compounds at 1410-1310 cm^{-1}, C–O–C vibrations of esters at 1280 cm^{-1}, C–OH stretching vibrations of secondary cyclic alcohols at 1070 cm^{-1}.

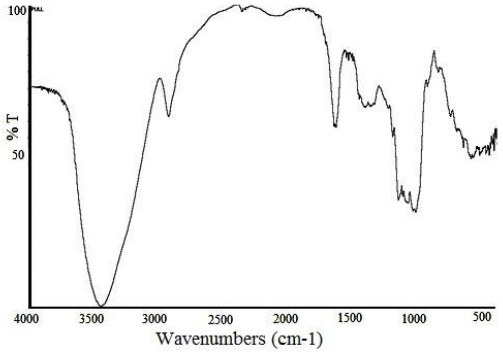

Figure 2. FT-IR spectrum of pullulan

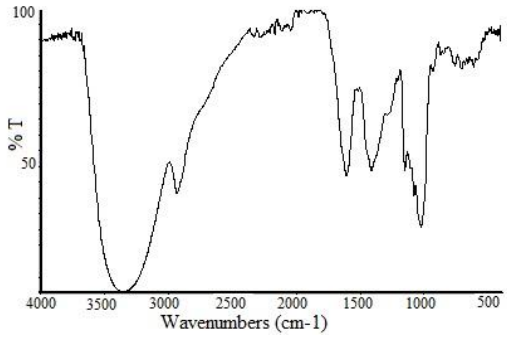

Figure 3. FT-IR spectrum of pullulan-thyme film

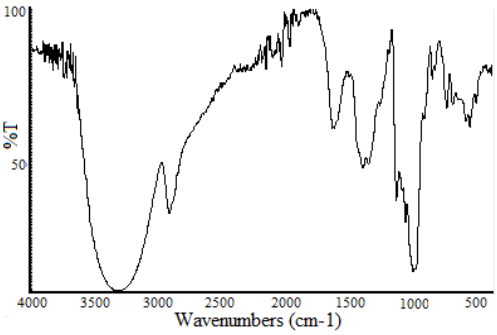

Figure 4. FT-IR spectrum of pullulan-sage film

Antioxidant capacity of prepared films was evaluated *in vitro* by two analytical assays: 1) DPPH (2, 2-diphenyl-1-picrylhydrazyl) free radical-scavenging capability and 2) the chelating ability on ferrous ions. With regard to scavenging ability on DPPH radicals, the samples of film pullulan-thyme and pullulan-sage showed scavenging ability as evidenced by their EC_{50} values were 0.11 and 0.14 mg/mL, respectively. For chelating ability on ferrous ions of these films EC_{50} values were found of 0.33, and 0.25 mg/mL, respectively. Films of native pullulan did not show any anti-oxidant activity.

Antimicrobial effectiveness of films. The antibacterial activity of the formed films was determined by test against *Staphylococcus aureus* ATCC 25923 and *Bacillus subtilis* ATCC 6633. Disks (10 mm diameter) cut from the films were placed on the nutrient agar plates previously surface spread

with inoculums of tested bacteria. After 24-hour incubation at 37 ºC, the zones of inhibition of bacterial growth were observed on both samples of prepared film containing plant extracts, while film of pure pullulan did not showed antimicrobial activity.

CONCLUSION

Pullulan based films containing aqueous extracts of medicinal plants thymus and sage were characterized by FT-IR spectroscopic data. Prepared samples showed antioxidant and antimicrobial activities which recommends these films as a promising candidate in food industry.

Acknowledgement

This work was supported by the Ministry of Education, Science and Technological Development of the Republic of Serbia through Project III 43004.

REFERENCES

[1] T. Bourtoom, International Food Res. J., 2008, **15**, 237-248.
[2] K. Cheng, A. Demirci, J.M. Catchmark, Appl. Microbiol. Biotechnol., 2011, **92**, 29–44.
[3] V. Coma, Polímeros, 2013, **23**, 287-297.
[4] D. M. Jakovljević, M. M. Vrvić, M. Đ. Radulović, M. S. Hranisavljević - Jakovljević, J. Serb. Chem. Soc., 2001, **66**, 377-383.
[5] M.N. Alam, N.J. Bristi, M. Rafiquzzaman, Saudi Pharm.J., 2013, **21**,143-152.
[6] G. Gudi, A. Krähmer, H. Krüger, H. Schulz, J. Agric. Food. Chem., 2015, **63**, 8743−8750.
[7] M. Mathlouthi, J.L. Koenig, Adv. Carb. Chem. Biochem., 1986, **44**, 7-89.

THE IONIZATION OF FLUOROQUINOLONES IN THE PRESENCE OF DIFFERENTLY CHARGED SURFACTANTS

M. Popović-Nikolić [1], G. Popović [2] and K. Berdon [2]

[1] Department of Pharmaceutical Chemistry, (majap@pharmacy.bg.ac.rs)
[2] Department of General and Inorganic Chemistry, Faculty of Pharmacy, University of Belgrade, Vojvode Stepe 450, 11000 Belgrade, Serbia

ABSTRACT

The pK_a values of ciprofloxacin (CPF) and norfloxacin (NRF) were determined potentiometrically, with and without the presence of differently charged micelles, as biomembrane mimetic models. The shift in protolytic equilibria are observed in the presence of surfactants, SDS (ΔpK_{a1} = +2.02; ΔpK_{a2} = +0.57); CTAB (ΔpK_{a1} = -0.09; ΔpK_{a2} = -0.23) and TX-100 (ΔpK_{a1} = +0.24; ΔpK_{a2} = +0.29). The change in distribution of equilibrium forms is most expressed in pH range 6 – 8 which may indicate on potential interactions with molecules of different polarity and charge under physiological conditions.

INTRODUCTION

Fluoroquinolones (FQs) are synthetic antimicrobial drugs which exhibit bactericidal effect by inhibition of the enzymes DNA gyrase and topoisomerase IV, resulting in nonfunctional DNA chains which leads to the death of bacterial cells [1]. The structural characteristics of FQs significantly

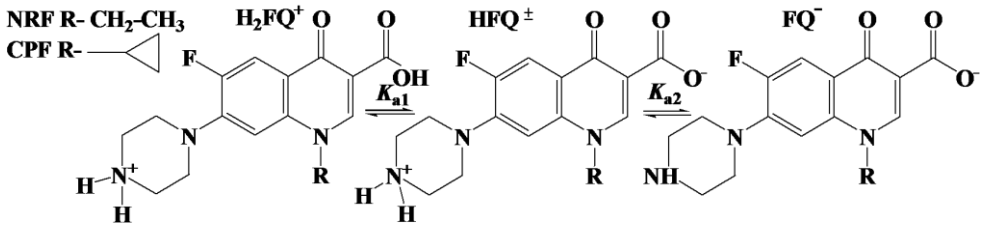

Figure 1. Ionization profile of NRF and CPF.

influence their antimicrobial effect and the pharmacokinetic properties. From a chemical point of view, NRF and CPF are ampholytes containing two ionization centers, the carboxylic group (acidic center) and secondary alkylamine (basic center) (Figure 1).

One of the most important physico-chemical parameters of drugs is pK_a value, which allows a quantitative assessment of the drug ionization at the given pH of the solution. The knowledge of the drug pK_a value plays a major role in the estimation of the pharmacokinetic parameters, definition of the experimental conditions in the analytical procedures, as well as in the development of pharmaceutical dosage forms. Under physiological conditions drugs can interact with biomolecules of different polarity and charge which could change the ionization profile in relation to aqueous solution. By investigating the interactions of drugs with biomembrane mymetic systems, such as micelles [2], a better insight into the behavior of drugs under physiological conditions could be provided. In this paper the pK_a values of NRF and CPF have been potentiometrically determined in the presence and in the absence of surfactants; anionic, sodium dodecylsulphate (SDS); cationic, cetyltrimethylammonium bromide (CTAB) and non-ionic, 4-octylphenol polyethoxylate (TX-100). The effect of differently charged micelles, as biomembrane mimetic systems, on the ionization of NRF and CPF was estimated.

EXPERIMENTAL

Potentiometric measurements were carried out on Automatic titrator 798 MPT Titrino (Metrohm, Switzerland) with a combined electrode LL unitrode Pt 1000 (Metrohm, Switzerland). Norfloxacin and ciprofloxacin were kindly donated from Medicines and Medical Devices Agency of Serbia (Belgrade, Serbia). The surfactants, SDS (J.T. Baker), CTAB (Acros Organic) and TX-100 (Acros Organic) were used for the preparation of micellar solutions. All solutions were prepared in double distilled water. Standard solutions of HCl and carbonate-free NaOH were standardized potentiometrically.

All solutions (5×10^{-4} M) of examined FQs, with and without the presence of 10^{-2} M surfactants (SDS, CTAB and TX-100), were titrated with 0.0998 M NaOH at a 25 °C and a constant ionic strength (0.1 M NaCl). Surfactants were used at a concentration higher than their critical micellar concentrations. Experimental data obtained by potentiometric titration were analyzed by the program Hyperquad.

RESULTS AND DISCUSSION

The pK_a values of NRF and CPF have been potentiometrically determined and ionization in aqueous media was defined. Due to the formation of the intramolecular hydrogen bond with the ketone at the C-4, the ionization of the carboxyl group is suppressed, resulting in a pK_{a1} values (pK_{a1} = 6.07 for NRF; pK_{a1} = 6.01 for CPF) greater than the usual for carboxylic acids. The pK_{a2} values (pK_{a2} = 8.24 for NRF; pK_{a2} = 8.22 for CPF) corresponds to the

secondary alkylamine in the side piperazinyl group. The only difference between structures of norfloxacin and ciprofloxacin is the substituent at position C-1 (Figure 1), which does not significantly affect the ionization. On the basis of the values determined in the micellar solutions (Table I), the shift in protolytic equilibria of examined FQs can be observed in the presence of all applied surfactants.

Table 1. The pK_a values of NRF and CPF potentiometrically determined in micellar solutions and differences with respect to values determined in surfactant free solutions (ΔpK_a).

FQ	pK_a	SDS	ΔpK_a	CTAB	ΔpK_a	TX-100	ΔpK_a
NRF	pK_{a1}	7.94	+1.87	5.98	-0.09	6.31	+0.24
	pK_{a2}	8.50	+0.26	8.01	-0.23	8.50	+0.26
CPF	pK_{a1}	8.18	+2.02	5.95	-0.06	6.15	+0.14
	pK_{a2}	8.65	+0.57	8.19	-0.03	8.51	+0.29

The anionic SDS micelles expressed the most pronounced effect on the ionization of the carboxylic group of CPF (ΔpK_{a1} = + 2.17), and the least pronounced effect exhibited the CTAB micelles on the ionization of NRF secondary alkylamine (pK_{a2} = -0.03). In the case of negatively charged SDS micelles the electrostatic interactions can be assumed: repulsion with the negatively charged ionized form of carboxylic group and attraction with a positively charged ionized form of the amino group. This kind of interactions shifted the equilibria toward the molecular form of carboxylic group (increased pK_a and lower acidity) and ionized form of amino group (increased pK_a and higher acidity). The cationic CTAB micelles, with a positively charged surface, did not express significant influence on NRF and CPF ionization (ΔpK_a up to -0.23). However, the protolytic equilibria have been slightly shifted in the opposite direction comparing to SDS, which indicate that ionizable centers of examined FQs could be also involved in electrostatic interactions with positively charged micelles. The change in pK_a values in the presence of TX-100 micelles, which are not charged, indicates on the possible dipole interactions and hydrogen bonds in the hydrophilic layer of nonionic micelles with the ionizable centers of FQs (ΔpK_a up to +0.29). The change in the distribution of the equilibrium forms under the influence of surfactants are the most expressed in pH range 6 – 8 which involves biopharmaceutically important pH values. This can be clearly seen on the distribution diagrams as a function of pH (Figure 2).

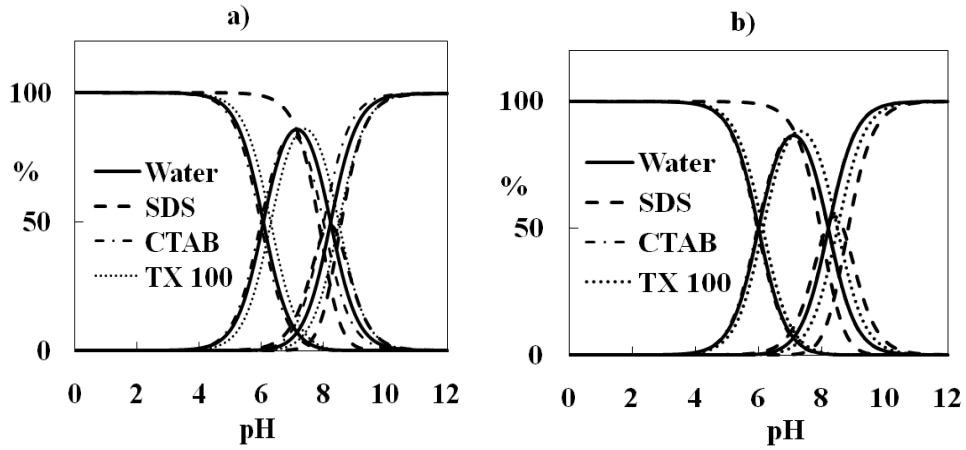

Figure 2. Distribution of a) NRF and b) CPF equilibrium forms as a function of pH.

CONCLUSION

The shift in pK_a values (ΔpK_a up to 2.02) indicates that the investigated FQs interact with micelles of different charge and polarity, which directly involve their ionization centers. The anionic micelles expressed the most pronounced effect, especially on the ionization of carboxylic group. On the basis of these results it can be assumed that negatively charged biomolecules in plasma potentially may shift the equilibria toward the molecular form of carboxylic group especially at pH values 6 - 8.

Acknowledgement

This work was supported by the Ministry of Education, Science and Technological Development of the Republic of Serbia, Contract No. 172033.

REFERENCES

[1] Lemke T. L., Williams D. A., Roche V. F., Zito S. W., Foye's Principles of Medicinal Chemistry, Lippincott Williams & Wilkins: Philadelphia, 2013.

[2] Fendler, J. H. Chem. Rev. 1987, 87, 877−899.

PHOSPHATES-COATED MAGNETIC NANOPARTICLES LABELED WITH YTTRIUM-90 AS MULTIFUNCTIONAL AGENTS FOR POSSIBLE USE IN MEDICINE

M. Radović, M. Mirković, M. Perić, A. Vukadinović, D. Janković, D. Stanković, Z. Milanović and S. Vranješ-Đurić

University of Belgrade, Vinča Institute of Nuclear Sciences, Laboratory for radioisotopes, P. O. Box 522, 11001 Belgrade, Serbia (magdalena.lazarevic@vinca.rs)

ABSTRACT

Radiolabeled magnetic nanoparticles (MNPs) coated with hydrophilic phosphates ligands: imidodiphosphate (IDP) and inositol hexaphosphate (IHP) were developed as multifunctional vectors to localize both radioactivity and magnetic energy at the tumor site. The coating of MNPs with phosphates increased their colloidal stability and prevented agglomeration, allowed the binding of the radionuclide ^{90}Y for the functional groups on the surface of MNPs and increased the stability of MNPs *in vivo*.

INTRODUCTION

Magnetic nanoparticles have been subjected to a variety of biomedical applications due to their remarkable nanoscale physicochemical properties. Their small size, high surface to volume ratio and magnetic properties make them ideal candidates for clinical applications, including magnetic resonance imaging (MRI), hyperthermia treatment of cancer, cell separation, tissue repair and magnetic force guided drug delivery [1, 2].

The phosphates have been used as coatings due to their strong chelating ability with metal ions, especially iron, and also due to the proven biocompatibility. The phosphates and phosphonates have been developed as pharmaceuticals due to their affinity for calcium which is abundant in bone [3]. In this work, however, we exploited the phosphates groups for its ability to bind to MNPs rather than for their bone targeting properties.

IDP and IHP (Fig. 1) have not hitherto been used for coating of MNPs and the results of this study showed that the phosphates groups influenced the modification of the surface of MNPs.

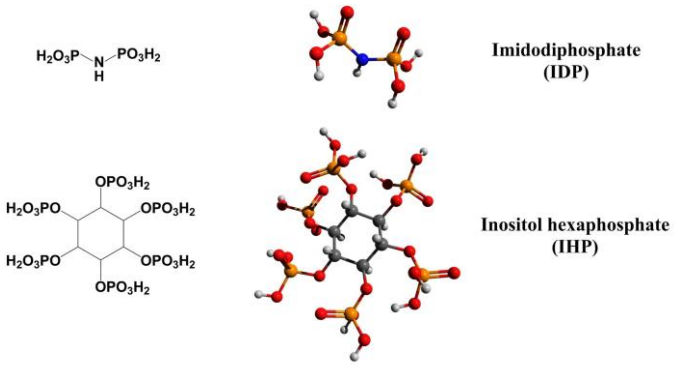

Figure 1. Structures of imidodiphosphate and inositol hexaphosphate used for a coating of MNPs

EXPERIMENTAL

Fe_3O_4 MNPs were synthesized by co–precipitation method [4]. After that, the coating reaction was carried out by the addition of 2 ml solution of IDP (Fe_3O_4:IDP = 1:2) and IHP (Fe_3O_4:IHP = 1:1), respectively. The pH of the mixture was adjusted to 8-9 by addition of 6 M NaOH. Then, the mixture was stirred overnight at room temperature. The excess of unreacted IDP and IHP was removed by dialysis against deionized water for 1 day. The stable suspension of phosphate-coated Fe_3O_4 particles, i.e., ferrofluid, was obtained. The heating ability of MNPs was quantified through the specific power absorption (SPA) measurements. The phosphate-coated MNPs were labeled with 37 MBq$^{90}YCl_3$, at room temperature for 1 h and were used in *in vivo* biodistribution studies in normal Wistar rats.

RESULTS AND DISCUSSION

The SPA values obtained for synthesized MNPs (46–81 W g^{-1}) in different physiological media such as phosphate buffered saline (0.01 M PBS, pH 7.4) and saline (0.15 M/0.9 % NaCl, pH 5.5) (Fig. 2), imply that the phosphate-coated MNPs could maintain their heating capacity in physiological environments and thus have great potential to be used in biomedical applications as magnetic fluid hyperthermia agents. Both types of coated MNPs were ^{90}Y-labeled in a reproducible high yield (>98%). The biodistribution pattern of the ^{90}Y-MNPs after intravenous administration to healthy Wistar rats was followed by the radiotracer method, showed high uptake in the liver and spleen as well as *in vivo* stability and long retention in these organs up to 72 h. The bidistributona of both MNPs are very similar.

Fig. 3 shows biodistribution profile for ^{90}Y-Fe_3O_4-IHP MNPs. An insignificant amount of radioactivity (<1.5 % injected dose (ID) per organ after 72 h) was detected in the femur, a target organ for free ^{90}Y, indicating that ^{90}Y was tightly attached to the surface of the MNPs.

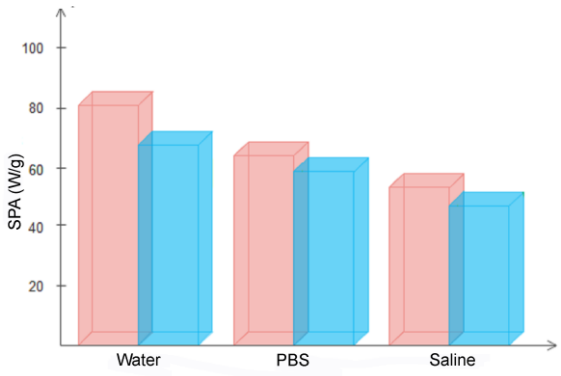

Figure 2. SPA values of Fe_3O_4-IDP (red) and Fe_3O_4-IHP (blue) MNPs in different physiological media under 23.9 kA m^{-1}, 577 kHz.

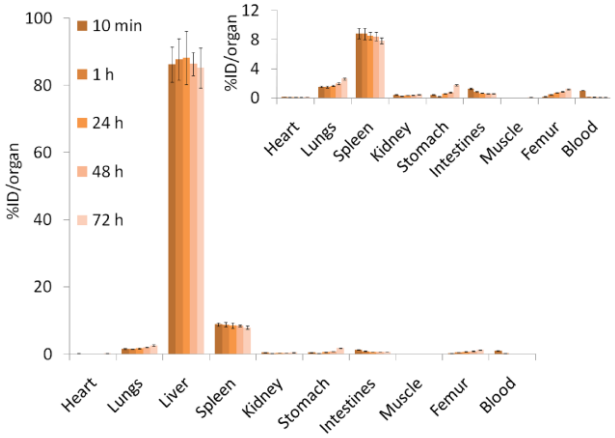

Figure 3. Biodistribution of ^{90}Y- Fe_3O_4-IHP MNPs in different tissues up to 72 h of intravenous administration in normal Wistar rats. The inset shows the results for tissues without the liver.

CONCLUSION

Phosphates on the surface of MNPs enabled their biocompatibility, especially colloidal stability in physiological media and successful binding of ^{90}Y radionuclide.^{90}Y-coated MNPs were radiolabeled for two purposes: to use the radiotracer to obtain an accurate biodistribution profile of the MNPs and to produce potential radiotherapeutical agents. ^{90}Y-MNPs will generally remain where they were initially deposited, thus allowing for repeated and concentrated hyperthermia treatments in the same area, leading to increased perfusion in the tumor region; therefore, higher radionuclide delivery and oxygenation are required to enhance free-radical-dependent cell death in radiotherapy. Both ^{90}Y-labeled phosphate-coated MNPs exhibited favorable properties that justify further investigations toward their potential use in combined radiotherapy–hyperthermia cancer treatment.

Acknowledgement

The Ministry of Education, Science and Technological Development of the Republic of Serbia supported this work financially through the Project Grant No. III45015.

REFERENCES

[1] I. Sharifi, H. Shokrollahi, S. Amiri, J. Magn. Magn. Mater., 2011, 324, 903–915.
[2] G. Chen, I. Roy, C. Yang, P. N. Prasad, Chem. Rev., 2016, 116, 2826–2885.
[3] T. Muthukumaran, J. Philip, J. Alloys Compd., 2016, 689,959–968.
[4] R. Massart and V. Cabuil, J. Chim. Phys. Phys.-Chim. Biol.,1987, 84, 967–973.

TWO NOVEL BISPHOSPHONATE-COATED MNPs LABELED WITH ^{99m}Tc DESIGNED AS POTENTIAL THERANOSTIC AGENTS

M. Mirković, M. Radović, D. Janković, Z. Milanović, M. Perić, A. Vukadinović, D. Stanković, Đ. Petrović and S. Vranješ-Đurić

University of Belgrade, Vinča Institute of Nuclear Sciences, Laboratory for radioisotopes, P. O. Box 522, 11001 Belgrade, Serbia (mmarija@vinca.rs)

ABSTRACT

The objective of this study is to prepare ^{99m}Tc–bisphosphonate–coated magnetic nanoparticles based on Fe_3O_4, assess their *in vitro* end *in vivo* stability and explore their potential application in the biomedical fields as theranostic nanoagent which combines magnetic hyperthermia and SPECT imaging.

INTRODUCTION

Nanometer-scale magnetic nanoparticles (MNPs) have unique properties such as biocompatibility, stability, long blood half-life, ability to enhance MR contrast and facile surface modification making them attractive as multifunctional nanoplatforms for medical applications. Key of the successful application of MNPs in biomedicine is surface functionalization which contributes to increase of the colloidal stability. Another requirement for *in vivo* use of the particles is to ensure nontoxicity and prevent opsonization by plasma proteins.

In order to radiolabel MNPs, their surface must be functionalized with radionuclide-binding molecules. In medicine, phosphonates complexes labeled with ^{99m}Tc are commonly used as bone-scanning agents due to theirs higher uptake in skeleton.

Magnetic nanoparticles have the application potentiality in innovative diagnostic and therapeutic modalities because of their multifunctionality [1,2]. In the present study, magnetite (Fe_3O_4) nanopaticles coated with two hydrophilic bisphosphonate ligands, i.e., methylene diphosphonate (MDP) and 1-hidroksietan diphosphonate (HEDP) were synthetized and labeled with ^{99m}Tc. The aim was to examine if the above nanosystems, can be used as theranostic nanoagents, for hyperthermia application and nuclear diagnostic imaging.

EXPERIMENTAL

The bisphosphonate coated MNPs were synthesized using co-precipitation method [3]. The obtained bisphosphonate-coated Fe_3O_4 MNPs were characterized by X-ray powder diffraction (XRD) and Fourier transform infrared spectroscopy (FTIR). The heating ability for cancer hyperthermia therapy application was quantified through the specific power absorption (SPA) measurement. Radiolabeling of both bisphosphonate-coated Fe_3O_4 nanoparticles with ^{99m}Tc was carried out using $SnCl_2$ as a reducing agent. ^{99m}Tc-MNPs were additionally used for i*n vitro* stability studies in saline and human serum and *in vivo* biodistribution studies in normal *Wistar* rats. The animals were intravenously injected into the tail vein with 0.1 ml (approx. 2.5 MBq) of ^{99m}Tc–MNPs (0.1 ml of suspension containing 0.2 mg of ^{99m}Tc–MNPs).

RESULTS AND DISCUSSION

The obtained bisphosphonate-coated MNPs were characterized by two techniques. The crystalline properties and phase identification were characterized by X-ray diffraction (XRD). Fig. 1. shows the X-ray powder diffractograms of the Fe_3O_4, Fe_3O_4-MDP and Fe_3O_4-HEDP MNPs. FTIR spectroscopy was used to study the functionalization of the magnetite nanoparticles with MDP and HEDP. Fig. 2. a i b illustrates the FT-IR spectra from the free ligands, Fe_3O_4 and functionalized Fe_3O_4 MNPs.

The obtained SPA values for Fe_3O_4–MDP and Fe_3O_4–HEDP were 183 W/g and 131 W/g, respectively, which indicate their potential in hyperthermia based cancer treatments (Table 1). Radiolabeling of both bisphosphonate-coated Fe_3O_4 nanoparticles with ^{99m}Tc was performed at high yields without purification (> 95 %). Incubation of both radiolabeled preparations in saline and serum showed that the bisphosphonate-iron oxide bonding was very stable with only 10 and 15 % of ^{99m}Tc detaching from the iron oxide after 24 h, respectively. The highest uptake was observed at 1 h p.i. in the liver followed by the spleen (Fig.3).

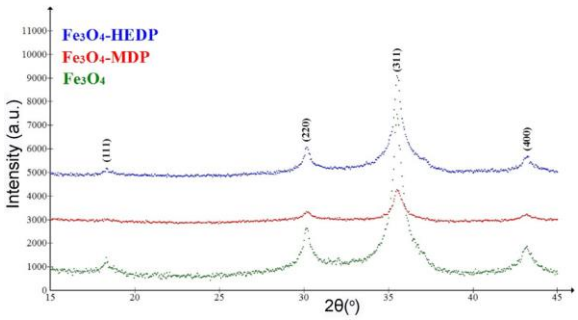

Figure 1. X-ray diffraction patterns of Fe_3O_4, Fe_3O_4-MDP and Fe_3O_4-HEDP MNPs

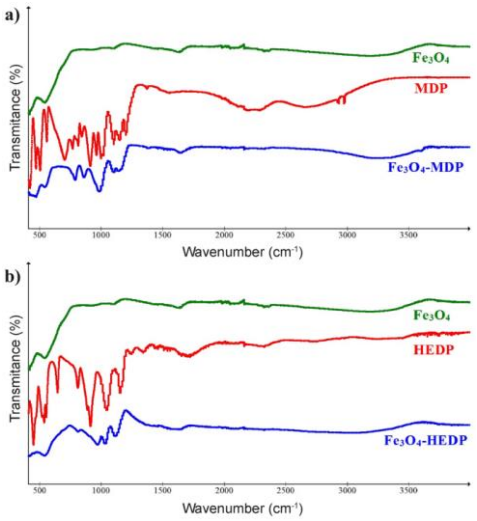

Figure 2. ATR-FTIR spectra: a) Fe_3O_4, MDP and Fe_3O_4-MDP b) Fe_3O_4, HEDP and Fe_3O_4-HEDP MNPs

Table 1. SPA values of the aqueous dispersion of MNPs in the applied magnetic field, 23.9 kA/m

MNPs	SPA (W/g)		
	252 kHz	397 kHz	577 kHz
Fe_3O_4-MDP	67.3	143	183
Fe_3O_4-HEDP	55	78.5	131

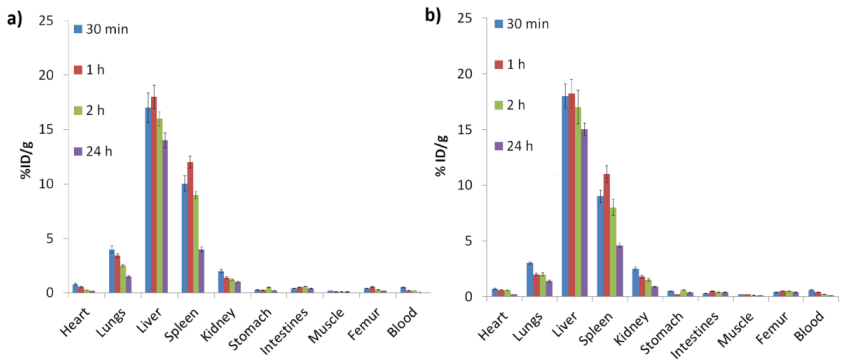

Figure 3. Biodistribution results of a) ^{99m}Tc-Fe_3O_4-MDP and b) ^{99m}Tc-Fe_3O_4-HEDP MNPs

CONCLUSION

The bisphosphonate coated MNPs showed good magnetic properties and colloidal stability even after a long period of time at physiological pH. The obtained results of specific power absorption demonstrate potential therapeutic applications of Fe_3O_4-MDP and Fe_3O_4-HEDP. ^{99m}Tc-Fe_3O_4-MDP and ^{99m}Tc-Fe_3O_4-HEDP MNPs, were obtained in a high radiolabeling yield (>95 %) and exhibit high *in vitro* stability in saline and human serum. As expected, the results of biodistribution showed high liver and spleen uptake almost immediately after i.v. administration due to their colloidal nature. Such radiolabeled biocompatible bisphosphonate MNPs with high labeling yield, *in vitro* and *in vivo* stability, showed the great promise as theranostic nanoagent which combines magnetic hyperthermia and SPECT imaging.

Acknowledgement

The Ministry of Education, Science and Technological Development of the Republic of Serbia supported this work financially through the Project Grant No. III45015.

REFERENCES

[1] K. Yahara, T. Ohguri, S. Yamaguchi, Int J Hyperthermia, 2015, 31, 600-608.

[2] U.I. Tromsdorf, O.T. Bruns, S.C. Salmen, U. Beisiegel, H. Weller, Nano Lett, 2009, 9, 4434-4440.

[3] R. Massart, V. J. Cabuil, Chim Phys, 1987, 84, 967-973.

SPECTRAL ANALYSIS OF EXTERNAL MAGNETIC FIELD INFLUENCE ON MAGNETITE AND COBALT-FERRITE NANO-PARTICLES IN FERROFLUID

M. Perić, A. Vukadinović, D. Janković, M. Radović, Z. Milanović, D. Stanković, Đ. Petrović and S. Vranješ-Đurić

University of Belgrade, Vinča Institute of Nuclear Sciences, Laboratory for radioisotopes, P. O. Box 522, 11001 Belgrade, Serbia
*(*markoperic1983@gmail.com*)*

ABSTRACT

Using simple optical measurements, the selective spectral sensitivity of suspended nano-particles of magnetite (Fe_3O_4) and cobalt-ferrite ($CoFe_2O_4$) coated with starch, was observed through switching on/off of external magnetic field. The field strength was varied in the interval 30 – 300 mT. In these transient regimes, the unexpected and unusually large changes of transmitted light occur. An explanation is suggested, within the model based on ordering of magnetic moments of nano-particles along the lines of magnetic field into magnetic chains and organization of magnetic chains into spatial structure - a quasi-lattice.

INTRODUCTION

The most frequently investigated nano-particles are certainly iron oxide nano-particles such as magnetite (Fe_3O_4) and hematite (Fe_2O_3), due to their biocompatibility, non-toxicity and non-immunogenicity in organism. Beside that cobalt-ferrite ($CoFe_2O_4$) magnetic nano-particles (MNPs) also showed remarkable magnetic properties. However key of the successful application of MNPs in medicine is surface functionalization which contributes to increase the colloidal stability. Due to their large surface area to volume ratio, MNPs have an inherent tendency to agglomerate. When injected intravascularly, these agglomerated particles are rapidly cleared away by macrophages of the mononuclear phagocyte system before they can reach the target cell of interest. To prevent aggregation of the particles and ensure nontoxicity under physiological conditions, magnetic nanomaterials require sophisticated coatings, which ideally should have a high affinity for the iron oxide core, be nonimmunogenic and nonantigenic, and prevent opsonization by plasma proteins. In the present study Fe_3O_4 and $CoFe_2O_4$ nanoparticles coated with starch have been successfully synthesized using co-precipitation method. The influence of the magnetic field on the behavior of MNPs was

tracked by measuring a transparence of ferrofluid suspension irradiated with white-light and laser beam [1-4]. Spectral range of 650-670 nm has been used. In this spectral region, there is number of semiconductor lasers which are being applied for the therapeutic purposes.

EXPERIMENTAL

Starch (6g) was dissolved in 40ml of doubly purified water at 100°C. 2.0 M NaOH solution was added into the mixture solution of 0.8 M Fe^{3+} ions and 0.4 M Co^{2+} (Fe^{2+} in the case of Fe_3O_4) ions under vigorous stirring until the pH of 9 for 1 hour. Then starch solution was poured into the reaction mixture and ultrasonically treated for 30 minutes. The resulting black suspension was neutralized with 0.1 M HCl.

RESULTS AND DISCUSSION

Ferrofluid sample reduces the intensity of the incident radiation uniformly throughout the spectrum and behaves as a neutral density filter. However, after switching on the external magnetic field, ferrofluid sample begins to act as a spectrally selective filter i.e. some wavelengths were attenuated more than others. The measured time dependence of transmitted light trough the ferrofluid in the wavelength interval of 300-900 nm forms a surface $I(\lambda, t)$ which, after normalization on the initial distribution (through the unperturbed ferrofluid), has a shape given in Fig. 1(a) and 1(c). During this study, special attention was focused on the spectral region 650-670 nm in which the most prominent changes of intensity of transmitted light occurs. For that purpose, the graphic of transmitted light intensity over time (Fig. 1 (b) and 1(d)) at the wavelength of 655nm was set aside.

Fig. 2 presents time dependence of intensity of transmitted light through the ferrofluid, under the influence of external magnetic field in the range of 30 – 300 mT when a laser diode on the same wavelength (λ = 655nm) was used instead of white light source.

Immediately after switching-on the magnetic field (MF) (Fig.2.), a rapid decrease of intensity of transmitted light occurred. Some mechanism after switching-on the MF leads to blurring of solution which reduces transparency and decreases intensity of transmitted light. In other words, in the region of the valley (Fig. 2.), the precipitate of ferrofluid samples was formed. The width of the valley and the amount of the precipitate depend on the applied magnetic field and the largest amount was observed at the strongest fields.

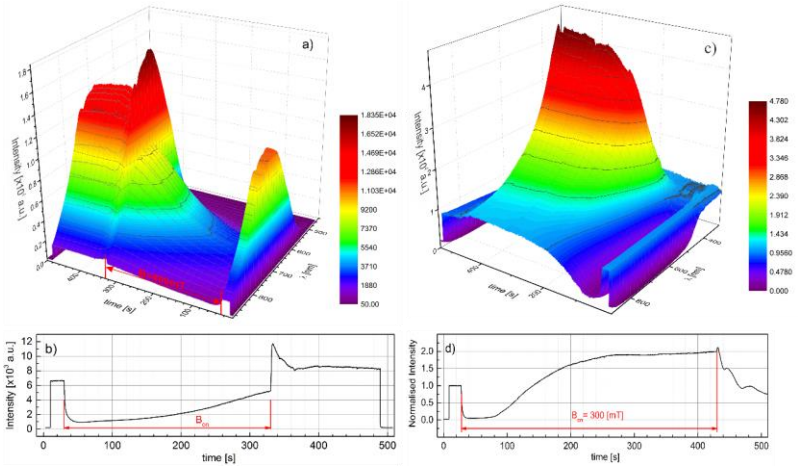

Figure 1. (a) Normalized intensity of transmitted white light through ferrofluid sample for Fe_3O_4, b) Intensity of transmitted light at λ=655nm in a function of time for Fe_3O_4, (c) Normalized intensity of transmitted white light through ferrofluid sample for $CoFe_2O_4$, d) Intensity of transmitted light at λ=655nm in a function of time for $CoFe_2O_4$

Also the valley minimum was affected by type of ferrofluid sample, i.e. the effect is much larger in the case of $CoFe_2O_4$. After some time (app. 100s), according to the MF used, the solution becomes more transparent and the intensity of transmitted light increases (see Fig. 2(a) and 2(b)).

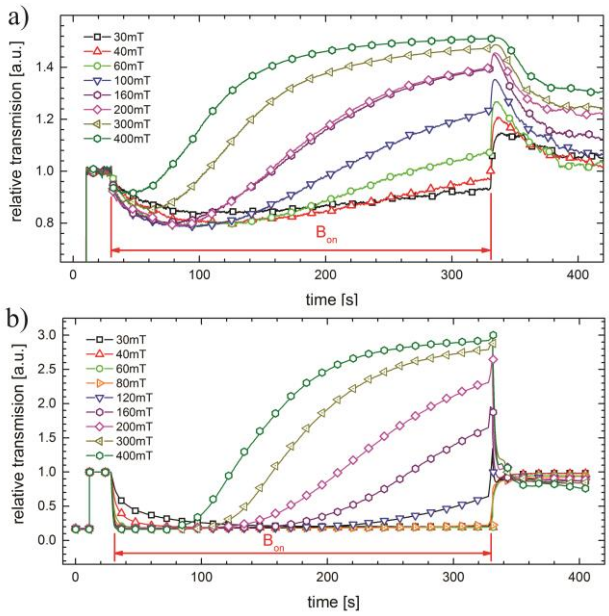

Figure 2. Time dependence of transmitted diode laser light (λ=655nm) for different magnetic field strength (a), for Fe_3O_4 coated with starch and (b) $CoFe_2O_4$ coated with starch

CONCLUSION

Within this paper we have presented measurements of spectral distribution of light transmitted through the ferrofluid suspensions of Fe_3O_4 and $CoFe_2O_4$ exposed to the external magnetic field. As it have been shown, nano-particles of $CoFe_2O_4$ coated with starch were more sensitive on switching on/off of magnetic field in the spectral range of 650-670 nm. In this spectral region, there is number of semiconductor lasers which are used for the therapeutic purposes, so further measurements were continued with a diode laser as a source of coherent light on the wavelength of λ=655 nm.

The unusually large changes were observed in the intensity of transmitted light during the transited regimes. An explanation is suggested within the classical electromagnetic theory based on Lenz's rule and response of the magnetic ferrofluid on the change in the magnetic flux. It can be concluded that in the rapidly changing magnetic field, for instance in the RF range, rapid change of orientation of magnetic domains of ferrofluid nanoparticles can find application in therapy, for instance for local heating of the tissue.

Acknowledgement

The Ministry of Education, Science and Technological Development of the Republic of Serbia supported this work financially through the Project Grant No. III45015.

REFERENCES

[1] C. Rablau, P.Vaishnava, C. Sudakar, R. Tackett, G. Lawes, R. Naik, Phys. Rev. E, 2008, 1-9.
[2] J. M. Laskar, J. Philip, B. Raj Phys. Rev. E, 2009, 1-8.
[3] J. Li, X. D. Liu, Y. Q. Lin, Y. Huang, L. Bai, Appl. Phys. B, 2006, 81-84.
[4] X. Bai, S. Pu, L. Wang, Opt. Commun., 2011, 4929-4935.

SPECTROPHOTOMETRIC QUANTIFICATION OF QUERCETINE USING A MICELLE SYSTEM

L. Pavun[1], S. Mićić, A. Janošević Ležaić, K. Kovačević, S. Uskoković-Marković and N. Pejić

University of Belgrade–Faculty of Pharmacy, Vojvode Stepe 450, 11000 Belgrade, Serbia

ABSTRACT

The current research provides the development of the new spectrophotometric method for the simple and affordable quercetin quantification. Proposed method based on formation of supramolecular assembles of quercetin (Q) and cetyl trimethylammonium bromide (CTAB). Under selected experimental conditions (λ = 378 nm, c_{CTAB} = 2 mM and T = 25 °C), Beer's law was obeyed in the quercetin concentration ranged $2 \times 10^{-6} - 8 \times 10^{-5}$ mol dm^{-3}. The method sensitivity was 2.1×10^4 dm^2 mol^{-1} (the molar absorptivity) as well as 1×10^{-6} mol dm^{-3} (the limit of detection). The method applicability to the direct Q determination in a pharmaceutical formulation (Quercetin+C capsules, Twinlab) was demonstrated.

INTRODUCTION

Among all the flavonoids, which display a significant array of biological and pharmacological activities (antioxidative, antinflamatory, antimicrobial, anticancerogeneous, etc.), quercetin (3,3′,4′,5,7-pentaxydroxyflavone) is commonly found in food and plant based beverages such as onions, apples, tea and red wine. Since quercetin possesses mentioned very important properties, and thus it is distributed in many pharmaceutical preparations, their quantification is of a significant importance.

Besides spectrophotometric method based on colored complexing reaction of Q with many different inorganic reagents [1], various methods have been described for the Q determination. However, some of the methods are time consuming since quercetin stability is time or pH dependent, while some of them require expensive instrumentation or sensing materials. As a result, simplified method for routine use, such as direct spectrophotometric method [2] is required for the Q determination in food and pharmaceutical dosage forms.

[1] email leposava.pavun@pharmacy.bg.ac.rs

It is well know that quercetin′s polyphenol structure like the other flavonoids, makes it very sensitive to changes in the surroundings, which can modulate quercetin properties and consequently its stability. In this since, a very recently, spectrofluorimetric method based on formation of stable supramolecular complexes between quercetin and micelles of surfactants (cetyl trimethylammonium bromide, sodium dodecyl sulfate and triton X-100) was proposed [3].

In this work, micelles of surfactant (CTAB) was used to improve quercetin UV-VIS spectrophotometric quantification. Thus, the aim of this work is development of a new UV-VIS spectrophotometric method for quercetin determination based on interactions of quercetin with cationic surfactant cetyl trimethylammonium bromide, and, in doing so its applicability.

EXPERIMENTAL

Quercetin×2 H_2O, methanol and ascorbic acid were obtained from Merck (Darmstadt, Germany) and were used without any further purification. Quercetin + C capsules were available from Twin Laboratories Inc., Ronkonkoma, New York, USA.

Spectrophotometric measurements were performed on UV-VIS Spectrophotometer Beckman DU-650 (Fullerton, USA), using a 1 cm quartz cuvette. For estimation of calibration curve for Q quantifications, absorption spectra of solutions with different Q concentrations in 3% methanolic solution (2.0×10^{-6} –8.0×10^{-5} mol dm^{-3}) and the constant CTAB concentration (2.0×10^{-3} mol dm^{-3}) were recorded in the range of wavelengths 220 – 500 nm.

For Q determination in a pharmaceutical preparation, the sample solution was prepared to dissolve an amount equivalent to the average weight of two capsules (containing 500 mg of quercetin and 1400 mg of vitamin C) in 200 cm^3 of methanol, shaking for 15 min in ultrasonic bath and filtered through filter paper Whattman No 1. The obtained solution is diluted with methanol/water and CTAB solution to the concentration of 5 μg cm^{-3}.

RESULTS ANS DISCUSSION

In the wavelength range 220 – 500 nm, 3% methanolic solution of Q shows two major absorption bands in the UV – VIS region: band I located in the wavelength range of 300 – 400 nm (ie. at 364 nm) is related to the cinnamoyl system, and band II located in the wavelength range of 240–300 nm (i.e. at 252 nm) is supposed to be associated with the light absorption of the benzoyl moiety (curve a, Fig. 1.).

UV-VIS quercetin absorption spectra showed hypochromic, hyperchromic and bathochromic effects upon addition of CTAB (Fig. 1, curves b-e). The absorbance of the band I increases (hyperchromic effect), while the band II is affected in two manners: there is decrease (hypochromic effect) and increase (hyperchromic effect) in the absorbance, for CTAB concentration smaller and higher than critical micelle concentration (CMC), respectively. Besides to that, there is a slight shift of bands towards higher wavelength region (bathochromic effect); presence of CTAB in concentration very close to CMC and higher then CMC cause a bathochromic shift of about 10-15 nm from the original band I in the absence of CTAB (curves c and d, Fig. 1.). Namely, formed CTAB spherical micelles (after CMC) shift band I from 364 nm to 379 nm. On the other hand, for CTAB concentration higher than 2 mmol dm^{-3}, the band I position is not changed (curve e, Fig. 1). It is obvious that the best conditions for Q quantification relate to the λ = 379 nm and c_{CTAB} = 2 mmol dm^{-3}. In addition, in the presence of CTAB micelles, no change of quercetin absorbance in the time at λ = 379 nm. Thus, the use of CTAB micelles provides enough stability to Q during its spectrophotometric quantification time.

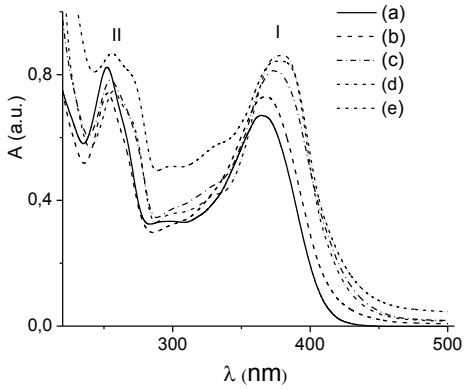

Figure 1. UV-VIS absorption spectra of 3% methanolic solution of Q (0.04 mmol dm^{-3}) alone (a) and in presence of different CTAB concentrations (in mmol dm^{-3}): 0.5 (b), 0.8 (c), 2.0 (d) and 4.0 (e)

It is evident that interaction between Q and CTAB promotes absorption of the former when the CTAB concentration is higher than the respective CTAB critical micellar concentration (about 1 mmol dm^{-3}). Thus, for quercetin quantification, the absorption spectra of solutions with constant CTAB concentration (2 mmol dm^{-3}) and different Q concentrations (2.0×10^{-6} – 8.0×10^{-5} mol dm^{-3}) at λ = 378 nm, were recorded.

The absorbance of these micellar systems at selected wavelength varies linearly with the Q concentration. Method validation was done in accordance with ICH guidelines (table 1). Under selected experimental conditions, Beer's law was valid within a concentration range of about two orders of magnitude (2×10^{-6} – 8×10^{-5} mol dm^{-3}). The calibration curve, has the regression equation, A = 21133 c – 0.025 (r = 0.9991). The sensitivity of the proposed method was 2.1×10^4 dm^2 mol^{-1} (the molar absorptivity) as well as 1×10^{-6} mol dm^{-3} (the limit of detection).

The stability of the supramolecular assembles between Q and CTAB micellar system allows to apply the method described above for the Q determination in pharmaceutical preparation (*Quercetin + Vitamin C capsules*). Although the presence of ascorbic acid may cause problem in measurements, quercetin has been determined successfully (Table 1).

Table 1. Precision and recovery of quercetin in capsules

Quercetin +Vitamin C capsules	Found Q-dihydrate (mg)	Recovery (%)	SD (%)	CV (%)
Declared 250 mg of per capsule	246.3	98.5	0.23	0.093

CONCLUSION

Our results demonstrate the feasibility of the proposed spectrophotometric method based on formation supramolecular CTAB–Q assembles for quercetin quantification in presence of ascorbic acid. The developed method shows good analytical features; the results are accurate and precise, and there are advantages in terms of short time required for each assay.

Acknowledgement

This work was partially supported by the Ministry for Education, Science and Technological Development of the Republic of Serbia (Grants no. 172015, 172016, 172043).

REFERENCES

[1] D. Malešev, V. Kuntić, J. Serb. Chem. Soc., 2007, **72**, 921-939.
[2] N. Pejić, V. Kuntić, Z. Vujić, S. Mićić, Il Pharmaco, 2004, **59**, 21-24.
[3] J.C. Alva-Ensastigue, M. Palomar-Pardavé, M. Romero-Romom, M.T. Ramirez-Silva, RCS Adv., 2018, **8**, 10980-10986.

FLUORESCENCE QUENCHING METHOD FOR DETERMINATION OF BROMIDE IN THE PHARMACEUTICAL PREPARATION

S. M. Blagojević[1], M. Minčić[1] and R. Daljević[2]

[1]*University of Belgrade–Faculty of Pharmacy, Department of Physical Chemistry and Instrumental Methods, Vojvode Stepe 450, Belgrade, Serbia*
[2]*Institute of General and Physical Chemistry, Studentski trg 12/V, Belgrade*

ABSTRACT

In the present paper the influence of bromide ion on the quenching of fluorescence intensity of quinine was investigated. Using fluorescence quenching method, applying the Stern–Volmer kinetics, the concentration of bromide in both bromide aqueous solution and sample of 2% homatropine hydrobromide eye drops determined. Result of determination of bromide content in selected pharmaceutical preparation obtained by the fluorescence quenching method are compared with result obtained by the ion chromatography method and are in excellent agreement.

INTRODUCTION

Fluorescence quenching refers to any process which decreases the fluorescence intensity of a certain fluorophore. Decrease in fluorescence intensity or lifetime of fluorophores can be measured and related directly to the quencher concentration via different quenching mechanism. The fluorescence of certain heterocyclic indicators such as those based on quinine and acridine type fluorophores are quenched by halide anion such as chloride, bromide and iodide [1,2]. The alkaloid quinine, an antimalarial drug and muscle relaxant with a bitter taste, is a strongly fluorescing compound in dilute acid solution which contains a quinolinium ring was sensitive to halide. The halide anions quench the quinine fluorescence by *collisional* deactivating the excited fluorophore (referred to as dynamic fluorescence quenching) [1], where both the intensity of fluorescence of quinine and lifetime are reduced in the presence of a quencher. The relationship between fluorescent intensity and the quencher concentration (halide anion) is represent by the Stern–Volmer equation [1]:

$$I_{oF}/I_F - 1 = K_{SV}\,c$$

where I_{oF} and I_F are the fluorescence intensities before and after adding the quencher, respectively, c is the molar concentration of quencher and K_{SV} is the dynamic Stern–Volmer quenching constant. This equation can be used to

obtain values of the Stern–Volmer halide quenching constant, by plotting $I_{oF}/I_F - 1$ as a function of bromide ion as quencher and for determination of the bromide ions in various samples. Fluorescence quenching method can give useful kinetic information of the investigated system flouorophora–quencher, but it can be applied for determining the concentration of the quencher in a variety of pharmaceutical and biological samples [1,3,4].The aim of this study is to investigate the influence of bromide ion on fluorescence quenching on quinine and application of fluorescence quenching method to determine the content of bromide ion quenchers in aqueous bromide solutions and selected pharmaceutical preparation 2% homatropine hydrobromide. Homatropine hydrobromide is an anticholinergic agent commonly used as a mydriatic and cycloplegic and is commonly formulated as 1.0 and 2.0% eye drops.

EXPERIMENTAL

Materials The quinine (Fluka), sulphuric acid (Merck), potassium bromide (Sigma–Aldrich), real sample 2% homatropine hydrobromide – the salt dissolved in 3% boric acid (Central Pharmacy-Clinical Center of Serbia). Deionized water (18 MΩ cm^{-1}, MilliQ, Millipore) was used for preparation of all solutions.

Preparations of the standard and sample solutions The series of aqueous standard solutions with constant quinine concentration 3.08×10^{-5} mol L^{-1} and varying bromide concentrations in the range 2.00×10^{-5} mol L^{-1} – 8.00×10^{-3} mol L^{-1} will be used to study collisional quenching and for determination of Stern–Volmer plot and determination of bromide ions in both sample solutions (bromide aqueous solution and selected pharmaceutical preparation 2% homatropine hydrobromide eye drops). The bromide standard solutions and both sample solutions with same concentration quinine (3.08×10^{-5} mol L^{-1}) were prepared in 5.00×10^{-2} mol L^{-1} sulphuric acid. 1.5 mL of real samples is transferred to 25 mL volumetric flask with 5 mL of quinine solution (1.54×10^{-4} mol L^{-1}) and diluted to volume with 5.00×10^{-2} mol L^{-1} sulphuric acid. ***Fluorimetry*:** The fluorescence intensity was measured using a filter *fluorimeter Spekol 10* (Carl Zeiss Jena, Germany), with excitation wavelength 365 nm. ***Ion chromatography***: The results of bromide determination using fluorescence quenching method were compared with those obtained by ion chromatography (IC). Bromide was determined by IC using a Dionex ICS–3000 system with suppressed conductivity detection. The column used was an IonPacAS14 with an eluent concentration of 3.5 mM Na_2CO_3 and 1.0 mM $NaHCO_3$ and flow rate is 1.2 mL min^{-1}. All measurements were performed at room temperature.

RESULTS AND DISCUSSION

The results presented in Figure 1a show that fluorescence intensity decreases in the presence of quencher bromide ion, in the frame of applied experimental conditions. A Stern–Volmer plot $I_{oF}/I_F - 1$ vs. c_{Br^-} of a bromide quenching of quinine is presented in Figure 1b. The parameters of validation of the fluorescence quenching method are summarized in Table 1. RSD are determined for three different concentrations of bromide aqueous solutions and real sample, with replicate measurements (n = 5). The value of dynamic Stern–Volmer constant, $K_{SV,}$ for bromide quenching of quinine, determined from the slop of the linear regression curve, is 254.2 mol^{-1} L and it is comparable to the previous results [3].

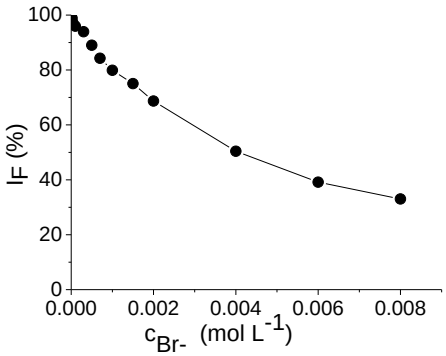

Figure 1. Bromide quenching of quinine

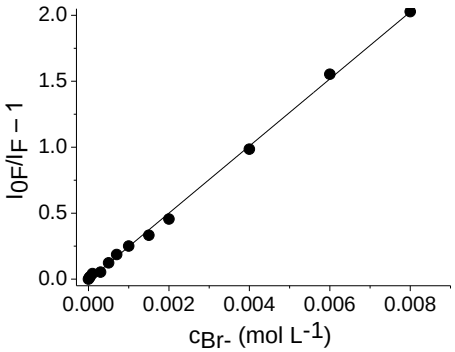

Figure 2. The Stern–Volmer plot of bromide quenching of quinine

Linear regression equation	$I_o/I - 1 = -0{,}0077 + 254.2c$
Correlation coefficients, *r*	0.9993
LOD (mol L^{-1})	1.16×10^{-4}
LOQ (mol L^{-1})	3.50×10^{-4}
Linearity range (mol L^{-1})	$3.55 \times 10^{-4} - 8.00 \times 10^{-3}$
RSD (%)	< 5.4
Recovery (%)	99.4 – 102.5

Table 1. The parameters of validation of the fluorescence quenching method

The results of fluorometric determination of bromide content in sample of selected pharmaceutical preparate were compared with those obtained with an ion chromatography method, as referral method. Figure 3 shows an ion chromatogram of 2.0% homatropine hydrobromide obtained using the IonPac AS14 column. The results for determination of bromide in real sample by both methods are reported as mean value and presented in Table 2. Measurement uncertainty for IC was determined on the basis of 32 measurements on 100 ppm solution and expressed as relative standard deviation (RSD). RSD was 4.5%.

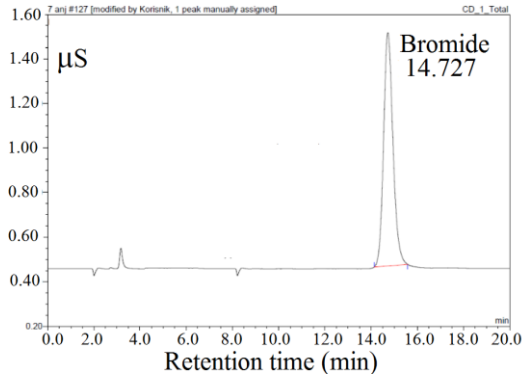

Figure 3. Ion chromatogram o 2.0% homatropine hydrobromide

Table 2. Determination of bromide ion concentration in the real sample

c(Br^-)					
2.0% homatropine hydrobromide		Fluorescence quenching method		Ion chromatography	
mol L^{-1}	ppm	mol L^{-1}	ppm	mol L^{-1}	ppm
5.16×10^{-2}	4123.0	4.92×10^{-2}	3931.3	4.98×10^{-2}	3979.5

CONCLUSION

The influence of bromide ions on fluorescence quenching of quinine can be described by Stern–Volmer kinetics. The results of both fluorescence quenching method and ionic chromatography as referral method, which were applied for determination of bromide content in solutions and selected pharmaceutical preparation, show that fluorescence quenching method because of its precision, accuracy, simplicity and short time of the analysis, can be applied for determination of bromide content in real samples.

Acknowledgement

The present investigations were supported by the Ministry of Education, Science and Technological Development of the Republic of Serbia, Grants no. 172015.

REFERENCES

[1] J. R. Lakowicz, Principles of Fluorescence Spectroscopy, (Eds.), Plenum Press, New York, 1999.
[2] A. Martin, R. Narayanaswamy, Sensors and Actuators B, 1997, **38**–**39**, 330–333.
[3] C. D. Geddes, Meas. Sci. Technol., 2001, **12**, 53–88.
[4] M. Wahba, N. El–Enany, F. Belal, **Anal. Methods**, 2015, **7**, 10445–10451.

P *– Education, History*

NIKOLAJ NIKOLAJEVICH BEKETOV

T. Halasi[1], S. Kalamković[2] and M. Kalamković[3]

[1]Faculty of Science, Department of Chemistry, Biochemistry and Environmental Protection, Methods of Teaching Chemistry, History of Chemistry, University of Novi Sad, Trg Dositeja Obradovića 3, 21000 Novi Sad, Serbia. (*tibor.halasi@dh.uns.ac.rs*)
[2]Primary School „Prva vojvođanska brigada", Seljačkih buna 51a, 21000 Novi Sad, Serbia
[3]School for elementary and secondary education with student's home "Milan Petrović", Novi Sad, Serbia

ABSTRACT

Becket is one of the pioneers of Physical Chemistry in Russia. He is known for his works in electrochemistry and metallurgy. He used methods of extrusion reactions, based on which he concluded the chemical affinity and behavior of certain metals in the process of electrolytic dissociation. On this basis, he compiled the Volta series, and at the same time, the table of electronegativity and electropositivity. He was the first one in Russia to take hydrogen as a zero point in a series of electronegativities. Of the properties of some ions he concluded based on the atomic mass and ionic radiuses. His work is important, because in his time, the exact structure of the atoms was not yet known. He compensated for that lack of knowledge with the results of very precise measurements. It belonged to the group headed by Mendeleev. His students, as well as his son, became famous physical chemists and important members - the pioneers of the Russian Physical Society.

BIOGRAPHY

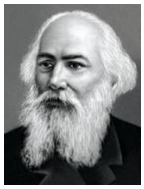

Figure 1. Nikolay Nikolayevich Beketov (1827 – 1911)

Nikolay Nikolayevich Beketov (*Николай Николаевич Бекетов*, 1827 - 1911) was a Russian physical-chemist academician. He was born in the village of Alferevka (*Алферьевка*, now - New Beketovka (*Новая Бекетовка*)) in the Penza province (*Пе́нза*) (Fig. 1). [1, 2]

His father was the former naval officer Nikolai Alekseevich Beketov (1794 - 1866) and mother was Ekaterina Andreevna Yakushkina. Beketov was the youngest of three brothers, each of whom became a celebrity Aleksey Beketov (1823 - 1898),

Andrei Beketov (1825 - 1902). He also had a sister Anna Nikolaevna Enisherlova (1828 - 1879) (Fig. 2).[2,3]

Figure 2. From left to right - Nikolai Alekseevich Beketov, Aleksey Beketov, Andrei Beketov and Anna Nikolaevna Enisherlova

In 1844, after he finished the 1st Petersburg Gymnasium, Beketov enrolled in St. Petersburg University (Faculty of Philosophy, Natural sciences II department). Two years later, he moved to Kazan University, where he was taught by an outstanding organic chemist, Zinin (*Никола́й Никола́евич Зи́нин*, 1812-1880). Beketov became interested in physical chemistry, at that time still an emerging field of chemical science. He graduated from Kazan University in 1849, in natural sciences with the thesis "Discourse on the effect of elevated temperature on organic compounds. He worked at the Medical and Surgical Academy (St. Petersburg), in the chemical laboratory of Zinin (1849-1853). In 1854 he completed his master's thesis "On some new cases of combination and general remarks on these phenomena". In 1855 he was appointed adjutant for the Department of Chemistry at Kharkov University, where in 1859 he became a Chemistry professor. The title of Becket's doctoral dissertation was "Studies on the phenomena of displacement of some elements by others" (1865) [1]. In this work, he established the effect of the concentration of reagents on the direction of chemical reactions, showing, in particular, that if it is good to conduct all known dissolution of marble ($CaCO_3$) in acetic acid, accompanied by the release of carbon dioxide, in sealed tubes, then when the CO_2 pressure reaches about 17 atmospheres the release of gas ceases, despite the presence of non-reacted acid and marble. And in the experiments that preceded the described, Beketov discovered that at a CO_2 pressure above 17 atmospheres in the solutions of calcium acetic acid, the reaction proceeds in the opposite direction, and calcium carbonate precipitates. Repeatedly stressing that he understands the effect of pressure as the influence of the concentration of gases, Beketov speaks of "the influence of pressure or, better, the density", introduces the notion of a change in the direction of the reaction "depending on the magnitude of the pressure". In this way the law of mass action was practically formulated practically simultaneously with Guldberg (*Cato Maximilian Guldberg*, 1836 - 1902) and Waage (*Peter Waage*, 1833 - 1900), and the arrangement of metals in a row by the ability to displace each other was the prototype of a certain number of

stresses. In Kharkov, Beketov worked until 1886 (the course "The ratio of physical and chemical phenomena among themselves", and the course "Physical Chemistry"), when he was elected an ordinary academician of the Petersburg Academy of Sciences. In 1886, Beketov moved to St. Petersburg, where he worked in the academic Chemistry laboratory and taught at the Higher Women's Courses. In 1890, Beketov organized course "Basic Principles of Thermochemistry", at the Moscow University. He was elected several times as the President of the Russian Physico-Chemical Society (1889-1890, 1896-1897, 1900, 1902, 1903, 1911) [2]. Beketov and his wife Elena Karlovna Beketova (*Елена Карловна Бекетова*, *Мильбофф*) had five children. Aleksei Nikolaevich Beketov (*Алексей Николаевич Бекетов*, February 19 (March 3), 1862, - November 23, 1941, Kharkov (*Харьков*)) was the oldest child and he was a Russian and Soviet architect and landscape painter, academician of architecture from 1894. Beketov died November 30 (December 13), 1911 in St. Petersburg. Now his grave at the Smolensk Orthodox cemetery, although protected by the state, is in a completely neglected state [1- 4].

BIBLIOGRAFY

Beketov had a great merit in the development of physical chemistry as an independent scientific and educational discipline. In 1852 he synthesized benzureid and aceturide. He discovered the displacement of metals from solutions of their salts by hydrogen under pressure, found that magnesium and zinc at other temperatures displace other metals from their salts. In 1859-1865 he showed that at high temperatures aluminum recovers metals from their oxides. Later these experiments served as a starting point for the appearance of aluminothermy. Beketov knew how to get classical results, using the simplest equipment. Thus, he investigated the phenomenon of aluminothermy by using a curved rifle barrel as a reaction vessel. He received the Lomonosov Prize for his work "On the effects of coal anhydride, carbon monoxide and mercury oxide on sodium oxide". Beketov organized thermochemical laboratories, in which, together with his students, he determined the heats of formation of oxides and chlorides of alkali metals. In 1870 he was the first to create anhydrous oxides out of alkali metals, which no one did before him. Beketov has published over 30 scientific papers. Scientific activity of this academician lasted 58 years, and all this time was devoted to Physical Chemistry [2].

STUDENTS

His students were: Eltekov (*Алекса́ндр Па́влович* Эльте́ков, 1846 - 1894), Flavitsky (*Флавиан Михайлович Флавицкий*, 1848 - 1917), Pogorelko (*Погоре́лко Алекса́ндр Костянти́нович*, 1848 - 1912), Chernaya (*Чернай*

Николай Александрович, 1849 - 1912), Osipov (*Ива́н Па́влович* О́сипов, 1855 - 1918), Timofeev (*Владимир Федорович Тимофеев*, 1858 - 1923) and many other famous scientists. Speaking of his teacher, Timofeev quoted Seneca's words: "All people are divided into two groups: those who die during life, and those who live after death" [1].

EDUCATION WORK

At Beketov's request, the first Physico-Chemical department in Russia was opened at Kharkov University at 1864. Beketov gave lectures and conducted practical classes in Physical Chemistry. In 1886, he published his textbook on this subject. On his initiative, the Society for Experimental Sciences at the Kharkov University was opened to conduct research and hold scientific conferences. Beketov believed that the theoretical study of science must necessarily be supported by practical experiments [1].

CONCLUSION

Beketov's biggest merit was his contribution into Physical Chemistry as an independent science. As one of the founders of physical chemistry and chemical dynamics, he laid the foundations of the principle of aluminotherm and metallurgy. With the tasks set, Beketov coped brilliantly. He managed to get acquainted with such outstanding scientists as: Wöhler (*Friedrich Wöhler*, 1800 - 1882), Kekule (*Friedrich August Kekulé von Stradonitz*, 1829 - 1896), Kopp (*Hermann Franz Moritz Kopp*, 1817 - 1892), Bunsen (*Robert Wilhelm Eberhard Bunsen*, 1811 - 1899), Berthelot (*Pierre Eugène Marcellin Berthelot*, 1827 - 1907), Balyar, Frankland (*Edward Frankland*, 1825 - 1899). All of Beketov's life, filled with the service of chemistry and his people, is forever imprinted in the history of science.

REFERENCES

[1] http://hrono.ru/biograf/bio_b/beketov_nn.html
[2] И. А., Беляев, Николай Николаевич Бекетов, выдающийся русский физико-химик и металлург, *1827-1911*, Москва, Государственное научно-техническое издательство литературы почерной и цветной металлургии, 1953.
[3] M. M, Andrusev, 150 Years since the birth of the eminent Russian physical chemist and metallurgist N. N. Beketov. *Metallurgist*, 1977, **21** 416–418. doi:10.1007/BF01132763.
[4] http://www.nasledie-rus.ru/podshivka/pics/9213-pictures.php? picture= 92130

HERMANN VON HELMHOLTZ

T. Halaši[1], S. Kalamković[2] and M. Kalamković[3]

[1]Faculty of Science, Department of Chemistry, Biochemistry and Environmental Protection, Methods of Teaching Chemistry, History of Chemistry, University of Novi Sad, Trg Dositeja Obradovića 3, 21000 Novi Sad, Serbia. (tibor.halasi@dh.uns.ac.rs)
[2]Primary School „Prva vojvođanska brigada", Seljačkih buna 51a, 21000 Novi Sad, Serbia
[3]School for elementary and secondary education with student's home "Milan Petrović", Novi Sad, Serbia

ABSTRACT
Hermann von Helmholtz was a German scientist and philosopher. He made fundamental contributions to philosophy, optics, electrodynamics, mathematics, meteorology and music. In 1842, he wrote a thesis in which he announced the discovery of nerve cells in the ganglia. This was his first significant research result, and from 1842 to the year of his death (1894), every year it was marked with more significant and published scientific achievements.

BIOGRAPHY
Hermann von Helmholtz (*Hermann Ludwig Ferdinand Helmholtz*, August 31 1821, Potsdam, Prussia - September 8 1894, Charlottenburg, Berlin) was born in Prussia (Fig. 1). His father was Julius (*August Ferdinand Julius Helmholtz*, 1792 (1797) - 1859 (1854)), the teacher of Philology and Philosophy in the gymnasium. M*other* Caroline Penn (*Karoline von Helmholtz* (*Penne*), 1797 - 1854) belonged to an emigrated English family. She was a Hanoverian lady, a descendant of the great Penn (*Quaker William Penn, 1644 - 1718).* Herman was the eldest child of his parents who had four children. His little brother, *Otto von Helmholtz* (1827 (1834) - 1913 (1919)), was an engineer who became the director of several steel mills for the modernization of steel production. Hermann's childhood had a strong influence on both his character and his later career. In particular the views on philosophy held by his father restricted Helmholtz's own views [1]. Hermann attended Potsdam Gymnasium. His interests at school were mainly in Physics. He wanted to study that subject at university. His financial position meant that he could study at university only if he received a scholarship. Hermann's father

persuaded him that he should study medicine which was supported by the government.

Figure 1. Hermann Ludwig Ferdinand Helmholtz (1821 - 1894)

Hermann liked to study Mathematics on his own, reading works by Laplace (*Pierre-Simon, comte de Laplace. Pierre-Simon, marquis de Laplace*, 1749 - 1827), Biot (*Jean-Baptiste Biot*, 1774 - 1862) and *Daniel Bernoulli* (1700 - 1782). He also read Philosophy works at this time, particularly the works of Kant (*Immanuel Kant*, 22. IV 1724 – 12. II 1804). His research career began in 1841 when he began work on his dissertation. Helmholtz graduated from the Medical Institute in Berlin in 1843. Helmholtz advocated for the law on energy conservation using both philosophical and physical arguments. He based many ideas on the earlier works by Carnot (*Nicolas Léonard Sadi Carnot*, 1. VI 1796. - 24. VIII 1832), Clapeyron (*Benoît Paul Émile Clapeyron*, 26. II 1799 - 28. I 1864), Joule (*James Prescott Joule*, 24. XII 1818 - 11. X 1889) and others. That philosophical arguments came right up front in this work was typical of all of Helmholtz's contributions. He argued that physical scientists had to conduct experiments to find general laws. He married *Olga von Velten* (1825 - 1859) on 26 August 1849 and settled down to an academic career and together they had two kids (*Katharina Caroline Juie Betty*, 1850 - 1877; *Richard Wilhelm Ferdinand von Helmholtz*, 1852 - 1934). She died in 1859. In 18 months he remarried with a sophisticated and attractive woman, *Anna von Mohl* (1834 - 1899) with whom he had three more kids (*Robert Julius von Helmholtz*, 1862 - 1889; *Ellen Ida Elisabeth Von Siemens*, 1864 - 1941, and *Friedrich Julius Von Helmholtz*, 1868 - 1901). Until his death in 1894 he made numerous discoveries and

achievements gaining him the title of one of the greatest scientist of the 19th century [2] [3].

BIBLIOGRAPHY

Helmholtz was involved in research in the following areas: Mechanics, Sensory physiology, Ophthalmic optics, Nerve physiology, Acoustics and aesthetics, Electromagnetism, Music.[1-4]

In mathematics, the Helmholtz equation, named for Hermann von Helmholtz, is the partial differential equation:

$$\nabla^2 A + k^2 A = 0$$

where ∇^2 is the Laplacian, k is the wavenumber, and A is the amplitude.

He showed that the assumption that work could not continually be produced from nothing led to the conservation of kinetic energy. He applied this principle to a variety of different situations. In various situations, where energy appears to be lost, energy is in fact converted into heat energy. This happens in collisions, expanding gases, muscle contraction, and other situations. Helmholt's equation has a wide range of applications – in the electrostatics, the galvanic phenomena and the electrodynamics. The equation was had significant in Helmholt's career. He was released from duty to serve as a military doctor, so that he could teach at the Chair of Physiology in Königsberg. In 1852 he published important work on Physiological Optics with his theory of colour vision. Experiments which he carried out at this time led him to reject Newton's theory (*sir Isaac Newton*, 25. XII 1642 - 20. III 1726/7) of colour. The paper was rightly criticised by Grassmann (*Hermann Günther Graßmann*; 15. IV 1809 - 26. IX 1877) and Maxwell (*James Clerk Maxwell*, 13. VI 1831 - 5. XI 1879). Helmholtz was always prepared to admit his mistakes, and indeed he did this when he published new experimental results showing those of his 1852 paper to be incorrect. He published the first volume of his *Handbook of Physiological Optics* in 1856. His important paper in *Crelle's Journal* "On the motion of a perfect fluid", he published in 1858.. Helmholtz's paper *Über Integrale der hydrodynamischen Gleichungen, welche den Wirbelbewegungen entsprechen* began by decomposing the motion of a perfect fluid into translation, rotation and deformation. Helmholtz defined vortex lines as lines coinciding with the local direction of the axis of rotation of the fluid, and vortex tubes as bundles of vortex lines through an infinitesimal element of area. Helmholtz showed that the vortex tubes had to close up and also that the particles in a vortex tube at any given instant would remain in the tube indefinitely so no matter how much the tube was distorted

it would retain its shape. Helmholtz was occupied with electrodynamics after his appointment to Berlin. He discussed the compatibility of Weber's electrodynamics and the principe of the conservation of energy (*Heinrich Friedrich Weber*, 7. XI 1843 - 24. V 1912). Helmholtz attempted to give a mechanical foundation to thermodynamics, and he also tried to derive Maxwell's electromagnetic field equations from the least action principle. Helmholtz's contributions to Physiological Optics are of great importance. He investigated the optical constants of the eye, measured by his invention, the ophthalmometer, the radii of curvature of the crystalline lens for near and far vision, explained the mechanism of accommodation by which the eye can focus within certain limits, discussed the phenomena of color vision, and gave a luminous account of the movements of the eyeballs so as to secure single vision with two eyes.

MUSIC AND MUSICIANS

Professor Helmholtz has invented a double harmonium with 24 vibrators to the octave, by means of which the musician can modulate into all keys quite as easily as on a single manual tuned by equal temperament, and without the dissonant thirds and sixths which that mode of tuning introduces.

CONCLUSION

Hermann made significant contributions in several scientific fields such as Physiology, Physiological Optics, Physiological Acoustics, Chemistry, Mathematics, electricity and magnetism, meteorology and theoretical mechanics. Helmholtz's thermodynamic theory of 1882–1883 was the pioneering work on which much of the new theoretical chemistry rests.

REFERENCES

[1] D. P. Schultz, S. E. Schultz, *A history of modern psychology* (7th ed.), New York: Harcourt College Publishers, 2000.
[2] E. Hiebert, The Helmholtz the Legacy in Physiological Acoustics, Archimedes 39, New Studies in the History and Philosophy of Science and Technology, New York, Springer, DOI 10.1007/978-3-319-06602-8
[3] D. Cahan, Hermann Von Helmholtz and the Foundations of nineteenth-Century Science, Berkeley: University of California Press, 1993.
[4] J. J. O'Connor, E. F Robertson, Hermann Ludwig Ferdinand von Helmholtz, University of St Andrews, Scotland, School of Mathematics and Statistics.
[5] J. F. Mulligan, *Hermann von Helmholtz and his students*, in: American Journal of Physics, 1989, **57**, 68-74.

GEORGE DE HEVESY

T. Halaši[1], S. Kalamković[2] and M. Kalamković[3]

[1]Faculty of Science, Department of Chemistry, Biochemistry and Environmental Protection, Methods of Teaching Chemistry, History of Chemistry, University of Novi Sad, Trg Dositeja Obradovića 3, 21000 Novi Sad, Serbia. (tibor.halasi@dh.uns.ac.rs)
[2]Primary School „Prva vojvođanska brigada", Seljačkih buna 51a, 21000 Novi Sad, Serbia
[3]School for elementary and secondary education with student's home "Milan Petrović", Novi Sad, Serbia

ABSTRACT
George Charles de Hevesy was a Hungarian radiochemist who received the Nobel Prize in chemistry, in 1943, for his work on radioactive markers of chemical processes in animal metabolism. Hevesy is known for discovering Hafnium in 1923 along with Dirk Coster.

BIOGRAPHY
George Charles de Hevesy (*György Hevesy*, 1. VIII 1885 - 5. VII 1966) was born in Budapest (Fig. 1.). His came from a wealthy family of Hungarian Jewish descendants. His parents Lajos (*Ludwig*, *Louis*) Bischitz (1832 - 1876) and Baroness Eugénie (*Jenny*) Schossberger (*De Tornya*) (1835 - 1877) had eight children (*Vilmos William Bischitz de Hevesy*; *André Andor Bischitz de Hevesy*; *Ödön Bischitz de Hevesy*; *Pál Paul Bischitz de Hevesy*; *George de Hevesy* and *Sarolta Hevesy*). He matriculated at the Gymnasium of the Piarist Order in 1903. Then he studied at Budapest University and Berlin Technical University. He gained his doctor's degree at the University of Freiburg in Breisgau in 1908. He worked for two years as an assistant at the Institute of Physical Chemistry, Technical University of Switzerland before having a short correspondence with Professor Fritz Haber (1868 - 1934). He travelled to England in 1910 to study under Professor Ernest Rutherford (*1st Baron Rutherford of Nelson*, 1871 - 1937) at Manchester. He paused his studies early in 1913 to carry out the first radioactive-tracer experiment at the Vienna Institute of Radium Research along with Paneth (*Friedrich Adolf Paneth*, 1887 - 1958). During his stay in Vienna he obtained the *Venia Legendi* (*permission to read*) in the University of Budapest. After the end of the war he was teaching for six months in the University of Budapest. At the spring of 1919 he went to Copenhagen to discuss his future activities at Niels Bohr's

Institute which were to be started. In 1926 he returned to Freiburg as the Professor of Physical Chemistry. In 1930 he was appointed the Baker Lecturer at Cornell University, Ithaca. He resumed his activities at the Niels Bohr's Institute from 1934 to 1952. He was living in Stockholm since 1943 and was an Associate of the Institute of Research in Organic Chemistry. In 1949 he was elected Franqui Professor in the University of Ghent. Professor de Hevesy married Pia Riis (1902 - 1979) in 1924. They had one son and three daughters. George de Hevesy died on July 5, 1966. One of daughters (Eugenie) married a grandson of the Swedish Nobel laureate Svante Arrhenius (*Svante August Arrhenius*, 19. II 1859 - 2. X 1927) [1], [2].

Figure 1. George Charles de Hevesy, 1885 - 1966

BIBLIOGRAPHY

Professor Hevesy worked with Fritz Haber to develop the process to synthesize ammonia. He also involved a study of the chemical behavior of molten salts and his introduction to practical radiochemistry came in Rutherford's laboratories at Manchester. His work in Manchester, Vienna and Budapest, mainly concerned the investigation and use of Radium and Lead isotopes. Rutherford gave Hevesy the task of separating out the Radium D from the large amount of Lead in a sample of Joachimsthal pitchblende which had been given as a gift by the Austrian government. Hevesy was not able to complete the separation. He was able to use Radium D and Radium E as a

radioactive tracer in investigations of the kinetics of Lead and Bismuth in plants. He was responsible for pioneer work in the use of isotopic indicators both in inorganic and life sciences. Later, in Freiburg, he was involved in the first clinical use of isotopes [3].

In 1923 together with Coster (*Dirk Coster*, 5. X 1889 - 12. II 1950), he discovered the element Hafnium [4].

He introduced a method of activation analysis based on neutron bombardment of the element to be investigated – the method was to replace X-ray analysis with fluorescent X-rays. He has studied, amongst other things, the effect of X-rays on the formation of nucleic acid in tumors and in normal organs, and iron transport in healthy and cancerous organisms. In 1923 Hevesy published the first study on the use of the naturally radioactive 212Pb as radioactive tracer to follow the absorption and translocation in the roots, stems and leaves of Vicia faba. [2]

He developed the X-ray fluorescence analytical method, and discovered the Samarium alpha-ray (Fig. 2.).

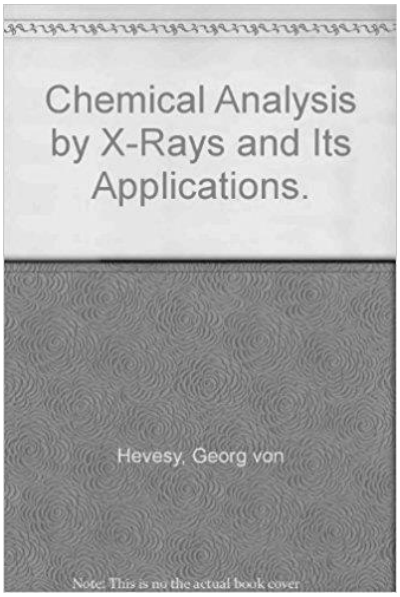

Figure 2. Hevesy's book

He began to calculate the relative abundance of the chemical elements. In 1934 after preparing a radioactive isotope of Phosphorus, he analyzed various physiological processes by tracing the course of "labeled" radioactive Phosphorus through the body. These experiments revealed the dynamic state

of the body constituents. George de Hevesy received his Nobel Prize for his work on the use of isotopes as tracers in the study of chemical processes in 1944 [5].

PRICES, MEDALS

- The Price *Cannizzaro* of the Academy of Science Italian in 1929
- The Nobel Prize of chemistry in 1943 for its work in the field of the radioactive tracers
- The Medal Copley of the Royal Society of London in 1949
- The *Faraday Lectureship* of the Royal Society off Chemistry British in 1950
- The Medal *Baily* in 1951
- The Medal *Sylvanus Thompson* in 1955
- The *Atoms for peace* award in 1959
- The Medal *Niels Bohr* in 1961.

CONCLUSION

Hevesy had published a total of 397 scientific publications, one of which was the Becquerel-Curie Memorial Lecture, in which he had reminisced about the careers of pioneers of radiochemistry.

REFERENCES

[1] George de Hevesy – Biographical. Nobelprize.org. Nobel Media AB 2014. Web. 30 Mar 2018; http://www.nobelprize.org/nobel_prizes/chemistry/laureates/1943/hevesy-bio.htm.

[2] Nobel Lectures, Chemistry 1942-1962, Amsterdam: Elsevier Publishing Company, Amsterdam, 1964.

[3] Hevesy G. Adventures in Radioisotope Research, The Collected Papers of George Hevesy in Two Volumes. New York: Pergamon Press, NY, 1962.

[4] B. Weintraub, George de Hevesy, Hafnium and Radioactive Traces, Chemistry in Israel. Bull. Isr. Chem. Soc., 2005, **18**, 41-43.

[5] https://www.britannica.com/biography/Georg-Charles-von-Hevesy.

Q *– Food Physical Chemistry*

PRESERVATION OF THE NATIVE STRUCTURES OF MEAT PROTEINS AFTER OSMOTIC DEHYDRATION AND REHYDRATION

S. Ostojić[1] , D. Micić[1], S. Zlatanović[1], B. R. Simonović[1] and Lj. B. Lević[2]

[1] University of Belgrade, Institute of General and Physical Chemistry, Studentski trg 12/ V, 11000 Belgrade, Serbia. (sostojic@iofh.bg.ac.rs)
[2]Department of Chemical Engineering, Faculty of Technology, University of Novi Sad, Bulevar Cara Lazara 1, 21000 Novi Sad, Serbia.,

ABSTRACT

Differential scanning calorimetry (DSC) method has been used to investigate the existence of the native state of meat proteins after osmotic dehydration, in sugar beet molasses, and during rehydration. It was shown, by obtained temperatures of protein denaturation (T_d) and enthalpies of denaturation (ΔH_d) that native protein structures have been preserved in the processes of dehydration by sugar beet molasses. In the processes of rehydration the existence of native protein structures was found in the rehydration at a temperature of 20 ° C and at a time of 15 min and 45 min, rehydration at 30 ° C at the time period of 15 min and rehydration at 40 ° C and for a period of 15 min. With further rehydration, the presence of protein native structures was not found.

INTRODUCTION

Water is essential for the formation of native protein structures. However, the effects of dehydration upon protein conformation have long been a point of controversy. It has been demonstrated, from theoretical considerations, that dehydration should result in significant conformational changes [1]. Several sorption isotherm studies of progressive rehydration of dried proteins employing vibrational spectroscopy, nuclear magnetic resonance, and hydrogen exchange techniques have indicated hydration-related changes in conformation and flexibility [1]. In particular, differences in the rehydration behaviour between α-lactalbumin and lysozyme were attributed to conformational differences in the dried state. Dehydration-induced changes in conformation-sensitive modes observed in a freeze-dried protein with Raman spectroscopy studies have also supported this claim, however, effects due solely to the removal of water could not be ruled out. Furthermore, it is well known that dehydration can completely and irreversibly inactivate some enzymes [1]. This inactivation occurs presumably through loss of structure.

Such dehydration-induced changes in tertiary and quaternary structure has been observed upon rehydration of dried myosin and catalase, respectively. [1]. Preservation of the native protein structure and biological activity in dry protein/excipient mixtures has been previously attributed to either the glass forming properties of the additives or to their ability to hydrogen bond to the protein. There is evidence that both processes are important but it has not yet been elucidated which is the limiting factor that determines the efficiency of a given molecule as a protectant [2]. In this work, differential scanning calorimetry (DSC) have been employed to investigate the preservation of native meat proteins structures after osmotic dehydration, by sugar been molasses, and during rehydration.

EXPERIMENTAL

Pork meat, *L. dorsi* muscle, was purchased from a local supermarket. Osmotic dehydration in sugar beet molasses and rehydration, of pork meat, *L. dors,i* has been conducted by the procedure described by Pezo [3]. A differential scanning calorimeter (DSC, Q1000, TA Instruments, New Castle, DE) was used to perform DSC experiments. Pork meat samples (7–11 mg) were subjected to heating, in hermetically sealed Al pans, in the temperature range from 20 ºC to 90 ºC, with controlled heating rate Hr= 2 ºC/min, under the N_2 purge flow of 50 ml/min. Each thermogram was analyzed by TA Advantage Universal analysis 2000 software to obtain the thermodynamical parameters of protein denaturation: temperature of denaturation (T_d) and enthalpies of denaturation (ΔH_d).

RESULTS AND DISCUSSION

The values obtained from DSC curves for the meat protein denaturation temperatures and enthalpies are shown on Table 1.

From the DSC results obtained for fresh and osmotically dehydrated pork meat three endothermic transitions with minima at 56 ° C, 67 ° C and 78 ° C can be seen in the DSC curves for fresh meat. They correspond to the following processes: the first denaturation of myosin, the second corresponds to the denaturation of sarcoplasmic proteins and collagen, and the third corresponds to actin (T_d = 78 ° C). The obtained values for temperatures and enthalpies of protein denaturation are in accordance to the literature [4].

It is evident that the denaturation temperatures (T_d), corresponding to the peak minimum of endothermal transition of a particular protein, are slightly higher in osmotically dehydrated meat compared to fresh meat and generally have close values during the beginning of rehydration. The rehydration process further reduced the enthalpy of denaturation (ΔH) of meat proteins

and lead to retention of a small amount of undenatured or minimally conformationally altered proteins.

Table 1. Enthalpy and temperature of denaturation of meat proteins (actin, myosin and collagen): fresh, osmotically dehydrated and rehydrated pork meat.

Meat sample	**Protein 1 (myosin)**		**Protein 2 (collagen)**		**Protein 3 (actin)**	
	T_{d1} (C°)	**ΔH_{d1} (J/g $_{sm}$)**	**T_{d2} (C°)**	**ΔH_{d2} (J/g $_{sm}$)**	**T_{d3} (C°)**	**ΔH_{d3} (J/g $_{sm}$)**
Fresh	56.3	23.10	67.1	2.90	78.19	5.90
Osmotic. dehyd.	64.25	6.03	74.6	1.35	83.11	9.80
Rehyd.20° °C/15 min	56.18	8.68	-	-	78.37	3.24
Rehyd.20° C /45 min	47.52	0.17	-	-	72.01	6.10
Rehyd.30° C/15min	49.70	1.91	-	-	79.03	1.06
Rehyd.40° C/15 min	50.60	1.35	-	-	74.28	1.20

These structures were preserved by rehydration at a temperature of 20 ° C and at a time of 15 min and 45 min, rehydration at 30 ° C for 15 min and rehydration at 40 ° C and for a period of 15 min, and with further rehydration the presence of such structures were not found. The disappearance of the protein denaturation transitions in the temperature range from 60ºC to 70ºC, during rehydration, is evident. (Table 1). Various salts addition have an influence on the stability of meat proteins, stabilization and destabilization-depending on the type of salt to be added, the concentration and percentage of protein hydration [5]. It is also known that sugars affect the proteins and interact with them as shown in the gelation of alginate, xanthan and myofibril proteins [6,7]. Chen et all [8] studied, by the DSC method, flaxseed gum / meat proteins interaction. Flaxseed gum, consisting mainly of xylose, ramosis, glucose, arabinose, fucose and galatoric acid, is known for its high water binding capacity [9]. They showed that the interaction of flaxseed gum with meat proteins leads to an increase in the temperature of meat proteins denaturation, what is also found in our work. The same authors have shown that these interactions with the protein come through disulfide bridges and

hydrogen bridges [8]. It can be assumed that this interaction with components of molasses (carbohydrates and salts) and proteins is obvious [10].

CONCLUSION

Thus, osmotic dehydration leads to conformational changes, partial denaturation of the protein of the meat, which is evident from the obtained enthalpy of denaturation (ΔH_d) of meat proteins that is reduced in the dehydration process. The rehydration process reduces the enthalpy of denaturation (ΔH_d) of meat proteins and preservation of amount of undenatured or minimally conformationally altered proteins was evident. These undenaturated structures were retained at rehydration at a temperature of 20 ° C and at a time of 15 min and 45 min, rehydration at 30 ° C for 15 min and rehydration at 40 ° C and for a period of 15 min, and with further rehydration the presence of such structures were not found. The decrease in the enthalpy of denaturation (ΔH_d) and an increase of temperature of denaturation (T_d) obtained for osmotically dehydrated meat is explained by the interactions of salts and carbohydrates with proteins that lead to conformational changes, and in this paper described, thermal properties of newly formed protein matrix.

Acknowledgement

This work was partially supported by the Ministry for Science of the Republic of Serbia (Grants no. 31055 and 31093).

REFERENCES

[1] S.J. Prestrelski, N. Tedeschi, T. Arakawa, J.F. Carpenter, 1993, **65**, 661–71.
[2] E.. López-Díez, S. Bone, 2004, **1673**, 139–148.
[3] L.L. Pezo, L.B. Levi, B.R. Cvetkovi, O.A. Kova, 2014, **53**, 260–270.
[4] T.-Y. Yu, J.D. Morton, S. Clerens, J.M. Dyer, 2017, **16**, 141–159.
[5] S. Kajitani, M. Fukuoka, N. Sakai, 2011, **12**, 19–26.
[6] S.A. Ensor, J.N. Sofos, G.R. Schmidt, 1991, **56**, 175–179.
[7] E.S. Dolinina, M.I. Vlasenkova, E.V. Parfenyuk, 2017, **527**, 101–108.
[8] H.-H. Chen, S.-Y. Xu, Z. Wang, 2007, **80**, 1051–1059.
[9] G. Mazza, C.G. Biliaderis, 1989, **54**, 1302–1305.
[10] Y.H. Roos, N. Potes, 2015, **119**, 7077–7086.

CHEMICAL PROFILE AND THERMAL BEHAVIOR OF CORIANDER AND SAGE ESSENTIAL OILS

S. Đurović[1], D. Micić [1], B. Simonović[1], S.N. Blagojević [1], B. Pavlić [2] and Z. Zeković [2]

[1] University of Belgrade, Institute of General and Physical Chemistry, Studentski trg 12-14, 11000 Belgrade, Serbia. (sasatfns@uns.ac.rs)
[2] University of Novi Sad, Faculty of Technology, Bulevar cara Lazara 1, 21000 Novi Sad, Serbia

ABSTRACT

Essential oils (EOs) of sage and coriander were isolated applying hydrodistillation and analyzed by GC/MS and differential scanning calorimeter (DSC). GC analysis confirmed domination of camphor (13.72%), α-thujone (9.45%), eucalyptol (8.31%), and β-thujone (3.48%) in sage EO and linalool (27.33%) in coriander EO. DSC curves revealed endothermic overlapping effects in temperature range of 20.7 to 223.8 °C (coriander) and 22.4 to 256.8 °C (sage). Endothermic effects of both EOs consist of two less intensive peaks, with T_p (peak temperature) at 45.5 and 114.3 °C for coriander, and 42.1 and 142.7 °C for sage, as well as one intensive peak, with T_p at 216.2 °C (coriander) and 222.5 °C (sage).

INTRODUCTION

Essential oils (EO) or volatile/ethereal oils are aromatic oily liquids prepared from plant material such as flowers, seeds, leaves, twigs, root, fruit, etc. EOs or their components have been shown to exhibit antioxidant, antimicrobial, antiviral, antimycotic, antitoxigenic, antiparasitic and insecticidal properties. These characteristics are possibly related to the function of these compounds in plants [1].

There is trend of introducing EOs into food as replacement for synthetic antioxidants. Relationship among activity and composition of EOs requires their characterization, while thermal processing of food indicates need for investigation of their thermal behavior. Thus, aim of this research was investigation of chemical composition and thermal stability of sage and coriander EOs using gas chromatography coupled with mass spectrometry (GC/MS) and differential scanning calorimetry (DSC).

EXPERIMENTAL

Plant material was acquired from Institute of Field and Vegetable Crops, Novi Sad, Serbia. Methylene chloride was purchased from Centrohem, Serbia. Isolation of volatile compounds from plant materials were performed according the standard procedure described in National Pharmacopoeia [2]. Sample (20.00 g) of plant material was distillated with water for 2 hours using Clevenger type apparaturs. Sample was stored in refrigerator at 4 °C to prevent possible evaporation or degradation of compounds.

GS/MS analysis - Coriander and sage EOs were analyzed using GC/MS (Thermo Fisher, USA) and TR WAX-MS (30 m x 0.25 mm x 0.25 μm) capillary column. Samples were dissolved in methylene chloride and introduced into GC through TriPlus AS autosampler (2 μl). Temperature program was as follows: initial temperature 45 °C (8 minutes), then 8.0 °C/min to 230 °C which was hold for 10 min. Temperatures of injector, mass transfer line and ion source were 250 °C, 200 °C and 220 °C, respectively. Compounds were identified using NIST database of MS spectra, while final results were expressed as relative content (%).

DSC analysis - Thermal characteristics of samples were studied on TA Instruments DSC Q1000 Differential Scanning Calorimeter (Delaware, USA), under N_2 purge flow of 50 ml/min, with TA Universal analysis 2000 software. DSC scans were conducted in temperature range from -90 to 300 °C, with heating rate of 5 °C/min. Analyzed samples of 3.0 ± 0.3 mg were weighed into hermetic Al pans and placed in the equipment's sample chamber. An empty hermetic Al pan was used as reference.

RESULTS AND DISCUSSION

Chromatograms showed presence of 73 and 49 compounds in sage and coriander EOs, respectively. Content of identified monoterpenes in sage and coriander EOs are shown in Table 1. Obtained results showed different profile of analyzed EOs. In the case of sage, camphor, eucalyptol and thujones were dominant compounds, while in the case of coriander EO, linalool was the main compound.

Such results are in accordance with the previously reported for investigated EOs [3–5]. Beside camphor and thujones, borneol, bornyl acetate and camphene were presented in significant amounts. In case of coriander, beside dominant linalool, α-pinene, γ-terpinene, nerol and camphor were also detected (Table 1) in higher amounts.

Table 1. Chemical composition of sage and coriander essential oils.

Sage		Coriander	
Compound	Content (%)	Compound	Content (%)
α-Pinene	0.77	*α*-Pinene	3.11
Camphene	1.60	Camphene	0.35
β-Pinene	0.15	3-Carene	0.13
Limonene	0.62	*β*-Pinene	0.29
Eucalyptol	8.31	Terpinolene	0.02
p-Cymene	0.77	Limonene	0.68
α-Thujone	9.45	Eucalyptol	0.08
β-Thujone	3.48	*γ*-Terpinene	2.40
Camphor	13.72	*p*-Cymene	1.63
Linalool	0.45	Camphor	1.80
Bornyl acetate	1.97	Linalool	27.33
Terpinen-4-ol	0.25	Terpinen-4-ol	0.11
Menthol	0.39	Geranyl acetate	0.06
Borneol	4.18	Terpineol acetate	0.13
Thymol	0.52	Borneol	0.02
Carvacrol	0.33	Nerol	2.43
		Geraniol	0.92

DSC curve profiles of sage and coriander essential oils are showed in Figures 1. Both samples showed endothermic overlapping effects in temperature range of 20.7 to 223.8 °C (coriander) and 22.4 to 256.8 °C (sage). These effects occur due to the evaporation process of analyzed EOs, since the GC/MS analysis showed that the EOs consist of a large number of components, the thermal effects of the evaporation of each component overlap with each other, resulting in a broad endothermal transition on the DSC curves.

It can be noticed that endothermic effects of both EOs consist of two less intensive peaks, with T_p (peak temperature) at 45.5 and 114.3 °C for coriander, and 42.1 and 142.7 °C for sage, as well as one intensive peak, with T_p at 216.2 °C (coriander) and 222.5 °C (sage). Less intensive peaks occur as a result of evaporation of components which present in less amounts, whereas intensive peaks appear due to evaporation of dominant compounds. Intensive peak of sage is broader than the peak of the coriander. The reason for this is that the sage EO contains several dominant compounds (thermal effects of their evaporation is overlapping), while coriander EO contains only one (linalool).

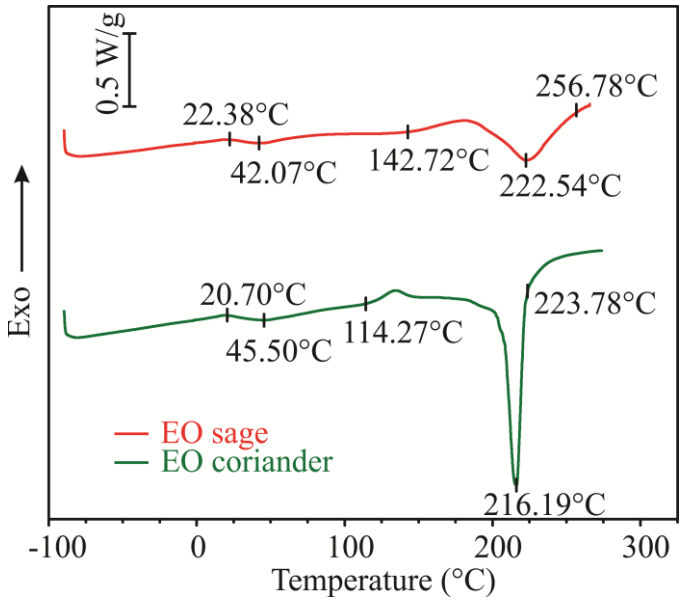

Figure 1. DSC curves of sage and coriander essential oils.

CONCLUSION

GC analysis confirmed domination of camphor, α-thujone, eucalyptol and β-thujone in sage EO and linalool in coriander EO. DSC analysis showed that coriander EO evaporated in range of 20.7 to 223.8 °C, while sage EO in range of 22.4 to 256.8 °C.

Acknowledgement

This work was partially supported by the Ministry for Science of the Republic of Serbia (Grants no. TR 31093, TR 31055 and TR 31013).

REFERENCES

[1] B. Šojić, B. Pavlić, Z. Zeković, V. Tomović, P. Ikonić, S. Kocić-Tanackov, N. Džinić, LWT, 2018, **89**, 749–755.
[2] Pharmacopoea Jugoslavica (Ph. Jug. IV). Savezni zavod za zaštitu zdravlja, 1984.
[3] B. Pavlić, S. Vidović, J. Vladić, R. Radosavljević, Z. Zeković, J. Supercrit. Fluids, 2015, **99**, 23–28.
[4] Z. Zeković, B. Pavlić, A. Cvetanović, S. Đurović, Ind. Crops Prod., 2016, **94**, 353–362.
[5] B. Pavlić, O. Bera, N. Teslić, S. Vidović, G. Parpinello, Z. Zeković, Ind. Crops Prod., 2018, **120**, 305–312.

DEHP EXTRACTION FROM MILK SAMPLES WITH DIFFERENT MILK FAT CONTENT

T. Anđelković[1], I. Kostić[1], D. Anđelković[1], H. Kocić[2] and G. Kocić[2]

[1] *University of Niš, Faculty of Sciences and Mathematics, Višegradska 33, 18000 Niš, Serbia. (ivana.kostic83@gmail.com)*
[2] *University of Niš, Faculty of Medicine, Bul. Zorana Đinđića 80, 18000 Niš, Serbia.*

ABSTRACT

In this study, four different extraction solvent combinations for di-(2-ethylhexyl) phthalate (DEHP) determination in milk samples with different milk fat content were compared. Combinations of methanol, ethanol, acetonitrile and ethanol/ammonium hydroxide with hexane were investigated. DEHP determination was carried out by gas chromatography – mass spectrometry (GC-MS). Effects of solvent extraction were studied by spiking of known amount of DEHP standard solution in concentration range 0.25 to 1.25 mg L^{-1}. Obtained results indicate that extraction method which included ethanol/hexane combination of solvents showed the best recovery for all spiked concentrations of DEHP: 73.08; 56.70 and 47.05% for samples with 0.50, 2.80 and3.80 % milk fat content. The lowest recovery (16.39%) was obtained for the sample with 3.80% milk fat content determined by methanol/hexane solvent combination.

INTRODUCTION

Plastic materials are widely used for producing packaging materials. A high percent of them are made from polymeric material that contains phthalates. Phthalates are substances that are often used as plasticizers in polymeric materials in order to increase their physical properties, flexibility and softness [1]. The most used phthalates are di-(ethylhexyl) phthalate (DEHP) and di-*n*-butyl phthalate (D*n*BP). Both, DEHP and D*n*BP, are listed as endocrine disruptors [2].

Milk as essential food for infants and children, that is packed into plastic bottles, can be exposure to phthalate contamination. Because of this determination of phthalates, especially DEHP, in milk is of increasing interest [3].

It is very important to find appropriate solvent or combination of few solvents to obtain high recovery for DEHP determination from milk samples.

Extraction techniques like liquid-liquid extraction, solid-phase extraction and dispersive liquid-liquid microextraction are the mostly used [4].

EXPERIMENTAL

DEHP standard, dibuthyl adipate (DBA), acetonitrile, hexane and ammonium hydroxide were purchased from Sigma Aldrich, USA. Methanol and ethanol were purchased from Baker, USA. All used solvents were HPLC grade and screened to determine the phthalate background. Amounts of DEHP and DBA standard were accurately weighted out by analytical balance with precision at ±0.0001 g (Kern, Germany) and stock solutions were prepared by hexane diluting and stored in the fridge.

Milk samples with three different content of milk fat (0.50; 2.80 and 3.80%) were purchased from local supermarket (Niš, Serbia). Effects of solvent extraction were studied by spiking with known amount of DEHP standard solution in ethanol at concentration range from 0.25 to 1.25 mg L^{-1}. A volume of 10 mL milk sample was put in a polypropylene centrifuge tube and 30 mL of solvent was added. Mixture was treated under ultrasonic conditions for 30 min and centrifuged for 10 min at 4000 rpm. After this step, 20 mL of supernatant was transferred into clean polypropylene tube, 10 mL of hexane was added, and mixture was shaken and centrifuged once more by the same conditions. Hexane layer was analyzed by GC-MS. All spiked samples and blank sample were analyzed in three replicates. This procedure was repeated for all solvents. In case of ethanol/ammonium hydroxide combination, ammonium hydroxide was added before adding of ethanol.

Analysis was carried out by gas chromatography coupled to mass spectrometer (Hewlett Packard 6890 series GC System with autosampler connected with Agilent 5973 Mass Selective Detector (Electron Ionization MSD-EI, single quadrupole). The separation was achieved with 30 m × 0.25 mm × 0.25 μm a non-polar AGILENT DB-5MS column coated with 5% phenyl, 95% dimethylpolysiloxane. The oven temperature was programmed from 65 °C (holding time 1 min) to 220 °C (1 min) at rate of 20 °C min^{-1}, then to 280 °C at rate of 5 °C min^{-1} (4 min). Volume of 1 μL was injected in the splitless mode. Helium was the carrier gas (1.0 mL min^{-1}) and the inlet temperature was 250 °C. The operating temperature of the MSD was 280°C with the emission energy of 70 eV. The MSD was used in the single ion-monitoring (SIM) mode and the identification of target compounds was based on the relative retention time, the presence of target ions and their relative abundance. The most abundant ion *m/z* 149 was chosen for quantification of DEHP, while ion *m/z* 185 was chosen as representative ion of DBA internal standard. The dwell time was 100 ms.

RESULTS AND DISCUSSION

All quantification was performed by an external calibration method based on response ratios between DBA, as internal standard, and DEHP. Calibration curve of DEHP standard series was obtained by standard solutions in a concentration range of 0.25 to 10 μg mL^{-1} and calibration curve showed linearity with correlation coefficient > 0.998.

Recovery values were calculated for all investigated systems. Mean values of recovery obtained by using four different combination of extraction solvents are given in Table 1.

Table 1. Recovery for spiked samples obtained by extraction with methanol, ethanol, acetonitrile and ethanol/NH_4OH in combination with hexane

Used solvent	Methanol /hexane	Ethanol /hexane	Acetonitrile /hexane	Ethanol/NH_4OH /hexane
Milk fat content (%)	Recovery (%)			
0.50	40.46	73.08	67.39	28.21
2.80	28.65	56.70	45.82	31.21
3.80	16.39	47.05	43.20	37.47

Obtained results indicate that extraction method which included ethanol/hexane combination of solvents showed the highest recovery for all investigated samples. Also, the lowest recovery for samples with the lowest milk fat content was obtained for extraction by ethanol/ammonium hydroxide and hexane combination of solvents, while for two other samples with 2.80 and 3.80% of milk fat content, the lowest recoveries were obtained with methanol/hexane combination of solvents.

By comparing all results, it can be concluded that in cases with solvent combination of ethanol, methanol and acetonitrile with hexane, recovery values decrease with increasing of milk fat content, while in case with ethanol/NH_4OH combination with hexane recovery value increases with increasing of milk fat content.

CONCLUSION

The effectiveness of four different solvent combinations on DEHP extraction in milk samples with different milk fat content was investigated. Applied combination ethanol/hexane showed the best recovery value (73.08%) for sample with the lowest milk fat content (0.50%), while methanol/hexane combination showed the lowest effectiveness (16.39%) for milk samples

with 2.80% milk fat content. Investigations with solvent combinations of ethanol, methanol and acetonitrile with hexane showed that recovery values decrease with increasing of milk fat content, while in case with ethanol/NH_4OH combination with hexane recovery value increases with increasing of milk fat content.

Acknowledgement
This work was partially supported by the Ministry for Education, Science and Technological Development of the Republic of Serbia (Grant no. TR 31060).

REFERENCES

[1] J. Lin, W. Chen, H. Zhu, C. Wang, J. Dairy Sci., 2015, 98, 1-7.
[2] D-P. Xu, S. Li, Y-H. Chen, H-B. Li, A-N. Li, X-R. Xu, Int. J. Modern Biol. Med., 2013, 4(1), 12-29.
[3] G. Mortensen, K. Main, A-M. Andersson, H. Leffers, N. Skakkebak, Anal. Bioanal. Chem., 2005, 382, 1084-1092.
[4] J. Zhu, S. Phillips, X-L. Cao in: Handbook of Dairy Foods Analysis, Chapter 37, L. Nollet, F. Toldra (Eds.), CRC Press, New York, 2010.

WATER BASED FREE ENERGY AS IMPORTANT FACTOR OF MAIZE GRAIN FILLING

V. Dragičević, M. Simić, B. Kresović and M. Brankov

Maize Research Institute "Zemun Polje", Slobodana Bajića 1, 1185 Zemun Polje, Serbia. (vdragicevic@mrizp.rs)

ABSTRACT

Kernel filling is important for achieving yield height and stability. It is firstly followed by the intensive accumulation of nutrients and water, up to the moment when polymerisation takes advantage, and added water tends to be loosed to the full ripening stage. The fluctuations of free energy of free, bulk and chemically boned water were measured in grains of different maize hybrids, grown at distinct densities, during grain filling. Free water gradually decreases during whole period, indicating that proper hydration is important for process continuity. Whereas bulk and chemically boned water are important for polymeriation phase. Maize growing at higher density enables higher water retention in kernels, with slower polymerisation.

INTRODUCTION

Kernel filling is important phase in maize lifecycle, defining yield height and stability. It is firstly followed by the intensive accumulation of assimilates and water, up to the moment when polymerisation takes advantage, when added water tends to be loosed to the full ripening stage. The dynamics of water fluctuation in kernel depends on genotype characteristics and agro-ecological conditions [1, 2]. One of the important factors that influence kernel moisture, and yield is crop density.

Besides the carrying of nutrients into kernels, water enables source (solute) for chemical reactions in kernels. Based on the water status, it could be assumed which processes take advantage, monomer accumulation or polymerization, i.e. endergonic over exergonic reactions [3]. Free energy presents the work necessary to make the sorption sites available, and so the higher the moisture content is, the number of available sites are lower [4].

The aim of this experiment was to test reaction of different maize hybrids, grown at distinct densities, based on fluctuations of free energy of free, bulk and chemically boned water in maize kernels, during grain filling.

EXPERIMENTAL

The experiment was performed with the aim to study how low and high crop density: 59523 plants ha^{-1} (D1) and 89286 plants ha^{-1} (D2) affects moisture fluctuation in kernel of ZP 366 (H1), ZP 555 (H2) and ZP 606 (H3) during vegetative season of 2017. After cob measuring, grains were sampled every 10 days (phase I to phase VI), starting from the 15^{th} day after full pollination. The moisture was determined after drying at 60°C (free water), 105°C (bulk) and 130°C (chemically boned water). Free energy (ΔGFW – free water; ΔGBW-bulk water; ΔGBonW-boned water) was calculated using sorption isotherm [5]:

$$\Delta G = -RT \ln(a_w)$$

where a_w is the relative water content achieved after drying at T (60, 105 and 130 °C), R is the gas constant (8.3145 J mol^{-1} K^{-1}) and ΔG is differential free energy. The experimental data were statistically processed by standard deviation.

RESULTS AND DISCUSSION

Grain filling is characterised by gradual accumulation of assimilates in the form of monomers and their further polymerisation, to the composition characteristic for each plant species (genotype). It is specific that ΔHFW increased mainly continually from phase I to phase VI (Table 1), indicating the presence of endergonic over exergonic reactions [3].

Lesser continuality in ΔHFW was present at H3. In grain of the same hybrid ΔHFW finished its increase in phase V at D1, meaning that lower density induces drop in available sorption sites, i.e water retention in grain, opposite to results obtained by Farnham [6].

ΔGBW and ΔGBonW expressed lesser gradation during grain filling, particularly ΔGBW at D1. The highest difference was present between phase I and II, when greater amounts of nutrients enter into kernels [2]. The further variations in ΔGBW were generally lower. This means that available sorption sites for bulk water reached their maximum and remained stable. Only for H3 at D2, increase in ΔGBW was somewhat continual, up to phase VI. In general, ΔGBonW had the highest values, since this kind of energy is the strongest one, bonding water to macromolecules [4, 7]. Similarly to ΔGBW, ΔGBonW rapidly increases between phase I and II and then slowly, up to phase VI. This could indicate that from phase II to VI saturation of sorption sites for water is present, so the polymerisation of storage molecules takes domination in regard to nutrients entering into kernel. Only H3 exhibits difference at D2, with stability of ΔGBonW reached in phase III. This indicates slower accumulation of storage substances.

Table 1. Fluctuations in free energy of free water (ΔGFW), bulk water (ΔGBW) and bound water (ΔGBonW) in maize grain during grain filling period of three maize hybrids (H1-H3) grown at twoi densities (D1 and D2)

	Dens.	Phase	ΔGFW (J mol^{-1})	ΔGBW (J mol^{-1})	ΔGBonW (J mol^{-1})
H1	D1	I	0.40 ± 0.15	4.07 ± 1.35	6.65 ± 1.09
		II	1.00 ± 0.22	10.98 ± 0.10	14.38 ± 0.16
		III	1.86 ± 0.20	11.20 ± 0.07	14.08 ± 0.18
		IV	3.17 ± 0.37	11.58 ± 0.07	15.28 ± 0.07
		V	3.87 ± 0.39	11.47 ± 0.10	15.32 ± 0.08
		VI	6.66 ± 0.89	11.89 ± 1.67	15.75 ± 1.47
	D2	I	0.39 ± 0.06	4.82 ± 1.38	7.43 ± 0.92
		II	0.79 ± 0.16	10.69 ± 1.19	12.65 ± 0.85
		III	1.93 ± 0.20	11.27 ± 0.13	13.85 ± 0.22
		IV	2.79 ± 0.28	11.46 ± 0.13	14.33 ± 0.25
		V	4.66 ± 0.35	12.02 ± 0.12	15.75 ± 0.45
		VI	6.27 ± 0.23	11.36 ± 0.15	17.92 ± 0.38
H2	D1	I	0.35 ± 0.16	3.96 ± 1.39	6.45 ± 0.96
		II	0.72 ± 0.23	10.11 ± 0.31	12.49 ± 0.33
		III	1.87 ± 0.28	11.89 ± 0.11	13.55 ± 0.25
		IV	3.01 ± 0.34	11.42 ± 0.08	15.13 ± 0.05
		V	4.67 ± 0.24	11.27 ± 0.11	15.39 ± 0.03
		VI	6.37 ± 0.85	11.72 ± 1.43	15.56 ± 1.41
	D2	I	0.40 ± 0.10	5.67 ± 1.14	7.60 ± 1.18
		II	1.11 ± 0.15	10.49 ± 1.02	14.30 ± 0.92
		III	1.85 ± 0.19	11.34 ± 0.17	13.66 ± 0.31
		IV	3.03 ± 0.29	11.36 ± 0.11	16.06 ± 0.31
		V	4.73 ± 0.26	11.94 ± 0.10	15.44 ± 0.08
		VI	5.63 ± 0.13	11.69 ± 0.06	15.86 ± 0.08
H3	D1	I	0.39 ± 0.12	4.44 ± 1.17	5.72 ± 1.03
		II	0.62 ± 0.18	9.50 ± 0.34	11.98 ± 0.46
		III	1.56 ± 0.27	11.16 ± 0.06	13.53 ± 0.28
		IV	2.41 ± 0.21	11.37 ± 0.02	15.66 ± 0.06
		V	4.20 ± 0.01	11.50 ± 0.02	15.22 ± 0.05
		VI	4.27 ± 0.55	11.41 ± 1.57	15.49 ± 1.74
	D2	I	0.40 ± 0.01	4.73 ± 0.92	5.67 ± 0.91
		II	0.48 ± 0.09	8.64 ± 0.94	10.80 ± 1.09

III	1.18 ± 0.20	10.20 ± 0.44	14.34 ± 0.57
IV	2.47 ± 0.23	11.26 ± 0.23	15.03 ± 0.09
V	3.49 ± 0.31	11.49 ± 0.07	14.45 ± 0.16
VI	5.55 ± 0.29	11.66 ± 0.04	15.76 ± 0.23

CONCLUSION

It could be concluded that maize grain filling is complex process, depending highly on grain water and its free energy. Free water is category with gradual decrease during whole period, indicating that proper hydration is important for process continuity. Whereas bulk and chemically boned water are important for polymerisation phase. In this study, growing at higher density enables higher water retention in kernels, with slower polymerisation, particularly for H3 (ZP 606). All these could contribute to greater yielding capacity.

Acknowledgement

This work was supported by the Ministry of Education, Science and Technological Development of the Republic of Serbia (Grant no. TR-31037).

REFERENCES

[1] I.R. Brooking, Field Crops Res., 1990, 23, 55-68.
[2] B.L. Gambín, L. Borrás, M.E. Otegui, Austral. J. Agric. Res., 2008, 59, 280–290.
[3] V. Dragičević, Recent Advances in Thermo and Fluid Dynamics, INTECH, Rijeka, Croatia, 2015, p. 195
[4] V. Worthington, J. Alter. Complement. Med., 2004, 7, 161-173.
[5] W.Q. Sun, in: Desiccation and Survival in Plants: Drying Without Dying, Black M. & Pritchard H. W. (Ed.), CABI Publishing, New York, USA, 2002, 47-91.
[6] D.E. Farnham, Agron. J., 2001, 93, 1049-1053.
[7] S. Ratkovic, P. Pissis, J. Material. Sci., 1997, 32, 3061-3068.

GLASS TRANSITION OF DEHYDRATED APPLE POMACE WITH DIFFERENT WATER CONTENT

S.Zlatanović [1], S. Ostojić [1], D. Micić [1] and P.Vukosavljević [2]

[1] *University of Belgrade, Institute of General and Physical Chemistry, Studentski trg 12 16, 11000 Belgrade, Serbia.*
[2]*University of Belgrade, Faculty of Agriculture, Nemanjina 6, 11000Belgrade, Serbia*
(snezana.zlatanovic@gmail.com)

ABSTRACT
Thermal behavior of fresh and dehydrated apple pomace (leftover after juice production from idared variety) was studied by differential scanning calorimetry (DSC). The purpose of the study was to evaluate thermal characteristics of apple pomace after dehydration in laboratory dehydrator at a temperature 55 ± 1 °C for 360 and 600 min. Temperature of glass transition (36.3 °C and 29,1 °C), water activity (0.45 and 0.20) and moisture content (9.52 % and 6.41 %) of apple pomace dehydrated 360 min and 600 min was assessed. According to glass transition temperature optimal dehydration time was 360 min.

INTRODUCTION
The apple processing industry, the production of juice, jam and apple candy generates enormous amounts of apple pomace mainly consisting of a complex mixture of peel, seed kernel, calyx, stem and soft tissue [1]. Apple pomace is a wet by-product most often used as animal feed or as a fertilizer and as a source of pectin, dietary fibre and polyphenols [2]. Drying, as the common preservation methods, was applied widely in processing of high moisture biomass. It is applied also to extend and preserve the shelf life of apple products as well as to preserve wet apple pomace thus enabling its further utilization as food ingredient.

Many food materials exist in a disordered amorphous solid state by their nature and due to processing. However, the glass transition behaviour of food systems may often be misleading in the prediction of characteristics of food components and their storage stability. The glass transition temperature is one of the most important parameters related to the stability of amorphous foods. It is relevant to such food processing operations such as drying, freezing and extrusion. It also affects quality attributes like texture, flavour and enzyme activity in low-moisture foods [3]. Some food changes are affected by

molecular mobility. Above the glass transition temperature, molecular mobility increases and viscosity decreases, which can be related to such structural changes as collapse and stickiness [3]. Foods with a Tg higher than room temperature (25 °C) can be considered stable [4]. The deterioration of dried foods is related to water content and water activity (aw), which have a strong influence on increasing the reaction rate that is similar to the effect of increasing temperature.

The state of water and its interaction with food ingredients plays a crucial role in food storage. The sorption isotherm characterises the relationship between water content and its activity at constant temperature [5]. The water sorption behaviour and glass transition temperature are parameters that can be employed in designing and optimising drying, packaging and storage of food powders [5,6].

The purpose of this study was to determine the effect of drying conditions on moisture content, water activity and glass transition temperature of apple pomace obtained from domestic apple juice factory.

EXPERIMENTAL

The starting material was the apple pomace (AP) originating from the fruit processing plant "Fruvita" from Smederevo, variety idared. Samples were dehydrated in laboratory dehydrator during 360 min and 600 min at a temperature 55 ± 1 °C, and digital thermometer indicator inside chamber provides at-a-glance temperature verification. Two samples of apple pomace were obtained: apple pomace dehydrated for 360 min (AP 360) and 600 min (AP 600).

A differential scanning calorimeter (DSC, Q1000, TA Instruments, New Castle, DE) was used to perform DSC experiments. Apple pomace samples (5-7 mg), were placed in Al pans, and cooled from 20 to -90 °C, then equilibrated for 5 min and scanned initially from -90 to 150 °C, with controled heating rate of Hr= 5 °C/min, under the N_2 purge flow of 50 ml/min. Each thermogram was analyzed by TA Advantage Universal analysis 2000 software to obtain - glass transition temperatures (T_{gon} – glass transition onset temperature, T_{g-} glass transition temperature and T_{gend}- glass transition end temperature) and ice melting temperatures (T_p).

Moisture content were determined according to standard procedure SRPS EN 12145:2005. Water activity has been determined by aw meter Testo 650 at 25 °C.

RESULTS AND DISCUSSION

DSC curves of apple pomace samples are shown in Fig. 1. For fresh apple pomace (moisture content 75 %) the heat flow curve obtained from DSC

showed two characteristic transition (Tab. 1.). Peak maxima at about -1.35°C and 75 °C represents ice melting and water evaporation (Fig. 1.). Glass transition of dried apple pomace samples obtained within the scope of this study, after period of dehydration of 360 min and 600 min was 36.3 °C and 29.1 °C while water activity was 0.45 and 0.2 respectively. Obtained result was in corroboration with previously published data related to apple puree powder produced from whole apple whose Tg was 34 °C at aw = 0 Jakubczyk et al [7]. Differences noticed in Tg are probably caused by various composition of samples. Dehydrated food with moisture content below 10 % and water activity below 0.6 is considered microbiologically stable. Apple pomace has high content of dietary fiber. Presence of high molecular polysaharides is known to increase glass transition temperature and provide stability and long term storage of food with low moisture content and water activity [3].

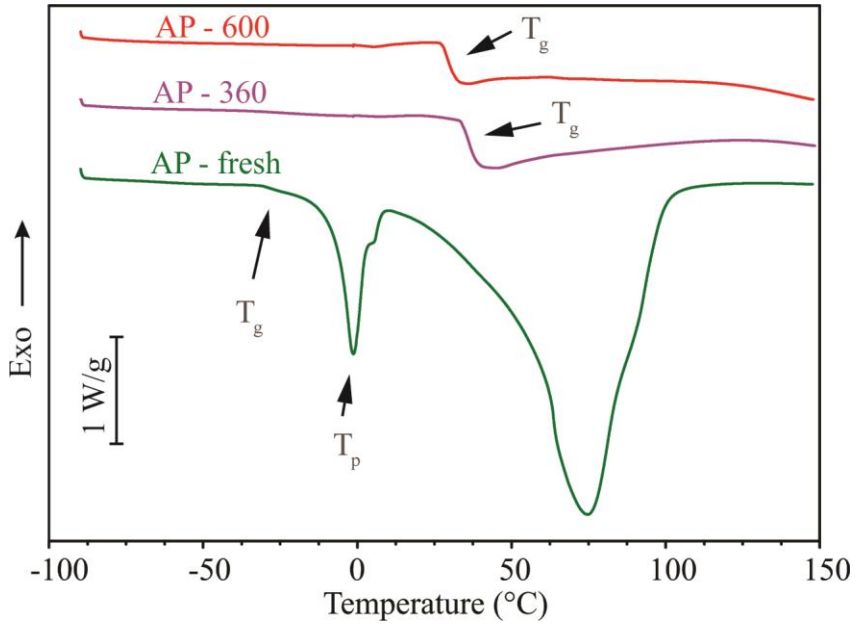

Figure 1. DSC curves of fresh and dehydrated apple pomace.

The glass transition temperature of foamed apple juice powder at low water activity was 20 °C [6] while Tg of other fruit powders reported previously varied significantly. The glass transition temperature of freeze-dried camu-camu pulp with aw = 0.11 was at 3.2 °C while the pulp with maltodextrin at the same water activity had a Tg of 62.7 °C [8]. The glass transition temperatures of foods are mainly dependent on the moisture content, water activity and chemical composition of the material. The food

industry uses water activity and the glass transition concept to determine food stability [5]. The same approach was used in this study.

Table 1. Water content, glass transition temperature, freezing point and water activity of fresh and dehydrated apple pomace.

Sample	Moisture (%) 105 °C	T_{gon} (°C)	T_{gmid} (°C)	T_{gend} (°C)	Ice melting T_p(°C)	aw
AP-fresh	75.0	-30.6	-28.3	-26.7	-1.35	0.91
AP-360	9.5	33.8	36.3	38.7	-	0.45
AP-600	6.4	27.6	29.1	31.8	-	0.20

CONCLUSION

According to obtained results in the present article it can be concluded that apple pomace obtained during dehydration process is stable for storage as it was achieved that product has glass transition (T_g) on temperature 36.3 °C and 29.1 °C for AP-360 and AP-600 respectivly. It is not necessary to extend the drying time for more than 360 minutes under given drying conditions, since obtained product were stable according to glass transition temperature, water activity and moisture content.

Acknowledgement

This work was partially supported by the Ministry for Science of the Republic of Serbia (Grants no. 31055 and 31093).

REFERENCES

[1] M. Yates, M. Ramos, M.A. Martin-luengo, A. Maria, M. Serrano, V. Zurdo, J. Clean. Prod., 2017, **143**, 847–853.
[2] G. Royer, E. Madieta, R. Symoneaux, F. Jourjon, LWT - Food Sci. Technol., 2006, **39**, 1022–1025.
[3] Y.H. Roos, in Water Act. Foods, Blackwell Publishing Ltd, 2008, 29–45.
[4] J.M. Aguilera, G. Levi, M. Karel, Biotechnol. Prog., 1993, **9**, 651–654.
[5] S.S. Sablani, S. Kasapis, M.S. Rahman, J. Food Eng., 2007, **78**, 266–271.
[6] N. Raharitsifa, C. Ratti, J. Food Process Eng., 2010, **33**, 341–364.
[7] E. Jakubczyk, E. Ostrowska-Ligeza, E. Gondek, Int. J. Food Sci. Technol., 2010.
[8] M.A. Silva, P.J.A. Sobral, T.G. Kieckbusch, J. Food Eng., 2006, **77**, 426–432.

COMPOSITION OF REISHI/GREEN TEA EXTRACT DETERMINED BY UHPLC-DAD-ESI-MS METHOD

S. Konstantinović[1], Lj. Stanojević[1], M. Zlatković[1], D. Stojiljković[2] and J. Zvezdanović[1]

[1]*University of Niš, Faculty of Technology, Bulevar oslobodjenja 124, 16000 Leskovac, Serbia. (sakisandra12@yahoo.com)*
[2]*Super Natura, Južnomoravskih brigade 156E, 16000 Leskovac, Serbia.*

ABSTRACT
Composition of Reishi/Green tea ethanolic extract (70:30 *v*/*v*) analyzed by UHPLC-DAD-ESI-MS/MS analysis (ultrahigh performance liquid chromatography coupled with diode array and mass spectrometry detectors) confirmed presence of significant amount of polyphenols with dominant contribution of flavonoids.

INTRODUCTION
Reishi (*Ganoderma lucidum*) is one of the most important mushroom used in China, Japan and Korea over the last 4000 years as a drug, additional remedy, or elixir [1,2]. Commercial *G. lucidum* products are available as powders, dietary supplements and tea and can be obtained from different parts of the mushroom, including mycelia, spores and fruit body. The main component of mushroom is water [3], with diverse chemical composition including polysaccharides, triterpenes, polyphenols which allows wide pharmaceutical properties such as antimicrobial, antioxidant, antiviral and anticancer [4]. Among cultivated mushrooms, *G.lucidum* is primarily known for its pharmaceutical rather than nutritional value. It has a significant impact on control the blood glucose levels, modulation of the immune system, hepatoprotection, bacteriostasis, etc. Addition of some biological active extracts in pure Reishi extract, could improve antioxidant and antimicrobial activity of extract itself. Considering this, the aim of this study was to evaluate the chemical composition of Reishi/Green tea extract by using UHPLC-DAD-ESI-MS analytical technique.

EXPERIMENTAL
Commercial ethanolic Reishi/Green tea extract (70:30 *v*/*v*) was obtained by Super Natura Company (Leskovac, Serbia). Standards quercetin, rutin and apigenin were purchased from (Sigma Chemical Company, St. Louis, USA). Solvents used in the UHPLC-experiments were of LC/MS grade. The chromatographic separation was performed on Hypersil gold C18 column

(50×2.1 mm, 1.9 μm) at 25 ^{o}C using a Dionex Ultimate 3000 UHPLC system equipped with a diode array (DAD) detector and LCQ Fleet Ion Trap Mass Spectrometer (Thermo Fisher Scientific, USA). A mobile phase consisted of two solvents, 0.1%, *v*/*v*, formic acid in water and methanol with a gradient program at 0.250 ml min^{-1} flow rate, according previously published method [5]. Absorption spectra were recorded on DAD-detector with total spectral range between 200 and 800 nm. Mass spectrometric analysis was performed using a 3D-ion trap with electrospray ionization (ESI) in negative ion mode (with source parameters given in [5]). MS-spectra were acquired in full range *m*/*z* 130–1300, with MS/MS analysis performed by a data dependent scan the collision-induced dissociation at 25 eV of detected molecular ions peaks (M-H]$^{-}$).Xcalibur software (version 2.1) was used for instrument control, data acquisition and data analysis. Qualitative analysis of the extract was achieved by using UV-Vis spectra of the DAD signals and the MS-spectra with the corresponding [M-H]$^{-}$ and also characteristic ion fragmentation within selected peaks (MS/MS), from the UHPLC chromatograms by comparison to literature data as well the standard compounds.

RESULTS AND DISCUSSION

UHPLC-DAD chromatogram of Reishi/Green tea extract is shown in Fig.1.

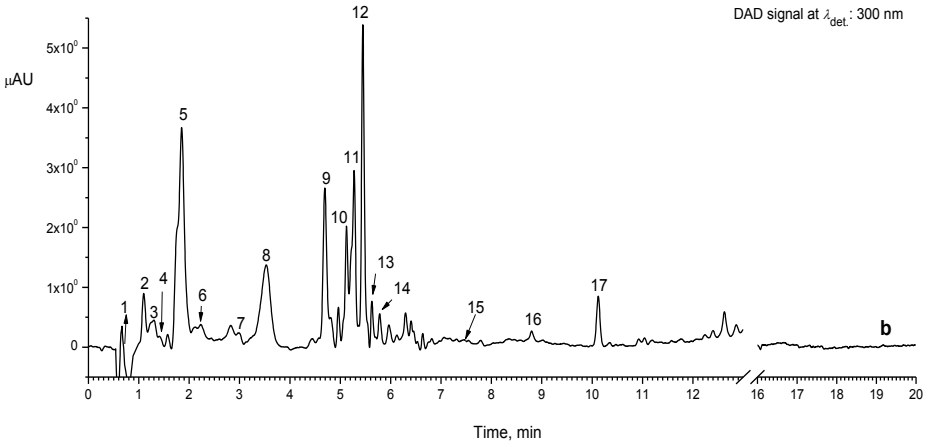

Figure 1. UHPLC-DAD chromatogram of Reishi/Green tea extract at DAD signal λ_{det} = 300 nm.

Dominant class of detected compounds in Reishi/Green tea extracts are flavonoids. Flavonols (kaempferol-3-*O*-rutinoside, kaempferol-3-*O*-glycoside, quercetin-glycoside and its quercetin-3-*O*-rutinoside derivative (rutin), as well as flavones such as apigenin-xyloside-glucoside and dihydroferuloyl

derivative of apigenin-diglucoside, were detected (peaks no. 13, 14, 12, 11 and 9, 10, with molecular ion peaks found at *m/z* 593, 447, 463, 609, 563 and 771, respectively, Fig. 1). Peaks no. 1,2,4,7 and 8 were assigned to 3-*O*-galloyl quinic acid, gallocatechin, epigallocatechin, catechin (or epicatechin) and epigallocatechin gallate with the molecular ions peaks detected at *m/z* 343, 305, 305, 289 and 457, respectively and the corresponding MS/MS fragmentation, in the MS-spectra. Spectral data for assignation were used from literature [6-10]. According to UV-Vis spectra, peaks no. 3, 5, 6, 15, 17 and 16 could be identified as derivatives of phenolic acids and flavonoids, respectively. This is only a presumption, since they could not be confirmed by using the corresponding MS/MS spectra.

For some identified compounds, recorded UV-Vis and MS/MS spectra were shown in Fig.2.

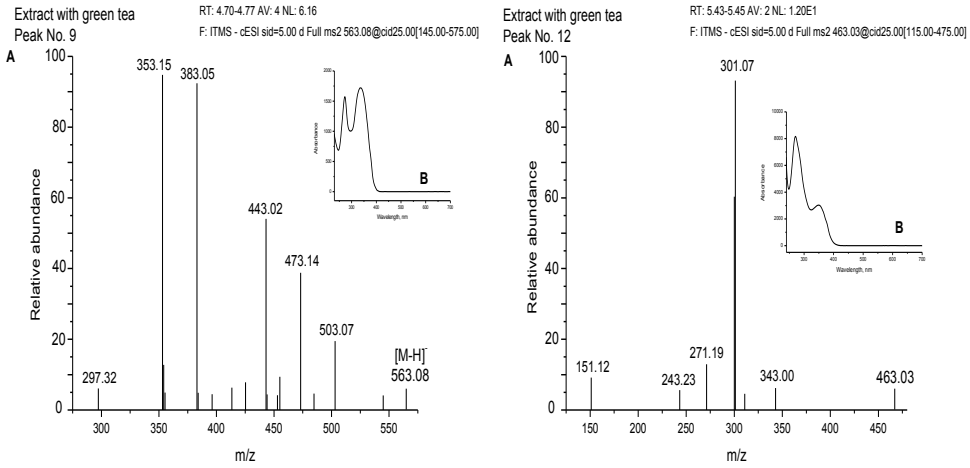

a) Compound No. 9 assigned as apigenin-xyloside-glucoside

b) Compound No. 12 assigned as quercetin-glycoside

Figure 2. Mass (A) and UV-Vis (B) spectra of selected compounds from chromatogram of Reishi/Green tea extract (peaks no. 9 and 12).

Apigenin-xyloside-glucoside, is also known as vicenin 1 (signal no. 9, Fig. 1). MS/MS-fragmentation pattern in negative mode for the same compound (Fig. 2a) represents molecular ion at *m/z* 563 fragmentation with the most abundant fragment-ions detected at *m/z* 443, 383 and 353 (100 %). The fragmentation is characteristics for a glucosyl and pentosyl residues in the molecule. The fragments ion signals observed at *m/z* 383 and *m/z* 353 are also typical for di-*C*-glycosyl-flavones [6]. UV/Vis spectra exhibited two absorption maxima (272 and 334 nm), which is also in accordance with some

previous works of similar research [6]. Quercetin-glycoside (signal no.12, Fig. 1), could be assigned to quercetin-7-*O*-glycoside, since fragment ion at *m/z* 301 is rather abundance in 7-*O*-glycoside than in 3-*O*-glycoside (Fig. 2b) [7]. Also, UV/Vis absorption maxima at 271 and 349 nm are in the range for this class of flavonols [7].

CONCLUSION

Chemical composition of Reishi/Green tea suggests significant amount of polyphenols, which are known to have antioxidant and antimicrobial activity. This study is strongly suggestive that extracts of *Ganoderma lucidum* can be used as antimicrobial and antioxidant agents in the development of new drugs with natural origin.

Acknowledgement

This work was partially supported by the Ministry for Science of the Republic of Serbia (Grants no.TR 34012).

REFERENCES

[1] A. Hasnat, M. Pervin, B.O. Lim, Molecules, 2013, 18, 6663-6678.
[2] K. Yan, W. Zhang, H. Yu, H. Wang, X. Zhang, Food Technology and Biotechnology, 2010, 48, 91-101.
[3] S.Wachtel-Galor, J. Yuen, J.A. Buswell, I.F.F. Benzie, *Ganoderma lucidum* (Lingzhi or Reishi), A Medicinal Mushroom, CRC Press/Taylor&Francic, Boca Raton, 2011.
[4] A. Kamra, A.B. Bhatt, International Journal of Pharmacy and Pharmaceutical Science, 2012, 4, 359-361.
[5] V. Tadić, I. Arsić, J.Zvezdanović, A.Zugić, D.Cvetković, S.Pavkov, Journal of Ethnopharmacology, 2017, 199, 138-148.
[6] Z. Benayad, C. Gómez-Cordovés, N.E. Es-Safi, International Journal of Molecular Science, 2014, 15, 20668-20685.
[7] H.Y. Zhao, J.H. Sun, M.X. Fan, L.Fan, L. Zhou, Z. Li, J. Han, B.R. Wang, D.A. Guo, Journal of Chromatography A, 2008, 1190, 157-181.
[8] C. C. Wyrepkowski, D. L. M. G. da Costa, A.P.Sinhorin, W.Vilegas, R. A. De Grandis,F.A.Resende, E.A.Varanda, L. C. dos Santos, Molecules, 2014, 19, 16039-16057.
[9] D. H. Markowicz Bastos, L. A. Saldanha, R R. Catharino, A. C. H. F. Sawaya, I. B. S. Cunha, P. O. Carvalho, M. N. Eberlin, Molecules, 2007, 12, 423-432.
[10] X. Jiang, Y. Liu, W. Li, L. Zhao, F. Meng, Y. Mang, H.Tan, H.Yang, C.Wei, X. Wei, X.Wan, L.Gao, T.Xia, Plos One, 2013.8, e62315.

THERMAL DEGRADATION KINETICS OF TOTAL ANTHOCYANINS IN TWO TYPES OF RASPBERRY JAMS

M. Nikolić, A. Pavlović, S.S. Mitić, S. Tošić, M. Mitić, E. Pecev-Marinković, A. Miletić and J. Mrmošanin

University of Niš, Faculty of Science and Mathematics, Department of Chemistry, Višegradska 33, 18 000 Niš, Serbia. (milenai.chem@gmail.com)

ABSTRACT

Fresh raspberries were processed into sugar and sugar-low jams at high temperatures (90, 95, 100 and 105 °C). Total anthocyanin (TA) content was significantly affected by the temperature, heating time and jam type, with the largest retention in sugar-low jam prepared at 90 °C for 5 minutes and with the largest decrease in sugar jam prepared at 105 °C for 30 minutes. In the temperature interval from 90 ºC to 105 ºC, degradation of total anthocyanins in both sugar and sugar-low jam type followed a first-order reaction, with activation energies (Ea) of 68.9 kJ/mol and 53.6 kJ/mol, respectively. The half-life values ($t_{1/2}$) of total anthocyanins ranged from 5.9 to 15.3 minutes for sugar jam and from 12.9 to 26.3 minutes for sugar-low jam. The degradation of total anthocyanins is more susceptible to temperature elevation in sugar jam comparing to sugar-low type.

INTRODUCTION

Raspberry fruits are a very rich source of health-beneficial polyphenolic phytochemicals – phenolic acids, tannins, anthocyanins [1]. Anthocyanins are potent antioxidants with anti-inflamatory and anticancer properties [2]. However, since anthocyanins are sensitive temperature-wise and undergo through significant changes during heating, it is important to determine whether thermally processed foods such as jams can also be considered as a good source of nutritional compounds.

Thermal degradation kinetic of anthocyanins follows first-order kinetic [3], where the rate constant increases with an increase in temperature.

According to our knowledge, influence of high temperatures, which are often applied during jam preparation, on the content of total anthocyanins has not been researched comparatively. So the aim of this research was to analyze the correlation between temperature, added sugar and total anthocyanin content, as well as total anthocyanin degradation kinetic in sugar and sugar-low raspberry jams.

EXPERIMENTAL

Frozen raspberry fruits were milled in the blender to obtained puree which was used for jam preparation. Two types of jams (sugar and sugar-low) were prepared according to slightly modified method described by de Moura et al. [3]. The sugar type implied 60% of fruit puree, 30% of saccharose, 9.8% of glucose and 0.2% of commercially available pectin for domestic use. The sugar-low type implied 94.2% of fruit puree, 5% of saccharose and 0.8% of commercially available pectin for domestic use. The mixtures were heated to temperatures of 90, 95, 100 and 105 ºC and stirred frequently in opened vessels. Samples were taken at different heating times: 5, 10, 15, 20 and 30 minutes, and immediately cooled to stop further thermal degradation. The ultrasonic extractions of jam samples were performed at room temperature (25 °C) for 15 minutes three times with acidified methanol (1% HCl). The fractions from three times repeated extractions were collected and evaporated to dryness by rotary evaporation under reduced pressure at 40 °C. Ultrapure water was added to 10 mL and these solutions were used for further analysis. The total anthocyanin (TA) content was determined using the pH-differential method [4] and was calculated as milligram of cyanidin-3-glucoside equivalents per gram of jam. All measurements were performed in triplicate on an Agilent 8453 UV/Vis spectrophotometer (Agilent Technologies, Santa Clara, California, USA) with optical cuvettes of 1 cm optical path.

RESULTS AND DISCUSSION

According to obtained results presented in the **Table 1**, TA content of jam samples decreased in time and temperature-dependent manners but being more pronounced in sugar than in sugar-low jam at all applied temperatures. The smallest loss in TA content was observed after 5 minutes of heating on 90 °C in sugar-low jam, yielding 6.3%. The greatest loss in TA content was observed after 30 minutes of heating on 105 °C in sugar jam, yielding 84.5%. Linear regression confirmed that the degradation of total anthocyanins in both sugar and sugar-low jam samples followed by a first-order reaction. The high R^2 values obtained from Arrhenius plot confirm that the degradation increased with increased temperature and time ($0.9410<R^2<0.9895$) (**Figure 1**). Therefore, the percentage of retention of anthocyanins strongly depends on heating time and temperature and was ranged from 48.4% to 71.1% at 90 °C, from 33.4% to 68.7% at 95 °C, from 24.0% to 62.4% at 100 °C and from 15.6% to 57.6% at 105 °C in sugar jam. TA have shown greater resistance towards high temperatures exposure in sugar-low jam, yielding from 65.6% to 93.8% at 90 °C, from 60.1% to 90.1% at 95 °C, from 51.3% to 87.1% at 100 °C and from 42.2% to 82.9% at 105 °C.

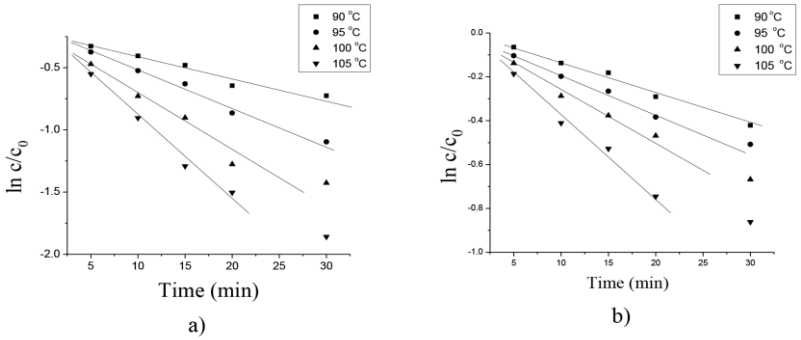

Figure 1. Degradation of total anthocyanins in sugar (a) and sugar-low raspberry jam (b)

Table 1. Changes in total anthocyanin content during processing of sugar and sugar-low raspberry jams

Temp. (°C)	Time (min)	Sugar jam		Sugar-low jam	
		c_{sr}±SD* (mg cy-3-glu/g)	RSD (%)	c_{sr}±SD* (mg cy-3-glu/g)	RSD (%)
		0.57±0.01**	1.75	0.69±0.01**	1.45
90	5	0.409±0.003	0.73	0.641±0.006	0.94
	10	0.38±0.01	2.63	0.596±0.008	1.34
	15	0.352±0.006	1.70	0.570±0.008	1.40
	20	0.298±0.003	1.01	0.52±0.01	1.92
	30	0.275±0.006	2.18	0.448±0.005	1.12
95	5	0.390±0.008	2.05	0.612±0.006	0.98
	10	0.336±0.008	2.38	0.560±0.004	0.71
	15	0.302±0.003	0.99	0.525±0.006	1.14
	20	0.239±0.004	1.67	0.466±0.008	1.72
	30	0.189±0.003	1.59	0.411±0.008	1.95
100	5	0.354±0.002	0.56	0.596±0.009	1.51
	10	0.274±0.004	1.46	0.511±0.008	1.57
	15	0.230±0.007	3.04	0.469±0.003	0.64
	20	0.158±0.002	1.27	0.428±0.006	1.40
	30	0.136±0.003	2.21	0.350±0.006	1.71
105	5	0.327±0.004	1.22	0.568±0.006	1.06
	10	0.230±0.005	2.17	0.454±0.006	1.32
	15	0.156±0.001	0.64	0.404±0.002	0.50
	20	0.126±0.001	0.79	0.324±0.004	1.23
	30	0.088±0.001	1.14	0.289±0.003	1.04

*Values represent mean±standard deviation (n=2)

**Initial concentration

The temperature-dependence degradation rate constant was represented by the Arrhenius equation:

$$k = k_0 \cdot e^{-Ea/RT}$$

The kinetic parameters are given in Table 2 and the Arrhenius plot is given on Figure 2. As it can be seen, larger amount of sugar in sugar jam resulted in twice as higher degradation rate constants and approximately twice as lower half-lives comparing to sugar-low jam at all applied temperatures. The value of the activation energy was 54 kJ/mol and 68 kJ/mol for sugar-low and sugar jam, respectively.

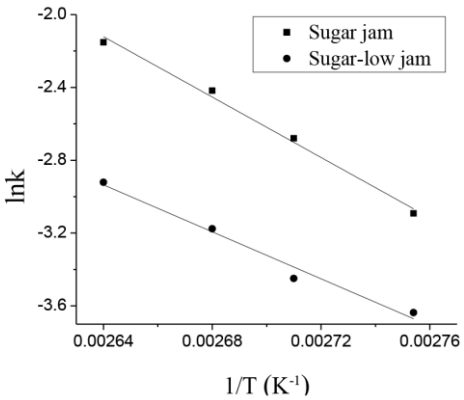

Figure 2. The Arrhenius plot for degradation of total anthocyanins in raspberry jam samples

Table 2. Effect of heating on the k, $t_{1/2}$ and Ea values of total anthocyanins degradation in sugar and sugar-low raspberry jams

Sugar jam				
Temp. (°C)	$kx10^{-2}$ (min^{-1})	R^2	$t_{1/2}$ (min)	Ea (kJ/mol)
90	4.5±0.1	0.9410	15.3	68±1
95	6.8±0.1	0.9835	10.1	
100	8.9±0.3	0.9678	7.8	
105	11.6±0.2	0.9799	5.9	
Sugar-low jam				
Temp. (°C)	$kx10^{-2}$ (min^{-1})	R^2	$t_{1/2}$ (min)	Ea (kJ/mol)
90	2.6±0.1	0.9871	26.3	54±2
95	3.2±0.1	0.9862	21.8	
100	4.2±0.1	0.9895	16.6	
105	5.4±0.1	0.9802	12.9	

CONCLUSION

Our finding implies that the degradation of anthocyanins is more susceptible to temperature elevation in sugar jam. Higher concentrations of TA are preserved in sugar-low jams, when being cooked at lower temperatures and shorter heating time.

Acknowledgement

This research was supported by grant number 172047 from the Serbian Ministry of Education, Science and Technological Development.

REFERENCES

[1] A.V. Rao, D.M. Snyder, J. Agric. Food Chem., 2010, **58**, 3871-3883.
[2] C.S. Bowen-Forbes, Y. Zhang, M.G. Nair, J. Food Compost. Anal., 2010, **23**, 554–560.
[3] S.C.S.R. de Moura, P.E. da Rocha Tavares, S.P.M. Germer, A.L.A.C. Nisida, A.B. Alves, A.S. Kanaan, Food Bioproc. Tech., 2012, **5**, 2488–2496.
[4] M.M. Guisti, R.E. Wrolstad, Curr. Prot. Food Anal. Chem. F1.2.1-F1.2.13.

EFFECT OF TEMPERATURE ON STABILITY OF INDIVIDUAL ANTHOCYANINS IN SUGAR-LOW STRAWBERRY JAM

M. Nikolić, A. Pavlović, M. Mitić, S. S. Mitić, S. Tošić, E. Pecev-Marinković and A. Miletić

University of Niš, Faculty of Science and Mathematics, Department of Chemistry, Višegradska 33, 18 000 Niš, Serbia. (milenai.chem@gmail.com)

ABSTRACT

High-performance liquid chromatography with diode array detection (HPLC-DAD) was used to study the stability of individual anthocyanins during preparation of sugar-low strawberry jam at high temperatures. The major anthocyanin was pelargonidin-3-glucoside, followed by cyanidin-3-glucoside, pelargonidin-3-rutinoside and cyanidin-3-malonylglucoside. The highest stability towards heating was observed at pelargonidin-3-rutinoside, while cyaniding-3-malonylglucoside was the least stable.

INTRODUCTION

Anthocyanins are water-soluble pigments which are responsible for blue, violet, pink and red colors of fruits of some plants [1]. They are found in strawberries [2], blackberries and raspberries [3]. The red color of strawberries is due to anthocyanins in their flavylium forms. The anthocyanins found in strawberries are glycosides of pelargonidin (λ_{max} at 502 nm) and cyanidin (λ_{max} at 516 nm) [4] (Figure 1). The aim of this work was to examine the influence of high temperatures and the time of heating on stability of individual anthocyanins during preparation of sugar-low strawberry jam.

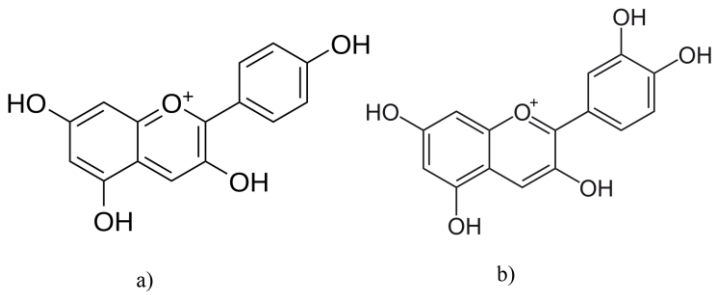

Figure 3. Chemical structure of a) pelargonidin and b) cyanidin

EXPERIMENTAL

Strawberry fruits were milled in the blender to obtained puree which was used for jam preparation. Flesh and seeds were not separated. Sugar-low strawberry jam was prepared according to a slightly modified method described by de Moura et al. [5] and it implied 94.2% of fruit purée, 5% of saccharose and 0.8% of commercially available pectin for domestic use. The mixtures were heated to the temperatures of 90, 95, 100 and 105 ºC and stirred frequently in opened vessels. The temperature was registered using a laboratory thermometer and stabilized at the process temperature (±1 ºC). Once isothermal conditions were achieved, the samples were taken at different heating times: 5, 10, 15, 20 and 30 minutes, and immediately cooled in cold water to stop further thermal degradation. The first sample was taken before the heating began (c_0). The analysis was done immediately. The ultrasonic extractions of jam samples were performed at room temperature (25 °C) for 15 minute, three times. Briefly, 5.0000 g ± 0.0001 g of each jam sample was weighed and mixed with 5 mL of acidified (1 % HCl) methanol. The flask with a sample was put into the ultrasonic bath and sonicated for 15 min. The extract was filtered and the clear supernatant was collected. The fractions from three times repeated extractions were collected and evaporated to dryness by rotary evaporation under the reduced pressure at 40 °C. Ultrapure water was added to 10 mL and these solutions were used for further analysis.

In order to identify and determine the individual anthocyanins content, Agilent-1200 series HPLC with the UV-Vis photodiode array detector (DAD) was used. The column was thermostated at 25 °C. After injecting 5 μL of the sample, the separation was performed in an Agilent-Eclipse XDB C-18 4.6×150 mm column. The mobile phase consisted of aqueous 5% formic acid (eluent A) and 80% acetonitrile/5% formic acid (eluent B). The elution program used was as follows: from 0 to 10 min 0% B, from 10 to 28 min gradually increases 0-25% B, from 28 to 30 min 25% B, from 30 to 35 min gradually increases 25-50% B, from 35 to 40 min gradually increases 50-80% B, and finally for the last 5 min gradually decreases 80-0% B. The identification of individual compounds was based on the retention time and spectral data with those of the standard cyanidin-3-glucoside. Quantitative determination of individual anthocyanins in the samples was calculated using a calibration curve of cyanidin-3-glucoside. Triplicate measurements were taken, and data were presented as mean ± standard deviation (SD).

RESULTS AND DISCUSSION

Obtained results are presented in Table 1. Several anthocyanins were identified: pelargonidin-3-glucoside (Pg-3-glu), cyanidin-3-glucoside (Cy-3-

glu), pelargonidin-3-rutinoside (Pg-3-rut) and cyanidin-3-malonylglucoside (Cy-3-malglu), which is in accordance with previously reported literature data on strawberry jams [6]. Pg-3-glu was found to be the most abundant anthocyanin, followed by Cy-3-glu, Cy-3-malglu and Pg-3-rut.

Table 1. Content of individual anthocyanins in sugar-low strawberry jam during processing (μg/kg)

Temp. (°C)	Time (min)	c_{sr}±SD*	RSD (%)	c_{sr}±SD*	RSD (%)	c_{sr}±SD*	RSD (%)	c_{sr}±SD*	RSD (%)
		219±9**	4.11	25.3±0.5**	1.98	11.8±0.3**	2.54	11.9±0.1**	0.84
	5	191±5	2.62	21.5±0.3	1.39	10.5±0.5	4.74	9.5±0.5	5.28
	10	167±6	3.59	19.9±0.7	3.51	9.8±0.1	1.02	8.9±0.2	2.24
90	15	161±4	2.48	18.9±0.5	2.65	9.5±0.3	3.17	8.4±0.3	3.57
	20	154±12	7.78	18.3±1	5.47	9.1±0.4	4.39	8.2±0.3	3.66
	30	132±4	3.02	16.4±0.3	1.83	8.1±0.7	8.69	7.5±0.6	8.03
	5	166±6	3.62	20±1	5.03	10.1±0.2	1.98	8.3±0.5	6.03
	10	156±10	6.42	18.4±0.2	1.09	9.0±0.4	4.47	8.0±0.2	2.51
95	15	153±9	5.88	17.7±0.3	1.69	8.7±0.5	5.75	7.5±0.2	2.66
	20	139±8	5.75	16.6±0.5	3.01	7.9±0.3	3.81	7.2±0.1	1.39
	30	123±7	5.70	14.2±0.3	2.11	7.0±0.6	8.55	6.6±0.4	6.06
	5	161±9	5.59	19.4±0.1	0.52	9.5±0.4	4.22	8.1±0.3	3.71
	10	151±5	3.30	17±1	5.81	9.0±0.5	5.57	7.6±0.5	5.26
100	15	150±8	5.32	17.1±0.7	4.10	8.8±0.7	7.95	6.8±0.5	7.30
	20	136±8	5.87	16±1	6.25	8.1±0.3	3.72	6.0±0.2	3.35
	30	120±9	7.51	13.4±0.7	5.21	7.4±0.4	5.38	4.9±0.1	2.05
	5	125±11	8.83	14.2±0.5	3.52	7.9±0.1	1.26	4.8±0.1	2.09
	10	119±4	3.38	13.1±0.3	2.28	7.2±0.2	2.77	4.6±0.2	4.38
105	15	104±8	7.72	12.1±0.5	4.13	6.7±0.2	3.01	3.9±0.1	2.58
	20	101±6	5.91	11.2±0.3	2.67	6.4±0.5	7.80	3.4±0.1	2.92
	30	99±7	7.05	10.9±0.1	0.91	6.3±0.3	4.7	3.4±0.1	2.97

*Values represent mean±standard deviation (n = 3)
**c_0 – initial concentrations

The highest concentration of all pigments was achieved by cooking the jam at 90 °C for 5 minutes with retention percentages yielding 87.2% of Pg-3-glu, 85.2% of Cy-3-glu, 89.5% of Pg-3-rut and 79.7% of Cy-3-malglu. However, preparation of strawberry jam at 105 °C for 30 minutes caused severe losses in anthocyanin content, where 45.4% of Pg-3-glu, 43.3% of Cy-3-glu, 53.4% of Pg-3-rut and 28.3% of Cy-3-malglu was retained. Obviously, the greatest stability towards thermal treatment was observed at Pg-3-rut. Pg-3-glu and Cy-3-glu exhibited relatively equable stability. Lower thermal

stability of Cy-3-malglu may be a consequence of the place of glycosylation and the presence of acylated substitutents [7]. However, Cy-3-malglu may degrade by losing the malonyl moiety and forming Cy-3-glu, so the real degradation rate of Cy-3-glu may be masked [8], which must be taken into consideration when interpreting these results.

CONCLUSION

This research showed that individual anthocyanins in strawberry fruits are significantly affected by heating. Longer time of exposure to high temperatures caused drastic loss of all identified pigments. Higher retention of all analyzed compounds was accomplished in lower temperatures and shorter heating time, which should be taken into consideration during domestic and industrial strawberry processing.

Acknowledgement

This research was supported by grant number 172047 from the Serbian Ministry of Education, Science and Technological Development.

REFERENCES

[1] A. Castañeda-Ovando, M.L. Pacheco-Hernández, M.E. Páez-Hernández, J.A. Rodríguez, C.A. Galán-Vidal, Food Chem., 2009, **113**, 859–871
[2] F. Lopes da Silva, M.T. Escribano-Bailón, J.J. Pérez Alonso, J.C. Rivas-Gonzalo, C. Santos-Buelga, Lebensm. Wiss. Technol., 2007, **40**, 374-382
[3] G.E. Pantelidis, M. Vasilakakis, G.A. Manganaris, G. Diamantidis, Food Chem., 2007, **102**, 777–783.
[4] K. Aaby, D. Ekeberg, G. Skrede, J. Agric. Food Chem., 2007, **55**, 4395-4406.
[5] S.C.S.R. de Moura, P.E. da Rocha Tavares, S.P.M. Germer, A.L.A.C. Nisida, A.B. Alves, A.S. Kanaan, Food Bioproc. Tech., 2012, **5**, 2488–2496.
[6] C. Garcia-Viguera, P. Zafrilla, F. Tomas-Barberan, J. Sci. Food Agric. 1997, **73**, 207-213.
[7] K. Torskangerpoll, O.M. Andersen, Food Chem., **89**, 2005, 427-440.
[8] A.-L. Gancel, A. Feneuil, O. Acosta, A. M. Perez, F. Vaillant, Food Res. Int., **44**, 2011, 2243–2251.

R *– Physico-Chemical Analysis*

INVESTIGATION OF RETENTION BEHAVIOR OF IMIDAZOLINE RECEPTOR LIGANDS ON MIXED-MODE HILIC STATIONARY PHASE

D. Obradović[1], S. Oljačić[1], M. Popović-Nikolić[1], G. Popović[2] and D. Agbaba [1]

[1] *Department of Pharmaceutical Chemistry. (darija2207@gmail.com)*
[2] *Department of General and Inorganic Chemistry, Faculty of Pharmacy, University of Belgrade, Vojvode Stepe 450, 11000 Belgrade, Serbia.*

ABSTRACT
Retention mechanism in the hydrophilic interaction liquid chromatography (HILIC) mode is complex and still a subject of many controversial interpretations. In order to describe the HILIC retention mechanism, different retention models can be employed. In this study, we investigated the partition mechanism for 7 imidazoline receptor ligands on the mixed mode HILIC stationary phase. Applicability of the assumed retention model in description of the HILIC retention behavior of the compounds was successfully demonstrated.

INTRODUCTION
The effect of mobile phase composition on the retention behavior can be described by different mathematical models, considering contribution of processes such as adsorption and partition to the investigated chromatographic mode [1, 2]. Complexity of retention processes in chromatography of hydrophilic interactions (HILIC) can involve different retention mechanisms and be reflected in a relationship between the retention factor of an analyte and the volume fraction of an aqueous modifier in mobile phase. The aim of this study was to investigate the influence of partition mechanism on the retention behavior of imidazoline-related compounds such, as amiloride, idazoxan, benazoline, moxonidine, cirazoline, tetrahydrozoline, oxymethazoline and clonidine [3] in the HILIC mode, using the mixed-mode HILIC column and the weakly acidic working conditions (pH 6).

EXPERIMENTAL
Amiloride hydrochloride, idazoxan hydrochloride, benazoline oxalate, moxonidine, cirazoline hydrochloride, tetrahydrozoline hydrochloride, oxymethazoline hydrochloride and clonidine hydrochloride were purchased from Sigma-Aldrich, St. Louis, MO, USA (Fig. 1).

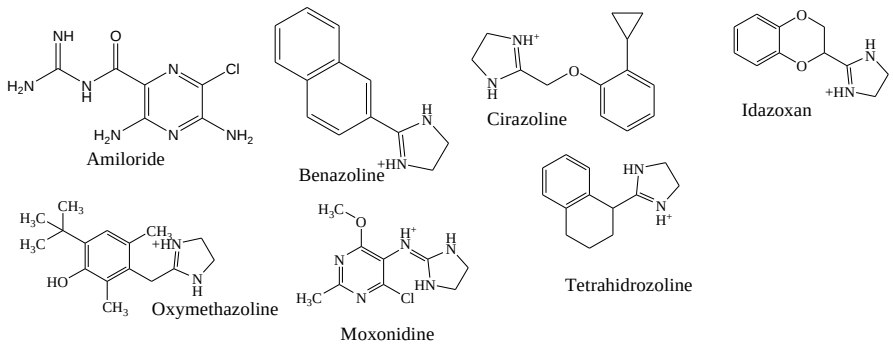

Figure 1. Dominant forms of investigated imidazoline receptor ligands at pH 6.

Acetonitrile (J.T. Baker, Deventer, The Netherlands) of HPLC grade and deionized water (TKA water purification system, Niederelbert, Germany) were used throughout this study. Ammonium acetate was obtained from Merck (Darmstadt, Germany). The HPLC analysis was performed using an Agilent Technologies 1200 HPLC system (Santa Clara, CA, USA). The analytical Acclaim Mixed-Mode HILIC-1 column 150mm × 4.6mm, silica particles size of 5µm (Thermo Fisher Scientific, Sunnyvale, CA USA) was used as stationary phase. Mobile phase consisted of acetonitrile and 20 mM ammonium acetate (pH 6). The flow rate was set to 1 mL min^{-1} and temperature to 25 °C. The UV detection was carried out at 225 nm.

The logk values were calculated from the obtained retention time (t_r) values for the three separate injections, using the below relationship:

$$\log k = \log ((t_r - t_0)/t_0) \quad (1)$$

where t_0 is the retention time of the dead time marker, KNO_3.

In order to find minimal concentrations of the buffered eluent from which the HILIC mechanism started, the retention factors of the investigated compounds were correlated with the volume fractions of the buffered eluent for a wide range of these fractions. The turning point (φ_{min}) at which the HILIC mechanism started was calculated from the following equation:

$$\log k = a_1 + m_1 \cdot \varphi - m_2 \cdot \log \varphi \rightarrow \varphi_{min} = 0.434\, m_2/m_1 \quad (2)$$

where a_1, m_1 and m_2 are the regression coefficients, and φ is the volume fraction of the buffered eluent. For low concentrations of aqueous phase (φ < 0.02), eq. 2 fails to properly describe the retention [2].

The solute partitioning mechanism on stationary phase in the HILIC mode depends on volume fraction of an aqueous solvent (φ) in a binary mobile phase and it can be given by the following equation [1, 2]:

$$\log k = a_2 + m_3 \cdot \varphi = \log k_{ACN} + m_3 \cdot \varphi \quad (3)$$

where a_2 holds for the logarithm of the retention factor of the solute in pure acetonitrile ($\log k_{ACN}$).

RESULTS AND DISCUSSION

The effect of volume fraction of the buffered eluent in the range of 0.10-0.75 was investigated in order to define its minimal concentration which influenced the beginning of the HILIC mode. The parameters of the relationship logk vs φ and the turning point (φ_{min}) for each compound are given in a Table 1.

Table 1. The regression coefficients and the turning point (φ_{min}) values of eq. 2 for the imidazoline receptor ligands.

Name of compounds	a_1	m_1	m_2	φ_{min}	R^2
Amiloride	-1.165	1.556	2.072	0.578	0.996
Idazoxan	-2.132	2.717	3.052	0.487	0.903
Tetrahydrzoline	-1.188	2.023	2.088	0.448	0.990
Benazoline	-1.222	2.286	2.145	0.407	0.980
Oxymethazoline	-1.804	3.400	2.577	0.329	0.984
Cirazoline	-1.329	2.514	2.144	0.370	0.981
Moxonidine	-0.527	0.824	0.912	0.480	0.986

At the next step of this study, the range 0.15-0.30 volume fraction of the buffered eluent showed high linearity of the relationship log k vs φ which was established. The influence of the volume fraction of the buffered eluent on the retention behavior of imidazoline derivatives was assessed with using eq. 3. In the determined chromatographic range, the retention factor values obtained from the isocratic process were linearly extrapolated to 100% volume fraction of acetonitrile ($\log k_{ACN}$). The obtained results are given in Table 2.

Table 2. Regression coefficients of eq. 3

Name of compounds	$logk_{ACN}$	m_3	R^2
Amiloride	1.074	-2.350	0.995
Benazoline	1.179	-2.109	0.994
Cirazoline	1.020	-1.072	0.986
Idazoxane	0.811	-1.355	0.982
Oxymethazoline	1.041	-1.692	0.993
Moxonidine	0.422	-0.732	0.983
Tetrahydrozoline	1.091	-2.043	0.989

The high R^2 values (Table 2) confirmed that the retention data fit well to the partition model. Therefore the predominant contribution of the partition mechanism to the overall retention process is confirmed, affecting the retention behavior of the imidazoline-related compounds.

CONCLUSION

The obtained retention data demonstrate the influence of the partition mechanism on the retention behavior of the imidazoline receptor ligands in the HILIC mode.

Acknowledgement

This work was supported by the Ministry of Education, Science and Technological Development of the Republic of Serbia, Contract No. 172033.

REFERENCES

[1] P Jandera. J. Sep. Sci., 2008, **31**, 1421 – 1437.
[2] G. Jin, Z. Guo, F. Zhang, X. Xue, Y. Jin, X.Liang, Talanta, 2008, **76**, 522-527.
[3] M. Krasavin, Eur. J. Med. Chem., 2015, **97**, 525-537.

QUANTIFICATION OF ORGANOPHOSPHORUS PESTICIDE AZAMETHIPHOS USING ELECTROANALYTICAL APPROACH

V. Vukojević[1], S. Đurđić[2], S. Jevtić[3], M. V. Pergal[4], B.B. Petković[3] and D.M. Stanković[1,5]

[1] Innovation center of the Faculty of Chemistry, University of Belgrade, Studentski trg 12-16, 11000 Belgrade, Serbia (vvukojevic@chem.bg.ac.rs) ;
[2]Faculty of Chemistry, University of Belgrade, Studentski trg 12-16, Belgrade, Serbia;
[3] Depatment of Chemistry, Faculty of Natural Science and Mathematics, University of Priština, Lole Ribara 29, 38220 Kosovska Mitrovica, Serbia;
[4] ICTM, Center of Chemistry, University of Belgrade, Njegoševa 12, 11000 Belgrade, Serbia;
[5] The Vinca Institute of Nuclear Sciences, University of Belgrade, Mike Petrovića Alasa 12-14, 11351 Vinča

ABSTRACT

In this work, for the first time, we proposed electrochemical behavior and development of analytical procedure for quantification of pesticide azamethiphos, using boron doped diamond (BDD) electrode. It was found that azamethiphos electrochemical behavior is irreversible oxidation at potential of around 1.70 V, in 1M nitric acid. Square wave voltammetric technique was most appropriate for azamethiphos quantification. Under optimized experimental conditions linear working range from 2 to 100 µM was estimated with detection limit of 1.38 µM. Negligible effect of possible interfering compound was observed. Obtained results clearly show that developed analytical methodology can be adequate replacement for the, up to date, used methods for detection of organophosphorous pesticide.

INTRODUCTION

Azamethiphos (AZA) is an organophosphorus pesticide which is used as spray for control flays and cockroaches or in veterinary medicine, in fish farming. Determination of this pesticide is mainly done by liquid chromatography or mass spectrometry [1]. Due to the high instrument costs, sometime complicated sample preparation of chromatographic methods and, on the other hand, low cost instrumentation and very often direct measurements of electrochemical methods only by sample dilution, the aim

of this paper was to offer rapid, sensitive and selective method for quantification of selected pesticide using electroanalytical detection.

In our work we used boron doped diamond (BDD) electrode, primarily due to its properties such as: wide potential window in aqueous solutions, low background current and negligible adsorption on electrode surface. This electrode has been widely used in electrochemical studies regarding vitamins, drugs and different class of pesticides [2,3]. Electrochemical behavior of AZA was studied using cyclic voltammetry and for quantification of this compound square wave voltammetry was used.

EXPERIMENTAL

All electrochemical experiments were done in conventional three electrode glass cell consist of boron doped diamond (BDD) electrode as working electrode, an Ag/AgCl electrode (3 M KCl) as reference electrode and Pt wire as counter electrode. For all electrochemical measurements CHI 760b (USA) potenciostat/galvanostat was used. All chemical used in this work were purchased from Sigma Aldrich and used as received. As supporting electrolyte Britton–Robinson buffer solutions and nitric acid solutions of different concentrations were examined.

RESULTS AND DISCUSSION

We examine electrochemical behavior of AZA at a BDD electrode using cyclic voltammetry (CV). AZA shows a well-defined oxidation peak with a potential of around +1.7 V in the anodic scan. In the reverse scan, no cathodic peak was observed indicating that the oxidation of this compound is electrochemically irreversible.

The effect of the pH value of the supporting electrolyte solution was investigated in the range from 0 to 12 using CV. For this purposes Britton–Robinson buffers (pH 2.0–12.0) and 0.1M and 1M solutions of nitric acid (pH 1 and 0) were used. The highest magnitude of peak current and the best peak shape, was achieved using 1M nitric acid, thus it was chosen as support electrolyte.

The effect of the scan rate (10-200 mV/s) on the oxidation peak current of AZA was also investigated (Figure 1). Dependence of peak current on the square root of the scan rate is linear, which indicate that the electrochemical reaction is controlled by diffusion.

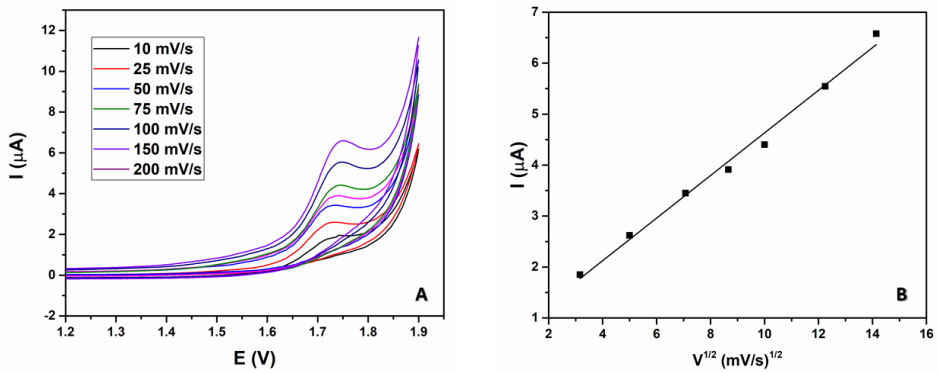

Figure 1. A) Cyclic voltammograms of 0.1 mM of AZA at BDD electrode in 1M nitric acid at various scan rates (10-200 mV/s). B) Dependence of the peak current from the square root of the scan rate.

Oxidation response of 0.1 mM AZA was investigated using differential pulse voltammetry (DPV) and square wave voltammetry (SWV). Significantly better response was obtained using SWV and this technique was chosen for all futher experiments. SWV operating parameters, pulse amplitude and frequency, were optimized. The best analytical response was obtained with pulse amplitude of 30 mV and frequency of 80 Hz and these parameters values were used in further studies.

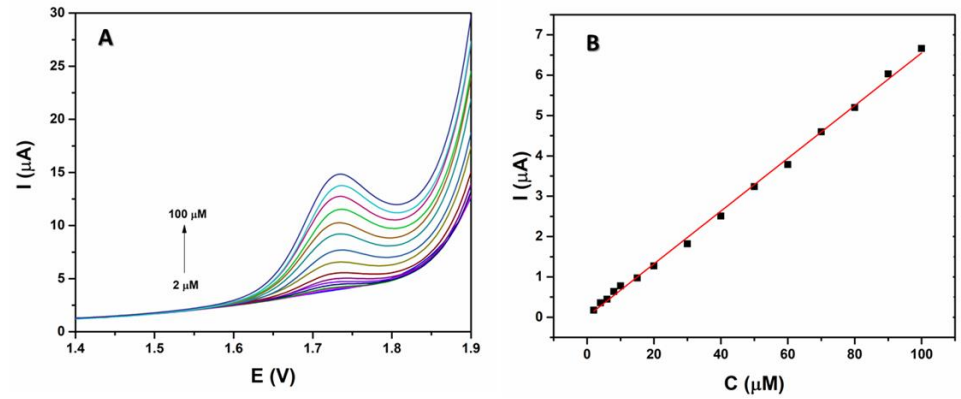

Figure 2. (A) Voltammograms obtained for different concentrations of AZA at BDD electrode in 1M nitric acid (SWV, pulse amplitude 30 mV, frequency 80 Hz). (B) Corresponding calibration curve.

Voltammograms for different AZA concentrations and corresponding calibration curve are shown in Figure 2. It was found that oxidation current

shows linear dependence with increase of AZA concentrations in the range of 2-100 μM. Calculated limit of detection (as 3σintercept/slope), was found to be 1.38 μM.

Selectivity of the proposed procedure toward detection of AZA was tested using SWV under optimized experimental conditions. Some other pesticides, clomazone and sulcotrione were investigated as possible interfering substances. Presences of clomazone significantly interfere determination of AZA and have influence on analytical performances of our method. In the case of the second tested compound, the presence of an interfering substance did not significantly effect on the signal of analyte.

The application of proposed method was examined on real water samples from the Danube River. Our sample did not show any pesticide content, so they were spiked with the analyte. Experiments were performed in triplicate. recoveries from our experiment were between 98% and 103%. From obtained results. can be concluded that our method can be used for detection of AZA in real samples.

CONCLUSION

In our work, we have developed a method for rapid, simple and reliable detection and quantification of azametiphos. Analytical characteristics of proposed method were quite good, with detection limit of 1.38 μM and wide linear range (2-100 μM). Also, this method was used for determination of AZA in three spiked real samples. In comparison with some other methods, such as HPLC, our method is simpler, less expensive and no complex preparation of samples is required.

Acknowledgement

This work was supported by the Ministry of Education, Science and Technology, the Republic of Serbia (Project No. OI 172030 and III45022) and Magbiovin project (FP7-ERAChairs-Pilot Call-2013, Grant agreement: 621375)

REFERENCES

[1] Ana Isabel García-Valcárcel, José Luis Tadeo, Anal. Chim. Acta., 2009, **641**, 117-123

[2] Dalibor Stanković, Kurt Kalcher, Sensor. Actuat. B-Chem., 2016, **233**, 144–147

[3] Ľubomír Švorc, Miroslav Rievaj, Dušan Bustin, Sensor. Actuat. B-Chem., 2013, **181**, 294–300

THE OPTIMIZATION OF INSTRUMENTAL PARAMETERS FOR MALDI-TOF MS of Au(III) PINCER TYPE COMPLEX

B. Rajčić [1], R. Masnikosa [1], F. Veljković [1], A. Rilak [2] and S. Veličković [1]

[1] University of Belgrade, VINČA Institute of Nuclear Sciences, P. O. Box 522, Belgrade, Serbia, (vsuzana@vin.bg.ac.rs).
[2]University of Kragujevac, Faculty of Science, R. Domanovića 12, P. O. Box 60, 34000 Kragujevac, Serbia

ABSTRACT
Coordination compounds of gold, among many applications, are synthesized as potential metallodrugs. We analyzed a newly-synthesized gold(III) pincer-type complex by matrix assisted laser desorption/ionization – time of flight mass spectrometry (MALDI-TOF MS) using both matrix and matrix-free (LDI) approach. Combinations of the instrumental settings were investigated to find the optimal conditions for obtaining the quality spectra of the studied compound. The typical quality spectrum possesses: a clearly visible molecular ion (or its protonated or deprotonated species), low number of fragment ions, a reasonably good isotopic distribution in the peak and few or no adducts with the matrix. In our experimental design, both LDI mass spectra and spectra acquired in dithranol provided the most valuable information on the molecular ion of the complex and its ligand.

INTRODUCTION
Gold(III) complexes have recently attracted a growing attention of scientists who design new metal-based therapeutics - metallotherapeutics. A number of structurally diverse gold(III) compounds were developed and tested both *in vitro* and *in vivo* with encouraging antitumor activities [1,2]. Few standard methods: X-ray crystallography (XRD), nuclear magnetic resonance (NMR), infrared (IR) and UV-Vis spectroscopy are continuously being used for (structural) characterization of metal complexes. However, these methods suffer from drawbacks such as: an extensive expertise is needed to resolve the spectra (NMR, XRD), obtained structural information is incomplete (IR, UV-Vis spectroscopy) and all require a substantial amount of sample. Hence, it is important to study the possibilities of all physicochemical methods that can provide useful structural information, such as MS techniques. These have become a leading trend for characterization of metallodrugs [3] and their

interactions with common biomolecules [4]. This is due to the accuracy, speed and specificity of MS, and, above all, its low sample consumption [3].

A novel monofunctional Au(III) pincer type complex with a bispyrazolate ligand: 2,6-bis(5-tert-butyl-1*H*-pyrazol-3-yl)pyridine - $[Au(H_2L^{tBu})Cl]Cl_2$ (Fig.1) where L is a bispyrazolate ligand, has been recently designed as a potential anticancer metallodrug (unpublished results). We acquired the spectra of the complex through MALDI-TOF MS using either matrix or no-matrix approach (LDI). Herein we present how to obtain quality spectra of the studied complex by optimizing instrumental settings on MALDI TOF DE Pro instrument: accelerating voltage, grid voltage (expressed as % of accelerating voltage), extraction delay time (time passed between the laser flash and ion extraction). We tried two matrices (dithranol and MTPP) and LDI approach.

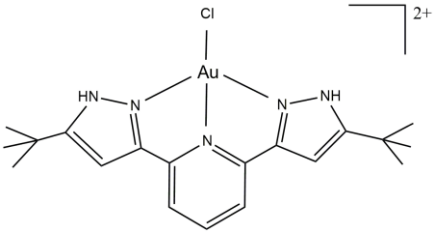

Figure 1. Structure of $[Au(H_2L^{tBu})Cl]$

EXPERIMENTAL

All the solutions were freshly prepared prior to use. Gold complex $[Au(H_2L^{tBu})Cl]Cl_2$ was dissolved in dimethyl sulfoxide (DMSO) to reach concentration of 5 mg/mL, whereas the matrix solutions were prepared as 10 mg/mL solutions also in DMSO. A small volume (0.5 µL) of the complex solution was applied to the 100-well sample plate and left to dry at room temperature. Then 0.5 µL of matrix solution was applied over the complex and left at room temperature to crystallize.

MALDI-TOF mass spectra were acquired on a commercial MALDI-TOF mass spectrometer (Voyager-DE PRO, AB Sciex, USA) equipped with a 20 Hz pulsed nitrogen laser operating at 337 nm. The spectra were recorded in the positive reflectron mode and each spectrum represented an average of 300 laser shots. The laser intensity was set to be 3000 arbitrary units (a.u.). Mass spectra were analyzed using Data Explorer Software 4.9.

RESULTS AND DISCUSSION

The recorded mass spectra of the gold complex were grouped into three categories: LDI mass spectra, MALDI mass spectra with dithranol and MALDI mass spectra with *mezo*-5,10,15,20-tetrakis(pentafluorophenyl)porphyrin (MTPP). LDI spectra and spectra acquired in dithranol were shown to be comparable under the experimental conditions applied in our study. Both LDI spectra and those recorded in dithranol were of a good quality and showed similar peak intensities.

The optimal values of accelerating voltage ranged between 7000 and 9000 V, grid voltage was 30-40% and extraction delay time was 100-200 ns. Applying aforementioned instrumental settings, two peaks (*m/z* signals) dominated the spectrum: i) one that originated from a protonated molecular ion of the complex - $[M+H]^+$, where M is a $[Au(H_2L^{tBu})Cl]^{2+}$ species (the complex ion without its outer chloride ions), observed at *m/z* 556.49; ii) other coming from the triple-protonated ligand ion of the gold complex (the complex ion lost AuCl) - $[M-AuCl+3H^+]^+$, observed at *m/z* 326.16 (Fig.2).

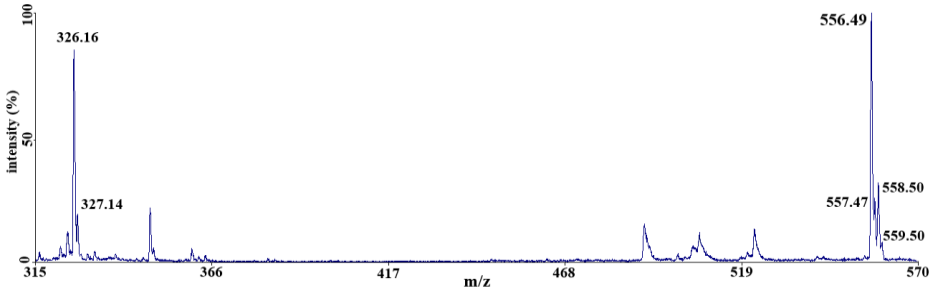

Figure 2. Reflectron positive ion LDI TOF mass spectrum of the gold complex. The spectrum represents the average of 300 laser shots with laser intensity of 3000 a.u., accelerating voltage 7000 V, grid voltage 30%, extraction delay time 100 ns

When the accelerating voltage of 7000 V was applied, the protonated molecular ion of the gold complex was the dominant peak in the spectra. When 8000 V was applied, the dominant peak was that from the protonated ligand ion. The identities of the detected signals were confirmed through comparison of experimental isotopic envelopes with those obtained from the theoretical models. The example for the *m/z* 556.49 is displayed in Fig. 3.

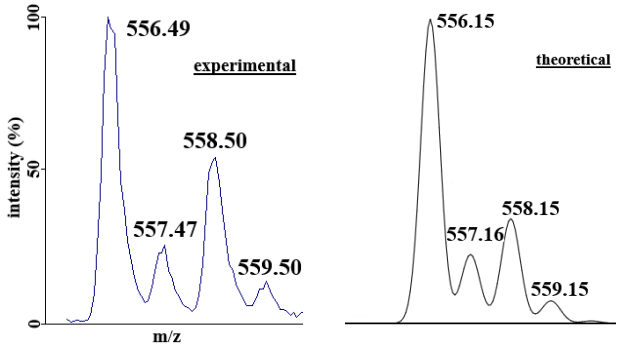

Figure 3. The comparison of experimentally observed and theoretical isotopic distribution of the signal at *m/z* 556.49 $[M+H]^+$

As can be seen there was a very good agreement between the theoretical and experimental isotopic distributions, which confirmed the identity of the *m/z* signals detected in the mass spectra.

CONCLUSION

In this work, (MA)LDI-TOF mass spectra of the novel gold complex - $[Au(H_2L^{tBu})Cl]Cl_2$) have been examined applying various instrumental settings. In order to acquire good quality mass spectra of the studied complex, they were recorded in the positive reflectron mode, while optimizing the instrumental settings of a commercial MALDI-TOF MS instrument. We found that both the LDI approach and dithranol-as-a-matrix approach resulted in the quality spectra, dominated by two peaks: one originating from the protonated complex ion and the other originating from the triple-protonated ligand ion.

Acknowledgement

This work was supported by the Ministry of Education, Science and Technological development of the Republic of Serbia (Projects Nos. 172019 and 172011).

REFERENCES

[1] T. Lazarević, A. Rilak, Ž.D. Bugarčić, Eur J Med Chem, 2017, 142, 8-31.
[2] B. Bertrand, A. Casini, Dalton Trans, 2014, 43, 4209-4219.
[3] M.F. Wyatt, J Mass Spectrom, 2011, 46, 712-719.
[4] M. Wenzel, A. Casini, Coord Chem Rev, 2017, 352, 432-460.

DEVELOPMENT OF KINETIC-SPECTROPHOTOMETRIC METHOD FOR HERBICIDE 4-CHLORO-2-METYLPHENOXY ACETIC ACID DETERMINATION

A. Miletić , M. Nikolić, E. Pecev-Marinković, Z. Grahovac, A. Pavlović, S. S. Mitić, S. Tošić and I. Rašić Mišić

Faculty of Natural Sciences and Mathematics, Department of Chemistry, University of Niš, Višegradska 33, 18000 Niš

ABSTRACT

This paper describes the development of kinetic spectrophotometric method for determining herbicide 4-chloro-2-metylphenoxy acetic acid (MCPA). Chosen indicatory reaction is based on oxidation reaction of sulfanilic acid (SA) by hydrogen peroxide in the presence of Co^{2+} ions as catalyst, in alkaline media. The reaction was monitored at 368 nm.By adding the MCPA pesticide to the investigated system, it was noticed that the reaction rate is more slowly, which indicated the inhibitory effect of pesticide in the reaction. The variables affecting the rate of the reaction were investigated and the optimum conditions were determined. MCPA can be measured in the concentration interval 0.14 – 2.0μg mL^{-1} and 2.0 – 20.0μg mL^{-1}. Thedetection LOD and quantification limitsLOQ of the method were calculated according to the 3σ criteria and found to be 0.035μg mL^{-1} and 0.106μg mL^{-1}, respectively. The relative standard deviations for five replicate determinations of 0.14, 1.0 and 2.0μg mL^{-1}MCPA were 4.35 %, 3.16% and 1.07 %, respectively for the first concentration interval. The recovery percentage were from 93.0 % to 98.57 %.

INTRODUCTION

MCPA is an herbicide in the phenoxy or phenoxyacetic acid family that is used postemergence for selective control of broadleaf weeds. Phenoxy herbicides act by simulating the action of natural hormones and produce uncoordinated plant growth. MCPA disrupts both seedling emergence and vegetative vigor, and can be used to control both dicots and moncots.The phenoxyacetic acid herbicides are one of the most commonly used groups of Plant Protection Products (PPPs) because of their low cost, effectiveness and good water solubility [1]. They are widely used in agriculture and recreational areas such as golf courses and watercourses. In addition, phenoxyacetic acid

herbicides readily degrade through biological and photolytic mechanisms, depending on the environmental conditions they are exposed to [2].

EXPERIMENTAL

The reaction was performed in a special glass four-compartment reaction vessel-mixer with a lapped flap. An aliquot solution of SA was transferred into the first compartment of the vessel; the second was filled with universal buffer solution; the third with Co^{2+} and MCPA and the fourth with H_2O_2 solution, then completed to volume of 10 mL with deionized water. The mixer-vessel was kept for 10 min at the temperature of (25.0 ± 0.1) °C. The solutions were mixed by shaking and then transferred into 10 cm constant temperature cell of spectrophotometer. The absorption at 368 nm was read over a period of 6 min at 30 seconds. In order to determine the lowest possible determinable concentration of insecticide diflubenzuron, working conditions needed to be optimized. Therefore, the dependence of the rate of reactions on the concentration of each of the reactants was determined.The dependence of the rate of reactions on the concentration of each of the reactants (H^+, H_2O_2, SA, Co^{2+}) obeyed the following rate equation:

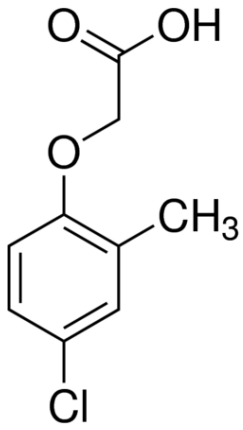

Figure 1. Chemical structure of 4-*chloro-2-methylphenoxy acetic acid*

$$rate = dA/dt = k \cdot c^n$$

where k is the rate constant, c is the concentration of each of the reactants, n is the order of reaction. The logarithmic form of the equation is written as:

$$log\ rate = logk + n \cdot logc$$

The value of "n" representing order of reaction in the regression equation.The rate of the reactions at different concentrations of reactants was obtained by measuring the slope of the linear part of kinetic curve absorbance – time plot(slope = dA/dt).For the processing of the kinetic data the differential variant of tangent method was used.

RESULTS AND DISCUSSION

By a spectrophotometric observation of the absorbance change with time in the system containing SA, H_2O_2 and Co^{2+} ions in universal buffer, it was noticed the formation of a yellow coloured product with maximum absorption at 368 nm. By adding the MCPAherbicide to the investigated system, it was

noticed that the colour was formed more slowly, which indicated the inhibitory effect of MCPA in the reaction.

In order to determine the lowest concentrations of the pesticide,the dependence of the rate of reactions on the concentration of each of the reactants was determined. For optimal concentration of each reactant, the one with the highest difference in reaction rate of catalyzed and inhibited reaction was chosen for further investigation.

Under the optimal experimental conditions: pH=9.66; $c(H_2O_2)$ = 0.25mol L^{-1}; $c(SA)=4\cdot10^{-3}$mol L^{-1}; $c(Co^{2+})=7\cdot10^{-5}$mol L^{-1}; t=(25.0±0.1) °C, the influence of MCPA concentration on the reaction rate was investigated. Two calibration curves with the linearity interval 0.14 – 2.0μg mL^{-1} and 2.0 – 20.0μg mL^{-1} were obtained. Figure 2. shows the calibration line in the interval 0.14-2.0μg mL^{-1}, at the temperature (25.0±0.1)°C, which can be used for the determination of MCPA concentration.The detection and quantification limits [3,4] of the method were calculated according to the 3σ criteria and found to be 0.035 μg mL^{-1} and 0.106 μg mL^{-1}, respectively.

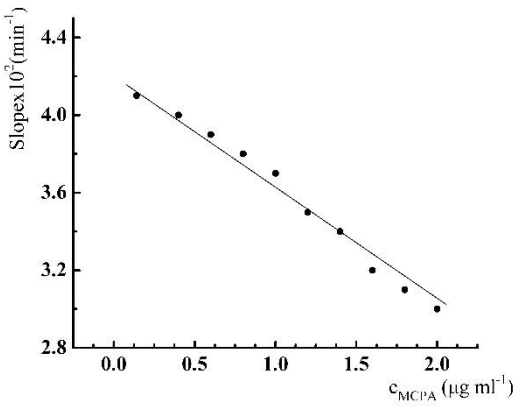

Figure 2. Dependence of the reaction rate on the MCPA concentration in the interval 0.14-2.0μg mL^{-1}

The equations of the calibration curves were:

$$Slope \cdot 10^2 = -0.628 \cdot c_{MCPA} + 4.26 \quad r = -0.9940 \quad (1)$$

$$Slope \cdot 10^2 = -0.105 \cdot c_{MCPA} + 3.24 \quad r = -0.9965 \quad (2)$$

where c_{MCPA} is the concentration of MCPA expressed in μg mL^{-1}. The calibration curves, at the temperature of (25.0±0.1) °C can be used for the determination of MCPA concentrations in the interval 0.14-2.0 μg mL^{-1} (Fig.2) and 2.0-20.0 μg mL^{-1}, respectively.The calibration curve (1) is more sensitive and it allows determination of lower concentration of MCPA.

Table 1. Accuracy and precision of the MCPA determination

Taken (μg/ml)	Found $\bar{x}$ (μg/ml)	n	RSD (μg/ml)	$\frac{\bar{x}-\mu}{\mu}\cdot 100$ (%)	Recovery (%)
0.14	0.138±0.006		4.35	-1.42	98.57
1.0	0.95±0.03	5	3.16	-5.0	95.0
2.0	1.86±0.02		1.07	-7.0	93.0

$\bar{x}$ - mean value; μ-true value; n-number of determinations; RSD-standard deviation;

The accuracy and precision of the measurements are presented in Table 1. It can be seen that the relative error ranges from 4.35 to 1.07 % for the concentration of MCPA in the range from 0.14 to 2.0 μg ml^{-1}.

CONCLUSION

A new reaction system for the kinetic spectrophotometric determination of MCPA was suggested. This method offers several distinct advantages namely, high selectivity and sensitivity, requiring cheap reagents, simple and inexpensive instruments, ease of operation and rapidity.

Acknowledgement

This research was supported by grant number 172061 from the Serbian Ministry of Science. The authors are grateful for the financial support provided by the Ministry.

REFERENCES

[1] P. Nadin, The Use of Plant Protection Products in the European Union Data 1992–2003, European Commission, Luxembourg, France, 2007.

[2] E. Sklivagou, K.Papadopoulou, A. Bakoulis, Determination of acid herbicides in water by LC/MS/MS, Desalin. Water Treat. 2010, **13**, 320–327.

[3] Motolla HA, Kinetic Aspect of Analytical Chemistry, New York, NY: John Wiley & Sons, 1998.

[4] V. Thomsen, D. Schatzlein,D. Mercuro, Limits of Detection in spectroscopy. Spectroscopy, 2003, **18**,112-114.

Author index

CIP - Каталогизација у публикацији - Народна библиотека Србије, Београд

544(082)
66.017/.018(082)
502/504(082)
663/664:658.56(082)
615.31:547(082)

INTERNATIONAL Conference on Fundamental and Applied Aspects of Physical Chemistry (14 ; 2018 ; Beograd)
Physical Chemistry 2018 : proceedings. Vol. 2 / 14th International Conference on Fundamental and Applied Aspects of Physical Chemistry, September 24-28, 2018, Belgrade ; [editors Željko Čupić and Slobodan Anić]. - Belgrade : Society of Physical Chemists of Serbia, 2018 (Belgrade : Jovan). - IV, 555-1073 str. : ilustr. ; 24 cm

Tiraž 200. - Bibliografija uz svaki rad.

ISBN 978-86-82475-37-8

1. Society of Physical Chemists of Serbia (Beograd)

a) Физичка хемија - Зборници b) Наука о материјалима - Зборници c) Животна средина - Заштита - Зборници d) Животне намирнице - Контрола квалитета - Зборници e) Фармацеутска хемија - Зборници

COBISS.SR-ID 267528716